Microsystems and Nanosystems

Harmeet Bhugra
Gianluca Piazza *Editors*

Piezoelectric MEMS Resonators

Microsystems and Nanosystems

Series editors

Roger T. Howe, Stanford, CA, USA
Antonio J. Ricco, Moffett Field, CA, USA

More information about this series at http://www.springer.com/series/11483

Harmeet Bhugra • Gianluca Piazza
Editors

Piezoelectric MEMS Resonators

Editors
Harmeet Bhugra
MEMS Division
Engineering Director, IDT Inc.
San Jose, CA, USA

Gianluca Piazza
Department of Electrical
and Computer Engineering
Carnegie Mellon University
Pittsburgh, PA, USA

ISSN 2198-0063 ISSN 2198-0071 (electronic)
Microsystems and Nanosystems
ISBN 978-3-319-28686-0 ISBN 978-3-319-28688-4 (eBook)
DOI 10.1007/978-3-319-28688-4

Library of Congress Control Number: 2016959445

© Springer International Publishing Switzerland 2017
This work is subject to copyright. All rights are reserved by the Publisher, whether the whole or part of the material is concerned, specifically the rights of translation, reprinting, reuse of illustrations, recitation, broadcasting, reproduction on microfilms or in any other physical way, and transmission or information storage and retrieval, electronic adaptation, computer software, or by similar or dissimilar methodology now known or hereafter developed.
The use of general descriptive names, registered names, trademarks, service marks, etc. in this publication does not imply, even in the absence of a specific statement, that such names are exempt from the relevant protective laws and regulations and therefore free for general use.
The publisher, the authors and the editors are safe to assume that the advice and information in this book are believed to be true and accurate at the date of publication. Neither the publisher nor the authors or the editors give a warranty, express or implied, with respect to the material contained herein or for any errors or omissions that may have been made.

Printed on acid-free paper

This Springer imprint is published by Springer Nature
The registered company is Springer International Publishing AG
The registered company address is: Gewerbestrasse 11, 6330 Cham, Switzerland

Preface

This book is meant to introduce piezoelectric microelectromechanical system (MEMS) resonators to a broad audience of engineers, graduate students, and researchers with the scope of offering a review of the field as well as generating excitement for future research work and stimulating entrepreneurial activities in this area.

The progress enabled by MEMS manufacturing methods has transformed the field of acoustic resonators. Piezoelectric materials have historically been the workhorse of practically any mechanical resonator on the market. The use of quartz crystals and ceramic resonators is widespread and can be found in electronic oscillators, filters, physical and gravimetric sensors, microphones, and ultrasonic transducers just to mention a few examples. These devices have been going through constant improvements and miniaturization since their first implementation approximately 100 years ago. Nonetheless, these piezoelectric acoustic resonant devices rely on bulk materials; hence they are hard to integrate with advanced manufacturing processes used in integrated circuits (IC). The use of micromachining techniques to manufacture micromechanical resonators offers the potential to build billions of these acoustic devices on silicon wafers, making them an extremely low-cost technology that could dramatically change the existing market dynamics. MEMS resonators have indeed received significant industrial attention and some of them are commercially available. Silicon-based resonators developed by several start-up companies are now sold in the millions for timing products. Piezoelectric-based resonators, namely bulk acoustic wave (BAW) resonators (covered in Chapters 8 and 16 of this book), are sold in billions for filtering applications.

Historically, the adoption of thin films of piezoelectric materials for manufacturing MEMS devices followed a relatively bumpy path. Many of the engineers working in the IC industry used to label piezoelectric materials as exotic. To add to this perception, many of the materials initially used for piezoelectric MEMS, such as zinc oxide and lead zirconate titanate (PZT), were indeed not compatible with semiconductor-focused manufacturing facility. The advent of new materials, such as aluminum nitride (see Chapter 1 of the book), has transformed the space and generated a growing interest in the use of piezoelectric materials for the making of

MEMS. At international MEMS conferences, it is quite impressive to witness the growing number of publications that rely on piezoelectric materials for the making of MEMS devices. Many foundries have also accepted the use of piezoelectric materials in their manufacturing line and products using PZT and AlN are commercially available. Similarly, in the field of acoustic resonators, MEMS researchers have developed new classes of piezoelectric miniaturized resonant devices that are deemed to transform the fields of radio frequency (RF) communication and sensing. Clear examples of this ongoing innovation are the thin-film bulk acoustic resonators (FBARs) that we can find in practically any modern phone as well as miniaturized contour-mode resonators, microphones, and ultrasonic transducers that several start-up companies are commercializing.

We believe we are at an inversion point of a trend that will see the explosion in the development of piezoelectric MEMS resonators. Commercial opportunities to replace existing products with smaller, lower cost, and higher performance piezoelectric MEMS resonators will continue to present themselves. Furthermore, the ability to manufacture these devices on large substrates and interconnect them in large systems will mark the development of integrated mechanical circuits that can transform existing paradigms of communication and sensing. For example, very low power RF sensor nodes that monitor the crowded electromagnetic spectrum as well as frequency-agile RF front ends that enhance the data capacity of our networks can be envisioned thanks to the continuous progress that researchers are making in the area of piezoelectric MEMS resonators.

This book captures some of the most exciting developments in the area of materials and devices for the making of piezoelectric MEMS resonators and offers direct examples of the technical challenges that need to be overcome in order to commercialize these types of devices. Part I reports on some of the most widely used piezoelectric materials that the research community has adopted for the making of MEMS resonators. This part focuses on well-established materials such as AlN (Chapter 1 by Muralt) and PZT (Chapter 2 by Polcawich and Pulskamp), but also discusses emerging interest in materials such as gallium nitride (GaN in Chapter 3 by Rais-Zadeh and Weinstein) and lithium niobate (LN in Chapter 4 by Gong). These two materials are representative of different emerging trends that aim at bringing "exotic" materials on silicon. GaN is an established electronic material. The ability to co-fabricate mechanical resonators in the same thin film on large silicon substrates will offer new opportunities to develop tightly integrated microsystems for RF and sensing applications. Thin films of LN on silicon are presented as representatives of emerging activities to exploit the unique properties of bulk materials and transfer them onto silicon substrates, hence enabling new capabilities not possible with films deposited by physical vapor deposition processes. A similar fabrication approach is described in Chapter 9 (by Chang) in regard to the use of thin films of quartz to make shear-mode MEMS resonators. Part II focuses primarily on the description of different kinds of resonators classified based on their mode of vibration. The main parameters that determine resonator performance, namely the quality factor (Q) and electromechanical coupling, are first introduced in Chapter 5 by Abdolvand. Flexural resonators used for low frequency

applications such as in ultrasonic transducers are described in Chapter 6 by Horsley. The focus is then switched to higher frequency resonators with a detailed description of contour-mode resonators (Chapter 7 by Rinaldi), thickness mode resonators (Chapter 8 by Hashimoto), and shear-mode resonators (Chapter 9 by Chang). Each subchapter describes the constitutive equations of motion of these resonators and guides the readers through the derivation of their electrical equivalent models. Examples of practical implementations of these classes of devices are described to showcase the level of performance that can be accomplished by these resonators. Chapters 10 and 11 deal with more advanced design concepts of piezoelectric MEMS resonators. In Chapter 10 Pan describes methods to temperature-compensate piezoelectric resonators so that they can operate over industrial temperature ranges. In Chapter 11 Kamon describes finite element methods for modeling the response of piezoelectric resonators with a focus on open challenges related to the modeling of Q and nonlinearity. Part III deals with more practical aspects associated with the fabrication (Chapter 12 by Tabrizian), test, and evaluation of piezoelectric MEMS resonators. Industry and academic perspectives are presented and details rarely found in the literature are provided on the requirement for test and evaluation of MEMS resonators (see Chapter 13 by Gubser on reliability and quality assessment and Chapter 14 by Pai on large volume testing and calibration). Finally, Part IV reports on two examples of commercialization paths for piezoelectric MEMS resonators. Chapter 15 by Kuypers reports on the initial efforts and lessons learned in commercializing piezoelectric MEMS resonators for the timing market. Chapter 16 by Aigner is focused on BAW resonators and their successful insertion into the filter and duplexer market. We believe that these two subchapters should serve as a source of inspiration and advice for future entrepreneurs in the space.

The editors would like to thank all the authors who have contributed to this book. There are no words to describe their sense of dedication to the topics covered in this book. It is through the commitment and excitement shown by the authors of this book that a community of researchers and engineers working on piezoelectric MEMS resonators could be built. Through this book, we hope to continue to educate new generations of graduate students, young engineers, and researchers and instill them with the same passion for piezoelectric MEMS resonators.

San Jose, CA, USA Harmeet Bhugra
Pittsburgh, PA, USA Gianluca Piazza

Contents

Part I Materials for Piezoelectric MEMS Resonators

1 AlN Thin Film Processing and Basic Properties 3
Paul Muralt

2 Lead Zirconate Titanate (PZT) for M/NEMS 39
Ronald G. Polcawich and Jeffrey S. Pulskamp

3 Gallium Nitride for M/NEMS 73
Mina Rais-Zadeh and Dana Weinstein

4 Lithium Niobate for M/NEMS Resonators 99
Songbin Gong

Part II Design of Piezoelectric MEMS Resonators

5 Quality Factor and Coupling in Piezoelectric MEMS Resonators 133
Reza Abdolvand, Hedy Fatemi, and Sina Moradian

6 Flexural Piezoelectric Resonators 153
David Horsley, Yipeng Lu, and Ofer Rozen

7 Laterally Vibrating Piezoelectric MEMS Resonators 175
Matteo Rinaldi

8 BAW Piezoelectric Resonators 203
Ken-ya Hashimoto

9 Shear Piezoelectric MEMS Resonators 221
D.T. Chang and D.J. Kirby

10 Temperature Compensation of Piezo-MEMS Resonators 243
Wanling Pan

11 Computational Modeling Challenges 257
Mattan Kamon

Part III Manufacturing and Reliability of Piezoelectric MEMS Resonators

12 Fabrication Process Flows for Implementation of Piezoelectric MEMS Resonators 283
Roozbeh Tabrizian

13 Reliability and Quality Assessment (Stability and Packages) 299
Robert Gubser

14 Large Volume Testing and Calibration 311
Minfan Pai

Part IV Real World Implementations

15 High Frequency Oscillators for Mobile Devices 335
Jan H. Kuypers

16 BAW Filters and Duplexers for Mobile Communication 387
Robert Aigner

Index 415

Contributors

Reza Abdolvand College of Engineering & Computer Science, University of Central Florida, Orlando, FL, USA

Robert Aigner Qorvo, Inc., Orlando, FL, USA

D.T. Chang HRL Laboratories LLC, Malibu, CA, USA

Hedy Fatemi College of Engineering & Computer Science, University of Central Florida, Orlando, FL, USA

Songbin Gong Department of Electrical and Computer Engineering, University of Illinois at Urbana-Champaign, Champaign, IL, USA

Robert Gubser PRA Inc., Norfolk, VA, USA

Ken-ya Hashimoto Department of Electrical and Electronic Engineering, Graduate School of Engineering, Chiba University, Chiba, Chiba Prefecture, Japan

David Horsley Department of Mechanical & Aerospace Engineering, University of California, Davis, CA, USA

D.J. Kirby HRL Laboratories LLC, Malibu, CA, USA

Jan H. Kuypers Sand 9, Inc., Boston, MA, USA

Yipeng Lu Department of Mechanical & Aerospace Engineering, University of California, Davis, CA, USA

Sina Moradian College of Engineering & Computer Science, University of Central Florida, Orlando, FL, USA

Paul Muralt Ecole Polytechnique Fédérale de Lausanne, EPFL, Lausanne, Switzerland

Mattan Kamon Coventor, Inc, Waltham, MA, USA

Minfan Pai Integrated Device Technology, Inc., San Jose, CA, USA

Wanling Pan Maxim Integrated, Inc., San Jose, CA, USA

Ronald G. Polcawich US Army Research Laboratory, Adelphi, MD, USA

Jeffrey S. Pulskamp US Army Research Laboratory, Adelphi, MD, USA

Mina Rais-Zadeh Department of Electrical Engineering and Computer Science, University of Michigan, Ann Arbor, MI, USA

Matteo Rinaldi Department of Electrical and Computer Engineering, Northeastern University, Boston, MA, USA

Ofer Rozen Department of Mechanical & Aerospace Engineering, University of California, Davis, CA, USA

Roozbeh Tabrizian University of Florida, Gainesville, FL, USA

Dana Weinstein Department of Electrical and Computer Engineering, Purdue University, West Lafayette, IN, USA

Part I
Materials for Piezoelectric MEMS Resonators

Chapter 1
AlN Thin Film Processing and Basic Properties

Paul Muralt

1.1 Introduction

Piezoelectric thin films are of interest for micro-electromechanical systems (MEMS) since the earliest developments in MEMS technology. This is quite natural or logic because the piezoelectric effect is an electromechanical effect. Resonators and ultrasound wave generators were among the first demonstrated MEMS devices [1–3]. In the 1970s and 1980s, the investigated thin film materials were mainly ZnO and AlN. In the 1990s, PZT was added to the list for having a stronger piezoelectric material for actuators (see, e.g., [4]). For higher-frequency applications, as, e.g., pass band filters for telecommunication in the GHz frequency range, the two wurtzite structures AlN and ZnO remained the champions, simply because they exhibit much higher mechanical quality factors than PZT, and in comparison to $LiNbO_3$, they are much more easily grown in thin film form. Moreover, integration and process compatibility with the rest of the device are less difficult using the relatively simple wurtzite materials. The strong polarity of their crystalline structure allows for a polar growth and a stable piezoelectric response with time, whereas ferroelectrics always risk depoling.

Today, AlN is the material of choice for practically all RF devices based on piezoelectric thin films [5–7]. There are two main reasons for this. Firstly, the deposition process of AlN thin films appears to be very well reproducible, and, secondly, AlN exhibits a high thermal conductivity for an electrically insulating material and is thus better suited for filters in the transmit line. As many nitrides, AlN has a high hardness and large stiffness constants. The relative dielectric constant of thin films amounts to typically 10–11. For thin film bulk acoustic wave resonators, the relevant piezoelectric coefficient is $e_{33}=1.55$ C/m^2. This is about

P. Muralt (✉)
Ecole Polytechnique Fédérale de Lausanne, EPFL, Lausanne, Switzerland
e-mail: paul.muralt@epfl.ch

© Springer International Publishing Switzerland 2017

H. Bhugra, G. Piazza (eds.), *Piezoelectric MEMS Resonators*,
Microsystems and Nanosystems, DOI 10.1007/978-3-319-28688-4_1

ten times less that in PZT thin films. However, combined with its roughly 100 times lower dielectric constant, AlN shows a relatively large coupling coefficient for the thickness vibration mode: $k_t^2 = 6.5\,\%$. Furthermore it is a hard material with light atoms and exhibits a high mechanical quality up to very large microwave frequencies. Moreover, it is CMOS compatible, in contrast to PZT and ZnO. A rather specific feature of AlN is its high sound velocity. This means that thickness mode resonators are made with thicker films for a given frequency. This is an advantage at frequencies beyond about 3 GHz. It turned out that considering all requirements beyond piezoelectric performance, like deposition process stability, thermal drift, power handling, chemical compatibility with semiconductor technology, etc., AlN came out as the clear winner for all RF MEMS applications. Over the last 10 years, AlN thin films became an established thin film material available in many semiconductor facilities. Future applications may also include devices operated at high temperature. AlN exhibits quite a large bandgap of 6.1 eV at room temperature. Consequently, it is a good dielectric material up to high temperatures.

In the following sections, an overview on AlN thin film processing will be given, discussing also piezoelectric characterization. Some years ago, AlScN was discovered as a stronger piezoelectric material than AlN and looks very promising for large band RF applications, as well as for energy harvesting devices. In principle, AlN can be grown by all major thin film techniques keeping the process free of oxygen. However, it is only magnetron sputtering that enables deposition at rather low temperatures. For this reason, this technique is now standardly applied for RF MEMS applications.

AlN has a very high melting point of 2470 K and grows in the wurtzite structure with the lattice constants of $a = 3.11$ Å and $c = 4.98$ Å [8, 9]. Wurtzites have a hexagonal crystal structure with the space group $P6_3mc$. In the binary compounds like AlN, the atoms are situated on threefold rotation axes. Equivalent ions are forming regular triangles with side-length a in the c-planes that are separated by $c/2$ (see Fig. 1.1). This distance is generated by the 6_3 axis, a screw axis rotating by 60° and translating by $c/2$. There are thus 2 Al and 2 N within the unit cell. All ions are fourfold coordinated, for which ionic radii of 132 pm for N^{3-} and 53 pm for Al^{3+} apply [10] considering AlN as an ionic structure. In reality, the ionicity is calculated as only 42 % from the electronegativities. However, the effective charge Z^* was found to be 2.7 [11, 12] and thus close to 3, meaning that the nitrogen ion is certainly larger than the Al ion. One can understand the structure as hexagonal close packed (hcp) layers of the bigger nitrogen ions with the aluminum ions occupying half of the interstitial sites of tetrahedral coordination, i.e., all the upper interstitial sites or all the lower interstitial sites with respect to such an hcp layer. This rule for occupancy has as consequence that the tetrahedrons of the same type are all pointing in the same direction along the threefold rotation axis, which is by definition the direction of the c-axis (see Fig. 1.1b). Important is to notice that there is no inversion center nor a mirror plane or a twofold axis that would turn the direction of a vector along the c-axis. This means that we deal with a polar structure, which allows for piezoelectricity and pyroelectricity. AlN is not ferroelectric, as we cannot switch the polar direction by the application of

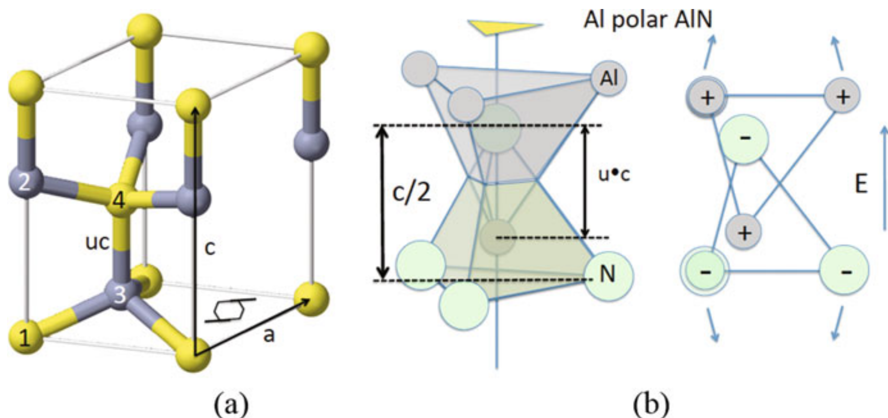

Fig. 1.1 (**a**) Basic elements of the wurtzite unit cell. Atoms are situated on threefold axes point along the *c*-direction. No atom is on the 6_3 axis, which is parallel to c as well and whose position is indicated on the base plane of the unit cell. (**b**) Both ion types are coordinated in tetrahedrons. Considering a surface situated on top of the drawing, the shown orientation is the one with the Al-polar surface. (**c**) Section spanned by the height of the tetrahedron and height of the regular base triangle lowest (dotted line in (**b**)), showing the charge sign and the ion displacement upon application of an electric field

an electric field, because the tetrahedrons cannot be inverted upside down by a small displacement of ions. An important structural parameter in wurtzites is the distance between different next-neighbor ions along the *c*-axis forming the top of a tetrahedron and its central ion (i.e., between ions 3 and 4 in Fig. 1.1a). This distance is defined as *uc*. Theoretically, one could form a "regular" wurtzite in which the tetrahedrons are regular ones (distance 1–3 would be equal to the distance 3–4 in Fig. 1.1a). In this case the parameters *c*/*a* and *u* are linked together: $c/a = 1.633$ and $u = 0.375$. But such regular tetrahedrons are not required by the wurtzite symmetry (in contrast to the zinc-blende structure which is also often realized by binary III/V compounds); the crystal has the possibility to deviate from these ideal values. The numbers for AlN are $u = 0.382$ and $c/a = 1.60$. It is found that the wurtzite phase is only stable when *c*/*a* is smaller than 1.633 and that the deviation from this ideal value is due to a lowering of the free energy by dipolar interactions [13]. As these depend on the effective ionic charges, the deviation increases with the difference in electronegativity.

The two surfaces of an (0001) oriented slab of AlN crystal are structurally different. The scientific community introduced the notions of N-polar and Al-polar for the two different polarities of (0001) faces [14]. It is defined as follows: as the crystal surface is approached from the bulk along the *c*-direction, if the bond parallel to the *c*-axis goes from the nitrogen atom to the group III atom, the crystal surface is nitrogen polar [15, 16]. In Fig. 1.1, the top face is thus Al-polar. In thin films, the top surface is giving the name of film polarity in case of (0001) oriented films.

The polarity of the film can be found by a simple etching test. In a number of etchants, typically diluted KOH, the N-polar film is much quicker etched than the Al-polar film [14]. To find the link between polarity and piezoelectricity, piezoelectric coefficients must be measured including their sign (see property section). What was found is that film thickness and in-plane film stress (tensile piezoelectric stress) are increasing when the electric field is applied as indicated in Fig. 1.1, thus pointing up for Al-polar films and pointing down for N-polar films. This appears to be very logic, as it means that the positive ions are displaced in direction of the electric field, and the negative ones are displaced in the opposite one. The tetrahedrons deform probably rather by rotation of the bonds near the basal plane, than by stretching and squeezing the rigid bonds along the *c*-axis. This could also explain the relatively large Poisson ratio of AlN. A good piezoelectric response requires indeed a periodic sequence of soft and hard springs [17] along a polar axis. As AlN is not a ferroelectric material, its internal or spontaneous electrical polarization cannot be measured. However, density functional theory allows for its calculation, following the "Berry's phase" method [18], yielding a value of $-9\ \mu C/cm^2$ [19, 20]. The negative value means that the direction is against the conventionally defined polar axis direction in the III/V wurtzite structures.

For thickness mode resonators and many other operation modes, the longitudinal effect $T_3 = -e_{33}E_3$ is exploited in a parallel plate capacitor structure. For such geometry one needs to grow (0001) oriented or textured thin films, either as Al-polar or as N-polar film. There are thus two challenges. The first one is to obtain the correct orientation and the second to have the whole film (all grains) in the same polarity. The first phenomenon going on when starting crystalline film growth is nucleation. In this stage, a new crystalline phase is formed on the substrate in the form of nuclei that become stable and are visible as tiny grains or single crystals. During the later film growth, these embryonic grains will grow, eventually merge with other grains, become dominating, or are overgrown by others.

For nucleation, interface and surface energies play an important role in combination with statistical probabilities given by thermodynamics. The latter criterion readily leads to the conclusion that surviving nuclei must have low-index planes parallel to the growth surface, simply because less atoms are needed to constitute such planes, and therefore the likelihood for their formation is larger than with complicated planes needing many atoms for their formation. Furthermore, next-neighbor coordination is better reflected in simple planes. Most of the crystalline structures—particularly ionic and metal ones—can be understood as a piling up of spheres in close packed structures or are at least derived from such close packed structures. Many thin films grow most easily in orientations that have the densest plane parallel to the surface. Well known are the (111) film orientations of face-centered cubic (fcc) structures like in Al, Cu, Pt, Au, etc.; the (0001) orientations cubic body centered of hexagonal structures like Ti, Zr, Hf, Ru, etc.; and the (110) orientations of Mo and W. Following this criterion, AlN should grow like other hexagonal structures in (0001) orientation. (For hexagonal structures, often 3 unit

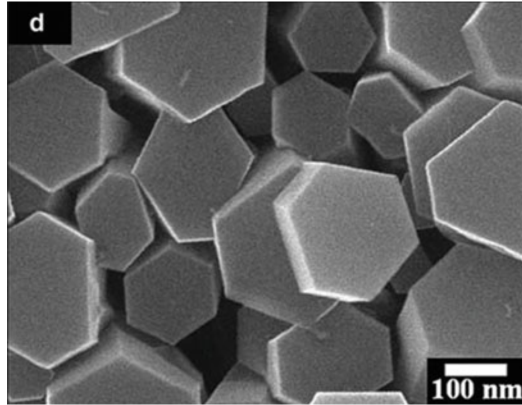

Fig. 1.2 AlN(0001) platelets grown on Au-coated silicon, as obtained by a thermal CVD technique (Al vapor + NH_3) at 1200 °C, and showing lateral (1,0,−1,0) facets (from [22])

vectors are used to describe the basal plane, enclosing an angle of 120° between each other. Four indices are then used to describe a plane: *h, j, k,* and *l*. The first three are not independent of each other: k is defined as $k = -h-j$.) AlN is, however, not as simple as a pure metal. The (0001) surface is a polar one and costs more energy. Recent ab initio calculations calculated surface energies of 6.31 J/m^2 for (0001) planes and 4.81 and 4.97 J/m^2 for {1,0,−1,0} and {1,1,−2,0} planes, respectively [23]. So the *c*-plane is not the one with the lowest energy. Nevertheless, even nuclei grown in a vapor at very high temperatures may show (0001) orientation having (1,0,−1,0) lateral facets [21]. Apparently, a low interface energy plays a major role for getting the (0001) orientation. In CVD-type techniques, the (0001) orientation can be obtained using gold films or particles as seed. Figure 1.2 shows a very nice crystal habitus of AlN plates obtained in this way. The lateral facets have surfaces with low surface energies with respect to the vapor phase, as expected.

When different orientations nucleate, some orientations grow often faster than others and will dominate after a certain thickness of the film. A certain ad-atom mobility to assure intergrain diffusion is required to make this happen. The rate of chemisorption on the surfaces of the dominating grains is then faster than on the surfaces of the grains to be overgrown. This is equivalent in stating that the winning surface has a higher activation energy for diffusion and is taking more than giving, whereas the perishing surface has a lower activation energy for diffusion and is giving more than taking. Such scenarios for growth of polycrystalline materials are described in Refs 24, 25. Needless to say that for good (0001) oriented AlN thin films, the exclusive nucleation of (0001) grains is a prerequisite.

In most cases, it is of no importance for applications which polar orientation is obtained in an AlN thin film, as long as it is the same everywhere in the film. In an actuator, the direction of the electric field can normally be used to create a positive or negative piezoelectric stress. The only need for having both orientations on a device is reported for the excitation of a true shear mode with interdigitated

electrodes. The periodic change of sign of the electric field was compensated by an AlN polarity changing sign in-phase with the electric field [26, 27]. In that work, the N-polar phase was obtained by sputter deposition on SiO_2, while the Al-polar phase was seeded by a very thin AlN layer grown by metal organic phase vapor epitaxy (MOPVE) and then increased in thickness by sputter deposition.

For achieving a perfect growth, it is of course better to understand why one of the polarities is preferred in a process. This may help to avoid regions or grains with the opposite (wrong) polarity. Often one can argue that the atoms that are first attached to the substrate will decide the polarity. For the case of AlN growing on silicon, it appears that N-Si bonds are much stronger than Al-Si bonds. The N triangles of N tetrahedrons would form first, thus obtaining the Al-polar version like in Fig. 1.1. This orientation is indeed obtained by the MOPVE process [26]. However, there is also another explication: the growth rate would be limited by the attachment rate of nitrogen species (N-Al molecules, NH_n groups) and not by the Al flux [22]. The Al-polar surface offering more dangling bonds to attach nitrogen would grow faster than the N-polar surface on which nitrogen species attach slower and diffuse more likely away. Hence, such mechanism would be similar to the one described for grain orientation preferences during growth. It is clear that once a stable grain is established after nucleation, it will keep its polarity during further growth. The formation of antiphase boundaries (where polarity would flip by 180°) is costing too much energy. This is also supported by the observation that a sputter process yielding normally N-polarity delivers Al-polar films when grown on an Al-polar seed layers. So it is quite clear that grain nucleation is the decisive step deciding about the complete grain, i.e., its crystallographic orientation including polarity.

There is evidence that the sputter process favors one of the polarities during growth. One polarity seems to grow quicker than the other one. In case of DC-pulsed sputter process, this is the N-polarity. Possibly, the nuclei have random polarity when growing on metal substrates, or passive amorphous substrates like silicon dioxide thin films, and that during the growth of the first tens of nanometers, the N-polar grains grow over the Al-polar grains, resulting in an overall N-polar, *c*-axis texture with highly parallel *c*-planes. Some TEM images suggest such a scenario (see Fig. 13 in Ref. [28]). A possible explanation could be that the growth is limited by the Al flux and that N-species are abundantly present. N-polar surfaces offer more dangling bonds to Al for attachment.

In the following, we present and discuss the sputter deposition method for growing AlN(0001) thin films in a very versatile polycrystalline, textured film microstructure. There is certainly much more literature on MBE- and CVD-type processes because most of the literature concerns AlN in III/V compound semiconductor structures for photonic and microelectronic applications. In this context, AlN is rather used for its structural than functional properties, serving as buffer and seed layer, as texturing layer, for concentrating dislocations in a passive insulator to keep

them away from the active semiconductor layer, to compensate mechanical stress, etc. The high deposition temperatures of such processes and also the frequently encountered high mechanical stresses are not suitable for MEMS applications. MEMS applications need a versatile process able to grow the films on many different substrates, at moderate temperatures (<400 °C), and with the possibility to tune the mechanical stress. All this can be achieved by reactive magnetron sputter deposition.

1.2 Growth of AlN Thin Films by Reactive Magnetron Sputter Deposition

1.2.1 Process for c-Axis Textured, Piezoelectric Thin Films

High-quality, *c*-axis-textured AlN thin films can be deposited by reactive magnetron sputtering. This technique is very suitable for MEMS applications as the deposition temperature can be kept quite low: typically 200–300 °C. In addition the film stress can be adjusted (in contrast to CVD techniques like MOPVE). When growing (0001) textured, dense polycrystalline thin films, the properties are identical to theoretical single crystal values, which were as a matter of fact, first measured in epitaxial AlN thin films on sapphire [29]. The reason for this equality is that the hexagonal point group of AlN yields isotropic properties in the plane up to fourth-order tensorial properties (like stiffness). The arbitrary in-plane orientation of (0001) oriented cylindrical grains (monocrystals) growing along the *c*-axis does not change in-plane properties as long as the structure is dense, and properties are not degraded by grain boundaries.

A schematic drawing of sputter hardware and process is given in Fig. 1.3. A pure aluminum target is mounted on a magnetron sputter source. The sputter down configuration as shown in Fig. 1.3 is mostly used in cluster tools. Sputter up or horizontal sputtering is employed as well. In industrial tools the target is larger than the substrate to achieve a good uniformity. In modern magnetrons, the magnets behind the target are rotated in order to erode the complete target for a better usage and to avoid zones without erosion where backscattered atoms would be deposited and very likely contribute to particle formation. The substrate is approximately 10 cm below on a substrate chuck. Anodes and shields are enclosing the discharge volume between target and substrate. In order to avoid particle formation by electrical breakdown through the insulating film deposited on anode, shields, and other parts that may charge up by electron bombardment, the source is powered by either radio frequency (RF) or more recently by pulsed direct current (DC) [30]. The substrate chuck is at the same time a heating chuck to bring the substrate up to 400–500 °C at maximum (for a typical industrial standard) and an electrode to which RF power can be supplied for controlling the substrate self-bias (negative voltage which is much smaller than the cathode voltage). Nitrogen gas (N_2) and most frequently also argon (Ar) are introduced into the chamber, the cathode

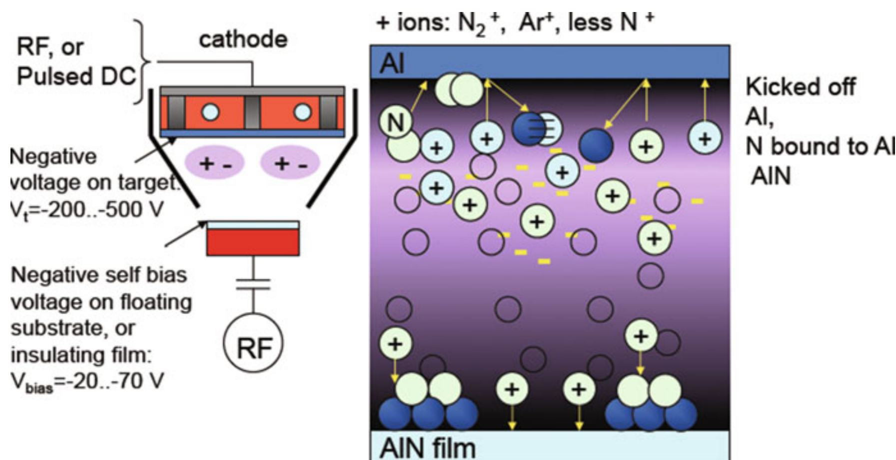

Fig. 1.3 Schematic drawing of reactive sputter deposition with a planar magnetron source (*left*), together with a symbolic drawing describing the basic phenomena going on in the glow discharge of the running source (*right*)

power is switched on, and a glow discharge is ignited. Positive ions are formed by collisions with fast electrons of 100 eV and more, which are secondary electrons emitted by the cathode and accelerated in the cathode sheath (the dark zone adjacent to the cathode, which has the largest electric field in the discharge). The so formed positive ions populate the interior of the plasma and make it the most positive region in the discharge. Arriving close to the cathode, i.e., to the border of the cathode sheath, they are accelerated toward the cathode, collide with it, and sputter off target atoms, causing also secondary electron emission. In this way the plasma is sustaining itself. The sputtered off atoms get quite some kinetic energy from the collision process, i.e., a few eV, i.e., energies that are two orders of magnitude higher than the thermal energy (kT) corresponding to the growth temperature. A very good insight into the phenomena of reactive discharges in sputter deposition is given by the analysis of ionic species in the discharge at the substrate position, as shown in Fig. 1.4 (from Ref. [31]) for the case of ZrN deposition. For studying the discharge in a broad nitrogen pressure range, Ar is added to the discharge. One can clearly differentiate two operation modes depending on the N_2 partial pressure. At low nitrogen pressure, no nitrogen ions are detected. The complete sputter process is based on Ar^+ and, in a minor degree, Ar^{++} ions. Nitrogen does not appear, because it is almost completely absorbed by the Zr target, and the Zr film that is deposited on substrate and shields. The fresh Zr surfaces getter the nitrogen gas much more efficiently than the pump of the sputter chamber. A small fraction of Zr atoms in the vapor is also ionized (Zr^+). The Zr^+ current allows monitoring the deposition rate. Upon increasing the pressure, there is a sudden drop of the Zr^+ current, thus deposition rate. At the same time, nitrogen ions $N_2{}^+$ and N^+ appear, indicating a rapid increase of the nitrogen pressure. This transition occurs all of a sudden when

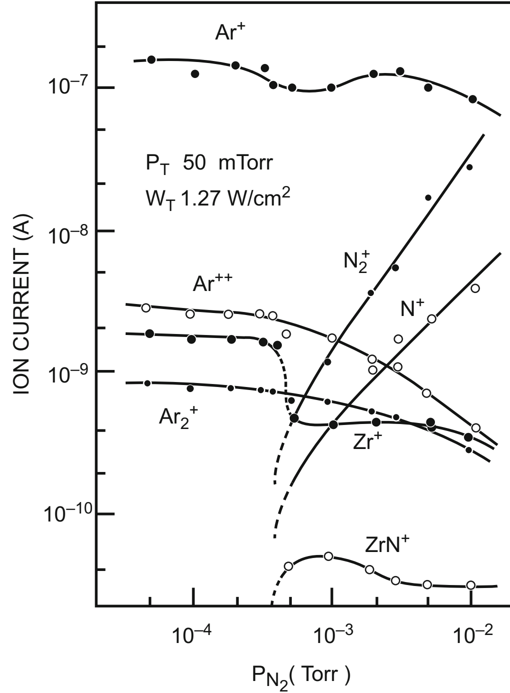

Fig. 1.4 Ionic current collected at the place of the substrate by a quadrupole mass spectrometer (from [31])

the target surface is saturated with nitrogen (close to ZrN). The pumping of nitrogen by target and film is dropping suddenly, even more, because the sputter yield of ZrN is smaller than the one for pure Zr. Above the transition, the target is completely nitrided (in a stoichiometric or slightly larger ratio), which is also true for the film on the substrate. Note the appearance of ZrN^+ ions, showing that about 10 % of the sputtered off species leave in the form of ZrN molecules, the rest as Zr and N atoms. Almost identical mechanisms are present in AlN sputtering. The ideal operation mode to get stoichiometric films is just above the instability. There is a hysteresis, meaning that the return path has the instability at lower nitrogen pressures. For a safe and optimal process, one usually approaches the working point from the high N_2 pressure side. The target surface is then fully nitrided, and most of the nitrogen in the film arrives from the target in the form of atomic nitrogen (N) and to a minor extent also in the form of molecules AlN. What is very special with AlN—possibly due to the stronger covalent nature of the bonds—is that stoichiometry is achieved easily when operating above but close to the instability (below the instability, the film looks metallic and is conducting). There is no stoichiometry concern like in TiN or ZnO when working above the transition.

Thin film morphology and crystal habits of individual grains depend on many parameters, starting with the growth substrate and including all sputter deposition parameters, such as temperature, sputter pressure, gas ratio (N_2/Ar), power density,

atom incidence angle distribution, ion bombardment intensity, and incidence direction. Apart from the surface energies, also diffusivities and growth speeds are of importance for the development of grain orientation and grain facets, as discussed and investigated in Ref. 25. It was found that grains show typically {11–20} and {0001} facets. For shear wave excitation, there is also an interest to grow films with tilted *c*-axis orientation, implying an ordering in the film plane (biaxial texture). The reader is referred to the literature on this topic [25, 33]. Here we focus on {0001} textured growth.

A well-balanced ion bombardment of the growing film is necessary for achieving *c*-axis orientation of the fiber grains and on top of this a polar texture. A typical $\theta-2\theta$ X-ray diffractogram (XRD) is shown in Fig. 1.5. From AlN, only the (0,0,0,2*n*) peaks of the *c*-axis orientation are observed. This is the first step needed for a good excitation of a longitudinal thickness mode resonator or transverse d_{31} resonator. X-ray diffraction (XRD) does not allow for the detection of polar orientation. In theory, high-resolution transmission electron microscopy (HR-TEM) could detect polar displacements; however, Al and N are too small ions to be detected precisely enough for the time being. The proof of the pudding lies in piezoelectric measurements. A further issue is mechanical film stress. Like in many sputter-deposited nitrides, a large compressive stress can be imposed by ion bombardment. The trade-off is shown in Fig. 1.5, showing residual stress and piezoelectric coefficient $d_{33,f}$ as a function of the DC self-bias installed at the floating, metallic substrate holder due to incoming electron and ion flux. In general, all floating surfaces exposed to a cold plasma (in a cold plasma, electrons and ions exhibit different temperatures: typically at 20,000–100,000 K for the electrons and typically at 500 K for the ions) are charged up negatively, because electrons have much higher velocities due to their smaller mass. Hence, all floating surfaces charge up negatively until the electrons are repelled sufficiently, and the ions attracted

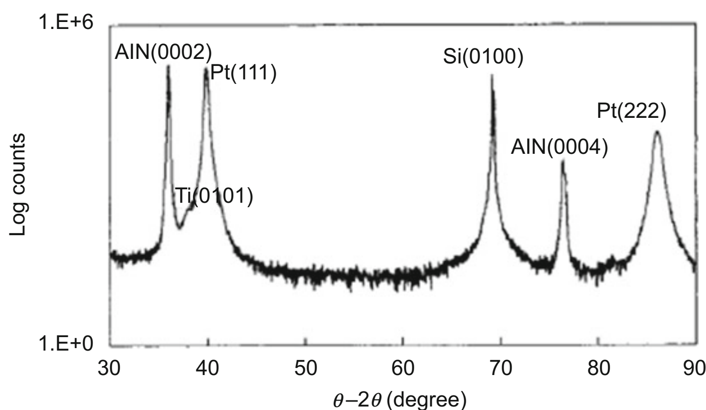

Fig. 1.5 $\theta-2\theta$ X-ray diffraction pattern of AlN thin film grown on a Pt(111) electrode layer attached to thermal oxide with a Ti adhesion layer (from [32])

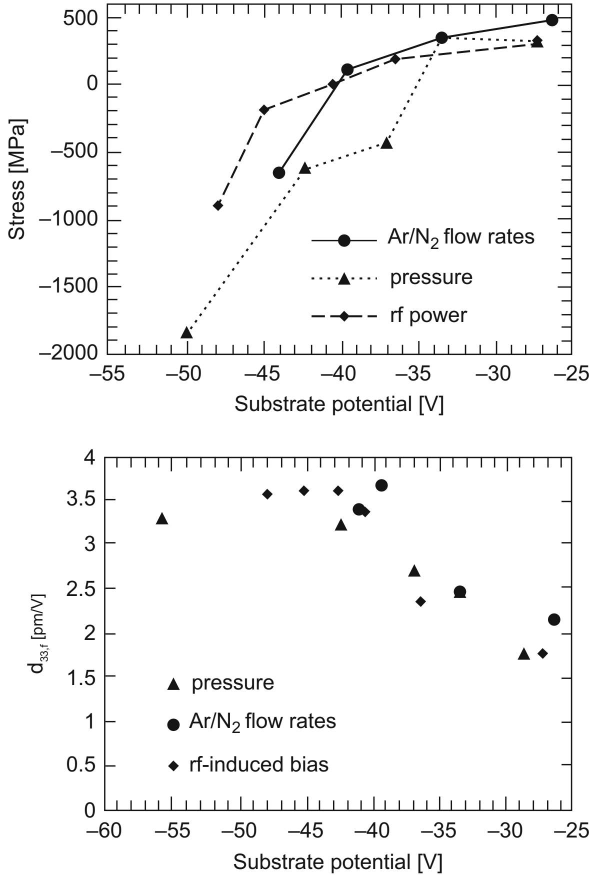

Fig. 1.6 Film stress and effective d_{33} ($d_{33,f}$) of (0001) textured AlN thin films obtained by DC pulsed magnetron sputtering. Important properties are the piezoelectric thickness coefficient ($d_{33,f}$) resulting from the polar order of the *c*-axis-oriented grains and the mechanical film stress. Keeping the cathode power constant, processes are influenced by the total sputter gas pressure (in this work varied between 1 and 5 mtorr), the ratio of N_2/Ar flow rates (50–100 %), and the rf bias applied to the substrate chuck. All the three parameters influence the ionic bombardment, as indicated by the measured chuck DC voltage (substrate potential). The trends show that most of the effects can be reduced to the energy of ions bombarding the film. More energy means more compressive stress and higher piezoelectric coefficients. An optimal situation is found at about −40 V substrate bias (from [30])

sufficiently to arrive at a zero total current. This stationary voltage is called self-bias. It is influenced by all parameters of the discharge: pressure, gas composition, cathode power, and substrate RF bias power. In Fig. 1.6, all these parameters are varied and represented in the graphs by the governing substrate potential during the process. The energy of the ions accelerated toward the substrate is the difference in plasma potential to film surface potential (approximated by the substrate potential).

The plasma potential is positive and amounts to roughly +20 V. The ion energy is thus rather higher than indicated by the substrate DC bias. More negative substrate potentials lead to larger compressive stresses, as ions with more energy are stronger peening the film or are even implanted. It is also observed that a minimal ion energy is needed to achieve a maximal piezoelectric response. Luckily, by choosing optimal parameters, including some substrate RF bias power, a working point is found with zero stress and maximal piezoelectric response (at about −40 V in this case). Note that there is a difference between substrate surface potential and the measured substrate chuck potential standardly provided by RF matchboxes connected to the substrate chuck. In large tools, the chuck is often well shielded from the plasma, and the chuck potential deviates from the substrate surface potential.

The microstructure of the AlN film grown at optimal conditions shows the typical features of zone T growth of Thornton's growth zone model for sputter deposition [34]. In this diagram, film morphology is depicted as a function of relative temperature T/T_M (melting point in K) and sputter gas pressure. It is clear that ion bombardment increases by lowering the latter. Zone T between low-temperature zone 1 and intermediate zone 2, and valid for lower sputter gas pressures, is characterized by the absence of bulk diffusion and weak thermally activated surface diffusion, but strongly activated surface diffusion by ion bombardment. Such conditions are well met in good AlN processes with typical $T/T_M \approx 0.25$ and sputter gas pressures below 1 Pa (see Fig. 1.7). Figure 1.7 shows a dark-field TEM cross section of a high-quality AlN thin film grown on a Pt substrate. The fiber grains are well-developed single crystals with a perfect c-axis orientation along the growth direction. The c-plane diffraction spots correspond to well-ordered c-planes parallel to the substrate plane (Fig. 1.8).

It is also possible to grow epitaxial films with this technique. Figure 1.9 shows a plan view image of an AlN thin film grown on a sapphire substrate. For realizing plan view images, the substrate is locally removed, and the film is thinned down so that the electron beam is transmitted through the film perpendicular to the film plane. It shows a rather smooth surface and the presence of threading dislocations (black spots). The diffraction pattern is the one of a hexagonal crystal, as it should be.

One of the basic questions about AlN growth concerns the mechanisms of film texturing. As stated above, one cannot advance a lower surface energy for (0001) surfaces to explain achieving a (0002) texture. (The texture is often named after the lowest-order Bragg peak. In case of (0001) texture, this is the (0002) peak). Hence, the driving mechanisms must be either related to a lowering of interface energies by epitaxial effects or a whatsoever impact of the sputtering process. These statements are supported by the finding that CVD processes without energetic stimulation of the growth results in general in (1,0,−1,0) textured films [37], thus corresponding to a prevailing surface energy and mechanisms as described by the capillarity theory. The impact of the plasma in sputter deposition, mainly ion bombardment as explained above, has obviously also an impact on the selection of film orientation. This was also observed using arc deposition by Takikawa et al. [38]. Voltages involved in arc deposition are quite low as compared to sputtering. The ionic current densities are, however, much higher. Faster ionic species can only be generated by a

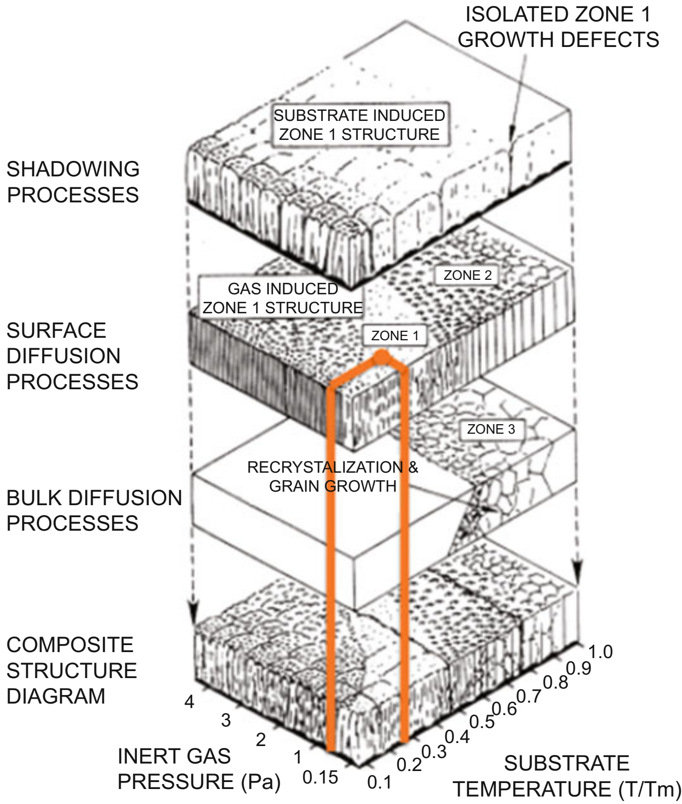

Fig. 1.7 Working point for AlN sputter in the Thornton's diagram [34]

substrate DC or RF bias. Both types were tested during growth of AlN on Mo(110) substrates in this work. It was found that at less than 20 V bias ($|U_{bias}|$<20 V), the dominating texture was (10–10) and that the (0002) texture had a window between −30 and −20 V (see Fig. 1.10). It is not clear why, at higher bias, the (0002) texture was lost again. Possibly, the ionic current was too strong and heated up the sample too much. The same threshold was also found with RF sputtering by Drusedau and Blasing [37], growing the films on silica (amorphous SiO_2). They did not observe an upper threshold, the (0002) texture covered the range from −20 to −40 V and higher. Growth on Pt(111) electrodes did not show a minimal threshold, but bias voltages of less than 20 V were not investigated [39, 40]. However, applying identical processes for AlN films grown on Mo(110) required a minimal bias voltage of 50 V for a good (0002) texture. The impact of ion bombardment is obvious. It was also observed that the gas ratio N_2/Ar plays a role, as it shifts the substrate bias as well. Drusedau and Blasing advanced the idea that fast neutrals of N_2 molecules would play a major role. However, in this case, the substrate bias voltage would not play a role. Fast neutrals are originally ions that are accelerated in the cathode sheath toward the

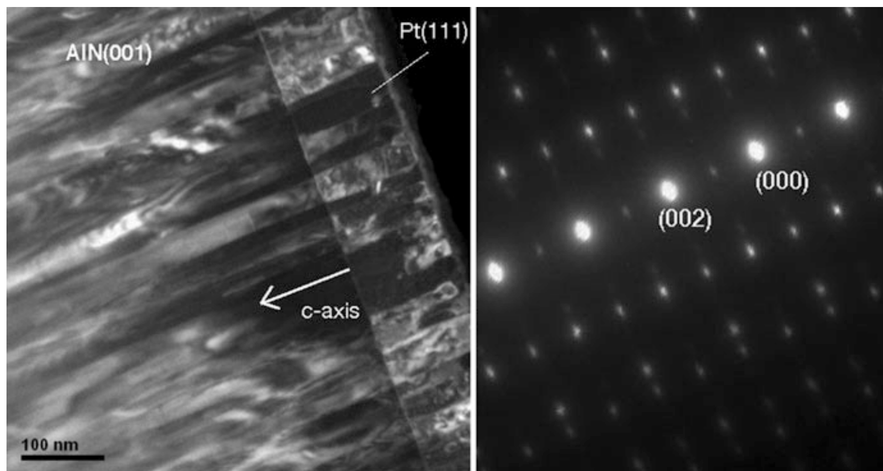

Fig. 1.8 TEM cross-sectional image and corresponding diffraction pattern of polycrystalline AlN thin film grown by reactive pulsed DC sputtering

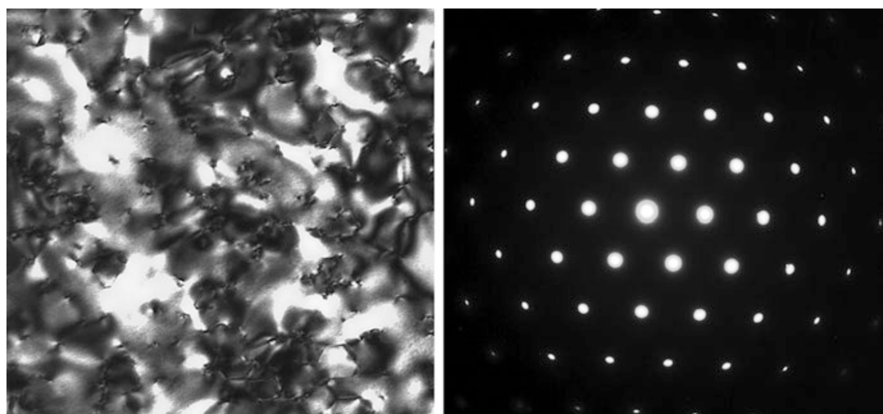

Fig. 1.9 TEM plan view image of epitaxial AlN grown by reactive pulsed DC sputter deposition on sapphire and corresponding diffraction pattern (from [35, 36])

target, neutralized during the collision, and quasi-elastically reflected from the target in direction of the growing film. Such processes are based on the elastic scattering at target atoms, and their likelihood increases with the mass of the target atoms. It is thus not clear why this should be an issue with the light Al atom having almost the same mass as N_2, meaning that the ion ${N_2}^+$ passes almost all its kinetic energy to the target atom.

After texture development, the next question concerns polarity. Pulsed DC operation usually leads to nitrogen polarity [26]. As stated before, it is very likely that the specific sputter process favors one of the polarities. It could be that N-polar grains would grow faster and thus overgrow the Al-polar grains. Such a mechanism would also explain that very thin sputter-deposited AlN thin films show

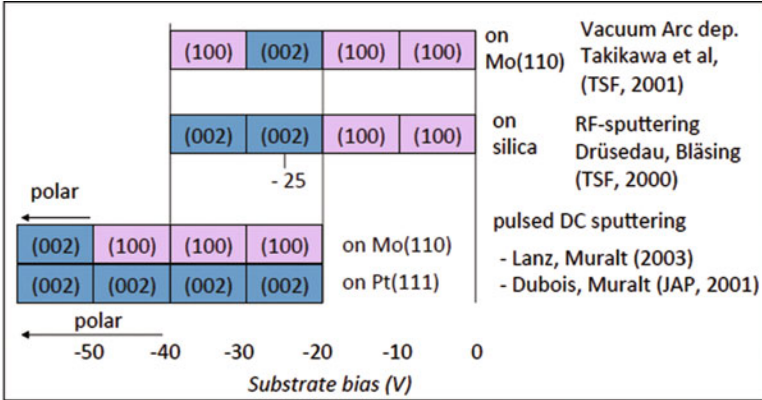

Fig. 1.10 Selection of orientation as a function of substrate self-bias voltage, collected from different works

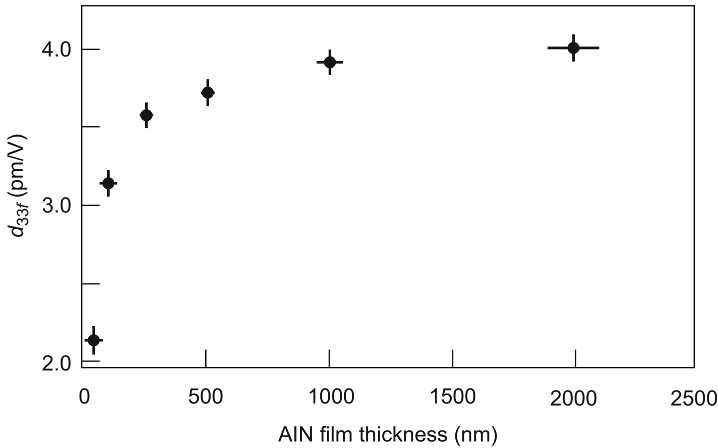

Fig. 1.11 Thickness extensional piezoelectric coefficient with full clamping $d_{33,f} = e_{33}/c_{33}^{E}$—as measured by double beam interferometry (DBLI)—as a function of AlN film thickness. The films were grown on Pt(111) electrodes (from [32]). The values were adapted according to new facts about the accuracy of DBLI

less piezoelectricity (Fig. 1.11) and that a higher degree of polarity is obtained with a higher partial nitrogen pressure. With typical growth rates of 1 nm/s, we deal with an Al flux of roughly 4 ML/s (sticking coefficient = 1). A nitrogen pressure of 3×10^{-3} mbar would mean an N_2 flux of 3000 ML/s. Such nitrogen is rather inert. The atomic nitrogen is much more reactive and found with a concentration of about 1 % in a nitrogen DC plasma [41] and is thus arriving with a flux density of 30 ML/s. Given that almost enough nitrogen arrives anyhow as atomic species or AlN species from the target, it is clear that the flux of reactive nitrogen atoms is much larger than the Al flux, corroborating the idea of a faster growth of N-polar surfaces.

1.2.2 The Impact of Substrate Roughness: Film Evolution with Thickness

The typical AlN thin film exhibits good piezoelectric properties when grown on a smooth surface. Several works report that the piezoelectric quality decreases with the width of the X-ray rocking curve. A rocking curve tells us how parallel crystal planes of the same type are. It includes a contribution due to the finite width of grains, but usually the tilt of grains is the dominating feature leading to a broadening of the rocking curve width. Figure 1.12 describes how the coupling coefficient of bulk acoustic wave resonators (k_t) scatters as a function of the rocking curve width of the AlN films used in the respective samples [42]. There is a clear trend saying that the more perfect the grains are aligned with their *c*-planes, the higher is the coupling k_t, which is proportional to the piezoelectric coefficient e_{33}. Many parameters were varied for the films used in this work.

When varying only one parameter, even clear linear correlations are found (Fig. 1.12b). Similarly, in Ref. [43], a nice linear correlation is found between film $d_{33,f}$ and rocking curve width when only the thickness is varied [43]. The increase of the $d_{33,f}$ with thickness is based on an improvement of crystal quality with film thickness. An explicit test was made with substrates on which a roughness was added in a controlled way, in the form of a very thin, amorphous silicon film growing with a rough surface morphology after nucleation of separated grains (island nucleation) on a very smooth thermal oxide film. The observed rocking curve width of AlN grown on such surfaces can directly be related to the surface roughness, apart of a small offset due to a limited in-plane coherence length caused by finite grain diameters. This is also well supported by HR-TEM showing the inclined *c*-planes of neighboring grains (Fig. 1.13). This work shows that grains

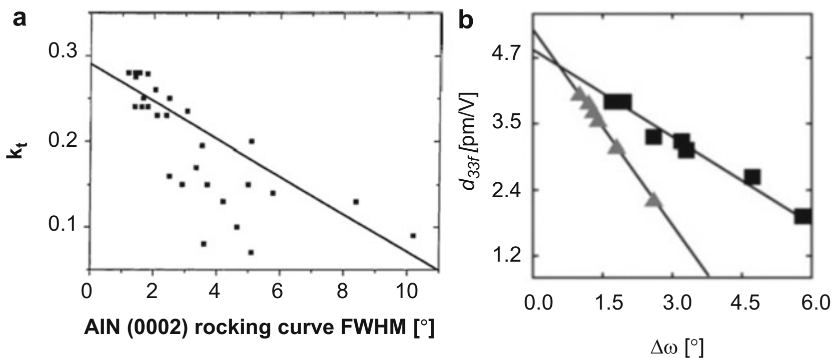

Fig. 1.12 (**a**) Electromechanical coupling coefficient k_t as determined from resonator measurements vs. the FWHM with of the (0002) rocking curve made at the respective films (from [42]). (**b**) Piezoelectric coefficient vs. rocking curve width $\Delta\omega$ combined from two different works: squares from variation in substrate surface roughness [28] and triangles from increasing the AlN film thickness [32]. The $d_{33,f}$ scale was corrected for the DBLI error

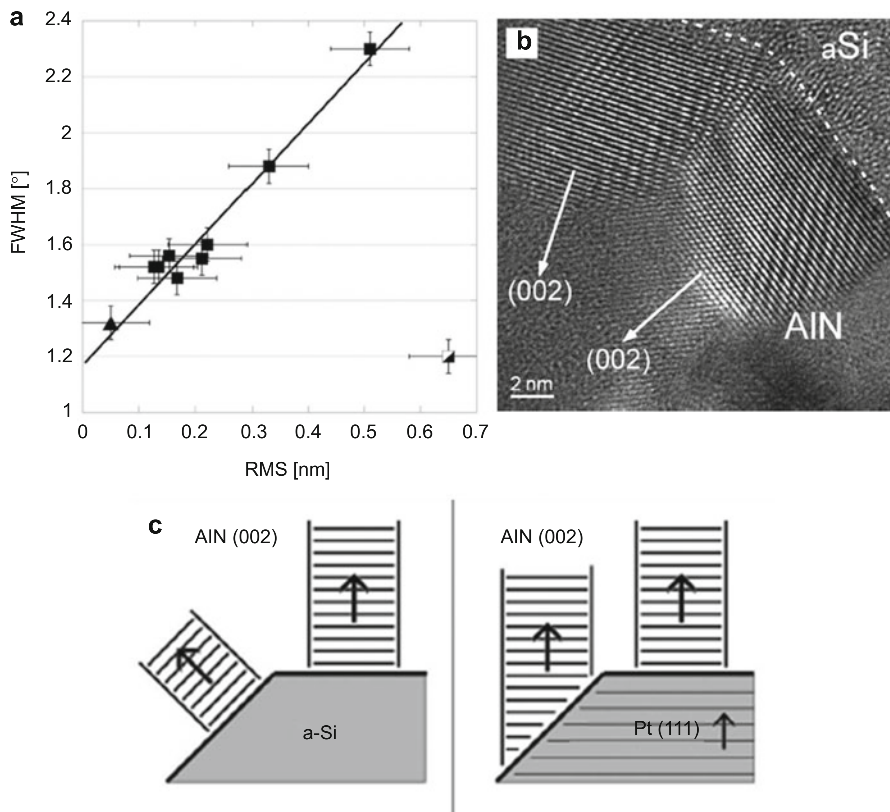

Fig. 1.13 (**a**) Rocking curve width (FWHM) as a function of surface roughness (RMS) for AlN film grown on a-Si/SiO_2/Si substrates having various surface roughness (from [44]). The half-filled square stands for a film grown on Pt(111). (**b**) High-resolution TEM of the AlN/s-Si interface of an extreme situation. (**c**) Explication for the difference between a-Si and Pt(111)

grow with the *c*-plane parallel to the local surface if epitaxial effects are absent. The same figure shows that on Pt(111), epitaxial nucleation leads to a smaller grain tilt at a given roughness, as explained in the schematic of Fig. 1.13. A linear correlation is found between piezoelectric coefficient and rocking curve width for the thickness experiment and for the roughness experiment.

A scenario that describes many features of AlN thin film growth is this one: embryonic grains of (0002) orientation may have some disorder at the beginning, depending on substrate type and roughness. Most likely, both polarities are represented. With increasing growth, grains having *c*-planes more parallel to the (global) substrate plane and those having N-polar surfaces (at least with DC pulsed sputtering) are growing faster up and into the width by covering the grains of bad orientation and polarity. The HR-TEM in Fig. 1.14 shows how the plane tilt

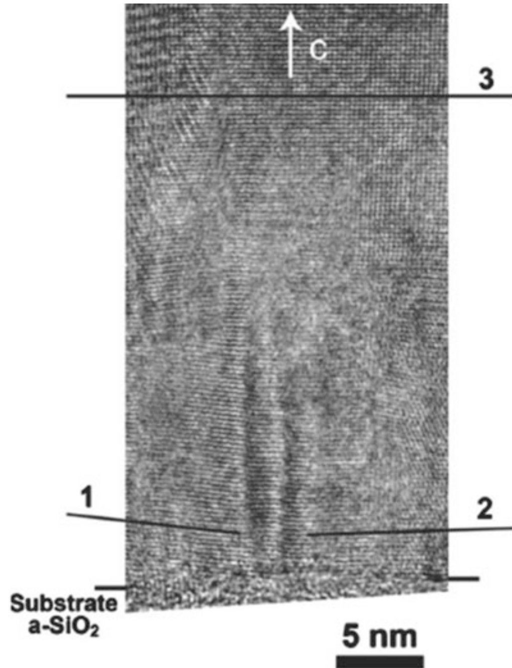

Fig. 1.14 Evolution of AlN thin film, starting from the growth interface. The smaller grains at the beginning have stronger tilted *c*-planes (lines 1, 2) than the larger grains growing over the "irregularities" (line 3). The vanishing grains in the center of the image, showing tip-like upper ends, exhibit a smaller growth rate than the other ones, which is possibly due to an opposite polarity

is disappearing, and some grains are overgrown. One can say that the process is somehow self-adjusting with time. The TEM image suggests a minimal thickness for perfect material of about 30 nm.

1.2.3 Further Growth Issues: Oxygen Impurities and Regrowth Issue

Oxygen is always a very disturbing gas during nitride synthesis. It is probably the reason why for a long time no good AlN crystals could be grown. In thin film growth, best possible vacuum conditions are chosen with a nitrogen gas purity of at least 57, i.e., with less than 3.0×10^{-6} impurity molecules. Interestingly, it was found that oxygen impurities invert the polarity of the grains, at least when the film is obtained by RF sputtering [45] (see Fig. 1.15). What is clear from this experiment is that a single grain has still a single polarity. Otherwise the opposite polarity could not be fully realized. So it is something that changes at the beginning of nucleation (by providing an oxide surface) or in the growth rate of Al-polar or N-polar surfaces.

In device fabrication, it may happen that an AlN thin film comes in contact with a developer solution for a positive resist containing an alkaline solution, typically KOH. It was tried to regrow AlN on an AlN surface after it was in contact with such a developer solution. However, the latter attacked the AlN surface forming cusp

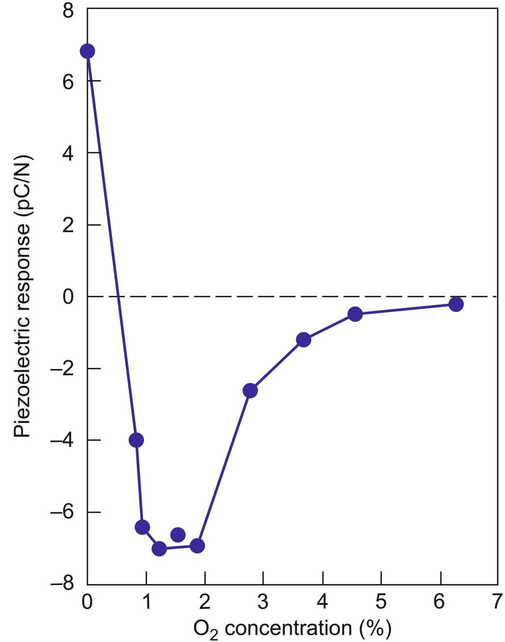

Fig. 1.15 Reversal of polarization with increasing oxygen concentration in the sputter gas [45]

structures (see Fig. 1.16). Continuing growth of AlN afterward, a very irregular grain growth was observed. Huge grains starting as cones and ending in a spherical surface grew out of the cusps. Astonishingly, these were single crystals, as shown in Fig. 1.16 by a TEM dark-field image [43]. It turned out that such grains had an opposite polarity, as concluded from $d_{33,f}$ measurements. High-resolution TEM images showed that the giant grain was in fact seeded by an underlying grain from the first AlN layer. Obviously the polarity changed when copying the structure from a wurtzite surface, which certainly had a monolayer of oxide. What is very astonishing is the absence of shadowing. Apparently, diffusion distances are large enough to fill up depressions from which grains grow that become higher than the side walls around.

1.3 Properties and Characterization

In general, a complete set of elastic, dielectric, and electromechanical coefficients is needed to describe quantitatively a problem that includes ultrasound wave propagation. Luckily, AlN exhibits a relatively high symmetry, and as a consequence, only a few elements of the rigidity tensor (or compliance tensor) are different from zero, and many are equal. For the hexagonal point symmetry 6 mm of AlN, there are only five different coefficients, as listed in Table 1.1. The shear coefficient

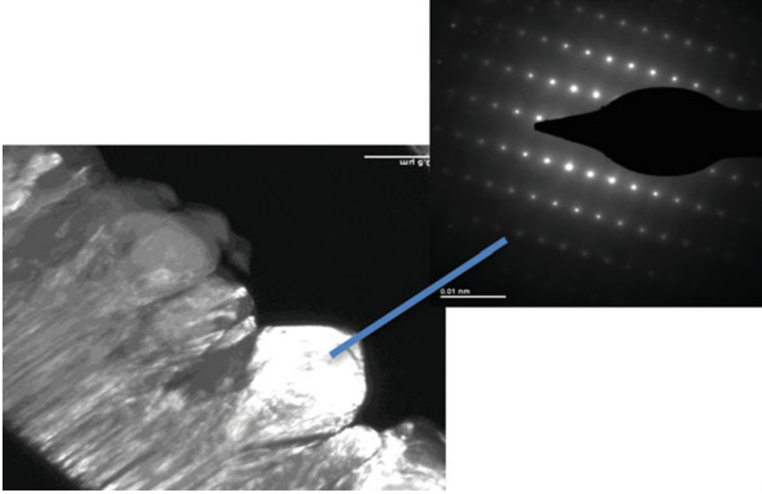

Fig. 1.16 Regrown film on slightly oxidized AlN surface with cusps leading to giant grain growth with polarity inversion (from [43])

c_{66} is not independent but is equal to $(c_{11} - c_{12})/2$. This means also that elastic properties are isotropic perpendicular to the *c*-axis. The sixfold axis is a high enough symmetry to give this partial isotropic property (like for a cylindrical shape) for a fourth-rank tensor (a fourfold axis is not sufficient) [46]. Also, there are only three different piezoelectric coefficients: e_{33} describing the longitudinal effect along the polar 3-axis (=*c* axis), $e_{31} = e_{32}$ describing the transverse effect, with the electric field along the polar 3-axis and the stress in the (1,2) plane, and $e_{15} = e_{24}$ describing the shear deformation when the electric field is perpendicular to the polar axis. There are two different dielectric constants (ε_{11} and ε_{33}), and together with the density required to derive wave velocities, we end up with 11 independent material constants. For a long time, there were no single crystals available for property measurements, and property data originated exclusively from epitaxial thin film data [29, 47]. Recently, sufficiently large and good crystals became available, and crystal properties were measured as well [48]. In addition, ab initio calculations based on density functional theories (DFT) become increasingly precise. In Table 1.1, the differently determined values are listed and compared to results of sputter-deposited thin films. Complete sets of electromechanical properties are listed as far as they are known.

In the thin film case, there are only very few efforts to get a complete parameter set, effectively only two: one for AlN [47] and one for $Al_{0.6}Sc_{0.4}N$ [49]. In most of the applications, AlN thin films are used in specific modes, depending on a few coefficients only. The most frequently fabricated devices with AlN thin films are thin film bulk acoustic resonators (TFBARs), also referred to as "solidly mounted

Table 1.1 Properties of AlN for the (*S, E*) system, evaluated from single crystals, epitaxial AlN thin films on sapphire (SAW device), from thin film data, and from ab initio studies

Material constant	Single crystal [48]	Epitaxial thin film [47] (T&M)	Sputter-deposited thin films [30, 51–54]	Density functional theory [19, 55–57]
ρ (kg/m^3)	3260	3260		3260
${c_{11}}^E = {c_{22}}^E$ (GPa)	402	345		.. |..| 397 | 410
${c_{12}}^E$	135	125		..| ..| 137 | 142
${c_{11}}^E + {c_{12}}^E$	537	470		506 |..| 534 | 552
${c_{13}}^E$	101	120		094 |..| 106 | 110
${c_{33}}^E$	387	395	382 ± 12	377 | 370 | 367 | 385
${c_{44}}^E = {c_{55}}^E$	123	118		.. |..| ..| 118 | 123
${c_{66}}^E = \left({c_{11}}^E - {c_{12}}^E\right)/2$	110	110		.. |..| 130 | 134
e_{15}	−0.32	−0.48		−0.351 |..|..| −0.39
e_{31}	−0.6	−0.58		−0.533 |..|..| −0.63
e_{33}	1.34	1.55		1.505 | 1.55 |..| 1.46
${\varepsilon_{11}}^S/\varepsilon_0$	9.0	9.0		
${\varepsilon_{33}}^S/\varepsilon_0$	9.5	10.7		10.2 [40]
α_{11} $\left(10^{-6}/\mathrm{K}\right)$		4.2		
α_{33} $\left(10^{-6}/\mathrm{K}\right)$		4.7		
$d_{33,f}$ (pN/V) $= e_{33}/{c_{33}}^E$	*3.5*	*3.92*	3.9	*4.0 | 4.2 |..| 3.8*
$e_{31,f}$ $\left(\mathrm{C/m^2}\right) = e_{31} - e_{33}{c_{13}}^E/{c_{33}}^E$	*−0.95*	*−1.05*	-1.07 ± 0.05	*−1.00 |..|..| −1.06*
${\varepsilon_{33}}^f/\varepsilon_0$ (film) $= \left({\varepsilon_{33}}^f + {e_{33}}^2/{c_{33}}^E\right)/\varepsilon_0$	*10.0*	*11.4*	10.3	*10.9*
${c_{33}}^D$	*408*	*420*	419 ± 4	*402 |..|..| 409*
${k_t}^2$ (%)	*5.23*	*6.05*	6.5–7.0 %	*6.2 |..|..| 5.8*

Values in italics stand for derived values, whereas the others are either measured or obtained from DFT. ${k_t}^2$ is specified for the basic thickness mode

resonators” (SMR) when they are mounted on an acoustic reflector stack, used in RF filters in mobile phones. The governing coupling coefficient of such resonators is valid for a pure thickness mode (no lateral deformations) and amounts to:

$$k_t^2 = \frac{e_{33}^2}{c_{33}^D \varepsilon_{33}^S} \tag{1.1}$$

The stiffness constant ${c_{33}}^D$ at constant D field is directly determined from the resonance frequencies of TFBARs and thus should come out quite precisely. It differs from ${c_{33}}^E$ (same coefficient at constant E-field) by a piezoelectric contribution as follows:

$$\begin{aligned} D_3 &= \varepsilon_{33}^S E_3 - e_{33} S_3 = 0 \\ T_3 &= c_{33}^E S_3 + e_{33} E_3 = \left[c_{33}^E + \frac{e_{33}^2}{\varepsilon_{33}^S}\right] S_3 \quad \Rightarrow c_{33}^D = c_{33}^E + \frac{e_{33}^2}{\varepsilon_{33}^S} \end{aligned} \tag{1.2}$$

Furthermore, thin films show a dielectric constant somewhere between fully clamped and free responses. When measuring capacitances at parallel plate condensers, the film is free in the 3-direction but clamped in the 1- and 2-directions (plane of the film) onto a thick, ideally infinitely rigid substrate. One calculates:

$$\varepsilon_{33,f} = \varepsilon_{33}^{S} + e_{33}^{2}/c_{33}^{E} \tag{1.3}$$

Piezoelectric coefficients are frequently measured with quasi-static methods below any film resonances (nevertheless one has to be sure that the substrate does not resonate!). For a film that is ideally clamped to a substrate (again rigid substrate), the thickness response is derived from

$$T_3 = c_{33}^{E} S_3 - e_{33} E_3 = 0 \quad \Rightarrow d_{33,f} = \frac{S_3}{E_3} = \frac{e_{33}}{c_{33}^{E}} \tag{1.4}$$

Finally, one can also determine a transverse thin film coefficient by measuring the bending of a piezoelectric laminated beam upon application of an electric field or the produced charge upon bending the beam.

$$\begin{aligned} & D_3 = e_{31}\left(S_1 + S_2\right) + e_{33} S_3 \\ & T_3 = c_{13}^{E}\left(S_1 + S_2\right) + c_{33}^{E} S_3 = 0 \\ & \Rightarrow D_3 = \left[e_{31} - \tfrac{c_{13}^{E}}{c_{33}^{E}} e_{33}\right]\left(S_1 + S_2\right) \quad e_{31,f} = e_{31} - \tfrac{c_{13}^{E}}{c_{33}^{E}} e_{33} \end{aligned} \tag{1.5}$$

This thin film coefficient can be measured directly without requiring the knowledge of the elastic constants of the piezoelectric film. Its value is larger than e_{31} because e_{31} is negative and e_{33} positive, reflecting the fact that the piezoelectric thin film is unclamped in the 3-direction ($T_3 = 0$).

Table 1.1 shows that crystal data, epitaxial film data, and ab initio data are rather underestimating the coupling coefficient ${k_t}^2$. Experiments yield that it is clearly above 6 % and below 7 % in sputter-deposited AlN. One can assume that AlN crystals are not 100 % perfect yet and thus still show some reduced piezoelectric activity. There is also a discrepancy in the dielectric constant. It appears that this value is lower than obtained by fitting resonance curves of epitaxial AlN on sapphire. In this case, single crystal data justify the lower values. There seems to be still a problem to analyze a dielectric response with DFT calculations (would require to add an electric field to the problem). There is only an elder work addressing the dielectric properties [50]. An overestimation of the dielectric constant could explain the lower coupling coefficient as derived from the epitaxial film data in Table 1.1.

The values in Table 1.1 correspond to the set of constituent equations having strain S and electric field E as variables (see, e.g., [58] for an introductory textbook). In piezoelectric materials, the elastic constants depend on whether they were determined at constant E or constant D fields, and the dielectric constants whether they were determined at constant stress T or constant strain S. Often, these conditions can be chosen by the external conditions, like measurement of voltage in an open circuit (constant D) or measurement of current with a charge amplifier in a

Table 1.2 Properties of AlN in the (*T, E*) system calculated from Ref. 47, i.e., second column of Table 1.1

Elastic compliance	$s_{11}^E = s_{22}^E$	3.53	Piezoelectric stress	d_{15}	−4.07
($10^{-12} m^2/N$)	s_{12}^E	−1.01	Constants (pC/N)	d_{31}	−2.66
	s_{13}^E	−0.77		d_{33}	5.54
	s_{33}^E $s_{44}^E = s_{55}^E$	3.00 8.48	Rel. dielectric permittivity	ε_{11}^T	9.44
	s_{66}^E	9.09		ε_{33}^T	11.5

The compliance values are obtained by inverting the rigidity tensor and the ε_{ij}^T and d_{ij} using algebra

virtual short-circuit scheme (constant *E*). In ultrasonic wave propagation, however, the conditions are given by the physics of the wave. Longitudinal waves occur at constant *D* (div$D = 0$ in a dielectric) and transversal waves at constant *E* (rot$E = 0$, no electromagnetic effects in the nonrelativistic case) (see, e.g., [59]). The (*T, E*) system is sometimes more practical than the (*S, E*) system, particularly if one knows that there are no stresses applied to a body. For convenience, the compliance values as derived from the rigidity values of Tsubouchi and Mikoshiba are given in Table 1.2.

Single crystal properties are measured at suitably oriented and cut crystals. Sound velocities (v_s) are obtained with pulse-echo methods [48] or derived from fundamental and overtone resonances. These methods allow a direct derivation of elastic constants though the simple relation:

$$v_{s,ij} = \sqrt{\frac{c_{ij}^x}{\rho}} \tag{1.6}$$

where c_{ij}^x means the relevant stiffness constant at either constant *D* or *E*. Analysis of admittance or impedance curves delivers dielectric constants and coupling coefficients.

Characterization of piezoelectric thin films is more complicated. One may try to determine properties at films as deposited on their substrates, which are usually much thicker than the film, or one may first liberate the film by some micro-fabrication method (keeping in mind that the electrodes are playing a mechanical role as well). One technique consists in analyzing surface acoustic wave resonators. It just requires the addition of interdigitated electrodes. A multitude of different SAW geometries, eventually also different substrates, combined with the simulation of wave propagation is needed to derive all property coefficients. The pioneering work of Tsubouchi and Mikoshiba [29, 47], whose results are given in Table 1.1 for the epitaxial film, shows that such work can be realized with very good results. In this work, made in the early 1980s, the AlN thin films were deposited by MOCVD at temperatures between 1000 and 1180 °C. Their values remained reference data, are reported in compendia of piezoelectric materials [60], and included in material

Table 1.3 Resonant plate structures allowing for the derivation of specific elastic and piezoelectric constants

MEMS resonator Type of plate resonator	Derived from resonance or antiresonance frequencies (sound velocity)	Derived from coupling constant
Thickness extensional mode	c_{33}^{D}	e_{33}
Length extensional mode	s_{11}^{E}	d_{31}
Width extensional mode	$s_{11}^{E}\left\{1-\left(S_{12}^{E}/S_{11}^{E}\right)^{2}\right\}$	d_{31}
Radius extensional mode	S_{12}^{E}/S_{11}^{E}	
Lateral shear mode	c_{44}^{E}	e_{15}

libraries of finite element modeling programs. For a long time, they were without competition by single crystal data.

Similar to single crystal characterization, one can produce shape resonators with thin films. It is not as straightforward as with crystals, though. Good AlN thin films have *c*-axis orientation, meaning that the *c*-axis stands vertical on liberated plate structures. Plates can be etched into various shapes by micromachining techniques. Rectangular shapes are suitable for length and width extensional modes [61], round shapes for radial extensional modes, various shapes for thickness extensional modes, and using two parallel top electrodes, also for the excitation of shear modes (see [49] for a work using all structures). In Table 1.3, these methods are listed together with the elastic and piezoelectric parameters to be derived. These methods have the advantage to be based on frequency measurements, which as such give accurate results. However, one needs to avoid or identify parasitic elements (such a parasitic capacities and inductances) and mass loading of resonators by electrodes. By careful analysis of electrical impedance data, varying design and dimensions, one can take care of such factors and calculate a correction to mass loading by finite element simulation or analytical methods. Resonance (f_r) and antiresonance (f_a) frequencies are easily and with high precision determined and depend essentially on material parameters (if parasitic elements are either absent or taken into account). For instance, f_a of a thin film bulk acoustic wave resonator (TFBAR) resonating at the fundamental resonance is in the ideal case obtained through the simple equation:

$$f_a = \frac{v_s}{2t} = \frac{1}{2t}\sqrt{\frac{c_{33}^{D}}{\rho}} \tag{1.7}$$

where t is the thin film plate thickness. The coupling coefficient is derived from the difference between f_a and f_r (for not too large values of k_t^2):

$$k_t^2 = \frac{e_{33}^2}{c_{33}^D \varepsilon_0 \varepsilon_{33}^S} \approx \frac{\pi^2}{4} \frac{f_a - f_r}{f_a} \tag{1.8}$$

There is tremendous data collection of such resonators, because they are the heart of a large portion of RF filters used in mobile phones. To cite two published results for the sound velocity reported as $v_s = 11.4 \times 10^3$ m/s [30] and 11.3×10^3 m/s [52], from which $c_{33}{}^D$ as 4.23 and 4.16×10^{11} N/m^2 are derived, confirming very well the T&M value. The coupling coefficient is frequently reported around 6.5 % for resonators around 2 GHz. Lakin et al. [52] reported even a value of 7.0 % obtained with solidly mounted resonators. Electrode material (acoustic impedance) and thickness need to be chosen optimally for getting the best possible coupling at a given frequency (AlN thickness). With higher frequency, electrodes tend to reduce the coupling as their relative volume in the resonator tends to increase. But even at 8 GHz, a coupling of $k_t{}^2 = 5.9$ % was realized [62]. The difference with respect to the T&M value is most likely due to a too high dielectric constant in the latter data set. A $\varepsilon_{33}{}^S$ of 9.6 (corresponding to $\varepsilon_{33,f} = 10.3$) would better fit to single crystal and sputtered thin film values and leads to a $k_t{}^2$ of 6.7 %. Important is to realize that polycrystalline (0001)-textured thin films are as good as single crystal films. In the former, each grain is a perfect single crystal in the form of a column or fiber (or nanowire). They are densely packed to give an excellent transverse piezoelectric response, and because of the hexagonal symmetry around the *c*-axis, the isotropic in-plane symmetry introduced by the random in-plane orientation of the grains does not even introduce a new symmetry aspect up to the 4th rank tensors, such as rigidity and compliance tensors.

Materials scientists are frequently using other methods. Device fabrication and characterization are a too large effort when tens or hundreds of differently processed films have to be analyzed in order to identify process-property relations. Most conveniently, films are analyzed with a minimal effort of photolithography and micro-fabrication, thus being clamped on a substrate having its complete thickness (typically 0.3–0.6 mm). For the measurement of $d_{33,f}$, piezoelectric films are grown on bottom electrodes, and circular electrodes (typically 0.5–0.6 mm in diameter) are deposited by evaporation or sputtering through a shadow mask. The thickness change upon application of an AC electric field between top electrode and bottom electrode is measured by means of a double side laser interferometer, which measures the phase change of an optical beam having a reflection from the top electrode and the precise opposite point of the wafer backside in its path. The applied voltage is sinusoidal with a frequency of a few kHz, in order to reduce $1/f$ noise and profit from powerful lock-in detectors. The clamped $d_{33,f}$ is then obtained as defined in Eq. 1.4. The method is only precise if the substrate is infinitely rigid. Deviations occur if this is not completely true, and for precise values, finite element calculations need to be done. The method is good and very efficient in comparing different qualities of films that have the same thickness, the same top electrode geometry, and the same substrate type and thickness.

The measurement of the transverse coefficient $e_{31,f}$ is carried out at flexural bending structures based on full substrate thickness and operated either in the

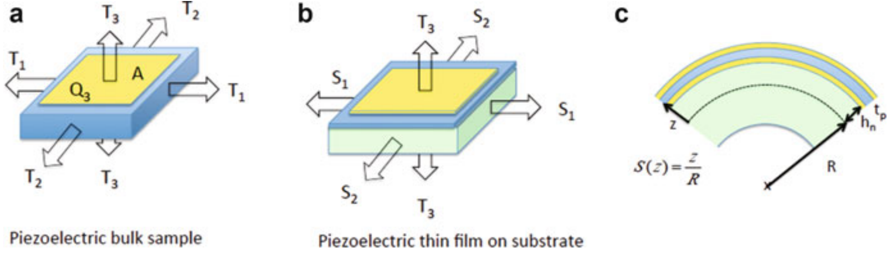

Fig. 1.17 Comparison of bulk and thin film situation requiring a different choice of mechanical variables: (**a**) bulk sample, (**b**) thin film on substrate, and (**c**) simple example of bent cantilever cross section with z-axis having zero at neutral plane

converse mode (measurement of deflection upon application of a voltage) or in the direct mode (collection of charge upon mechanical bending). Different versions were proposed for the direct effect: single-side clamped cantilever and bending by a calibrated actuator at the other side [63], flexibly clamped cantilever in a four-point fixation [64], and a wafer flexure technique by application of a pressure behind a clamped sample [65]. For the converse mode, the curvature of single-side clamped cantilevers is measured [66, 67]. These techniques are rather accurate, provided that cantilever dimensions and elastic properties of the substrate are known correctly.

However, this approach is not as simple as measuring a bulk sample. Let us point out the difference considering the assessment of the direct piezoelectric effect with a bulk sample equipped with two parallel electrodes (see Fig. 1.17) and which is based on the following constituent equation:

$$D_3 = \varepsilon_{33}^T E_3 + d_{31}\,(T_1 + T_2) + d_{33} T_3 \tag{1.9}$$

D_3 means the displacement field or charge density produced at electrodes perpendicular to the 3-axis, equal to the charge Q_3 divided by the electrode area. When applying an exclusive T_3 stress and measuring the charge at a virtual short (which is the case when using a charge amplifier), then we get $d_{33} = D_3/T_3$, or when applying an exclusive stress T_1, then we can derive also $d_{31} = D_3/T_1$.

When we try to do the same with a thin film sample, we have several problems. In theory, it is possible to apply T_3, because the stress will be the same in the substrate and in the thin film. However, the substrate will expand in the transverse direction (S_1 and S_2 are different from zero as $T_1 = T_2 = 0$) differently as the piezoelectric thin film would do alone, because the respective s_{31} compliance values are different in general. The strain of the substrate is imposed to the piezoelectric thin film, causing more charges on the electrodes due to the transverse piezoelectric effect. So for taking care about the influence of the substrate, the strain variables would be more suited, and we thus have to consider the e-coefficients in this case:

$$D_3 = \varepsilon_{33}^S E_3 + e_{31}\,(S_1 + S_2) + e_{33} S_3 \tag{1.10}$$

It is clear that strain S_3 cannot be controlled well as an input parameter. The ideal variables for the thin film problem are thus T_3, S_1, and S_2. One can show that the constituent equation can be transformed to the following form:

$$D_3 = \varepsilon^{s}_{33,f} E_3 + e_{31,f}\left(S_1 + S_2\right) + d_{33,f} T_3 \tag{1.11}$$

The coefficient $d_{33,f}$ is difficult to measure in the direct mode, because the substrate will always react upon applying a pressure T_3, and as shown in literature, S_1 and S_2 can be much larger than from T_3 [68]. Using a curved support and stamp, the bending can be avoided [69]. Nevertheless, as the substrate reacts with lateral extension to pressure, d_{33} will be measured too high on a softer substrate and too small on a harder substrate, as shown by the following equation derived from (Eqs. 1.9 and 1.11):

$$D_3 = 2e_{31,f} s^{(s)}_{13} T_3 + d_{33,f} T_3 = \left[2e_{31,f}\left(s^{(s)}_{13} - s^{E}_{13}\right) + d_{33}\right] T_3 \tag{1.12}$$

where $s_{31}{}^{(s)}$ means the substrate compliance component. For measuring $e_{31,f}$ one has to provide an experiment with a well-known substrate deformation, to put $T_3 = 0$ (this is the case at 1 atmosphere pressure (=0.1 MPa)) and $E_3 = 0$ when using a charge amplifier, and to evaluate according to Eq. 1.11. The controlled deformation is conveniently achieved by a bending experiment. The most simple experiment with a well-defined strain is the four-point bending test [64], resulting in a constant curvature reproducing the situation as sketched in Fig. 1.17c. It works also by single point bending [63] and flexural plate bending [65]. The cantilevers for bending experiments exhibit a defined long direction along which the main strain develops (say S_1). Then, in a wide range of thickness to width ratios, the strain S_2 is then given by the Poisson ratio ν_{sub} of the substrate: $S_2 = -\nu_{\text{sub}} S_1$. It follows that

$$e_{31,f} = \frac{D_3}{\left(1 - \upsilon_{sub}\right) S_1}$$

So besides the curvature, one needs to know also the Poisson ratio of the substrate. In case of cantilevers obtained from (001) silicon wafers, the Poisson ratio amounts to 0.28 when the cantilevers point along [100] and 0.064 when they point along [110] [70, 71].

For measuring $d_{33,f}$ we consider the converse effect:

$$S_3 = \frac{s^{E}_{13}}{s^{E}_{11} + s^{E}_{12}}\left(S_1 + S_2\right) + d_{33,f} E_3, \text{ when } T_3 = 0 \tag{1.13}$$

Applying E_3 (voltage V_3) and measuring the thickness change Δt_p by double side interferometry, we can derive $d_{33,f}$ as $\Delta t_p / V_3$ provided that (1) $S_1 = S_2 = 0$ and (2) the substrate does not change its thickness. The reason is that one measures the complete thickness change, the sum of the substrate and of the thin film. Unfortunately, these two conditions are normally not met. They would be true in the limiting case of an infinitely stiff substrate (much stiffer than the piezoelectric film). For AlN/Si this is definitely not the case. So the only way to come around

this problem is to perform finite element calculations. The elastic properties of the substrate are usually well known, and $e_{31,f}$ can be measured before. Let us call this new method *FEM-supported double beam laser interferometry* (*FEM-DBLI*).

1.3.1 Efforts in Ab Initio Calculations

Sporadic efforts were made over the years to calculate AlN properties by density functional theories. With the discovery of improvement of piezoelectric constant by Sc doping, the efforts are being done more systematically in order to predict AlScN properties. In an early paper, Kamiya [50] calculated the piezoelectric coefficient d_{33} of AlN to be 6.7 pC/N, which is about 20 % higher than the T&M experimental values. The d_{31} coefficient (-2.71 pC/N, $+2$ %), however, was obtained close to experimental data. Later, Bernardini and Fiorentini calculated d_{31} and d_{33} as -2.1 and 5.4 pC/N, respectively. The latter value is very close to the experimental value. Tasnadi et al. [55] published an e_{33} value of 1.55 C/m^2, identical to the experimental value. The most complete work was published by Caro et al. [57]. The values for e_{33}, d_{31}, and d_{33} were obtained as 1.46 C/m^2, -2.32 pC/N, and 5.12 pC/N. All values are thus about 10 % smaller than in reality. Most difficulties seem to be encountered in calculating the elastic properties. In two works, the rigidity constant $c_{11}{}^E$ is calculated much higher than the T&M experimental value: 500 GPa [72] and 420 GPa [57] vs. 345 GPa found experimentally. $C_{33}{}^{\mathrm{E}}$, however, is calculated rather accurate: 370 [55] to 385 [57] vs. 370 to 395 GPa observed experimentally.

1.4 AlN-ScN Alloy Thin Films

Recently, it was discovered that Al substitution by Sc allows for an increase of the piezoelectric response [69, 73]. This was predicted earlier for the (Ga,Sc)N system based on first principle calculations [74] motivated by the idea that a solid solution system going from a piezoelectric wurtzite structure on the Ga-rich side to a non-piezoelectric rock-salt structure on the Sc-rich side would exhibit somewhere a region within the wurtzite phase where piezoelectricity would peak, similar to a para- to ferroelectric phase transition, occurring in this case, however, as a morphotropic phase transition. Sc is a strictly 3-valent cation like Al but is larger. Applying rules for ionic crystals (with the reserve expressed before) and using the large ionic radius of N^{3-} (132 pm in tetrahedral coordination), one concludes that Al^{3+} (32 pm) has most likely a tetrahedral coordination with nitrogen, which is indeed the case. Sc^{3+} is in general not found in tetrahedral coordination, its radius is too large (88.5 pm in octahedral coordination), and the natural ScN structure is the rock-salt (NaCl) structure with octahedral coordination [75]. Sc is less electronegative than Al, and its bonds have a larger ionic nature (50 % covalent). It is interesting to note that also Ga^{3+} and In^{3+} are larger ions than Al^{3+}, forming as well

a wurtzite structure with nitrogen (although their ionic radii indicate a preference for octahedral coordination), but their piezoelectric coefficients are smaller than the ones of AlN. The increase of piezoelectricity with Sc doping must be ascribed firstly to a smaller electronegativity than the one of Al, Ga, and In and, secondly, as pointed out by Tasnadi et al. [55], to a distortion of the unit cell which lowers the c/a ratio and softens the elastic properties. Sc in AlN spreads the nitrogen tetrahedron to find more space. It is mainly the lattice constant a that increases. The length of c is almost untouched [53, 76]. The Sc ion thus tends to approach the nitrogen base plane, increasing the u-parameter from 0.38 toward 0.5, as shown by ab initio calculations [55]. Centering the Sc in the base plane would cause a fivefold coordination. It was indeed proposed that there exists an intermediate non-piezoelectric hexagonal structure with this coordination before reaching the NaCl structure at high Sc content [77]. However, no experimental evidence has been published so far. DFT works advance the interpretation that there is a competition of Al^{3+} and Sc^{3+} ions about the coordination of nitrogen resulting in a kind of frustrated system [55]. With increasing Sc concentration in the wurtzite phase, the potential wells of the ions become shallower, and thus the ionic displacements in an electric field become larger, leading to larger piezoelectric strains and dielectric responses.

In the first works, the deposition processes for AlScN were based on RF co-sputtering from two magnetron sources with metallic Al and Sc targets, operated in a nitrogen-argon gas mixture [69, 73]. Later, the same method was used supplying pulsed DC power to the two magnetrons instead of RF power [54]. For high-throughput industrial processes, a single source using an alloy target is preferred. Such processes were successfully applied with either RF or DC pulsed power supplies [53, 78], however, with a limited Sc concentration of less than 17 %. It was found in the latter case that the identical growth mode and microstructure type as with pure AlN can be reproduced, at least up to 17 % of Sc. X-ray diffraction (XRD) pattern and transmission electron microscopy (TEM) reveal a pure c-axis orientation with columnar microstructure, similarly to what is observed for un-doped AlN thin films. The favorable microstructure is maintained as long as the Sc concentration is not too large, and the growth temperature is not too high, i.e., not above about 500 °C.

For the first piezoelectric characterization of AlScN, the sample was squeezed between two spherically shaped stamps being at the same time the contacts for charge collection [73] (this according to Eq. 1.12). As stated above, this approach yields too large values on softer substrates (such as Si in the case of AlN thin films). Hence the obtained d_{33} value was larger than in reality. This is indeed suggested when comparing the experimental values with the ab initio ones (Fig. 1.18). The interesting point is that the s_{13} values of AlScN and Si are very close at 40 % Sc, according to the predicted $s_{13}{}^{E}$ of Caro et al. This would mean that the value of 21.1 pm/V published in [69] for this composition would be free of d_{31} contributions! DFT calculations are predicting an even higher value of 29.3 pm/V [57]. Both are extraordinary high values for a non-ferroelectric material and even more spectacular considering the low dielectric constant!

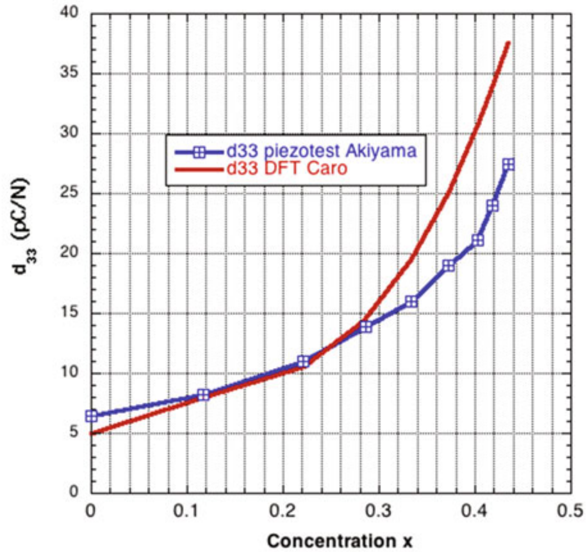

Fig. 1.18 Comparison of results for d_{33}: Experimental values from Ref. 69 and ab initio values from Ref. 57

High Sc concentrations are probably more of an advantage in flexural bending actuators, sensors, and energy harvesters [53, 79] governed by $e_{31,f}$. As it is also very much the custom to determine as well, $d_{33,f}$, the two thin film coefficients are plotted in Fig. 1.19, comparing measurements and DFT literature values. The curves were corrected for giving correct values for pure AlN in the cases where major deviations to higher values were published. Figure 1.19 shows that experiments tend to give higher values for the clamped longitudinal response than predicted by DFT, at least at lower Sc concentrations. In contrast, $e_{31,f}$ data are quite the same up to 20 % Sc concentration. Above, DFT proposes lower values. Differences could arise from the predicted stiffness constants. For instance, a too large s_{13} could lower $d_{33,f}$ in the DFT prediction. A further problem of present state of research is the fact that it is not known what the "true" or optimal AlScN thin film should deliver as properties. In any case, the discovery of piezoelectricity in AlScN alloys opened a very interesting field in experimental and theoretical materials research and allows for well-justified dreams in applications.

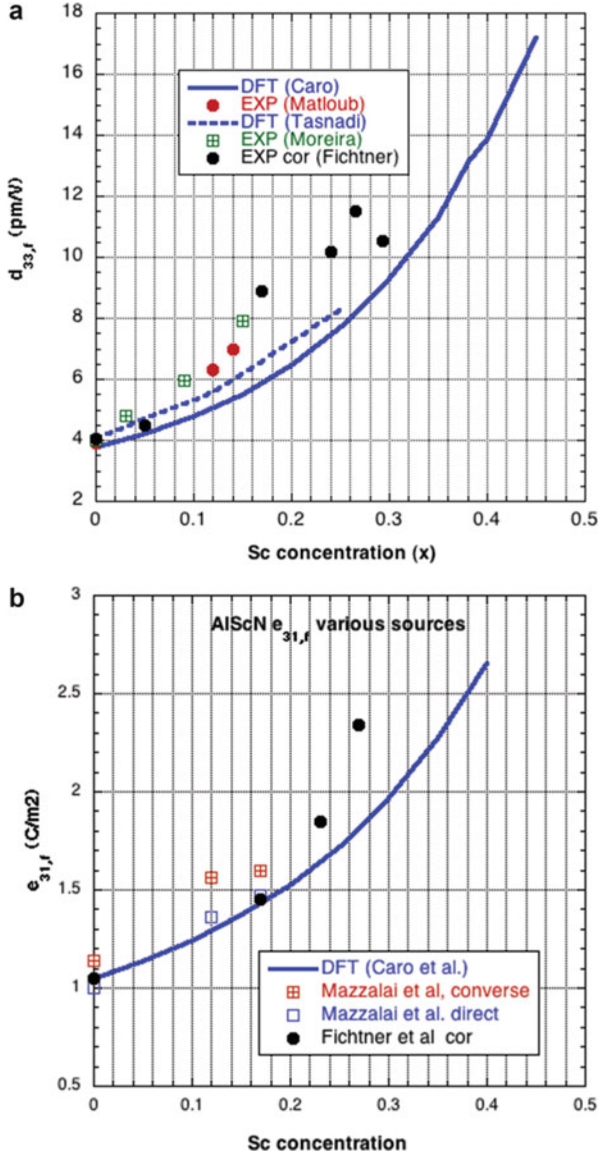

Fig. 1.19 (**a**) Longitudinal, clamped coefficient $d_{33,f} = e_{33}/c_{33}{}^{E}$. The DFT Caro curve is from Ref. 57 and the DFT Tasnadi curve from Ref. 55. The experimental values from Matloub et al. were obtained by FEM-assisted DBLI. The values of Moreira were derived from thin film bulk acoustic wave resonators [54]. The DBLI values of Fichtner et al. were proportionally adjusted to result in 4 pC/N. (**b**) Transverse coefficient $e_{3,1f}$. The experimental $e_{31,f}$ values from Mazzali et al. are from Ref. 51. Fichtner's values were adjusted for getting 1.05 C/m^2 for pure AlN

References

1. Grudkowski TW, Black JF, Reeder TM, Cullen DE, Wagner RA (1980) Fundamental-mode VHF-UHF miniature acoustic resonators and filters on silicon. Appl Phys Lett 37:993–995
2. Uozumi K, Ohsone K, White RM (1983) Generation and detection of ultrasonic lamb waves in a thin deposited film using interdigital transducers. Appl Phys Lett 43:917–919
3. Nakamura K, Sasaki H, Shimizu H (1981) ZnO/SiO2-diaphragm composite resonator on a silicon wafer. Electron Lett 17(14):507–509

4. Muralt P (2008) Recent progress in materials issues for piezoelectric MEMS. J Am Ceram Soc 91:1385–1396
5. Lakin KM, Mccarron KT, Rose RE (1995) Solidly mounted resonators and filters. In: IEEE ultrasonics symposium. IEEE, Seattle, Washington, USA
6. Ruby R, Bradley P, Larson JD, Oshmyansky Y (1999) PCS 1900MHz duplexer using thin film bulk acoustic resonators (FBARs). Electron Lett 35:794–795
7. Aigner R, Ella J, Timme H-J, Elbrecht L, Nessler W, Marksteiner S (2002) Advancement of MEMS into RF applications. In: Electron devices meeting IEDM'02
8. Schulz H, Thiemann KH (1977) Crystal structure refinement of AlN and GaN. Solid State Comm 23:815–819
9. Jeffrey GA, Parray GS, Mozzi RL (1955) Study of the wurtzite-type binary compounds. I. Structures of AlN ad BeO. J Chem Phys 25(5):1024–1031
10. Shannon (1976) Acta Cryst A 32:75
11. Sengstag T, Binggeli N, Baldereschi A (1995) Anomalies in the pressure dependence of the effective charge in cubic semiconductors. Phys Rev B 52(12):R8613–R8616
12. Ferrara P, Binggeli N, Baldereschi A (1997) Band discontinuities in zinc-blende and wurtzite AlN/SiC. Phys Rev B 55(12):R7418–R7421
13. Keffer F, Portis AM (1957) Study of the wurtzite-type binary compounds. II. Macroscopic theory of the distortion and polarization. J Chem Phys 27(3):675–682
14. Zhuang D, Edgar JH (2005) Wet etching of GaN, AlN, and SiC: a review. Mater Sci Eng R 48:1–46
15. Bernardini F, Fiorentini V, Vanderbilt D (1997) Phys Rev B 56:R10024
16. Hellman ES (1998) MRS Internet J Nitride Semicond Res 3:11
17. Muralt P (2001) Stress coupled phenomena. In: Encyclopedia of materials: science and technology. In: Buschow JKH, Cahn RW, Flemings MC, Ilschner B (ed) Elsevier, pp 8894–8897
18. King-Smith RD, Vanderbilt D (1993) Theory of polarization of crystalline solids. Phys Rev B 47:1651–1654
19. Bernardini F (2007) Spontaneous and piezoelectric polarization: basic theory vs. practical recipes. In: Piprek J (ed) Nitride semiconductor devices, Wiley-VCH, Newark, USA, pp 49–68
20. Zoroddu A, Bernardini F, Ruggerone P, Fiorentini V (2001) First-principles prediction of structure, energetics, formation enthalpy, elastic constants, polarization, and piezoelectric constants of AlN, GaN, and InN: comparison of local and gradient-corrected density functional theory. Phys Rev B 64:045208
21. Jin L, Zhang H-Y, Han J-C, Yao T, Song B (2015) Control of AlN single crystal nucleation: an insight into the crystal growth habit in the initial stages of the physical vapor transport method. Mater Express 5(2):129–136
22. Shi S-C, Chattopadhyay S, Chen C-F, Chen K-H, Chen L-C (2006) Structural evolution of AlN nano-structures: nanotips and nanorods. Chem Phys Lett 418:152–157
23. Dreyer CE, Janotti A, Van De Walle CG (2015) Brittle fracture toughnesses of GaN and AlN from first-principles surface-energy calculations. Appl Phys Lett 106:212103
24. Mahieu S, Ghekiere P, Dewinter G, Heiwegh S, Depla D, Degryse R, Lebedev O, Vantendeloo G (2005) Mechanism of preferential orientation in sputter deposited TiN and YSZ. J Cryst Growth 279:100–109
25. Deng R, Muralt P, Gall D (2012) Biaxial texture development in aluminum nitride layers during off-axis sputter deposition. J Vac Sci Techn A 30:051501
26. Milyutin E, Harada S, Martin D, Carlin JF, Grandjean N, Savu V, Vasquez-Mena O, Brugger J, Muralt P (2010) Sputtering of (001) AlN thin films: control of polarity by a seed layer. J Vac Sci Techn B 28(6):L61–L63
27. Milyutin E, Muralt P (2011) Electro-mechanical coupling in shear mode FBAR with piezoelectric modulated thin film. IEEE Trans UFFC Lett 685(4):685–688
28. Artieda A, Sandu CS, Muralt P (2010) Highly piezoelectric AlN thin films grown on amorphous, insulating substrates. J Vac Sci Techn A 28:390–393
29. Tsubouchi K, Sugai K, Mikoshiba N (1981) AlN material constants evaluation and SAW properties of AlN/Al2O3 and AlN/Si. In: IEEE ultrasonics symposium

30. Dubois M-A, Muralt P (1999) Properties of AlN thin films for piezoelectric transducers and microwave filter applications. Appl Phys Lett 74:3032–3034
31. Shinoki F, Itoh A (1975) Mechanisms of rf reactive sputtering. J Appl Phys 46(8):3381–3384
32. Martin F, Muralt P, Dubois M-A, Pezous A (2004) Thickness dependence of properties of highly c-axis textured AlN thin films. J Vac Sci Techn A 22:361–365
33. Bjurstrom J, Wingqvist G, Katardjiev I (2095) Synthesis of textured thin piezoelectric AlN films with a nonzero c-axis mean tilt for the fabrication of shear mode resonators. IEEE Trans UFFC 53(11):2095–2100
34. Thornton JA (1986) The microstructure of sputter deposited coatings. JVSTA 4:3059–3065
35. Dubois M, Muralt P, Sagalowicz L (1999) Aluminum nitride thin films for microwave filter and microsystem applications. In: Wun-Fogle KUM, Ito Y, Gotthardt R (eds) Materials research meeting. Materials Research Society, Boston, pp 9–14
36. Engelmark F, Iriarte GV, Katardjiev I, Ottossen M, Muralt P, Berg S (2001) Structural and electroacoustic studies of AlN thin films during low temperature radio frequency sputter deposition. J Vac Sci Techn A 19:2664–2669
37. Drusedau TP, Blasing J (2000) Optical and structural properties of highly c-axis oriented nitride prepared by sputter deposition in pure nitride. Thin Solid Films 377:27–31
38. Takikawa H, Kimura K, Miyano R, Sakakibara T, Bendavid A, Martin PJ, Matsumuro A, Tsutsumi K (2001) Effect of substrate bias on AlN thin film preparation in shielded reactive vacuum arc deposition. Thin Solid Films 386:276–280
39. Dubois M-A, Muralt P (2001) Stress and piezoelectric properties of AlN thin films deposited onto metal electrodes by pulsed direct current reactive sputtering. J Appl Phys 89:6389–6395
40. Dubois M, Muralt P, Matsumoto H, Plessky V (1998) Solidly mounted resonator based on AlN thin film. In: IEEE ultrasonics symposium. Sendai, Japan
41. Ricard A (1995) Plasma réactifs. Société Françai s du Vide (sfv). 156
42. Löbl HP, Klee M, Metzmacher C, Brand W, Milsom R, Lok P (2003) Piezoelectric thin AlN films for bulk acoustic wave resonators. Mater Chem Phys 79:143–146
43. Martin F, Muralt P, Dubois M (2004) Investigation of highly c-axis orientated AlN thin film regrowth. In: Ultrasonics symposium. IEEE, Montreal (Can)
44. Artieda A, Barbieri M, Sandu CS, Muralt P (2009) Effect of substrate roughness on c-oriented AlN thin films. J Appl Phys 105:024504
45. Akiyama M, Kamohara T, Kano K, Teshigahara A, Kawahara N (2008) Influence of oxygen concentration in sputter gas on piezoelectric response of aluminum nitride thin films. Appl Phys Lett 93:021903
46. Newnham RE (2004) Properties of materials: anisotropy, symmetry, structure. Oxford University Press, New York, p 380
47. Tsubouchi K, Mikoshiba N (1985) Zero-temperature coefficient SAW devices on AlN epitaxial films. IEEE Trans Sonics Ultrasonics SU-32:634–644
48. Sotnikov AV, Schmidt H, Weihnacht M, Smirnova EP, Chemekova TY, Makarov YN (2010) Elastic and piezoelectric properties of AlN and LiAlO2 single crystals. IEEE Trans UFFC 57(4):808–811
49. Konno A, Kadota M, Kushibiki J-I, Ohashi Y., Esashi M, Yamamoto Y, Tanaka S (2014) Determination of full material constants of ScAlN thin film from bulk and leaky lamb wavesin MEMS based samples. In: IEEE international ultrasonics symposium. IEEE, Chicago
50. Kamiya T (1996) Calculation of crystal structures, dielectric constants and piezoelectric properties of Wurtzite-Type crystals using ab-initio periodic Hartree-Fock method. Jpn J Appl Phys 41:4421–4426
51. Mazzalai A, Balma D, Chidambaram N, Matloub R, Muralt P (2015) Characterization and fatigue of the converse piezoelectric effect in PZT films for MEMS applications. J MEMS 24:831–838
52. Lakin KM, Belsick J, Mcdonald JF, Mccarron KT (2001) Improved bulk wave resonator coupling coefficient for wide bandwidth filters. In: IEEE ultrasonics symposium. IEEE, Atlanta, GA, USA

53. Matloub R, Hadad M, Mazzalai A, Chidambaram N, Moulard G, Sandu C, Metzger T, Muralt P (2013) Piezoelectric AlScN thin films: a semiconductor compatible solution for mechanical energy harvesting and sensors. Appl Phys Lett 102:152903
54. Moreira M, Bjurstrom J, Katardjiev I, Yantchev V (2011) Aluminum scandium nitride thin film bulk acoustic resonators for wide band applications. Vacuum 86:23–26
55. Tasnadi F, Alling B, Höglund C, Wingqvist G, Birch J, Hultman L, Abrikosov A (2010) Origin of the anomalous piezoelectric response in wurtzite ScAlN alloys. Phys Rev Lett 104:137601
56. Zhang S, Fu WY, Holec D, Humphreys CJ, Moram MA (2013) Elastic constants and critical thicknesses of ScGaN and ScAlN. J Appl Phys 114:243516
57. Caro MA, Zhang S, Ylilammi M, Riekkinen T, Moram M, Lopez-Acevedo O, Molarius J, Laurila T (2015) Piezoelectric coefficients and spontaneous polarization of AlScN. J Phys Condens Matter 27:245901
58. Moulson AJ, Herbert JM (1990) Electroceramics. Chapman & Hall, London
59. Ikeda T (1990) Fundamentals of piezoelectricity. University Press, Oxford
60. Gualtieri JG, Kosinski JA, Ballato A (1994) Piezoelectric materials for acoustic wave applications. IEEE UFFC 41:53–59
61. Piazza G, Pisano AP (2007) Two-port stacked piezoelectric aluminum nitride contour-mode resonant MEMS. Sensor Actuator A 136:638–645
62. Lanz R, Muralt P (2005) Bandpass filters for 8 GHz using solidly mounted bulk acoustic wave resonators. IEEE Trans UFFC 52:936–946
63. Dubois M-A, Muralt P (1999) Measurement of the effective transverse piezoelectric coefficient e31, f of AlN and PZT thin films. Sensor Actuator A 77:106–112
64. Prume K, Muralt P, Schmitz-Kempen CFT, Tiedke S (2007) Piezoelectric thin films: evaluation of electrical and electromechanical characteristics for MEMS devices. IEEE Trans UFFC 54:8–14
65. Shepard JF, Moses PJ, Trolier-Mckinstry S (1998) The wafer flexure technique for the determination of the transverse piezoelectric coefficient (d31) of PZT thin films. Sensor Actuator A 71:133–138
66. Kanno I, Fujii S, Kamada T, Takayama R (1997) Piezoelectric properties of c-axis oriented PZT thin films. Appl Phys Lett 70:1378–1380
67. Fujii E, Takayama R, Nomura K, Murata A, Hirasawa T, Tomozawa A, Fujii S, Kamada T, Torii H (2007) Preparation of (001)-oriented PZT thin films and their piezoelectric applications. IEEE Trans UFFC 54:2431–2438
68. Barzegar A, Damjanovic D, Ledermann N, Muralt P (2003) Piezoelectric response of thin film determined by charge integration technique: substrate bending effects. J Appl Phys 93:4756–4760
69. Akiyama M, Kano K, Teshigahara A (2009) Influence of growth temperature and scandium concentration on piezoelectric response of ScAlN alloy thin films. Appl Phys Lett 95:162107
70. Hopcroft MA, Nix WD, Kenny TW (2010) What is the Young's modulus of silicon? J Microelectromech Syst 19:229–238
71. Chidambaram N, Mazzalai A, Muralt P (2012) Measurement of effective piezoelectric coefficients of PZT thin films for energy harvesting applications with interdigitated electrodes. IEEE Trans UFFC 59:1624–1631
72. Bernardini F, Fiorentini V (2002) First-principles calculation of the piezoelectric tensor d of III-V nitrides. Appl Phys Lett 80:4145–4147
73. Akiyama M, Kamohara T, Kano K, Teshigahara A, Takeuchi Y, Kawahara N (2009) Enhancement of piezoelectric response in scandium aluminum nitride alloy thin films prepared by dual reactive cosputtering. Adv Mat 21:593–596
74. Alsaad A, Ahmad A (2006) Piezoelectricity of ordered Sc-Ga-N alloys from first principles. Eur Phys J B 54:151–156
75. Gall D, Petrov I, Hellgren N, Hultman L, Sundgren JE, Greene JE (1998) Growth of poly-and single crystal ScN on MgO(001): role of low-energy (N2)+ irradiation in determining texture, microstructure evolution, and mechanical properties. J Appl Phys 84:6034–6041

76. Deng R, Evans SR, Gall D (2013) Bandgap in AlScN. Appl Phys Lett 102:112103
77. Farrer N, Bellaiche L (2002) Properties of hexagonal ScN versus wurtzite GaN and InN. Phys Rev B 66
78. Matloub R, Artieda A, Milyutin E, Muralt P (2011) Electromechanical properties of Al0.9Sc0.1N thin films evaluated at 2.5 GHz film bulk acoustic wave resonators. Appl Phys Lett 99
79. Akiyama M, Umeda K, Honda A, Nagase T (2013) Influence of Sc concentration on power generation figure of merit of ScAlN thin films. Appl Phys Lett 102:021915

Chapter 2
Lead Zirconate Titanate (PZT) for M/NEMS

Ronald G. Polcawich and Jeffrey S. Pulskamp

2.1 PZT Thin Films

This section concentrates on the leading ferroelectric material used in thin-film piezoelectric MEMS: lead zirconate titanate ($PbZr_xTi_{1-x}O_3$) or PZT. PZT-based MEMS technology has been explored extensively for a variety of actuator applications [1] but has received less attention for RF MEMS resonator and filter applications. Despite the long and successful history of bulk PZT resonators [2], the process complexity/compatibility issues and high mechanical losses have discouraged the exploitation of this strong piezoelectric for these applications. However, for select MEMS resonator and filter applications, thin film PZT offers many unique advantages due to the high electromechanical coupling factors, permittivity, piezoelectric stress constants, and the DC-bias electric field dependence of these properties. Significant progress has also been made in developing materials deposition and processing technologies that address the fabrication challenges with PZT thin films. The goals of this section include an analysis of the deposition of these materials, patterning techniques, identification of device design and processing concerns, and finally a detailed subsection covering examples of how PZT thin films have been incorporated into resonant-based devices.

R.G. Polcawich (✉) • J.S. Pulskamp
US Army Research Laboratory, RDRL-SER-L, 2800 Powder Mill Road, Adelphi, MD 20783, USA
e-mail: ronald.g.polcawich.civ@mail.mil

© Springer International Publishing Switzerland 2017

H. Bhugra, G. Piazza (eds.), *Piezoelectric MEMS Resonators*,
Microsystems and Nanosystems, DOI 10.1007/978-3-319-28688-4_2

2.1.1 Deposition

PZT thin films have been successfully deposited by a wide variety of processes with a majority of the early development done through various sputtering techniques with a strong focus on RF or ion-beam deposition using bulk ceramic targets [3–6]. Current research efforts primarily utilize sputtering [7, 8], metal-organic-chemical vapor deposition (MOCVD) [9–11], and chemical solution deposition (CSD) techniques [12–17] with many of the techniques summarized in Table 2.1. Each of these three techniques has and is used in commercial fabrication of PZT-based devices with ferroelectric random access memory (FRAM) initially using either CSD or sputtering and then migrating to MOCVD for ultrathin layers. For PZT-based MEMS devices, CSD and sputtering are both used in commercial production and foundry facilities. PZT deposition methods require strict control of the stoichiometry to prevent nucleation of non-ferroelectric fluorite and pyrochlore structures [18, 19]. Furthermore, lead oxide (PbO) becomes highly volatile above 500 °C, so one must take care to provide enough excess lead to compensate for lead loss through the release of PbO during any high-temperature processing and annealing [20].

A variety of substrates can be used for PZT deposition. However, there are requirements for both the substrate and metallization layers. Growth of PZT is strongly nucleation controlled, and with proper control of the nucleation, crystal orientation of the film can be manipulated [21, 22]. Single-crystal substrates (i.e., MgO, $SrTiO_3$) can be used to nucleate epitaxial, single-crystal PZT thin films [23].

For most MEMS applications, silicon is the substrate of choice. Furthermore, when it comes to resonant devices, PZT is often integrated with silicon-on-insulator (SOI) substrates to couple the high electromechanical coupling of the PZT with

Table 2.1 Deposition methods and parameters for PZT thin films

Deposition parameter	DC sputter (reactive)	RF sputter	MOCVD	CSD
Reference	[7]	[7, 39, 99]	[11]	[15]
Target stoichiometry	Pb, Zr, Ti (3 metal targets)	$Pb_{1.20}(Zr_{0.53}Ti_{0.47})O_3$		
Excess Pb %		20		10 and 30
RF power (W)		100		
Bias (V or W)				
Pressure (Pa or T)		1–2	5 T	
Gas		O_2 (1–3 sccm)	O_2 (1 L/min)	O_2
Deposition rate (nm/min)		10–20	12	
Temperature (°C)	570 Followed by post-dep RTA	550–700	550	RT → 350 → 650

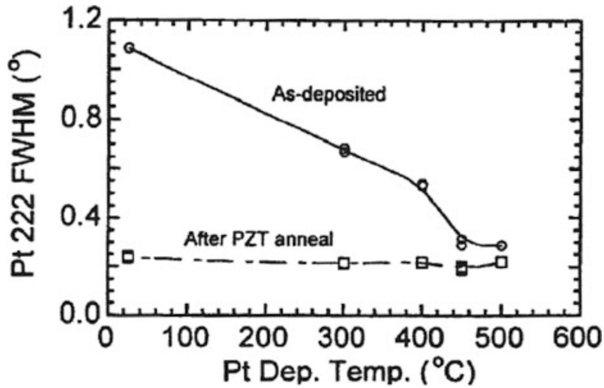

Fig. 2.1 Texture, FWHM of the sputtered Pt (222) peak, as a function deposition temperature and after thermal processing of a PZT film deposited atop the Pt film [24] (Reprinted with permission. Copyright 2004)

the high mechanical quality factor of the single-crystal silicon. When using Si, it is important to prevent the formation of lead silicide at the substrate interface by using buffer layers and/or metal layers. In most instances, a layer of silicon dioxide is used as a buffer layer in combination with a bilayer of TiO_2/Pt to serve as the base electrode for the PZT deposition. With the lattice constant of platinum being close to that of PZT (2–3 % mismatch for c-axis-oriented PZT), Pt can be an excellent template for (111) oriented PZT films as Pt tends to grow with a strong (111) texture. In order to maximize the texture within the Pt, the preferred material stack is SiO_2/TiO_2/Pt [24]. The layer of TiO_2 serves as a buffer layer and template that allows higher degree of texture within the Pt. For detailed information on the method required for achieving highly textured (111) Pt, the readers are directed to Ref. [24] with one of the key figures reproduced in Fig. 2.1. It is noted that although Pt is great at seeding (111) PZT growth, the preferred orientation to maximize the piezoelectric properties of PZT is (001) orientation [22]. Methods of manipulating the texture of the PZT away from (111) orientation when using Pt layers will be discussed later within this section.

There are several metal and/or conducting oxides (i.e., Ru and RuO_2 and Ir and IrO_2) that can be used in place of Pt. These alternative electrodes can exhibit a higher resistance to Pb interdiffusion and thus provide a better barrier. Oxide electrodes are commonly used for the top electrode to reduce ferroelectric fatigue (reduction of switchable polarization with bipolar cycling, especially in excess of the coercive field of the PZT) [25]. Note, ferroelectric fatigue can be mitigated by simply using one of the electrodes as a conductive oxide (e.g., IrO_2 or RuO_2). An additional benefit of IrO_2 electrodes is it can serve as a barrier of hydrogen damage within PZT thin films [26].

Sputter deposition of PZT thin films has been completed through either reactive deposition using three metal targets (Pb, Zr, and Ti) or RF sputtering using ceramic targets. In either case, PZT thin films with excellent ferroelectric and piezoelectric

properties can be obtained. One challenge with sputter deposition is accurate control of the Pb and O content within the films. Lead has a higher sputter yield and higher volatility (i.e., PbO) compared to Zr and Ti. As a result, the lead loss must be compensated with either higher fluxes sputtered from pure Pb targets or excess Pb incorporated in ceramic targets. An additional item of note is the substrate temperature during deposition. The use of high temperatures during deposition results in higher Pb loss and typically requires higher excess lead content targets. If the substrate temperature can be maintained greater than 600 °C, pure perovskite phase PZT thin films can be achieved. Otherwise, a crystallization anneal is required on the sputtered film to convert the deposited layer into the desired perovskite phase.

MOCVD processes for PZT thin films have been researched as a key technology for mass production of ferroelectric random access memory (FeRAM) especially for device architectures requiring exceptional step coverage. For PiezoMEMS applications, there has been limited information reported on the piezoelectric properties of MOCVD-deposited thin films. For a summary of the MOCVD deposition process, readers are directed to Refs. [9] and [11] for more detail.

Chemical solution deposition (CSD) methods for ferroelectric thin films have been developed based on a variety of methods (i.e., sol-gel and metallorganic decomposition) and precursors [27]. The CSD techniques can be categorized into three main groups: sol-gel, chelating process, and metallorganic decomposition [15, 16]. The two most widely used approaches are based on a sol-gel approach using 2-methoxyethanol as a solvent and the inverted mixing order process using methanol as a solvent. Sol-gel methods have been primarily based on the research of Budd, Dey, and Payne in 1985 [12].

With the inverted mixing order (IMO) process, the lead, titanium, and zirconium precursors are combined in the opposite order from those developed in the original sequential addition process by Budd, Dey, and Payne [12, 28, 29]. In addition, the solvent used for the IMO process is primarily methanol with slight additions of acetic acid and deionized water for additional solution stability. The use of methanol instead of 2-MOE enables a less toxic solution preparation and the deposition process for the user [28]. Additionally, a commercial source of solutions is now available through Mitsubishi Materials using a proprietary solvent that is also less toxic than 2-MOE [30]. The PZT-N solution offered by Mitsubishi Materials is currently one of the most widely used solutions within the available foundries.

The most heavily researched processes for the deposition of PZT films use 2-MOE as a solvent and lead acetate trihydrate, titanium isopropoxide, and zirconium n-propoxide as the precursors [12, 31, 32]. This process has been used to produce PZT films with the highest piezoelectric coefficients to date. A general version of the 2-MOE-based solution process flow is highlighted in Fig. 2.2. To begin, the lead precursor (lead acetate trihydrate) is dissolved in 2-MOE followed by vacuum distillation to remove the water. The dehydrated lead acetate is allowed to redissolve in a portion of the 2-MOE solvent before being mixed with Zr and Ti precursors. Prior to being added to the lead precursor, Zr and Ti precursors are mixed in the desired stoichiometric ratio at room temperature with 2-MOE. The combined solution is refluxed for two to three hours at 120 °C

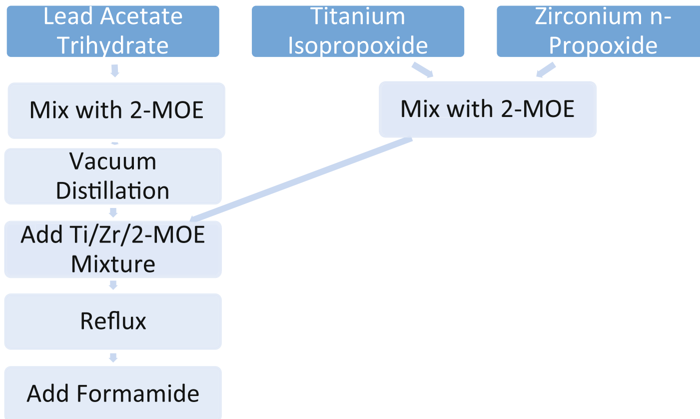

Fig. 2.2 Schematic process flow for creating a 2-MOE-based solution for PZT thin films

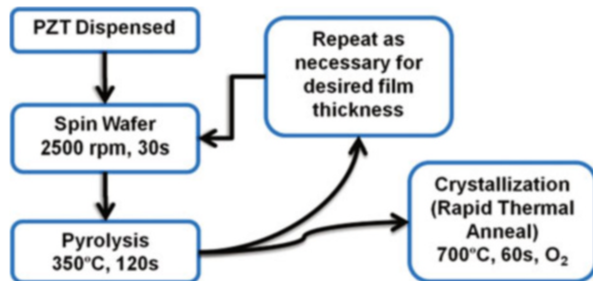

Fig. 2.3 Deposition and thermal treatment process flow for chemical solution deposition of PZT thin films based on a 2-methoxyethanol solvent system

using a rotary evaporator or comparable setup. Next, the solution undergoes a short vacuum distillation to remove a small amount of reaction by-products and adjust the concentration, typically 0.4 M. The final step is to add 4 volume percent of formamide, which serves as a drying control agent [33]. Additionally, a small percentage of acetylacetate may be added to the solution to assist in the long-term stability of the solution [34].

Regardless of the solution chemistry, the deposition processes are quite similar and graphically represented in Fig. 2.3. The only discrepancies are minor changes to the pyrolysis temperature or the crystallization temperature. Using automated solution coating machines (similar to those developed for photoresists), the deposition process usually begins by prefiltering the solution into the deposition canisters or syringes. The solution is statically dispensed onto the substrate and then spun to achieve a uniform film thickness across the substrate. Following the spin, the film is pyrolyzed on a hot plate to remove the volatile organics. The spin and pyrolysis steps are repeated as required (i.e., one to four layers) prior to the crystallization anneal in flowing oxygen. Using a 0.4 M solution, a four-layer spin process typically yields a final film thickness close to 0.25 μm. The process is continuously repeated until the desired film thickness is achieved.

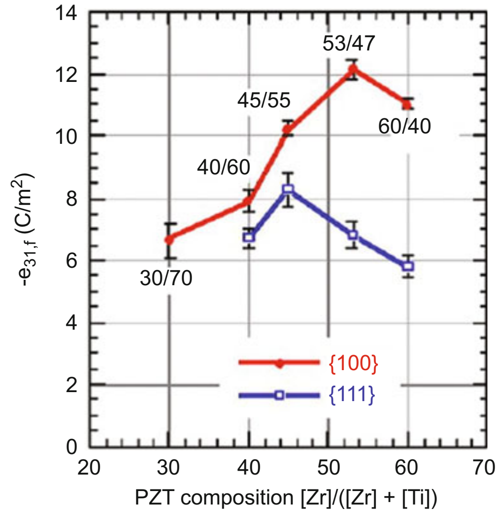

Fig. 2.4 Transverse piezoelectric stress constant, $e_{31,f}$, of a 1 μm PZT thin film as a function of Zr/Ti ratio for both (100)/(001) and (111) oriented thin films [22, 23] (Reprinted with permission. Copyright 2003, Elsevier)

Regardless of deposition method, there are several key material parameters with which to judge the quality of the PZT thin film. The first is the crystalline quality of the film via X-ray diffraction (XRD). The best quality piezoelectric films will possess a high degree of texture in the (100)/(001) orientation (see Fig. 2.4). The easiest method of assuring a high degree of (100) texture is through templating the nucleation and growth with a $PbTiO_3$ seed layer and proper attention to the amount of excess lead present during any high-temperature annealing or crystallization processes [21, 33, 35]. An example XRD pattern of a highly textured CSD PZT thin film is shown in Fig. 2.5.

Optimizing material quality and properties requires controlling the stoichiometric gradients through the thickness of the PZT film. Figure 2.6 illustrates the importance of controlling these gradients, as these gradients represent deviations of the average properties of the film from the intended composition. As stated earlier, PZT films are strongly nucleation controlled. With heterogeneous nucleation occurring at the electrode interface, Ti-rich compositions nucleate first [21]. The end result is a sawtooth Zr/Ti gradient through the PZT thickness with a Ti-rich layer at the electrode interface and a Zr-rich layer at the film surface (see Fig. 2.6) [15]. To compensate for the gradient, Calame and Muralt developed a process to reduce the gradient by manipulating the stoichiometry of each of the four CSD layers (63, 58, 48, and 43 % Zr content) deposited prior to the crystallization step [15]. As shown in Fig. 2.6, the average composition through the entire 2 μm thickness closely resembles the MPB desired composition of 53/47. Alternatively, recent work has demonstrated gradient-free films using process optimization with a ZnO buffer layer beneath a Pt electrode layer [36, 37].

For comparison, a list of the material properties achieved for each deposition method has been compiled in Table 2.2. Note, that quite often, the ferroelectric property, namely, the remnant polarization, is similar for the different techniques.

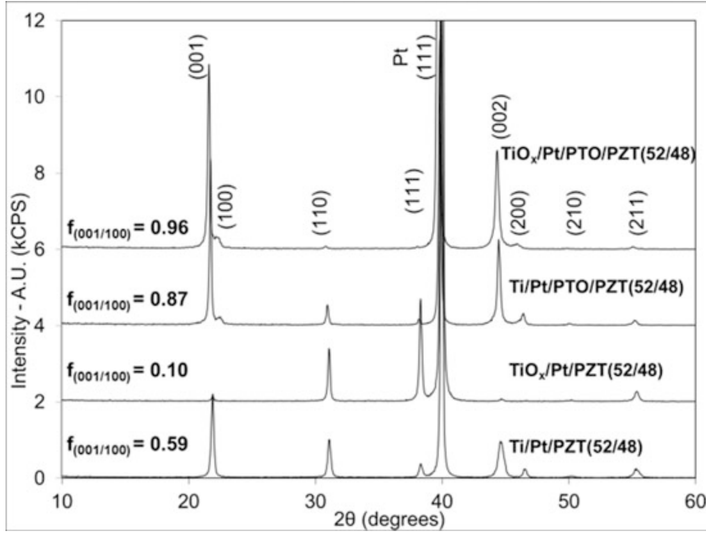

Fig. 2.5 Θ–2Θ X-ray diffraction pattern for PZT (52/48) thin films (∼0.5 μm) using a $PbTiO_3$ seed layer to promote a highly textured (100) orientation [36] (Reprinted with permission. Copyright 2013 MRS).

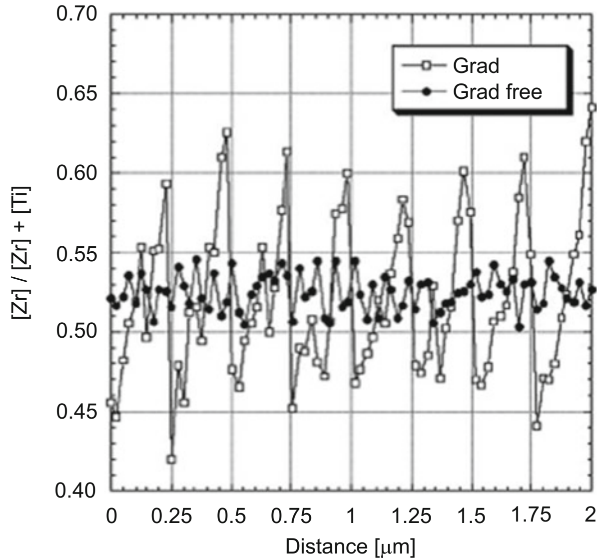

Fig. 2.6 Zr content in two different PZT (53/47) films, one with a standard 2-MOE process using a crystallization anneal every four layers and the other using an optimized process to reduce the Zr/Ti gradient in the film [15] (Reprinted with permission. Copyright 2007 American Institute of Physics)

Table 2.2 Material properties as a function of deposition method

Technique	Stoichiometry (Zr/Ti)	P_r (μC/cm^2)	E_c (kV/cm)	$e_{31,f}$ (C/m^2)	d_{33} (pC/N)	ε_{33}	tan δ	Ref.
Sputter-RF magnetron	50/50	22–26	40–50	−25.1	100	800–1200	0.02	[7, 100]
CSD (N-PZT)	53/47	26.2	43.3					[29]
CSD (2-MOE)	53/47			−12.0	85	1180	0.029	[33]
				−17.7		1650	0.023	[15]

Table 2.3 Etch parameters for PZT thin films

Etching parameter	ECR-RIE	ICP-RIE	ICP-RIE	Wet	Ar ion mill
Reference	[46]	[48]	[49]	[43]	[101]
RF power (W)	10–200	400–800	500–800		150
Bias (V or W)	100–1000 V	100–400 V	200–350 V		36 V
Pressure (Pa or mT)	5e^{-4} to 1 Pa	1–10 mT	0.1–2.0 Pa		0.7 mT
Gas(es)	CCl_4, CF_4, Ar	Cl_2/C_2F_6/Ar	BCl_3:Ar Cl_2:Ar	BOE:2HCl:4NH_4Cl: 4H_2O +2HNO_3 :H_2O	Ar
Etch rate (nm/min)	20–95	100–180	63–193	960	25
Resist selectivity (PR/PZT)	3:1–13:1	1.5–3:1	3–6 :1	1.5:1	1:1

However, the piezoelectric coefficients tend to be higher in the highly textured, gradient controlled CSD techniques.

2.1.2 Patterning Techniques

Patterning PZT thin films along with many other ferroelectrics remains one of the more challenging aspects of incorporating these compounds with MEMS. Not only are these compounds rather difficult to etch and pattern, but contamination from the heavy metal elements, especially lead, poses additional problems for most clean rooms. Specific to PZT, regardless of the Zr/Ti ratio, this material can be etched with all of the common etching techniques including wet processing, electron cyclotron resonance-based reactive ion etching (ECR-RIE), inductively coupled plasma (ICP)-based RIE, and ion milling as indicated in Table 2.3.

Wet etching techniques remain one of the easiest solutions to patterning PZT especially when selectively stopping the etch on a platinum electrode. However, this technique is limited to larger areas (several microns to tens of microns) because most etch chemistries are highly isotropic or can even have faster lateral etch rates.

Typical chemistries involve mixtures of hydrochloric (HCl) and hydrofluoric (HF) acids resulting in combinations of fluorine- and chlorine-containing by-products [38–40]. One of the most common chemistries with relatively high etch rate and excellent selectivity to platinum is a mixture of deionized H_2O:HCl:HF (2:1:0.05). The HCl acid is used to remove lead and titanium, while the HF is used to remove titanium and zirconium. One problem that can occur with this etch combination occurs in films with excess lead where a white powdery lead residue remains on the wafer surface [42]. This lead-rich residue can be removed by adding small amounts of ammonium chloride and/or nitric acid to the solution [42]. Note that this etchant has a lateral etch rate nearly 2–3 times that of the film thickness.

Chemical and physical etching via reactive ion etching (RIE) and ion milling can provide the necessary dimensional control necessary for creating MEMS and NEMS structures. Similar to the wet etch chemistry, reactive ion etch techniques utilize combinations of fluorine- and chlorine-containing compounds (such as CF_4 and CCl_4) [19, 41–43]. A major challenge with a purely chemically based RIE is the extremely low volatility of the Zr and Ti by-products, namely, ZrF_4, $ZrCl_4$, TiF_4, and $TiCl_4$. To counter, the most successful etching techniques use combinations of RF-bias power in excess of 50 W, low pressures (<0.1 Pa), and elevated temperature. One leading technique is to etch the PZT in an electron cyclotron resonance/radio frequency (ECR/RF) reactor with 40 % CCl_4, 40 % CF_4, and 20 % Ar gases [19]. As shown in Fig. 2.7, thistechnique can achieve etching rates approaching 100 nm/min using 100 W_{RF} operating at a pressure of 1 mPa. Another chemistry for RIE is outlined by the ferroelectric random access memory (FRAM) community using

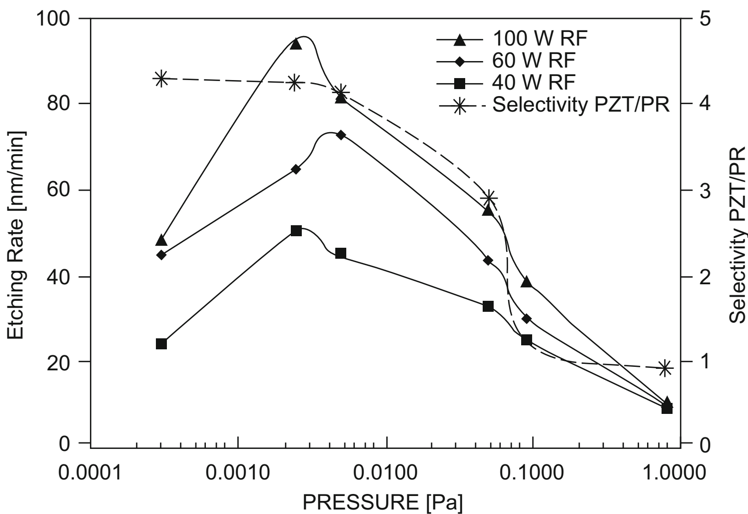

Fig. 2.7 Etching characteristics of PZT thin films as a function of processing pressure using an electron cyclotron resonance/radio frequency (ECR/RF) reactor [98] (Reprinted with permission. Copyright 2000)

inductively coupled plasma (ICP) RIE reactors with 70 % BCl_3 and 30 % Ar gas [44–46]. In addition to etching PZT layers, RIE can be used to etch the electrode layers such as Pt, RuO_2, and IrO_2. In general, the leading etch chemistries use chlorine-containing gases such as Cl_2, CCl_4, and BCl_3 with the etch mechanism being mostly physical in nature [19, 47–49].

The two biggest challenges with a chemical RIE approach to patterning PZT are controlling redeposition of the nonvolatile etch by-products and achieving the necessary resist selectivity. Processing at higher temperatures and using low pressures combined with high-throughput vacuum pumps increase the percentage of the by-products remaining in the gaseous phase. However, increasing the temperature causes severe resist degradation or even carbonization of the photoresist. As a result a hard mask needs to be employed. Further evidence of this is shown in Figs. 2.7 and 2.8 where resist selectivity dramatically decreases with increases in processing pressure or incident ion energy or RF bias. Resist degradation is yet another challenge with RIE etches of PZT. To preserve the resist integrity, any masking must be done with either hard-cured photoresist or hard masks to avoid degradation in soft-cured photoresist. Early work on hard masks included TiO_2 coatings with the FRAM community moving toward TiN or TiAlN coatings [49, 50]. The use of hard coatings enables a single mask layer etching process to etch the entire capacitor (electrode/PZT/electrode) (see Fig. 2.9). The same process can be used for MEMS actuators. However, care must be taken to account for the elevated voltages (electric fields) that the actuators require compared to that of FRAM. The gap separation between the two electrode layers is defined by the PZT thickness. Because this separation can be in the range of 0.25–2 μm, breakdown across the air gap becomes

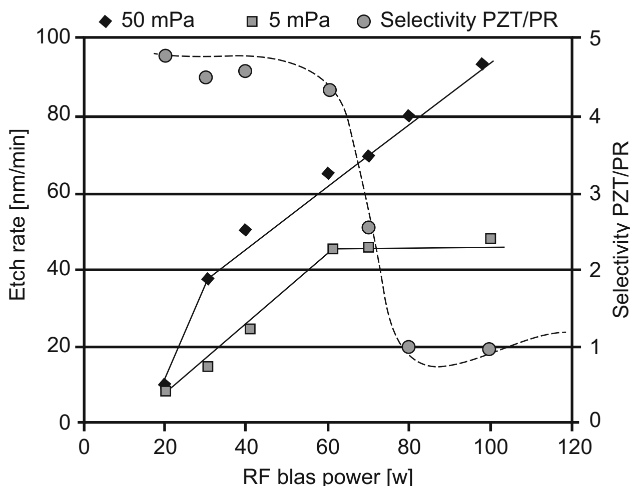

Fig. 2.8 Etching characteristics of PZT thin films as a function of RF-bias power using an electron cyclotron resonance/radio frequency (ECR/RF) reactor [54] (Reprinted with permission. Copyright 2000)

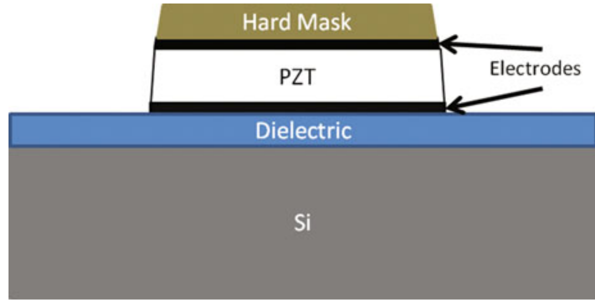

Fig. 2.9 Cross-sectional image/schematic of an FRAM capacitor (Ir/IrOx/PZT/IrOx/Ir) patterned using a single-layer hard-etch mask of TiAlN

Fig. 2.10 Schematic cross section of PZT stack actuators patterned using (**a**) a single-etch process and (**b**) a multiple-step etch process.

a concern during device operation. For example, actuators comprised of a 0.5 μm PZT film with Pt electrodes fabricated with a single-etch process have breakdown voltages on the order of 10 V (~200 kV/cm). In contrast, employing a multiple-step etching (see Fig. 2.10) process to define the top electrode and the actuator separately increases the breakdown voltage for a 0.5 μm thick PZT actuators to approximately 100 V (~2000 kV/cm). This effect is primarily due to the fact that the PZT overlap required for the multistep etch/masking process increases the distance between the top and bottom electrodes. Alternatively, an interlayer dielectric coating such as an atomic layer deposited coating of alumina (Al_2O_3) can be employed to also mitigate breakdown across the air gap between the top and bottom exposed electrodes.

The final method of patterning PZT thin films is through a physical etch using Argon ion milling. Although this technique does not provide any significant selectivity to photoresist, PZT, or the electrode layers, it has several key advantages including the ability to etch the entire metal/PZT/metal stack and variable control of the angle of incidence [51]. For hard-to-etch compounds, especially materials with low volatility such as PZT and Pt, the accelerated Ar ions can be used to break the atomic bonds, while the variable angle control is used to push free atoms away from the wafer surface. Furthermore, the angle of incidence can be altered during the final stages of the etching to remove any redeposited materials. Similar to the chemical-based RIE procedures, the masking material for the ion mill must either be hardened photoresist or a hard mask as ion damage and redeposited heavy metal ions prevent clean removal of a soft photoresist. Although the ion mill generally has poor selectivity and a difficulty to accurately endpoint on the desired layer, an ion mill reactor can be configured with a secondary ion mass spectrometer (SIMS)

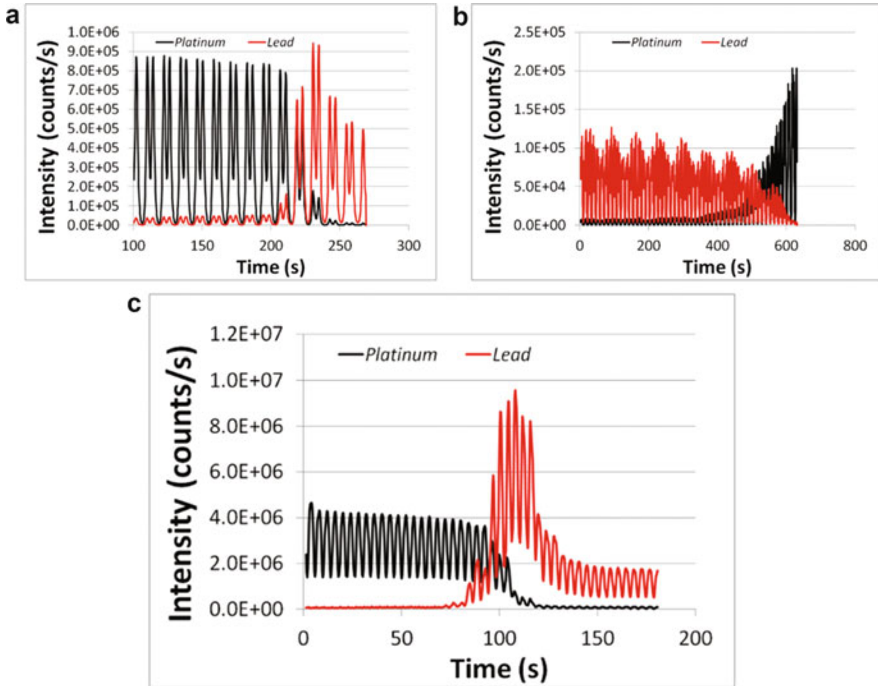

Fig. 2.11 Examples of using SIMS endpoint detection in conjunction with ion milling of (**a**) Pt etching and stopping on a PZT thin film using the falling edge of Pt, (**b**) etching PZT and stopping on a Pt thin film using the rising edge of Pt, and (**c**) etching PZT and Ti/Pt stopping on the underlying SiO_2 using the falling edge of Pt. Note the double peaks in the SIMS signal are the result from monitoring two substrates that are rotated under the beam during the etching process

endpoint detection system. The SIMS system analyzes the etched material as it is removed from the wafer surface and yields an accurate depiction of the depth of the current etch. An example of the endpoint detection is illustrated in Fig. 2.11 for a sample etching the top Pt electrode stopping on the PZT and for a sample etching the PZT and stopping on the bottom Pt electrode.

2.1.3 Device Design Concerns

An area of concern for PZT-based MEMS devices is degradation in the material properties during the device fabrication. The research on ferroelectric random access memory (FRAM) has advanced the understanding of the leading degradation mechanisms including ion damage, H_2 damage, and surface contaminants [52, 53, 55]. In many instances, the manifestation of damage in the PZT can be observed through characterization of the ferroelectric and dielectric properties. In cases where

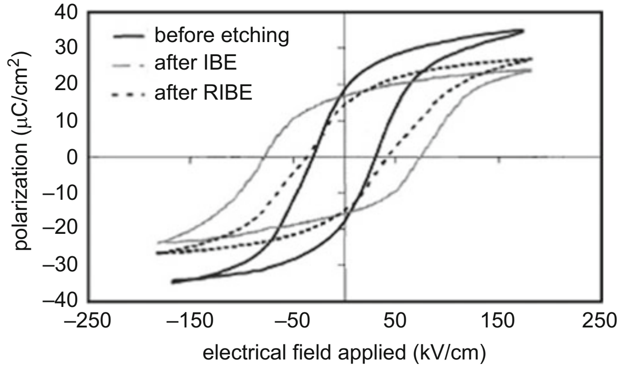

Fig. 2.12 Change in the polarization electric field hysteresis loop observed for virgin (before etching) PZT thin films, for a PZT film exposed to ion milling (after IBE), and for a PZT film exposed to a reactive ion etch (after RIBE). For both etched samples, the testing was done after depositing and annealing a top Pt electrode layer on the etched surface [56] (Reprinted with permission. Copyright 2005 American Institute of Physics)

the PZT surface is exposed to etch conditions and then electroded, reductions in the remnant polarization, increases in the coercive field, and decreases in the dielectric constant are observed resulting from the creation of a damaged surface layer lying beneath the top electrode (see Fig. 2.12) [55, 56]. The presence of the damaged surface layer is severely detrimental to the performance of the PZT, and consequently the preferred process deposits and patterns the top electrode onto the as-deposited, pristine surface of the PZT film.

For piezoelectric devices patterned after the top electrode has been deposited, degradation remains a potential problem. The PZT sidewalls are damaged during the patterning process and can introduce defects into the material. More importantly, exposure to H_2 through contact with the hydrocarbons in photoresist and forming gas anneals introduces protons in the PZT via diffusion, adversely affecting the ferroelectric and dielectric properties through domain pinning. Additionally, the feature size of the active device area can play a significant role in the degree of damage that exists in the PZT layer [54].

Regardless of the damage created by processing, in most instances the ferroelectric and dielectric properties can be recovered using a thermal anneal. To approach full recovery, the anneal must be done above the Curie temperature of the ferroelectric (e.g., T_c (PZT) ∼365 °C). An example of how effective the recovery anneal can be is shown in Ref. [55]. In this example, the material properties are recovered to the initial conditions using a 500 °C anneal (Fig. 2.13).

Another key aspect with PZT devices is the aligning of the ferroelectric domains or poling. Unlike the pure polar materials discussed previously (i.e., AlN and ZnO), the polarization in ferroelectric materials can be configured in a multitude of orientations. In order to optimize the piezoelectric coefficient of the PZT, the ferroelectric domains need to be aligned in a single preferred direction. For an

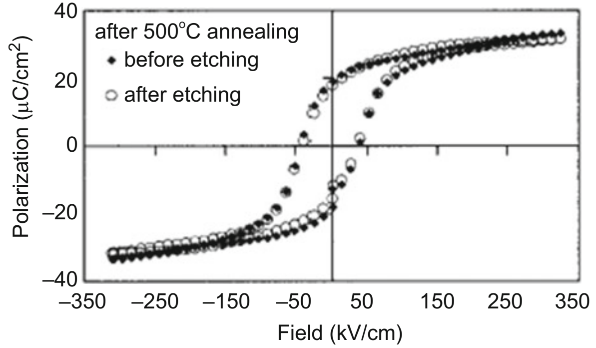

Fig. 2.13 Illustration of how high-temperature annealing can be used to recover the ferroelectric properties of PZT thin films after damage induced by the patterning process [55] (Reprinted with permission. Copyright 2002 American Institute of Physics)

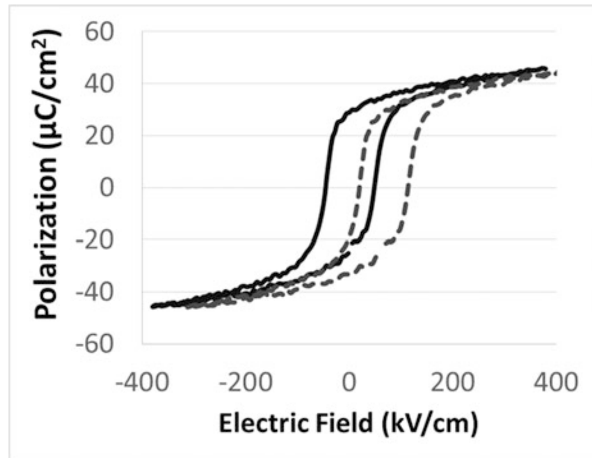

Fig. 2.14 Example of imprint in a ferroelectric illustrated by a shift in the polarization electric field response of the material

actuator in a parallel plate configuration (d_{31} mode), the poling direction is along the film thickness. The most direct method of poling is the application of an electric field nominally 3–4 times the coercive field for 10–15 min (i.e., 10–15 V for a 0.5 μm thick film). With respect to resonators and especially filters, the poling process post-fabrication can be a concern especially with very complicated device and circuit topologies. One possible approach that is of interest is to use heavily imprinted PZT films such that they are poled following the fabrication process. Imprint is defined as the presence of a strongly preferred polarization direction in a ferroelectric material such that the ferroelectric and piezoelectric hysteresis loops are shifted laterally along the electric field axis (see the example in Fig. 2.14). Essentially, the film has an internal bias field acting upon the polar domains resulting in a preferred orientation. If the imprint can be pushed toward extreme levels pushing toward and beyond the coercive field, the film will essentially always be in a preferred polarization state and achieving a near-optimal piezoelectric coefficient. An additional benefit especially for resonant devices is that the dielectric constant and dielectric loss are reduced under these internal biasing conditions enabling reduced parasitic capacitances and reduced loss in the devices.

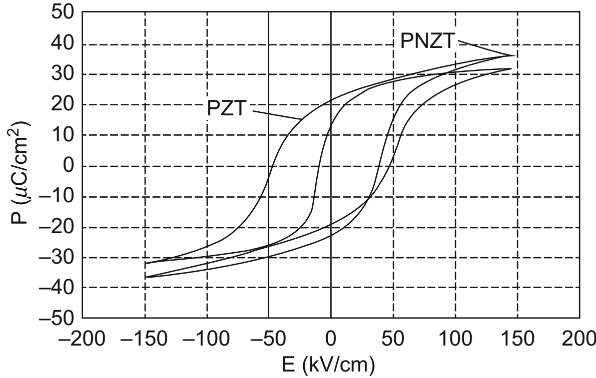

Fig. 2.15 Example of imprint in sputter deposited Nb-doped PZT (Reprinted with permission. Copyright FUJIFILM Corporation 2014) [25]

Imprint techniques fall essentially into two categories: in situ controlled and post-processed. In situ controlled are typically limited for use with sputtered films where the bombardment conditions can be refined to control the adatom mobility and manipulate the growth strains as well as the local defect chemistry (i.e., oxygen vacancies). An example of the imprint achieved in sputtered PZT is illustrated in Fig. 2.15. In contrast, post-processing imprint can be employed on films deposited by many methods and include thermal poling and exposure to ultraviolet radiation consisting of a wavelength smaller than the absorption bandgap of the material (i.e., approximately 365 nm for PZT [55]). With thermal poling, the electric field for poling is applied while the PZT is held at temperatures approaching half of the Curie temperature or higher, nominally 125–150 °C. Generally, thermal poling procedures have a longer duration and stability compared to the UV-assisted poling procedures.

2.1.4 PZT-Based Resonant Devices

Table 2.4 includes select published results for PZT MEMS resonators since 1997 [56–71], and Fig. 2.16 plots the corresponding center frequencies versus the year the results were obtained. As highlighted in Fig. 2.16, PZT thin film for SAW and FBAR resonators was investigated during the late 1990s and early 2000s for cell phone RF filtering [70–75]. k_t^2 values as high as 35 % were demonstrated in PZT FBARs [71]; however, the poor quality factor performance of these devices (<237) resulted in inferior filter performance. PZT MEMS flexure-mode resonators [73] were also first investigated during this time. Since the late 2000s, several groups have explored PZT contour-mode resonators with much of the research motivated by certain defense applications at lower frequencies (<500 MHz).

Table 2.4 Representative published results for PZT MEMS resonators

Ref.	Year	Type	f_c (MHz)	k_{eff}^2 (%)	Max $\|S_{21}\|$ (dB)	Q_m	R_m (Ω)	Method and composition	Material stack	FOM
[60, 61]	2016	Z-flexure	22	1.41 %	1.4	1856	3.3	Sol-gel 52/48	0.5 μm PZT/10 μm Si	26.5
[60, 61]	2016	Z-flexure	22	2.10 %	1	815	9	Sol-gel 52/48	0.5 μm PZT/10 μm Si	17.5
[60]	2016	Contour	56	8.15 %	2.7	289	8.5	Sol-gel 52/48	0.5 μm PZT on 1 μm SiO_2	25.6
[60]	2016	Contour	10.7	0.05 %	8	6575	143	Sol-gel 52/48	0.5 μm PZT/10 μm Si	3.3
[62]	2016	Contour	10.7	0.48 %	1.7	3000	16	Sol-gel 52/48	0.5 μm PZT/10 μm Si	14.5
[63]	2013	Contour	15	3 %	2.1	541	11	Sol-gel 52/48	0.5 μm PZT/2 μm Si	16.7
[63]	2013	Contour	15.9	0.85 %	5.1	738	101	Sol-gel 52/48	0.5 μm PZT/4 μm Si	6.3
[63]	2013	Contour	18.9	0.38 %	3.7	2850	23	Sol-gel 52/48	0.5 μm PZT/10 μm Si	10.9
[64]	2013	Contour	382	–	–	–	542	Pulsed laser	0.5 μm PZT/3 μm Si	–
[65]	2010	Contour	834	–	12	314	296	Sol-gel 52/48	0.5 μm PZT/3 μm Si	–
[66]	2009	FBAR	790	10 % k_t^2	–	52	8.2	Sol-gel 53/47	2 μm PZT	4.0
[67]	2008	Contour	21	–	5	2023	50	Sol-gel 52/48	0.5 μm PZT/10 μm Si	–
[67]	2008	Contour	20	–	10	148	207	Sol-gel 52/48	0.5 μm PZT/0.5 μm SiO_2	–
[68]	2008	FBAR	3724	52.7 % k_t^2	–	114	–	Sputtered 45/55	–	68.8
[69]	2008	Contour	15.9	–	–	5040	167	CSD: Sol-gel	0.5 μm PZT/10 μm Si	–
[70]	2004	FBAR	2000	9 % k_t^2	–	220	–	Sputtered 58/42	0.35–0.43 μm PZT	15.1
[71]	2004	FBAR	600	35 % k_t^2	–	45	–	Sol-gel 30/70	2.3 μm PZT	15.0
[71]	2004	FBAR	1100	17 % k_t^2	–	125	–	Sputtered 40/60	1.4 μm PZT	17.3
[71]	2004	FBAR	2100	22 % k_t^2	–	30	–	MOCVD 30/70	0.4 μm PZT	5.6
[72]	2001	FBAR	1581	19.1 % k_t^2	–	53	–	Sol-gel 30/70	0.8 μm PZT	8.4
[74]	2001	SMR	900	25 % k_t^2	–	67	–	Sol-gel 35/65	1.3 μm PZT	14.6
[75]	1997	FBAR	1700	9.6 % k_t^2	4	237	–	Sol-gel 52/48	0.8 μm PZT	17.4

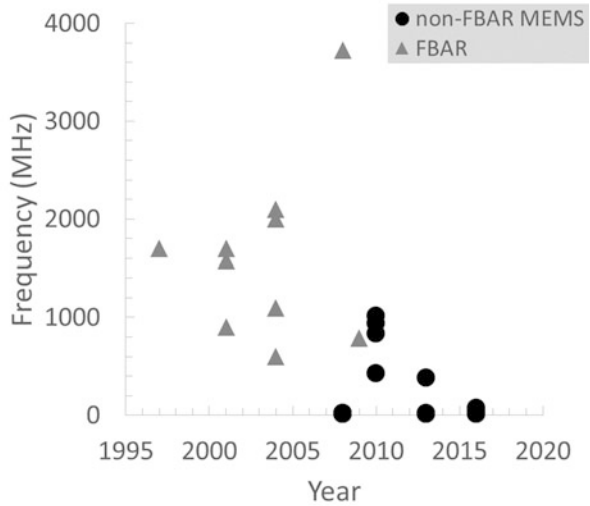

Fig. 2.16 Select published results for PZT MEMS resonators since 1997; resonator center frequency versus the year the results were obtained

The unique capabilities of thin film PZT MEMS resonators arise from the high electromechanical coupling factors, permittivity, piezoelectric stress constants, and the DC-bias electric field dependence of these properties. The very high piezoelectric coefficients of thin film PZT enable strong electromechanical coupling despite the relatively large dielectric constants. PZT bulk ceramics vary in electromechanical coupling with composition, but typical quasi-static material values at low electric field are 48 % k_{33}^2, 22 % k_t^2, 12 % k_{31}^2, and 39 % k_p^2 [74]. The subscripts for the electromechanical coupling are related to the directions of electrical and mechanical quantities. For k_{33}, the polarization and vibration are along the same direction (i.e., the 3 direction in this case) and as an example consider a ceramic rod polarized along its length and electrode at the ends. Related to k_{33} is k_t, which is used in cases where the surface area of device is substantially larger than its thickness. In cases where the polarization direction and vibration direction are orthogonal to one another, the k_{31} term is appropriate where the polarization is along the three directions. Finally, k_p is associated with discs with the polarization in thickness direction (i.e., 3 direction) and the mechanical vibration in the in-plane radial directions (i.e., 1 and 2). There are limited published results for thin film PZT quasi-static material coupling factors due to the difficulties in directly measuring these properties. However, k_{31}^2 values as high as 29.8 % [22] (based on permittivity and piezoelectric coefficient measurements and assuming s_{11}^E from [75]) and 27.9 % [79] (based on micro-tensile specimen testing of s_{11}^E and s_{11}^D) have been reported for low electric fields. The larger values for thin film PZT can be explained by the fact that thin-film piezoelectric properties have been shown to exceed those of bulk ceramic material [33], and the reported coupling factors for bulk material k_{ij}^2 are not identical to the effective film value. The film clamping effect [22] responsible for the discrepancy between e_{31} and the larger $e_{31,f}$

constants also influences the electromechanical coupling, resulting in an effective film coupling value that can exceed the bulk material k_{ij}^2. The film clamping serves to enhance electromechanical coupling through the participation of additional piezoelectric coefficients in transduction. The largest electromechanical coupling factor reported with thin film PZT was achieved with a 3.7 GHz FBAR resonator with sputtered 45/55 PZT that exhibited a k_t^2 of 52.7 % and a $k_t^2 Q_m$ product of 57 [68]. For contour-mode MEMS resonators, a k_{eff}^2 of 8.2 % was achieved with a 0.5 μm PZT on 1 μm silicon dioxide/silicon nitride multilayer operating at 56 MHz with a Q_m of 289 [60] and motional resistance of 9 Ω.

The strong electromechanical coupling and high dielectric constants of PZT enable very compact filters, facilitating the design of resonators and filters for appropriate port impedances to avoid matching network losses, parasitic capacitance sensitivity, and large voltage swings [76]. High performance is also possible with direct 50 Ω termination without the need for any external matching networks [60]. The size of commercially available acoustic filters such as quartz and SAW at HF to low-UHF frequencies is rather large, and the performance of SAW filters is significantly degraded relative to higher frequencies. The size of impedance matching components at these low frequencies also presents a challenge to realize the benefits of small MEMS filters in large filter banks. PZT is particularly well suited to these low frequencies where high-performance low-loss filters can be directly interfaced with 50 Ω systems without the need for external matching. The size advantage of PZT MEMS filters over SAW filters is illustrated in Fig. 2.17 where a 70 MHz length-extensional 2-pole PZT MEMS filter [60] is seen atop a commercially available 70 MHz SAW filter.

The combination of strong electromechanical coupling and poor mechanical quality factor has led to the development of PZT-on-silicon resonator technology [60–62, 64, 65, 67, 69, 77–84]. PZT-on-silicon resonators (see Fig. 2.18) permit the tradeoff of resonator effective electromechanical coupling, k_{eff}^2, and quality factor while nearly maintaining constant figure of merit (FOM) for similar resonator designs [82]. The largest FOM, non-FBAR PZT MEMS resonators published to date (FOM of 27) have utilized 0.5 μm PZT on 10 μm single-crystal silicon stacks [60, 61]. Trading electromechanical coupling for quality factor with comparable

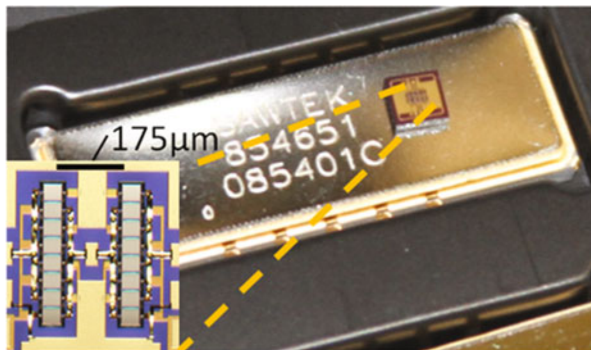

Fig. 2.17 Size comparison between 70 MHz length-extensional 2-pole PZT MEMS filter atop a commercially available 70 MHz SAW filter [60] (Reprinted with permission. Copyright IEEE 2016)

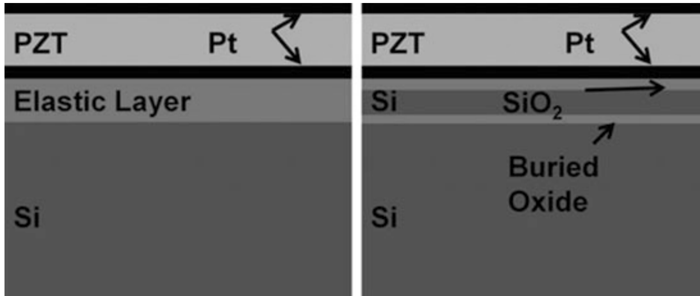

Fig. 2.18 Cross-sectional illustrations of typical PZT (*left*) and PZT-on-single-crystal silicon (*right*). PZT resonators are commonly implemented with various elastic layers, typically silicon dioxide or silicon nitride, and PZT-on-silicon resonators are realized with silicon-on-insulator substrates

figure of merit permits the development of resonators that would otherwise possess insufficient quality factors. Figures 2.19 and 2.20 plot the reported mechanical *Qs* of the resonators from Fig. 2.16 versus the year the results were obtained and center frequency, respectively. The apparent trend of decreasing *Q* versus frequency is interesting but is likely due to recently published high *Qs* at low frequencies with PZT-on-silicon devices. Furthermore, the largest reported FBAR *Q* results are not the lowest frequency devices. The significant improvements in resonator *Qs* since 2008 are largely due to the development of PZT-on-silicon MEMS resonator technology at lower frequencies (<1 GHz). The highest mechanical *Q* reported to date, 6575 in air, was achieved with a 10.7 MHz length-extensional mode and 0.5 μm PZT on 10 μm single-crystal silicon resonator with a k_{eff}^2 of 0.05 % (see Fig. 2.21) [60]. Moreover, PZT-on-silicon technology dramatically improves resonator power handling and linearity [61, 63]. Length-extensional [63] and disc Z-flexural [61] PZT-on-silicon resonators have demonstrated >+10 dBm and >+15 dBm 1 dB compression points at 16 and 22 MHz, respectively. These results compare very favorably to similar AlN MEMS resonators at these frequencies (−15.6 dBm) [85]. The addition of silicon to the resonator also significantly increases the average acoustic velocity that facilitates the design of higher-frequency contour-mode resonators [65].

The very high $e_{31,f}$ constants of PZT thin films enable the integration of RF MEMS acoustic filters with high-performance MEMS actuators such as RF MEMS switches, varactors, and tunable inductors. PZT resonators with and without single-crystal silicon (see Fig. 2.18) have been monolithically integrated with high-performance tunable RF MEMS passives that utilize the state-of-the-art actuation capabilities of PZT MEMS [86–89]. The low-loss and low-parasitic integration of piezoelectric MEMS acoustic filters with varactors and MEMS inductors could enable novel tunable filters via reconfigurable matching networks or facilitate the impedance matching and adjustment of rejection of filters in future complex RF system architectures [80].

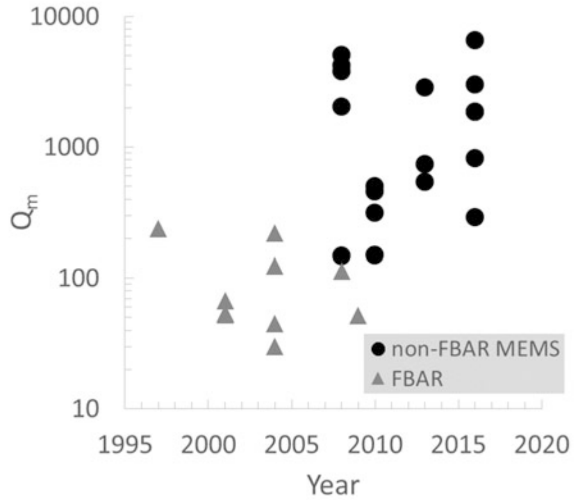

Fig. 2.19 Select published results (see Fig. 2.16) for PZT MEMS resonators since 1997; reported mechanical quality factor versus the year the results were obtained (*semilog plot*)

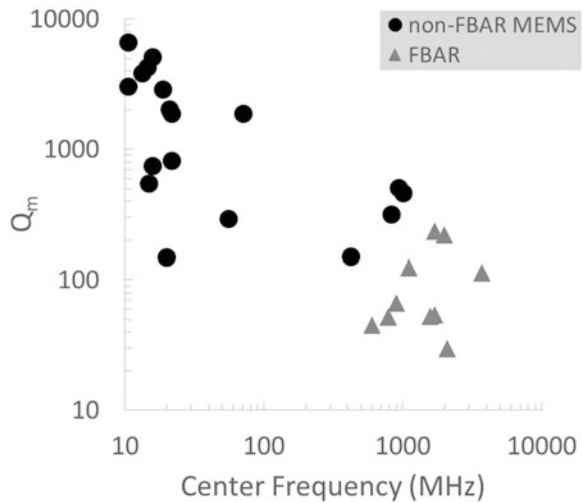

Fig. 2.20 Select published results (see Fig. 2.16) for PZT MEMS resonators since 1997; reported mechanical quality factor versus resonator center frequency (*log-log plot*)

The ferroelectric behavior of PZT induces both high electric field nonlinearity of the permittivity and piezoelectric properties [90]. These nonlinearities are only significant near or above the coercive field (high field) of PZT. High-quality PZT thin films tend to exhibit breakdown strengths that are far larger than those of similar composition bulk ceramic materials. This allows the application of bias electric fields that are many times the coercive field of the material to tune the dielectric constant, piezoelectric coefficients, and coupling factors. The significance is clear when considering the simple 2-port BVD model of a thin film PZT MEMS resonator as illustrated in Fig. 2.22. The DC-bias tuning of the permittivity enables

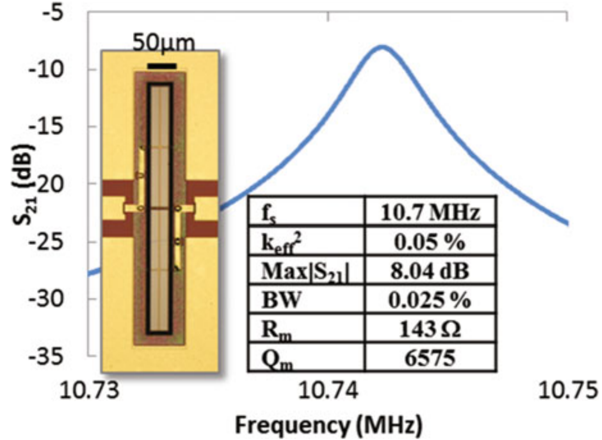

f_s	10.7 MHz
k_{eff}^2	0.05 %
Max|S_{21}|	8.04 dB
BW	0.025 %
R_m	143 Ω
Q_m	6575

Fig. 2.21 Example result of high-*Q* PZT-on-silicon MEMS resonator from [60]. Measured frequency response of a 10.7 MHz gold-laced, length-extensional resonator when biased at 15 V. The device utilizes a 0.5 µm, 52/48, CSD sol-gel PZT film on 10 µm silicon (Reprinted with permission. Copyright IEEE 2016)

the static capacitances of the resonator to function as solid-state varactors. The tuning of the material electromechanical coupling factors result in tunable motional resistance, inductance, capacitance, and resonator effective coupling. The mobility and polarization switching of ferroelectric domains of the material, at high fields, lead to electric field dependence of the permittivity as illustrated in Fig. 2.23. Figure 2.23 plots the unipolar responses of the k_{33} dielectric constant and dielectric loss tangent for increasing and decreasing DC electric fields applied to a 0.5 µm, 52/48, CSD sol-gel deposited PZT film. The permittivity and loss tangent at high fields generally decreases as a result of a reduction in the number of domains not aligned with the applied field and the reduced movement of domain walls due to the bias electric field. It should be noted that while the dielectric loss of thin film PZT is commonly reported at low electric fields, significant improvements in the loss tangent, and hence the equivalent series resistance of resonator shunt capacitance, can be obtained with DC bias. The switching and wall mobility of non-180° domains (i.e., ferroelastic) result in both changes in polarization and strain. These processes tend to be nonlinear and hysteretic as well. At very large electric fields, electrostriction can also contribute to the strain response. All of these effects result in electric field dependence of the piezoelectric coefficients of PZT as illustrated in Fig. 2.24 for the same material plotted in Fig. 2.23. The tuning of both permittivity and piezoelectric coefficients leads to the tuning of the material electromechanical coupling factors. Figure 2.24 also plots the extracted $k_{31}{}^2$ from the $e_{31,f}$ and k_{33} results plotted in Figs. 2.23 and 2.24, assuming the measured dielectric constant is clamped and utilizing the $s_{11}{}^E$ from [79]. The material coupling is seen to be highly dependent on the bias voltage. The particularly low coupling and piezoelectric constants in this example at low electric fields are not representative of most thin film PZT. Many groups have demonstrated the DC-bias tunability of PZT MEMS resonators. Center frequency tuning of 5.1 % was demonstrated in contour-mode resonators in [67] as shown in Fig. 2.25. The tuning of both series and parallel resonance frequencies of a PZT FBAR [66] is shown in Fig. 2.26. DC bias was used

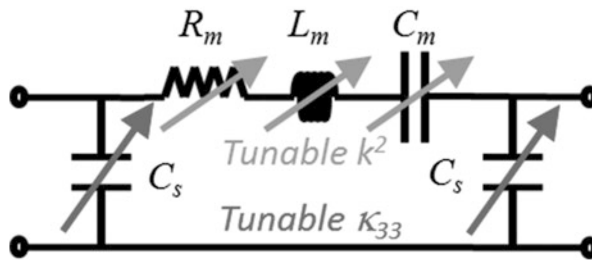

Fig. 2.22 Simplified equivalent circuit of thin film PZT MEMS two-port resonator highlighting effect of tunable material electromechanical coupling and permittivity. The static capacitances of the piezoelectric behave as varactors, and the motional *R*, *L*, and *C* also tune with DC-bias voltage

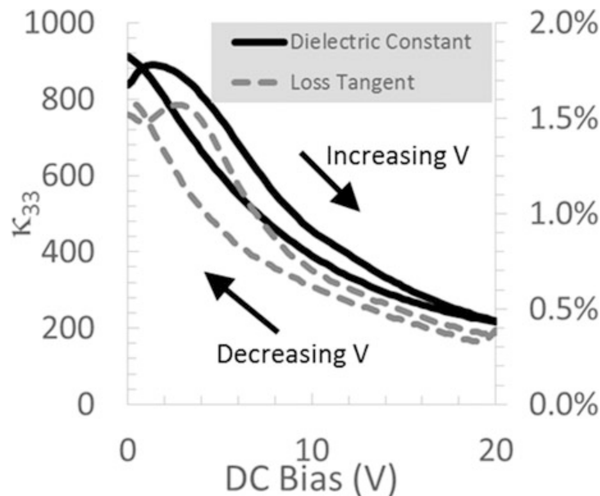

Fig. 2.23 Unipolar responses of the k_{33} dielectric constant and dielectric loss tangent for increasing and decreasing DC electric fields applied to a 0.5 μm, 52/48, CSD sol-gel PZT film

to tune the bandwidth of a low-loss 22 MHz out-of-plane disc flexure PZT-on-Si resonator array (see Figs. 2.27 and 2.28) [60, 61]. The bandwidth and maximum S_{21} vary from 24.3 kHz/16.8 dB at 1 V bias to 240 kHz/1.0 dB at 14 V bias. For bias voltages between 7 and 14 V, the bandwidth varies by a factor of 1.7× for a variation of max S_{21} from 1.0 to 1.4 dB. Furthermore, ferroelectric-based MEMS resonators can be depoled by applying the coercive field that is the opposite of the current remnant polarization state resulting in an "off-state" for the resonator by tuning the material electromechanical coupling to zero.

Contour-mode and FBAR PZT MEMS resonators have been utilized to demonstrate filters [60, 64, 72, 90, 91]. An example result of a 10.8 MHz PZT-on-silicon 2-pole IF filter is shown in Figs. 2.29 and 2.30 [60]. Figures 2.29 and 2.30 display the wideband and narrowband measured S_{21} and S_{11} responses, respectively. The filter design is based on a self-coupled design [92] utilizing 0.5 μm PZT (52/48 sol-gel) on 10 μm silicon, higher-order length-extensional resonators. Table 2.5 lists

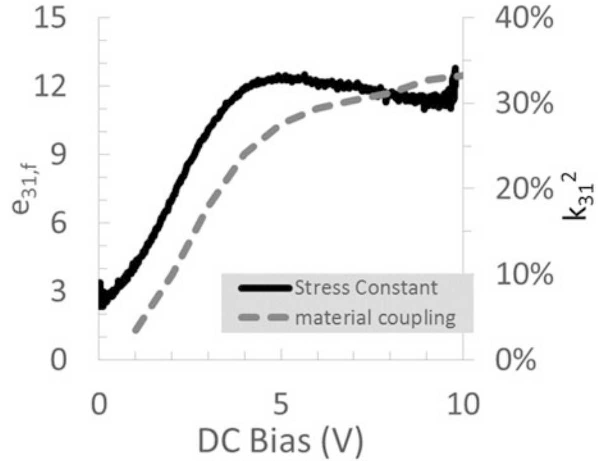

Fig. 2.24 Unipolar response under increasing applied voltage of the $e_{31,f}$ piezoelectric stress constant and extracted $k_{31}{}^2$ material electromechanical factor of the same film plotted in Fig. 2.23. The $k_{31}{}^2$ is extracted from $e_{31,f}$ and k_{33} assuming the measured dielectric constant is clamped (i.e., $k_{33}{}^S$) and utilizing the $s_{11}{}^E$ from [79]

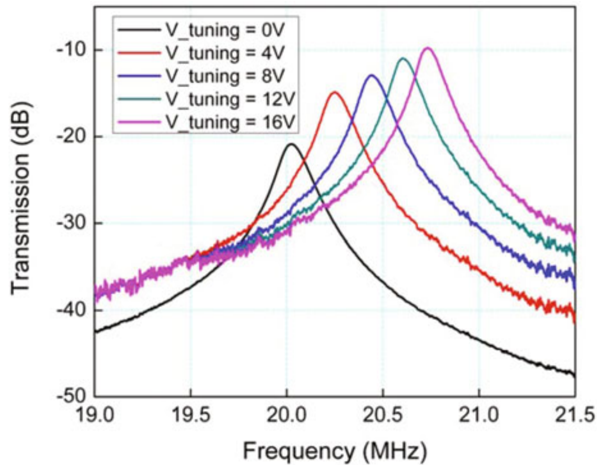

Fig. 2.25 Measured transmission of PZT MEMS resonator from [67], exhibiting 5.1 % center frequency voltage tunability (Reprinted with permission. Copyright IEEE 2008)

the performance of this filter as compared to similar low-frequency commercially available acoustic filters, including monolithic quartz, SAW, and ceramic technologies [93]. The PZT-on-silicon IF filter without external impedance matching outperforms the competing technologies in all categories except insertion loss (quartz for same number of poles) and power handling (SAW at a higher frequency). The performance listed for the commercially available filters is for the case of external impedance matching, while the PZT MEMS filter is directly terminated to 50 Ω. The component size listed accounts for the size of the required discrete matching elements for the commercially available filters and the input and output bias tees for the PZT MEMS filter (assumes 0402 size components). Despite the relatively high insertion loss, the PZT MEMS filter performance was reported to meet the requirements of the intended IF filter application.

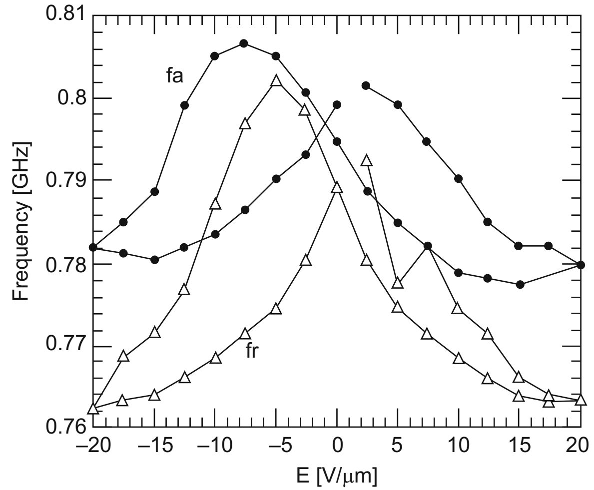

Fig. 2.26 Measured series (*fr*) and parallel (*fa*) resonance frequency tunability with applied DC-bias electric field for thin film PZT FBAR from [66]. The device utilized 2 μm 53/47 PZT deposited by CSD sol-gel technique and exhibited a maximum k_t^2 of 10 % with applied bias (Reprinted with permission. Copyright IEEE 2008)

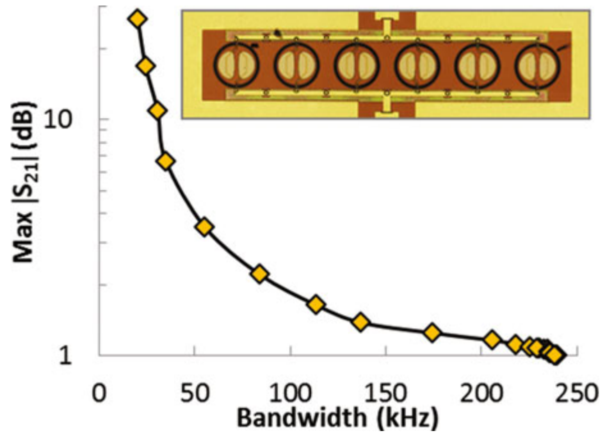

Fig. 2.27 Measured bandwidth tuning response of out-of-plane flexural disc array resonator from [60] with DC-bias voltages from 0 to 14 V. The maximum $|S_{21}|$ at 14 V bias is 1.0 dB (Reprinted with permission. Copyright IEEE 2016)

The primary limitations of PZT for resonator applications are the low mechanical (<~200) and dielectric *Qs* (~1–10 %). In addition, the low acoustic velocity (~2800 m/s) and high dielectric constants (~300–1600) and losses make it challenging to achieve high performance at high frequencies (>1 GHz). Furthermore, the need to provide DC bias for optimal material properties can provide unwanted complications. In light of these limitations and the aforementioned advantages, PZT resonators and filters are best suited to lower frequencies of operation (<500 MHz) where the small size and ease of design for 50 Ω termination provide unique benefits for acoustic filter applications and are well suited to applications that can leverage the integration of high-performance MEMS actuators. The figures of merit of PZT FBAR and MEMS resonators have been improving since the late 1990s, and PZT-on-silicon technology has provided resonator *Qs* that are relevant for some filter applications (see Fig. 2.31). Promising efforts in recent

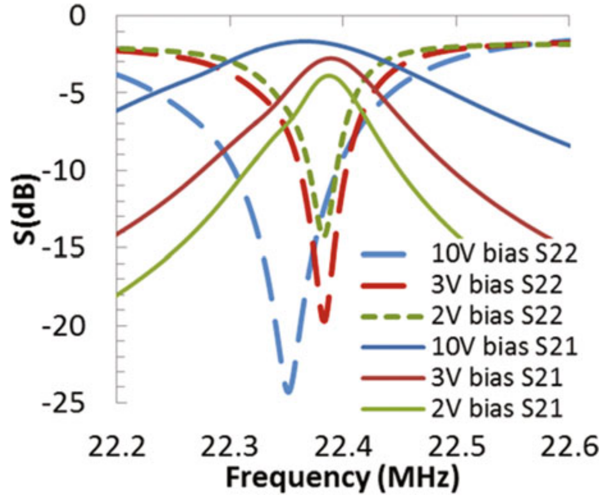

Fig. 2.28 Measured bandwidth tuning of S_{21} and S_{11} responses of an out-of-plane flexural disc array resonator (similar to Fig. 2.27) with bias voltages of 10, 3, and 2 V from [60]. (Reprinted with permission. Copyright IEEE 2016)

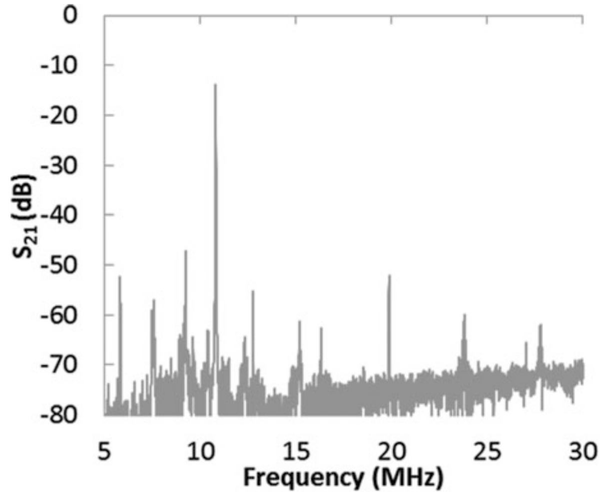

Fig. 2.29 Measured wideband S_{21} response of the 10.8 MHz PZT-on-Si filter from (Reprinted with permission. Copyright IEEE 2016) [60]

years with manganese/niobium doping [94–96] and ternary compounds based on thin film PZT and relaxor ferroelectrics [97] have demonstrated improvements in most material properties relevant to resonators including mechanical and dielectric loss, electromechanical coupling, and piezoelectric coefficients. FBAR resonators based on sputtered PMnN-PZT have demonstrated k_t^2 (49 %)–Q_m (185) products of 91 at 3.9 GHz with Curie temperatures that well exceed typical PZT [101]. Yet even this performance does not approach the best material k^2Q_m performance of commercially available bulk material PZTs. As stated earlier, thin film PZT has demonstrated piezoelectric coefficients and electromechanical coupling that are superior to similar bulk ceramic materials; however, thin films have yet to achieve the high-quality factors obtained with certain bulk PZT compositions. Figure 2.32

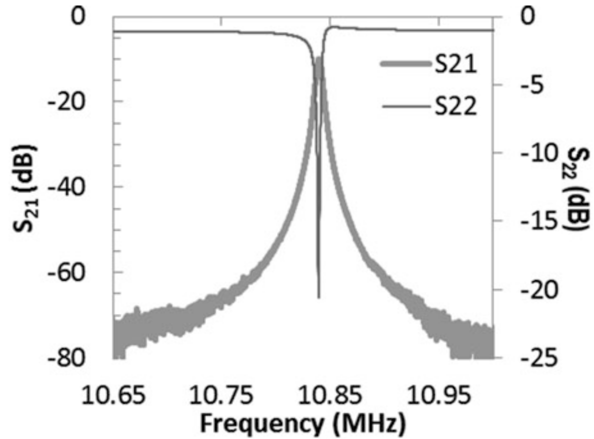

Fig. 2.30 Measured narrowband S_{21} and S_{22} responses of 10.8 MHz PZT-on-silicon 2-pole IF filter from [60]; response is from the same device in Fig. 2.29

plots the Q_m and material $k_p{}^2-Q_m$ product versus the electrical Q (1/loss tangent) of commercially available bulk PZT compositions including modified PZTs [78]. The reported properties/results of the highest figure of merit thin film PZT resonator (FBAR from [68]) are plotted for comparison. It is evident that if similar Q_m and k^2Q_m performance can be achieved in thin films as in bulk material, that as much as an order of magnitude in improvement in PZT MEMS resonator FOM can be expected. Future improvements in the quality factor and figure of merit of PZT-based contour-mode MEMS resonators are expected to utilize such modified PZT materials.

2.1.5 Summary

This chapter has introduced the reader to the leading ferroelectric material used in thin-film piezoelectric MEMS: lead zirconate titanate ($PbZr_xTi_{1-x}O_3$) or PZT. An overview of the material deposition and patterning techniques were provided as an introduction to the complex nature of processing PZT thin films. Additionally, device design considerations related to processing have also been addressed with respect to PZT-based resonant devices. With increasing interest in PZT-based PiezoMEMS technology from the major MEMS manufacturers, it is anticipated that PZT thin-film-based resonant devices could become a commercial product in the coming years.

Acknowledgment The authors would like to thank Dr. Brett Piekarski and Dr. Paul Amirtharaj of the US Army Research Laboratory for their support and encouragement in writing this chapter. The authors also acknowledge the effort of their colleagues Dr. Sarah Bedair, Dr. Madan Dubey, Dr. Ryan Rudy, Dr. Daniel Potrepka, Dr. Luz Sanchez, Joel Martin, and Brian Power of the US Army Research Laboratory, Steven Isaacson of General Technical Services, and Dr. Glen Fox of Glen Fox Consulting in assisting with this chapter.

Table 2.5 Comparison of PZT MEMS filter [60] with commercially available acoustic filters

Filter technology	# Poles	fc (MHz)	BW (%)	Insertion loss (dB)	Roll-off (dB/kHz)	Ultimate attenuation (dB) (±1.5 MHz)	Term. Imp. (Ω)	Size (mm^3)	Max. power (dBm)
PZT MEMS	2	10.8	0.04	6.8	2.1	60	50	5.2	13
Monolithic quartz	2	10.7	0.07	1.5	1.1	35	1800	587.3	−10
Ceramic	–	10.7	1.03	9	0.2	30	330	339.0	–
SAW	–	43.8	6.86	14.8	0.04	42	2000	826.1	27

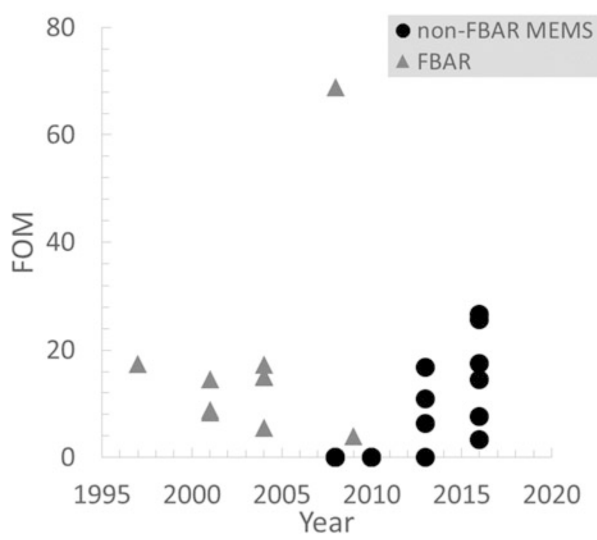

Fig. 2.31 Select published results for PZT MEMS resonators since 1997; resonator figure of merit ($k_{eff}^2/(1-k_{eff}^2)Q_m$) versus the year the results were obtained. For results where only k_t^2 was provided, k_{eff}^2 was approximated as ~70 % of k_t^2 based on [101]

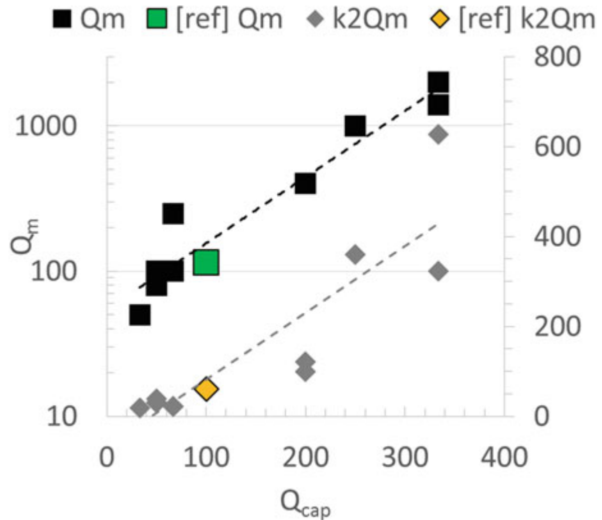

Fig. 2.32 Mechanical quality factor (Q_m) (*logy axis*) and material k^2-Q_m product versus capacitor electrical quality factor (1/loss tangent). The black and gray points are reported properties of commercially available bulk PZT compositions including modified PZTs [78] based on k_p^2. The green and orange points are the properties reported for the highest figure of merit thin film PZT resonators to date from [68] for comparison. The lines are only intended to guide the eye

References

1. Pulskamp J et al (2012) Piezoelectric PZT MEMS technologies for small-scale robotics and RF applications. MRS Bull 37(11):1062–1070
2. Fujishima S (2000) The history of ceramic filters. IEEE Trans UFFC 47(1):1–7
3. Castellano RN, Feinstein LG (1979) Ion-beam deposition of thin films of ferroelectric PZT. J Appl Phys 50:4406–4411

4. Krupanidhi SB et al (1983) RF planar magnetron sputtering and characterization of ferroelectric PZT films. J Appl Phys 54:6601–6609
5. Okuyama M et al (1979) Preparation of PbTiO3 ferroelectric thin film by RF sputtering. Jpn J Appl Phys 18:1633–1634
6. Sreenivas J, Sayer M, Garrett P (1989) Properties of dc magnetron-sputtered PZT thin films. Thin Solid Films 172:251–267
7. Hiboux S, Muralt P, Setter N (2000) Orientation and composition dependence of piezoelectric dielectric properties of sputtered $Pb(Zr_xTi_{1-x})O_3$ thin films. Mat Res Soc Symp Proc 596:499–504
8. Kanno I, Kotera H, Wasa K (2003) Measurement of transverse piezoelectric properties of PZT thin films. Sens Act A 107:68–74
9. Okada M et al (1989) Preparation of c-axis oriented $PbTiO_3$ thin films by MOCVD. Ferroelectrics 91:181–192
10. Kuwabara H, Menou N, Funakubo H (2008) 1 V saturated Pb(Zr, Ti)O3 films with (111) orientation using lattice-matched (111) SrRuO3/(111) Pt bottom electrode prepared by pulsed metal organic chemical vapor deposition. Appl Phys Lett 93:152901-1–152901-3
11. Otani Y, Okamura S, Shiosaki T (2004) Recent developments on MOCVD of ferroelectric thin films. J Electroceram 13:15–22
12. Budd KD, Dey SK, Payne DA (1985) Sol-gel processing of PT, PZ, PZT, and PLZT thin films. Br Ceram Proc 36:107
13. Spierings GAMC et al (1991) Preparation and ferroelectric properties of PZT by spin coating and metal organic decomposition. J Appl Phys 70:2290–2298
14. Tuttle BA et al (1992) Microstructural evolution of PZT thin films prepared by hybrid metallorganic decomposition. J Mater Res 7:1876–1882
15. Tuttleand BA, Schwartz RW (1996) Solution deposition of PZT ferroelectric thin films prepared by hybrid metallorganic decomposition. MRS Bull 7:1876–1882
16. Schwartz JW (1997) Chemical solution deposition of perovskite thin films. Chem Mater Sci 209:2325–2340
17. Calame F, Muralt P (2007) Growth and properties of gradient free sol-gel lead zirconate titanate thin films. App Phys Lett 90:062907
18. Klissurska RD et al (1995) Effect of Nb doping on the microstructure of sol-gel derived PZT thin films. J Am Ceram Soc 78:1513–1520
19. Muralt P, Baborowski J, Lederman N (2002) Piezoelectric micro-electro-mechanical systems with PbZrxTi1-xO3 thin films: integration and application issues, piezoelectric materials and devices, EPFL Swiss Federal Institute of Technology, Switzerland, pp 231–260
20. Hartl KH, Rau H (1969) PbO vapour pressure in the Pb(Zr, Ti)O3 system. Solid State Commun 7:41–45
21. Muralt P (2006) Texture control and seeded nucleation of nanosize structures of ferroelectric thin films. J Appl Phys 100:051605
22. Trolier-McKinstry S, Muralt P (2004) Thin film piezoelectrics for MEMS. J Electroceram 12:7–17
23. Kim DM, Eom CB, Nagarajan V, Ouyang J, Ramesh R, Vaithyanathan V, Schlom DG (2006) Thickness dependence of structural and piezoelectric properties of epitaxial $Pb(Zr_{0.52}Ti_{0.48})O_3$ films on Si and SrTiO3 substrates. Appl Phys Lett 88:142904-1–142904-3
24. Fox G, Suu K (2004) High temperature deposition of Pt/TiOx for bottom electrodes, US Patent 6,682,772
25. Nakamura T, Nakao Y, Kamisawa A, Takasu H (1994) Preparation of Pb(Zr, Ti)O3 thin films on electrodes including IrO2. Appl Phys Lett 65:1522
26. Fox GR, Sun S, Eastep B, Hadnagy TD (1999) Comparison of CSD and sputtered PZT with iridium electrodes. Integr Ferroelectr 26:215–223
27. Whatmore RW, Zhang Q, Huang Z, Dorey RA (2003) Ferroelectric thin and thick films for microsystems. Mater Sci Semi Proc 5:65–76

28. Schwartz RW, Assink RA, Headley TJ (1992) Spectroscopic and microstructural characterization of solution chemistry effects in PZT thin film processing. Ferroelectric Thin Films II Mat Res Soc Symp Proc 243:245–254
29. Assink RA, Schwartz RW (1993) 1H and 13C NMR investigations of Pb(Zr, Ti)03 thin-film precursor solutions. Chem Mater 5:511–517
30. http://www.mmc.co.jp/adv/ele/en/products/assembly/solgel.html
31. Zhou QF, Hong E, Wolf R, Trolier-McKinstry S (2001) Dielectric and piezoelectric properties of PZT 52/48 thick films with (100) and random crystallrographic orientation. Ferroelectric Thin Films IX Mater Res Soc Proc 655:CC11.7.1–CC11.7.6
32. Ledermann N, Muralt P et al (2003) {100}-Textured, piezoelectric $Pb(Zr_x, Ti_{1-x})O_3$ thin films for MEMS: integration, deposition and properties. Sens Act A 105:162–170
33. Orcel G, Hench L (1986) Effect of formamide additive on the chemistry of silica-gels. Part 1. NMR of silica hydrolysis. J Non-Cryst Solids 79:177–194
34. Schwartz RW, Assink RA, Dimos D, Sinclair MB, Boyle TJ, Buchheit CD (1995) Effects of acetylacetone additions on PZT thin film processing. Ferroelectric Thin Films IV MRS Symp 377–387
35. Sanchez L, Potrepka D, Fox G, Takeuchi I, Polcawich RG (2013) Optimization of $PbTiO_3$ seed layers and Pt metallization for PZT based PiezoMEMS actuators. J Mater Res 28:1920–1931
36. Shelton CT et al (2012) Chemically homogeneous complex oxide thin films via improved substrate metallization. Adv Funct Mater 22:2295–2302
37. Ihlefeld J, Shelton C (2012) Chemical homogeneity effects on the nonlinear dielectric response of lead zirconate titanate thin films. Appl Phys Lett 101:052902
38. Mancha S (1992) Chemical etching of thin film PLZT. Ferroelectrics 135:131–137
39. Miller R, Bernstein J (2000) A novel wet etch for patterning PZT thin films. Integr Ferroelectr 29:225–231
40. Zheng K, Lu J, Chu J (2004) A novel wet etching process of Pb(Zr, Ti)O3 thin films for applications in microelectromechanical system. J Appl Phys 43:3934–3937
41. Vijay DP, Desu SUB, Pan W (1993) Reactive ion etching of lead zirconate titanate (PZT) thin film capacitors. J Electrochem Soc 140:2535–2539
42. Pan W et al (1994) Reactive ion etching of PZT and RuO_2 films by environmentally safe gases. J Mater Res 9:2976–2980
43. Baborowski J et al (2001) Mechanisms of PZT thin film etching with ECR/RF reactor. Int Ferroelectr 31:261–271
44. Joo SH, Lee JJ et al (2001) Stacked FRAM capacitor etching process for high density application. Integr Ferroelectr 37:103–111
45. Chung CW (1998) Reactive ion etching of $Pb(Zr_xTi_{1-x})O_3$ thin films in an inductively coupled plasma. J Vac Sci Tech B 16:1894–1900
46. Koo S, Kim D, Kim K, Song S, Kim C (2004) Etching properties of $Pb(Zr_xTi_{1-x})O_3$lead–zirconate–titanate thin films in an inductively coupled plasma Cl_2/Ar and BCl_3 /Ar gas chemistries. J Vac Sci Tech B Technol A 1622:1519–1523
47. Baborowski J, Muralt P, Lederman N (1999) Etching of platinum thin films with dual frequency ECR/RF reactor. Integ Ferroelectr 27:243–256
48. Baborowski J et al (2000) Etching of RuO_2 and Pt with ECR/RF reactor. Vacuum 56:51–56
49. Chung CW, Chung I (2001) Etch behavior of $Pb(Zr_xTi_{1-X})O_3$ films using a TiO_2 hard. J Electrochem Soc 148:C353–C356
50. Joo SH, Lee JJ, Lee KM, Nam SD, Lee SW, Oh SJ, Lee YT, Park SO, Kang HK, Moon JT (2001) Stacked FRAM capacitor etching process for high density application. Integr Ferro 31:103–111
51. Soyer C, Cattan E, Rémiens D, Guilloux-Viry M (2002) Ion beam etching of lead–zirconate–titanate thin films: correlation between etching parameters and electrical properties evolution. J Appl Phys 92:1048–1055
52. Soyer C, Cattan E, Rémiens D (2005) Electrical damage induced by reactive ion-beam etching of lead-zirconate-titanate thin films. J Appl Phys 97:114110–114117

53. Udayakumar KR, Moise TS, Summerfelt SR (2007) Ferroelectric capacitor hydrogren barriers and methods for fabricating the same. US Patent No. 7,183,602
54. Yang J, Polcawich RG, Sanchez LM et al (2015) Effect of feature size on dielectric nonlinearity of patterned $PbZr_{0.52}Ti_{0.48}O_3$ films. J Appl Phys 117:014103
55. Polcawich RG, Trolier-McKinstry S (2000) Piezoelectric and dielectric reliability of lead zirconate titanate (PZT) thin films. J Mater Res 15(11):2505–2513
56. Pulskamp J et al (2016) Ferroelectric PZT MEMS HF/VHF resonators/filters. Frequency Control and the European Frequency and Time Forum (FCS). Joint Conf IEEE Int
57. Rudy RQ et al (2016) Disk Flexure resonator with 1 dB insertion loss. Frequency control and the European Frequency and Time Forum (FCS). Joint Conf IEEE Int
58. Rudy RQ et al (2016) Low-loss gold-laced PZT-on-silicon resonator with reduced parasitics. 2016 IEEE 29th international conference on micro electro mechanical systems (MEMS)
59. Bedair S, Pulskamp J, Polcawich R, Judy D, Gillon A, Bhave S, Morgan B (2012) Low loss micromachined lead zirconate titanate, contour mode resonator with 50 ω termination. MEMS 2012, Paris, France, pp 708–712. Accessed 29 Jan–2 Feb 2012
60. Yagubizade H et al (2013) A 4th-order band-pass filter using differential readout of two in-phase actuated contour-mode resonators. Appl Phys Lett 103(17):173517
61. Chandrahalim H et al (2010) PZT transduction of high-overtone contour-mode resonators. Ultrason Ferroelectrics Freq Contr IEEE Trans 57(9):2035–2041
62. Conde J, Muralt P (2008) Characterization of sol-gel Pb (Zr 0.53 Ti 0.47) O 3 in thin film bulk acoustic resonators. Ultrason Ferroelectr Freq Contr IEEE Trans 55(6):1373–1379
63. Chandrahalim H et al (2008) Influence of silicon on quality factor, motional impedance, and tuning range of PZT-transduced resonators. 2008 Solid State sensor, actuator and microsystems workshop
64. Wasa K et al (2008) Thin films of PZT-based ternary perovskite compounds for MEMS. Ultrason Symp IUS 2008 IEEE
65. Chandrahalim H, Bhave S, Polcawich R, Pulskamp J, Judy D, Kaul R (2008) Performance comparison of Pb(Zr0.52Ti0.48)O3-only and Pb(Zr0.52Ti0.48)O3-on-silicon resonators. Appl Phys Lett 93
66. Schreiter M et al (2004) Electro-acoustic hysteresis behaviour of PZT thin film bulk acoustic resonators. J Eur Ceram Soc 24(6):1589–1592
67. Larson JD, III, Gilbert SR, Xu B (2004) PZT material properties at UHF and microwave frequencies derived from FBAR measurements. Ultrason Symp 2004 IEEE 1
68. Kirby PB et al (2001) PZT thin film bulk acoustic wave resonators and filters. 2001 IEEE international frequency control symposium and PDA exhibition, vol 687
69. Qing-Xin S et al (2001) Thin-film bulk acoustic resonators and filters using ZnO and lead-zirconium-titanate thin films. Microw Theor Tech IEEE Trans 49(4):769–778
70. Löbl HP et al (2001) Materials for bulk acoustic wave (BAW) resonators and filters. J Eur Ceram Soc 21(15):2633–2640
71. Hanajima N et al (1997) Ultrasonic properties of lead zirconate titanate thin films in UHF-SHF range. Jpn J Appl Phys 36(9S):6069
72. Aigner R (2003) MEMS in RF filter applications: thin-film bulk acoustic wave technology. Sens Update 12(1):175–210
73. Piekarski B et al (2001) Surface micromachined piezoelectric resonant beam filters. Sens Actuator A Phys 91(3):313–320
74. [Online]. www.piceramic.com/download/PI_Ceramic_Material_Data.pdf
75. Yagnamurthy S et al (2011) Mechanical and ferroelectric behavior of PZT-based thin films. Microelectromech Syst J 20(6):1250–1258
76. Aigner R (2015) Tunable filters? Reality check foreseeable trends in system architecture for tunable RF filters. Microw Mag IEEE 16(7):82–88
77. Polcawich R, Pulskamp J (2011) Additive processes for piezoelectric materials: piezoelectric MEMS. In: Ghodssi R, Lin P (eds) MEMS materials and processes handbook, 1st edn. Springer, New York, pp 273–344

78. Bedair S et al (2013) Thin-film piezoelectric-on-silicon resonant transformers. J Microelectromech Syst 22(6):1383–1394
79. Bedair S, Pulskamp J, Polcawich R, Rudy R, Puder J (2015) Thin-film piezoelectric transformers operating in harmonics of out-of-plane flexure modes. In: Solid-state sensors, actuators and microsystems, transducers-2015 18th international conference on IEEE, pp 714–717
80. Pulskamp J, Bedair S, Polcawich R, Judy D, Bhave S (2011) Ferroelectric PZT RF MEMS resonators. IEEE Frequency Control Symposium, San Francisco, CA, pp 1–6
81. Puder J et al (2015) Higher dimensional flexure mode for enhanced effective electromechanical coupling in PZT-on-silicon MEMS resonators. Solid-state sensors, actuators and microsystems (TRANSDUCERS), 2015 transducers-2015 18th international conference on IEEE
82. Pulskamp J, Bedair S, Polcawich R, Smith G, Martin J, Power B, Bhave S (2012) Electrode-shaping for the excitation and detection of arbitrary modes in arbitrary geometries in piezoelectric resonators. IEEE Trans Ultrason Ferro Freq Control 59:1043–1060
83. Bedair S, Judy D, Pulskamp J, Polcawich RG, Gillon A, Hwang E, Bhave S (2011) High rejection, tunable parallel resonance in micromachined lead zirconate titanate on silicon resonators. App Phys Lett 99:103509
84. Kaul R et al (2014) A bi-phase MEMS resonator modulator. IEEE Microw Wirel Compon Lett 24(1):41–43
85. Kim B, Olsson RH, Wojciechowski KE (2013) AlN microresonator-based filters with multiple bandwidths at low intermediate frequencies. J Microelectromech Syst 22(4):949–961
86. Pulskamp J, Judy D, Kaul R, Polcawich R, Chandrahalim H, Bhave S (2009) Monolithically integrated piezo-MEMS SP2T switch and contour-mode filters. IEEE MEMS Trans 900–903
87. Pulskamp J, Bedair S, Polcawich R, Meyer C, Kierzewski I, Maack B (2014) High-Q and capacitance ratio multilayer metal-on-piezoelectric RF MEMS varactors. IEEE Electron Device Lett 35:871–873
88. Bedair S, Pulskamp J, Meyer C, Polcawich R, Kierzewski I (2014) Modeling, fabrication and testing of MEMS tunable inductors varied with piezoelectric actuators. J Micromech Microeng 24:095017, 12 pp
89. Bedair S, Pulskamp J, Meyer C, Mirabelli M, Polcawich R, Morgan B (2012) High-performance, micromachined inductors tunable by lead zirconate titanate actuators. IEEE Electron Dev Lett 33:1–3
90. Damjanovic D (1998) Ferroelectric, dielectric and piezoelectric properties of ferroelectric thin films and ceramics. Rep Prog Phys 61(9):1267
91. Chandrahalim H, Bhave S, Polcawich R, Pulskamp J, Judy D, Kaul R (2009) A Pb(Zr0.52Ti0.48)O3 transduced fully-differential mechanical-coupled frequency-agile filter. IEEE Electron Device Lett 30(12):1296–1298
92. Zuo C, Sinha N, Piazza G (2010) Very high frequency channel-select MEMS filters based on self-coupled piezoelectric AlN contour-mode resonators. Sens Actuator A Phys 160(1):132–140
93. [Online]. http://www.digikey.com/product-search/en/filter
94. Fujii T et al (2010) Characterization of Nb-doped Pb (Zr, Ti) O 3 films deposited on stainless steel and silicon substrates by RF-magnetron sputtering for MEMS applications. Sens Actuator A: Phys 163(1):220–225
95. Fujii T et al (2009) Preparation of Nb doped PZT film by RF sputtering. Solid State Commun 149(41):1799–1802
96. Benhadjala W et al (2015) Sol-gel doped-PZT thin films for integrated tunable capacitors. International symposium on microelectronics, vol 2015. No. 1. International Microelectronics Assembly and Packaging Society

97. Wasa K et al (2013) PZT-based high coupling with low permittivity thin films. Applications of ferroelectric and workshop on the piezoresponse force microscopy (ISAF/PFM), 2013 IEEE international symposium on the IEEE
98. Baborowski J, Muralt P, Ledermann N, Colla E, Seifert A, Gentil S, Setter N (2000) Mechanisms of $Pb(Zr_{0.53}Ti_{0.47})O_3$ thin film etching with ECR/RF reactor. Integr Ferroelectr 31:261–271
99. Fujii T et al. Fuji Research and Development, No. 59-2014
100. Tsuchiya K, Kitagawa T, Uetsuji Y, Nakamachi E (2006) Fabrication of smart material PZT thin films by RF magnetron sputtering method in micro actuators. JSME Intern J 49:201–208
101. Polcawich RG (2007) Design, fabrication, test, and evaluation of RF MEMS series switches using lead zirconate titanate (PZT) thin film actuators, Ph.D. Thesis, Pennsylvania State University

Chapter 3
Gallium Nitride for M/NEMS

Mina Rais-Zadeh and Dana Weinstein

3.1 Introduction

3.1.1 A Bit of History

The holy grail of seamless monolithic integration of MEMS with supporting circuitry has driven the development of electromechanical devices in compound semiconductors. Piezoelectricity manifests itself in the majority of compound semiconductors due to the inherent crystal asymmetry of the two or more atomic species comprising the material. The interaction of acoustic waves with charge carriers in these piezoelectric semiconductors was investigated as early as 1953 [1] and revealed interesting phenomena such as reduced electron effective mass due to phonon drag [2] and wave amplification and velocity shift in the presence of free carriers [3–5]. The unique properties of piezoelectric semiconductors and their implications for resonant devices are explored in this chapter.

In the late 1980s and early 1990s, commercialization of III–V heterostructure-based integrated circuit technology (particularly gallium arsenide (GaAs)) boomed, resulting in more widespread implementation of piezoelectric semiconductors for electromechanical systems. At the time, researchers focused on surface acoustic wave (SAW) devices, likely due to ease of fabrication since the piezoelectric film did not need be etched. Acoustic charge transport (ACT) [6] and heterojunction

M. Rais-Zadeh (✉)
Department of Electrical Engineering and Computer Science, University of Michigan,
Ann Arbor, MI, USA
e-mail: minar@eecs.umich.edu

D. Weinstein
Department of Electrical and Computer Engineering, Purdue University,
West Lafayette, IN, USA
e-mail: danaw@purdue.edu

© Springer International Publishing Switzerland 2017

H. Bhugra, G. Piazza (eds.), *Piezoelectric MEMS Resonators*,
Microsystems and Nanosystems, DOI 10.1007/978-3-319-28688-4_3

acoustic charge transport (HACT) [7] devices were developed, using SAWs to generate potential wells for packets of electrons propagating at acoustic velocities in the semiconductor. These packets could be manipulated via biasing on Schottky electrodes at the wafer surface and could be detected nondestructively using image charges on these electrodes. In this way, one could perform discrete-time analog signal processing, including phase shifting, filtering, correlation, and signal predistortion. Intimate integration with control circuits for switching and biasing electrodes for charge injection and readout was critical for speed and size and to alleviate I/O constraints. Ultimately, with the successful scaling of CMOS (complementary metal-oxide semiconductor) and the ultralow-power circuits afforded by digital processing, ACT and HACT devices were largely abandoned by 2000. More recently, several advances in growth and fabrication technology for III–V semiconductors have reinvigorated interest in these materials specifically for resonant MEMS devices.

3.1.2 GaN Technology Enabling MEMS

There has been a substantial effort to grow InP and GaN heterostructures on silicon substrates for reduced cost and toward the goal of heterogeneous integration with CMOS [8, 9]. These films are typically grown by metalorganic chemical vapor deposition (MOCVD) or by molecular beam epitaxy (MBE) at high temperatures of more than 700° necessitating substrates that are closely matched in lattice constants and thermal expansion coefficients to those of the thin films [10].

Figure 3.1 illustrates a typical AlGaN/GaN heterostructure used for both RF and power applications. A thin nucleation layer (commonly AlN) establishes an interface between the substrate. A transition or buffer layer of GaN is generally necessary to accommodate for lattice mismatch and high-density dislocations. A thin AlGaN layer grown on top of the high-quality GaN above the transition layer then establishes a 2D potential well due to band bending as shown in

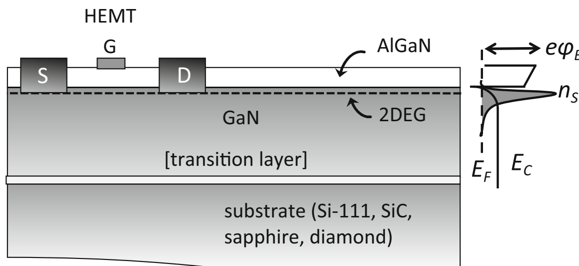

Fig. 3.1 Sample cross section of GaN HEMT heterostructure, showing the conduction band bending between AlGaN and GaN resulting in a 2D confined electron gas (2DEG). A HEMT on the left includes Ohmic (S/D) and Schottky (G) contacts to control the 2DEG channel

the figure. The 2D electron gas (2DEG) formed at this potential well exhibits high charge density (1×10^{13} cm^{-2}), mobility (2000 cm^2/Vs), and saturation velocity (3×10^7 cm/s), which is ideal for high-speed high electron mobility transistors (HEMTs) that use the 2DEG to form the transistor channel.

Favored substrates for GaN growth include silicon carbide (SiC) and sapphire, which can be prohibitive in cost. However, toward the goal of developing GaN on 200 mm and even 300 mm substrates, recent developments in epitaxial growth have enabled stress compensation and termination of dislocations stemming from lattice mismatch at the interface with the silicon substrate [11]. To prevent unintentional doping of the GaN, the Si substrate must be high resistivity, which is additionally beneficial for RF characteristics. To further increase electrical isolation, the GaN layer may be compensation doped (e.g., Fe, C).

The shift of implementing monolithic microwave integrated circuits (MMICs) to silicon substrates is beneficial not only in terms of cost but also enables the release of the piezoelectric film from the substrate. This can be achieved either by a front-side isotropic etch (e.g., using xenon difluoride (XeF_2)) or etching through the back of the wafer (e.g., using deep reactive ion etching (DRIE) or potassium hydroxide (KOH)) to freely suspend the desired MEMS structure. This opens the door for high-Q resonators in piezoelectric semiconductors beyond the limits of SAW devices.

A second development in fabrication enabling piezoelectric semiconductor MEMS resonators involves the etch recipes for these materials. Previously, etching the piezoelectric substrate was avoided, and metallization on top of the film provided both transducers and acoustic isolation structures. However, inductively coupled plasma (ICP) reactive ion etching (RIE) using metal masks has been shown to provide smooth, vertical sidewalls on GaN resonators—a key characteristic for high-Q resonance [12, 13].

Finally, the industrial push toward heterogeneous integration of III–V materials with CMOS has also sparked the development of gold-free technology for both Ohmic and Schottky contacts for transistors. The corresponding elimination of gold from resonator electrodes results in higher Q and reduced distortion of the targeted resonant mode due to mass loading and acoustic mismatch [12–15].

These factors are mutually beneficial both electrically for HEMTs and mechanically for MEMS devices. With minor additions to the standard III–V HEMT process, including a deep GaN etch and a release step from the substrate, one can achieve seamless integration of high-Q MEMS resonators with active mm-wave circuits.

3.1.3 Benefits of GaN

As previously mentioned, the majority of compound semiconductors exhibit piezoelectric properties due to the asymmetry in their crystal structure. While there is a range of compound semiconductors to choose from, GaN stands out overall in both electrical and mechanical performance. Figure 3.2 shows the bandgaps (E_g) of several IV–IV, III–V, and II–VI compound semiconductors ($E_g < 4$ eV).

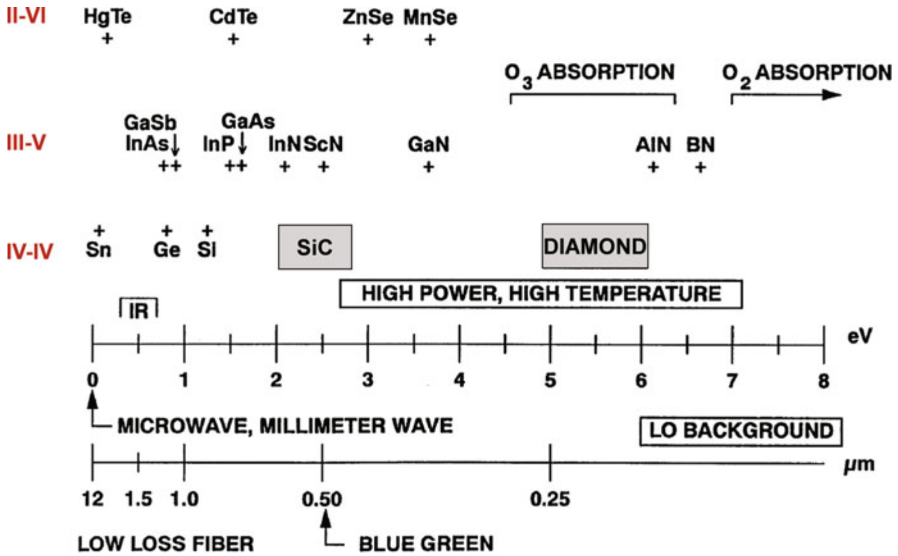

Fig. 3.2 Bandgaps of various IV–IV, III–V, and II–VI semiconductors ($E_g < 4$ eV). Compound semiconductors exhibit piezoelectric effect [16]

The wide direct bandgap of GaN (3.4 eV) makes it ideal for solid-state lighting and optoelectronics but also translates to a high breakdown field (3.3 MV/cm) and subsequent large power-handling capabilities (>10 W/mm). Additionally, the GaN HEMT technology is maturing and quickly becoming the preferred solution for MMICs and power electronics.

In addition to its impressive electrical performance, GaN also has favorable electromechanical properties. Like AlN, GaN has a *c*-axis wurtzite crystal structure, which exhibits a large piezoelectric effect relative to other common compound semiconductors used in analog, RF, mm-wave, THz, and mixed signal ICs, as well as in power applications. Table 3.1 compares the piezoelectric coupling coefficient (k^2) of several compound semiconductors under consideration. The larger the k^2, the more energy can couple from an electrical signal into a mechanical vibration (or vice versa).

While GaAs and InP are historically more common in MMIC technology, they are zinc blende crystals with weak piezoelectricity and consequently poor coupling coefficient. ZnO provides the highest transducer coupling among the III–V semiconductors shown in Table 3.1, but also has high leakage prohibiting its use at high frequencies. In addition, zinc is a dopant of silicon and its monolithic integration with silicon CMOS is not desirable. Among piezoelectric III–V materials, GaN offers a distinct combination of high-performance electrical properties with high piezoelectric coupling. Coupled with high acoustic velocity comparable to silicon and low acoustic loss [17], the benefits of this material have catapulted GaN MEMS into the spotlight over the past few years.

Table 3.1 Comparison of elastic properties (c_{33}, c_{13}, c_{11}) and piezoelectric properties (e_{33}, e_{13}, $k_{33}{}^2$) and permittivity (ε) of various compound semiconductors

Material	Crystal	c_{33} (GPa)	c_{11} (GPa)	c_{13} (GPa)	e_{33} (C/m^2)	e_{13} (C/m^2)	ε	$k_{33}{}^2$ (%)
BeO	W	488	454	77	0.02	−0.02	7.74	0.001
ZnO	W	210.9	193	105.1	0.89	−0.51	10.9	8.5
GaAs	ZB	118	118	–	−0.12	–	12.9	0.106
InP	ZB	101	101	–	0.04	–	12.5	0.014
GaN	W	398	293	106	0.65	−0.33	9.5	2.00
AlN	W	373	304	108	1.46	−0.6	9.4	6.87

AlN (an insulator) is shown for comparison. Material properties are taken from Refs. [17–20]. Here, crystal structure W stands for wurtzite and ZB for zinc blende

The following sections of this chapter highlight important features and successes of GaN MEMS resonators and puts them in the context of key applications ranging from sensors to clocks. These applications tie back to the need for monolithic integration of MEMS with supporting circuitry, with benefits in size, weight, and cost, frequency of operation, dynamic range, and relaxed constraints on impedance matching networks. Furthermore, transduction mechanisms unique to GaN MMIC technology are discussed, including the use of the 2DEG in AlGaN/GaN heterostructures for piezoresistive sensing and switchable piezoelectric transduction. Transistor sensing of acoustic resonance is also covered in the context of scaling of resonators to multi-GHz frequencies of operation. These distinctive attributes of GaN MEMS devices enable a versatile class of sensor and RF tools in a platform increasingly used for high-power, high-frequency electronics [17].

3.2 Transduction Mechanisms in Resonant GaN Devices

3.2.1 Passive Piezoelectric Transduction

There are various ways in which electrodes can be configured to piezoelectrically drive and sense elastic modes in thin-film *c*-axis wurtzite crystals, such as GaN. While the details of resonator design will be covered in Part 2, it is worth discussing key GaN resonator configurations to highlight the capabilities and performance of the material within the framework of an Integrated Circuit (IC) platform.

Passive Piezoelectric GaN Resonators with Top and Bottom Electrodes

AlN and ZnO thin films are most commonly deposited by reactive sputtering or pulsed laser deposition (see Chap. 1) which can be done on top of a metallic surface, resulting in a piezoelectric film sandwiched between bottom and top electrodes. This configuration naturally excites the thickness mode of vibration along the *c*-axis of

the wurtzite film, commonly termed the film bulk acoustic resonator or FBAR mode [21, 22]. This mode of vibration yields the highest transduction efficiency and is commonly used for filter applications requiring large bandwidth, as discussed in Part 4. However, since the resonance frequency is set by the thickness of the constituent films, FBARs are limited to a small range of frequencies on each wafer, achieved using mass loading with metal [23]. To achieve multiple frequencies on a single chip, contour mode resonators can be realized using the metal-piezoelectric-metal sandwich either by patterning the entire stack to excite certain in-plane modes [24] or by patterning the electrodes to form interdigitated transducers for Lamb-mode excitation [25].

High-quality GaN is typically grown epitaxially either by MBE or MOCVD. In either case, the high temperatures and purity of the epitaxial chamber often preclude the presence of a bottom metal electrode prior to GaN growth. Instead, researchers have demonstrated GaN FBAR [26] and Lamb wave resonators [27] by back-etching through the handle wafer to suspend the GaN film and depositing a bottom electrode from the back (Fig. 3.3a, b) or by using silicon as the bottom electrode using a starting SOI wafer [28].

The required back etch through the wafer to deposit the bottom electrode on GaN after growth can be limiting with regard to substrate material and embedded etch stop. However, this electrode configuration achieves highest transduction coupling coefficient Alternately, meshed electrodes can be embedded inside the GaN film prior to the active GaN growth to realize a bottom electrode (Fig. 3.3c). This method relies on regrowth of GaN on a meshed metal electrode and may be a promising alternative to through-wafer etching [14]. However, it remains to be seen what effect this approach has on 2DEG concentration and HEMT operation in an AlGaN/GaN heterostructure.

Lateral Excitation of GaN Resonators

For simplicity of fabrication and ease of seamless integration in GaN MMIC technology, Lamb-mode resonators with no bottom electrode have been designed

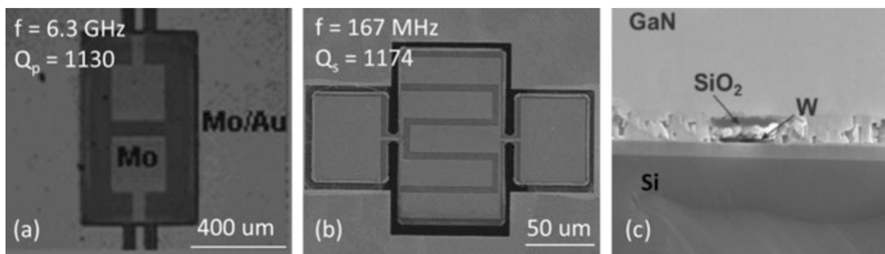

Fig. 3.3 GaN bulk acoustic resonators with grounded bottom electrodes in (**a**) FBAR mode [26] (**b**) Lamb mode [27]. (**c**) Bottom mesh electrode embedded in GaN film during growth [14]

and demonstrated, exhibiting multiple frequencies on a single chip side by side with HEMTs. The fabrication of these resonators requires only two additional steps to the standard GaN-on-Si MMIC process, including a deep GaN etch to define the resonant cavity and an isotropic etch (e.g., using XeF_2) to release the device from the handle wafer. In gold-free technology increasingly used for compatibility with CMOS processing, GaN Lamb-mode resonators with no bottom electrode can achieve exceptionally high f·Q products [13, 15] partially due to the reduced acoustic losses associated with metal in the resonant structure. f·Q values up to 1.56×10^{13} have been reported for Lamb-mode GaN resonators centered at 1.9 GHz and operated in vacuum [29]. This is one of the highest values recorded and comes very close to the fundamental limit of f·Q defined by phonon-phonon losses in the material (see Sect. 3.4 of this chapter).

Of course, this enhanced Q comes at the cost of transduction efficiency. The effect of the bottom electrode on Lamb-mode resonator k^2 has been studied in AlN [30] and GaN [12, 13]. Figure 3.4 shows a comparison of transducer efficiency for GaN Lamb-mode resonators with and without a grounded bottom electrode. The symmetric (S0) mode is attractive due to high Q relative to the asymmetric (A0) mode which undergoes large thermoelastic dissipation. It can be seen that the S0 Lamb mode has a maximum transduction efficiency at a frequency corresponding

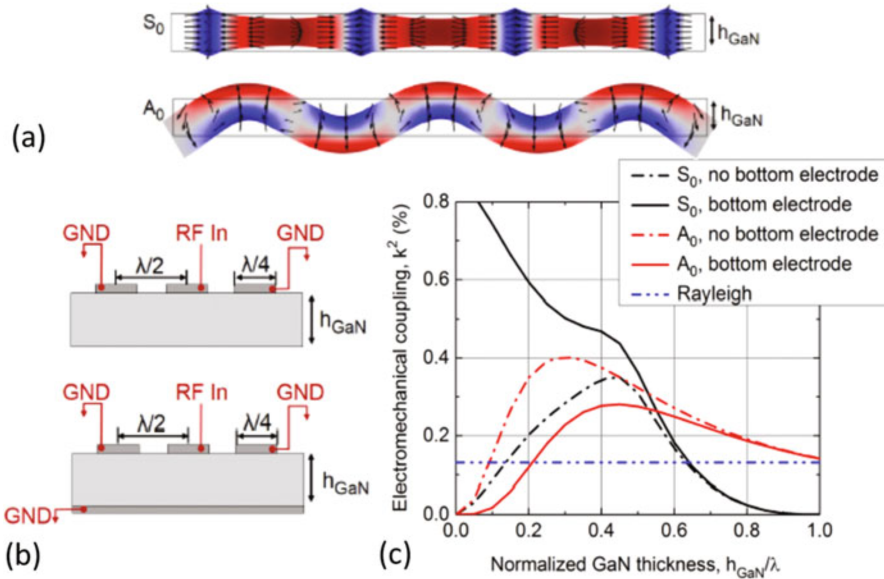

Fig. 3.4 Comparison of transduction efficiency between GaN (**a**) symmetric (S0) and asymmetric (A0) Lamb-mode resonators (**b**) with and without bottom electrode [29]. (**c**) Transduction efficiency of symmetric Lamb wave more is highest when thickness of the GaN (h_{GaN}) is 0.45× the resonance wavelength (λ)

to $h_{GaN}/\lambda \sim 0.45$, where h_{GaN} is the thickness of the GaN film and λ is the acoustic wavelength.

For applications with bandwidth requirements below ~0.4 % including timing, notch and channel-select filtering, and sensor applications, this resonator design may be ideal due to high quality factor and ease of integration with control circuitry in standard MMIC technology. For higher bandwidth applications, a bottom electrode is required as described previously.

Metal-Free Transduction with 2DEG

A unique aspect of piezoelectric compound semiconductors is their ability to form a 2DEG sheet at the interface of certain heterojunctions, as discussed in Sect. 3.1 of this chapter. In the AlGaN/GaN heterostructure, this 2DEG exhibits high carrier concentration and high mobility, resulting in sheet resistance between 200 and 400Ω/□. The 2DEG can be defined in various ways, including (1) a shallow "mesa" etch to remove the thin AlGaN layer on top of GaN to eliminate the quantum well generating the 2DEG; (2) implantation of the AlGaN, which may result in local destruction of the lattice [31]; and (3) selective depletion of the 2DEG using a negative bias voltage applied to a patterned Schottky contact above the AlGaN [32–34]. The 2DEG must have an Ohmic contact nearby for successful depletion.

The patterned 2DEG can form electrodes for piezoelectric transduction. Though the sheet resistance in GaN HEMT technology is currently too high for 2DEG electrodes in RF applications, the mesa etch can be used to realize metal-free resonators necessary for interrogating fundamental material properties and loss mechanisms in the GaN resonator and may have additional benefits in sensor applications.

A comparison of quality factor was performed between Lamb-mode resonators with gold metal electrodes and those with 2DEG-based IDTs [32, 33]. A consistent drop in mechanical Q of approximately 3× was observed in resonators containing metal transduction electrodes relative to 2DEG-based transducers. This helps parse out the loss in metal electrodes relative to thermoelastic dissipation, anchor losses, and phonon-phonon scattering which are common to resonators using both types of transducers. Since GaN MMIC technology is still a maturing field, feedback from fundamental studies enabled by 2DEG electrodes can help refine growth processes and heterostructure optimization for concurrent high-performance MEMS and HEMTs.

3.2.2 Piezoresistive Transduction

GaN, in contrast to the other commonly used piezoceramics, is a semiconductor that exhibits piezoresistive effect [35, 36] in addition to the piezoelectric behavior [37]. The large piezoresponse—combined piezoelectric and piezoresistive effects—of

GaN points out possible applications of GaN-based material systems in resonant devices. With its large spontaneous polarization, several effects can contribute to the piezoresponse of GaN. For example, bending a bulk GaN beam induces a vertical stress gradient, which in turn induces polarization doping (similar to the case of a graded AlGaN layer [38]). Second, there is the energy band structure realignment with its associated carrier redistribution in the transversal and longitudinal valleys [39]. In an AlGaN/GaN heterostructure, there is additionally the modulation of the interfacial 2DEG density by stress modulation of the heterostructure interface [39]. A combination of these effects results in large changes in the resistance and therefore a large gauge factor (GF) for a passive resistor or a significant shift in the 2DEG density of a transistor placed on a high-stress region of a bending beam. While static piezoresistive response of GaN is small [35, 36], time-dependent piezoresponse of GaN electromechanical devices is much larger than that of its other semiconductor rivals, silicon, and SiC, as a result of significant piezoelectric contribution to the overall response. Hence, GaN having a large GF of nearly 3500 in a heterostructure [40] has an advantage over other piezoresistive materials for time-dependent applications. Micromechanical resonators are classic examples of such time-dependent systems.

The first electromechanical device type that utilized the piezoresponse of GaN was a cantilever beam with a piezoresistor or a transistor structure (HEMT or HFET) at the pivot point of the cantilever [39, 41] (Fig. 3.5). Early prototypes focused on the static response of the cantilever beam upon application of pressure or a strain force. In such a device, several effects contribute to the bending response. First, the donor/conducting valley pairs shift causing redistribution of carriers in the longitudinal and transversal energy valleys in the bulk, which is the result of the direct piezoresistive effect in GaN. As discussed earlier, the contribution of this effect is presumed to be small in n-type GaN [35, 36]. This is due to the premise that the donor states in n-type GaN are close to the conduction band, and the donor energy levels shift together with the conduction band under stress. Consequently, the donor activation energy does not change under strain, leading to a small static piezoresistive effect [35, 36].

Second, bending a cantilever induces a vertical stress gradient across the beam, generating a polarization gradient, which in turn generates a distribution of free carriers (holes or electrons) [38] across the beam. The corresponding donors or acceptors are represented by the stress-induced change in the bonded polarization charge distribution. This effect was first introduced in [39]. In the same article, Zimmerman et al. discussed that upward bending of the Ga-face-oriented GaN cantilever shows p-type polarization doping in the bulk. Similarly, downward bending will result in n-type polarization doping, both generating bulk conduction paths in parallel to the piezoresistive channel.

Third, in the case where a HEMT is used to sense the bending strain, in addition to the aforementioned effects, the piezoresponse of the AlGaN/GaN interface needs to be considered [42]. Bending changes the stress magnitude of the already prestressed AlGaN barrier layer, shifting the piezo-induced 2DEG density. In summary, the piezoresponse of a GaN cantilever to static bending is a result of a combination of these three major effects in GaN.

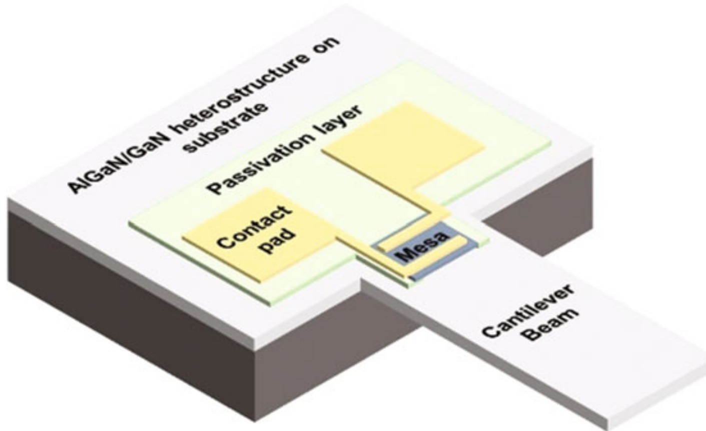

Fig. 3.5 A schematic showing the position of the piezoresistor for sensing the deflection of an AlGaN/GaN cantilever beam. This is the basic structure used for early demonstration of GaN-based MEMS and measurement of GaN GF

Although only the static piezoresponse of the cantilever beam was reported in early demonstrations of GaN MEMS, it is clear that the same device can be operated in a dynamic resonance mode [40]. Piezoresistive signal pickup is especially useful when implementing resonators at multi-GHz frequencies, where large-signal feedthrough prohibits effective signal detection using other sensing schemes [43, 44]. With the piezoresistive effect being a sense mechanism only, the device should be excited through other means, such as piezoelectric transduction using electrodes sandwiching the entire piezo stack or using only a portion of the piezo stack as the transducer. For the latter approach, the 2DEG sheet can be used as one of the electrodes. This is the main mechanism used for the resonant body HEMTs discussed later in this chapter.

Faucher et al. demonstrated the first time-varying resonant beam whose resonance response was sensed through monitoring the drain-source current of a HEMT placed on the pivot points of the clamped-clamped beam [45]. In their doubly clamped structure, the flexural resonance mode was excited piezoelectrically using the AlGaN layer with a Schottky top electrode and the 2DEG sheet as the bottom electrode. In this device, the piezoresistor was basically the region between the drain and the source, with the drain Ohmic contact on the beam and the other located below the anchoring point (Fig. 3.6). This choice was motivated by the fact that strain is concentrated in that region. In such a device, two mechanisms contribute to a change in the drain-source current: (1) the dynamic strain causes modulation of the 2DEG density due to the difference between the AlGaN and GaN piezoelectric coefficients. (2) Surface charges generated by the entire GaN buffer layer further modulate the current [46]. We leave a more detailed discussion on the resonant HEMTs to the next section and only note here that the same principle could be

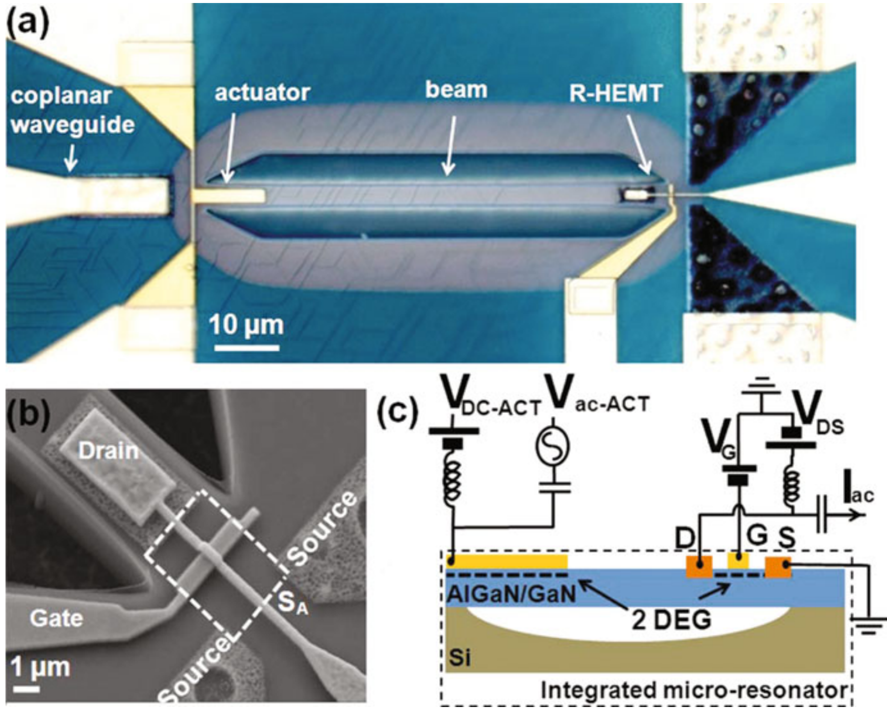

Fig. 3.6 (**a**) Optical image of the first GaN doubly clamped beam resonator. The device exploits the 2DEG at the AlGaN-GaN interface located between drain and source contacts, with a top gate to control the carrier density. (**b**) A scanning electron microscope (SEM) image of the device. The drain electrode is separated from the surface and gate thanks to a dielectric layer nonvisible here. (**c**) Resonator measurement setup. (Reproduced from [45])

used to detect the resonance response if a simple piezoresistor (a gate-less HEMT) was employed for sensing instead [47]. The change in the resistance could then be converted to a voltage response using the popular Wheatstone bridge configuration or a transimpedance amplifier (TIA). Since the gate gives an extra control knob for tuning the resonance response, devices with piezoresistive readout have almost exclusively used a gated HEMT for sensing.

3.2.3 GaN Resonant Body Transistors

Passive piezoelectric transduction is an energy-conserving transduction mechanism and is by far the most common method of driving and sensing in piezoelectric resonators. This approach is discussed at length throughout this book and offers a simple, low-power, low-noise solution for piezoelectric resonator design. However, the finite transduction efficiency k^2 of such devices typically falls in the range

of 0.1–10 %, limited by material properties such as piezoelectric coefficients, permittivity, and compliance. In GaN, the maximum achievable k^2 is a moderate 2 % [17]. In practical terms, this means that to achieve sufficiently low motional impedance or insertion loss, a large transducer capacitance is required. Among other things, this transducer capacitance poses a limit on rejection of the broadband signal floor off-resonance, assuming a 50Ω termination, which becomes a significant concern as resonators scale to GHz frequencies of operation. To overcome the low-signal-to-floor ratio at high frequencies, transistor sensing of acoustic vibrations can be employed, which provides an electromechanical amplification of the resonance prior to electrical parasitics and enables detection of acoustic resonators at 10–100× higher frequencies than possible with passive transduction. To date, resonators up to 37 GHz have been demonstrated with this two-port electrical readout, using silicon FinFETs [48, 49]. Fundamental frequency scaling of the RBT is limited primarily by the cutoff frequency of the sense transistor, which can read hundreds of GHz.

Transistor Sensing in Piezoelectric Resonators

The concept of transistor sensing in electromechanical resonators dates back to some of the first MEMS devices. In 1967, Nathanson et al. demonstrated the resonant gate transistor (RGT), driving resonance in a conductive cantilever with a gap-closing electrostatic transducer [50]. The RGT cantilever served as the gate of an air-gap transistor, with output drain current modulated by the cantilever resonant motion. In 2003, Chang and Bhave extended this concept to devices in which the resonance was excited in the body of the transistor rather than the gate [51]. The resulting resonant body transistor (RBT) can generate an electromechanical transconductance based on field-effect, piezoresistive, or electrostrictive modulation and piezoelectric modulation in the case of compound semiconductors such as GaN. Transistor sensing has since been implemented in a variety of micromechanical devices, including RGTs and RBTs in silicon [48, 49, 52–54] and in GaN [32, 33, 45, 55].

A small-signal equivalent circuit of the RBT is shown in Fig. 3.7. This four-terminal device includes a source S, drain D, and gate G2 associated with the sense transistor in addition to a driving gate G1. The left hand side of the equivalent circuit looks like a standard Butterworth—van Dyke (BVD) model which describes the mass-spring-damper represented by a series RLC tank and input capacitance to drive resonance. This BVD model applies to both electrostatic and piezoelectric energy-conserving transducers. The right hand side of the RBT model presents the transistor sensing. The device is typically operated with the transistor gate voltage G2 held constant such that any modulation in the drain current is attributed to mechanical vibrations. This small-signal drain current is represented by a voltage-dependent current source with *electromechanical* transconductance g_{α} and the small-signal voltage v_{CM} across the motional capacitance C_m corresponding to stress in the resonant body.

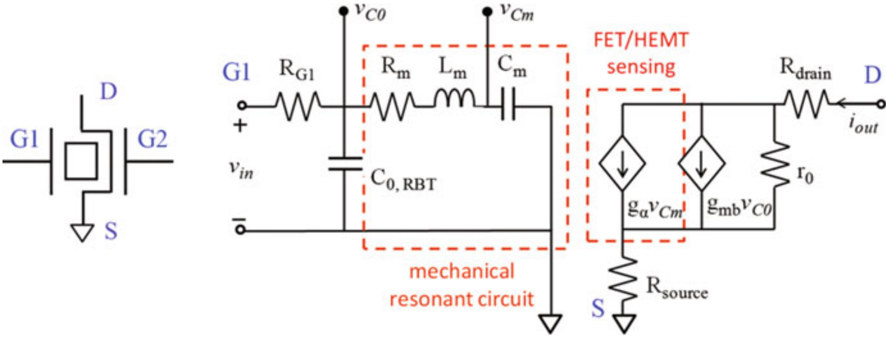

Fig. 3.7 Equivalent circuit of a RBT

In GaN HEMT-based RBTs, the electromechanical transconductance arises primarily from a change in 2DEG charge density due to polarization in the GaN and AlGaN layers as the resonator vibrates. Secondary effects include the piezoresistance between source and gate and drain and gate regions over which the drain current must travel [46]. The decoupling between input and output afforded by this active sensing and the boost in the mechanical signal due to the electromechanical transconductance are key in enabling high-frequency detection of acoustic resonance.

Flexural Resonant Body Transistors

The first GaN RBT was demonstrated by Faucher et al. [45] (Fig. 3.6). An out-of-plane flexural vibration was induced in a doubly clamped beam resonator by applying an AC field across the AlGaN of an AlGaN/GaN HEMT stack at one end of the beam. This field was established between a Schottky contact on top of the AlGaN (using the gate metal of the HEMT process) and the 2DEG inherent at the AlGaN/GaN interface. At the other end of the beam, a HEMT was designed to sense vibrations as discussed above. The resonator achieved Q of 1850 at 1.49 MHz and showed explicitly the effect of electromechanical gain due to HEMT sensing under different biasing conditions.

Bulk Wave Resonant Body Transistors

To truly leverage HEMT sensing at higher frequencies of operation, bulk mode GaN RBTs were then explored in the range of L and S bands. Figure 3.8 shows a (a) Lamb wave resonant body transistor at 1 GHz with Q over 3000 (no bottom electrode) and (b) thickness mode resonant body transistor with Q of 250 at 4.23 GHz. In the Lamb wave RBT, the AlGaN was selectively removed in the drive region so that interdigital transducers (IDTs) could generate fields penetrating

deep into the GaN for lateral actuation. HEMT sensing was performed on a second, identical resonance cavity coupled strongly to the drive via mechanical coupling beams to ensure synchronized resonance with minimal direct electrical feedthrough capacitance. Consequently, good off-state rejection is achieved and is independent of HEMT biasing. As in the case of the flexural GaN RBT, the electromechanical transconductance at resonance is strongly dependent on DC biasing of the sense HEMT. Here, the HEMT is positioned to maximize strain under the gate, with maximum g_α in saturation. More recently, a Lamb wave RBT was demonstrated using Schottcky IDT contacts biased in depletion as the transducer and a HEMT as the sense placed on a low-loss acoustic phonon trap [15]. This device showed a *Q* exceeding 7000 at 740 MHz, which is one of the highest f.*Q* values seen for GaN-based RBTs so far. The thickness mode RBT similarly sees a strong dependence on HEMT biasing. With the HEMT positioned to maximize strain under the drain, optimal performance is obtained with the HEMT near cutoff. The advantage of the thickness mode RBT (Fig. 3.8b) is its higher electromechanical coupling efficiency resulting in higher acoustic transconductance. Relying on the thickness resonance modes, this structure can reach higher frequencies without the need for advanced submicron lithography [55].

The use of active transistor sensing to amplify mechanical resonance prior to electrical parasitics has been shown to enable frequency scaling deep into the Ka band, limited by transistor rather than acoustic performance. Fundamentally, electromechanical transconductance and subsequent frequency scaling can be achieved using piezoresistive sensing [44] with lower power consumption. However, transistor sensing provides reduced noise induced from piezoresistive sensing and potentially higher gain [57]. GaN technology offers high-frequency HEMTs with intrinsically low noise due to reduced surface scattering relative to Si FETs, further improving performance relative to passive piezoelectric and piezoresistive sensing of acoustic resonance in the multi-GHz range.

3.3 Applications

3.3.1 GAN-Based Physical Resonant Sensors

It is readily understandable that any mechanical resonator can be used in a frequency synthesizer (discussed in the next sub-section) or as a frequency-shifting sensor. In fact, micromechanical resonators have been widely used for sensing temperature, humidity, pollution, etc. The challenge in developing resonant sensors has been to improve the device sensitivity to the measurand(s) of interest while also improving the specificity and reducing noise. This has been achieved through surface functionalization, differential signal pickup, and/or calibrating the response using a reference resonator. In Part 4, general and commercial applications of piezoelectric micromechanical resonators are discussed. In this section, we focus on a few that are enabled by specific properties of GaN [58]—properties that are either not present or sufficiently strong to make these applications common to

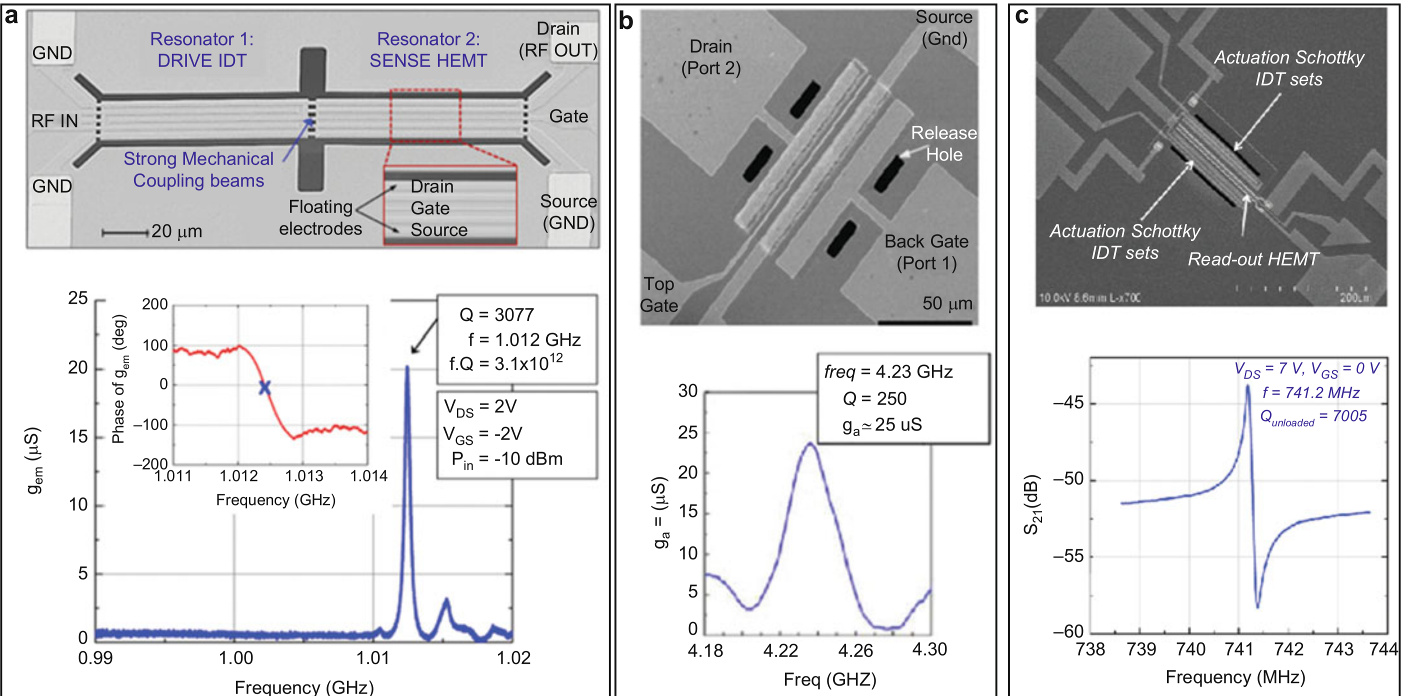

Fig. 3.8 Bulk wave GaN RBTs including (**a**) Lamb wave [12, 13] (**b**) thickness [56] modes of vibration and integrated HEMT sensing. (**c**) Measured S_{21} response of a resonant HEMT, showing the ninth-order width-extensional resonance mode at 741.2 MHz with a high Q of 7005, at $V_{DS} = 7$ V and $V_{GS} = 0$ V of the readout HEMT

other piezoceramics. First, as discussed earlier, GaN is a piezoelectric and also a piezoresistive material, facilitating resonant signal transduction in a homogenous GaN-based film. The word piezo makes it an obvious candidate for detecting any change in the mechanical stress induced through vibration, pressure [41, 59], or static bending (as is the case in AFM cantilevers [45]).

Most materials exhibit a change in elasticity with temperature. In timing applications discussed later, the temperature coefficient of elasticity (TEC) has to be nulled or accounted for to realize a stable clock. In sensors, however, the intrinsic TCE and the resulting temperature coefficient of frequency (TCF) can be used to detect a change in temperature. This is the basis of resonant temperature sensors using silicon [60]. The same idea can be extended to GaN, which interestingly has an acoustic velocity and a TCF very close to moderately doped silicon [17].

GaN is also a strong pyroelectric material [35, 36, 61]. In fact, it is shown that GaN is one of the strongest pyroelectric ceramics with pyroelectric voltage coefficient of 10^4 V/mK ([35, 36] (vol. 69)). The most immediate application of pyroelectric materials is in uncooled infrared (IR) sensing [62, 63]. Since pyroelectricity is a transient response, resonant pyroelectric detectors require a chopper for signal detection. The chopper adds to the weight and size of the system, but it eliminates the need for any external calibration. In pyroelectric bolometers, the frequency shift of the detecting element can be compared to the non-radiated response of the same element when the chopper is off to remove the effect of any other mechanism which may also cause a shift in frequency (e.g., a change in the ambient temperature). In cases where having a chopper or a modulator is undesirable, the TCF of the resonator can be used to detect the temperature change induced by IR radiation [64, 65]. In that case, a reference resonator can be used for differential sensing. Rais-Zadeh was the first to report on resonant IR sensors using pyroelectric response of GaN [66]. Since GaN is a wide-bandgap material and is not an efficient absorber of short to mid-wavelength IR, an IR absorber coating was used to enhance the detectivity of the sensor. Note that if an absorber of terahertz or ultraviolet (UV) radiation was used instead, terahertz/UV detection could have been possible. In a later article, Gokhale and Rais-Zadeh further noted that the electrostrictive property of GaN combined with its pyroelectric behavior was the main contributor to the large frequency shift of GaN resonators with IR radiation [67]. Although, there is some debate about the actual value of electrostrictive coefficients of GaN, with theoretical estimates being orders of magnitude different from the experimentally extracted values [68, 69], it is recognized that this multifunctional material exhibits a significant electrostrictive effect. The nonlinear electrostrictive mechanism can be used to enhance the sensitivity of other resonant devices based on GaN. It should be noted that IR sensors along with an IR radiation source can also be used for gas sensing [70] as most gases have a unique *fingerprint*—absorption at a specific wavelength—in the IR range. For example, active IR detectors can be used to sense carbon dioxide with absorption wavelength in the 3–5 μm range [71].

In a heterostructure of a doped GaN and an insulating AlGaN, the presence of a 2DEG at AlGaN/GaN interface provides another strong sensing mechanism. As the 2DEG is very close to the surface of the heterostructure and is confined within a

few nanometers (2 nm), it is extremely sensitive to any changes in the free surface charge [72]. For example, if ions are absorbed at the free surface, a similar number of electrons are gained or lost in the 2DEG. Therefore, any change in the surface charge prevails as a change in the 2DEG conductivity, but amplified by several orders of magnitude (due to the mobility difference of electrons and ions). This is the basic operation principle of sensors based on AlGaN/GaN HEMTs [72] or GaN ion-sensitive field-effect transistor (ISFETs) [73]. In addition to the intrinsic sensitivity of 2DEG to changes in the surface charge, other mechanisms can be used to enhance the sensitivity of a HEMT for sensing other chemicals, gases, and bio samples. As an example, the gate can be made out of a material that exhibits catalytic activity, such as Pd or Pt. Absorption of gases on the surface of an AlGaN/GaN heterostructure equipped with such a catalytic gate influences the Schottky barrier height of the catalytic metal contact, a mechanism that is used to sense a large variety of gases [74]. In a similar approach, pH sensors can be made. Although in [75], it is suggested that the native oxide on the nitride surface was responsible for the pH sensitivity of the gateless HEMT to electrolyte solutions [41].

Through monitoring the capacitance (instead of the resistance) of a HEMT channel on a released membrane, pressure change or mechanical strain can also be sensed [76]. Although the 2DEG is an excellent marker for detecting a variety of measurands, GaN devices relying on the 2DEG channel for sensing have been stationary piezodevices rather than resonators. There is a wealth of knowledge in the GaN/AlGaN solid-state devices and sensors domain that could be used to implement similarly powerful or even higher performance sensors using AlGaN/GaN resonant transistors or resonators with 2DEG electrodes. More importantly, similarity in the device structure of such GaN sensors and AlGaN/GaN transistors opens up a possible route for monolithic integration of both sensor functions and analog and digital data processing and transmission on the same chip or inside the same package [72].

3.3.2 Frequency Synthesizers and Timing

The GaN-based sensors outlined in the previous section hold great potential for autonomous sensor networks in the context of the Internet of Things and lab-on-a-chip diagnostics. Research in this space has so far focused on demonstration of sensitivity and selectivity of this material system to the desired measurands. To readout the response of these resonant sensors, one common method is to build a closed-loop system in which the mechanical resonators' oscillations are sustained by an amplifier. The ease of monolithic integration of GaN MEMS resonators within MMIC technology commonly used for high-frequency, low-noise amplifiers makes such oscillators readily accessible.

First demonstration of an all-GaN oscillator incorporated a SAW device in a feedback loop with an off-the-shelf amplifier [77]. With a resonator Q of 1730 at

a resonance frequency of 1 GHz, a phase noise of −115 dBc/Hz was recorded at 10 kHz offset from the carrier with noise floor of −165 dBc/Hz.

Towards the goal of implementing a single-chip oscillator, a GaN BAW resonator was monolithically integrated with a HEMT in 2012 [78]. Using a similar platform, the first monolithically integrated GaN MEMS-based oscillator was demonstrated by Bahr et al. [57]. Pierce and Colpitts crystal oscillators were realized using Lamb wave resonators with no bottom electrode described in [12, 13] with Qs exceeding 5000 at 1 GHz and piezoelectric coupling coefficient k_{eff}^2 of 0.23 %. Figure 3.9 shows an optical micrograph of a Pierce oscillator, with a GaN MEMS resonator, oscillator core, and 50 Ω buffer for readout fabricated side by side on the same chip. The resonator and core occupy an area of $268 \times 214\ \mu\mathrm{m}^2$ with low-phase-noise floor of −130 dBc/Hz. Close to carrier, the noise has a characteristic slope of −30 dB/dec, corresponding to flicker noise in the system.

The high Q, compact footprint, and capacity for intimate integration with ICs of GaN MEMS resonators make them ideally suited for monolithic low-phase-noise clocks. The application space for such clocks is vast, ranging from sensors to communications and navigation and beyond. Part 4 delves into more detail of piezoelectric resonators for high-frequency oscillators and their commercial opportunities.

3.4 Future Outlook

In recent years, we have seen an increasing interest in GaN-based heterostructures for mm-wave circuits, power electronics, and optoelectronics. While the use of GaN as an electromechanical material is a relatively new technology direction [17], similarity in the device structure of GaN resonators and AlGaN/GaN transistors paves the way for adoption of the more mature transistor technology for implementing complementary GaN MEMS and microsystems. In fact, the electromechanical resonators that have been demonstrated so far have resorted to using the stacks optimized for electronic devices [12, 13, 55, 79], and any custom-made GaN epilayer used in resonators had a very similar structure to those commercially available for fabricating GaN/AlGaN HEMTs [27, 28, 45, 77, 78, 80]. Therefore, the ever-improving processes developed for GaN epitaxy or deposition equally impact the performance of GaN micromechanical devices as those of transistors, diodes, and optical devices the industry mainly targets. Having said that, there are several factors that are exclusively important when implementing a micromechanical device that may not even be monitored if a streamline process is used. For example, with the HEMT being a surface device, bulk properties of the materials in question are of minor importance. For this reason, most GaN HEMT stacks include a relatively thick layer of an unintentionally doped (UID) GaN layer with the exact doping concentration not monitored or characterized. Before we discuss possible improvements that could be made to GaN resonators, we first need to see how such material parameters affect the device performance.

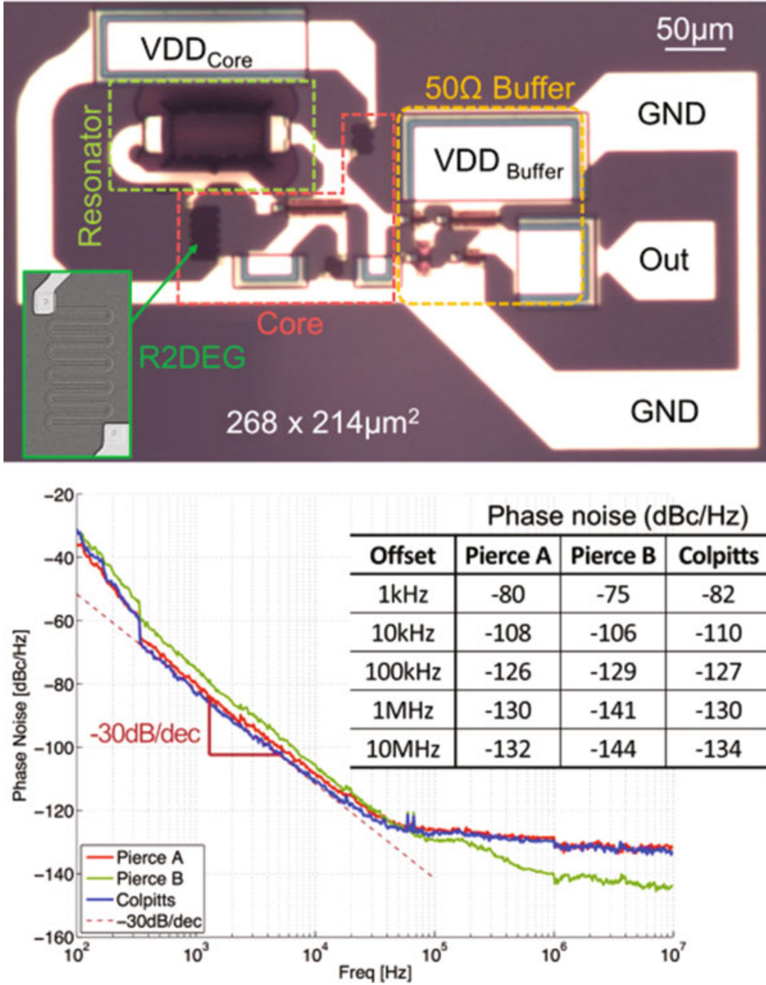

Offset	Pierce A	Pierce B	Colpitts
1kHz	-80	-75	-82
10kHz	-108	-106	-110
100kHz	-126	-129	-127
1MHz	-130	-141	-130
10MHz	-132	-144	-134

Fig. 3.9 Monolithic GaN MEMS-based oscillators in standard MMIC technology [57]

One of the most important figure of merits for mechanical resonators is the product of frequency and Q (i.e., the f.Q value). The Q of an acoustic resonator is directly related to the total energy lost in each resonance cycle. There are a few intrinsic energy dissipation mechanisms that cannot be overcome by optimizing the resonator design or the phonon-trapping efficiency. Thermoelastic damping (TED) and loss of phonon energy to the material lattice (phonon-phonon loss) and to conduction electrons (phonon-electron loss) are examples of intrinsic losses and are considered the ultimate limiting factors of the Q for a micromechanical resonator. The measured values of the resonator f.Q (having the non-intrinsic losses accounted

for) are a good indicator of how close the properties of the resonator material are to the ideal bulk values.

At low frequencies, when the resonance period is much larger than the lattice relaxation time of the material crystal, it is found theoretically that the f.Q remains constant with frequency [81]. The frequency range at which the acoustic phonons interact with ensembles of lattice phonons and the f.Q stays constant is known as the Akhieser regime [82]. For GaN, this regime should be valid for frequencies as high as 5 GHz (at room temperature and ambient pressure). At higher frequencies, it is considered that acoustic phonons interact with individual lattice phonons and the limiting value of f.Q is given by the Landau-Rumer (L-R) regime. For high-frequency longitudinal wave resonators made from GaN, the TED is not significant [83]; however, it is generally a dominant damping mechanism for lower-frequency flexural-mode resonators [84, 85]. For GaN, a semiconductor, electron scattering is also a significant loss mechanism [86], which is highly dependent on the free carrier concentration, the carrier mobility, and the coupling between the electrical and mechanical domains (due to piezoelectric or deformation potential coupling) [65]. In addition, in piezoelectrically transduced resonators, phonon losses due to charge redistribution can significantly affect the Q [87].

Figure 3.10 shows the f.Q limit of GaN set by phonon-phonon and phonon-electron interactions and compares that to the measured data (red circles) from GaN resonators presented in the previous sections. Material properties used for calculation of f.Q limits are given in Table 3.2 [17]. The reason that the doping concentration of GaN for measured data points is not given is because the bulk doping level is not monitored or specified for the films used. The gap between the theoretical and measured results may be due to this or other effects that also play a role in damping the device resonance. All measured data points are for GaN resonators or AlGaN/GaN resonant HEMTs on silicon substrates. We emphasize here that the plot merely shows an estimate of the resonator performance limit and the exact values of f.Q are dependent on the quality of the GaN film, the carrier concentration of GaN, the specific design of the resonator, the phonon relaxation time in that specific phonon branch, and the fitting Grüneisen parameter. Other parameters, such as dislocation density, electron mobility in the bulk, and homogeneity of the stack, also affect acoustic phonon interactions with the lattice phonons and electrons but are not considered here as little is known about the effect of such nonidealities on the Q. Yet, the measured and theoretical values corroborate well, proving the quality of GaN films epitaxially grown on (111) silicon is decent. Any improvement to GaN on silicon growth processes further improves the limits on the resonator f.Q value and its ultimate performance.

Another figure of merit, specifically for piezoelectrically transduced resonators, is the piezoelectric coupling coefficient. The effective coupling coefficient k_{eff}^2 is extracted from the mechanical response of the resonators and includes the effects of metal electrode loading, nonideal electrode area coverage, and anisotropic effects. The measured values of k_{eff}^2 in prior literature are seen to be close to the calculated maximum values for both the thickness modes (measured 1.9 % vs. theoretical limit of 2 %) and in-plane modes (measured 0.9 % vs. theoretical limit of 1.3 %)

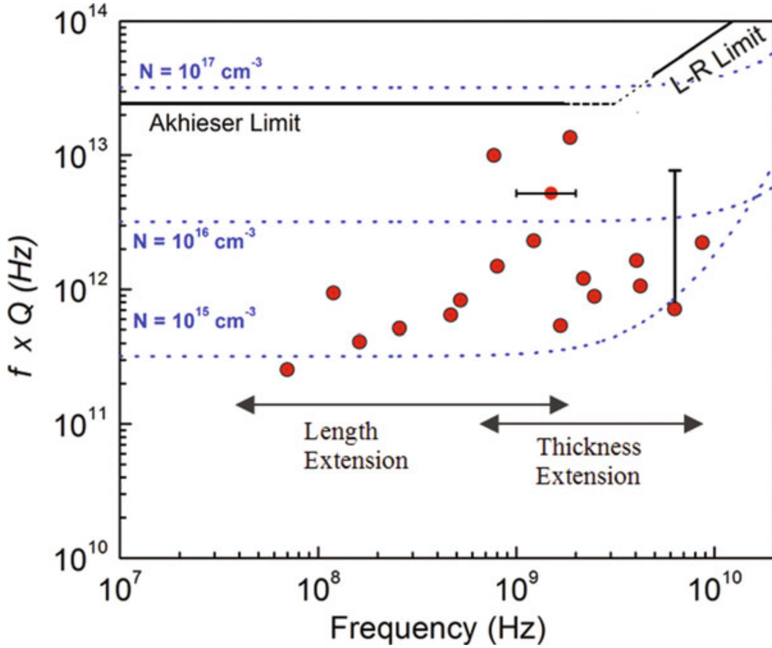

Fig. 3.10 Estimated values of the f.Q limits for the dominant intrinsic dissipation mechanisms in GaN ($\gamma = 1.18$, $\tau = 2$ ps). Red dots show measured values for GaN-based resonators (theoretical limits reproduced from [17])

Table 3.2 Material properties used for calculation of theoretical f.Q values of GaN [17]

Material property	Values
ρ (mass density)	6150 kg/m^3
C_s (specific heat)	490 J/kg K
μ (electron mobility (bulk GaN))	200 cm^2/V s
N (free electron concentration)	1×10^{16} cm^{-3}
k (Piezoelectric coupling coefficient)	0.02
ε (dielectric constant of GaN)	9.5
τ (phonon relaxation time)	(2–6) $\times 10^{-12}$ s
k (thermal conductivity)	130 W/m K
β (coefficient of linear expansion)	5.6×10^{-6} K^{-1}
s (acoustic velocity)	8000 m/s
γ (Grüneisen parameter)	0.74–1.18
Ξ (deformation potential constant)	12 eV
τ_R (intervalley relaxation time)	1.2×10^{-12} s

(Fig. 3.11a) [17]. Another related metric that is used often for characterizing the applicability of a piezoelectric material for use in RF electromechanical filters is the product of k_{eff}^2 and Q with higher values of this parameter more desired for widerband filters. In this regard, measured GaN resonators have demonstrated

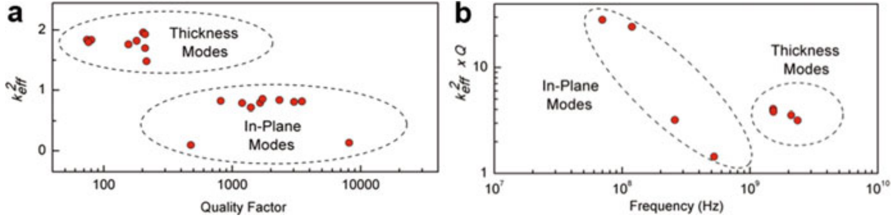

Fig. 3.11 Measured values of (**a**) k_{eff}^2 as a function of Q and (**b**) $k_{eff}^2 \times Q$ as a function of frequency for reported GaN piezoelectric resonators. (Reproduced from [17])

similar numbers (Fig. 3.11b) in comparison with quartz, diamond, AlN-on-Si, and Si-based internal dielectric transduction. However, it is significantly lower than stronger piezoelectric materials such as $LiNbO_3$ [88–90] or single crystalline AlN resonators [21, 22]. Therefore, for wideband frequency filtering, GaN does not provide sufficient coupling efficiency, and its application should be reduced to sensors, resonators, and perhaps narrowband channel-select filters.

In this chapter, we have shown that GaN is quickly becoming a strong contender for implementing piezoelectric resonators. These devices in conjunction with AlGaN/GaN HEMTs could enable low-noise, high-speed, and power devices and circuits for use in sensing, surveillance, electronic warfare, multifunctional RF systems, communications, and power applications. Such GaN resonators and systems can be especially attractive for mining and harsh environment resource exploration, aerospace, and defense. With the recent push to heterogeneously integrated GaN devices with CMOS, several other applications open up taking advantage of the unique functionalities of both material systems.

References

1. Parmenter RH (1953) The acousto-electric effect. Phys Rev 89(5):990–998
2. Hutson AR (1960) Piezoelectricity and conductivity in ZnO and CdS. Phys Rev Lett 4(10):505–507
3. Hutson AR, McFee JH, White DL (1961) Ultrasonic amplification in CdS. Phys Rev Lett 7(6):237–240
4. Hutson AR, White DL (1962) Elastic wave propagation in piezoelectric semiconductors. J Appl Phys 33(1):40–47
5. White RM (1967) Surface elastic-wave propagation and amplification. IEEE Trans Electron Dev 14(4):181–189
6. Miller R, Nothnick CE, Bailey DS (1992) Acoustic charge transport: device technology and applications. Artech House, Boston, MA, USA
7. Tanski WJ, Merritt SW, Eschrich TC et al (1988) Heterojunction acoustic charge transport devices on GaAs. Appl Phys Lett 52(18):18–20
8. Kazior TE, Laroche JR, Lubyshev D et al (2009) A high performance differential amplifier through the direct monolithic integration of InP HBTs and Si CMOS on silicon substrates. IEEE International Microwave Symposium, Boston, MA, pp 1113–1116. Accessed 7–12 June 2009

9. Li JC, Royter Y, Elliot KR et al (2008) Heterogeneous wafer-scale integration of 250nm, 300GHz InP DHBTs with a 130nm RF-CMOS technology. IEEE International Electron Devices Meeting, San Francisco, CA, pp 1–3. Accessed 15–17 Dec 2008
10. Ambacher O (1998) Growth and applications of group III-nitrides. J Phys D Appl Phys 31(20):2653
11. Feltin E, Beaumont B, Gibart P et al (2001) Stress control in GaN grown on silicon (111) by metalorganic vapor phase epitaxy. Appl Phys Lett 79(20):3230–3232
12. Popa L, Weinstein D (2014) L-Band lamb mode resonators in gallium nitride MMIC technology. IEEE International Frequency Control Symposium, Taipei, Taiwan, pp 1–4. Accessed 19–22 May 2014
13. Popa LC, Weinstein D (2014) 1 GHz GaN resonant body transistors with enhanced off-resonance rejection. Solid-State Sensors, Actuators and Microsystems Workshop, Hilton Head, South Carolina, pp 269–272. Accessed 8–12 June 2014
14. Ansari A, Liu CY, Rais-Zadeh M et al (2015) GaN micromechanical resonators with meshed metal bottom electrode. Materials 8(3):1204–1212
15. Ansari A, Tabrizian R, Rais-Zadeh (2015) A high-Q AlGaN/GaN phonon trap with integrated HEMT read-out. Inter Solid-State Sensors, Actuators and Microsystems Conf (Transducers), Anchorage, Alaska, pp 1–4. Accessed 21–25 June 2015
16. Ballato A (1995) Piezoelectricity: old effect, new thrusts. IEEE Trans Ultrason Ferroelectrics Freq Control 42(5):916–926
17. Rais-Zadeh M, Gokhale V, Ansari A et al (2014) Gallium nitride as an electromechanical material. J Microelectromech Syst 23(6):1252–1271
18. Bernardini F, Fiorentini V, Vanderbilt D (1997) Spontaneous polarization and piezoelectric constants of III-V nitrides. Phys Rev B 56(16):24–27
19. Hanada T (2009) Basic properties of ZnO, GaN, and related materials. Adv Mater Res 12:1–19
20. Lakin KM (1999) Thin film resonators and filters. IEEE Ultrasonics Symposium, Caesars Tahoe, NV, pp 895–906. Accessed 17–20 Oct 1999
21. Ruby R, Bradley P, Larson J et al (2001) Ultra-miniature high-Q filters and duplexers using FBAR technology. IEEE International Solid-State Circuits Conference, San Francisco, CA, pp 120–121. Accessed 5–7 Feb 2001
22. Ruby RC, Bradley P, Oshmyansky Y, Chien A, Larson III JD (2001) Thin film bulk wave acoustic resonators (FBAR) for wireless applications. IEEE International Ultrasonics Symposium, Atlanta, Georgia, pp 813–821. Accessed 7–10 Oct 2011
23. Pan W, Ayazi F (2008) Multiple-frequency thickness-mode thin-film piezoelectric-on-substrate filter array. IEEE International Frequency Control Symposium, Honolulu, Hawaii, pp 259–262. Accessed 19–21 May 2008
24. Piazza G, Stephanou PJ, Pisano AP (2006) Piezoelectric aluminum nitride vibrating contour-mode MEMS resonators. J Microelectromech Syst 15(6):1406–1418
25. Bjurstrom J, Katardjiev I, Yantchev V (2005) Lateral-field-excited thin-film lamb wave resonators. Appl Phys Lett 86:154103
26. Muller A, Neculoiu D, Tsagaraki K et al (2009) 6.3-GHz film bulk acoustic resonator structures based on a gallium nitride/silicon thin membrane. IEEE Electron Dev Lett 30(8):799–801
27. Gokhale VJ, Roberts J, Rais-Zadeh M (2011) High performance bulk mode gallium nitride resonators and filters. Inter Solid-State Sensors, Actuators and Microsystems Conference (Transducers), Beijing, China, pp 926–929. Accessed 5–9 June 2011
28. Ansari A, Gokhale VJ, Thakar VA et al (2011) Gallium nitride-on-silicon micromechanical overtone resonators and filters. IEEE International Electron Devices Meeting, Washington, DC, pp 20.3.1–20.3.4. Accessed 5–7 Dec 2011
29. Popa LC (2015). Gallium nitride MEMS resonators. Doctoral dissertation, Massachusetts Institute of Technology, Cambridge, MA, USA
30. Lin CM, Yantchev V, Chen YY, Felmetsger VV, Pisano AP (2011) Characteristics of AlN lamb wave resonators with various bottom electrode configurations. IEEE International Frequency Control Symposium, San Francisco, CA, pp 1–5. Accessed 2–5 May 2011

31. Wong KY, Tang W, Lau KM, Chen KJ (2007) Surface acoustic wave device on AlGaN/GaN heterostructure using two-dimensional electron gas interdigital transducers. Appl Phys Lett 90:213506
32. Popa LC, Weinstein D (2013) 2DEG electrodes for piezoelectric transduction of AlGaN/GaN MEMS resonators. IEEE International Frequency Control Symposium, Prague, pp 922–925. Accessed 21–25 July 2013
33. Popa LC, Weinstein D (2013) Switchable piezoelectric transduction in AlGaN/GaN MEMS resonators. International Solid-State Sensors, Actuators and Microsystems Conference (Transducers), Barcelona, Spain, pp 2461–2464. Accessed 16–20 June 2013
34. Ansari A, Rais-Zadeh M (2016) Depletion-mediated piezoelectric AlGaN/GaN resonators. Phys Status Solidi. doi:10.1002/pssa.201532746
35. Bykhovski AD, Kaminski VV, Shur MS et al (1996) Pyroelectricity in gallium nitride thin films. Appl Phys Lett 69(21):3254–3256
36. Bykhovski AD, Kaminski VV, Shur MS et al (1996) Piezoresistive effect in wurtzite n-type GaN. Appl Phys Lett 68(6):818–819
37. Gualieri JG, Kosinski JA, Ballato A (1994) Piezoelectric materials for acoustic wave applications. IEEE Trans Ultrason Ferroelectr Freq Control 41(1):53–59
38. Jena D, Heikman S, Green D et al (2002) Realization of wide electron slabs by polarization bulk doping in graded III–V nitride semiconductor alloys. Appl Phys Lett 81(23):4395–4397
39. Zimmermann T, Neuburger M, Benkart P et al (2006) Piezoelectric GaN sensor structures. IEEE Electron Dev Lett 27(5):309–312
40. Talukdar A, Qazi M, Koley G (2012) High frequency dynamic bending response of piezoresistive GaN microcantilevers. Appl Phys Lett 101(25):252102
41. Kang BS, Kim S, Kim J et al (2003) Effect of external strain on the conductivity of AlGaN/GaN high-electron-mobility transistors. Appl Phys Lett 83(23):4845–4847
42. Eickhoff M, Ambacher O, Krötz G et al (2001) Piezoresistivity of AlxGa1−xN layers and AlxGa1−xN/GaN heterostructures. J Appl Phys 90(7):3383–3386
43. Lin AT-H, Lee JE-Y, Yan J et al (2010) Methods for enhanced electrical transduction and characterization of micromechanical resonators. Sensor Actuator A 158(2):263–272
44. van Beek JTM, Steeneken PG, Giesbers B (2006) A 10MHz piezoresistive MEMS resonator with high Q. IEEE International Frequency Control Symposium Expo, Miami, FL, pp 475–480. Accessed 4–7 June 2006
45. Faucher M, Grimbert B, Cordier Y et al (2009) Amplified piezoelectric transduction of nanoscale motion in gallium nitride electromechanical resonators. Appl Phys Lett 94(23):233506-1–233506-3
46. Faucher M, Cordier Y, Werquin M et al (2012) Electromechanical transconductance properties of a GaN MEMS resonator with fully integrated HEMT transducers. J Microelectromech Syst 21(2):370–378
47. Gray JM, Rogers CT, Bertness KA et al (2011) Gallium nitride nanowire electromechanical resonators with piezoresistive readout. J Vac Sci Tech B 29(5):052001-1–052001-4
48. Weinstein D, Bhave SA (2010) The resonant body transistor. Nano Lett 10(4):1234–1237
49. Weinstein D, Bhave SA (2010) Acoustic resonance in an independent-gate FinFET. Solid-State Sensors, Actuators and Microsystems Workshop, Hilton Head, SC, pp 459–462. Accessed 6–10 June 2010
50. Nathanson HC, Newell WE, Wickstrom RA, Davis JR Jr (1967) The resonant gate transistor. IEEE Trans Electron Dev 14(3):117–133
51. Chang L (2003) Nanoscale thin-body CMOS devices. Unpublished doctoral dissertation, University of California, Berkeley, CA
52. Colinet E, Durand C, Ionescu AM (2009) J Solid-State Circ 44(1):247–257
53. Durand C, Casset F, Buchaillot L (2008) Electron Device Lett 29(5):494–496
54. Grogg D Mazza M, Tsamados D, Ionescu AM (2008) Multi-gate vibrating-body field effect transistor (VB-FETs). IEEE International Electron Devices Meeting, San Francisco, CA, pp 1–4. Accessed 15–17 Dec 2008

55. Ansari A, Rais-Zadeh M (2013) HEMT-based read-out of a thickness-mode AlGaN/GaN resonator. IEEE International Electron Devices Meeting, Washington, DC, p 18.3.1–18.3.4. Accessed 9–11 Dec 2013
56. Ansari A, Rais-Zadeh M (2014) A thickness-mode AlGaN/GaN resonant body transistor. IEEE Trans Electron Dev 61(4):1006–1013
57. Bahr B, Popa LC, Weinstein D (2015) 1 GHz GaN-MMIC monolithically integrated MEMS-based oscillators. IEEE International Solid State Circuits Conference, San Francisco, California, pp 1–3, 22–26 Feb 2015
58. Cimalla V, Pezoldt J, Ambacher O (2007) Group III nitride and SiC based MEMS and NEMS: materials properties, technology and applications. J Phys D Appl Phys 40:6386–6434
59. Kang BS, Kim J, Ren F et al (2004) Pressure-induced changes in the conductivity of AlGaN/GaN high-electron mobility-transistor membranes. Appl Phys Lett 85(14):2962–2964
60. Jha CM, Bahl G, Melamud R et al (2007) High resolution microresonator-based digital temperature sensor. Appl Phys Lett 91(7):074101-1–074101-3
61. Shur MS, Bykhovski AD, Gaska R (1999) Pyroelectric and piezoelectric properties of GaN-based materials. MRS Internet J Nitride Semicond Res 4. doi: 10.1557/PROC-537-G1.6
62. Mchenry TF (1969) Pyroelectric radiation detector providing compensation for environmental temperature changes. US Patent 3,453,432. Accessed 1 July 1969
63. Obara H, Kon T, Murayama N (1981) Pyroelectric infrared detector. US patent 4,258,260. Accessed 24 Mar 1981
64. Gokhale V, Rais-Zadeh M (2014) Uncooled infrared detectors using gallium nitride on silicon micromechanical resonators. J Microelectromech Syst 23(4):803–810
65. Gokhale VJ, Rais-Zadeh M (2014) Phonon-electron interactions in piezoelectric semiconductor bulk acoustic wave resonators. Sci Rep 4(5617):5617:1–5617:10
66. Rais-Zadeh M (2012) Gallium nitride micromechanical resonators for IR detection. Proceedings of SPIE 8373, micro- and nanotechnology sensors, systems, and applications IV, 83731M, Baltimore, MD. Accessed 1 May 2012. doi: 10.1117/12.919941
67. Gokhale VJ, Rais-Zadeh M (2012) Sensitive uncooled IR detectors using gallium nitride resonators and silicon nitride absorbers. Solid-State Sensors, Actuators and Microsystems Workshop, Hilton Head, South Carolina, pp 46–49. Accessed 3–7 June 2012
68. Guy IL, Goldys EM, Muensit S (2000) Measurements of piezoelectric coefficients of nitride semiconductor films. International Semiconducting and Insulating Materials Conference, Canberra, ACT, pp 55–58. Accessed 3–7 July 2000
69. Kornev I, Willatzen M, Lassen B et al (2010) Electrostriction coefficients of GaN, AlN, MgO and ZnO in the wurtzite structure from first principles. AIP Conference Proceedings 1199(1), Rio de Janeiro, Brazil, pp 71–72. Accessed 27 July–1 Aug 2009. doi: http://dx.doi.org/10.1063/1.3295559
70. Luft KF (1943) Über eine neue methode der registrierenden gasanalyse mit hilfe der absorption ultraroter strahlen ohne spektrale zerlegung. Z Tech Phys 5:97–104
71. Auble DL, Meyers TP (1992) An open path, fast response infrared absorption gas analyzer for H2O and CO2. Bound-Lay Meteorol 59(3):243–256
72. Stutzmann M, Steinhoff G, Eickhoff M et al (2002) GaN-based heterostructures for sensor applications. Diamond Relat Mater 11:886–891
73. Neuberger R, Müller G, Ambacher O et al (2001) Ion-induced modulation of channel currents in AlGaN/GaN high-electron-mobility transistors. Phys Stat Sol (a) Appl Res 183(2):R10–R12
74. Schalwig J, Müller G, Ambacher O et al (2001) Group-III-nitride based gas sensing devices. Phys Stat Sol (a) 185(1):39–45
75. Steinhoff G, Hermann M, Schaff WJ et al (2003) pH response of GaN surfaces and its application for pH-sensitive field-effect transistors. Appl Phys Lett 83(1):177–179
76. Kang BS, Kim J, Jang S et al (2005) Capacitance pressure sensor based on GaN high-electron-mobility transistor-on-Si membrane. Appl Phys Lett 86(25):253502-1–253502-3
77. Faucher M, Martin G, Friedt JM et al (2013) A 1 GHz SAW oscillator on epitaxial GaN/Si substrate: Toward co-integrated frequency sources. Joint European Frequency and Time Forum & Inter Frequency Control Symposium, Prague, pp 21–24. Accessed 21–25 July 2013

78. Ansari A, Gokhale VJ, Roberts J et al (2012) Monolithic integration of GaN-based micromechanical resonators and HEMTs for timing applications. IEEE International Electron Devices Meeting, San Francisco, CA, pp 15.5.1–15.5.4. Accessed 10–13 Dec 2012
79. Gokhale VJ, Shim Y, Rais-Zadeh M (2010) Observation of the acoustoelectric effect in gallium nitride micromechanical bulk acoustic filters. IEEE International Frequency Control Symposium, Newport Beach, CA, pp 524–529. Accessed 1–4 June 2010
80. Palacios T, Calle F, Grajal J et al (2002) High frequency SAW devices on AlGaN: fabrication, characterization and integration with optoelectronics. IEEE Ultrasonics Symposium, Munich, Germany, pp 57–60. Accessed 8–11 Oct 2002
81. Tabrizian R, Rais-Zadeh M, Ayazi F (2009) Effect of phonon interactions on limiting the f.Q product of micromechanical resonators. International Solid-State Sensors, Actuators and Microsystems Conference (Transducers), Denver, Colorado, pp 2131–2134. Accessed 21–25 June 2009
82. Akhieser A (1939) On the absorption of sound in solids. J Phys USSR 1:277–278
83. Braginsky VB, Mitrofanov VP (1986) Systems with small dissipation. Thorne KS (ed) The University of Chicago Press, Chicago, IL, USA
84. Srikar VT, Senturia SD (2002) Thermoelastic damping in fine-grained polysilicon flexural beam resonators. J Microelectromech Syst 11(5):499–504
85. Chandorkar S, Agarwal M, Melamud R et al (2008) Limits of quality factor in bulk-mode micromechanical resonators. International Conference Micro Electro Mechanical Systems, Tucson, Arizona, pp 74–77. Accessed 13–17 Jan 2008
86. Pomerantz M (1965) Ultrasonic loss and gain mechanisms in semiconductors. Proc IEEE 53(10):1438–1451
87. Tabrizian R, Rais-Zadeh M (2015) The Effect of charge redistribution on limiting the kt2.Q product of piezoelectrically transduced resonators. International Solid-State Sensors, Actuators and Microsystems Conference (Transducers), Anchorage, Alaska, pp 1–4. Accessed 21–25 June 2015
88. Gong S, Piazza G (2013) Figure-of-merit enhancement for laterally vibrating lithium niobate MEMS resonators. IEEE Trans Electron Dev 60(11):3888–3894
89. Olsson RH, Hattar K, Homeijer SJ et al (2014) A high electromechanical coupling coefficient SH0 lamb wave lithium niobate micromechanical resonator and a method for fabrication. Sens Actuators A Phys 209:183–190
90. Wang R, Bhave SA, Bhattacharjee K (2015) Design and fabrication of S0 lamb-wave thin-film lithium niobate micromechanical resonators. J Microelectromech Syst 24(2):300–308

Chapter 4
Lithium Niobate for M/NEMS Resonators

Songbin Gong

Piezoelectric Radio frequency (RF) microelectromechanical systems (MEMS) resonators are chip-scale components embedded in the modern RF front ends to carry out the function of frequency selection and interference rejection. They are the building blocks of RF filters and oscillators. Their working principle leverages piezoelectric thin films to covert resonance phenomenon from the mechanical to the electrical domain. Piezoelectric MEMS resonators are still being extensively researched with the main focus placed on attaining the optimal combination of electromechanical coupling, higher Q, and wafer-level frequency agility. The intense development of piezoelectric MEMS resonators was triggered in the past decade by the demand for high-precision timing sources and high-performance filtering devices to address telecommunication needs in an already-crowded RF spectrum. Particularly, fueled by the fast growth of consumers and services in the mobile marketplace, the demand for bandwidth has resulted in increasingly stringent performance specifications for front-end filters and duplexers. In order to accommodate the emerging standards in the RF spectrum, the development of piezoelectric MEMS resonators faces many new challenges, including lower loss, wider bandwidth performance, better temperature stability, high power handling and linearity, and most important of all, frequency tunability and agility.

Lithium Niobate ($LiNbO_3$) has recently gained significant interest as a promising material platform to simultaneously deliver high electromechanical coupling (k_t^2) and quality factor (Q) [1]. Its higher k_t^2, Q, and resulting FoM ($k_t^2 \cdot Q$) can serve to address all of the above-mentioned challenges. For example, the high FoM leads to a lower insertion loss for the comprising filters and multiplexers, thus placing less burden on power amplifiers to compensate the loss and reducing

S. Gong (✉)
Department of Electrical and Computer Engineering, University of Illinois
at Urbana-Champaign, Champaign, IL, USA
e-mail: songbin@illinois.edu

© Springer International Publishing Switzerland 2017

H. Bhugra, G. Piazza (eds.), *Piezoelectric MEMS Resonators*,
Microsystems and Nanosystems, DOI 10.1007/978-3-319-28688-4_4

the overall power consumption of RF front ends. The lower insertion loss and high Q also permit the implementation of higher order filters (typically more cascaded resonators) with a sharper roll-off for duplexing closely spaced bands (e.g. coexistence of WIFI and LTE band 40). Additionally, k_t^2 directly determines the maximum achievable bandwidth of the filter. Therefore, device platforms with a larger k_t^2 can accommodate existing or emerging standards that require wider bandwidth and a higher data rate (e.g. LTE band 41 with fractional bandwidth of 7.5 %). Moreover, differently from other materials commonly employed for piezoelectric MEMS resonators, the high k_t^2 and Q can be achieved in $LiNbO_3$ thin films for lateral modes, in addition to the thickness/breathing mode that has been demonstrated with high k_t^2 in Aluminum Nitride (AlN). The lateral mode supports lithographical definition of the resonator and filter center frequency, thus allowing wafer-level frequency diversity. Coupled with an integrated switching mechanism, such wafer-level frequency diversity can be harnessed to implement a reconfigurable and frequency agile apparatus. Finally, it is also worth emphasizing that the aforementioned technical benefits of $LiNbO_3$ MEMS resonators come with temperature stability, linearity, and power handling performance that are on par with commercially available devices.

This chapter discusses the historical development, material properties, micromachining processes, design considerations, and at last the suitable applications of $LiNbO_3$-based MEMS resonators.

4.1 Historical Development of Lithium Niobate Material and Thin Films

Even though $LiNbO_3$-based MEMS resonators have only been recently demonstrated, the material has been widely used for acoustic devices for several decades. It first gained tremendous interest in the late 1960s as surface acoustic wave (SAW) devices rose to serve many applications that required analog signal processing in the acoustic domain (e.g. pulse compression radars [2]). Based on the design considerations of SAW devices that include acoustic velocity, electromechanical coupling, temperature coefficient of elasticity, diffraction effects, coupling to unwanted modes, a wide range of materials was investigated. Among these materials, $LiNbO_3$ was chosen for wideband applications due to its pronounced piezoelectric properties. In the meanwhile, the optical community also had invested interests in $LiNbO_3$ due to its excellent electro-optic properties and added fuel to the material development [3].

The bulk $LiNbO_3$, as a synthetic material, was first grown with the Czochralski technique in the 1960s [4]. Similar to the growth method of Si, pure compounds are placed in a crucible with the optimal composition ratio and heated to a temperature slightly above the melting point of $LiNbO_3$ [5]. The growth is then initiated by dipping a seed crystal into the melt and gradually extracting the rod. The size of the

growing crystal rod can be controlled by setting the crucible temperature. Growth was first done along *Z*-axis, and later along other orientations by employing a seed crystal with the intended orientation. The grown crystal rod can be then sliced into wafers of different cuts for the manufacturing of devices.

Different cuts of $LiNbO_3$ provide for different material properties as $LiNbO_3$ is highly anisotropic as it will be discussed in the next section. Having access to different cuts of $LiNbO_3$ allows for an additional degree of freedom in designing the acoustic devices and harnessing the high piezoelectric properties of the material. For example, a 41° rotated Y-cut is desired for attaining high k_t^2 and wide bandwidth devices.

In the mid 1990s, anticipating the fast growing mobile and wireless industry, researchers in both academia and industry started to look into devices that could support wider bandwidth, lower loss, and higher frequency RF front end filtering and duplexing, and could compete with the rising AlN FBAR technology [6]. Naturally, $LiNbO_3$, which had already been shown as a successful SAW platform, was considered for enabling new types of piezoelectric bulk acoustic wave devices. However, it was largely unfruitful due to the lack of integration approaches that could result in high-quality thin films on carrier substrates for the subsequent micromachining steps. Research on the material integration was then re-initiated after the topic was first heavily researched in the 70s for making optical waveguides. A wide range of techniques, including sputtering [7, 8], chemical vapor deposition (CVD) [9, 10], and epitaxial growth [11–13], have been attempted or revisited on various substrates. The film quality, as characterized by X-ray diffraction (XRD) rocking curve measurements, was far from approaching bulk quality. Moreover, techniques of this nature are inherently limited to growing c-axis (Z-cut) film, which is not the optimal cut for building bulk acoustic wave devices.

Inspired by the success of Silicon-on-insulator technology and motivated by demonstrating chip-scale optical waveguide rather than acoustic devices, scholars around the globe attempted to develop a Smart-cut alike technology for $LiNbO_3$ and showed great success (Fig. 4.1). Since then, different versions of the so-called crystal-ion-slicing technique, either with H^+ and He^+ ions, have been utilized in combination with either direct or adhesive bonding techniques to attain single crystal $LiNbO_3$ on a carrier substrate [14]. The implantation process is carefully designed with the proper energy so that the ions can penetrate the surface and come to rest at a desired depth (up to a few μm) below the surface. The implanted ions serve to generate defects and further form platelets or micro cavities that can be expanded under thermal conditions. The dose of implantation thus plays an important role as it directly determines the density of the implantation induced micro-cavities (Fig. 4.1).

In order to process and handle the thin film for later steps, the implanted wafers are often bonded to carrier substrates using direct or adhesive bonding. Early experiments focused on using another $LiNbO_3$ with the identical cut as the carrier substrate to avoid a large mismatch in coefficient of thermal expansion (CTE). Later on, Si was successfully shown to support transferred $LiNbO_3$ thin film. In either

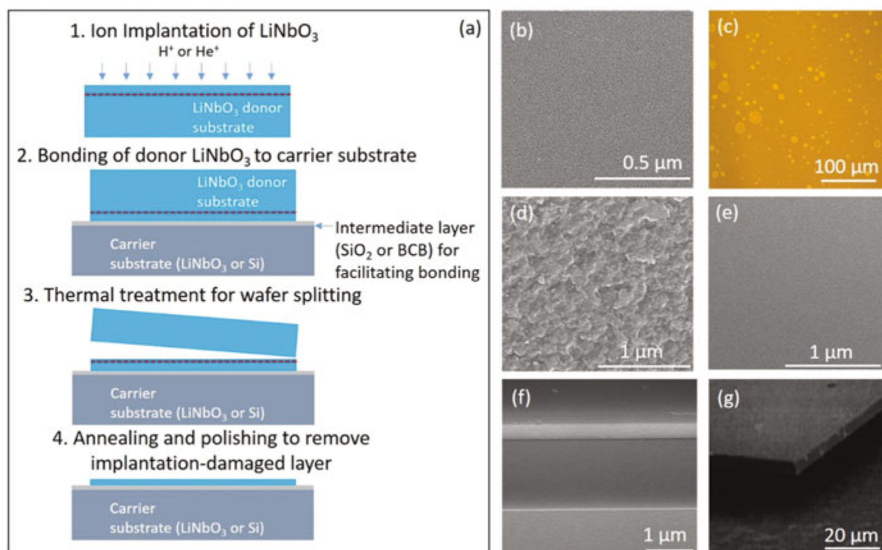

Fig. 4.1 (**a**) Typical process of ion slicing and transferring $LiNbO_3$ thin films. (**b**) SEM and (**c**) optical images of the blistering on the $LiNbO_3$ surface induced by ion-implantation and annealing. (**d**) Unpolished and (**e**) polished surfaces of the transferred $LiNbO_3$ thin film. (**f**) Cross-sectional view of the transferred film stack. Images (**b–f**) are kindly provided by Prof. Hui Hu at Shandong University. (**g**) Ion-sliced and transferred $LiNbO_3$ thin film suspended using HF-based selective etching of the implantation-damaged $LiNbO_3$ layer, courtesy of Prof. Richard Osgood at Columbia University

cases, a SiO_2 intermediate layer is generally used, although direct bonding to silicon is also possible. The wafer bonding process requires the surfaces of the donor and carrier wafers to be thoroughly cleaned and free of contaminants. Once bonded, the wafer stack is then thermally treated to expand the micro-cavities into micro-cracks and induce splitting. The donor wafer eventually detaches from the wafer stack completely, leaving the transferred $LiNbO_3$ of a few µm on the carrier wafer.

Surprisingly though, the success in $LiNbO_3$ film integration did not immediately translate to bulk acoustic device demonstrations, most likely due to remaining technical hurdles in micromachining of $LiNbO_3$. It is speculated that the telecomm market, which had been well served by the low-cost SAWs and high-performance FBARs, de-incentivized research community to pursue $LiNbO_3$ MEMS/BAW resonators as they seem to be a high-cost and low-yield option that is years of high-risk development away. However, the pervasion of smart phones and ever-increasing demand from customer for more bandwidth have pushed the RF front ends to accommodate more tightly packed communication bands, which in turn imposes more stringent requirements on the loss, bandwidth, roll-off, and out-of-band rejection of front-end filters and duplexers. This technical evolution in the telecomm marketplace calls for high-integration, low-loss, and frequency diverse/agile platforms for front-end filtering. Thus, $LiNbO_3$, with its pronounced

piezoelectric properties, has to be revisited as an RF-MEM platform. By introducing the material properties of $LiNbO_3$ in the next section, we can then investigate the acoustic wave propagation characteristics in $LiNbO_3$ and subsequently engineer the optimal device performance.

4.2 Material Properties of Lithium Niobate

Before discussing the design of LN resonators, it is important to familiarize ourselves with the material properties of $LiNbO_3$. Only first-order material properties are discussed given that the focus is towards MEMS devices operating in the linear regime. Second-order elastic constants can be found in [15, 16] for readers who are interested in investigating their effects on MEMS resonators' performance. For the design of $LiNbO_3$ resonators, the relevant properties, as listed in Table 4.1, include the stiffness constants and their temperature coefficients, the piezoelectric coupling constants and their temperature coefficients, dielectric constants, coefficient of thermal expansion, density, and thermal conductivity. These material constants

Table 4.1 Material constants of $LiNbO_3$

Parameter	Symbol	$LiNbO_3$ (Z-cut) 0° to $+X$ axis	
		Stiffness	Temp
Stiffness constants (10^{11} N/m^2) and their temp coefficients (ppm/K)	c_{11}	2.030	−174
	c_{12}	0.573	−252
	c_{13}	0.752	−159
	c_{14}	0.085	−214
	c_{33}	2.424	−153
	c_{44}	0.595	−203
	c_{66}	0.728	−143
Coupling constants (C/m^2) and temp coefficients (ppm/K)	e_{15}	3.76	147
	e_{22}	2.43	79
	e_{31}	0.23	221
	e_{33}	1.33	887
Dielectric constants	ε_{11}	43.60	N/A
	ε_{33}	29.16	N/A
Coefficient of thermal expansion (ppm/K)	α_x	14.4	N/A
	α_y	15.9	N/A
	α_z	7.5	N/A
Density (kg/m^3)	ρ	4700	N/A
Specific heat (J/(kg K))	c	628	N/A
Thermal conductivity (W/m K)	k	5.6	N/A

either directly or cooperatively determine the device electromechanical coupling, phase velocity and resonant frequencies, temperature coefficient of frequency (TCF) and power handling. There have been numerous reports, documenting these material properties using different methods [16, 17]. Table 4.1 lists material constants that have been used for the demonstration and modeling of LN laterally vibrating resonators in [1]. The material constants by default are measured for c-axis grown $LiNbO_3$ (in the z-cut plane), and the subscripts of 1, 2, and 3 correspond to *x*, *y*, and *z* (*c*-axis) of the Cartesian coordinates.

To attain the piezoelectric and elastic constants for various orientations in different cut planes, basic matrix rotations can be performed using the following transformation formulas:

$$\tilde{c} = M \cdot c \cdot M^T \tag{4.1}$$

$$\tilde{e} = a \cdot e \cdot M^T \tag{4.2}$$

$$\tilde{\varepsilon} = a \cdot \varepsilon \cdot a^T \tag{4.3}$$

Where c, e, and ε are stiffness, coupling, and permittivity matrices of un-rotated $LiNbO_3$. $\tilde{c}$, $\tilde{e}$ and $\tilde{\varepsilon}$ are the rotated matrices. a is the transformation matrix, and can be determined by the Euler angles pertaining to intended direction of wave propagation. Typically, a rotation convention by which the axis rotation is done sequentially about z, x, and z axes is adopted and Euler angles are defined correspondingly as α, β, and γ. To attain a device orientation of θ in the *X*-cut plane, Euler angles of (θ, 90°, −90°) are used to derive the transformation matrix (a), the bond matrix M, and their transposed versions (a^T and M^T) [18].

The rotated coefficients can then be input into the FEM tools for the modeling of resonators. State of the art commercial FEM tools come with either a matrix rotation tool or a coordinate rotation tool for simulating 3D resonator structures oriented in an arbitrary angle within the anisotropic piezoelectric crystal.

In comparison to some other piezoelectric materials discussed in this book (e.g. AlN and GaN), $LiNbO_3$ has significantly higher piezoelectric coupling coefficients and thus allows for the implementation of resonators with much higher k_t^2. It suggests that much wider bandwidth that could not be attained with AlN and GaN can be achieved with $LiNbO_3$. The higher k_t^2 also implies a higher energy transduction efficiency and therefore lower impedance than AlN and GaN devices, given that similar Qs are attained. Different from AlN and GaN, $LiNbO_3$ is anisotropic even within the Z-cut plane. Therefore, the design and modeling of $LiNbO_3$ for optimal performance is a more complex problem and the orientation of the device plays an important role. $LiNbO_3$ also has higher permittivity and higher temperature coefficients of elastic and piezoelectric constants. Unfortunately, this means LN resonators have worse temperature stability than AlN- [19] or GaN [20]-based resonators. $LiNbO_3$ is also a slightly "softer" material than AlN and GaN, suggesting an on-average slower phase velocity for various types of bulk acoustic

Table 4.2 Comparison of theoretically predicted and experimentally demonstrated *f·Q* products for various low-loss acoustic materials

Material	Gruneisen coefficient [22]	Longitudinal velocity (m/S)	Thermal conductivity (W/m K)	Theoretical *f·Q* (Hz) [22]	Experimental *f·Q* (Hz)
3C-SiC	1.1	11,000	360	5.6×10^{13}	8.8×10^{12} [23]
AlN	0.9	9000	280	5.6×10^{13}	1.2×10^{13} [24]
Sapphire	1.1	10,500	36	5.9×10^{14}	1.1×10^{14} [25]
$LiNbO_3$	2	6500	5.6	2.3×10^{14}	7.8×10^{13} [26]

waves. The thermal conductivity of $LiNbO_3$ is more than an order of magnitude smaller than the values of AlN and GaN, leading to a more pronounced thermal management issue, particularly for meeting the requirement of sufficient power handling [21].

Another important comparison that might be difficult to carry out relates to the acoustic loss in these materials. In the field of micro-acoustic resonators, the acoustic loss in the material imposes the ultimate limit on the product of resonance and quality factor (*f·Q*), one of the important figure of merits (FoM) for evaluating device performance across different material platforms. The acoustic loss in thin film materials is particularly challenging to study as it highly depends on a wide range of factors, including the carrier substrate, deposition/integration method, and its resulting crystallinity and defect density. There have been numerous theoretical reports on analyzing the complex loss mechanisms in various piezoelectric materials, and speculating the ultimate *f·Q* product limit for different materials [22].

One reliable way to gauge the bulk acoustic wave loss in materials is through measuring the quality factors of high or lateral overtone bulk acoustic wave resonators (HBARs or LOBARs). HBARs are generally formed by stacking a piezoelectric transducer on the surface of a bulk substrate. LOBARs use a large thin film as the acoustic waveguide with a much smaller piezoelectric transducer in the center. The piezoelectric transducer can launch bulk acoustic waves into the bulk substrate or the plate waveguide and introduce standing waves via the reflection off the backside of the substrate or edges of the plate waveguide. The dominating loss mechanism in HBARs and LOBARs is the acoustic propagation loss in the bulk substrate and the plate waveguide, thus allowing experimental characterization of the wave attenuation. Table 4.2 shows a short list of the materials that have been characterized by this method, among which $LiNbO_3$ is the piezoelectric material with the highest theoretical and experimental *f·Q* [26].

4.3 Bulk Acoustic Modes in Lithium Niobate Thin Films

Now we have introduced the piezoelectric and elastic properties, it is not difficult to notice that the $LiNbO_3$ has very high piezoelectric coupling coefficients. As

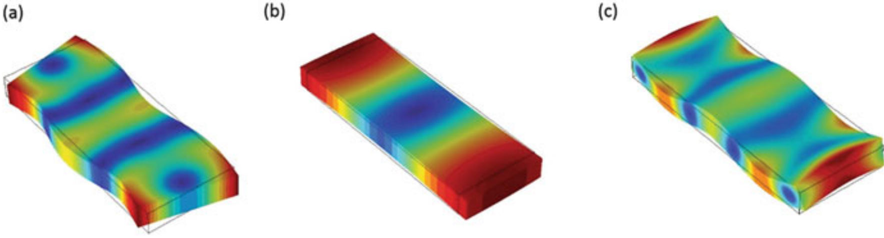

Fig. 4.2 Acoustic modes in $LiNbO_3$ thin plates. (**a**) Shear horizontal mode. (**b**) Symmetrical lateral mode. (**c**) Asymmetrical flexural mode

previously discussed, the desirable piezoelectric properties are the reason why $LiNbO_3$ is used for the implementation of SAW in the first place. However, SAW modes do not maximally harness the piezoelectric transduction capability of $LiNbO_3$, even though they do provide a high k_t^2 (∼10 %). It has been known since mid-1990s that some bulk acoustic wave (BAW) modes in $LiNbO_3$ theoretically feature higher K^2 than SAW modes [27, 28]. Later, more accurate models were used to predict even larger K^2 for several other BAW modes (e.g. lamb wave modes) [29, 30]. These high K^2 BAW modes, with their displacement mode shapes generated using eigen mode finite element analyses and shown in Fig. 4.2, include Shear Horizontal (SH), longitudinal Symmetrical (S), and Asymmetrical (A) modes.

Despite the obvious advantages of $LiNbO_3$ for enabling BAW devices, the high electromechanical coupling of $LiNbO_3$ can be a double-sided sword in the sense that a variety of bulk acoustic modes is often excited concurrently. The designer efforts have to be focused on selecting the mode with desired propagation characteristics for the targeted applications, and later engineering the optimal electrode patterns and resonator structures so that the intended acoustic mode is predominantly excited while the unwanted modes are sufficiently suppressed or removed. This calls for analytical studies of the various acoustic modes that can be supported by the $LiNbO_3$ thin film. These studies first investigate the intrinsic electromechanical coupling (K^2) pertaining only to material properties and independent of the transducer configuration. K^2 measures the energy conversion efficiency between electrical and mechanical domains and is given by [31]:

$$K = \frac{e^2}{c^E \varepsilon^S} \tag{4.4}$$

where e, c, and ε are the piezoelectric coefficients, stiffness constants, and permittivity of the material. Note that all material properties are tensors. Calculations of K^2 for different modes have to resort to the enabling (e_{ij}) and corresponding (c_{ij} and ε_{ij}) components. For a highly piezoelectric material such as $LiNbO_3$, more than one component often contribute or determine the intrinsic coupling. Thus, K^2 of different modes can be more conveniently estimated using Alder's approach [32],

which compares the phase velocities of the same acoustic mode in a thin $LiNbO_3$ plate with and without perfect metallized boundary condition on the top surface:

$$K^2 = \frac{\upsilon_0^2 - \upsilon_m^2}{\upsilon_0^2} \tag{4.5}$$

where υ_m is the phase velocity in a $LiNbO_3$ plate with a top metalized surface, and υ_0 is the phase velocity in the identical $LiNbO_3$ plate with free boundary conditions. The phase velocities can be computed using eigen mode analysis in a finite element tool with the metalized and free boundary conditions applied. Finite element analysis generally allows the mode identification via inspecting displacement modeshapes and streamlines the process of predicting the K^2 for modes of interest. Due to anisotropic piezoelectric and elastic material properties of $LiNbO_3$, K^2 and phase velocity for different modes vary with respect to the direction of acoustic wave propagation in various cut planes. Rotated coupling, stiffness, and permittivity can be incorporated in FEA to compute K^2 dependence on propagation direction.

In the context of searching for the next generation frequency agile filtering platform, we will first narrow our scope of discussion to two primary BAW modes in $LiNbO_3$: zero order Shear Horizontal mode (SH0) and symmetrical lateral mode (S0), and use the above analytical method to derive their propagation and excitation characteristics. These two modes are of primary interest for the development of $LiNbO_3$ MEMS resonators as their displacement is predominately in-plane and their resonances can be predominately defined by the pitch of the top electrodes. To be differentiated from other MEMS resonator technologies in this book, we categorize $LiNbO_3$ SH0 and S0 devices as laterally vibrating resonators (LVRs) and will reference the term onward. In addition to these two intended modes, one should also be keen on the characteristics of the asymmetrical mode (A0) as it presents a thorny problem to the design of $LiNbO_3$ LVRs. It does not have the desirable wave characteristics (lower K^2 and phase velocity). More troublesomely, it often shows up in the resonator response as spurious vibration and creates undesirable ripples in the passband of the comprising filters [33]. Therefore, some discussion on A0 will follow the analysis on lateral modes.

First, let us exam the symmetrical longitudinal (S0) mode. The results, as shown in Fig. 4.3 for X, Y, Z cuts $LiNbO_3$, indicates the K^2 and phase velocity of S0 both vary as the direction of prorogation is set from 0° to 180° within each cut plane. The X-cut $LiNbO_3$ with a 30° to $+Y$ orientation has the highest (35 %) among all cuts and orientations [1, 29]. Y and Z-cut $LiNbO_3$ also feature some high coupling orientations, such as 45° to $\pm X$ axis in Y-cut, and exhibit symmetrical response about Z and Y axis respectively. This analysis indicates that the X-cut is the optimum cut of $LiNbO_3$ for enabling high electromechanical coupling microresonators for S0 mode. This K^2 value is significantly higher than the ones of AlN and GaN platforms for the S0 mode. Given an optimal transducer configuration, the K^2 can be translated into device level electromechanical coupling approximately by $k_t^2 = K^2/(1 + K^2)$.

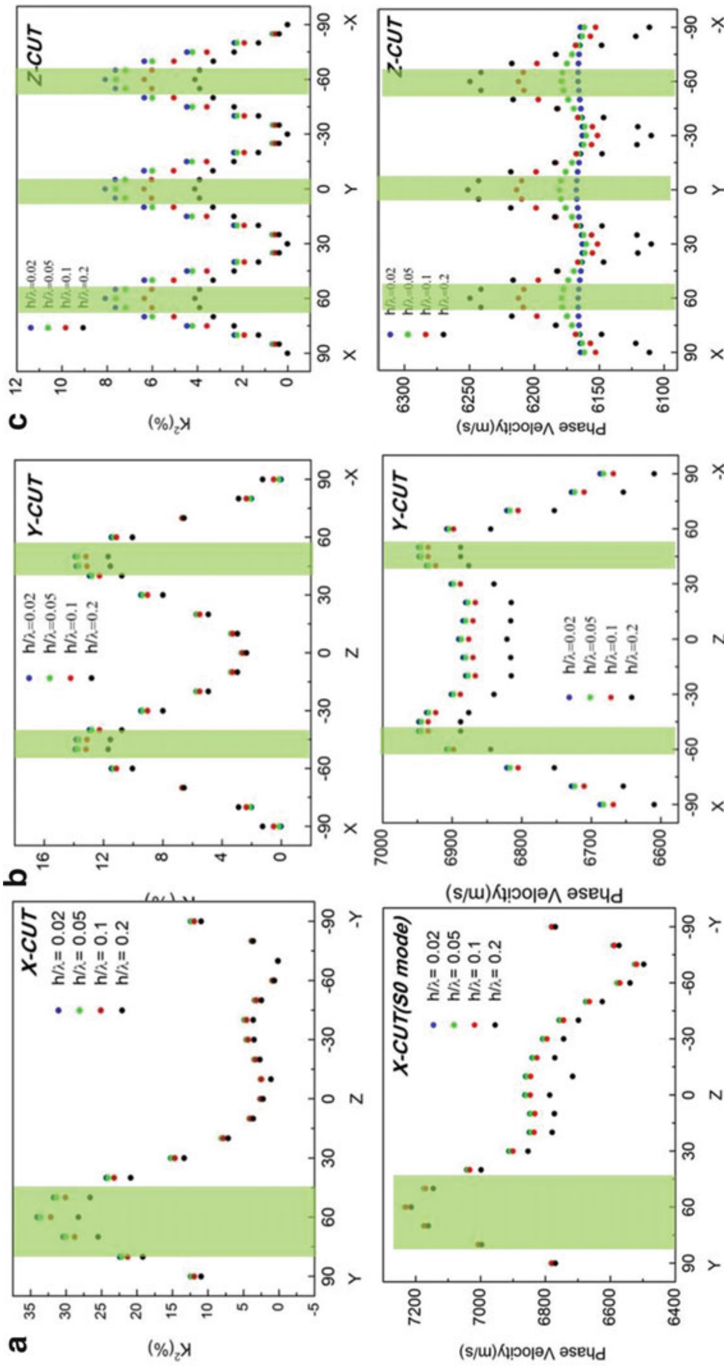

Fig. 4.3 **(a–c)** Simulated K^2 and phase velocity of the S0 mode in **(a)** X-cut **(b)** Y-cut and **(c)** Z-cut of $LiNbO_3$. h is the thickness of the $LiNbO_3$ thin film and λ is the wavelength

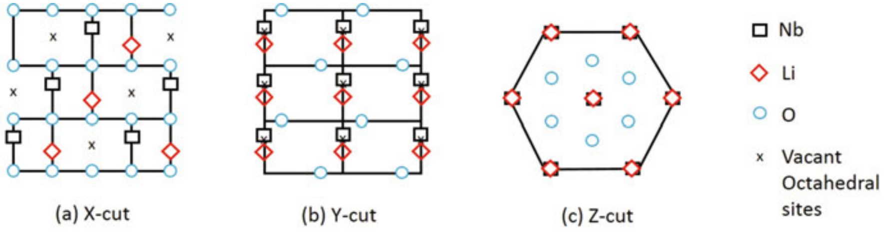

Fig. 4.4 In-plane arrangement of Nb, Li, and O atoms for X, Y, and Z cuts $LiNbO_3$. (**a**) X-cut. (**b**) Y-cut. (**c**) Z-cut

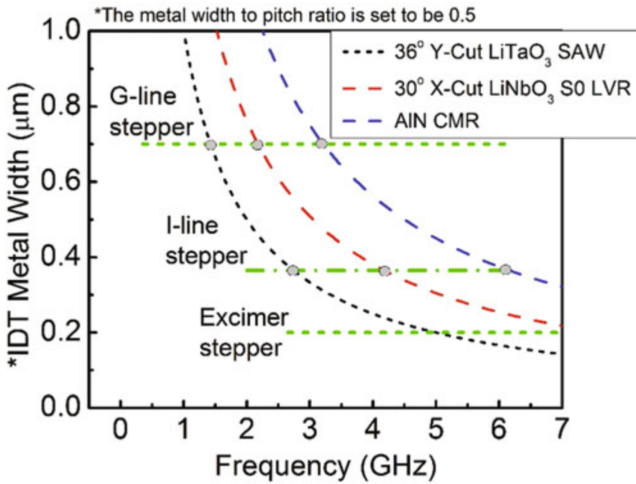

Fig. 4.5 Resonant frequency range of $LiNbO_3$ SAWs, $LiNbO_3$ LVRs, and AlN CMRs given the different limits imposed by photolithography tools

The phase velocity of S0-mode lamb waves in $LiNbO_3$ is between 6400 and 7200 m/s, with X-cut having the highest average phase velocity. The nonsymmetrical characteristics about Z axis in X-cut plane, and the symmetrical response in Y and Z-cut planes can be explained by the arrangement of Li, Nb, and O atoms in these cut planes depicted in Fig. 4.4. The acoustic velocity for S0 mode in $LiNbO_3$ is faster than SAW devices ($\sim$3500 m/s) and slower than the AlN-based CMRs ($\sim$9000 m/s). Given the limit of standard photolithography tools, the scaling of center frequency for these technology platform is illustrated in Fig. 4.5. S0 mode $LiNbO_3$ LVRs have the potential to be scaled up to 4 GHz using low-cost manufacturing tools.

The high K^2 in $LiNbO_3$ shown above is not a feature exclusively of the S0 mode. Similar calculations done for SH0 acoustic waves also identify X-cut as the optimal plane for attaining high K^2 at an orientation of 10° to $-Y$ axis [29]. The K^2 is the

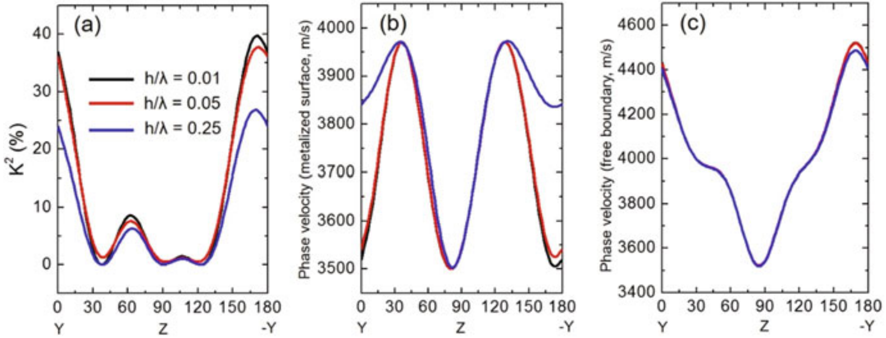

Fig. 4.6 (**a**) Simulated K^2 and (**b**, **c**) phase velocity of the SH0 mode in X-cut $LiNbO_3$. h is the thickness of the $LiNbO_3$ thin film and λ is the wavelength

highest for lateral bulk acoustic modes in $LiNbO_3$, more than three times the K^2 of $LiTaO_3$ SAW (Fig. 4.6).

The average phase velocity of SH0 acoustic waves for various h/λ values is about 3500 m/s, slower than the one of S0 mode acoustic waves and on par with the phase velocity of SAWs in $LiTaO_3$. The lower phase velocity and shorter wavelength suggests SH0 mode devices require the definition of smaller features at the same design frequency. The smaller feature might present a challenge in attaining high-frequency filters. Nonetheless, devices based on SH0 mode bulk acoustic waves in $LiNbO_3$ should have the comparable frequency scalability as the $LiTaO_3$ SAWs, making them the ideal candidate for wider bandwidth and more versatile filtering than what is currently served by SAWs [34].

The last mode that will be studied is the first asymmetrical mode (A0). A0 mode electromechanical coupling as a function of the orientation in the X-cut plane, as seen in Fig. 4.7a, suggests that the electromechanical coupling for A0 mode vibrations reduces to near-zero at an orientation of 50° to $+Y$-axis, while the K^2 for the main S0 mode remains above 20 % at this orientation. Therefore, a design trade-off can be made to minimize A0 spurious mode presence at the expense of a lower K^2 for the intended S0 mode [33]. For applications where a lower K^2 is not acceptable, mitigation of A0 resonances has to resort to other techniques such as engineering the dispersion curves of A0 and S0.

As shown in Fig. 4.2, A0 mode exhibits out of plane displacement and therefore has dispersive characteristics pertaining to the thickness of the $LiNbO_3$ plate (in relation to wavelength). The investigation of A0 mode propagation in $LiNbO_3$ thin film has confirmed the dispersion relationship as seen in Fig. 4.7b. The dispersion curve of A0 mode vibrations for 1 μm electrode-less $LiNbO_3$ thin films indicates that the wave numbers of an A0 overtone and the intended S0 mode will coincide, suggesting the presence of both modes. Fortunately, the dispersion of A0 can be engineered by changing the film stack to create a large dispersion disparity between A0 and S0 modes [33].

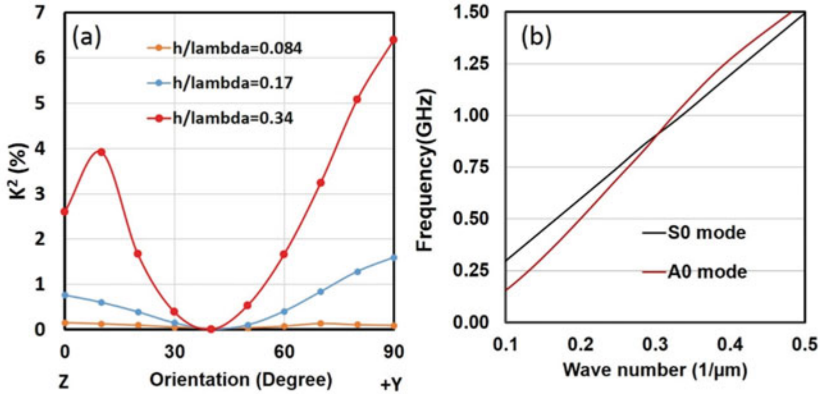

Fig. 4.7 (**a**) Electromechanical coupling (K^2) versus orientation for the A0 mode in the X-cut plane, and (**b**) dispersion curve in a 1 μm electrode-less $LiNbO_3$ thin film

At the beginning of this Section, we state that the motivation for pursuing $LiNbO_3$ BAW or lamb wave devices comes from the potentially higher K^2 than that of SAW. It is also worth noting that BAW modes in $LiNbO_3$, given the prerequisite of excitation (a plate structure or mechanically suspended thin film), intrinsically imply a better acoustic confinement. Propagation of BAW in thin plate/thin film will not suffer the acoustic energy leakage that has been commonly identified in SAW devices [35]. Consequently, $LiNbO_3$ LVRs employing BAW modes are likely to have high *Qs* comparable to those of AlN FBARs, particularly considering that single crystal AlN and $LiNbO_3$ have comparable theoretical limits on $f{\cdot}Q$ (as seen in Table 4.2).

Despite of all the promises of higher performance in both K^2 and Q, the challenge at the time (late 1990s), namely attaining highly crystalline $LiNbO_3$ thin films, prevented experimental validations of these high K^2 and Q modes on chip scale. With the high-quality film integration techniques discussed in Sect. 4.1, it seems that a new MEMS resonator technology simultaneously featuring high Q and k_t^2 is within reach. The only missing piece of the puzzle is a reliable micromachining process of $LiNbO_3$, which will be the focus of the next section.

4.4 Micromachining Lithium Niobate Thin Films

With the success of ion slicing and film-transfer technique, the major roadblock associated with the demonstration of suspended MEMS-like structures made out of $LiNbO_3$ consists in the lack of a micromachining process capable of defining the acoustic geometries of interest and releasing them from the carrier substrate. Etching of $LiNbO_3$ has been proven a tougher task than the etching of other piezoelectric materials. It is a notoriously inert material and reacts with very few chemicals at a

Table 4.3 Wet etching recipes for various cuts of $LiNbO_3$

$LiNbO_3$, cut plane	Chemical	Temperature (°C)	Etch rate (μm/h)	Etch mask	Ref.
Z cut, Ti-diffused	HF, HNO_3, ethanol	22	0.8	Chromium	[36]
Z cut, domain inverted	HF, HNO_3	60	0.8	None	[37]
Y-cut, proton exchanged	HF, HNO_3	Room temperature	Orientation dependent	None	[38]

moderate rate. As a matter of fact, developing an effective etch technique to attain high etch rate, smooth and straight etch surfaces in $LiNbO_3$ has been a very active research topic. Most of the etch efforts that preceded the synthesis of MEMS devices originated from the need to make optical wedge waveguide in $LiNbO_3$, and thus were mostly focused on c-axis $LiNbO_3$ substrates. The only well know wet etching technique uses a mixture of hydrofluoric acid (HF) and Nitric acid (HNO_3) with a slight dose of ethanol to improve the smoothness of the etched surfaces. More importantly, the wet etching relies on the proton exchange, often by Ti-diffusion, to accelerate the etch rate of $LiNbO_3$. Nonetheless, such wet etching only produces a very moderate etch rate of 10 nm/min. What is more discouraging for the acoustic device researchers is the fact that none of the wet etching approaches (see Table 4.3) can produce the straight sidewalls that are essential for optimal acoustic boundaries and high Qs.

On the other hand, dry etching techniques, including ion milling, UV laser ablation, and reactive ion etching (RIE) with inductively coupled plasma (ICP), have been shown to be more effective and more versatile on different cuts and configurations of $LiNbO_3$. They have all shown faster etching rates, finer control of the sidewall profile, and scalability to mass manufacturing.

Ion milling was first tested as a dry etching approach for $LiNbO_3$ in the 1970s [39]. Due to the high physical nature of ion milling, the process has very limited selectivity and it is generally not scalable to large substrates. Laser assisted micromachining of $LiNbO_3$ has also been investigated as an alternative method [40, 41]. Several issues have obstructed its employment for making $LiNbO_3$ acoustic devices. First, the laser ablation could not directly remove $LiNbO_3$ and still requires a HF-based wet etch to remove the laser damaged $LiNbO_3$. In addition, the laser ablation has been reported to amorphize the regions in the vicinity of the area exposed to the laser and produce crystalline defects [41]. Lastly, the etched sidewalls have a slanted profile and are far from ideal in enabling the desired sharp and smooth acoustic boundaries.

RIE-ICP is so far the optimal approach that offers great control in the etched profile. The ICP is essential in attaining anisotropic etch characteristics. As seen in Fig. 4.8, the process generally employs hard etch masks (SiO_2, Cr, Ni, or Au) that can be patterned by either wet etch and RIE with photoresist as the mask. PR is not directly used as the etch mask to micro-machine $LiNbO_3$ due to its low selectivity to

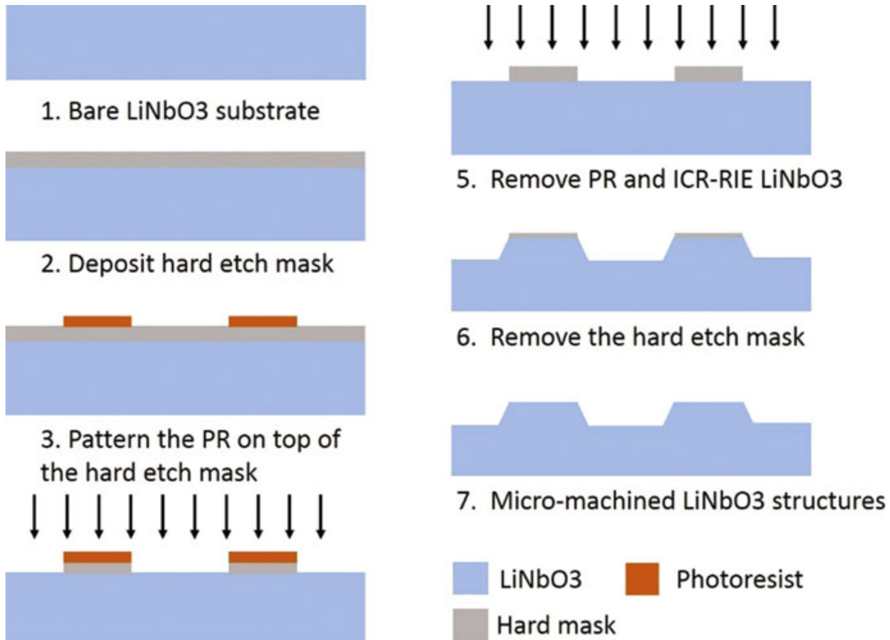

Fig. 4.8 Processing steps for etching $LiNbO_3$ with ICP-RIE

$LiNbO_3$ in a typical high ICP power RIE recipe. In addition, the PR-based etching requires operating at a low temperature that often limits the etch rate to a very moderate value. The hard masks that have been selected are either dielectrics or metals, depending on their compatibility with the other micromachining steps and the etch chemistry. Most importantly, the hard masks offer sufficient selectivity (often >1:1) against $LiNbO_3$ in the corresponding RIE chemistry, and can endure high temperatures (>120 °C).

Two gas chemistries, either fluorine or chlorine, have been reported to effectively etch $LiNbO_3$. Fluorine-based chemistry utilizes either SF_6 [42], CHF_3 [42], or C_4F_8 [43] with high ICP power to produce a reasonable etch rate. As seen in Table 4.4, 4.5, and 4.6, the etch rates reported using fluorine chemistry are generally between 20 and 100 nm/min for various cuts. The reaction of Fluorine plasma and $LiNbO_3$ produces mostly volatile fluorinated niobium species at a temperature higher than 200 °C, except for LiF. LiF has a melting temperature higher than 800 °C. It gets re-deposited on etched surfaces and subsequently lowers the etch rate (Fig. 4.9). Thus, it is extremely challenging to attain vertical sidewalls. To mitigate this effect, etching of $LiNbO_3$ with fluorine gases requires intermittently pausing the etch and cleaning the sample in SC-1 solution (70 % H_2O, 20 % H_2O_2, 10 % NH_4OH) to remove the re-deposited LiF [43].

Table 4.4 Dry etching recipes for Z-cut of $LiNbO_3$

Approach	[44]	[39]	[45]	[1]
$LiNbO_3$ cut plane	Z-cut	Z-cut	Ti-diffused Z-cut	Z-cut
Etch mask	Chromium	Titanium	Chromium	PECVD SiO2
Etch technique	Focused Ion milling	Ion milling	RIE	RIE-ICP
Tool	Orsay Physics LEO FIB4400	Technics Inc. Model MIM TLA 5.5	ME-3A	Trion Phantom III
Chamber pressure	2×10^{-6} Torr	1.1×10^{-4} Torr	N/A	10 mTorr
Temperature	N/A	50 °C	N/A	70 °C
Power	Current: 2 μA, Biasing voltage: 30 kV	100 W RIE 500 W ICP	350 W RIE	RIE 250 W ICP 600 W
Etch rate	160 nm/min	0.45 μm/h	46 nm/min	110 nm/min
Etch selectivity to mask[a]	N/A	1:3	2.5:1	2.2:1
Gas mixture or relevant settings	Ga^+ ions current: 2 μA Acceleration voltage: 30 kV	Ar+ and O+ Acceleration voltage and ion current: 1.1 kV and 0.97 mA/cm^2	$SF_6$40 sccm	Cl_2 5 sccm $BCl_3$15 sccm Ar 20 sccm
Sidewall angle	N/A	N/A	60°	75°

[a]Etch selectivity is defined as the ratio between $LiNbO_3$ and mask etch rates

Cl_2-based RIE was first demonstrated in [1] for micromachining MEMS resonators, using a mixture of Cl_2, BCl_3, and Ar. The ratios between gases were carefully selected to attain a desired balance of the physical and chemical etch of $LiNbO_3$. Due the anisotropic properties of $LiNbO_3$, the same etch recipe would produce different etched profiles for different cuts $LiNbO_3$, as seen in Fig. 4.10. In addition, as seen in Fig. 4.11, the optimization of the gas ratios has a significant impact on the sidewall profile, ranging from 20° to near 90°. The chamber pressure is generally reduced to below 10 mTorr for maximizing the etch rate.

The ICP-RIE, similar to all the aforementioned techniques, exhibits varying etch characteristics for different cuts of $LiNbO_3$ substrates. The orientation dependent nature of the etch arises from the anisotropic crystal properties [53]. Optimizing the etch rate relies on fine-tuning the balance of physical (with Ar) and chemical etching (with F_2 or Cl_2) [51]. None of the reported etching techniques has caused the processed thin film to change polarization.

After the etching windows are defined by using one of the aforementioned etching techniques, the final step of the process is to remove the sacrificial layer and suspend the device via critical point drying (if a wet etch is used) [54, 55]. For processes using transferred $LiNbO_3$ thin films, the sacrificial layer removal depends on the materials used for the intermediate layer(s) between the transferred

Table 4.5 Dry etching recipes for Y-cut of $LiNbO_3$

Approach	[46]	[47]	[1]	[48]
$LiNbO_3$ cut plane	Y-cut	Y-128°	Y-cut	Y-cut
Etch mask	Electroplated nickel	Electroplated nickel	PECVD SiO_2	Thick photoresist
Etch technique	RIE	RIE-ICP	RIE-ICP	Ion milling
Tool	Plassys MG 200	STS multiplex AOE	Trion Phantom III	AJA Ion Mill
Chamber pressure	1.5 mTorr	N/A	10 mTorr	8–10 Torr
Temperature	N/A	20–80 °C	70 °C	N/A
Power	RIE 150–250 W	N/A	RIE 250 W ICP 600 W	N/A
Etch rate	40 nm/min at 150 W 50 nm/min at 200 W	0.5 μm/min	80 nm/min	42 nm/min
Etch selectivity to mask[a]	10:1–16:1	N/A	1.7:1	N/A
Gas mixture	SF6 10 sccm	CF4/ He	Cl_2 5 sccm BCl_3 15 sccm Ar 20sccm	N/A
Sidewall angle	68° at RIE 150 W 73° at RIE 200 W 79° at RIE 200 W	75°	40°	Near 90°

[a]Etch selectivity is defined as the ratio between $LiNbO_3$ and mask etch rates

$LiNbO_3$ thin films and the supporting substrates. So far, BCB [56], SiO_2 [57], and a proprietary glue [55] are used and all have been removed with wet etch processes based on either Nanostrip or HF. The removal of the sacrificial layer somewhat limits the choice of metal material for the top electrodes unless additional steps are taken to protect the metal electrode during wet etching. For example, neither Nanostrip nor HF allows for Al top electrodes. The size of the release region can only be limited via timing the isotropic wet etch, thus lacking the fine control required for device optimization purposes.

There is an alternative process that also requires ion-implantation, similarly to the aforementioned process based on micromachining transferred $LiNbO_3$ thin film. However, it uses the ion-implantation with properly chosen energy and dose to embed a thin layer of damaged $LiNbO_3$, which is subsequently used as the sacrificial layer to suspend the $LiNbO_3$ structures [52]. It has been reported that ion-damaged $LiNbO_3$ can be selectively etched by HF at a much higher rate than virgin $LiNbO_3$ [58]. Therefore, the damaged $LiNbO_3$ can be exploited as the sacrificial layer for releasing the structure, as long as the sidewalls are sufficiently protected (e.g. using a thin layer of gold) during the selective etching. This approach is

Table 4.6 Dry etching recipes for X-cut of $LiNbO_3$

Approach	[43, 49]	[50]	[51]	[52]
$LiNbO_3$ cut plane	H^+ proton exchanged	H^+ proton exchanged	X-cut	X-cut
Etch mask	Chromium	Chromium	PECVD SiO_2	PECVD SiO_2
Etch technique	RIE	ICP-RIE	ICP-RIE	ICP-RIE
Tool	Oxford Plasmalab 80+	Plasma-Therm SLR 770	Trion Phantom III	Plasma-Therm SLR 770
Chamber pressure	100 mTorr	5 mTorr	10 mTorr	5 mTorr
Temperature	200 °C	50 °C	65 °C	65 °C
Power	350 W RIE	100 W RIE 500 W ICP	250 W RIE 600 W ICP	280 W RIE 900 W ICP
Etch rate	55 nm/min	94 nm/min	40 nm/min	170 nm/min
Etch selectivity to mask[a]	N/A	16:1	1:1	1:1.1
Gas mixture or relevant settings	CHF_3 50 sccm Ar 50 sccm	CF4 25 sccm Ar 20 sccm	Cl_2 5 sccm BCl_3 15 sccm Ar 20sccm	Cl_2 5 sccm BCl_3 15 sccm Ar 18 sccm
Sidewall angle	Sloped	>80°	Orientation Dependent 30–90°	80°

[a]Etch selectivity is defined as the ratio between $LiNbO_3$ and mask etch rates

capable of lithographically defining the release region through hard masking of the ion implantation, and thus creating more precise acoustic boundary conditions for optimizing device performance [52]. The inherent challenges with this approach include fabricating large devices and incorporating bottom electrodes. The selective etching can only create a very small gap and it takes a long time for the etchant to access the damaged layer under the center of the resonator and accomplish the full release. The surface roughness induced by the selective etching has also been characterized and proven not a limiting factor for the device Q [52]. Any ion-implantation-induced damages in the resonator body can be significantly reduced by rapid thermal annealing (>300 °C), as experimentally validated by the measured Q enhancement before and after annealing [59]. Other studies targeting the measured defect density have shown similar conclusions.

So far, the resonant devices that have exhibited the highest performance were built with the aforementioned processes or some slight variations of such. These variations are mainly related to releasing or suspending the device structures. Several approaches either create the release cavities in $LiNbO_3$ [60] before the $LiNbO_3$ thin film integration on a carrier substrate, or utilize through Si deep RIE process to suspend the thin film of $LiNbO_3$ on a Si carrier [61]. These approaches

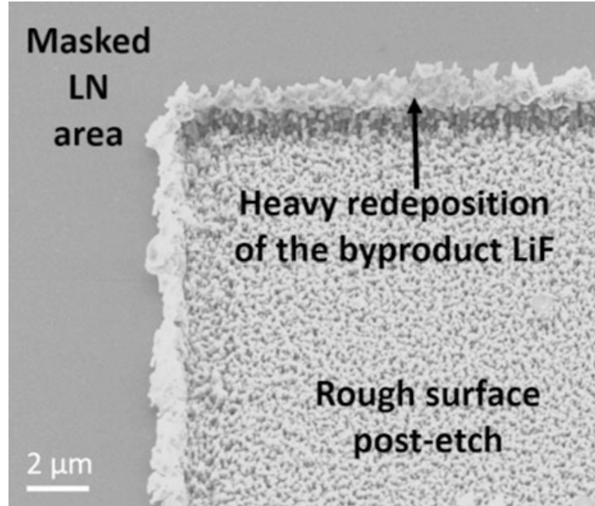

Fig. 4.9 Dry etch of X-cut $LiNbO_3$ using SF_6-based ICP-RIE

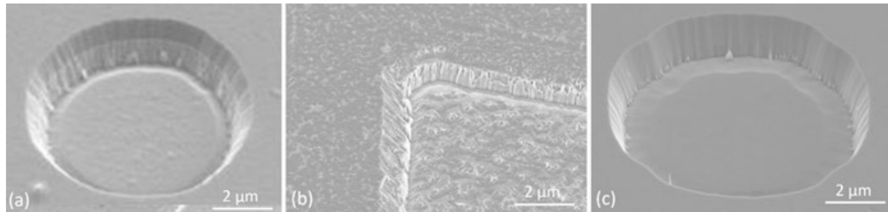

Fig. 4.10 Etched profiles of (**a**) X-cut, (**b**) Y-cut, and (**c**) Z-cut $LiNbO_3$ after being processed with the identical ICP-RIE recipe

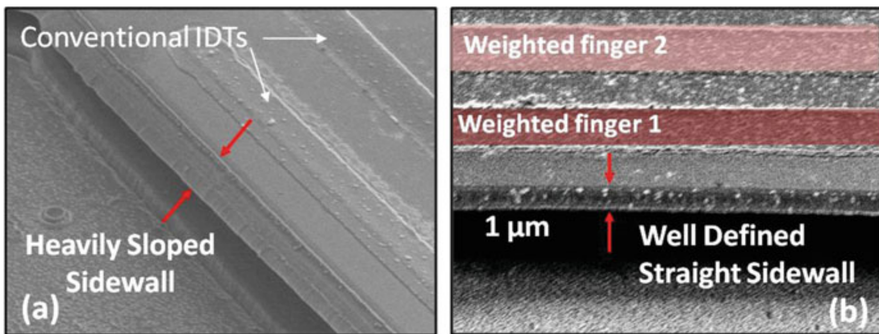

Fig. 4.11 Sidewalls of etched resonators using (**a**) a gas mixture that has low Ar content (**b**) a gas mixture that has high Ar content

can define the region with lithographical accuracy, and possibly allows for the integration of bottom electrodes.

Micromachining epitaxially grown $LiNbO_3$ thin films has also been attempted. In principle, the etching process can be the same used for transferred or ion-implanted thin films. The epitaxially grown $LiNbO_3$ thin films have not shown comparable crystallinity as ion-sliced, ion-implantation enabled, or even chemical mechanical polishing (CMP) thinned $LiNbO_3$ thin films. This is particularly reflected in the measured Q of the fabricated devices [62]. As mentioned before, the epitaxially grown thin films are limited to *c*-axis or Z-cut. From a device performance perspective, they are not suitable as a platform for high k_t^2 S0 or SH0 mode devices, although A1 mode has been experimentally demonstrated to feature high acoustic velocity and high k_t^2 [62].

4.5 Design and Performance of Lithium Niobate Devices

The design of LiNbO3 LVRs leveraged the know-hows of AlN-CMRs [19, 63]. As seen in Fig. 4.12, a typical one-port $LiNbO_3$ LVR consists of a suspended $LiNbO_3$ thin film with inter-digitated electrodes (IDE) patterned on the top surface. In operation, the IDEs are alternatingly connected to the signal and ground, introducing electric fields in the $LiNbO_3$ thin film. Differently from the typical AlN CMRs, the $LiNbO_3$ LVRs are lateral electric-field excited devices so that the high in-plane (X-cut) piezoelectric constants can be harnessed. For S0 mode devices, the lateral electric fields excite the $LiNbO_3$ thin film into longitudinal expansion and contraction under alternating electrode pairs, as depicted in Fig. 4.13a. For SH0 devices, the electric fields, introduced by virtually identical electrode configuration, excite in-plane opposite-direction transverse motions under alternating electrodes (Fig. 4.13b). Even though S0 and SH0 devices appear similar in configuration, they differ in the device orientation at which the wave propagation characteristics are optimal (detailed in Sect. 4.3).

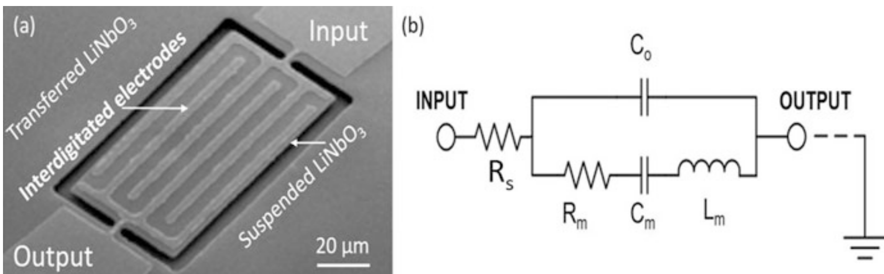

Fig. 4.12 (**a**) SEM image and (**b**) MBVD model of a typical $LiNbO_3$ LVR

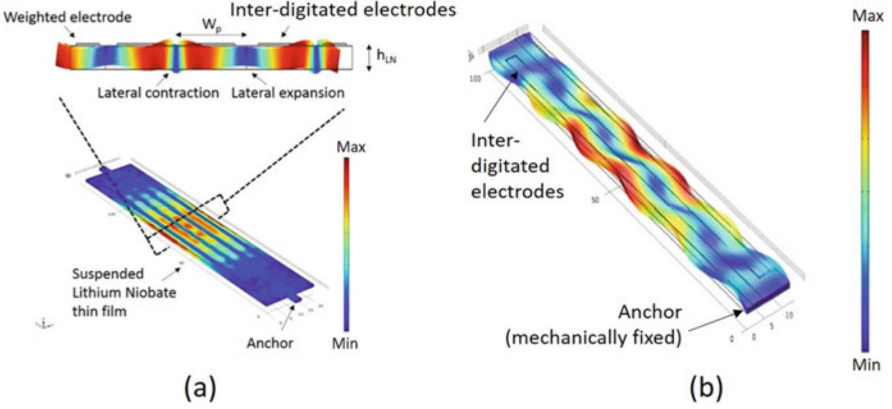

Fig. 4.13 Typical structures and modeshapes of (**a**) S0 and (**b**) SH0 $LiNbO_3$ LVRs

The resonant frequency of these devices is predominately determined by the transducer pitch and the phase velocity of the intended acoustic mode in the electrode-on-$LiNbO_3$ film stack. For example, the resonance of the longitudinal mode order *i* and transverse mode order *j*, can be estimated by:

$$f_{ij} = v_0 \sqrt{\left(\frac{i}{2W}\right)^2 + \left(\frac{j}{2L}\right)^2} \tag{4.6}$$

where *W* and *L* are the width and length of the resonator and v_0 is the acoustic velocity. In most cases, $LiNbO_3$ LVRs are designed with several pairs of electrodes so that the static capacitance, C_0, is sufficiently high to interface with 50Ω. As a result, the intended resonance is typically a higher order longitudinal mode with the transverse mode order $j = 1$ (modes with $j = 3, 5, \ldots$ are considered spurious modes). Given that *L* is typically larger than *W* and *i* is larger than *j*, the series resonant frequency (f_s) can be approximated by:

$$f_s = \frac{v_0 i}{2W} = \frac{v_0}{2W_p} \tag{4.7}$$

where W_p is the pitch of the transducer. Note that Eq. 4.6 is an approximation because acoustic velocities along most orthogonal directions in the X-cut plane of $LiNbO_3$ are not the same. For more precise prediction of the resonance for a given mode, one has to resort to a 3D finite element simulation of the resonator structure.

In addition to the resonant frequency, the performance of $LiNbO_3$ LVRs is characterized by the device or transducer electromechanical coupling (k_t^2) and device quality factor (*Q*). It is important to note that k_t^2, different from K^2, is dependent on the mode of operation, electrode configuration, and material properties. K^2 typically sets the maximum achievable k_t^2 for a given mode. On

the other hand, the device Q is collectively determined by various involved loss mechanisms, including thermal elastic dissipation, anchor loss, attenuation loss in electrodes and the piezoelectric material, and electrical loss (R_s). The ultimate limit on Q for devices based on a certain piezoelectric material is set by the attenuation loss in the piezoelectric material, which is often overshadowed by anchor loss and damping at the interface between electrodes and the piezoelectric material. For more information on Q modeling and optimization of laterally vibrating MEMS resonators, please refer to a later chapter of this book.

k_t^2 and Q are the key parameters in constructing the Modified Butterworth-Van Dyke (MBVD) model that is commonly applied as the equivalent circuit representing piezoelectric MEMS resonators. More on MBVD model will be also discussed in the following chapters. As seen in Fig. 4.12b, the MBVD model typically allows accurate extraction of k_t^2 and Q values from measurements as the motional components (R_m, C_m, and L_m) in the MBVD model are related to k_t^2 and Q [19]. In most cases, it sufficiently captures the electrical performance of resonators and thus can be embedded in circuit simulations for predicting the performance of resonator-comprised subsystems.

From the MBVD model of $LiNbO_3$ LVRs, we can define k_t^2 as:

$$k_t^2 = \frac{\pi^2}{8}\frac{C_m}{C_0} \tag{4.7}$$

It directly measures *device* transduction efficiency from the electrical to mechanical domain as the mechanical and electrical energy is stored in the motional and static capacitors, respectively.

Q, similar to the definition used for any resonant system, is defined as the ratio of stored energy versus dissipated energy per cycle. In both models and experiments, Q is characterized by the ratio between the resonance and its 3 dB bandwidth.

So far, we have discussed the operation and performance characterization of $LiNbO_3$ LVRs in the general sense. Next, we will focus on understanding the state of the art performance of both S0 and SH0 mode devices.

The first experimental demonstration of S0 mode devices came in [56], and was immediately optimized in [1, 51]. As seen in Fig. 4.14, the measured resonant frequency of 485 MHz for a device with 6 μm electrode pitch at the orientation of 30° to $+Y$-axis verifies the acoustic velocity of S0 to be 5820 m/s, on par with the value predicted in Sect. 4.2 for a metalized $LiNbO_3$ plate with an infinitely thin top electrode. Such a high velocity should permit the electrode definition of devices up to 3.5 GHz using stepper-based lithography, while devices have been demonstrated to operate up to 0.88 GHz for X-cut [33] and 1 GHz for Y-cut devices [48].

Given our discussion on the material properties of $LiNbO_3$, it is no surprise that the S0 mode LVRs achieve the maximum k_t^2 at the orientation of 30° to $+Y$-axis in the X-cut plane. To further maximize the k_t^2, an electrode weighting technique (depicted in Fig. 4.13) has to be employed for any overmoded resonator structures. The electrode weighting technique uses two electrodes close to the edges of the device, each having a width less than the conventional electrode pitch ($\lambda/2$).

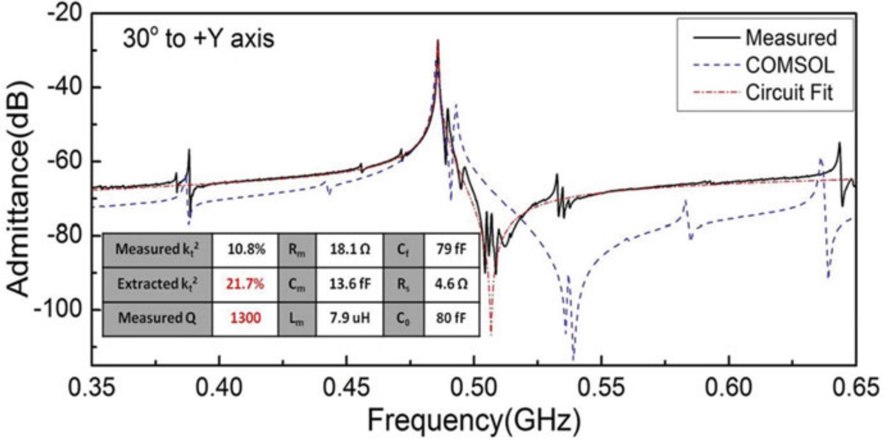

Fig. 4.14 Measured performance of a S0 $LiNbO_3$ LVR with an orientation of 30° to $+Y$ axis and the weighted electrode configuration

The weighted electrodes on the edges modify the acoustic boundary conditions and maximize the electric field distribution between the electrodes. It therefore excites largest compression or expansion right underneath the electrodes. A similar technique has also been applied to Y-cut S0 LVRs and proven effective in enhancing k_t^2 [48].

The measured *Qs* of S0 $LiNbO_3$ LVRs are typically between 1000 and 2000, far from the ultimate limit imposed by the intrinsic loss in the material. It is believed that *Q* is still largely limited by micromachining. Upon improving the straightness of etched sidewalls and reducing the residual stress accumulated in thin film during processing, *Q* is expected to be further enhanced. Other factors, including the electrode material and anchoring/acoustic boundaries, can also be leveraged to enhance *Q* given that fabrication processes can accommodate the implementation of the optimized designs. Because of the simultaneously attained high k_t^2 and *Q* of S0 $LiNbO_3$ LVRs, record-breaking FoMs have been achieved for both X-cut (FoM = 280) [51] and Y-cut (FoM = 110) [48] devices.

Following the success demonstration of high k_t^2 S0 $LiNbO_3$ LVRs, SH0 mode devices have also been explored as they are predicted with higher k_t^2 and potentially an even larger FoM. Additionally, they typically feature less spurious modes than S0 mode devices, when both modes are excited using a conventional electrode configuration. So far, the lower phase velocity of SH0 mode has limited device demonstrations to below 1 GHz [64], although finer lithography tools could scale SH0 to even higher frequencies.

As shown in Fig. 4.15, the k_t^2 of SH0 mode devices reaches optimum at 10° to $-Y$ axis with a value larger than 20 % [65]. Given an optimized electrode configuration, the achieved k_t^2 can be even larger, for example, 23.6 % in [59]. Further optimizations in the electrode configuration (e.g. metal coverage and

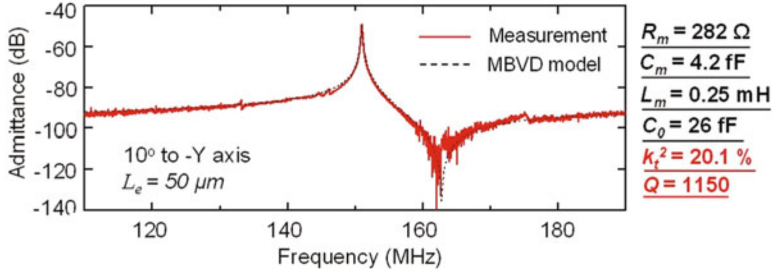

Fig. 4.15 Measured performance of a SH0 $LiNbO_3$ LVR with an orientation of 10° to $-Y$ axis and the length-controlled electrode configuration

electrode weighting) and device structure are expected to yield k_t^2 closer to the limit set by the calculated K^2. Moreover, suppressing unwanted modes can also help to concentrate the coupling into the intended mode. For example, the device with its response shown in Fig. 4.15 has a length-controlled electrode configuration for minimizing the third order transverse SH0 spurious mode [66]. As a result, the k_t^2 of intended SH0 mode is increased.

The measured Qs of SH0 devices are comparable to those of S0 mode devices, ranging from 1000 to 2200 and dependent of the resonant frequency. SH0 mode devices currently hold the record for the highest experimental FoM at a value of 420, owing to the simultaneously achieved high k_t^2 (23.6 %) and Q (2200) [59]. Similar to S0 mode devices, there is still room for improving the Q of SH0 mode devices. Better processing or more sophisticated designs of acoustic confinement are all potentially effective approaches and are going to be explored for this purpose.

Beyond the SH0 and S0 modes that we have discussed, readers might be curious about other higher order S and A modes, such as the degenerate S1 (FBAR mode) or A1. As a matter of fact, these two modes have been experimentally demonstrated with high k_t^2 [10, 67], but neither of them has the feature of lithographically definable center frequencies. The resonances of S1 and A1 mode devices are predominately set by the thin film thickness. In the case of S1 mode, a bottom electrode is also required. A patterned bottom electrode under a transferred $LiNbO_3$ thin film is difficult to implement as transferring $LiNbO_3$ thin films requires planarized surfaces. The existing S1 mode device demonstrations used a back-side Si etch to release the device and included a bottom electrode through the etched via. This process introduces additional fabrication complications and large parasitic effects from the Through-Si-vias. Scaling and interconnecting these devices for forming filters would need a more sophisticated method of including bottom electrodes.

4.6 Discussion and Potential Applications of Lithium Niobate Devices

The previous sections have offered a comprehensive overview of $LiNbO_3$ as a material for RF-MEMS platform. The potential of $LiNbO_3$ devices is better appreciated with a discussion on the most promising applications for this technology, namely RF front-end filtering and duplexing.

As also discussed in other chapters of this book, it is evident that SAWs and AlN FBARs are the existing commercial solution for RF front-end filtering, respectively. SAWs can be manufactured with very simple and low-cost fabrication processes and offer sufficient bandwidth and low-loss performance for current standards (<2 GHz). AlN FBARs is pervasive due to its desirable piezoelectric properties and low-cost CMOS-compatible sputtering process of AlN [68, 69]. These devices vibrate in a thickness extensional mode and leverage the high d_{33} piezoelectric coefficient of AlN to attain high electromechanical coupling. However, FBARs lack wafer-level frequency diversity because the resonant frequency of FBARs is determined by thickness of the AlN thin film. Low-cost batch fabrication can only yield resonators of one resonance across the substrate. Motivated by having access to a resonator technology that can have wafer level frequency diversity, AlN contour mode resonators (CMRs) and filters were developed [70]. Similar to FBARs, AlN CMRs consist of suspended AlN thin film with top and bottom electrodes. Different from the operation of AlN FBARs, AlN CMRs vibrate in a lateral extensional mode of which resonant frequency can be lithographically defined via electrode pitch. However, one major drawback of AlN CMRs is their moderate electromechanical coupling due to limited d_{31} coefficient of AlN. The moderate k_t^2 results in a lower figure of merit even though AlN CMRs have comparable high Qs to FBARs. Moreover, the moderate k_t^2 has also limited the maximum FBW that AlN CMRs-based filters can achieve, and restricted AlN CMRs to applications that have narrower bandwidth requirement than most of existing telecomm standards.

The $LiNbO_3$ LVR technology essentially combines the technological benefits of AlN FBARs and CMRs. It shares the same fundamental working principle of AlN CMRs and offers higher electromechanical coupling than AlN FBARs. These advantages fundamentally originate from material properties and the method of integrating high-quality $LiNbO_3$ thin films for micromachining. As seen in Fig. 4.16, the high electromechanical coupling and lateral mode of operation of $LiNbO_3$ LVRs ensures attaining wide bandwidth and low-loss filtering with unprecedented wafer-level frequency-diversity.

It is evident from an application perspective that $LiNbO_3$ LVRs can be a key enabler for the next generation of RF front-end filtering. The main concern is about how rapidly the $LiNbO_3$ LVRs can be placed into the market place. Benchmarked to the development history of AlN FBARs, which started in early 1980s by Ken Lakin [71], and became a commercial RF filtering solution in the early 2000s (thanks to an Agilent semiconductor division now owned by now known as Broadcom), the $LiNbO_3$ technology is still very much in its early adolescence. Several challenges

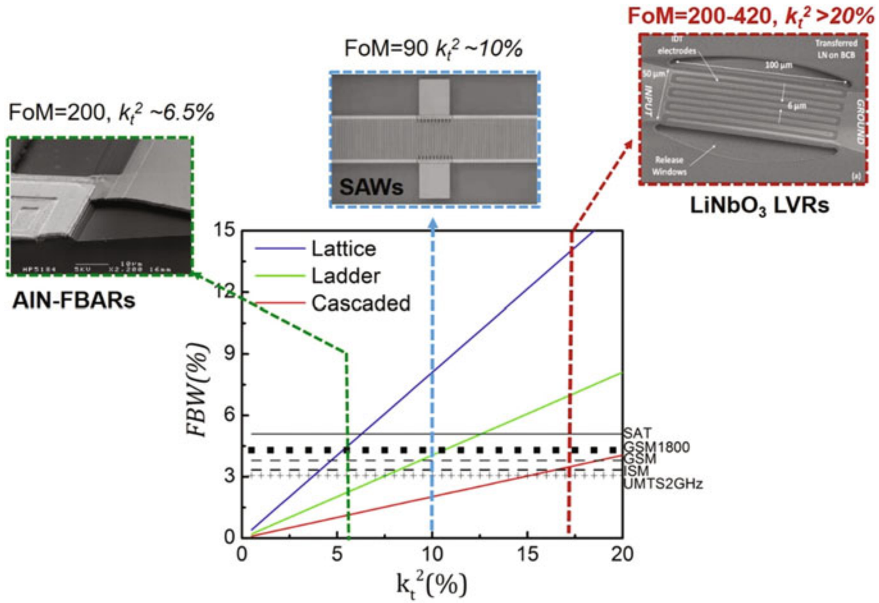

Fig. 4.16 Comparison of performance for various types of filters based on SAWs, AlN FBARs, and $LiNbO_3$ LVRs

still need to be addressed, either on the material side or device level optimization, before $LiNbO_3$-based resonators become ready for prime time. These challenges involve suppression of spurious modes, enhancement of power handling, and improvement of temperature stability.

As seen in the last section, the S0 and SH0 $LiNbO_3$ devices are prone to spurious responses. The spurious response stems from a number of causes that have been already investigated for AlN CMRs [72–75]. Completely suppressing or appreciably subduing the spurious response is essential for engineering high-performance filters and remains a major bottleneck for $LiNbO_3$ LVRs. In addition, the techniques to be developed have to be effective without substantially increasing the fabrication complexity or compromising the chip-level frequency diversity. There have already been a few reports on this research topic [66, 76–78] and substantial progress should be expected in the next few years.

The second challenge is the power handling of $LiNbO_3$ LVRs. $LiNbO_3$ LVRs are formed by thermally isolated thin films, hence suffering from self-heating caused by electrical losses and thermo-elastic damping [21]. Depending on the size and anchoring, $LiNbO_3$ LVRs can operate in the nonlinear regime at low power levels due to the thermal nonlinearity. This issue is more evident when $LiNbO_3$ LVRs are compared with $LiNbO_3$ SAWs and AlN FBARs. $LiNbO_3$ SAWs are built on bulk substrates that are heat sinked through packages. They have access to a higher thermal conductance path to dissipate the self-heating. AlN FBARs enjoy

Table 4.7 The comparison between measured TCF of micro-resonators

Resonator technology	Measured TCF
AlN-FBARs	−25 to 30 pmm/K [69]
AlN-CMRs	−25 to 30 ppm/K [19]
LN-LVRs	−75 to 90 ppm/K [79]

the extremely high thermal conductivity of AlN material and therefore can easily disperse heat even in a suspended thin film configuration. AlN FBARs are often fully anchored in the peripherals, further allowing a low thermal resistance path from the resonator body to the surroundings.

The last technological issue for $LiNbO_3$ LVRs is the temperature instability induced by the negative temperature coefficients of elastic constants seen in Table 4.1. A comparison of measured temperature coefficients of frequency is listed in Table 4.7. It is foreseeable that a TCF larger than −20 ppm/K might become insufficient in the near future as more closely spaced bands are placed into the RF spectrum.

Temperature compensation techniques that were developed in the past for creating ultra-stable on chip oscillators can be readily applied to $LiNbO_3$ devices. Particularly, passive compensation techniques that do not require power for enhancing temperature stability are of great interest. They typically involves stacking sputtered or thermally grown SiO_2 with the piezoelectric thin film [80]. There have been demonstrations of temperature compensated Y-cut $LiNbO_3$ LVRs at the expense of a reduced electromechanical coupling [57]. However, the impact of passive temperature compensation on the device quality factor is still unclear. Further studies are required to determine if a trade-off between the filter temperature stability and insertion loss exists.

All of the aforementioned challenges are identified by tracing back to the historical development of successful acoustic filters and targeting the specifications of existing standards. However, it is not unforeseeable that the capabilities of $LiNbO_3$ platform may offer a new paradigm for front-end filtering that does not need to conform to the conventional design space. For example, widely tunable resonators based on $LiNbO_3$ have been proposed with several mechanisms and shown promising results [81–83]. The frequency tunability, if implemented with acceptable tradeoff, could revolutionize the RF design space, reduce cost, and enable new radio architectures. Because of these benefits, it should definitely be part of the future work on $LiNbO_3$-based devices.

References

1. Gong S, Piazza G (2013) Design and analysis of lithium-niobate-based high electromechanical coupling RF-MEMS resonators for wideband filtering. IEEE Trans Microw Theor Tech 61:403–414

2. Klauder JR, Price AC, Darlington S, Albersheim WJ (1960) The theory and design of chirp radars. Bell Lab Tech J 39(4):745–808
3. Arizmendi L (2004) Photonic applications of lithium niobate crystals. Phys Status Solidi 201:253–283
4. Nassau K, Levinstein HJ, Loiacono GM (1966) Ferroelectric lithium niobate-1 growth, domain structure, dislocations and etching. Solid State Commun 4:19
5. Carruthers JR, Peterson GE, Grasso M, Bridenbaugh PM (1971) Nonstoichiometry and crystal growth of lithium niobate. J Appl Phys 42:1846–1851
6. Ruby RC, Bradley P, Oshmyansky Y, Chien A, Larson JD (2001) Thin film bulk wave acoustic resonators (FBAR) for wireless applications. In: 2001 IEEE international ultrasonics symposium. Proceedings of the international symposium (Cat. No. 01CH37263), vol 1
7. Takada S, Ohnishi M, Hayakawa H, Mikoshiba N (1974) Optical waveguides of single crystal LiNbO3 film deposited by RF sputtering. Appl Phys Lett 24(10):490–492
8. Huang CH, Rabson TA (1993) Low-loss thin-film LiNbO(3) optical waveguide sputtered onto a SiO(2)/Si substrate. Opt Lett 18:811–813
9. Jiang YD, McGee J, Polley TA, Schwerzel RE, Hunt AT (2001) Fabrication and properties of epitaxial lithium niobate thin films by combustion chemical vapor deposition (CCVD). In: MRS Proc 688
10. Kadota M, Ogami T, Yamamoto K, Tochishita H, Negoro Y (2010) High-frequency lamb wave device composed of MEMS structure using LiNbO 3 thin film and air gap. IEEE Trans Ultrason Ferroelectr Freq Control 57:2564–2571
11. Yablonovitch E, Gmitter T, Harbison JP, Bhat R (1987) Extreme selectivity in the lift-off of epitaxial GaAs films. Appl Phys Lett 51:2222–2224
12. Callejo D, Bermúdez V, Serrano MD, Diéguez E (2002) Lithium niobate films on periodic poled lithium niobate substrates prepared by liquid phase epitaxy. J Cryst Growth 237–239:596–601
13. Betts RA, Pitt CW (1985) Growth of thin-film lithium niobate by molecular beam epitaxy. Electron Lett 21(21):1985
14. Levy M, Osgood RM, Liu R, Cross LE, Cargill GS, Kumar A, Bakhru H (1998) Fabrication of single-crystal lithium niobate films by crystal ion slicing. Appl Phys Lett 73(16):2293–2295
15. Weis R, Gaylord T (1985) Lithium niobate: summary of physical properties and crystal structure R. Appl Phys A Mater Sci Process 37:191–203
16. Kovacs G, Anhorn M, Engan HE, Visintini G, Ruppel CCW (1990) Improved material constants for LiNbO3 and LiTaO3. In: Proceedings of the Ultrasonics Symposium 1990, pp 435–438
17. Weis RS, Gaylord TK (1985) Lithium niobate: summary of physical properties and crystal structure. Appl Phys A 203:191–203
18. Auld BA (1990) Acoustic fields and waves in solids, vol 1. RE Krieger, Malabar, FL
19. Piazza G, Stephanou PJ, Pisano AP (2006) Piezoelectric aluminum nitride vibrating contour-mode MEMS resonators. J Microelectromech Syst 15:1406–1418
20. Rais-Zadeh M, Gokhale VJ, Ansari A, Faucher M, Théron D, Cordier Y, Buchaillot L (2014) Gallium nitride as an electromechanical material. J Microelectromech Syst 23(6):1252–1271
21. Lu R, Gong S (2015) Study of thermal nonlinearity in lithium niobate-based MEMS resonators. In: 2015 18th international solid-state sensors, actuators and microsystems conference (TRANSDUCERS), pp 1993–1996
22. Chandorkar SA, Agarwal M, Melamud R, Candler RN, Goodson KE, Kenny TW (2008) Limits of quality factor in bulk-mode micromechanical resonators. In: 2008 IEEE 21st international conference on micro electro mechanical systems, 2008
23. Gong S, Kuo NK, Piazza G (2011) A 1.75 GHz piezoelectrically-transduced SiC lateral overmoded bulk acoustic-wave resonator. In: 2011 16th international solid-state sensors, actuators and microsystems conference, TRANSDUCERS'11, 2011, pp 922–925
24. Gong S, Kuo NK, Piazza G (2011) GHz AlN lateral overmoded bulk acoustic wave resonators with a f·Q of 1.17×10^{13}. In: Proceedings of the IEEE international frequency control symposium and exposition, 2011

25. Lakin KM, Kline GR, McCarron KT (1993) High-Q microwave acoustic resonators and filters. IEEE Trans Microw Theor Tech 41:2139–2146
26. Pijolat M, Reinhardt A, Defay E, Deguet C, Mercier D, Aid M, Moulet JS, Ghyselen B, Gachon D, Ballandras S (2008) Large Qxf product for HBAR using smart cut transfer of LiNbO3 thin layers onto LiNbO3 substrate. In: 2008 IEEE ultrasonics symposium, 2008
27. H. Search, C. Journals, A. Contact, M. Iopscience, S. Mater, and I. P. Address. Investigation of quasi-shear-horizontal acoustic waves in thin plates of lithium niobate, vol 739.
28. Jin Y, Joshi SG (1996) Propagation of a quasi-shear horizontal acoustic wave in Z-X lithium niobate plates [and conductivity sensor application]. IEEE Trans Ultrason Ferroelectr Freq Control 43(3):491–494
29. Kuznetsova IE, Zaitsev BD, Joshi SG, Borodina IA (2001) Investigation of acoustic waves in thin plates of lithium niobate and lithium tantalate. IEEE Trans Ultrason Ferroelectr Freq Control 48(1):322–328
30. Kuznetsova IE, Zaitsev BD, Borodina IA, Teplyh AA, Shurygin VV, Joshi SG (2004) Investigation of acoustic waves of higher order propagating in plates of lithium niobate. Ultrasonics 42(1–9):179–182
31. Hashimoto K (2009) RF bulk acoustic wave filters for communications. Artech House, Norwood, MA
32. Adler EL (1989) Electromechanical coupling to lamb and shear-horizontal modes in piezoelectric plates. IEEE Trans Ultrason Ferroelectr Freq Control 36(2):223–230
33. Gong S, Piazza G (2014) An 880 MHz ladder filter formed by arrays of laterally vibrating thin film lithium niobate resonators. In: 2014 IEEE 27th international conference on micro electro mechanical systems, Jan 2014, pp 1241–1244
34. Campbell C (2012) Surface acoustic wave devices and their signal processing. Elsevier, Amsterdam
35. Knuuttila JV, Tikka PT, Salomaa MM (2000) Scanning Michelson interferometer for imaging surface acoustic wave fields. Opt Lett 25(9):613–615
36. Hu H, Ricken R, Sohler W, Wehrspohn RB (2007) Lithium niobate ridge waveguides fabricated by wet etching. IEEE Photon Technol Lett 19:417–419
37. Sones CL, Mailis S, Brocklesby WS, Eason RW, Owen JR (2002) Differential etch rates in z-cut LiNbO3 for variable HF/HNO3 concentrations. J Mater Chem 12:295–298
38. Cheng R-S, Wang T-J, Wang W-S (1997) Wet-etched ridge waveguides in Y-cut lithium niobate. J Light Technol 15(10):1880–1887
39. Minakata M (1979) Efficient $LiNbO_3$ balanced bridge modulator/switch with an ion-etched slot. Appl Phys Lett 35:40
40. Christensen FK, Mullenborn M (1995) Sub-band-gap laser micromachining of lithium niobate. Appl Phys Lett 66(21):2772–2773
41. Malshe A, Deshpande D, Stach E, Rajurkar K, Alexander D (2004) Investigation of femtosecond laser-assisted micromachining of lithium niobate. CIRP Ann Manuf Technol 53:187–190
42. Deng J, Si G, Danner AJ (2010) Dry etching of LiNbO 3 using inductively coupled plasma. In: IEEE photonics global conference, 2010, pp 1–5
43. Hui H, Ricken R, Sohler W (2008) Etching of lithium niobate: from ridge waveguides to photonic crystal structures. In: 14th European conference on integrated optics and technical exhibition, contributed and invited papers, ECIO'08 Eindhoven, 11 Jun 2008 to 13 Jun 2008, pp 75–78
44. Lacour F, Courjal F, Bernal M-P, Sabac A, Bainier C, Spajer M (2005) Nanostructuring lithium niobate substrates by focused ion beam milling. Opt Mater 27:1421–1425
45. Jianjie W, Jinyang L, Yanqing Y, Zhimei Q (2013) Reactive ion etching of Ti-diffused LiNbO3 slab waveguides. J Semicond 34(8):096001
46. Benchabane S, Robert L, Rauch JY, Khelif A, Laude V (2009) Highly selective electroplated nickel mask for lithium niobate dry etching. J Appl Phys 105:094109
47. Queste S, Courjon E, Ulliac G, Salut R, Petrini V, Rauch J, Besançon Cedex F (2008) Deep reactive ion etching of quartz, lithium niobate and lead titanate. In: JNTE proceedings

48. Wang R, Bhave SA, Bhattacharjee K (2015) Design and fabrication of S0 lamb-wave thin-film lithium niobate micromechanical resonators. J Microelectromech Syst 24(2):300–308
49. Pal S, Das B (2010) Fabrication of ridge waveguide in X-cut LiNbO3 for nonlinear optic applications. In: International conference on fiber optics and photonics, 2010, p 81730W
50. Deng J, Si G, Danner AJ (2010) Dry etching of LiNbO3 using inductively coupled plasma. In: Photonics global conference (PGC), 2010, pp 1–5
51. Gong S, Piazza G (2013) Figure-of-merit enhancement for laterally vibrating lithium niobate MEMS resonators. IEEE Trans Electron Dev 60(11):3888–3894
52. Olsson RH, Hattar K, Homeijer SJ, Wiwi M, Eichenfield M, Branch DW, Baker MS, Nguyen J, Clark B, Bauer T, Friedmann TA (2014) A high electromechanical coupling coefficient SH0 Lamb wave lithium niobate micromechanical resonator and a method for fabrication. Sensor Actuat A Phys 209:183–190
53. Randles AB, Esashi M, Tanaka S (2010) Etch rate dependence on crystal orientation of lithium niobate. IEEE Trans Ultrason Ferroelectr Freq Control 57:2372–2380
54. Gong S, Piazza G (2012) Weighted electrode configuration for electromechanical coupling enhancement in a new class of micromachined lithium niobate laterally vibrating resonators. In: 2012 international electron devices meeting, Dec 2012, pp 15.6.1–15.6.4
55. Wang R, Bhave RA, Bhattacharjee K (2014) Etch-a-sketch resonator. 2014 solid state sensor, actuator microsystems work (hilt Head 2014), no. 101–102
56. Gong S, Shi L, Piazza G (2012) High electromechanical coupling MEMS resonators at 530 MHz using ion sliced X-cut LiNbO3 thin film. Microw Symp Dig (MTT) 1:2–4
57. Shi L, Piazza G (2014) Lithium niobate on silicon dioxide suspended membranes: a technology platform for engineering the temperature coefficient of frequency of high electromechanical coupling resonators. J Microelectromech Syst 1
58. Schrempel F, Gischkat T, Hartung H, Höche T, Kley E-B, Tünnermann A, Wesch W (2009) Ultrathin membranes in X-cut lithium niobate. Opt Lett 34(9):1426–1428
59. Olsson RH, Hatta K, Baker MS, Wiwi M, Nguyen J, Padilla C, Homeijer SJ, Wendt JR, Friedmann TA (2014) Lamb wave micromechanical resonators formed in thin plates of lithium niobate. In: Hilton head solid-state sensors, actuators and microsystems workshop, 2014, pp 281–284
60. Gachon D, Lengaigne G, Benchabane S, Majjad H, Ballandras S, Laude V (2006) High frequency bulk acoustic wave resonator using thinned monocrystalline lithium niobate. In: Proceedings of the 20th European frequency and time forum, pp 14–17
61. Pijolat M, Loubriat S, Queste S, Mercier D, Reinhardt A, Defaÿ E, Deguet C, Clavelier L, Moriceau H, Aïd M, Ballandras S (2009) Large electromechanical coupling factor film bulk acoustic resonator with X-cut LiNbO3 layer transfer. Appl Phys Lett 95:182106
62. Kadota M, Ogami T, Yamamoto K, Negoro Y, Tochishita H (2009) 4.5 GHz lamb wave device composed of LiNbO3 thin film. In: IEEE MTT-S international microwave symposium digest, 2009, pp 333–336
63. Rinaldi M, Zuniga C, Zuo C, Piazza G (2010) Super-high-frequency two-port AlN contour-mode resonators for RF applications. IEEE Trans Ultrason Ferroelectr Freq Control 57:38–45
64. Gong S, Piazza G (2014) Overmoded shear horizontal wave MEMS resonators using X-cut lithium niobate thin film. In: 2014 IEEE international ultrasonics symposium (IUS), 2014, pp 568–571
65. Song YH, Gong S (2016) Arraying SH0 lithium niobate laterally vibrating resonators for mitigation of higher order spurious modes. In: IEEE 29th international conference on micro electro mechanical systems (MEMS), Jan 2016, vol 7, pp 111–114
66. Song YH, Gong S (2016) Analysis and removal of spurious response in SH0 lithium niobate MEMS resonators. IEEE Trans Electron Dev 63(5):2066–2073
67. Gachon D, Lengaigne G, Gauthier-Manuel L, Laude V, Ballandras S (2007) Development of high frequency bulk acoustic wave resonator using thinned single-crystal lithium niobate. In: Proceedings of the IEEE international frequency control symposium and exposition, 2007, pp 810–812

68. Aigner R, Kaitila J, Ella J, Elbrecht L, Nessler W, Handtmann M, Herzog T-R, Marksteiner S (2003) Bulk-acoustic-wave filters: performance optimization and volume manufacturing. Int Microw Symp Dig 3:2003
69. Ruby R (2007) Review and comparison of bulk acoustic wave FBAR, SMR technology. In: Proceedings – IEEE ultrasonics symposium, 2007, pp 1029–1040
70. Piazza G, Stephanou PJ, Pisano AP (2006) AlN contour-mode vibrating RF MEMS for next generation wireless communications. In: 2006 European solid-state device conference, 2006
71. Lakin KM (2005) Thin film resonator technology. IEEE Trans Ultrason Ferroelectr Freq Control 52:707–716
72. Branch D, Wojciechowski K, Olsson RH (2014) Elucidating the origin of spurious modes in aluminum nitride microresonators using a 2-D finite-element model. IEEE Trans Ultrason Ferroelectr Freq Control 61(5):729–738
73. Giovannini M, Yazici S, Kuo NK, Piazza G (2014) Apodization technique for spurious mode suppression in AlN contour-mode resonators. Sensor Actuat A Phys 206:42–50
74. Olsson RH, Nguyen J, Pluym T, Hietala VM (2014) A method for attenuating the spurious responses of aluminum nitride micromechanical filters. J Microelectromech Syst 23(5):1198–1207
75. Gao A, Gong S (2016) Harnessing mode conversion for spurious mode suppression in AlN laterally vibrating resonators. J Microelectromech Syst 25(3):450–458
76. Song YH, Gong S (2016) Arraying SH0 lithium niobate laterally vibrating resonators for mitigation of higher order spurious modes. In: IEEE 28th international conference on micro electro mechanical systems (MEMS), 2016, pp 111–114
77. Song YH, Gong S (2015) Spurious mode suppression in SH0 lithium niobate laterally vibrating MEMS resonators. In: 2015 IEEE international electron device meeting (IEDM), 2015, pp 18.5.1–18.5.4
78. Song YH, Gong S (2015) Elimination of spurious modes in SH0 lithium niobate laterally vibrating resonators. IEEE Electron Dev Lett 36(11):1198–1201
79. Gong S, Piazza G (2013) Multi-frequency wideband RF filters using high electromechanical coupling laterally vibrating lithium niobate MEMS resonators. In: 2013 IEEE 26th international conference on micro electro mechanical systems, MEMS, pp 785–788
80. Lin C-M, Yen T-T, Lai Y-J, Felmetsger VV, Hopcroft MA, Kuypers JH, Pisano AP (2010) Temperature-compensated aluminum nitride lamb wave resonators. IEEE Trans Ultrason Ferroelectr Freq Control 57:524–532
81. Gong S, Piazza G (2013) Large frequency tuning of lithium niobate laterally vibrating MEMS resonators via electric boundary reconfiguration. In: 2013 transducers and eurosensors XXVII: the 17th international conference on solid-state sensors, actuators and microsystems, transducers and eurosensors 2013, pp 2465–2468
82. Kadota M, Ogami T (2011) 5.4 GHz Lamb wave resonator on LiNbO3 thin crystal plate and its application. Jpn J Appl Phys 50
83. Reinhardt A, Defay E, Perruchot F, Billard C (2012) Tunable composite piezoelectric resonators: a possible holy grail of RF-filters. Int Microw Symp Dig 2012:1–3

Part II
Design of Piezoelectric MEMS Resonators

Chapter 5
Quality Factor and Coupling in Piezoelectric MEMS Resonators

Reza Abdolvand, Hedy Fatemi, and Sina Moradian

5.1 Introduction

A piezoelectric-based resonator is an electromechanical device in which electrical and mechanical energies are reciprocally converted to each other at a resonance frequency through the two-way coupling between stress and electric field in a piezoelectric material. Moreover, the mechanical energy in the resonator body and the applied electrical energy through the metallic electrodes convert from potential to kinetic and back in every vibration half cycle (Fig. 5.1). Therefore, the overall performance of a resonant system is determined by both of the energy conversion mechanisms mentioned above. To quantify the efficiency of these energy conversions in a resonator, there are two specific parameters defined as *electromechanical coupling factor* and *quality factor (Q)*.

In this chapter we will define Q and coupling factor for resonators and explain how they affect the performance of the systems in which the resonators are implemented. Also, we briefly study the mechanisms that could influence each of the two parameters and reference some of the research carried out aiming at improving these parameters.

5.2 Quality Factor

Quality factor (Q) is a measure of energy loss in a resonator. As the energies convert from one form to the other, a portion of the energy contained in the system will either

R. Abdolvand (✉) • H. Fatemi • S. Moradian
College of Engineering & Computer Science, University of Central Florida, 4000 Central Florida Blvd, Orlando, FL 32816, USA
e-mail: reza@eecs.ucf.edu

© Springer International Publishing Switzerland 2017

H. Bhugra, G. Piazza (eds.), *Piezoelectric MEMS Resonators*,
Microsystems and Nanosystems, DOI 10.1007/978-3-319-28688-4_5

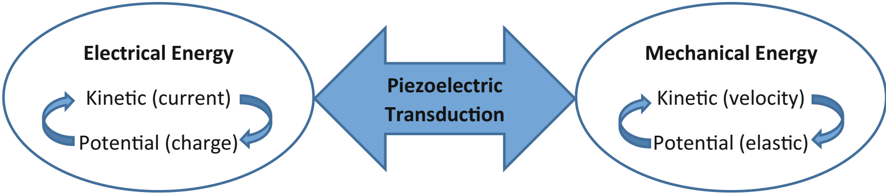

Fig. 5.1 A block diagram representing the energy flow in a piezoelectric resonator

directly escape or it's repetitive turn into a form that could no longer be restored (e.g., heat). The Q is generally defined as [1]:

$$Q = 2\pi \frac{\text{peak energy stored}}{\text{energy dissipated per cycle}}$$

There are several distinct dissipation mechanisms in a resonator. Thus, the overall quality factor of a system can be found by summing up the dissipated energies [1]:

$$Q_{\text{total}} = 2\pi \frac{E_{\text{stored}}}{\Sigma_{\text{i}}\, E_{\text{dissipated}_i}/\text{cycle}} = \left(\Sigma_i \frac{1}{Q_i}\right)^{-1}$$

An equivalent description of Q in a damped mass-spring system governed by a second-order differential equation of $M\ddot{x} + C\dot{x} + Kx = 0$ is:

$$Q = \frac{1}{2\zeta},$$

where ζ is the damping ratio equal to C/C_{c} and C_{c} is the value of critical damping equal to $C_{\text{c}} = 2\sqrt{KM}$ [2].

Since resonators are commonly characterized by their frequency response, it is practically convenient to develop alternative formulas for Q based on the features of the frequency response plot. One such equation is:

$$Q = \frac{f_0}{\text{BW}_{3\text{dB}}},$$

where f_0 is the resonance frequency and BW stands for the frequency bandwidth.

The Q of a resonator can also be extracted from the slope of the phase response ($\angle H$) at resonance:

$$Q = \frac{\omega_0}{2} \frac{\partial \angle H}{\partial f}\bigg|_{\omega_0}.$$

Both of the equations above indicate that as the Q increases in a resonator the frequency response becomes sharper or in other words the energy is more confined to the resonance frequency as expected.

To understand how the resonator Q will affect the performance of a system that contains the resonator, it should be recalled that any loss mechanism is a coupling between the energy of the resonator and other forms of undesirable energy that randomly fluctuate. Therefore, the same mechanism can create a path for such energy fluctuations to perturb the energy of the system [3]. Such random influx of energies are sources of noise/interference. This concept is known as the fluctuation-dissipation theorem in thermodynamic [4]. A simple example for this physical concept is the energy that is transferred from the resonator to the surrounding air molecules (i.e., air damping). Reversely, the random movement of air molecules (Brownian motion) could couple back into the resonator generating noise [5]. With that, we can conclude that lower resonator Q will ubiquitously result in higher system noise/interference.

5.2.1 Sources of Loss

In a piezoelectric resonator, three distinctive sources of loss could be identified within the three main components of the resonator (refer to Fig. 5.1) [6, 7], namely:

1. Electrical losses including resistive losses associated with the finite resistance of the conductive material used as electrodes and dielectric losses associated with the generation of heat in the static capacitances of the device
2. Electromechanical (i.e., piezoelectric) losses associated with non-ideal mutual conversion of electrical and mechanical energies
3. Mechanical/elastic losses including any mechanism for the conversion of mechanical energy to heat or leakage of mechanical energy from the system

Among the three categories of loss mentioned above, the electrical losses are the most straightforward to understand and characterize. On the other hand, piezoelectric loss is the last to have been recognized as an independent source of loss [8] and although attributed to the moving domain walls and defects [9], the origin of the loss is not fully understood. Piezoelectric loss appears to be a considerable source of loss in ferroelectrics such as lead zirconate titanate (PZT) [10] and is negligible in other types of piezoelectric material. Lastly, the mechanical losses are the most complicated to study as there are a variety of physical mechanisms that contribute to mechanical energy dissipation.

In the following two sections, most common loss mechanisms in a resonator are reviewed by grouping them into intrinsic (i.e., the dissipative process is fundamentally linked to the material properties) and extrinsic (i.e., the dissipative process is dependent on the design and implementation of the resonator) as shown in the table below:

Intrinsic loss	Extrinsic loss
Dielectric loss (“dielectric loss”)	Anchor loss (“support loss”)
Piezoelectric loss (“piezoelectric loss”)	Air/fluidic loss (“air/fluid damping”)
Phonon-phonon interaction loss (“loss due to phonon-phonon interaction”)	Surface loss (“surface loss”)
Phonon-electron interaction loss (“loss due to phonon-electron Interaction”)	Ohmic loss (“ohmic loss”)

Intrinsic Losses

In a piezoelectric resonator, there are several fundamental dissipative processes at work, which cannot be avoided even if the most ideal design of a resonator could be accurately implemented. Once the dimensions and the material contained in the resonator are chosen, one could estimate an upper limit for the quality factor of the resonator based on such dissipative processes, and that is the rationale for using the term “intrinsic loss” to classify them. In the following, most common intrinsic losses are described.

Dielectric Loss

The operation of piezoelectric resonators is fundamentally based on the coupling between the electric field and the stress field inside a piezoelectric material. The electric field established within the piezoelectric material (which is also a dielectric) will polarize it, and the energy will be partially conserved in the form of opposite charges on the metallic electrodes (electrical potential energy). The polarization process involves movement of centers of charge within the material during which some of the applied energy will be directly transformed to heat through a process classically described as dielectric relaxation [11]. Losses associated with dielectric loss are represented by a complex permittivity value [12]:

$$\epsilon = \epsilon' - j\epsilon''$$

Based on this representation, a material constant known as loss tangent is cited for dielectrics which is defined as:

$$tg\delta = \frac{\epsilon''}{\epsilon'},$$

where δ is known as the loss factor. Based on this definition, material with lower loss tangent exhibit lower dielectric loss and therefore are more desirable for achieving higher Q resonators. It is of practical importance to note that loss tangent is usually

a function of electric field frequency. The dielectric loss is a relatively small source of loss in dielectric piezoelectric resonator such as AlN-based resonators [13], but that is not the case for ferroelectrics [14].

Piezoelectric Loss

The energy loss in piezoelectric material for which the electric field to strain field coupling is strong (e.g., PZT) has been reported to be inadequately captured by dielectric losses (through a complex permittivity) and acoustic losses (through a complex stiffness). Therefore, researchers in the field have suggested extending the concept of complex representation of the material properties to the piezoelectric coefficient [8] in order to better model the operation of devices that utilize such material [15]. It is postulated that the piezoelectric loss is a result of damped motion of domain walls in ferroelectrics such as PZT [9, 16]. However, there is no consensus among researchers whether the piezoelectric loss is an independent loss that exists without any connection to dielectric and elastic losses [17, 18].

Loss Due to Phonon-Phonon Interaction

In quantum mechanics, a quanta of vibrational energy is referred to as a phonon. The arrangement of atoms and the overall shape of a solid body define what specific (and quantized) vibration modes/energy levels are allowed in that system. At finite temperatures above 0 K, atoms vibrate around their equilibrium position (i.e., lowest potential energy position). These random lattice vibrations are viewed as phonons that occupy the allowed levels of vibrational energy. Since these phonons are generated by heat, they are sometimes labeled as thermal phonons. The overall distribution of the phonons at different energy levels (i.e., vibration modes) is known to be governed by the Planck distribution at equilibrium [19]. With the excitation of acoustic vibration modes in the solid body, the distance between atoms periodically changes around the equilibrium value. The acoustic waves causing coherent movement of the atoms in a lattice can also be viewed as phonons generated in the solid (elastic phonons). Therefore, the equilibrium phonon distribution is disturbed as a result of such acoustic waves. In any inelastic system, the resulted non-equilibrium status will resettle to a new equilibrium through a relaxation process. It is during this relaxation process that the elastic phonons interact with inelastic phonons (i.e., thermal phonons). This interaction could be divided into two regimes based on the relative value of the phonon scattering time and the period of vibration as will be discussed below.

Scattering Regime

As mentioned above, in a resonator at resonance, the spatial distance of atoms periodically varies above and below its equilibrium. In parts of the solid where the

volume decreases (i.e., compressive strain), the average phonon frequency/energy increases locally, and the opposite happens at areas where the volume increases. The resulting non-equilibrium/perturbed thermal phonon distribution function will resettle into a new equilibrium given there is enough time in each period of the vibration (i.e., mean phonon scattering time (τ_s) is shorter than one period of vibration (τ_v); $\tau_s < \tau_v$) [20]. In the process of restoring the thermal equilibrium, phonons interact with each other (i.e., scattering) resulting in the irreversible loss of elastic energy. This process was first described and formulated by Akheiser [21]. Given a set of simplifying assumptions, the quality factor associated with this loss can be calculated from the following formula:

$$Q_{\text{AKE}} = \frac{\rho c^4}{2\pi f \gamma_{\text{avg}}^2 kT},$$

where ρ is the material density, c is the acoustic velocity, f is the frequency of vibration, γ_{avg} is the average Grüneisen's parameter (a dimensionless thermal parameter that explains the dependency of the thermal properties on pressure and temperature), and k is the thermal conductivity. This loss mechanism exists in all resonant structures regardless of the resonator design and the mode of vibration. The distinctive feature of the Akheiser Q is the $1/f$ proportionality, which predicts that loss will increase at higher frequencies.

The Akheiser loss mechanism is limited to situations in which the assumption of $\tau_s < \tau_v$ is valid. If the vibration frequencies are scaled higher so that this assumption no longer holds, then a thermal equilibrium can't be achieved during a half cycle of the wave. The earliest notion of treating this new regime of high-frequency loss is found in the work published by Landau and Rumer [22]. Their approach is based on treating the acoustic waves as a beam of phonons and limiting the phonon interaction to a "three-phonon process" where an elastic phonon (associated with the elastic wave) collides with a thermal phonon and a third phonon is generated. The simplified result of their approach is a loss that is no longer a function of frequency, and therefore the limit of intrinsic Q at extremely high frequencies is expected to be relaxed considerably compared to what is predicted by Akheiser effect [23]. This loss regime is dominant at frequencies beyond 500 MHz for most relevant material, and its onset (i.e., $\tau_s = \tau_v$) is a function of the material properties and the crystalline orientation [24].

Diffusion Regime

A nonuniform instantaneous temperature field could result from a nonuniform strain field within a resonating body. Under the same original assumption of $\tau_s < \tau_v$, such local temperature gradients drive irreversible heat flow. In other words to reinstitute an overall thermal equilibrium, the phonons diffuse from higher temperature spots toward lower temperature spots (i.e., thermal transport). This specific loss mechanism is known classically as thermoelastic damping (TED) [23].

TED is a significant source of loss if the period of the acoustic wave is close to the thermal transport time constant (τ_{th}), with the maximum loss corresponding to the case of $\tau_{th} = \tau_v$ [25]. For $\tau_{th} \ll \tau_v$ (i.e., low vibration frequencies), the aforementioned temperature gradients will no longer develop (system is always in thermal equilibrium), and therefore the energy dissipation is absent. Reversely, for $\tau_{th} \gg \tau_v$, the temperature gradients vary much faster than the thermal transport process. As a result, heat flow is diminished and the TED becomes negligible. The bending mode of thin solid beams is one of the cases in which the maximum TED loss could be easily observed as the frequency of vibration for maximum loss could be relatively low. This case was first studied by Zener in his seminal work in 1937 [26] in which he offered an equation for calculation of Q_{TED}. Zener's equation has been evaluated by many researchers and is proved quite accurate despite the simplifications that were made [27]. In practice the distance between local extremums of temperature developed in a resonant body is not uniform, and therefore more than one thermal time constant would be required to capture the TED effect [28]. Finite element analysis offers a relatively accurate method for estimating the TED in situations that an analytical solution is out of reach [29].

Most commonly used piezoelectric resonators operate in shear mode or bulk-extensional modes. TED is not present in shear mode resonators as the change of volume driving the inhomogeneous temperature field is absent in such modes. Contribution of TED in bulk-mode resonator is also negligible in the range of frequency they are normally utilized.

Loss Due to Phonon-Electron Interaction

As described earlier, the mechanical oscillation of a resonating body results in periodic oscillation of atoms about their equilibrium position. This oscillation modulates the discrete quantum mechanical energy levels that are occupied by the electrons, driving the electron distributions out of their equilibrium state (distorting fermi surfaces). Similar to what was earlier described for non-equilibrium phonon distributions, the non-equilibrium electron distribution also relaxes back to a new equilibrium (through interaction of electrons with thermal phonons) given the electron relaxation time (τ_e) is significantly smaller than the period of vibration (τ_v). Predictably, the electron relaxation process and the magnitude of the loss associated with this process vary in metals and semiconductors. For metals in which the free career concentration is high, the equilibrium reestablishment of the disturbed electron distribution will result in a significant internal loss that is proportional to the frequency of vibration [30]. In semiconductors, however, this loss is understandably a strong function of doping concentration (increases for higher doping) [31] and in general is a less significant source of loss. Very similar to the case of phonon-phonon interaction loss, for the regime of $\tau_e > \tau_v$ (very high acoustic frequencies), the quality factor associated with this loss mechanism is no longer a function of frequency as the electron relaxation vanishes [32].

It should also be noted that there is an additional mechanism for loss in piezoelectric semiconductors associated with the coupling of strain field to electric field. In this case, the developed strain in the material will result in an internal electric field, and assuming that the carrier concentration is not negligible, this electric field will generate an internal current (acoustoelectric current) and subsequently gives rise to loss [33]. This loss has been extensively studied for CdS in the past [34] and more recently is reported for GaN-based resonator [35].

Extrinsic Losses

In addition to the sources of loss described in the last section, there are several other dissipation processes that are not fundamentally bound to the material properties, and rather they depend on practical aspects of design and implementation. As such, these loss mechanisms are labeled as "extrinsic loss" and described below.

Support Loss

Support loss (also known as anchor loss) quantitatively represents the amount of acoustic energy that radiates from the body of a resonator to the frame that holds the resonator in place (Fig. 5.2). Based on this description, it is perceivable that the support loss is strongly dependent on the position, shape, and the dimensions of the anchors. Analytical calculation of support loss has been attempted for a variety of designs [36, 37] and is useful in providing general guidelines for reducing support loss.

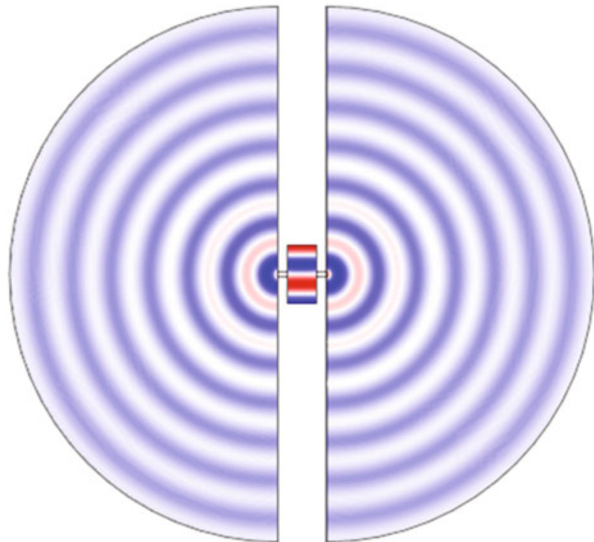

Fig. 5.2 2D model of a third harmonic lateral-extensional resonator including the supporting substrate. The strain is color coded on the resonator and the substrate, but the color intensity is not a true representation of the strain intensity (it is manipulated on the substrate region to enhance visibility of waves penetrating the substrate)

A general rule for mitigation of support loss is to place the anchors at nodal points of the resonator mode shape, where the displacement of the resonator boundary is virtually zero. Numerous examples of this design methodology can be found in literature such as in center-supported bulk-mode disk resonator [38], free-free flexural beam resonators supported at the nodal points [39], or notched attachments in a ring resonator [40]. The success of this technique is restricted by misalignment, the practical limitations on the dimensions of the anchors, and also the invalidity of assuming a perfect nodal point in a 3D resonant structure. Considering such non-idealities, it is not surprising for the support loss to be one of the most significant factors limiting the quality factor of resonators especially at high frequencies. Operation at high frequencies necessitates scaling down of the frequency defining feature. To keep the support loss at the same level, the support will need to shrink at the same rate. This is because as the frequency defining feature of a resonator shrinks at high frequencies the anchor dimension should also shrink at the same rate for the anchor loss to not grow relatively. However, scaling down the anchor dimension is restricted by the smallest features that could be fabricated and also by the mechanical integrity of the structure. Therefore, alternative techniques have been suggested to circumvent excessive support loss at high frequencies.

A prevailing approach undertaken by many researchers is centered on the hypothesis that given a portion of the acoustic waves will radiate from the anchors, one could focus on reflecting some of that energy back to the resonator. This idea is commonly used in solidly mounted thin-film piezoelectric bulk acoustic resonators in which the acoustic cavity (i.e., the piezoelectric film sandwiched between metal electrodes) is placed on top of a Bragg reflector [41, 42]. The Bragg reflector is an alternating stack of high- and low-acoustic impedance films, each usually quarter wavelength thick. In a Bragg reflector, a large portion of the wave penetrating into the substrate will be reflected back at every interface between the two films that exhibit a large acoustic mismatch.

For the bulk waves that travel in the plane of the substrate (as is the case for most bulk-mode MEMS resonators), a reflector could be implemented by simply etching vertical trenches into the substrate. This idea has been implemented in disk resonator [43] as well as lateral-mode piezoelectric-on-silicon resonators [44]. Other researchers have proposed the use of 2D phononic crystals for implementation of acoustic reflectors in the plane of a substrate [44, 45]. Phononic crystals are structures designed to create acoustic bandgaps in which propagation of certain acoustic wave modes or frequencies is prohibited. Phononic crystals have also been used to design anchors that efficiently reflect the acoustic waves generated at the resonance frequency of the resonator [46, 47].

Air/Fluid Damping

A resonator vibrating in gaseous/fluid medium will lose some energy to the medium as a result of movement relative to the surrounding molecules. This interaction with the surrounding exerts damping forces on the vibrating structure that become a

dominant source of loss as the ratio of the surface area to the volume of resonator increases in microscale resonators [48]. If the resonator's surface movement is in parallel with respect to the fluid, a shear force is applied to the structure, whereas for perpendicular vibrations, squeezed film damping occurs [49].

To eliminate air damping, MEMS resonators are often operated and packaged in partial vacuum [50, 51]. Air damping is dependent on the frequency of vibration and is less effective at higher frequencies [52]. Therefore, the complexity and the cost of vacuum packaging (and the electronic frequency multiplication) could be alleviated by directly increasing the fundamental frequency of the resonator when possible.

Surface Loss

Properties of material on the surface are always different relative to what is measured and cited for the bulk. Such differences could be intuitively understood by considering the asymmetric nature of the physical variables on the surface as a result of the discontinuity of the medium at the boundary. With that, one could imagine that the effect of surface-related phenomenon on the overall properties of material (including intrinsic loss mechanisms) is dependent on the surface to volume ratio of the resonator body. As this ratio becomes larger, the resonator quality factor will be more dominated by the surface-related dissipation processes [53]. The physics of loss on the surface of resonators is rather complicated as it strongly depends on a variety of non-idealities such as roughness, contamination, native oxide films, and adsorbents to name a few. However, there has been an effort to analyze all of the surface-related dissipation mechanism using a unified model [54]. In this treatment it is postulated that the loss on the surface could be described by a model that was originally developed to explain the nature of loss in amorphous material. The rationale for this assumption is that all the non-idealities associated with the surface of the material will result in formation of an amorphous-like layer on the surface.

Regardless of the true nature of the loss, it has been shown that vacuum annealing can substantially improve the quality factor of the resonators that are influenced by surface-related loss [55, 56]. Also, a general guideline to alleviate the surface-related loss is to avoid resonators with high surface to volume ratios.

Ohmic Loss

The relatively thin films of metals used as electrodes in piezoelectric resonators introduce a considerable resistive load that directly turn electrical energy to heat. This loss mechanism can obviously be managed by thickening the metal layers and by utilizing low-resistivity metals when possible.

5.2.2 Discussion on Loss

As discussed, intrinsic loss processes in solids predict an upper limit for a resonator quality factor, which is set by the basic properties of the material used in the resonant body (hence it is design independent). The intrinsic mechanical losses are well captured by a constant known as acoustic attenuation coefficient (α) that could be found in literature for most relevant material. Attenuation coefficient is defined as the ratio of mean energy dissipation to twice the mean energy flux for the acoustic wave traveling in the material [27]. It could be shown that α sets the rate of the exponentially decaying amplitude of the traveling acoustic wave:

$$A(x) = A_0 \mathrm{e}^{-\alpha x}$$

As expected from the discussions in Sect. 5.2.1, the acoustic attenuation coefficient is a function of frequency and has been studied/measured for a variety of material by researchers [57–60]. Such measurements can guide designers in choosing the material with lower intrinsic loss when the goal is to achieve high Q piezoelectric resonators. Generally speaking, dielectric piezoelectric material such as quartz, AlN, lithium niobate (LN), and ZnO tends to exhibit lower acoustic attenuation compared to ferroelectrics such as PZT. Due to relative ease of integrating AlN into well-established micro-fabrication facilities, sputtered AlN is the most commonly used piezoelectric material for micro-fabricated resonators today [61, 62]. It should be noted that sputtered films are polycrystalline and intrinsic loss in polycrystalline material could be considerably different than the measured bulk values. Depending on the ratio of the acoustic wavelength to the average grain size, the intrinsic loss could be affected differently by the granularity of the media [63, 64].

In a piezoelectric resonator, there are usually more than one layer of material incorporated in the resonant body (i.e., other than the piezoelectric material), and as a result the intrinsic loss for each of those material will affect the overall Q of the resonator. For example, a bulk acoustic wave (BAW) piezoelectric resonator consists of a thin piezoelectric layer sandwiched between two metallic films which is either suspended over a cavity or formed on top of a multilayer Bragg reflector [41]. In both cases the acoustic wave travels in materials other than the piezoelectric layer; hence, the intrinsic loss associated with metallic electrodes or the layers of the reflector will play an important role and should be considered. It is needless to say that the selection criteria for the metal used in a piezoelectric resonator is not solely based on lowering the acoustic attenuation as other factors such as electrical resistivity, acoustic impedance, and process compatibility are also of critical importance. Today, the more common choices of metal for micro-fabricated acoustic resonators are aluminum, molybdenum, and tungsten which offer process compatibility as well as relatively low-acoustic attenuation compared to the more traditional metal films used in microelectronics such as copper and gold [65–68].

The significant impact of metal films on the quality factor of piezoelectric resonators was first experimentally demonstrated by Besson in quartz crystal

resonators [69]. In his groundbreaking design, Besson avoided direct contact of the metallic electrodes with the quartz substrate, and instead the electric field was applied through small capacitive gaps. Such “electrodeless” quartz resonators (also known as BVA quartz crystal resonators) were shown to demonstrate record-breaking quality factors and are now the unparalleled choice of resonator for applications where extremely stable oscillators are required [70]. The same concept of spacing the metal electrode from the piezoelectric resonant body has been successfully implemented in thin-film AlN resonators in recent years [71, 72].

An alternative path taken by researchers to improve the quality factor of the micro-fabricated thin-film piezoelectric resonators is to incorporate a substrate with low-acoustic loss in the structural body of the resonator. This class of resonators (sometimes referred to as thin-film piezoelectric-on-substrate or TPoS) has been implemented on single crystal silicon [73, 74], nano-crystalline diamond [75, 76], and polycrystalline silicon carbide [77] and has presented some of the highest quality factors ever reported from thin-film piezoelectric bulk acoustic resonators [78–80].

5.3 Coupling Factor

The electromechanical coupling factor in a resonator is the second parameter (after the quality factor) that describes the efficiency of energy conversion processes in a resonator. There are a variety of approaches in defining the coupling factor for a piezoelectric material, most of which result in similar analytical expressions despite the seemingly different description [81]. It is critical to recognize that the electromechanical coupling factor of a piezoelectric resonator is different than the coupling factor of the piezoelectric material used in the resonator; the latter is solely dependent on material properties (as expected) and is not a function of the resonator design/implementation. With this introduction the piezoelectric coupling factor is described first in the next section before moving on to the electromechanical coupling factor of a resonator.

5.3.1 Piezoelectric Coupling Factor

The piezoelectric coupling factor (K^2) is a unitless quantity that could be used to compare the efficiency of different piezoelectric material in mutually converting electrical energy to mechanical energy. One way to define the piezoelectric coupling factor is as follows (in a loss-free scenario):

$$K^2 = \frac{W_{\mathrm{M}}}{W_{\mathrm{M}} + W_{\mathrm{E}}}$$

where W_M is the work that is delivered to a mechanical load by a piezoelectric actuator that is preloaded with potential energy ($W_\mathrm{M} + W_\mathrm{E}$) by connecting it to an electrical source, while it is mechanically free to move [82]. It could be shown that this ratio is a function of material properties as follows (given the stress is only non-zero in one direction or in other words in a 1D scenario):

$$K^2 = \frac{e^2}{c^E \epsilon^T},$$

where e is the piezoelectric constant (with the unit of $\frac{C}{m^2}$) in the direction of the electric field and mechanical stress, c^E is the stiffness (i.e., elastic constant with the unit of $\frac{N}{m^2}$) at zero electric field, and e^T (with the unit of $\frac{F}{m} = \frac{C}{V \times m}$) is the dielectric constant in the direction of electric field at zero stress. The strong dependency (i.e., second-order proportionality) of the coupling factor on the piezoelectric coefficient is fully expected as it is the same piezoelectric coefficient that relates stress from mechanical domain to electric field in the electrical domain. The inverse proportionality to the stiffness could be understood by the smaller mechanical displacement for a unit applied electric field as the stiffness of the piezoelectric material increases (less displacement results in less mechanical work delivered to the load or in other words smaller W_M). Finally, the inverse proportionality to the dielectric constant could be intuitively described by the larger portion of the total potential energy that is conserved in the electrical domain (i.e., not converted to mechanical energy) as the dielectric constant grows for a piezoelectric material.

The piezoelectric coupling factor is the upper bound of energy conversion efficiency in a resonator that uses a certain type of piezoelectric material (the effective energy conversion efficiency in the resonator is always smaller than this value). The nominal maximum piezoelectric coupling factor is listed in the table below for a few piezoelectric materials commonly used in fabrication of resonators [41, 83].

Material	Quartz	AlN	ZnO	PZT	LN (36° rotated)
K^2 (%)	0.86	6.5	8.5	23	23

5.3.2 Effective Electromechanical Coupling Factor

Once a piezoelectric material is used in a resonant device, the energy conversion efficiency at resonance is of great interest to the designers. To quantify this conversion efficiency, an effective electromechanical coupling factor is customary to be defined as [82]:

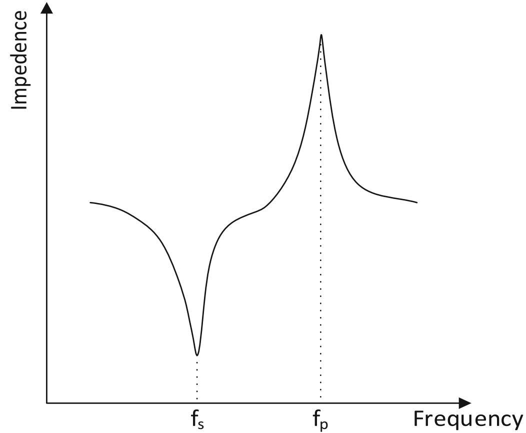

Fig. 5.3 Schematic diagram represents a typical measured impedance (magnitude) for a one-port piezoelectric resonator

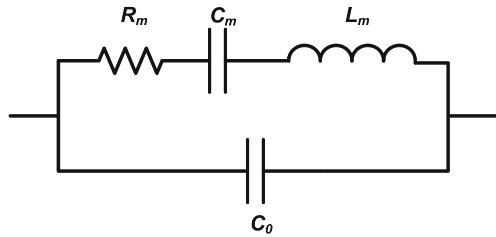

Fig. 5.4 Basic BVD model of a piezoelectric resonator

$$k_{\text{eff}}^2 = \frac{f_\text{p}^2 - f_\text{s}^2}{f_\text{p}^2},$$

where f_s and f_p are the frequencies at which the magnitude of the impedance is minimum and maximum, respectively (Fig. 5.3). This coupling factor is largely affected by piezoelectric material properties (i.e., the piezoelectric coupling coefficient), but it is also affected by the design of the resonator.

An alternative definition for the resonator coupling factor is developed based on the equivalent electrical circuit representing the electrical characteristic of the resonator. The most common equivalent circuit of a resonator (one-port) known as the BVD model [84] consists of a series RLC circuit (the motional branch) in parallel with an static capacitance (C_0) (Fig. 5.4).

The electromechanical coupling factor of the resonator could then be defined as [85, 86]:

$$k_{\text{eff}}^2 = \frac{C_\text{m}}{C_0},$$

where C_m and C_0 are the motional capacitance and the static capacitance of the resonator, respectively. Both of the above definitions for the effective coupling factor originate from the fact that for an ideal 1D loss-less piezoelectric resonator in which the resonator solely consists of a piezoelectric body with thin electrodes the

piezoelectric coupling factor can be approximated by the same equations described in this section. Therefore, it is reasonable to use the same equations to derive the coupling factor for any piezoelectric-based resonators.

5.3.3 Discussion on Coupling Factor

The coupling factor in piezoelectric MEMS resonators is dependent on both the piezoelectric material used as the transducer and the design of the resonator.

In order to achieve the highest possible coupling factor while using a certain crystalline piezoelectric material, the orientation that offers the highest piezoelectric coefficient should be used if possible. However, incorporation of single crystalline material in standard silicon-MEMS processes is not trivial, and the piezoelectric film is usually deposited as a polycrystalline thin film using techniques such as RF magnetron sputtering. The application of thin-film ZnO sputtered on silicon substrate for fabrication of micromachined resonators dates back to early days of micromachining [87]. Despite their extensive presence in research, ZnO-based micro-resonators have not been manufactured in large scales mainly due to the fact that zinc is a high-diffusivity metal that could contaminate other materials and also because ZnO is chemically unstable. The commercial use of piezoelectric-based micromachined resonators became a reality only after the development of RF-sputtered piezoelectric AlN [88]. The maximum piezoelectric coefficient of AlN is slightly lower than that of ZnO, but AlN is a very chemically stable material with excellent acoustic properties such as large stiffness and low loss. Nowadays, AlN-based thin-film piezoelectric resonators are commonly used in wireless devices for filtering application in the form of bulk acoustic wave (BAW) filters [89]. BAW filters are designed based on the thickness extensional modes of a plane and therefore take advantage of e_{33} of the C-plane-oriented-sputtered AlN film which is the largest of the piezoelectric coefficients in AlN. The sputtered AlN films have also been used to design lateral-extensional (or contour) mode resonators in which the e_{31} coefficient is utilized [76, 90]. Predictably, such devices offer lower coupling factor compared to BAW resonators as e_{31} is smaller than e_{33} for AlN.

Beyond the choice of piezoelectric material, the proper design of the resonator could play an important role in optimizing the coupling factor. The design guideline for achieving the highest possible coupling factor for a specific resonator design is conceptually simple. Consider a third harmonic lateral-extensional resonator such as the one presented in Fig. 5.5a. The presented resonant structure is made of a thin film of AlN on top of a relatively thick layer of silicon [74]. Thin-film metallic electrodes should be patterned on the two surfaces (i.e., bottom ad top) of the AlN film with the objective of maximizing the charge-to-stress conversion (i.e., maximizing coupling factor). Assuming that a one-port design is targeted, all surface areas with the same stress polarity should be covered with metal in order to collect the maximum charge and consequently maximize the coupling factor (Fig. 5.5b). Covering areas with opposing stress polarity would reduce the coupling factor and should be avoided to the extent possible.

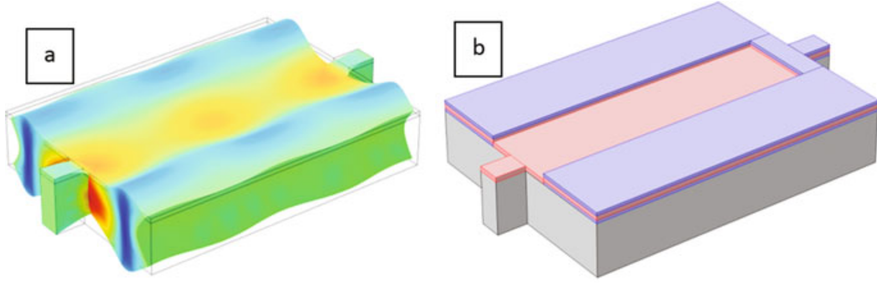

Fig. 5.5 The third-order harmonic lateral-extensional resonant mode of a thin-film AlN on silicon block (**a**) and a suggested electrode pattern for maximized coupling factor (**b**)

5.4 Conclusion (Figure of Merit)

Based on the material presented in this chapter, it is reasonable to expect the definition of the figure of merit (FoM) for a piezoelectric-based resonator be proportional to both Q and coupling factor. One standard definition for the resonator FoM is [82]:

$$\mathrm{FoM} = \frac{k_{\mathrm{eff}}^2 \cdot Q}{1 - k_{\mathrm{eff}}^2}$$

For small values of k_{eff}^2, this equation reduces to:

$$\mathrm{FoM} = k_{\mathrm{eff}}^2 \cdot Q$$

The usefulness of this FoM in quantifying the performance of a resonator could be intuitively understood by recalling that a large coupling factor signifies efficient mutual conversion of electrical to mechanical energy, while a large Q indicates a weak coupling between the energy of the system and undesired forms of fluctuating energy. Therefore larger coupling and Q directly contribute to a better signal-to-noise ratio (the ultimate figure of merit for any electrical system).

References

1. Brand O, Heinrich S, Hierold C, Korvink JG, Dufour I, Fedder GK, Tabata O, Josse F (2015) Resonant MEMS. Wiley, New York, NY
2. Bahreyni B (2008) Fabrication & design of resonant microdevices. William Andrew, New York, NY
3. Djurić Z (2000) Mechanisms of noise sources in microelectromechanical systems. Microelectron Reliabil 40(6):919–932
4. Callen HB, Welton TA (1951) Irreversibility and generalized noise. Phys Rev 83(1):34

5. Vig JR, Yoonkee K (1999) Noise in microelectromechanical system resonators. IEEE Trans Ultrason Ferroelectr Freq Control 46(6):1558–1565
6. Ballato A, Joseph K, John B, Ahmad S (1996) Dissipation in ceramic resonators and transducers. In: 50th, Proceedings of the 1996 IEEE international frequency control symposium, pp 371–378
7. Uchino K, Hirose S (2001) Loss mechanisms in piezoelectrics: how to measure different losses separately. IEEE Trans Ultrason Ferroelectr Freq Control 48(1):307–321
8. Holland R (1967) Representation of dielectric, elastic, and piezoelectric losses by complex coefficients. IEEE Trans Sonics Ultrason 14(1):18–20
9. Smits JG (1976) Influence of moving domain walls and jumping lattice defects on complex material coefficients of piezoelectrics. IEEE Trans Sonics Ultrason 23(3):168–173
10. Ballato A et al (1996) Dissipation in ceramic resonators and transducers. In: 50th, Proceedings of the 1996 IEEE international frequency control symposium, 1996
11. Jonscher AK (1999) Dielectric relaxation in solids. J Phys D Appl Phys 32(14):R57
12. Raju GG (2003) Dielectrics in electric fields, vol 19. CRC Press, London
13. Loebl HP, Metzmacher C, Milsom RF, Lok P, Van Straten F, Tuinhout A (2004) RF bulk acoustic wave resonators and filters. J Electroceram 12(1–2):109–118
14. Sherrit S, Wiederick HD, Mukherjee BK (1997) Accurate equivalent circuits for unloaded piezoelectric resonators. In: Proceedings of the IEEE ultrasonics symposium, 1997, vol. 2, pp 931–935
15. Kelly J, Ballato A, Safari A (1996) The effect of a complex piezoelectric coupling coefficient on the resonance and antiresonance frequencies of piezoelectric ceramics. In: Proceedings of the 10th IEEE on applications of ferroelectrics, 1996, pp 825–828
16. Arlt G, Dederichs H (1980) Complex elastic, dielectric and piezoelectric constants by domain wall damping in ferroelectric ceramics. Ferroelectrics 29(1):47–50
17. Mezheritsky AV (2004) Elastic, dielectric, and piezoelectric losses in piezoceramics: how it works all together. IEEE Trans Ultrason Ferroelectr Freq Control 51(6):695–707
18. Tsurumi T, Kil YB, Nagatoh K, Kakemoto H, Wada S, Takahashi S (2002) Intrinsic elastic, dielectric, and piezoelectric losses in lead zirconate titanate ceramics determined by an immittance-fitting method. J Am Ceram Soc 85(8):1993–1996
19. Brennan KF (1999) The physics of semiconductors: with applications to optoelectronic devices. Cambridge University Press, Cambridge
20. Ghaffari S, Chandorkar SA, Wang S, Ng EJ, Ahn CH, Hong V, Yang Y, Kenny TW (2013) Quantum limit of quality factor in silicon micro and nano mechanical resonators. Sci Rep 3:3244
21. Akhiezer A (1939) On the absorption of sound in solids. J Phys (Moscow) 1(1):277–287
22. Landau LD, Rumer YB (1937) On sound absorption in solids. Phys Zs Soviet Un 11:8–15
23. Nowick A, Berry D (1972) Anelastic relaxation in crystalline solids. Academic, New York, NY
24. Tabrizian R, Rais-Zadeh M, Ayazi F (2009) Effect of phonon interactions on limiting the fQ product of micromechanical resonators. In: International solid-state sensors, actuators and microsystems conference, 2009. Transducers 2009, pp 2131–2134
25. Lifshitz R, Roukes ML (2000) Thermoelastic damping in micro-and nanomechanical systems. Phys Rev B 61(8):5600
26. Zener C (1937) Internal friction in solids. I. Theory of internal friction in reeds. Phys Rev 52(3):230
27. Yasumura KY, Stowe TD, Chow EM, Pfafman T, Kenny TW, Stipe BC, Rugar D (2000) Quality factors in micron-and submicron-thick cantilevers. J Microelectromech Syst 9(1):117–125
28. Abdolvand R, Johari H, Ho GK, Erbil A, Ayazi F (2006) Quality factor in trench-refilled polysilicon beam resonators. J Microelectromech Syst 15(3):471–478
29. Guo X, Yi Y-B, Pourkamali S (2013) A finite element analysis of thermoelastic damping in vented MEMS beam resonators. Int J Mech Sci 74:73–82
30. Pippard AB (1960) Theory of ultrasonic attenuation in metals and magneto-acoustic oscillations. Proc R Soc Lond 257(1289):165–193

31. Mason WP, Bateman TB (1964) Ultrasonic wave propagation in doped n-germanium and p-silicon. Phys Rev 134(5A):A1387
32. Morse RW, Bohm HV (1957) Superconducting energy gap from ultrasonic attenuation measurements. Phys Rev 108(4):1094
33. Hutson AR, White DL (1962) Elastic wave propagation in piezoelectric semiconductors. J Appl Phys 33(1):40–47
34. Nine HD, Truell R (1961) Photosensitive-ultrasonic properties of cadmium sulfide. Phys Rev 123(3):799
35. Gokhale VJ, Rais-Zadeh M (2014) Phonon-electron interactions in piezoelectric semiconductor bulk acoustic wave resonators. Sci Rep 4:5617
36. Hao Z, Erbil A, Ayazi F (2003) An analytical model for support loss in micromachined beam resonators with in-plane flexural vibrations. Sensors Actuat A Phys 109(1):156–164
37. Hao Z, Ayazi F (2007) Support loss in the radial bulk-mode vibrations of center-supported micromechanical disk resonators. Sensors Actuat Phys 134(2):582–593
38. Jing W, Ren Z, Nguyen CTC (2004) 1.156-GHz self-aligned vibrating micromechanical disk resonator. IEEE Trans Ultrason Ferroelectr Freq Control 51(12):1607–1628
39. Kun W, Wong AC, Nguyen CTC (2000) VHF free-free beam high-Q micromechanical resonators. J Microelectromech Syst 9(3):347–360
40. Li S-S, Lin Y-W, Xie Y, Ren Z, Nguyen CT-C (2004) Micromechanical "hollow-disk" ring resonators. In: 17th IEEE international conference on (MEMS) micro electro mechanical systems, 2004, pp 821–824
41. Lakin KM (2005) Thin film resonator technology. IEEE Trans Ultrason Ferroelectr Freq Control 52(5):707–716
42. Newell WE (1965) Face-mounted piezoelectric resonators. Proc IEEE 53(6):575,581
43. Pandey M, Reichenbach RB, Zehnder AT, Lal A, Craighead HG (2009) Reducing anchor loss in MEMS resonators using mesa isolation. J Microelectromech Syst 18(4):836–844
44. Harrington BP, Abdolvand R (2011) In-plane acoustic reflectors for reducing effective anchor loss in lateral–extensional MEMS resonators. J Micromech Microeng 21(8):085021
45. Mohammadi S, Eftekhar AA, Khelif A, Hunt WD, Adibi A (2008) Evidence of large high frequency complete phononic band gaps in silicon phononic crystal plates. Appl Phys Lett 92(22):221905
46. Mohammadi S et al (2010) Support loss suppression in micromechanical resonators by the use of phononic band gap structures. In: OPTO, international society for optics and photonics, 2010
47. Sorenson L, Fu JL, Ayazi F (2011) One-dimensional linear acoustic bandgap structures for performance enhancement of AlN-on-silicon micromechanical resonators. In: 16th International solid-state sensors, actuators and microsystems conference (TRANSDUCERS), 2011, pp 918–921
48. Lin C-M et al (2014) Anchor loss reduction in AlN Lamb wave resonators using phononic crystal strip tethers. In: IEEE international frequency control symposium (FCS), 2014
49. Cho YH, Pisano AP, Howe RT (1994) Viscous damping model for laterally oscillating microstructures. J Microelectromech Syst 3(2):81–87
50. Vibration transmission and support loss in MEMS sensors by Benjamin Chouvion
51. Candler RN, Hopcroft M, Kim B, Park W-T, Melamud R, Agarwal M, Yama G, Partridge A, Lutz M, Kenny TW (2006) Long-term and accelerated life testing of a novel single-wafer vacuum encapsulation for MEMS resonators. J Microelectromech Syst 15(6):1446–1456
52. Esashi M (2008) Wafer level packaging of MEMS. J Micromech Microeng 18(7):073001
53. Verbridge SS, Ilic R, Craighead HG, Parpia JM (2008) Size and frequency dependent gas damping of nanomechanical resonators. Appl Phys Lett 93(1):013101
54. Ekinci KL, Roukes ML (2005) Nanoelectromechanical systems. Rev Sci Instrum 76(6):061101
55. Seoánez C, Guinea F, Castro-Neto AH (2008) Surface dissipation in nanoelectromechanical systems: unified description with the standard tunneling model and effects of metallic electrodes. Phys Rev B 77(12):125107

56. Yang J, Ono T, Esashi M (2002) Energy dissipation in submicrometer thick single-crystal silicon cantilevers. J Microelectromech Syst 11(6):775–783
57. Landau LD, Lifshitz EM (1986) Theory of elasticity, vol 7. Course Theor Phys 3:109
58. Lücke K (1956) Ultrasonic attenuation caused by thermoelastic heat flow. J Appl Phys 27(12):1433–1438
59. Mason WP, Bateman TB (1964) Ultrasonic-wave propagation in pure silicon and germanium. J Acoust Soc Am 36(4):644–652
60. Oliver DW, Slack GA (1966) Ultrasonic attenuation in insulators at room temperature. J Appl Phys 37(4):1542–1548
61. Papadakis EP (1965) Ultrasonic attenuation caused by scattering in polycrystalline metals. J Acoust Soc Am 37(4):711–717
62. Robert A (2004) Volume manufacturing of BAW-filters in a CMOS fab. In: Acoustic wave device symposium, pp 129–34
63. Ruby R (2011) A decade of FBAR success and what is needed for another successful decade. In: Symposium on piezoelectricity, acoustic waves and device applications (SPAWDA), 2011, pp 365–369
64. Bhatia AB, Moore RA (1959) Scattering of high frequency sound waves in polycrystalline materials II. J Acoust Soc Am 31(8):1140–1141
65. Bhatia AB (1967) Ultrasonic absorption: an introduction to the theory of sound absorption and dispersion in gases, liquids, and solids. Courier Corporation, North Chelmsford, MA
66. MacFarlane RE, Rayne JA (1967) Ultrasonic attenuation in the noble metals. Phys Rev 162(3):532
67. Hepfer KC, Rayne JA (1971) Ultrasonic attenuation in aluminum. Phys Rev B 4(4):1050
68. Jones CK, Rayne JA (1964) Ultrasonic attenuation in tungsten and molybdenum up to 1 Gc/s. Phys Lett 13(4):282–283
69. Mansfeld GD, Alekseev SG, Kotelyansky IM (2001) Acoustic HBAR spectroscopy of metal (W, Ti, Mo, Al) thin films. IEEE Ultrason Symp 1:415–418
70. Besson R (1976) A new piezoelectric resonator design. In: IEEE 30th annual symposium on frequency control, pp 78–83
71. Besson RJ, Moutrey M, Galliou S, Marionnet F, Gonzalez F, Guillemot Ph, Tjoelker R, Diener W, Kirk A (1999) 10 MHz hyperstable quartz oscillators performances. In: Proceedings of the 1999 joint meeting of the European frequency and time forum, 1999 and the IEEE international frequency control symposium, 1999, vol 1, pp 326–330
72. Hung L-W, Nguyen CTC (2011) Capacitive-piezoelectric AlN resonators with Q> 12,000. In: 2011 IEEE 24th international conference on micro electro mechanical systems (MEMS), pp 173–176
73. Yen T-T, Pisano AP, Nguyen CTC (2013) High-Q capacitive-piezoelectric AlN Lamb wave resonators. In: 2013 IEEE 26th international conference on micro electro mechanical systems (MEMS), pp 114–117
74. Humad S, Abdolvand R, Ho GK, Piazza G, Ayazi F (2003) High frequency micromechanical piezo-on-silicon block resonators. In: IEDM'03 technical digest IEEE international electron devices meeting, 2003, pp 39–3
75. Abdolvand R, Lavasani HM, Ho GK, Ayazi F (2008) Thin-film piezoelectric-on-silicon resonators for high-frequency reference oscillator applications. IEEE Trans Ultrason Ferroelectr Freq Control 55(12):2596–2606
76. Abdolvand R, Ho GK, Butler J, Ayazi F (2007) ZnO-onnanocrystalline-diamond lateral bulk acoustic resonators. IN: Proceedings of the 20th IEEE International conference on Micro electro mechanical systems, Kobe, Japan, Jan 2007, pp 795–798
77. Fatemi H, Zeng H, Carlisle JA, Abdolvand R (2013) High-frequency thin-film AlN-on-diamond lateral–extensional resonators. J Microelectromech Syst 22(3):678–686H
78. Lin CM, Chen YY, Felmetsger VV, Senesky DG, Pisano AP (2012) AlN/3C–SiC composite plate enabling high-frequency and high-Q micromechanical resonators. Adv Mater 24(20):2722–2727

79. Pan W, Ayazi F (2010) Thin-film piezoelectric-on-substrate resonators with Q enhancement and TCF reduction. In: 2010 IEEE 23rd international conference on micro electro mechanical systems (MEMS), pp 727–730
80. Shahmohammadi M, Harrington BP, Abdolvand R (2013) Turnover temperature point in extensional-mode highly doped silicon microresonators. IEEE Trans Electron Dev 60(3):1213–1220
81. Baborowski J, Bourgeois C, Pezous A, Muller C, Dubois MA (2007) Piezoelectrically activated silicon resonators. In: 2007 Joint with the 21st European frequency and time forum. IEEE international frequency control symposium, pp 1210–1213
82. Smits JG (1978) Eigenstates of coupling factor and loss factor of piezoelectric ceramics IEEE standard on piezoelectricity (ANSI/IEEE Standard 176-1987). The Institute of Electrical and Electronics Engineers, Inc, New York, NY
83. Muralt P, Antifakos J, Cantoni M, Lanz R, Martin F (2005) Is there a better material for thin film BAW applications than A1N? IEEE Ultrason Symp 1:315–320
84. Van Dyke KS (1925) The electric network equivalent of a piezoelectric resonator. Phys Rev 25(6):895
85. Rosenbaum JF (1988) Bulk acoustic wave theory and devices. Artech House, Boston, MA
86. IEEE (1966) IEEE standard definitions and methods of measurement for piezoelectric vibrators. IEEE Std No. 177, p 1
87. Newell WE, Wickstrom RA (1969) The tunistor: a mechanical resonator for microcircuits. IEEE Trans Electron Dev 16(9):781–787
88. Wang JS, Lakin KM (1981) Sputtered AlN films for bulk-acoustic-wave devices. Ppresented at the 1981 ultrasonics symposium, pp 502–505
89. Ruby RC, Bradley P, Oshmyansky Y, Chien A, Larson JD (2001) Thin film bulk wave acoustic resonators (FBAR) for wireless applications. IEEE Ultrason Symp 1:813–821
90. Piazza G, Stephanou PJ, Pisano AP (2007) Single-chip multiple-frequency ALN MEMS filters based on contour-mode piezoelectric resonators. J Microelectromech Syst 16(2):319–328

Chapter 6
Flexural Piezoelectric Resonators

David Horsley, Yipeng Lu, and Ofer Rozen

6.1 Introduction

Flexural piezoelectric resonators can be broadly classified as being one-dimensional devices, such as bars [1–4], and tuning forks [5], or two-dimensional devices, such as round or square diaphragms [6–8]. Models for the static deflection of piezoelectrically actuated one-dimensional beams are presented in [9, 10], while a lumped-element model for flexural plate-wave resonators is presented in [11]. This chapter focuses on developing lumped-element equivalent circuit models for vibration of continuous one-dimensional and two-dimensional resonators. These models allow the designer to predict various aspects of resonator behavior such as the natural frequency and vibration amplitude of the various vibration modes.

6.2 Mechanics of Laminates

One common feature of flexural piezoelectric resonators is that they are usually multilayer laminates in which at least one layer exhibits piezoelectricity. The out-of-plane vibration and cross section of a vibrating laminate are illustrated in Fig. 6.1 along with a cross-sectional SEM image of a piezoelectric laminate resonator [12]. Following the standard notation, the *x, y, z* coordinate axes are also numbered with indices 1,2,3.

D. Horsley (✉) • Y. Lu • O. Rozen
Department of Mechanical & Aerospace Engineering, University of California, Davis,
1 Shields Ave, Davis, CA 95616, USA
e-mail: dahorsley@ucdavis.edu

© Springer International Publishing Switzerland 2017

H. Bhugra, G. Piazza (eds.), *Piezoelectric MEMS Resonators*,
Microsystems and Nanosystems, DOI 10.1007/978-3-319-28688-4_6

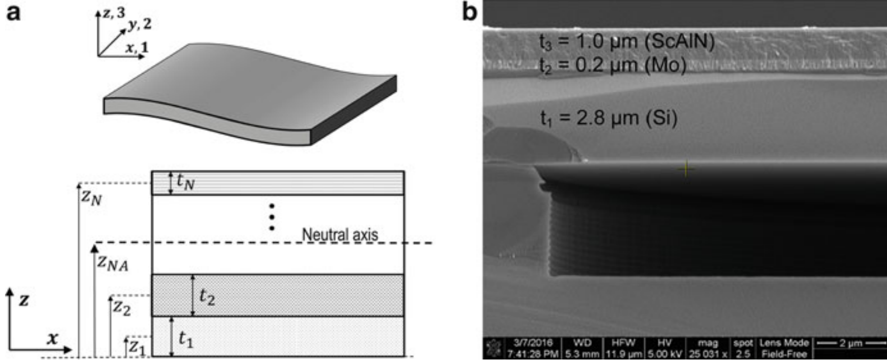

Fig. 6.1 (**a**) Laminate cross section and coordinate definitions. z_n denotes the distance from the bottom plane to the mid-plane of the *n*-th layer and t_n is the thickness of this layer. (**b**) Flexural resonator with three layers (Si, Mo, and ScAlN piezo layer), SEM image adapted from [12]

We describe a planar laminate having *N* layers, and denote the thickness and mass density of the *n*-th layer as t_n and ρ_n. We assume that the materials are isotropic in the *x*/*y* plane, and denote the in-plane (*x*/*y* plane) and out-of-plane (*z*-axis) Young's moduli of the *n*-th layer as $Y_{11,n}$ and $Y_{33,n}$ and the in-plane Poisson's ratio as $\nu_{12,n}$. When a short, wide beam (length less than five times the width) or plate is modeled, the Young's modulus is replaced by the plate modulus,

$$Y'_{11,n} = \frac{Y_{11,n}}{1 - \nu_{12,n}^2} \tag{6.1}$$

Following [13], we define the location of the mid-plane (z_n) and top (h_n) of each layer relative to the bottom of the laminate as

$$z_n = \sum_{j=1}^{n-1} t_j + \frac{1}{2} t_n \qquad h_n = \sum_{j=1}^{n-1} t_j + t_n \tag{6.2}$$

and the mass per unit area is

$$\mu = \sum_{n=1}^{N} t_n \rho_n. \tag{6.3}$$

The location of the neutral axis is then

$$z_{NA} = \frac{\sum_{n=1}^{N} t_n z_n Y_{11,n}}{\sum_{n=1}^{N} t_n Y_{11,n}} \tag{6.4}$$

The flexural rigidity of a homogeneous plate of thickness t is defined as:

$$D = \frac{Y_{11}t^3}{12\left(1-\nu_{12}^2\right)} = \frac{Y'_{11}t^3}{12} \tag{6.5}$$

while a laminate's flexural rigidity is found from [14]

$$D = \int_0^{t_{total}} Y'_{11,n} z^2 dz = \frac{1}{3}\sum_{n=1}^{N} Y'_{11,n}\left(\bar{h}_n^3 - \bar{h}_{n-1}^3\right) \tag{6.6}$$

where $\overline{h}_n = h_n - z_{\mathrm{NA}}$ is the distance from the top of the n-th layer to the neutral axis. Note that in Eq. (6.6), $h_0 = 0$. For a homogeneous plate, $h_1 = t$, $z_{\mathrm{NA}} = t/2$, and Eq. (6.6) simplifies to Eq. (6.5).

6.2.1 Natural Frequencies

The natural frequencies of a two-dimensional plate are given by [15]:

$$\omega_{i,j} = \frac{\lambda_{i,j}^2}{l^2}\sqrt{\frac{D}{\mu}} \tag{6.7}$$

where i, j are the mode indices, $\lambda_{i,j}$ is a constant that depends on the vibration mode, and l is the length or diameter of the square or circular plate.

For a one-dimensional resonator such as a beam, only a single index, i, is needed. Some intuition for how the resonant frequencies scale with the beam geometry can be gained considering a homogeneous beam, for which $D = Y_{11}t^3/12$ and $\mu = \rho t$. Substituting these values into the equation for natural frequency, we find that the frequency of the i-th vibration mode is:

$$\omega_i = \frac{\lambda_i^2}{l^2}\sqrt{\frac{D}{\mu}} = \lambda_i^2\frac{t}{l^2}\frac{1}{2\sqrt{3}}\sqrt{\frac{Y_{11}}{\rho}} = \frac{1}{2\sqrt{3}}\lambda_i^2\frac{t}{l^2}c \tag{6.8}$$

where $c = \sqrt{Y_{11}/\rho}$ is the acoustic velocity. Equation (6.8) reveals that the natural frequencies scale linearly with thickness and with the inverse square of length.

6.2.2 Thin-Film Piezo-Coefficient

Thin-film flexural piezoelectric devices must be modeled using the effective thin-film piezoelectric coefficients, which are different from the ordinary piezoelectric coefficients due to the boundary conditions experienced by the thin piezoelectric

layer. In a thin-film piezoelectric device, the piezoelectric film is free to deform in the vertical direction but is clamped in the plane of the substrate. Therefore, the out-of-plane stress σ_3 is equal to zero, and the in-plane stress can be described as [16]:

$$\sigma_1 = -\frac{d_{31}E_3}{s_{11}^E + s_{12}^E} = (e_{31} - \nu_{12}e_{33})\,E_3 = -e_{31,f}E_3 \tag{6.9}$$

$$e_{31,f} = e_{31} - \nu_{12}e_{33} = \frac{d_{31}}{s_{11}^E + s_{12}^E} \tag{6.10}$$

where s_{ij}^E are the coefficients of the piezoelectric layer's compliance matrix S which is related to the stiffness matrix C via $S = C^{-1}$, and d_{31}, e_{31}, e_{33} are the piezoelectric coefficients.

As an example, for AlN, the stiffness matrix is:

$$C_{\mathrm{AlN}} = \begin{pmatrix} c_{11} & c_{12} & c_{13} & 0 & 0 & 0 \\ c_{12} & c_{11} & c_{13} & 0 & 0 & 0 \\ c_{13} & c_{13} & c_{33} & 0 & 0 & 0 \\ 0 & 0 & 0 & c_{44} & 0 & 0 \\ 0 & 0 & 0 & 0 & c_{44} & 0 \\ 0 & 0 & 0 & 0 & 0 & (c_{11} - c_{12})/2. \end{pmatrix}$$

where c_{11}= 410 GPa, c_{12}= 149 GPa, c_{13}= 120 GPa, c_{33} =395 GPa, and c_{44}= 125 GPa [17, 18]. Note that Young's modulus and Poisson's ratio are given by $Y_{11} = s_{11}^{-1} = 345$ GPa and $\nu_{12} = s_{21}/s_{11}$=0.32.

The AlN piezo coefficients are $e_{31} = -0.58\frac{C}{m^2}$, $e_{33} = 1.55\frac{C}{m^2}$ [19]. Substituting these parameters into Eq. (6.9) yields $e_{31,f} = -1.08$ C/m^2. To verify the accuracy of $e_{31,f}$ in analytical modeling, a finite element method (FEM) model was created for a 385 μm radius circular plate consisting of 1 μm thick AlN on varying thicknesses of Si. The FEM model uses the compliance matrix C_{AlN} listed above along with the standard piezoelectric coefficients e_{31} and e_{33}, whereas the analytical model uses the thin-film coefficient $e_{31,f}$ and lumped-element parameters derived later in this chapter. The deflections predicted by the FEM and analytical models agree very closely for all the studied thicknesses, as shown in Fig. 6.2.

6.3 Vibration Analysis via Energy Methods

We use an energy method to derive the parameters of a Butterworth–van Dyke (BVD) equivalent circuit model for a resonator, shown in Fig. 6.3. The equivalent circuit parameters are developed in the mechanical domain and represent the mass (L_m), stiffness (k_m), and damping (R_m) of a particular vibration mode. These mechanical parameters can be converted to electrical parameters having the usual

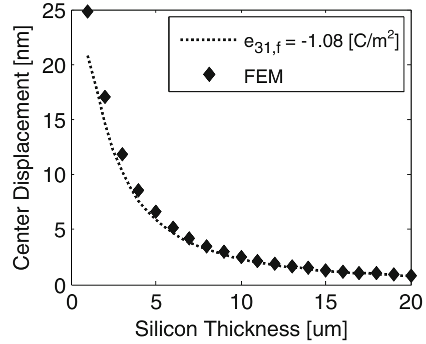

Fig. 6.2 Static displacement of a Si/AlN (1 μm) clamped plate at different silicon thickness

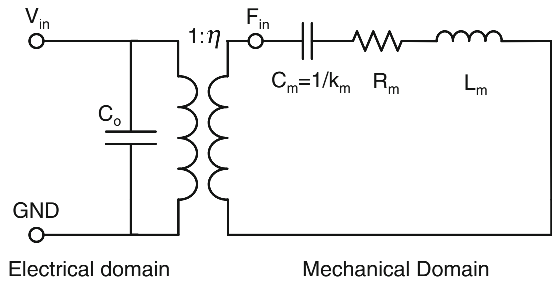

Fig. 6.3 BVD equivalent circuit model

units of H, F, and Ω using the electromechanical coupling constant (η) to transform each mechanical impedance to an equivalent electrical impedance.

Referring to Fig. 6.3, we begin by developing a quasi-static model for the resonator that considers only the piezoelectric force ($F_{\text{in}} = \eta V_{\text{in}}$) and the stiffness ($k_{\text{m}}$). The resonator vibration is separated into spatial and temporal components, $w(x,t) = w(x)e^{j\omega t}$, where $w(x)$ is the vibration mode shape and ω is the frequency. In the lumped-parameter model, we assume that the vibration occurs in a known mode shape with unknown amplitude $w(x) = w_0\varphi(x)$, where $\varphi(x)$ is the normalized mode shape and w_0 is the unknown vibration amplitude.

When the piezoelectric force creates a deflection w_0, the work done is $U_{\text{piezo}} = (\eta V_{\text{in}})w_0$ and the elastic strain energy stored in the resonator's stiffness is $U_{\text{elastic}} = \frac{1}{2}k_{\text{m}}w_0^2$. We define an energy function $U = U_{\text{elastic}} - U_{\text{piezo}}$. When the exact displacement is known, and the piezoelectric force is the only force acting on the resonator, the stored strain energy must be exactly equal to the work done by the piezoelectric force and $U = 0$. Here, we assume the resonator deflection matches an assumed mode shape and seek the approximate solution w_0 that minimizes U,

$$\frac{\mathrm{d}U}{\mathrm{d}w_0} = k_{\text{m}}w_0 - \eta V_{\text{in}} = 0 \tag{6.11}$$

$$w_0 = k_{\text{m}}^{-1}\eta V_{\text{in}} = C_{\text{m}}\eta V_{\text{in}} \tag{6.12}$$

where $C_m = k_m^{-1}$ is the mechanical compliance. Equation (6.12) shows that the static deflection w_0 resulting from input voltage V_{in} can be predicted based on the compliance C_{m} and electromechanical coupling η. The deflection at the resonance frequency $w(\omega)$ will be amplified by the quality factor Q of the given vibration mode, $w(\omega) = Qw_0$. Modeling the quality factor depends on many parameters and is the subject of a separate chapter. In the following sections, we use the elastic strain energy and piezoelectric work to develop expressions for C_{m} and η for common flexural resonators.

6.4 One-Dimensional Resonators

We begin by analyzing a one-dimensional beam resonator, illustrated in Fig. 6.4. The beam is a unimorph structure of width b and length l with an elastic layer of thickness t_e and a piezoelectric layer of thickness t_{p}. The piezoelectric layer is covered by a central electrode whose length is a fraction of the total beam length, $l_{\text{e}} = \gamma l$. While the figure shows a clamped–clamped beam, the following analysis applies to a beam with any boundary conditions.

The elastic strain energy is computed by integrating the strain energy over the volume of the beam:

$$U_{\text{elastic}} = \frac{1}{2}\int_V Y\varepsilon^2 dV \tag{6.13}$$

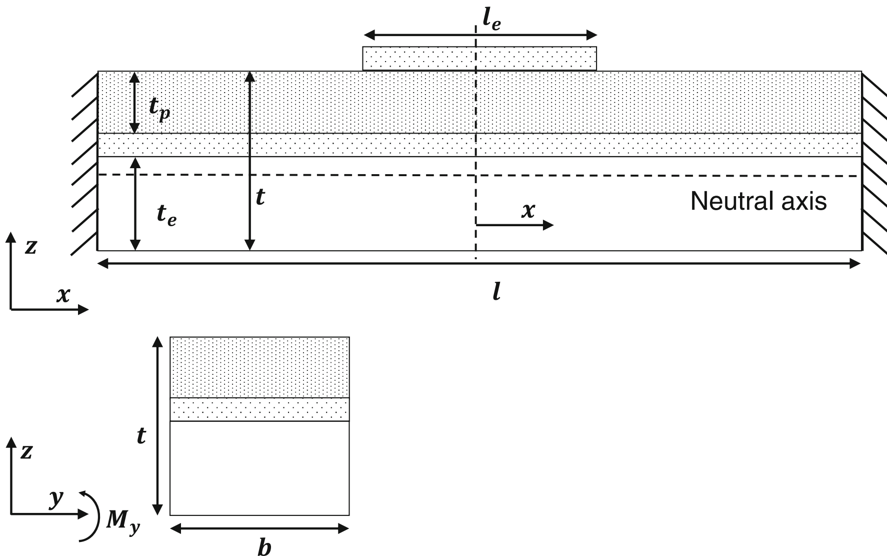

Fig. 6.4 A clamped–clamped beam of length l, x spans from $\frac{-l}{2}$ to $\frac{+l}{2}$

For a beam in pure bending, the strain in the x-axis is

$$\varepsilon_1(z) = \frac{z}{R} = z\frac{\mathrm{d}^2 w(x)}{\mathrm{d}x^2} \tag{6.14}$$

where z is the distance to the neutral axis and R is the radius of curvature. The strain energy is

$$U_{\mathrm{elastic}} = \frac{1}{2}\int Yz^2\mathrm{d}z \iint \left(\frac{d^2 w(x)}{dx^2}\right)^2 \mathrm{d}x\mathrm{d}y = \frac{1}{2}Db\int_{-l/2}^{l/2}\left(\frac{\mathrm{d}^2 w(x)}{\mathrm{d}x^2}\right)^2 \mathrm{d}x \tag{6.15}$$

To collect all the geometric parameters together, we introduce a normalized coordinate, $\bar{x} = x/l$, and substitute $w\left(\bar{x}\right) = w_0\varphi\left(\bar{x}\right)$ for the mode shape,

$$U_{\mathrm{elastic}} = \frac{1}{2}\frac{Db}{l^3}w_0^2\int_{-1/2}^{1/2}\left(\frac{\mathrm{d}^2\varphi\left(\bar{x}\right)}{\mathrm{d}\bar{x}^2}\right)^2 \mathrm{d}\bar{x} = \frac{1}{2}k_{\mathrm{m}}w_0^2 \tag{6.16}$$

The stiffness k_{m} of every mode has the same dependence on the rigidity and beam dimensions. The effect of a particular mode shape on the stiffness is captured by the integral

$$I_{\mathrm{elastic}} = \int_{-1/2}^{1/2}\left(\frac{d^2\varphi\left(\bar{x}\right)}{\mathrm{d}\bar{x}^2}\right)^2 \mathrm{d}\bar{x} \tag{6.17}$$

so that the stiffness is simply

$$C_{\mathrm{m}}^{-1} = k_{\mathrm{m}} = \frac{Db}{l^3}I_{\mathrm{elastic}} \tag{6.18}$$

Note that for a homogeneous beam, $D = Y'_{11}t^3/12$ and k_{m} is proportional to $(t/l)^3$.

Similarly, the work done by the piezoelectric layer is computed from the piezoelectric strain energy integral

$$U_{\mathrm{piezo}} = \iiint_{V_{\mathrm{p}}} \frac{1}{2}\sigma\varepsilon dV \tag{6.19}$$

Where V_{p} is the volume of the piezoelectric layer that is covered by the electrode and therefore exposed to electric field $E_3 = V_{\mathrm{in}}/t_{\mathrm{p}}$.

The in-plane piezoelectric stress is $\sigma = e_{31,f}E_3$ and the piezoelectric energy is

$$U_{piezo} = \iiint\limits_{V_p} \frac{1}{2}\left(e_{31,f}E_3\right)\left(\frac{d^2w(x)}{dx^2}\right)dV = \frac{M_p b}{2l}w_0 \int\limits_{-\gamma/2}^{\gamma/2} \frac{d^2\varphi\left(\bar{x}\right)}{d\bar{x}^2}d\bar{x} = \left(\eta V_{in}\right)w_0 \tag{6.20}$$

In the equation above, M_p is the piezoelectric bending moment,

$$M_\mathrm{p} = \int_{z_\mathrm{b}}^{z_\mathrm{t}} e_{31,f}E_3 z\mathrm{d}z = e_{31,f}\bar{z}_\mathrm{p}V_\mathrm{in} \tag{6.21}$$

where $\bar{z}_\mathrm{P}$ is the distance from the mid-plane of the piezoelectric layer to the neutral axis (z_NA) and V_in is the input voltage.

The electromechanical coupling, η, is given by:

$$\eta = \frac{e_{31,f}\bar{z}_\mathrm{p}b}{2l}I_\mathrm{piezo} \tag{6.22}$$

where the effect of the electrode layout and the particular mode shape is captured by the integral

$$I_\mathrm{piezo} = \int\limits_{-\gamma/2}^{\gamma/2} \frac{\mathrm{d}^2\varphi\left(\bar{x}\right)}{\mathrm{d}\bar{x}^2}d\bar{x} \tag{6.23}$$

6.4.1 Clamped–Clamped Beam Analysis

For a clamped–clamped beam, the exact mode shape of the *i*-th vibration mode is [15]:

$$\varphi_i\left(\bar{x}\right) = \kappa_i\left[\sin h\left(\lambda_i\bar{x}\right) - \sin\left(\lambda_i\bar{x}\right) - \sigma_i\left(\cos h\left(\lambda_i\bar{x}\right) - \cos\left(\lambda_i\bar{x}\right)\right)\right] \tag{6.24}$$

where the values of the constants λ_i, κ_i, and σ_i for the first three vibration modes are given in Table 6.1 below.

However, the resonator can also be analyzed without knowledge of the exact mode shape. Instead, approximate mode shapes may be used. These approximate mode shapes only need to satisfy the geometric boundary conditions (i.e., the slope and displacement at the resonator boundaries). For the first vibration mode of a clamped–clamped beam, an approximate mode shape is

Table 6.1 Constants for the first three modes of a clamped–clamped one-dimensional beam resonator

Mode	λ_i	κ_i	σ_i
$i = 1$	4.730	0.618	1.018
$i = 2$	7.853	0.663	0.999
$i = 3$	10.996	0.711	1.000

$$\varphi\left(\bar{x}\right) = \left(1 - 4\bar{x}^2\right)^2 \tag{6.25}$$

which yields

$$C_\mathrm{m} = \frac{5}{1024}\frac{l^3}{Db}$$

and

$$\eta = 16\gamma\left(\gamma^2 - 1\right)\frac{e_{31,f}\,\bar{z}_\mathrm{p} b}{2l}$$

The expression for η can be used to determine the electrode coverage that maximizes the coupling of the piezoelectric bending moment into the desired vibration mode, thereby maximizing the vibration amplitude per unit voltage. The maximum occurs where

$$\frac{\mathrm{d}\eta}{\mathrm{d}\gamma} = 3\gamma^2 - 1 = 0 \Rightarrow \gamma = \sqrt{1/3} = 0.58$$

However, maximizing η does not consider the input power (input current and voltage) required to achieve a given vibration amplitude. The electromechanical coupling constant, ${k_\mathrm{t}}^2$, which measures the mechanical vibration energy as a fraction of the total input energy, can be used to find the electrode coverage that achieves the maximum vibration amplitude per unit input power. In terms of the equivalent circuit parameters,

$${k_\mathrm{t}}^2 \cong \frac{\eta^2 C_\mathrm{m}}{C_0 + \eta^2 C_\mathrm{m}} \tag{6.26}$$

For a 1D beam, the electrical capacitance is given by $C_0 = \varepsilon_{33}\varepsilon_0\gamma lb/t_\mathrm{p}$. For most micromachined devices, $C_0 \gg \eta^2 C_\mathrm{m}$, and Eq. (6.26) can be simplified to ${k_\mathrm{t}}^2 \approx \eta^2 C_\mathrm{m}/C_0$. Since C_m is independent of γ, the value of γ that maximizes ${k_\mathrm{t}}^2$ can be found from η^2/C_0. Hence, the value of γ that maximizes ${k_\mathrm{t}}^2$ is found from

$$\frac{\mathrm{d}}{\mathrm{d}\gamma}\left(\frac{\eta^2}{C_0}\right) = 0 \Rightarrow \frac{\mathrm{d}}{\mathrm{d}\gamma}\frac{\left(3\gamma^2 - 1\right)^2}{\gamma} = 0$$

This equation has several roots; however, the root that maximizes η^2/C_0 is $\gamma = \sqrt{1/5} = 0.45$. Because the electrical capacitance appears in the denominator of ${k_\mathrm{t}}^2$, it can be seen that the electrode size which maximizes ${k_\mathrm{t}}^2$ is smaller than the size used to maximize η.

6.4.2 Natural Frequencies

The resonator's dynamic behavior can be analyzed by adding terms representing damping and mass to the equivalent circuit model. The modal mass is found by integrating the square of the vibration mode shape weighted by the density

$$L_{\mathrm{m}} = \iiint \rho\,(x, y, z)\, w(x, y)^2 \mathrm{d}V \tag{6.27}$$

Continuing the example of the 1D beam, the modal mass simplifies to:

$$L_{\mathrm{m}} = bl\mu \int_{-1/2}^{1/2} \varphi\left(\bar{x}\right)^2 \mathrm{d}\bar{x} = m \int_{-1/2}^{1/2} \varphi\left(\bar{x}\right)^2 \mathrm{d}\bar{x} \tag{6.28}$$

where $m = bl\mu$ is the total mass of the beam. Using the approximate mode shape from Eq. (6.25),

$$L_{\mathrm{m}} = \frac{128}{315} m \tag{6.29}$$

The natural frequency of the first vibration mode found from the equivalent circuit parameters is

$$\omega_1 = \sqrt{\frac{1}{L_{\mathrm{m}} C_{\mathrm{m}}}} = \frac{6\sqrt{14}}{l^2} \sqrt{\frac{D}{\mu}} \tag{6.30}$$

In comparison with the exact natural frequencies of a clamped–clamped beam from Eq. (6.7) using $\lambda_1 = 4.73$ for the first mode, the error between the approximate solution and the exact solution for ω_1 is less than 0.5 %.

6.4.3 Two-Port Resonators

A two-port resonator having two top electrodes is illustrated in Fig. 6.5 along with an image of a two-port circular resonator [20]. The equivalent circuit model of a two-port resonator is shown in Fig. 6.6. The central electrode, identical to the electrode analyzed for the one-port beam above, forms the first electrical port. The second electrode is located at the right and left boundaries of the beam. In the beam's first vibration mode, the beam's curvature beneath the central electrode has opposite sign from the curvature beneath the right and left electrodes, resulting in a sign reversal between η_1 and η_2, the electromechanical coupling of the first and second ports. One method to use this beam is to differentially excite vibration, using voltages of

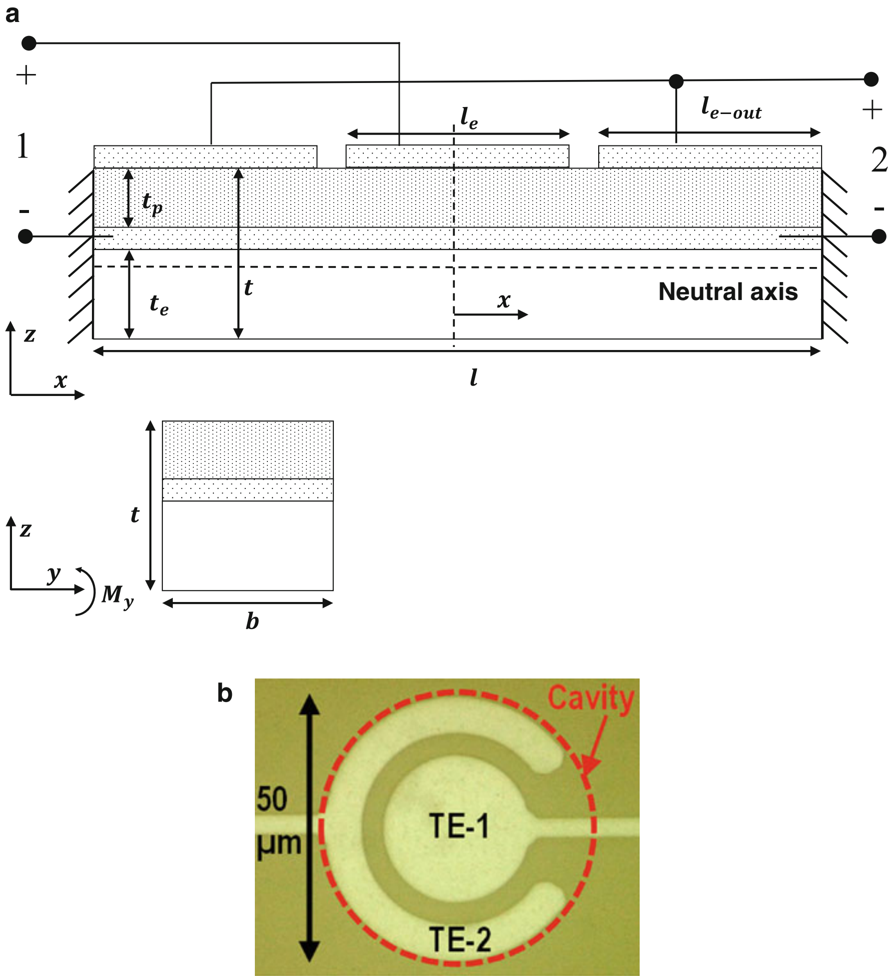

Fig. 6.5 (**a**) Cross section of a two-port resonator. The center electrode is identical to the electrode of the one-port beam and forms the first electrical port, while the second electrode is located at the left and right edges of the resonator. (**b**) Optical image of a two-port circular resonator with two top electrodes, TE-1 and TE-2 [20]

opposite polarity to excite the two ports, thereby doubling the output displacement at a given voltage level [21]. More commonly, one of the ports is used as an input, while the second port is used as an output, allowing the resonator to be driven into oscillation in a feedback loop [2].

Referring to Eq. (6.22), the second port's electromechanical coupling η_2 is computed through the corresponding piezoelectric coupling integral, I_{piezo}. For a 2-port linear beam resonator, the integral is

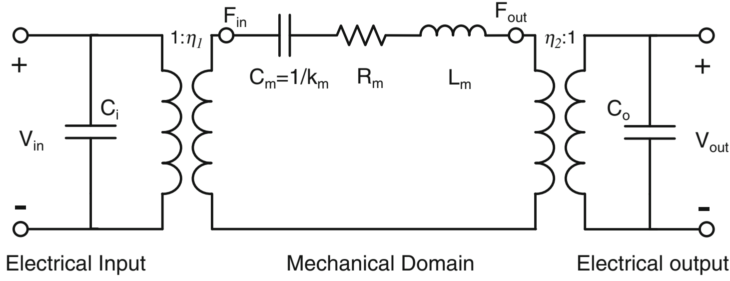

Fig. 6.6 Equivalent circuit of two-port transducer

$$I_{\mathrm{piezo}} = \int_{\beta/2}^{1} \frac{\mathrm{d}^2\varphi\left(\bar{x}\right)}{\mathrm{d}\bar{x}^2} \mathrm{d}\bar{x} + \int_{-1}^{-\beta/2} \frac{\mathrm{d}^2\varphi\left(\bar{x}\right)}{\mathrm{d}\bar{x}^2} \mathrm{d}\bar{x} \tag{6.31}$$

At resonance, the impedances L_{m} and C_{m} cancel, leaving only R_{m}. To find the output voltage in this case, we use R_l to denote the load impedance attached to the output terminal and solve

$$\frac{V_{\mathrm{out}}}{V_{\mathrm{in}}} = \frac{1}{1 + \eta_2^2 R_{\mathrm{m}}/R_l} \left(\frac{\eta_1}{\eta_2}\right) \tag{6.32}$$

If the load impedance (R_l) is large relative to the motional resistance ($\eta_2^2 R_{\mathrm{m}}$), Eq. (6.32) shows that $V_{\mathrm{out}}/V_{\mathrm{in}} \approx \eta_1/\eta_2$ and the device acts as a resonant transformer. This typically requires a high quality factor to achieve low R_{m}. Note that while reducing η_2 will increase the voltage gain, it may also degrade the impedance matching since the motional resistance is scaled by η_2^2.

6.5 Two-Dimensional Resonators

For a two-dimensional resonator vibrating with mode shape $w(x, y)$ shown in Fig. 6.1, the in-plane strain and stress components are:

$$\varepsilon_x = \tfrac{z}{R_x} \; \varepsilon_y = \tfrac{z}{R_y} \; \varepsilon_{xy} = \tfrac{z}{R_{xy}} = 0 \tag{6.33}$$

$$\sigma_x = Y'_{11,n}\left(\varepsilon_x + v_{12}\varepsilon_y\right) \quad \sigma_y = Y'_{11,n}\left(\varepsilon_y + v_{12}\varepsilon_x\right) \tag{6.34}$$

The elastic strain energy is:

$$U_{\mathrm{elastic}} = \frac{1}{2} \iint \left(\sigma_x\varepsilon_x + \sigma_y\varepsilon_y\right) \mathrm{d}x\mathrm{d}y \tag{6.35}$$

Substituting the stress and strain components yields [22]:

$$U_{\text{elastic}} = \frac{1}{2}D \iint \left[\left(\frac{\mathrm{d}^2 w(x,y)}{\mathrm{d}x^2} \right)^2 + \left(\frac{\mathrm{d}^2 w(x,y)}{\mathrm{d}y^2} \right)^2 + 2v_{12} \frac{\mathrm{d}^2 w(x,y)}{\mathrm{d}x^2} \frac{\mathrm{d}^2 w(x,y)}{\mathrm{d}y^2} \right] \mathrm{d}x\mathrm{d}y \tag{6.36}$$

Similarly, the piezoelectric strain energy is:

$$U_{\text{piezo}} = \frac{1}{2} \int_{z_b}^{z_t} \left(e_{31,f} E_3 \right) z\mathrm{d}z \iint_{A_p} \left[\frac{\mathrm{d}^2 w(\mathrm{x},\mathrm{y})}{\mathrm{d}x^2} + \frac{\mathrm{d}^2 w(\mathrm{x},\mathrm{y})}{\mathrm{d}y^2} \right] \mathrm{d}x\mathrm{d}y \tag{6.37}$$

$$U_{\text{piezo}} = \frac{1}{2} M_p \iint_{A_p} \left[\frac{d^2 w(\mathrm{x},\mathrm{y})}{dx^2} + \frac{d^2 w(\mathrm{x},\mathrm{y})}{dy^2} \right] dxdy \tag{6.38}$$

where the integration is performed only over A_{p}, the area of the piezoelectric layer that is spanned by the electrodes. These equations may be used to compute the modal compliance and electromechanical coupling as was shown for a one-dimensional beam above. In what follows, we consider two simple structures that are commonly encountered, square plates and round plates.

6.5.1 Square Plates

For a clamped–clamped square plate, we use normalized coordinates $\bar{x} = x/l$ and $\bar{y} = y/l$ and write the vibration mode shape as $\varphi\left(\bar{x}, \bar{y}\right)$

$$\begin{aligned} U_{\text{elastic}} = \frac{1}{2} \frac{D}{l^2} w_0^2 \iint [(\frac{\mathrm{d}^2 \varphi(\bar{x}, \bar{y})}{\mathrm{d}\bar{x}^2})^2 + (\frac{\mathrm{d}^2 \varphi(\bar{x}, \bar{y})}{\mathrm{d}\bar{y}^2})^2 \\ + 2v_{12} \frac{\mathrm{d}^2 \varphi(\bar{x}, \bar{y})}{\mathrm{d}\bar{x}^2} \frac{\mathrm{d}^2 \varphi(\bar{x}, \bar{y})}{\mathrm{d}\bar{y}^2}] \mathrm{d}\bar{x}\mathrm{d}\bar{y} \end{aligned} \tag{6.39}$$

Following the one-dimensional example,

$$I_{\text{elastic}} = \int_{-1/2}^{1/2} \int_{-1/2}^{1/2} \left[\left(\frac{\mathrm{d}^2 \varphi\left(\bar{x}, \bar{y}\right)}{\mathrm{d}\bar{x}^2} \right)^2 + \left(\frac{\mathrm{d}^2 \varphi\left(\bar{x}, \bar{y}\right)}{\mathrm{d}\bar{y}^2} \right)^2 + 2v_{12} \frac{\mathrm{d}^2 \varphi\left(\bar{x}, \bar{y}\right)}{\mathrm{d}\bar{x}^2} \frac{\mathrm{d}^2 \varphi\left(\bar{x}, \bar{y}\right)}{\mathrm{d}\bar{y}^2} \right] \mathrm{d}\bar{x}\mathrm{d}\bar{y} \tag{6.40}$$

and

$$k_{\mathrm{m}} = \frac{D}{l^2} \mathrm{I}_{\mathrm{elastic}} \tag{6.41}$$

Similarly,

$$U_{\mathrm{piezo}} = \frac{1}{2} M_p w_o \int_{-\gamma/2}^{\gamma/2} \int_{-\gamma/2}^{\gamma/2} \left[\frac{\mathrm{d}^2 \varphi\left(\bar{x}, \bar{y}\right)}{\mathrm{d}\bar{x}^2} + \frac{\mathrm{d}^2 \varphi\left(\bar{x}, \bar{y}\right)}{\mathrm{d}\bar{y}^2} \right] \mathrm{d}\bar{x}\mathrm{d}\bar{y} = (\eta V_{\mathrm{in}})\, w_0 \tag{6.42}$$

$$I_{\mathrm{piezo}} = \int_{-\gamma/2}^{\gamma/2} \int_{-\gamma/2}^{\gamma/2} \left[\frac{\mathrm{d}^2 \varphi\left(\bar{x}, \bar{y}\right)}{\mathrm{d}\bar{x}^2} + \frac{\mathrm{d}^2 \varphi\left(\bar{x}, \bar{y}\right)}{\mathrm{d}\bar{y}^2} \right] \mathrm{d}\bar{x}\mathrm{d}\bar{y} \tag{6.43}$$

and

$$\eta = \frac{1}{2} e_{31,f}\, \bar{z}_{\mathrm{p}} I_{\mathrm{piezo}} \tag{6.44}$$

The final parameter of the equivalent circuit model, the modal mass, is defined analogously,

$$L_{\mathrm{m}} = l^2 \mu \int_{-1/2}^{1/2} \int_{-1/2}^{1/2} \varphi\left(\bar{x}, \bar{y}\right)^2 \mathrm{d}\bar{x}\mathrm{d}\bar{y} = m \int_{-1/2}^{1/2} \int_{-1/2}^{1/2} \varphi\left(\bar{x}, \bar{y}\right)^2 \mathrm{d}\bar{x}\mathrm{d}\bar{y} \tag{6.45}$$

The mode shapes of the first six vibration modes for a square plate are illustrated in Fig. 6.7. We assume that the two-dimensional mode shape is separable into two one-dimensional functions, $\varphi_{ij}\left(\bar{x}, \bar{y}\right) = \varphi_i\left(\bar{x}\right) \varphi_j\left(\bar{y}\right)$. For example, the first mode can be analyzed using the same mode shapes used to analyze the beam, $\varphi_{11}\left(\bar{x}, \bar{y}\right) = \varphi_1\left(\bar{x}\right) \varphi_1\left(\bar{y}\right) = \left(1 - 4\bar{x}^2\right)^2 \left(1 - 4\bar{y}^2\right)^2$. Substituting the mode shape function, $\varphi_{11}\left(\bar{x}, \bar{y}\right)$, into the elastic energy integral I_{elastic}, and piezoelectric coupling integral I_{piezo} we find

$$k_{\mathrm{m}} = (166.4 + 47.6 v_{12}) \frac{D}{l^2}$$

$$\eta = 16 e_{31,f}\, \bar{z}_{\mathrm{p}} \left[\gamma^2 \left(\gamma^2 - 1\right) \left(\frac{\gamma^4}{5} - \frac{2\gamma^2}{3} + 1 \right) \right]$$

$$\mathrm{L}_{\mathrm{m}} = 0.165 m$$

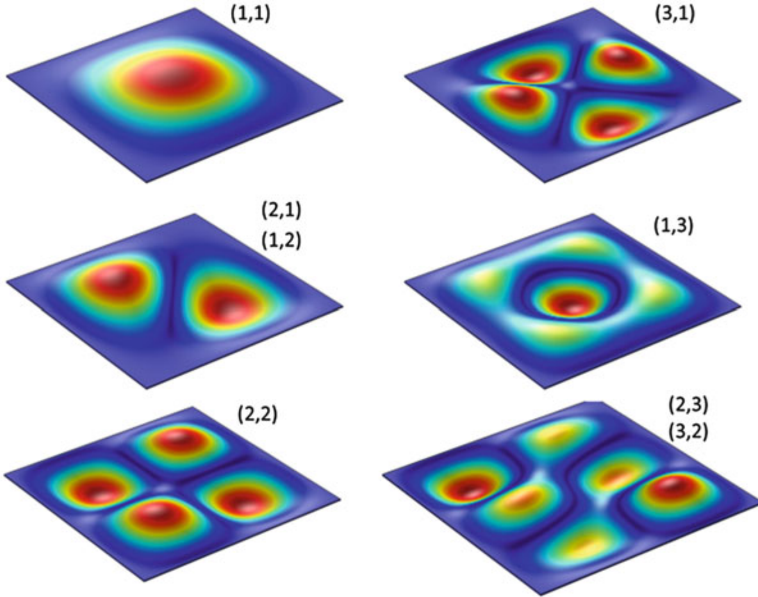

Fig. 6.7 mode-shapes of a rectangular plate, obtained via FEM modeling

Table 6.2 Eigenvalues λ_{ij}^2 of the first four modes of a square plate with clamped boundary conditions

λ_{ij}^2	$i = 1$	$i = 2$
$j = 1$	35.99	73.41
$j = 2$	73.41	108.3

where m is the total mass of the plate. The resulting natural frequency is

$$\omega_{11} = \sqrt{\frac{1}{L_m C_m}} = \frac{12\sqrt{2v_{12} + 7}}{l^2} \sqrt{\frac{D}{\mu}} \tag{6.46}$$

To allow comparison with the natural frequency predicted using Eq. (6.7), the eigenvalues λ_{ij}^2 of a square plate with clamped boundary conditions for $i, j = (1,2)$ are listed in Table 6.2. The error between the approximate solution from Eqs. (6.46) and (6.7) is 8 % assuming that $v_{12} = 0.3$.

Comparing a square 2D resonator with a 1D beam, the fundamental frequency of a square plate is approximately eight times higher than that of a 1D beam of the same length. By comparing Eq. (6.22) with Eq. (6.44), it can be seen that the electromechanical coupling η of the square plate resonator is l/b times larger than that of the beam resonator, assuming I_{piezo} is similar (I_{piezo} is -5.7 for a square plate resonator and -6.2 for a beam resonator when $\gamma = 0.58$).

6.5.2 Round Plates

Round plates may be solved using similar methods, with the vibration mode shape defined in polar coordinates, $\varphi_{ij}\left(\overline{r},\theta\right) = \varphi_i\left(\overline{r}\right)\varphi_j(\theta)$. Here, we define the normalized radial coordinate as $\overline{r} = r/a$ where a is the plate's radius. In polar coordinates, the elastic strain energy is

$$U_{\text{elastic}} = \frac{1}{2}\frac{D}{a^2}I_{\text{elastic}}w_0^2 \tag{6.47}$$

$$I_{\text{elastic}} = \int_0^{2\pi}\int_0^1 \Big\{\Big(\frac{\partial^2\varphi}{\partial\overline{r}^2} + \frac{1}{\overline{r}}\frac{\partial\varphi}{\partial\overline{r}} + \frac{1}{\overline{r}^2}\frac{\partial^2\varphi}{\partial\theta^2}\Big)^2$$
$$-2(1-\text{v}_{12})\Big[\frac{\partial^2\varphi}{\partial\overline{r}^2}\Big(\frac{1}{\overline{r}}\frac{\partial\varphi}{\partial\overline{r}} + \frac{1}{\overline{r}^2}\frac{\partial^2\varphi}{\partial\theta^2}\Big) - \Big(\frac{1}{\overline{r}^2}\frac{\partial\varphi}{\partial\theta} - \frac{1}{\overline{r}}\frac{\partial^2\varphi}{\partial\overline{r}\partial\theta}\Big)^2\Big]\Big\}\overline{r}\,\mathrm{d}\overline{r}\,\mathrm{d}\theta \tag{6.48}$$

and the piezoelectric energy is:

$$U_{\text{piezo}} = \frac{1}{2}M_{\text{p}}I_{\text{piezo}}w_0 \tag{6.49}$$

$$I_{\text{piezo}} = \int_0^{2\pi}\int_0^{\gamma}\left(\frac{\partial^2\varphi}{\partial\overline{r}^2} + \frac{1}{\overline{r}}\frac{\partial\varphi}{\partial\overline{r}} + \frac{1}{\overline{r}^2}\frac{\partial^2\varphi}{\partial\theta^2}\right)\overline{r}\,\mathrm{d}\overline{r}\,\mathrm{d}\theta \tag{6.50}$$

In the case of the axisymmetric mode shapes $\varphi_j(\theta) = 1$, and the integrals are simplified:

$$I_{\text{elastic}} = 2\pi\int_0^1\left[\left(\frac{\partial^2\varphi}{\partial\overline{r}^2}\right)^2 + \frac{2v_{12}}{\overline{r}}\frac{\partial^2\varphi}{\partial\overline{r}^2}\frac{\partial\varphi}{\partial\overline{r}} + \left(\frac{1}{\overline{r}}\frac{\partial\varphi}{\partial\overline{r}}\right)^2\right]\overline{r}\,\mathrm{d}\overline{r} \tag{6.51}$$

$$k_{\text{m}} = \frac{D}{a^2}I_{\text{elastic}} \tag{6.52}$$

$$I_{\text{piezo}} = 2\pi\int_0^{\gamma}\left(\frac{\partial^2\varphi}{\partial\overline{r}^2} + \frac{1}{\overline{r}}\frac{\partial\varphi}{\partial\overline{r}}\right)\overline{r}\,\mathrm{d}\overline{r} \tag{6.53}$$

$$\eta = \frac{1}{2}e_{31,f}\overline{z}_{\text{p}}I_{\text{piezo}}$$

The mode shapes of the first four vibration modes for a circular plate are illustrated in Fig. 6.8 along with the mode shapes and corresponding natural frequencies of a 510 μm diameter circular piezoelectric resonator measured via scanning laser Doppler vibrometer (LDV).

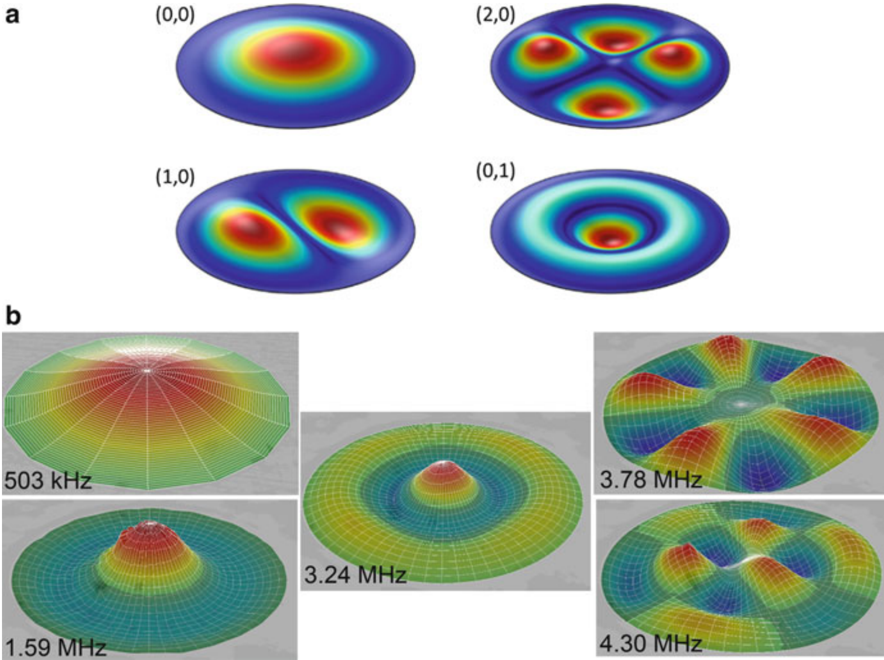

Fig. 6.8 (**a**) Mode shapes of a circular plate, obtained via FEM. (**b**) Vibration mode shapes and corresponding natural frequencies of a 510 μm diameter circular piezoelectric resonator

Table 6.3 Eigenvalues λ_{ij}^2 of the first 16 modes of a circular plate with clamped boundary conditions.

λ_{ij}^2	$i = 0$	1	2	3
$j = 0$	10.22	21.26	34.88	51.04
1	39.77	60.82	84.58	111.0
2	89.1	120.1	153.8	190.3
3	158.2	199.1	242.7	289.2

The exact equation for a circular plate's mode shape is

$$\varphi_{ij}\left(\bar{r},\theta\right) = \left[J_i\left(\lambda_{ij}\bar{r}\right) - \frac{J_i\left(\lambda_{ij}\right)}{I_i\left(\lambda_{ij}\right)} I_i\left(\lambda_{ij}\bar{r}\right)\right]\cos\left(j\theta\right) \tag{6.54}$$

where I_i and J_i are Bessel functions and the eigenvalues λ_{ij} are the solutions of

$$J_i\left(\lambda\right) I_{i+1}\left(\lambda\right) + I_i\left(\lambda\right) J_{i+1}\left(\lambda\right) = 0 \tag{6.55}$$

The eigenvalues for the first several modes are summarized in Table 6.3.

Considering the first vibration mode of a clamped circular plate $\left(\lambda_{00}^2 = 10.22\right)$, the mode shape is given by

$$\varphi_{00}\left(\bar{r}\right) = J_0\left(3.2\bar{r}\right) + 0.0555 I_0\left(3.2\bar{r}\right) \tag{6.56}$$

We use a simplified mode shape that is identical to the one used to analyze the beam and square plate,

$$\varphi\left(\bar{r}\right)=\left(1-\bar{r}^2\right)^2 \tag{6.57}$$

which yields

$$\mathrm{C_m}=\frac{1}{\pi}\frac{3}{64}\frac{\mathrm{a}^2}{\mathrm{D}} \tag{6.58}$$

$$\eta=4\pi\gamma^2\left(\gamma^2-1\right)\mathrm{e_{31,f}}\bar{\mathrm{z}}_\mathrm{p} \tag{6.59}$$

$$\mathrm{L_m}=\frac{\pi\mathrm{a}^2\mu}{5}=0.2\mathrm{m} \tag{6.59}$$

The resulting natural frequency for this mode is

$$\omega_0=\frac{10.327}{a^2}\sqrt{\frac{D}{\mu}} \tag{6.60}$$

In comparison with the exact natural frequency from Eq. (6.7), the approximate solution for the natural frequency is within 1 % of the exact value.

Note that in deriving the values of C_m and L_m above we have used the displacement at the center of the circular plate, w_0. In modeling acoustic resonators, some authors [23, 24] use the average displacement, $\bar{w}=w_0/3$, which results in different motional impedance values, $\bar{L}_\mathrm{m}=9L_\mathrm{m}$ and $\bar{C}_\mathrm{m}=C_\mathrm{m}/9$.

6.5.3 Example – Predicting Coupling to Multiple Vibration Modes

A circular piezoelectric micromachined ultrasonic transducer (PMUT) [25] with a single central electrode covering 70 % of the PMUT ($\gamma=0.7$) was designed to excite transducer's (0,0) vibration mode. The device has a 255 µm radius and is composed of a 1 µm AlN layer on a 4 µm Si elastic layer. The measured frequency response, Fig. 6.9, shows both the (0,0) mode at f_0 =402.8 kHz and the (0,1) vibration mode at f_1 =1517 kHz. Using the analysis presented above, the expected amplitude ratio for these modes can be computed from

$$\frac{w\left(f_0\right)}{w\left(f_1\right)}=\frac{Q_0}{Q_1}\frac{C_{\mathrm{m}0}}{C_{\mathrm{m}1}}\frac{\eta_0}{\eta_1}$$

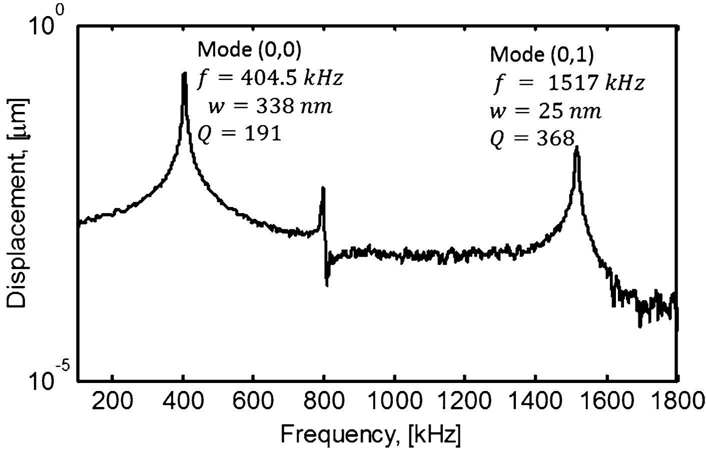

Fig. 6.9 Measured PMUT displacement frequency response showing the (0,0) and (0,1) vibration modes

where the subscripts 0 and 1 denote the appropriate parameters for the (0,0) and (0,1) modes. Similarly, the frequency ratio of these modes is given by:

$$\frac{f_1}{f_0} = \sqrt{\frac{L_{m0}}{L_{m1}} \frac{C_{m0}}{C_{m1}}}$$

To compute these parameters, we use the following approximate mode shapes in the integrals for modal mass, modal compliance, and electromechanical coupling constant.

$$\varphi_{00}\left(\bar{r}\right) = 0.5\left(1 + \cos\left(\pi \bar{r}\right)\right) \tag{6.61}$$

$$\varphi_{01}\left(\bar{r}\right) = 0.5\left(\cos\left(\pi \bar{r}\right) + \cos\left(2\pi \bar{r}\right)\right) \tag{6.62}$$

The resulting ratios are:
$C_{m0}/C_{m1} = 11.6$, $L_{m0}/L_{m1} = 1.25$, $\eta_0/\eta_1 = 0.74$
where only the last ratio depends on the electrode geometry.
Using these values, and assuming that both modes have the same Q, we calculate the amplitude and frequency ratios of the two modes to be:

$\frac{w(f_0)}{w(f_1)} = 8.6$ and $\frac{f_0}{f_1} = 0.26$.

The measured frequency ratio is 0.27 while the measured amplitude ratio is 26:1, after correcting for the measured difference in Q between the two modes. The difference between the predicted and experimental amplitude ratio may be due

to the fact that η_1, the piezoelectric coupling to the (0,1) mode, is very sensitive to the electrode diameter—reducing γ from 0.7 to 0.62 reduces η_1 by a factor of 3, producing better agreement with the experiment.

References

1. Karabalin RB, Matheny MH, Feng XL, Defay E, Le Rhun G, Marcoux C, Hentz S, Andreucci P, Roukes ML (2009) Piezoelectric nanoelectromechanical resonators based on aluminum nitride thin films. Appl Phys Lett 95:103111 (3 pp.)-103111 (3 pp.)
2. Piazza, G., Abdolvand, R., Ho, G. K. & Ayazi, F. 2004. Voltage-tunable piezoelectrically-transduced single-crystal silicon micromechanical resonators. Sens Actuat A Phys, A111,71–78.
3. Leighton GJT, Kirby PB, Fox CHJ (2007) In-plane excitation of thin silicon cantilevers using piezoelectric thin films. *Applied Physics Letters* 91:183510–1–183510-183510-3
4. Sokmen, U., Stranz, A., Waag, A., Ababneh, A., Seidel, H., Schmid, U. & Peiner, E. 2010. Evaluation of resonating Si cantilevers sputter-deposited with AlN piezoelectric thin films for mass sensing applications. J Micromech Microeng, 20**,** 064007 (7 pp.)-064007 (7 pp.).
5. Vigevani G, Goericke FT, Pisano AP, Izyumin II, Boser BE (2012) Microleverage DETF aluminum nitride resonating accelerometer. Frequency Control Symposium (FCS), 2012 IEEE International, 21–24 May 2012, pp 1–4
6. Griffin BA, Williams MD, Coffman CS, Sheplak M (2011) Aluminum nitride ultrasonic air-coupled actuator. IEEE/ASME J Microelectromech Syst 20:476–486
7. Guedes, A., Shelton, S., Przybyla, R., Izyumin, I., Boser, B. & Horsley, D. (2011) Aluminum nitride pMUT based on a flexurally-suspended membrane. The 16th International Conference on Solid-State Sensors and Actuators (Transducers), Bejing, China, 6 Jun 2011
8. Shelton S, Chan ML, Park H, Horsley D, Boser B, Izyumin I, Przybyla R, Frey T, Judy M, Nunan K, Sammoura F ,Yang K (2009) CMOS-compatible AlN piezoelectric micromachined ultrasonic transducers. IEEE ultrasonics symposium, Rome, Italy, September 2009 pp 402-405.
9. Devoe DL, Pisano AP (1997) Modeling and optimal design of piezoelectric cantilever microactuators. J Microelectromech Syst 6:266–270
10. Weinberg MS (1999) Working equations for piezoelectric actuators and sensors. J Microelectromech Syst 8:529–533
11. Weinberg MS, Cunningham BT, Clapp CW (2000) Modeling flexural plate wave devices. J Microelectromech Syst 9:370–379
12. Wang Q, Lu Y, Fung S, Jiang X, Mishin S, Oshmyansky Y, Horsley DA (2016) Scandium doped aluminum nitride based piezoelectric micromachined ultrasonic transducers. Solid State Sensor, Actuator and Microsystems Workshop. Hilton Head, SC
13. Muralt P, Ledermann N, Paborowski J, Barzegar A, Gentil S, Belgacem B, Petitgrand S, Bosseboeuf A, Setter N (2005) Piezoelectric micromachined ultrasonic transducers based on PZT thin films. IEEE Trans Ultrasonics Ferroelectrics Frequency Control 52:2276–2288
14. Reddy JN (1997) Mechanics of laminated composite plates: theory and analysis. CRC press, Boca Raton
15. Blevins RD (2001) Formulas for Natural Frequency and Mode Shape. Krieger Pub Co, Malabar,FL
16. Muralt P, Kholkin A, Kohli M, Maeder T (1996) Piezoelectric actuation of PZT thin-film diaphragms at static and resonant conditions. Sens Actuat A Phys 53:398–404
17. Mcneil LE, Grimsditch M, French RH (1993) Vibrational spectroscopy of aluminum nitride. J Am Ceram Soc 76:1132–1136

18. Wright AF (1997) Elastic properties of zinc-blende and wurtzite AlN, GaN, and InN. J Appl Phys 82:2833–2839
19. Tsubouchi K, Sugai K, Mikoshiba N (1981) AlN material constants evaluation and SAW properties on AlN/A2O3 and AlN/Si. Ultrasonics Symposium
20. Lu Y, Wang Q, Horsley DA (2015) Piezoelectric micromachined ultrasonic transducers with increased coupling coefficient via series transduction. Ultrasonics Symposium (IUS), 2015 IEEE Int 21–24 Oct 2015.pp 1–4
21. Sammoura F, Shelton S, Akhbari S, Horsley D, Lin L (2014) A two-port piezoelectric micromachined ultrasonic transducer. Applications of Ferroelectrics, International Workshop on Acoustic Transduction Materials and Devices & Workshop on Piezoresponse Force Microscopy (ISAF/IWATMD/PFM), 2014 Joint IEEE International Symposium on the. 12–16 May 2014, pp 1–4
22. Timoshenko S, Woinowsky S (1959) Theory of plates and shells. McGraw-Hill, New York
23. Smyth K, Kim SG (2015) Experiment and simulation validated analytical equivalent circuit model for piezoelectric micromachined ultrasonic transducers. IEEE Trans Ultrason Ferroelectr Freq Control 62:744–765
24. Wygant, I. O., Kupnik, M. & Khuri-Yakub, B. T (2008) Analytically calculating membrane displacement and the equivalent circuit model of a circular CMUT cell. 2008 IEEE Ultrasonics Symposium, 2–5 Nov 2008, pp 2111–2114
25. Rozen O, Shelton SE, Guedes A & Horsley, D. A. (2014) Variable thickness diaphragm for a stress insensitive wideband piezoelectric micromachined ultrasonic transducer. Solid-state sensors, actuators & microsystems workshop. Hilton Head

Chapter 7
Laterally Vibrating Piezoelectric MEMS Resonators

Matteo Rinaldi

7.1 Introduction

Sensors are found in a wide variety of applications, such as smart mobile devices, automotive, healthcare, and environmental monitoring. The recent advancements in terms of sensor miniaturization, low power consumption, and low cost allow envisioning a new era for sensing in which the data collected from multiple individual smart sensor systems are combined to get information about the environment that is more accurate and reliable than an individual sensor data. By leveraging such sensor fusion it will be possible to acquire complete and accurate information about the context in which human beings live, which has huge potential for the development of the Internet of Things (IoT) in which physical and virtual objects are linked through the exploitation of sensing and communication capabilities with the intent of making life simpler and more efficient for human beings.

This trend towards sensor fusion has dramatically increased the demand of new technology platforms, capable of delivering multiple sensing and wireless communication functionalities in a small foot print. In this context, Micro- and Nanoelectromechanical systems (MEMS/NEMS) technologies can have a tremendous impact since they can be used for the implementation of high-performance sensors and wireless communication devices with reduced form factor and Integrated Circuit (IC) integration capability.

This chapter describes a particular class of laterally vibrating piezoelectric MEMS resonators that can address some of the most important challenges in the areas of physical, chemical, and biological detection and can be simultaneously used to synthesize high-Q multifrequency radio frequency (RF) resonant devices. Particular attention is dedicated to the basic concepts needed to understand the working

M. Rinaldi (✉)
Department of Electrical and Computer Engineering, Northeastern University, Boston, MA, USA
e-mail: rinaldi@ece.neu.edu

© Springer International Publishing Switzerland 2017

H. Bhugra, G. Piazza (eds.), *Piezoelectric MEMS Resonators*,
Microsystems and Nanosystems, DOI 10.1007/978-3-319-28688-4_7

principle, design, fabrication, and testing of such laterally vibrating piezoelectric resonant MEMS/NEMS devices including structural mechanics, piezoelectric sensing and actuation principles, lumped modeling of mechanical vibration, material properties, and fabrication technologies. Furthermore, key applications and ongoing challenges are identified and discussed through a state of the art review of demonstrated device prototypes including sensors and RF components.

7.2 Operating Principle

A typical laterally vibrating piezoelectric resonator is formed by a thin-film piezoelectric film sandwiched between metallic electrodes (Fig. 7.1). The application of a potential across the thickness of the piezoelectric film induces a lateral strain in the plane of the device. When the frequency of the excitation signal coincides with the mechanical resonance of the piezoelectric body, the device exhibits enhanced amplitude of vibration, which is translated to an electrical signal by the direct piezoelectric effect and generates a charge proportional to the amplitude of the displacement.

The modes and the resonant frequencies of the lateral vibrating structure can be determined by solving the wave equation with proper boundary conditions. For a longitudinal bar resonator vibrating along its width (width-extensional) the wave equation in one space dimension can be written as:

$$\rho \frac{\partial^2 u}{\partial t^2} = E_{\mathrm{p}} \frac{\partial^2 u}{\partial x^2} \tag{7.1}$$

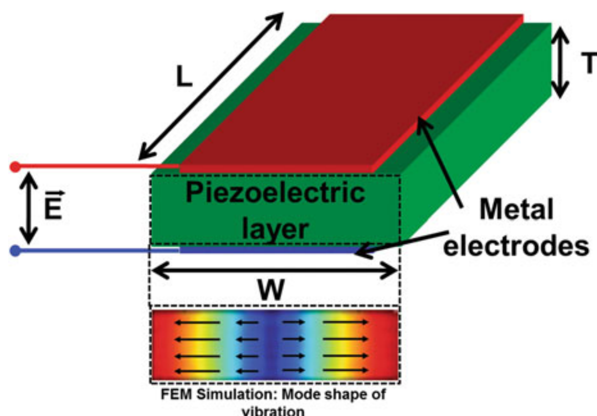

Fig. 7.1 Mock-up view of a typical laterally vibrating piezoelectric resonator

Where ρ and E_{p} are respectively the equivalent density and Young's modulus of the material stack forming the bar, u is the displacement, t is time, and x is the one-dimensional space dimension (direction of vibration). A general solution for Eq. 7.1 is:

$$u\,(x,t) = [a \sin\,(\beta x) + b \cos\,(\beta x)]\, e^{j\omega_0 t} \tag{7.2}$$

Considering a bar of width, W, and applying the boundary conditions that there is no stress and no stress gradient at the free lateral boundaries of the bar ($x = \pm W/2$) the solution of the wave equation for the width-extensional vibration of the bar becomes:

$$u\,(x,t) = U(x)X(t) = \sin\,(\beta_n x)\, e^{j\omega_0 t} \tag{7.3}$$

$$\beta_n = (2n-1)\,\frac{\pi}{W} \tag{7.4}$$

By substituting Eq. 7.3 into Eq.7.1, the resonant frequencies of the width-extensional bar can be readily found. In particular, by computing the solution for $n = 1$ the fundamental mode of vibration of the structure (at frequency f_0) can be derived:

$$f_0 = \frac{1}{2W}\sqrt{\frac{E_{\mathrm{p}}}{\rho}} \tag{7.5}$$

Equation 7.5 highlights a key feature of laterally vibrating resonators: the operating frequency of the resonator is set by the in-plane lateral geometrical dimension of the structure (width in the case of a width-extensional bar). This enables the possibility of lithographically defining multiple frequency devices on the same substrate and effectively producing components that are capable of operating over a broad spectrum independently from the thickness, T, and length, L, of the piezoelectric structure. Therefore, the device thickness and length can be independently selected to define the electrical static capacitance, C_0, of the piezoelectric transducer and therefore its electrical impedance.

A laterally vibrating resonator, as any other second order mechanical system, can be represented by an equivalent lumped mass, a spring and a damper that depend on the mode of vibration of the structure. An equivalent mass, m_{eff}, that has the same characteristic of the overall resonator but lumped at a specific location of interest (typically at the point of maximum displacement, $x = x_{\max}$) can be derived bay equating the kinetic energy at the point of interest (i.e. point of maximum displacement) to the overall kinetic energy of the vibrating body:

$$\frac{1}{2} m_{\mathrm{eff}} \left(\frac{\mathrm{d}X}{\mathrm{d}t}\right)^2 = \frac{1}{2}\int_{-W/2}^{W/2} \rho LT \left(\frac{\mathrm{d}X}{\mathrm{d}t}\right)^2 U(x)^2 \mathrm{d}x \tag{7.6}$$

$$m_{\text{eff}} = \rho LT \int_{-W/2}^{W/2} \sin^2(\beta x)\,\mathrm{d}x = \frac{\rho LTW}{2} \tag{7.7}$$

Since the mass and the spring of a second order mechanical system are intrinsically related by the resonance angular frequency, ω_0, of the structure ($\omega_0 = \sqrt{k_{\text{eff}}/m_{\text{eff}}}$), the equivalent spring constant, k_{eff}, can be readily found:

$$k_{\text{eff}} = \frac{\pi^2}{2}\frac{E_{\text{p}}TL}{W} \tag{7.8}$$

Furthermore, for a given quality factor, Q (ratio of the energy stored in the oscillating resonator to the energy dissipated per cycle by damping processes), the effective damping coefficient of the resonator can be expressed as:

$$b_{\text{eff}} = \frac{m_{\text{eff}}\omega_0}{Q} \tag{7.9}$$

These lumped mechanical variables of the laterally vibrating resonator can be made to correspond to equivalent electrical variables in order to model the behavior of the mechanical structure in terms of circuit parameters (resistance, inductance, and capacitance), for which well-established and powerful analysis tools and design techniques already exist (Fig. 7.2).

Furthermore, the intrinsic capability of the piezoelectric structure to convert mechanical displacement into an electrical signal (and vice versa) can be represented

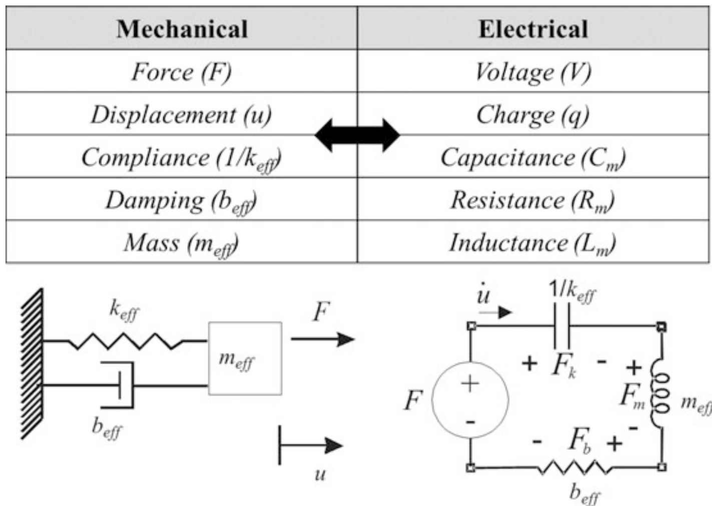

Mechanical	Electrical
Force (F)	*Voltage (V)*
Displacement (u)	*Charge (q)*
Compliance ($1/k_{eff}$)	*Capacitance (C_m)*
Damping (b_{eff})	*Resistance (R_m)*
Mass (m_{eff})	*Inductance (L_m)*

Fig. 7.2 Electrical equivalents for mechanical lumped elements

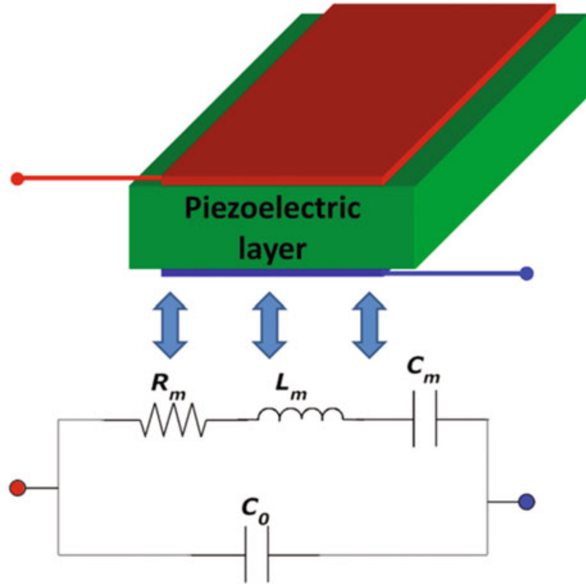

Fig. 7.3 Equivalent electrical circuit of a laterally vibrating piezoelectric resonator

by an electromechanical transduction factor, η, that relates force to voltage and charge to displacement:

$$\eta = \frac{F}{V} = \frac{q}{u} \tag{7.10}$$

$$F = m_{\text{eff}}\ddot{u} + b_{\text{eff}}\dot{u} + k_{\text{eff}}u \;\rightarrow\; V = \frac{m_{\text{eff}}}{\eta^2}\ddot{q} + \frac{b_{\text{eff}}}{\eta^2}\dot{q} + \frac{k_{\text{eff}}}{\eta^2}q \tag{7.11}$$

Therefore, the piezoelectric laterally vibrating resonator can be represented by the equivalent electrical circuit in Fig. 7.3 consisting of two branches in parallel: an acoustic branch, composed by the series combination of the motional resistance, $R_{\text{m}} = b_{\text{eff}}/\eta^2$ (quantifying dissipative losses), motional capacitance, $C_{\text{m}} = \eta^2/k_{\text{eff}}$ (inversely proportional to the effective stiffness), and motional inductance, $L_{\text{m}} = m_{\text{eff}}/\eta^2$ (proportional to the effective mass), and an electrical branch composed by the static electrical capacitance, C_0, of the piezoelectric transducer (i.e. parallel plate capacitance formed by the piezoelectric material sandwiched between two metal electrodes).

For a given geometry and material properties of the mechanical structure, the value of the electromechanical transduction factor, η, determines the equivalent electrical impedance of the resonator. In general, for piezoelectric resonators, η can be computed through a three-dimensional analysis of the piezoelectric constitutive equations that determine the relationship between the stress, the strain, and the electric field in the piezoelectric material employed. A matrix formalism is typically

required to account for the anisotropic nature of piezoelectric materials and the three-dimensional spatial distribution of the electric field. Nevertheless, a one-dimensional analysis, assuming displacement only in one direction and a uniform distribution of electric field in one dimension, provides a relatively simple model that well approximates the actual behavior of the majority of practical piezoelectric resonators.

In the case of a piezoelectric laterally vibrating resonator (i.e. width-extensional) it is possible to assume that an uniform electric field applied across the thickness of the piezoelectric layer, E_3, generates an orthogonal stress along the width of the structure, T_1 (the axis direction x, y, and z are indicated with numbers *1*, *2,* and *3* respectively). Therefore, the piezoelectric constitutive equations can be simplified to:

$$T_1 = c_{11}S_1 - e_{31}E_3 \tag{7.12}$$

$$D_3 = \epsilon_{33}E_3 + e_{31}S_1 \tag{7.13}$$

where c_{11} is the longitudinal stiffness coefficient of the material forming the resonator, S_1 is the longitudinal strain, e_{31} is the piezoelectric coefficient (in C/m^2) relating the electric field along the z direction ('3') to the longitudinal stress along the x direction ('1'), D_3 is the electric displacement field along the z direction and ϵ_{33} is the dielectric constant of the material in the direction of the electric filed. Therefore, the general relationship between the voltage applied across the thickness of the piezoelectric layer, V, and the generated longitudinal force, F, is given by:

$$F = e_{31}LV \tag{7.14}$$

where L is the length of the longitudinal bar (along the y dimension).

Nevertheless, the efficiency of this force in exciting the vibration mode described by Eq. 7.3 depends on the location it is applied along the width of the bar. Indeed, the structure is most efficiently actuated from the two ends ($x = \pm W/2$) that have the highest vibration amplitude, while the same force applied in the center of the bar ($x = 0$), where the displacement is zero (nodal point), will not excite the resonant mode. Therefore, the location of the transducer must be taken into account when computing the electromechanical transduction factor of the distributed laterally vibrating bar resonator. Assuming that the electrode covers the entire surface of the bar and accounting for the force on both the electrode edges (at $x = \pm W/2$) and the mode shape in Eq. 7.3, the relationship between the effective force acting on the resonator, F_{eff}, and the applied voltage, hence the electromechanical transduction factor of the resonator, η, can be calculated as shown in Eqs. 7.15 and 7.16 (where $U(x)$ is the normalized mode shape of vibration with maximum amplitude equal to 1).

$$F_{\text{eff}} = e_{31}LV\left(U\left(\frac{W}{2}\right) - U\left(-\frac{W}{2}\right)\right) = 2e_{31}LV \tag{7.15}$$

$$\eta = \frac{F}{V} = 2e_{31}L \tag{7.16}$$

The relationship between charge, q, and displacement, u, of a laterally vibrating resonator (i.e. width-extensional) can be found by integrating Eq. 7.13 along the direction of displacement (i.e. assuming displacement only along the width of the bar, $u(x,t) = X(t)U(x)$, and an uniform electric field distribution across its thickness):

$$\int_{-W/2}^{W/2} D_3 \mathrm{d}x = \int_{-W/2}^{W/2} \varepsilon_{33} E_3 \mathrm{d}x + \int_{-W/2}^{W/2} e_{31} S_1 \mathrm{d}x \tag{7.17}$$

$$D_3 = \varepsilon_{33}\frac{V}{T} + \frac{e_{31}}{W}\left[u\left(\frac{W}{2}\right) - u\left(-\frac{W}{2}\right)\right] \tag{7.18}$$

$$i = \dot{q} = \varepsilon_{33}\frac{WL}{T}\dot{V} + e_{31}L\dot{X}\left[U\left(\frac{W}{2}\right) - U\left(-\frac{W}{2}\right)\right] \tag{7.19}$$

$$i = \dot{q} = \varepsilon_{33}\frac{WL}{T}\dot{V} + 2e_{31}L\dot{X} \tag{7.20}$$

Therefore, the electromechanical transduction factor, η, relating force, F, to voltage, V, and charge, q, to displacement, X, in width-extensional laterally vibrating resonator is given by:

$$\eta = \frac{F}{V} = \frac{q}{X} = 2e_{31}L \tag{7.21}$$

By substituting Eqs. 7.7–7.9 and 7.21 in Eq. 7.11 it is possible to find expressions for the equivalent circuit elements, describing the width-extensional resonator, as functions of the device geometrical dimensions and material properties (assuming $E_\mathrm{p} \approx c_{11}$ in case of one-dimensional longitudinal displacement along the width):

$$R_\mathrm{m} = b_\mathrm{eff}/\eta^2 = \frac{\pi}{8}\frac{T}{L}\frac{\sqrt{E_\mathrm{p}\rho}}{Qe_{31}^2} \tag{7.22}$$

$$C_\mathrm{m} = \eta^2/k_\mathrm{eff} = \frac{8}{\pi^2}\frac{WL}{T}\frac{e_{31}^2}{E_\mathrm{p}} \tag{7.23}$$

$$L_\mathrm{m} = m_\mathrm{eff}/\eta^2 = \frac{\rho}{8}\frac{WT}{L}\frac{1}{e_{31}^2} \tag{7.24}$$

$$C_0 = \varepsilon_{33}\frac{WL}{T} \tag{7.25}$$

It is worth noting that this simple model neglects the intrinsic coupling between transversal and axial strains determined by the Poisson's ratio, ν, of the material which, for an electric field applied across the thickness of the bar, induces an additional lateral stress, $T_1 \approx \nu e_{33} E_3$, that effectively increases the electromechanical coupling factor of the laterally vibrating resonator to $\eta \approx 2L\,(e_{31} + \nu e_{33})$.

Two parameters that best describe the performance of any electromechanical resonator are the quality factor, Q, and electromechanical coupling coefficient, k_t^2. The quality factor is a dimensionless parameter representing the ratio of the energy stored in the vibrating resonant structure to the energy dissipated per cycle by the damping processes (the higher is the Q, the lower is the energy loss), while the electromechanical coupling coefficient is a quantitative measure of the conversion between the electrical and mechanical energy in the electromechanical resonator:

$$k_\mathrm{t}^2 = \frac{\pi^2}{8}\frac{C_\mathrm{m}}{C_0} \tag{7.26}$$

$$\frac{C_\mathrm{m}}{C_0} = \frac{\frac{1}{2}k_\mathrm{eff}\frac{\eta^2 V^2}{k_\mathrm{eff}{}^2}}{\frac{1}{2}C_0 V^2} = \frac{\frac{1}{2}k_\mathrm{eff}\left(\frac{F}{k_\mathrm{eff}}\right)^2}{\frac{1}{2}C_0 V^2} = \frac{\frac{1}{2}k_\mathrm{eff}x^2}{\frac{1}{2}C_0 V^2} \tag{7.27}$$

For a given geometrical capacitance, C_0 and angular resonance frequency, ω_0, the motional resistance (R_m), capacitance (C_m) and inductance (L_m) of the resonator are determined by the values of Q and k_t^2.

$$R_\mathrm{m} = \frac{\pi^2}{8}\frac{1}{\omega_0 C_0 k_\mathrm{t}^2 Q} \tag{7.28}$$

$$C_\mathrm{m} = \frac{8}{\pi^2}C_0 k_\mathrm{t}^2 \tag{7.29}$$

$$L_m = \frac{\pi^2}{8}\frac{1}{\omega_0^2 C_0 k_t^2} \tag{7.30}$$

In particular the device equivalent motional resistance, R_m, is inversely proportional to the $k_\mathrm{t}^2 \cdot Q$ product. The achievement of a low value of motional resistance, in a radio frequency electromechanical resonator, is of crucial importance for the direct interface of the device with compact and low-power 50-Ω electronics. Therefore, the figure of merit (FOM) of an electromechanical resonator is defined as the $k_\mathrm{t}^2 \cdot Q$ product. The FOM is the main factor in determining the performance of the system in which it will be used, and affects parameters such as insertion loss and bandwidth in a filter, and power consumption and phase noise in an oscillator or resonant sensor.

In the case of a piezoelectric laterally vibrating resonator, k_t^2 can be readily calculated from Eq. 7.23 and 7.25, highlighting the important results that the energy conversion process in this kind of resonators is completely determined by material properties:

$$k_t^2 = \frac{\pi^2}{8}\frac{C_m}{C_0} = \frac{e_{31}^2}{E_p \varepsilon_{33}} \tag{7.31}$$

7.3 Materials

Laterally vibrating piezoelectric resonators are formed either entirely by a thin-film piezoelectric film sandwiched between metallic electrodes [1, 2] or by a composite constituted by the same piezoelectric film stacked on top of another structural layer such as a semiconducting or insulating material (Fig. 7.4). This layer has generally been introduced to enhance the quality factor, Q, of the pure piezoelectric device. In various demonstrations, materials with intrinsically high Q have been used, such as silicon [3–6], diamond [7], and silicon carbide [8]. Although beneficial, its insertion introduces a trade-off between Q and the electromechanical coupling coefficient, k_t^2. In fact, in the case of purely piezoelectric laterally vibrating resonator, the k_t^2 is set exclusively by material properties (for a given mode of vibration) as shown in Eq. 7.31. In the case of a composite, the intrinsic electromechanical coupling is approximately scaled by the ratio of the thickness of the piezoelectric layer, T_p, to the total thickness of the composite, $T_p + T_s$ (being T_s the thickness of the structural layer). Therefore, composite structures typically show FOM values similar to the ones of purely piezoelectric resonators, but, within fabrication limits, they enable the tuning of k_t^2 and Q values by varying the thickness of the structural layer, T_s (depending on the resonator application, T_s can be tailored to either enhance the device Q or maintain a certain k_t^2).

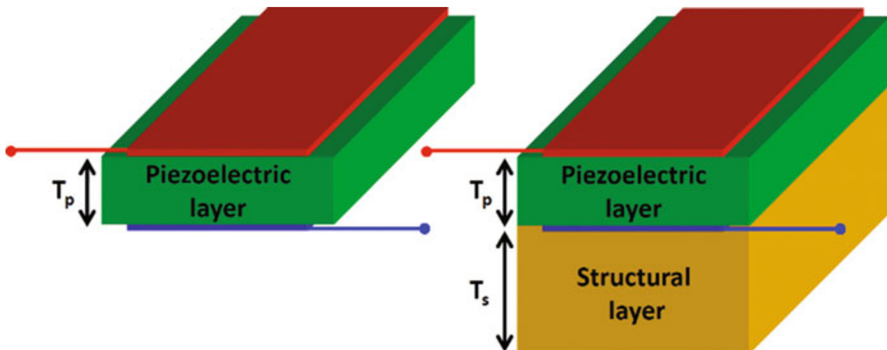

Fig. 7.4 Mock-up view of laterally vibrating piezoelectric resonators formed either by a pure piezoelectric material (*left*) or (*right*) a composite stack of a piezoelectric and semiconducting or insulating material (structural layer)

Various thin-film piezoelectrics have been used for making laterally vibrating resonators, with zinc oxide (ZnO), lead zirconate titanate (PZT), gallium nitride (GaN), aluminum nitride (AlN) and, recently, lithium niobate (LN), being the most commonly available. The selection of one over the others is dictated by material properties, process compatibility, reproducibility, and specific application of interest. For example, PZT offers a very large k_t^2, but exhibits very low Q and therefore is exclusively used in a composite configuration with other materials such as silicon showing values of FOM < 30. On the other side, GaN based laterally vibrating resonators showing high $f_0 \cdot Q$ product values up to 5.5×10^{12} (comparable to the ones of commercially available microacoustic AlN thin-film bulk acoustic resonators, FBARs) have been demonstrated [9, 10]. GaN resonators take also advantage of intrinsic integration capability with GaN HEMTs, which has great potential for the implementation of monolithic microwave ICs (MMICs) platforms in which passive devices (such as resonators and filters) are integrated with GaN active electronics to enable advanced functionalities for high-power and high-frequency applications. Nevertheless, due to the relatively low piezoelectric coupling coefficients of GaN ($\sim 3\times$ lower than AlN), resonators based on this material have shown low values of FOM < 10 [9]. Furthermore, the high temperature (800–1100 °C) epitaxial process needed to grow GaN on a crystalline substrate makes the use of bottom electrodes (commonly employed with sputtered piezoelectric materials, such as AlN) challenging (only possible with post-processing) and has so far required the use of buffer layers, not optimized for MEMS applications, in order to mitigate stress issues in the piezoelectric thin-film. Laterally vibrating resonators with high values of FOM approaching ∼500 have been recently demonstrated using LN thin films [11–13]. This technology suffers from the lack of a deposition technique capable of producing a piezoelectric LN thin film on a substrate which requires the use of complex fabrication techniques involving either wafer bonding and grinding of LN or high energy ion implantation to create an ion damaged release layer below the wafer surface. Nevertheless, the high electromechanical coupling of this new class of laterally vibrating resonators show great promise for the implementation of multifrequency wideband multiplexers and filter banks for reconfigurable RF front-ends. In this context, AlN offers some unique advantages compared with other piezoelectric materials: high-quality AlN thin-films of various thicknesses (from 10s *nm* to several μm) can be easily deposited on a substrate by low-temperature sputtering process showing very reproducible properties with high Q and intermediate values of k_t^2. Laterally vibrating AlN resonator with $f_0 \cdot Q > 5 \times 10^{12}$ and FOM > *30* have been demonstrated [14–16]. Furthermore, the low-temperature sputtering deposition process of thin-film AlN enables staking of multiple AlN and electrode layers which can be properly configured to efficiently transduce the desired mode of vibration of the structure and simultaneously achieve the optimum input and output impedance values. For these reasons AlN has been often considered as a preferred material for the fabrication of purely piezoelectric laterally vibrating resonators.

7.4 Frequency Scaling

In order to attain higher frequency of operation, the frequency setting dimension of the laterally vibrating resonator (i.e. W) needs to be made smaller (Eq. 7.5) (Fig. 7.5a). At the same time, taking into accounts the constraints on C_0 (Eq. 7.25), the surface area of the structure needs to be increased and its thickness reduced in order to maintain a low device electrical impedance (Eq. 7.25). For this purpose the following criteria are proposed as guidelines for the frequency scaling of a laterally vibrating resonator:

- Mechanically couple a large number, n, of subresonators whose width, W, has been scaled to operate at higher frequency (Fig. 7.5b). In this way a higher order mode of vibration is excited in the piezoelectric plate (f_0 is set by W), but the capacitance of the device is n times larger (total width equal to $n \cdot W$).
- Reduce the thickness, T, of the piezoelectric film (Fig. 7.5c). This is extremely important in order to further increase the device capacitance while simultaneously keeping small the effective area occupied by the device.
- Reduce the length, L, of the resonator (Fig. 7.5d) to avoid loading the quality factor of the device with the electrical resistance of the metal electrodes. The reduction in the length of the electrode compensates for the increase in resistance associated with the scaling of the electrode width.

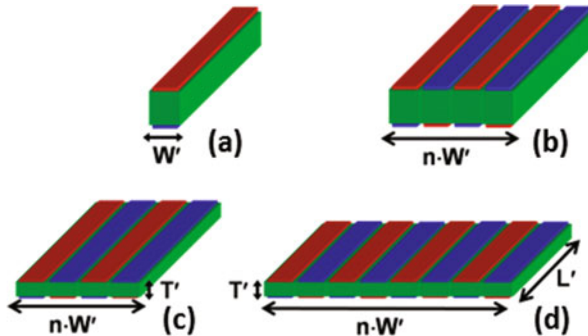

Fig. 7.5 Schematic representation of the scaling criteria for a piezoelectric laterally vibrating resonator [17]: (**a**) scaling of the width to increase the frequency; (**b**) mechanical coupling of a large number of scaled subresonators to increase the device capacitance; (**c**) reduction of the AlN film thickness to increase capacitance and reduce device form factor; (**d**) reduction of the device length to compensate for increase in electrode resistance due to scaling of the width

7.5 Fabrication Techniques

Laterally vibrating piezoelectric resonators are generally fabricated by micromachining techniques. Although each process has its own specific implementation, there are common steps. In particular, standard integrated circuit (IC) processes are used for the deposition and patterning of the metals that sandwich the piezoelectric film. The production and micromachining of the piezoelectric thin-film are the two most challenging steps and require the most attention since the most important resonator characteristics are affected by the property of this film.

Bulk piezoelectric substrates such as quartz and lithium niobate can be micromachined to attain suspended thin films. For example, few groups [17, 18], have successfully demonstrated the capability to transfer high-quality thin film LN on either Si [19, 20], or LN [18] substrates using the crystal ion slicing technique. High-quality LN thin films have also been produced by wafer bonding and grinding of LN or high-energy ion implantation to create an ion damaged release layer below the wafer surface [12, 13, 21]. Nevertheless, the complexity associated with these processes poses some significant challenges in terms of yield and reproducibility of the device fabrication process, miniaturization, and dense integration of resonators on micromachinable substrates. In this context, the use of a piezoelectric material that can be produced as a thin film on a silicon substrate (such as AlN or GaN) can potentially reduce significantly the complexity of the micro-fabrication process (using conventional micro-machining of thin-film materials) and enable the implementation of high performance, miniaturized, and highly integrated resonant devices on a silicon substrate. It is worth noting that compatibility with standard IC processes is crucial for large-scale manufacturing of these devices, which will be ultimately required for commercialization (production of billions of devices is needed for filtering or frequency setting applications). In addition, the monolithic integration of these laterally vibrating resonators with complementary metal oxide semiconductors (CMOS) electronics is highly desirable since it provides circuit designer with an extended library of passive devices (resonators, filters, and sensors) that can be broadly employed for design of high-performance systems with more than Moore functionalities. In this context, aluminum nitride (AlN) offers some unique advantages compared with other piezoelectric materials: high-quality AlN thin-films of various thicknesses (from 10s nm to several μm) can be easily deposited on a substrate by low-temperature sputtering process showing very reproducible properties. Since it is very stable and is not considered to be a contaminant, AlN is already employed in some CMOS facilities. A simple schematic of the fabrication process for an AlN laterally vibrating resonator is shown in Fig. 7.6.

Figure 7.7 is a scanning electron micrograph of a 9.9 GHz AlN laterally vibrating resonator. This is an individual resonator formed by a 250 nm thick AlN nano-plate with a top interdigital electrode properly patterned (99 aluminum fingers with a pitch of 500 nm) to excite an acoustic wave (lamb-wave) in the nano-plate and operate at

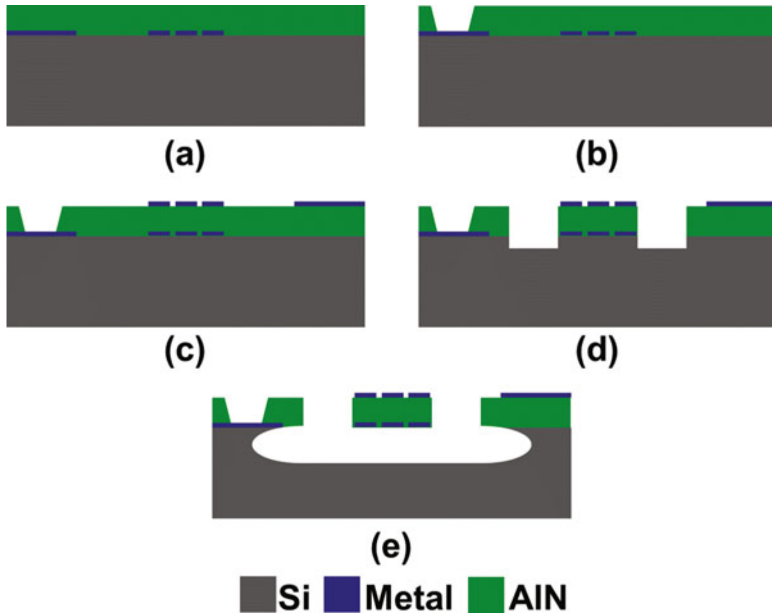

Fig. 7.6 Post-CMOS compatible 4-mask fabrication process for a typical AlN laterally vibrating resonator: (**a**) deposition and patterning of the bottom metal electrode on a high resistivity Si substrate; sputter deposition of the thin AlN piezoelectric layer; (**b**) open vias in AlN to access the bottom electrode; (**c**) deposition and patterning of the top metal electrode; (**d**) dry etching of AlN in Cl_2-based chemistry; (**e**). XeF_2 dry release of the AlN resonator from the Si substrate

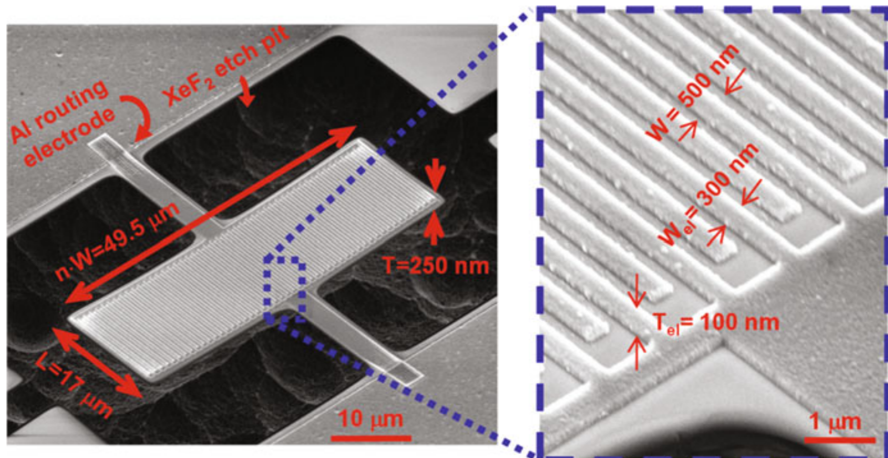

Fig. 7.7 SEM picture of a fabricated 9.9 GHz AlN laterally vibrating NEMS resonator [14] with zoomed view of the nano-patterned interdigital electrode (electrode pitch is 500 nm, electrode width is 300 nm)

a frequency around 9.9 GHz. In this case, only a top electrode is employed (lateral field excitation scheme [14, 15]). The release of this kind of AlN laterally vibrating resonators is straightforward and is generally performed by a dry fluorine etch chemistry that removes the underlying silicon. In the case of a composite structure incorporating silicon, an additional etch step is required to define the structural layer (bulk micromachining of silicon via a Bosch-type process) and generally a silicon dioxide sacrificial layer is employed which is removed by a wet etch step to accomplish device release [4].

7.6 Examples of Demonstrated Prototypes

The piezoelectric laterally vibrating resonator technology has emerged as one of the most promising in enabling the fabrication of multiple frequency and high-performance resonators on the same silicon chip. This is a crucial feature for advanced wireless communication systems, for which single-chip, multiband RF solutions are becoming the dominant trend. The reproducibility of AlN deposition and its compatibility with CMOS fabrication have made it the piezoelectric of choice for such laterally vibrating resonators. These devices have exhibited k_t^2 around 2 % and Q factors as high as 4000 in ambient conditions, with values of FOM > 30 [1, 16, 22, 23]. More recently the frequency of operation of these resonators has been extended around 10 GHz [2, 14, 24] (Fig. 7.7) and there is no fundamental limit to operating them at higher frequencies. This implies that this technology is effectively broadband and could be employed to synthesize filters and oscillators for a wide range of communication systems that operate over different frequency bands. The demonstrated k_t^2 and Q values of AlN laterally vibrating resonators are sufficient to satisfy the stringent power and phase noise requirements for oscillators and have proven adequate to meet the specifications for narrowband filtering. Nevertheless, the development of laterally vibrating resonators with improved FOM would enable a broader range of applications including wideband multiplexers and ultra-low power and high-resolution resonant sensors. Therefore, a significant research effort has been recently devoted to the investigation of advanced materials and design solutions capable of delivering laterally vibrating resonators with increased k_t^2 and Q values. For example, LN material has attracted considerable attention due to its high piezoelectric coefficients that directly enable the implementation of laterally vibrating resonators with increased k_t^2 (Eq. 7.31). Despite the challenges in terms of complexity, yield, and reproducibility of the device fabrication process, laterally vibrating resonators based on thin film LN have shown $k_t^2 > 20$ % and *FOM* as high as ~ 500 [11–13]. The simultaneous achievement of such high values of k_t^2 and Q has great potential for the implementation of multifrequency band select filters with percent bandwidths of 2–5 % and duplexers with narrow frequency gaps between the transmit and receive bands.

Another interesting approach recently proposed to increase the k_t^2 of laterally vibrating piezoelectric resonators involves the transduction of a single

2-dimensional (2D) mechanical mode of vibration based on the coherent combination of multiple piezoelectric coefficients of the material [25–27]. In particular, the AlN cross-sectional Lamé-mode resonator (CLMR) technology [25, 26] has been recently proposed and developed. This technology relies on the transduction of a Lamé-mode in the cross-section of an AlN plate through the coherent combination of the e_{31} and e_{33} piezoelectric coefficients of AlN. Thanks to the opposite sign of these two piezoelectric coefficients, in-phase charge components are generated by vibration along both the cross-sectional directions (thickness and width) of the plate. As a consequence, the k_t^2 attained by AlN CLMRs is function of both the e_{31} and e_{33} piezoelectric coefficients of AlN and it is higher than the k_t^2 achieved by conventional laterally vibrating AlN resonators. Similarly to conventional laterally vibrating resonators, CLMRs can be excited through either a Lateral-Field-Excitation (LFE) [25] or a thickness-field-excitation (TFE) scheme [26, 27]. CLMRs achieve maximum k_t^2-value of ~7 % when the pitch of the IDTs (W) is set to a specific value (W^{opt}) similar to the thickness (T_{AlN}) of the AlN plate [26]. In fact, in this scenario, a nondegenerate Lamé-mode is excited in the cross-section of the AlN plate. However, due to the capability of exciting high-k_t^2 *degenerate* cross-sectional Lamé-modes in plates, CLMRs can attain high k_t^2 (>5 %) also when W is different from W^{opt} [26]. Since the device resonance frequency, f_{res}, depends on W, the transduction of such degenerate modes also enables a significant lithographic tunability of f_{res} (~40 % while maintaining $k_t^2 > 5$ %). The capability of achieving high FOM (comparable to the ones of commercially available AlN FBAR devices) and multiple operating frequencies on the same chip without additional fabrication costs (lithographic tunability of the resonance frequency), makes this technology one of the best candidate for the implementation of monolithic integrated contiguous and not-contiguous pre-select filters for platforms adopting carrier-aggregation (CA).

These unique features have been recently exploited for the experimental demonstrations of: (1) a LFE CLMR operating around 2.8 GHz and showing k_t^2 and FOM in excess of 2.5 % and 45, respectively, which are the is the highest ever reported among LFE AlN MEMS resonators employing a single top interdigital electrode (2-maskfabrication process) [25]; (2) a TFE CLMR operating around 920 MHz and showing k_t^2 and FOM in excess of 6.2 % and 108, respectively, which are the highest ever demonstrated in AlN resonators operating in the same frequency range (Fig. 7.8) [28]; (3) two contiguous ladder filters operating around 900 MHz, fabricated on the same silicon substrate and showing a fractional bandwidth (BW_{3dB}) as high as 3.3 % and an insertion loss as low as 0.4 dB [27]; (4) a Cross-Sectional Lamé-Mode Transformer (CLMT), showing a record-high open-circuit voltage-gain ($G_v^{(max)}$) in excess of 39, which is suitable for the implementation of low-loss narrow-band matching networks and voltage-amplification stages in miniaturized AC-to-DC and DC-to-DC converters [29].

Another key challenge in the development of laterally vibrating piezoelectric resonators has been the isolation of energy-dissipating mechanisms limiting the device quality factor, Q [23, 30–33]. It has been shown that, especially for devices operating in the ultra-high frequency (UHF) band or above, most of the energy

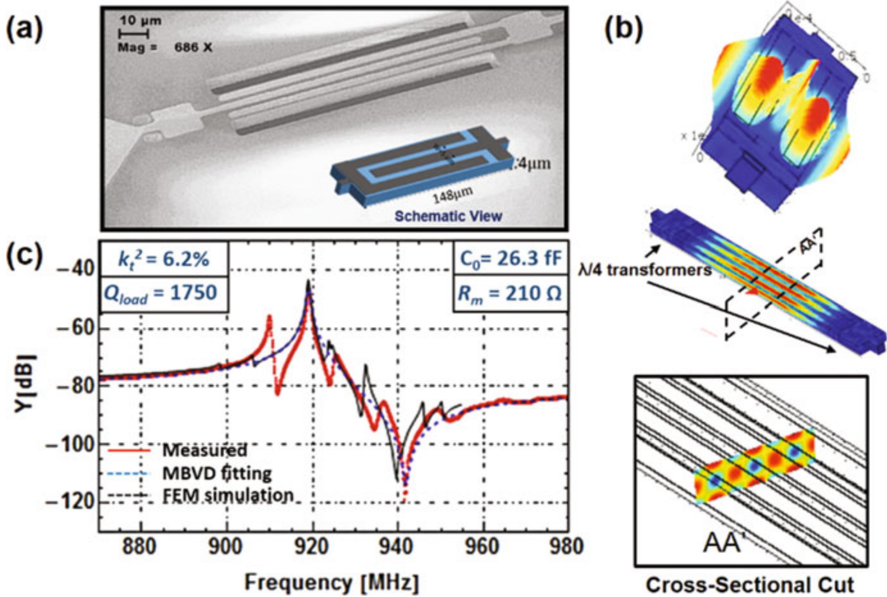

Fig. 7.8 Prototype of AlN Cross-Sectional Lamé-Mode Resonator (CLMR) operating around 920 MHz and showing k_t^2 and FOM in excess of 6.2 % and 108, respectively [28]: (**a**) SEM picture; (**b**) 3D FEM simulation of the Lame' Mode excited in the cross-section of the AlN plate; (**c**) measured and 3D FEM-simulated admittance curves and BVD fitting (Images courtesy of Dr. Cristian Cassella, Northeastern University)

loss is attributed to bulky metal-electrodes attached to the resonant body, which induce damping and interfacial strain that limit the resonant frequency f_0 and the quality factor Q [30–32, 34]. Moreover, the physical and electrical properties of the metal electrodes fundamentally limit the volume and frequency scaling since, with current nano-fabrication techniques, the thickness of metal layers cannot be arbitrarily reduced. The most promising approach for overcoming the deleterious effects of metal electrodes, beyond optimizing the type of metal [30], has been the elimination of the mechanical contact between metal electrodes and piezoelectric layer by artificially creating a nano-scale air gap [31, 34]. Although this floating-electrode approach is effective in increasing Q (∼5× improvement demonstrated), it also reduces (by a similar factor) the effective electromechanical coupling coefficient, k_t^2 of the resonant system (due to the physical separation between the electrode and the vibrating body of the structure), which limits the benefit in terms of improved FOM. Therefore, designing "ideal electrodes" that simultaneously guarantee low mechanical damping and electrical loss as well as high electromechanical coupling in ultra-low-volume piezoelectric micro and nano mechanical structures can be considered to be a key challenge in the field. Recently it has been shown that mechanically transferred graphene, floating at van der Waals proximity, closely mimics "ideal electrodes" for ultra-high frequency

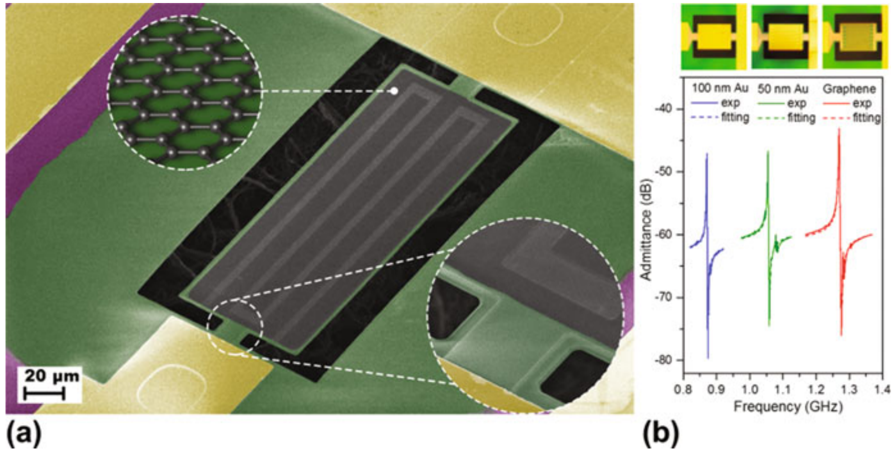

Fig. 7.9 Laterally vibrating AlN NEMS resonator using an atomically thin and virtually massless graphene electrode [35]. (**a**) False-color SEM image: a bottom metal interdigitated electrode (shown in *dark gray* underneath the AlN nanoplate), connected to the two electrical terminals of the device, and a top electrically floating graphene electrode (the *gray rectangular* area on top of AlN nanoplate), are employed for the piezoelectric actuation and sensing of a high-frequency lateral-extensional mode of vibration in the AlN nanoplate. The zoomed-in views highlight the boundary of the patterned graphene electrode on the anchor region of the device and the honeycomb lattice of the atomically thin and virtually massless graphene electrode. (**b**) Frequency response of admittance in graphene and reference devices with 100 and 50 nm thick gold top-electrode. A significant enhancement of resonant frequency is obtained ($f_0 \sim 1.27$ GHz) in the graphene-electrode devices compared to the reference devices ($f_0 \sim 0.87$ and 1.05 GHz), without any loss of resonance amplitude which immediately outlines the superiority of graphene as an electrode in piezoelectrically driven MEMS/NEMS devices (Images courtesy of Zhenyun Qian, Northeastern University)

(0.2 GHz $< f_0 <$ 2.6 GHz) laterally vibrating piezoelectric resonators (Fig. 7.9) with negligible mechanical mass and interfacial strain and perfect radio-frequency electric field confinement [35]. These unique attributes have enabled graphene-electrode based laterally vibrating piezoelectric resonators to operate at their theoretically "unloaded" frequency-limits, with significantly improved electromechanical performance compared to metal-electrode counterparts, despite their reduced volumes [35]. This represents a spectacular trend inversion in the scaling of piezoelectric laterally vibrating resonators, opening up new possibilities for the implementation of micro and nano electro mechanical systems with unprecedented performance.

Although the capability to fabricate on the same silicon chip multiple frequency and high-performance AlN laterally vibrating resonators has been demonstrated, the implementation of dynamically reconfigurable solutions based on AlN micro-acoustic resonant devices remains an open challenge due to the intrinsic static nature of such resonant structures: the operating frequency and electrical impedance of the device are set by material properties and geometrical dimensions that cannot be dynamically controlled to a large extent. Only very limited frequency tuning due to

piezoelectric [36–38] and thermal effects has been demonstrated [39–41]. A broader coverage of the RF spectrum could potentially be achieved by developing a bank of multifrequency laterally vibrating AlN micro-acoustic resonators in an electrically programmable matrix in which RF switches are used for frequency selection. The major limitation to the implementation of such reconfigurable architectures is the need of a dense integration of resonators and switches which necessarily increases size and complexity of the system and negatively affects its RF performance due to the resistive losses and capacitive loading effects introduced by the switches and the interconnections. In this perspective, the monolithic integration of RF switches and laterally vibrating AlN MEMS resonators in a single technology platform is highly desirable since it would eliminate the loading effect introduced by the conventional hybrid integration with other RF CMOS-MEMS tunable components (i.e. switches and capacitors), and significantly reduce the area required, allowing the achievement of the highest level of reconfigurability with minimum possible effect on the resonator electromechanical performance. Therefore, in recent years, a significant research effort, has been devoted towards the development of technology platforms in which high-performance laterally vibrating AlN resonators and RF switches are monolithically integrated to minimize complexity and losses to enable new radio architectures with enhanced spectrum coverage [42, 43]. In particular, effective ON/OFF switching of the acoustic resonance, with minimal effect on the electromechanical performance of the device, has been recently demonstrated with the monolithic integration of chalcogenide phase change material (PCM) switches in the design of AlN laterally vibrating resonators [44–49]. PCM (specifically $Ge_{50}Te_{50}$ [50–53]) RF switches have been recently demonstrated, showing ON resistance values of less than 1 Ω [53], the ability to cycle between ON and OFF states over 10,000 times [52], insertion loss values of less than 0.2 dB [51], and a figure of merit as high as 12.5 THz which is rapidly approaching the best reported (∼40 THz) for RF MEMS switches [54]. Furthermore, PCMs do not require constant power to maintain either the ON (low resistance) or the OFF (high resistance) state (i.e. behave as latching switches) and can be fabricated using a relatively simple and post-CMOS compatible process which, differently from RF MEMS switches, does not require the implementation of air-gaps [44, 47]. Recently RF PCM switches, with a small form factor (2 μm × 2 μm) and cut-off frequencies in the *THz* range, have been monolithically integrated in the design of an AlN laterally vibrating resonator and used to switch the terminal connections of the individual metal fingers composing the device top interdigital electrode [46, 47] (Fig. 7.10). This innovative approach not only enabled ON/OFF switching of the acoustic resonance, but also effective reconfiguration of the device electrical impedance (electromechanical coupling coefficient, k_t^2, and static capacitance, C_0) and operating frequency [45, 47, 48] (Fig. 7.10).

These prototypes have set a milestone towards the demonstration of highly reconfigurable filter architectures, exclusively based on the same micro-acoustic resonator technology, in which order, bandwidth and roll-off can be dynamically adjusted to adapt to the needs of different wireless communication standards: filter order can be modified by reconfiguring into a short circuit of one or more resonators

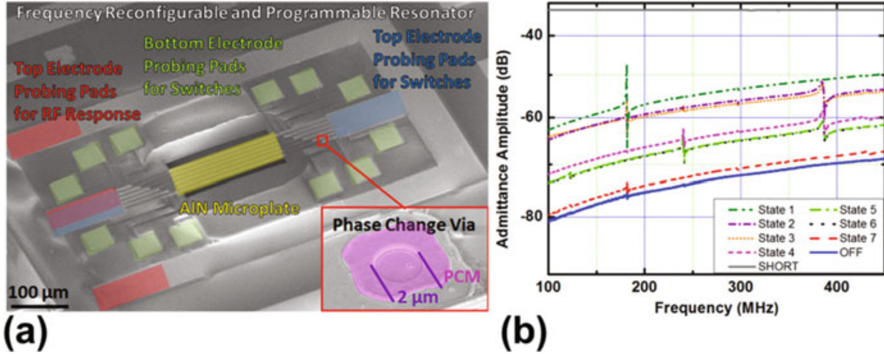

Fig. 7.10 Highly reconfigurable AlN laterally vibrating resonator using 12 monolithically integrated phase change material switches [47]. (**a**) SEM image; (**b**) Admittance response measured in nine different programmable states (Images courtesy of Gwendolyn Hummel, Northeastern University)

composing the filter, while the positions of the poles and zeroes that set the filter bandwidth and roll-off can be adjusted by reconfiguring the electromechanical coupling coefficient, k_t^2, and static capacitance, C_0, of the individual resonant elements.

Piezoelectric laterally vibrating resonators have also shown great potential for the development of high-resolution and low-power chemical physical and biological sensors. In general, micro- and nano-electro mechanical resonators have been used successfully as ultra-sensitive detectors for sensing mass, fluids flow, and specific chemical or biological agents [55–63]. The fundamental advantage of MEMS/NEMS resonant sensors over other existing sensor technologies is related to the unique combination of extremely high sensitivity to external perturbations (due to their very reduces dimensions) and ultra-low noise performance (due to the intrinsically high-quality factor, Q, of such resonant systems). Nevertheless, the greatly reduced dimensions of these devices often render their transduction extremely difficult, requiring the use of cumbersome, complex, and power-inefficient readout techniques, and limiting the effective interaction between the sensor and the environment (extremely reduced sensing area). This limits the performance of MEMS/NEMS resonant sensors, which should ultimately be evaluated in terms of limit of detection per unit area. In this perspective, optimal sensor performance is attained by synthesizing a transducer that occupies a relatively large area (which facilitates efficient transduction) and is very thin (which allows fabricating low mass devices with ultra-high sensitivity). Suspended membranes with thickness in the nanometer range are therefore desirable [56, 57, 64, 65]. Flexural plates (instead of beams) are a good compromise [59, 66], but higher frequencies and power handling are achieved in bulk mode acoustic resonators [67–69]. Laterally vibrating piezoelectric resonators belong to this category and represent one of the most suitable technologies to devise high-performance resonant sensors.

The substantial difference between laterally vibrating piezoelectric resonant sensors and the other MEMS/NEMS resonant sensors technologies is that the sensitivity of a laterally vibrating resonator, to the particular external perturbation of interest, can be set independently of its vibration frequency. In fact, differently from more conventional piezoelectric resonant sensors, such as quartz crystal microbalances (QCMs), FBARs, or flexural beam resonators, whose sensitivity per unit area and operating frequency are highly dependent on the thickness of the structure, in a laterally vibrating resonant sensor the sensitivity per unit area can be adjusted by varying the thickness of the piezoelectric layer without any significant effect on the chosen optimal operating frequency of the device. This is an important and unique feature that offers a degree of flexibility in the sensor design when operation is constrained to a particular frequency dictated by the application requirements such as in wireless or radio frequency identification (RFID) components. Furthermore, attaining high sensitivity at a low frequency translates in the use of lower power electronic readout circuits than what is possible with other devices, such as FBARs, which require operating at approximately two orders of magnitude higher frequencies in order to achieve the same levels of sensitivity. In fact, the power consumption of the CMOS circuitry used as readout typically increases with the square of the operating frequency. In addition, for typical flexural beam resonators, FBARs and QCMs an increase in sensitivity per unit area, due to a reduction in thickness and an increase in the frequency of operation, does not translate in an improvement of the overall sensor performance. In fact, the noise level of a resonant sensor (which ultimately limits the detection capability for a given sensitivity) is intrinsically related to the frequency stability of the device, hence to the inverse of its quality factor, Q [64, 65, 70]. Since FBARs and QCMs are generally characterized by a constant $f_0 \cdot Q$ product (at least for a wide range of frequencies), an increase in sensitivity per unit area, is typically accompanied by a reduction in Q (due to the associated increase in the resonance frequency), hence rendering unaltered the sensor limit of the detection per unit area. On the contrary, for laterally vibrating resonators, once the desired frequency of operation, f_0, has been set, the performance of the sensor can be improved by reducing the thickness, T, of the piezoelectric layer up to the limit for which a high Q is preserved.

For example, Q comparable to thicker films and in the order of 1000 has been attained for AlN Nano-Plate Resonator (NPR) employing an AlN layer as thin as 50 nm [71]. The efficient on-chip piezoelectric actuation and sensing of lateral-extensional bulk acoustic modes of vibration in AlN nano plate structures, instead of more conventional beams, have enabled the fabrication of ultra-low volume (high sensitivity) and high Q (low noise) nano-plate resonators that can be directly connected to compact and power-efficient electronic readouts [56, 57, 72] (without the need of off-chip bulky piezoceramic disks for actuation and complex and power-inefficient optical readouts for displacement detection), which is a key requirement for the implementation of miniaturized, multifunctional integrated sensing platforms.

Thanks to these unique features, the same core AlN NPR technology has been successfully used for the implementation of multiple high-performance physical [40, 73, 74], chemical [55–57, 61], and biological sensors [62, 75]. Recently, the extraordinary transduction properties of the AlN NPR technology have also been combined with the unique physical, optical, and electrical properties of advanced materials such as graphene, photonic metamaterials, and magnetic materials, to devise laterally vibrating resonant sensors with unprecedented sensitivity to infrared radiation and magnetic field [76–80]. For example, high frequency and high electromechanical performance (quality factor, $Q > 1000$ and electromechanical coupling coefficient, $k_t^2 > 1.0\,\%$) magnetoelectric laterally vibrating micro-mechanical resonators based on self-biased Aluminum Nitride/Iron-Gallium-Boron (AlN/FeGaB) bilayer nano-plates (250 nm/250 nm) have been implemented (Fig. 7.11) and used to synthesize miniaturized and low-power MEMS-CMOS resonant sensors capable of detecting magnetic field at the pico-Tesla level [79, 80].

Furthermore, the use of a thin piezoelectric plasmonic metasurface forming the resonant body of a laterally vibrating nanomechanical resonator with simultaneously tailored optical and electromechanical properties has also been demonstrated (Fig. 7.12) [76, 77]. Differently from all the previously proposed plasmonically enhanced MEMS devices [82], such unique nano-structure simultaneously acts as

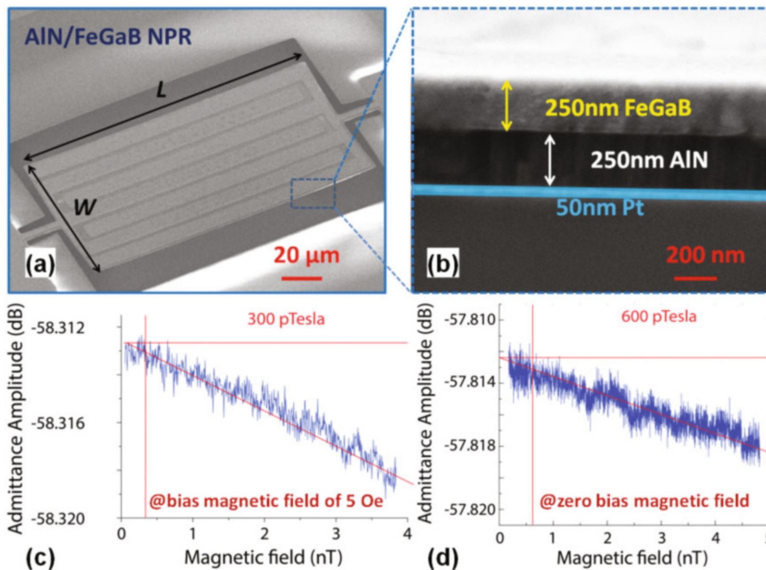

Fig. 7.11 Magnetoelectric AlN/FeGaB laterally vibrating resonator for high-resolution magnetic field sensing [79–81]. (**a**) SEM image; (**b**) Cross sectional view of the AlN/FeGaB laterally vibrating nano-plate; (**c**) resonator admittance amplitude as a function of a minute varied DC magnetic field superimposed to a fixed bias DC field of 5 Oe; (**d**) resonator admittance amplitude as a function of a minute varied DC magnetic at zero bias magnatic field (Images courtesy of Dr. Yu Hui and Dr. Tianxiang Nan, Northeastern University)

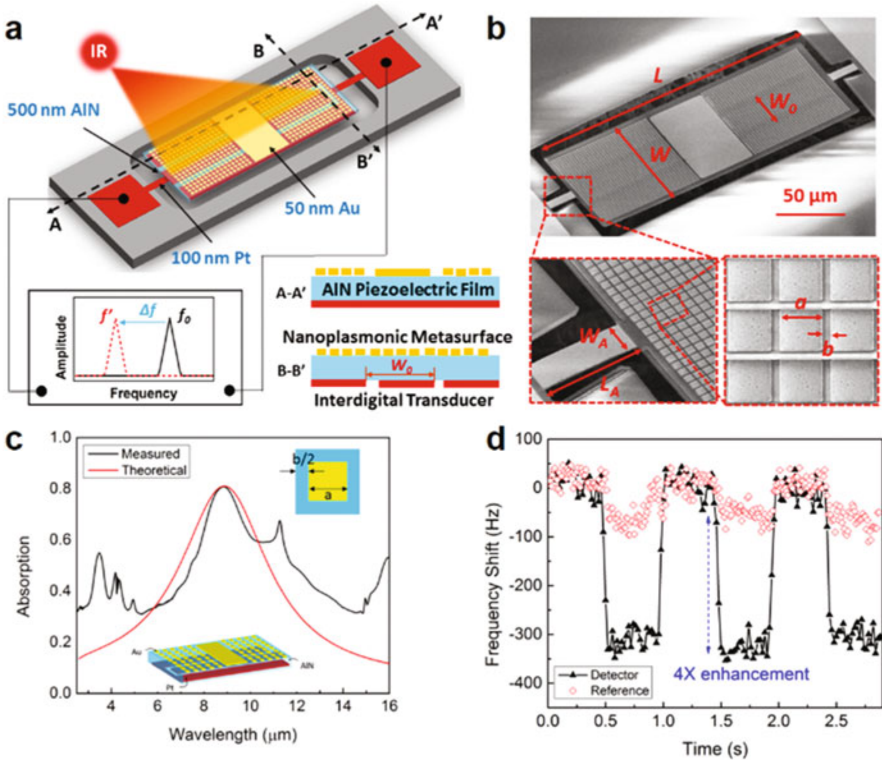

Fig. 7.12 Plasmonic piezoelectric laterally vibrating resonator for high-resolution and spectrally selective uncooled infrared sensing [76, 77]. (**a**) Mock-up view: an aluminum nitride nano-plate is sandwiched between a bottom metallic interdigitated electrode and a top nanoplasmonic metasurface. The incident IR radiation is selectively absorbed by the plasmonic metasurface and heats up the resonator, shifting its resonance frequency from f_0 to f' due to the temperature dependence of its resonance frequency. (**b**) SEM images of a fabricated plasmonic piezoelectric resonator with fully metallic anchors. The dimensions of the resonator are: $L = 200$ μm, $W = 75$ μm, $W_0 = 25$ μm (19 μm + 6 μm), $L_A = 20$ μm, $W_A = 6.5$ μm. The dimensions of the unit cell of the plasmonic metasurface are: $a = 1635$ nm, $b = 310$ nm. (**c**) Simulated and measured absorption spectra of the fabricated plasmonic piezoelectric nanomechanical resonator. The dimensions of the gold (Au) patches which compose the metasurface area = 1635 nm b = 310 nm, and the thickness of the Au, AlN, and Pt layers are 50, 500, and 100 nm, respectively. (**d**) Measured response of the plasmonic piezoelectric resonator and a conventional AlN MEMS resonator to a modulated IR radiation emitted by a 1500 °K globar (2–16 μm broadband spectral range) (Images courtesy of Dr. Yu Hui, Northeastern University)

an efficient piezoelectric transducer (without the need of off-chip actuation and sensing techniques), a high-frequency and high-Q laterally vibrating resonator and a subwavelength, strong and spectrally selective infrared (IR) absorber (without the need of integrating any additional IR absorbing materials). The combination of nanoplasmonic and piezoelectric resonances in such an ultra-thin planar structure, enabled the simultaneous achievement of efficient transduction (electromechanical

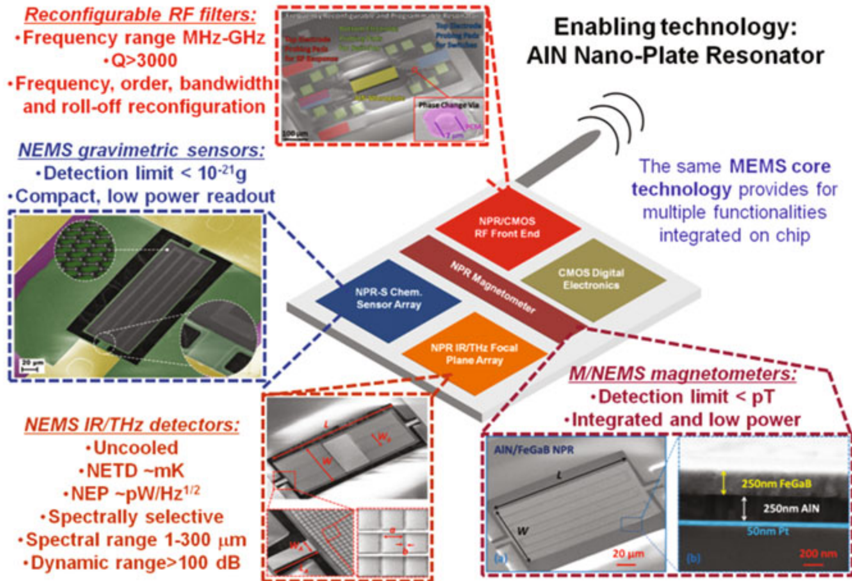

Fig. 7.13 Schematic representation of the envisioned miniaturized, low-power, multifunctional, and reconfigurable wireless sensing platform enabled by the core AlN nano-plate laterally vibrating resonator technology

coupling coefficient >1 %), high quality factor (>1000), low detection limit (noise equivalent power ∼100s pW/Hz$^{1/2}$) and strong, polarization independent, and spectrally selective absorption of long wavelength infrared (LWIR) radiation over an ultrathin thickness, addressing all fundamental challenges associated with the development of performing resonant IR detectors which could potentially lead to a new paradigm for high-performance, miniaturized, power-efficient IR spectroscopy and multispectral imaging systems.

The unique capability of such AlN NPR technology to deliver high performance and CMOS compatible sensors and RF components makes it the best candidate for the realization of the next generation miniaturized, low-power, multifunctional, and reconfigurable wireless sensing platforms (Fig. 7.13) that can fully leverage sensor fusion to acquire more accurate and reliable information about the context in which we live.

References

1. Piazza G, Stephanou PJ, Pisano AP (2006) Piezoelectric aluminum nitride vibrating contour-mode MEMS resonators. J Microelectromech Syst 15:1406–1418
2. Rinaldi M, Zuniga C, Zuo C, Piazza G (2010) "Super-high-frequency two-port AlN contour-mode resonators for RF applications. IEEE Trans Ultrason Ferroelectr Freq Control 57:38–45

3. Harrington BP, Shahmohammadi M, Abdolvand R (2010) Toward ultimate performance in GHZ MEMS resonators: low impedance and high Q. In: IEEE 23rd international conference on micro electro mechanical systems (MEMS), 2010, pp 707–710
4. Ho GK, Abdolvand R, Sivapurapu A, Humad S, Ayazi F (2008) Piezoelectric-on-silicon lateral bulk acoustic wave micromechanical resonators. J Microelectromech Syst 17:512–520
5. Chandrahalim H, Bhave SA, Polcawich RG, Pulskamp JS, Kaul R (2010) PZT transduction of high-overtone contour- mode resonators. IEEE Trans Ultrason Ferroelectr Freq Control 57:2035–2041
6. Chandrahalim H, Bhave SA, Polcawich R, Pulskamp J, Judy D, Kaul R, Dubey M (2008) Performance comparison of Pb(Zr0.52Ti0.48)O3-only and Pb(Zr0.52Ti0.48)O3-on-silicon resonators. Appl Phys Lett 93:233504
7. Abdolvand R, Ho GK, Butler J, Ayazi F (2007) ZNO-on-nanocrystalline diamond lateral bulk acoustic resonators. In: IEEE 20th international conference on micro electro mechanical systems, MEMS, 2007, pp 795–798
8. Songbin G, Nai-Kuei K, Piazza G (2011) A 1.75 GHz piezoelectrically-transduced SiC lateral overmoded bulk acoustic-wave resonator. In: 2011 16th international solid-state sensors, actuators and microsystems conference (TRANSDUCERS), 2011, pp 922–925
9. Rais-Zadeh M, Gokhale VJ, Ansari A, The X, Faucher M, Ron D, Cordier Y, Buchaillot L (2014) Gallium nitride as an electromechanical material. J Microelectromech Syst 23: 1252–1271
10. Popa LC, Weinstein D (2014) L-band lamb mode resonators in gallium nitride MMIC technology. In: 2014 IEEE international frequency control symposium (FCS), 2014, pp 1–4
11. Songbin G, Piazza G (2013) Design and analysis of lithium-niobate-based high electromechanical coupling RF-MEMS resonators for wideband filtering. IEEE Trans Microw Theory Tech 61:403–414
12. Olsson III RH, Hattar K, Baker MS, Wiwi M, Nguyen J, Padilla C, Homeijer SJ, Wendt JR, Friedmann TA (2014) Lamb wave micromechanical resonators formed in thin plates of lithium niobate. In: Solid state sensors, actuators, and microsystems workshop (Hilton Head 2014), Hilton Head, South Carolina, 2014, pp 281–284
13. Renyuan W, Bhave SA, Bhattacharjee K (2013) High k_t^{2*}Q, multi-frequency lithium niobate resonators. In: IEEE 26th international conference on micro electro mechanical systems (MEMS), 2013, pp 165–168
14. Rinaldi M, Zuniga C, Piazza G (2009) 5–10 GHz AlN contour-mode nanoelectromechanical resonators. In: IEEE 22nd international conference on micro electro mechanical systems, 2009. MEMS 2009, pp 916–919
15. Rinaldi M, Zuniga C, Zuo C, Piazza G (2010) GHz range nanoscaled AlN contour-mode resonant sensors (CMR-S) with self-sustained CMOS oscillator. In: Proceedings of solid-state sensors, actuators and microsystems workshop (Hilton Head 2010), Hilton Head, USA
16. Rinaldi M, Zuo C, Van der Spiegel J, Piazza G (2011) Reconfigurable CMOS oscillator based on multifrequency AlN contour-mode MEMS resonators. IEEE Trans Electron Dev 58: 1281–1286
17. Levy M, Osgood RM, Liu R, Cross LE, Cargill GS, Kumar A, Bakhru H (1998) Fabrication of single-crystal lithium niobate films by crystal ion slicing. Appl Phys Lett 73:2293–2295
18. Poberaj G, Koechlin M, Sulser F, Guarino A, Hajfler J, Günter P (2009) Ion-sliced lithium niobate thin films for active photonic devices. Opt Mater 31:1054–1058
19. Diest K, Archer MJ, Dionne JA, Park Y-B, Czubakowski MJ, Atwater HA (2008) Silver diffusion bonding and layer transfer of lithium niobate to silicon. Appl Phys Lett 93:092906
20. Solal M, Pastureaud T, Ballandras S, Aspar B, Biasse B, Daniau W, Hode JM, Calisti S, Laude V (2002) "Oriented lithium niobate layers transferred on 4" [100] silicon wafer for RF SAW devices. In: Proceedings of the 2002 IEEE ultrasonics symposium, 2002, vol 1, pp 131–134
21. Olsson Iii RH, Hattar K, Homeijer SJ, Wiwi M, Eichenfield M, Branch DW, Baker MS, Nguyen J, Clark B, Bauer T, Friedmann TA (2014) A high electromechanical coupling coefficient SH0 Lamb wave lithium niobate micromechanical resonator and a method for fabrication. Sensor Actuat A Phys 209:183–190

22. Olsson RH, Fleming JG, Wojciechowski KE, Baker MS, Tuck MR (2007) Post-CMOS compatible aluminum nitride MEMS filters and resonant sensors. In: IEEE international frequency control symposium, 2007 joint with the 21st European frequency and time forum, 2007, pp 412–419
23. Cassella C, Segovia-Fernandez J, Piazza G, Cremonesi M, Frangi A (2013) Reduction of anchor losses by etched slots in aluminum nitride contour mode resonators. In: European frequency and time forum & international frequency control symposium (EFTF/IFC), 2013 Joint, 2013, pp 926–929
24. Wojciechowski KE, Olsson RH, Nordquist CD, Tuck MR (2009) Super high frequency width extensional aluminum nitride (AlN) MEMS resonators. In: 2009 IEEE international ultrasonics symposium (IUS), 2009, pp 1179–1182
25. Yu H, Zhenyun Q, Rinaldi M (2013) A 2.8 GHz combined mode of vibration aluminum nitride MEMS resonator with high figure of merit exceeding 45. In: European frequency and time forum & international frequency control symposium (EFTF/IFC), 2013 Joint, pp 930–932
26. Cassella C, Hui Y, Qian Z, Hummel G, Rinaldi M (2016) Aluminum nitride cross-sectional lame' mode resonators. J Microelectromech Syst 25:275–285
27. Cassella C, Chen G, Qian Z, Hummel G, Rinaldi M (2016) Cross-sectional lame' mode ladder filters for UHF wideband applications. IEEE Electron Dev Lett 37:681–683
28. Cassella C, Chen G, Qian Z, Hummel G, Rinaldi M (2016) Unprecedented figure of merit in excess of 108 in 920 MHz aluminum nitride cross-sectional lamé mode resonators showing kt2 in excess of 6.2%. In: 2016 solid-state sensors, actuators and microsystems workshop (Hilton Head 2016), Hilton Head Island, 2016, pp 94–96
29. Cassella C, Chen G, Qian Z, Hummel G, Rinaldi M (2016) 920 MHz aluminum nitride cross-sectional lamé mode piezoelectric MEMS transformer with high open-circuit voltage gain in excess of 39," in 2016 solid-state sensors, actuators and microsystems workshop (Hilton Head 2016), Hilton Head Island, 2016, pp 412–415
30. Segovia-Fernandez J, Nai-Kuei K, Piazza G (2012) Impact of metal electrodes on the figure of merit ($k_t^{2*}Q$) and spurious modes of contour mode AlN resonators. In: 2012 IEEE international ultrasonics symposium (IUS), pp 299–302
31. Ting-Ta Y, Pisano AP, Nguyen CTC (2013) High-Q capacitive-piezoelectric AlN lamb wave resonators. In: 2013 IEEE 26th international conference on micro electro mechanical systems (MEMS), 2013, pp 114–117
32. Segovia-Fernandez J, Cremonesi M, Cassella C, Frangi A, Piazza G (2015) Anchor losses in AlN contour mode resonators. J Microelectromech Syst 24:265–275
33. Cassella C, Singh N, Soon BW, Piazza G (2015) Quality factor dependence on the inactive regions in AlN contour-mode resonators. J Microelectromech Syst
34. Li-Wen H, Nguyen CTC (2015) Capacitive-piezoelectric transducers for high-Q micromechanical AlN resonators. J Microelectromech Syst 24:458–473
35. Qian Z, Liu F, Hui Y, Kar S, Rinaldi M (2015) Graphene as a massless electrode for ultrahigh-frequency piezoelectric nanoelectromechanical systems. Nano Lett 15:4599–4604
36. Karabalin RB, Matheny MH, Feng XL, Defaÿ E, Le Rhun G, Marcoux C, Hentz S, Andreucci P, Roukes ML (2009) Piezoelectric nanoelectromechanical resonators based on aluminum nitride thin films. Appl Phys Lett 95:103111
37. Defay E, Ben Hassine N, Emery P, Parat G, Abergel J, Devos A (2011) Tunability of aluminum nitride acoustic resonators: a phenomenological approach. IEEE Trans Ultrason Ferroelectr Freq Control 58:2516–2520
38. Songbin G, Piazza G (2013) Large frequency tuning of lithium niobate laterally vibrating MEMS resonators via electric boundary reconfiguration. In: The 17th international conference on solid-state sensors, actuators and microsystems (TRANSDUCERS & EUROSENSORS XXVII), 2013 Transducers & Eurosensors XXVII, 2013, pp 2465–2468
39. Tazzoli A, Rinaldi M, Piazza G (2012) Experimental investigation of thermally induced nonlinearities in aluminum nitride contour-mode MEMS resonators. IEEE Electron Dev Lett 33:724–726

40. Hui Y, Rinaldi M (2013) Fast and high resolution thermal detector based on an aluminum nitride piezoelectric microelectromechanical resonator with an integrated suspended heat absorbing element. Appl Phys Lett 102:093501
41. Bongsang K, Olsson RH, Wojciechowski KE (2010) Ovenized and thermally tunable aluminum nitride microresonators. In: Ultrasonics symposium (IUS), 2010 IEEE, 2010, pp 974–978
42. Rashed M, Nipun S, Marcelo BP, Gianluca P (2008) Dual-beam actuation of piezoelectric AlN RF MEMS switches monolithically integrated with AlN contour-mode resonators. J Micromech Microeng 18:105011
43. Nordquist CD, Olsson RH, Scott SM, Branch DW, Pluym T, Yarberry V (2013) On/off micro-electromechanical switching of AlN piezoelectric resonators. In: 2013 IEEE MTT-S international microwave symposium digest (IMS), 2013, pp 1–4
44. Hummel G, Hui Y, Qian Z, Rinaldi M (2014) Switchable aluminum nitride MEMS resonator using phase change materials. In: 2014 solid-state sensors, actuators and microsystems workshop (Hilton Head 2014), Hilton Head Island, South Carolina, 2014, pp 431–434
45. Hummel G, Yu H, Rinaldi M (2014) Phase change material programmable vias for switching and reconfiguration of aluminum nitride piezoelectric MEMS resonators. In: 2014 IEEE international frequency control symposium (FCS), 2014, pp 1–3
46. Hummel G, Rinaldi M (2015) Switchable 2-port aluminum nitride MEMS resonator using monolithically integrated 3.6 THz cut-off frequency phase-change switches. In: 2015 Joint conference of the IEEE international frequency control symposium & the european frequency and time forum (FCS), 2015, pp 706–708
47. Hummel G, Hui Y, Rinaldi M (2015) Highly reconfigurable aluminum nitride MEMS resonator using 12 monolithically integrated phase change material switches. In: 18th international conference on solid-state sensors, actuators and microsystems (TRANSDUCERS), 2015 transducers – 2015, pp 323–326
48. Hummel G, Yu H, Rinaldi M (2014) Reconfigurable mode of vibration in AlN MEMS resonators using phase change materials. In: 2014 IEEE International, ultrasonics symposium (IUS), pp 799–802
49. Hummel G, Hui Y, Rinaldi M (2015) Reconfigurable piezoelectric MEMS resonator using phase change material programmable vias. J Microelectromech Syst 24:2145–2151
50. Raoux S, Xiong F, Wuttig M, Pop E (2014) Phase change materials and phase change memory. MRS Bull 39:703–710
51. Jeong-Sun M, Seo HC, Le D (2014) High linearity 1-ohm RF switches with phase-change materials. In: 2014 IEEE 14th topical meeting on silicon monolithic integrated circuits in RF systems (SiRF), 2014, pp 7–9
52. El-Hinnawy N, Borodulin P, Jones E, Wagner B, King M, Mason J, Hartman J, Howell R, Lee M, Young R (2014) Improvements in GeTe-based inline phase-change switch technology for RF switching applications. In: CS MANTECH conference, Denver, CO, USA, 2014, pp 401–403
53. Jeong-Sun M, Hwa-Chang S, Duc L (2014) Development toward high-power sub-1-ohm DC-67 GHz RF switches using phase change materials for reconfigurable RF front-end. In: 2014 IEEE MTT-S international microwave symposium (IMS), pp 1–3
54. Rebeiz GM, Entesari K, Reines I, Park SJ, El-Tanani MA, Grichener A, Brown AR (2009) Tuning in to RF MEMS. IEEE Microw Mag 10:55–72
55. Rinaldi M (2012) NEMS resonant chemical sensors. In: Bhushan B (ed) Encyclopedia of nanotechnology. Springer, Amsterdam, pp 1888–1895
56. Rinaldi M, Duick B, Zuniga C, Zuo C, Piazza G (2010) SS-DNA functionalized ultra-thin-film ALN contour-mode resonators with self-sustained oscillator for volatile organic chemical detection. In: IEEE 23rd international conference on micro electro mechanical systems (MEMS 2010) 2010, pp 132–135

57. Rinaldi M, Zuniga C, Piazza G () ss-DNA functionalized array of ALN contour-mode NEMS resonant sensors with single CMOS multiplexed oscillator for sub-ppb detection of volatile organic chemicals. In: IEEE 24th international conference on micro electro mechanical systems (MEMS 2011), 2011, pp 976–979
58. Li M, Tang HX, Roukes ML (2007) Ultra-sensitive NEMS-based cantilevers for sensing, scanned probe and very high-frequency applications. Nat Nanotechnol 2:114–120
59. Lee HJ, Park KK, Oralkan O, Kupnik M, Khuri-Yakub BT (2008) CMUT as chemical sensor for DMMP detection. In: 2008 IEEE international frequency control symposium, pp 434–439
60. Rahafrooz A, Pourkamali S (2010) Fabrication and characterization of thermally actuated micromechanical resonators for airborne particle mass sensing: I. Resonator design and modeling. J Micromech Microeng 20
61. Zuniga C, Rinaldi M, Khamis SM, Johnson AT, Piazza G (2009) Nanoenabled microelectromechanical sensor for volatile organic chemical detection. Appl Phys Lett 94:223122–223123
62. Zuniga C, Rinaldi M, Piazza G (2011) Reduced viscous damping in high frequency piezoelectric resonant nanochannels for sensing in fluids. In: 2011 IEEE 24th international conference on micro electro mechanical systems (MEMS), 2011, pp 960–963
63. Lee J, Shen W, Payer K, Burg TP, Manalis SR (2010) Toward attogram mass measurements in solution with suspended nanochannel resonators. Nano Lett 10:2537–2542
64. Rinaldi M, Piazza G (2011) Effects of volume and frequency scaling in AlN contour mode NEMS resonators on oscillator phase noise. In: 2011 Joint conference of the IEEE international frequency control and the european frequency and time forum (FCS), 2011, pp 1–5
65. Rinaldi M, Zuniga C, Piazza G (2009) Ultra-thin-film AlN contour-mode resonators for sensing applications. In: 2009 IEEE international ultrasonics symposium (IUS), 2009, pp 714–717
66. Lee HJ, Park KK, Cristman P, Oralkan O, Kupnik M, Khuri-Yakub BT (2009) A low-noise oscillator based on a multi-membrane CMUT for high sensitivity resonant chemical sensors. In: IEEE 22nd international conference on micro electro mechanical systems, 2009 (MEMS 2009), pp 761–764
67. Ruby RC, Bradley Y, Oshmyansky Y, Chien A, Larson JD (2001) Thin film bulk wave acoustic resonators (FBAR) for wireless applications. In: Proceedings of the 2001 IEEE international ultrasonics symposium, 2001, pp 813–821
68. Lin A, Hongyu Y, Waters MS, Eun Sok K, Goodman SD (2008) Explosive trace detection with FBAR-based sensor. In: 21st IEEE international conference on micro electro mechanical systems (MEMS 2008), 2008, pp 208–211
69. Clark JR, Wan-Thai H, Abdelmoneum MA, Nguyen CTC (2005) High-Q UHF micromechanical radial-contour mode disk resonators. J Microelectromech Syst 14:1298–1310
70. Vig JR, Walls (FL) A review of sensor sensitivity and stability. In: Proceedings of the 2000 IEEE/EIA international frequency control symposium and exhibition, 2000, pp 30–33
71. Rinaldi M (2010) Piezoelectric aluminum nitride nano plate resonant sensors for next generation miniaturized sensing platforms. Ph.D., Electrical and Systems Engineering, University of Pennsylvania, ProQuest, 2010
72. Rinaldi M, Zuniga C, Duick B, Piazza G (2010) Use of a single multiplexed CMOS oscillator as direct frequency read-out for an array of eight AlN contour-mode NEMS resonant sensors. In: Proceedings of IEEE sensors 2010, pp 2666–2670
73. Hui Y, Rinaldi M (2013) High performance NEMS resonant infrared detector based on an aluminum nitride nano-plate resonator. In: 2013 transducers & eurosensors XXVII: the 17th international conference on solid-state sensors, actuators and microsystems (TRANSDUCERS & EUROSENSORS XXVII), 2013, pp 968–971
74. Zhenyun Q, Vyas R, Yu H, Rinaldi M (2014) High resolution calorimetric sensing based on aluminum nitride MEMS resonant thermal detectors. In: 2014 IEEE sensors, 2014, pp 986–989
75. Zuniga C, Rinaldi M, Piazza G (2010) High frequency piezoelectric resonant nanochannel for bio-sensing applications in liquid environment. In 2010 IEEE sensors, 2010, pp 52–55
76. Hui Y, Gomez-Diaz JS, Qian Z, Alu A, Rinaldi M (2016) Plasmonic piezoelectric nanomechanical resonator for spectrally selective infrared sensing. Nat Commun 7

77. Yu H, Rinaldi M (2015) Spectrally selective infrared detector based on an ultra-thin piezoelectric resonant metamaterial. In: 2015 28th IEEE international conference on micro electro mechanical systems (MEMS), 2015, pp 984–987
78. Qian Z, Hui Y, Liu F, Kai S, Rinaldi M (2015) 1.27 GHz graphene-aluminum nitride nano plate resonant infrared detector. In: 2015 18th international conference on solid-state sensors, actuators and microsystems (TRANSDUCERS), 2015 transducers, 2015, pp 1429–1432
79. Yu H, Tianxiang N, Sun NX, Rinaldi M (2015) High resolution magnetometer based on a high frequency magnetoelectric MEMS-CMOS oscillator. J Microelectromech Syst 24:134–143
80. Nan T, Hui Y, Rinaldi M, Sun NX (2013) Self-biased 215MHz magnetoelectric NEMS resonator for ultra-sensitive DC magnetic field detection. Scientific Rep 3:1985
81. Hui Y, Nan TX, Sun NX, Rinaldi M (2013) MEMS resonant magnetic field sensor based on an AlN/FeGaB bilayer nano-plate resonator. In: 2013 IEEE 26th international conference on micro electro mechanical systems (MEMS), 2013, pp 721–724
82. Yi F, Zhu H, Reed RC, Cubukcu E (2013) Plasmonically enhanced thermomechanical detection of infrared radiation. Nano Lett 13:1638–1643

Chapter 8
BAW Piezoelectric Resonators

Ken-ya Hashimoto

8.1 Introduction

This chapter describes basic properties and modeling of resonators using acoustic waves propagating in a solid body. This type of waves is called the bulk acoustic wave (BAW), which can be excited and detected efficiently using piezoelectricity. The resonators are widely used in various applications such as clock generation, frequency filtering, and sensing. The most popular ones are crystal quartz resonators [1] for relatively low frequency applications (<100 MHz). Recently BAW resonators fabricated by thin film and micromachining technologies, i.e., film bulk acoustic resonators (FBARs) [2], are getting popular for relatively high frequency applications (>1–3 GHz) such as duplexers used in mobile and smart phones.

BAWs can be also excited and detected electrostatically, and some devices have already been mass produced and applied to various frequency control applications [3]. However, owing to the very weak electromechanical coupling, electrostatically driven BAW devices are not feasible for low-loss and wideband applications.

First basic device operation is discussed using a very simple phenomenological model, and a one-dimensional model based on the wave theory is introduced for detailed discussions. Then typical device structures and fabrication steps are explained, and choice of piezoelectric and electrode materials are also discussed. Finally, wave propagation in three-dimensional structures is explained, and possible spurious and loss mechanisms including their countermeasures are discussed.

K.-y. Hashimoto (✉)
Department of Electrical and Electronic Engineering, Graduate School of Engineering, Chiba University, Chiba, Chiba Prefecture, Japan
e-mail: k.hashimoto@faculty.chiba-u.jp

© Springer International Publishing Switzerland 2017

H. Bhugra, G. Piazza (eds.), *Piezoelectric MEMS Resonators*,
Microsystems and Nanosystems, DOI 10.1007/978-3-319-28688-4_8

8.2 BVD Model

Let us consider acoustic wave propagation in a plate with thickness h. It is known that the plate causes a mechanical resonance (thickness resonance) at frequencies satisfying the condition of

$$f_r = \frac{nV}{2h}, \tag{8.1}$$

where V is the acoustic wave velocity, and n is an integer called the order of resonance modes. Equation (8.1) indicates that in addition to a lowest order resonance ($n = 1$) called the fundamental resonance, a series of higher-order ($n \neq 1$) ones exist. Since f_r for $n \neq 1$ will be an integer times f_r for $n = 1$, higher-order resonances are often called harmonic resonances or overtones. When the longitudinal BAW is responsible for the thickness resonance, it is called the thickness extensional (TE) resonance while it is called the thickness shear (TS) resonance when the shear BAW is responsible. In general, V of the longitudinal BAW is faster than that of the shear BAW for the identical propagation direction in the identical material.

When the plate is piezoelectric and sandwiched in between two parallel electrodes (see Fig. 8.1a), we can excite and detect the resonances electrically. This device can be used as an impedance element in electronic circuits. This type of electronic components is called BAW resonators.

In the structure shown in Fig. 8.1a, when a sinusoidal voltage v with the frequency f is applied to two electrodes, a mechanical force v_m is generated through piezoelectricity, and the displacement u is generated in the plate as a reaction. The relation might be written as

$$v \propto v_m = M\frac{d^2u}{dt^2} + \eta\frac{du}{dt} + Ku, \tag{8.2}$$

where M, η, and K are an effective mass, effective viscosity, and effective spring constant of the plate, respectively. In the right hand side of the equation, first to third terms correspond to inertia, friction, and elasticity, respectively.

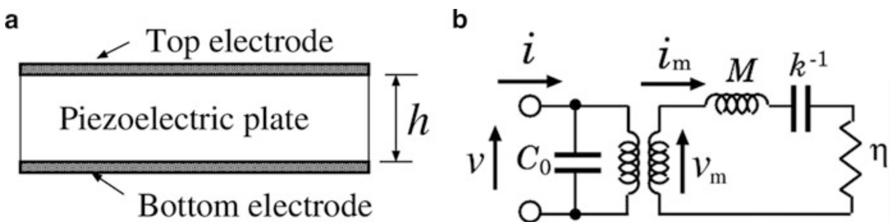

Fig. 8.1 Simplified model for BAW resonators. (**a**) Physical model. (**b**) Electromechanical equivalent circuit

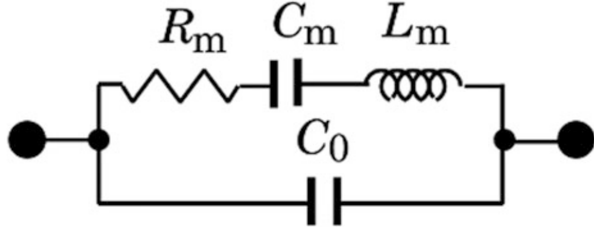

Fig. 8.2 Electrical equivalent circuit model (BVD model)

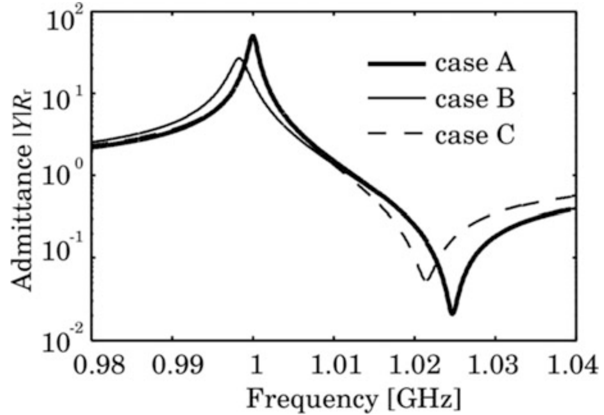

Fig. 8.3 Frequency dependence of input admittance $|Y|$ derived from the BVD model. Case A: calculated by the original BVD model, Case B: calculated by the modified BVD model (see Fig. 8.5) with $R_e \neq 0$, and Case C: calculated by the modified BVD model with $R_0 \neq 0$

Due to the reciprocity of piezoelectricity, electrical charges q_m proportional to u will be induced on the electrodes.

From these relations, we may derive an electromechanical equivalent circuit shown in Fig. 8.1b. In the figure, $i_m = du/dt$ is a mechanical current, and C_0 is called the clamped capacitance which expresses the electrostatic coupling between two electrodes.

Since we are only interested in electrical characteristics, the equivalent circuit can be simplified as shown in Fig. 8.2, where C_m, L_m, and R_m are called the motional capacitance, inductance, and resistance, respectively. This circuit is called the Butterworth–Van Dyke (BVD) model [4], and is quite often used as the simplest model for one-port acoustic resonators.

Case A in Fig. 8.3 shows a typical frequency dependence of the input admittance Y calculated from the BVD model. In the figure, R_r is an impedance used for the normalization. A series resonance where $|Y|$ takes a maximum is seen at 1 GHz while a parallel resonance where $|Y|$ takes a minimum is seen at 1.025 GHz.

From the BVD model, we can express Y in a form of

$$Y = 2\pi jfC_0 \frac{1 - (f/f_a)^2 + j(f/f_a)Q_a^{-1}}{1 - (f/f_r)^2 + j(f/f_r)Q_r^{-1}}. \quad (8.3)$$

In the equation, f_r is the resonance frequency where the series resonance occurs, and f_a is the anti-resonance frequency where the parallel resonance occurs. From the equivalent circuit, these frequencies are given by

$$f_r = \frac{1}{2\pi\sqrt{L_m C_m}} \tag{8.4}$$

and

$$f_a = \frac{1}{2\pi\sqrt{L_m\left(C_m^{-1} + C_0^{-1}\right)^{-1}}}, \tag{8.5}$$

respectively. In Eq. (8.3), Q_r and Q_a are called the resonance and anti-resonance quality factors, respectively, and are given by

$$Q_r = \frac{2\pi f_r L_m}{R_m} \tag{8.6}$$

and

$$Q_a = \frac{2\pi f_a L_m}{R_m}. \tag{8.7}$$

They give steepness of the resonance peaks, and influence the minimum insertion loss and steepness of the passband edges for filter applications [5].

Here we define the capacitance ratio γ, which is defined as

$$\gamma = \frac{C_0}{C_m} = \frac{1}{(f_a/f_r)^2 - 1}. \tag{8.8}$$

Figure 8.2 implies that γ gives the weakness of piezoelectricity. For filter applications, it influences the minimum insertion loss and determines the maximum passband width [5].

When multiple resonances exist, their influences can be taken into account by increasing the number of *LCR* branches as shown in Fig. 8.4, where the *n*th branch expresses the *n*th order mechanical resonance [4].

It is important to note that Eqs. (8.6) and (8.7) imply that Q_r is almost equal to Q_a. This is not true in general. This is because only the viscous loss is considered in the original BVD model shown in Fig. 8.2.

Figure 8.5 shows the modified BVD model taking the difference in Q_r and Q_a into account [6]. In the figure, R_e stands for the ohmic resistance of electrodes, and R_0 considers the dielectric loss in the piezoelectric film. Other loss mechanisms such as the acoustic leakage discussed in Eq. (8.6) may be also included in R_e and/or R_0.

Figure 8.2 also shows influence of these resistances on the resonance characteristics. In the figure, R_e is considered for case B while R_0 is included for case C. It

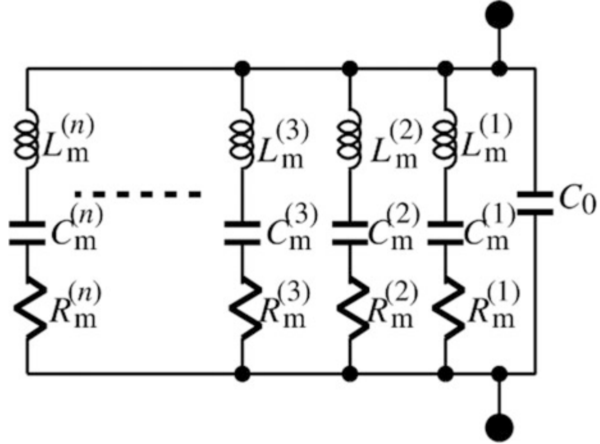

Fig. 8.4 BVD model taking multiple resonances into account

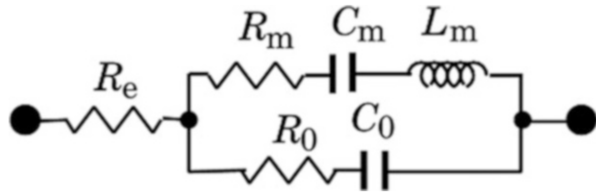

Fig. 8.5 Modified BVD model

is seen that R_e influences only the response at $f \sim f_r$ while R_0 influences only the response at $f \sim f_a$. Traces for cases B and C are mostly overlapped with that for case A at the remaining frequency ranges.

Existence of these resistances modifies Eqs. (8.6) and (8.7) as

$$Q_r = \frac{2\pi f_r L_m}{R_m + R_e} \tag{8.9}$$

and

$$Q_a = \frac{2\pi f_a L_m}{R_m + R_0}. \tag{8.10}$$

These equations indicate that $Q_r > Q_a$ when $R_e < R_0$ while $Q_r < Q_a$ when $R_e > R_0$.

Equation (8.3) indicates that

$$Y_{max} \equiv Y|_{f=f_r} \sim 2\pi f_r C_0 Q_r \left\{1 - (f_r/f_a)^2\right\} \sim 2\pi f_r C_0 M_r, \tag{8.11}$$

and

$$Y_{min} \equiv Y|_{f=f_a} \sim -2\pi f_a C_0 \frac{Q_a^{-1}}{1 - (f_a/f_r)^2} \sim 2\pi f_a C_0 M_a^{-1}, \tag{8.12}$$

where $M_r = Q_r/\gamma$ and $M_a = Q_a/\gamma$ are the figure of merit for BAW resonators at the resonance and anti-resonance, respectively. Equations (8.11) and (8.12) indicate that when R_r is chosen as $2\pi f_r C_0$ or $2\pi f_a C_0$, M_r and M_a are approximately given by $Y_{max} R_r$ and $(Y_{min} R_r)^{-1}$, respectively, and thus we can estimate them graphically from the $|Y|R_r$ curve shown in Fig. 8.3. Since γ are estimated from f_r and f_a, we can calculate Q_r and Q_a from estimated M_r and M_a.

For better understanding of device behavior, we often want to know how the Q factor changes with the frequency. For the purpose, Feld et al. proposed the following frequency dependent Q factor for device characterization [7];

$$Q(f) = 2\pi f \tau(f) \frac{|S_{11}|}{1 - |S_{11}|^2}, \tag{8.13}$$

where S_{11} is the electrical reflection coefficient measured by a vector network analyzer and τ is the group delay estimated by

$$\tau(f) = -\frac{\partial \angle S_{11}}{2\pi \partial f}. \tag{8.14}$$

Variation of f_r with temperature T is one of the most important characteristics of acoustic resonators. Equation (8.1) indicates that the temperature coefficient of frequency (TCF) of the acoustic resonator is given by

$$\mathrm{TCF} = f_r^{-1} \frac{\partial f_r}{\partial T} = V^{-1} \frac{\partial V}{\partial T} - h^{-1} \frac{\partial h}{\partial T}. \tag{8.15}$$

In the right hand side of the equation, the first and second terms correspond to the temperature coefficient of the BAW velocity (TCV) and the thermal expansion coefficient of the plate toward the thickness direction, respectively. Equation (8.15) indicates that choice of the plate medium and propagation mode is determinative for the TCF.

It is known that TCF can be very small for a wide temperature range when single-crystal quartz is chosen as a plate material and its crystallographic orientation is set properly [1]. This is the main reason why quartz resonators are widely used for frequency control applications. However, materials with good TCF possess weak piezoelectricity in general, and this is also true for quartz. Thus we must choose an appropriate piezoelectric material under a compromise between TCF and k_t^2 (or γ) as we will discuss in Sect. 8.5.

It should be noted that the TCF at $f = f_r$ ($\mathrm{TCF_r}$) is different from that at $f = f_a$ ($\mathrm{TCF_a}$). Equation (8.8) indicates that $\mathrm{TCF_r}$ and $\mathrm{TCF_a}$ are related to each other by the temperature coefficient of γ (TCF_γ) as

$$\mathrm{TCF_a} = \mathrm{TCF_r} - \frac{1}{2(1+\gamma)} \mathrm{TCF}_\gamma. \tag{8.16}$$

This equation indicates that difference between $\mathrm{TCF_r}$ and $\mathrm{TCF_a}$ becomes large when γ is small.

8.3 Mason's Equivalent Circuit Model

As for one-dimensional case, the rigorous analysis is possible by using the Mason equivalent circuit [8, 9]. Figure 8.6 shows the equivalent circuit of the resonator structure shown in Fig. 8.1a for the TE vibration. In the figure,

$$n^2 = k_t^2 C_0 Z_\mathrm{p} V_\mathrm{p} S/h,\ \ Z_\mathrm{ap} = -jZ_\mathrm{p} S \csc\left(\beta_\mathrm{p} h\right),\ \ Z_\mathrm{bp} = jZ_\mathrm{p} S \tan\left(\beta_\mathrm{p} h/2\right)$$
$$Z_\mathrm{ae} = -jZ_\mathrm{e} S \csc\left(\beta_\mathrm{e} h_\mathrm{e}\right),\ \ Z_\mathrm{be} = jZ_\mathrm{e} S \tan\left(\beta_\mathrm{e} h_\mathrm{e}/2\right),$$

Z_p and Z_e are the acoustic impedance [9] (mass density × BAW velocity) of the piezoelectric layer and electrodes, β_p and β_e are the wavenumbers ($2\pi f$/BAW velocity) in the piezoelectric layer and electrodes, and h_e and S are the thickness and surface area of the electrodes, and k_t^2 is the "intrinsic" electromechanical coupling factor of the piezoelectric layer for the TE vibration [9]. In the figure, both ends of acoustic ports are short-circuited because the mechanical voltage (stress) is zero at the top and bottom surfaces.

We can derive the input admittance Y (=i/v) from this circuit as

$$\begin{aligned} Y &= \frac{2\pi jfC_0}{1+jn^2(\omega C_0)^{-1}\left[Z_\mathrm{ap}+Z_\mathrm{bp}/2+\left\{Z_\mathrm{be}+\left(Z_\mathrm{be}^{-1}+Z_\mathrm{ae}^{-1}\right)^{-1}\right\}/2\right]^{-1}} \\ &= \frac{2\pi jfC_0}{1-k_t^2\left(\beta_\mathrm{p}h/2\right)^{-1}\left\{\cot\left(\beta_\mathrm{p}h/2\right)-R\right\}^{-1}}, \end{aligned} \tag{8.17}$$

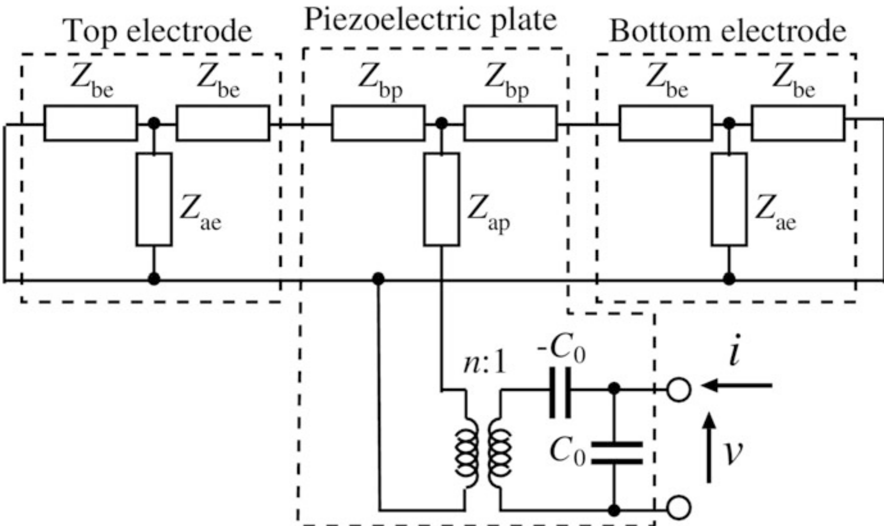

Fig. 8.6 Mason equivalent circuit model of the BAW resonator

where $R = Z_e Z_p^{-1}\tan(\beta_e h_e)$ is a factor giving influence of the electrodes on the resonance characteristics. It should be noted that when $\beta_e h_e \ll 1$, $R \sim 2\pi f Z_p^{-1}(\rho_e h_e)$, where ρ_e is the mass density of the electrode material.

From Eq. (8.17), the resonance frequency f_r is given as a solution of

$$\cot\left(\beta_p h/2\right) = R \tag{8.18}$$

while the anti-resonance frequency f_a is given as a solution of

$$\cot\left(\beta_p h/2\right) - k_t^2\left(\beta_p h/2\right)^{-1} = R. \tag{8.19}$$

Figure 8.7 shows calculated variation of f_r and f_a of the fundamental resonance with R at $f = f_a$. In the figure, the calculated frequencies are normalized by f_a when $h_e = 0$, and k_t^2 was set at 0.05. In the calculation, we assume R is proportional to f. It is seen that f_r and f_a decrease monotonically with R at $f = f_a$. The frequency decrease is due to an increase in the total mass of the resonator structure.

When $h_e = 0$, Eq. (8.17) reduces to

$$Y = \frac{2\pi j f C_0}{1 - k_t^2 \tan\left(\beta_p h/2\right) / \left(\beta_p h/2\right)}. \tag{8.20}$$

This equation relates f_r/f_a with k_t^2 as

$$k_t^2 = \frac{(n\pi f_r/2f_a)}{\tan\left(n\pi f_r/2f_a\right)}, \tag{8.21}$$

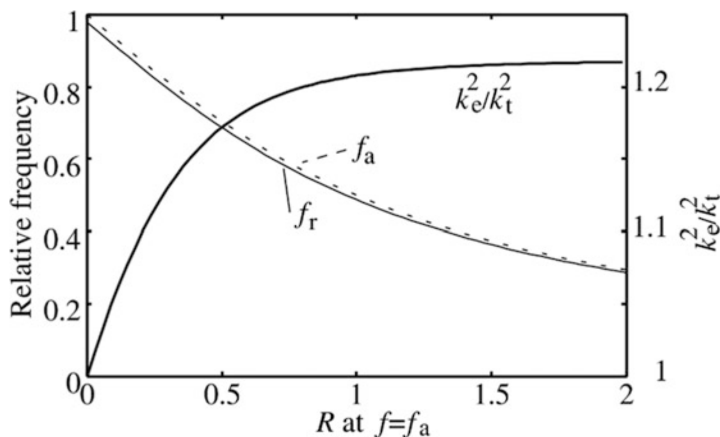

Fig. 8.7 Variation of resonance and anti-resonance frequencies, and k_e^2 with the electrode related parameter R at $f = f_a$

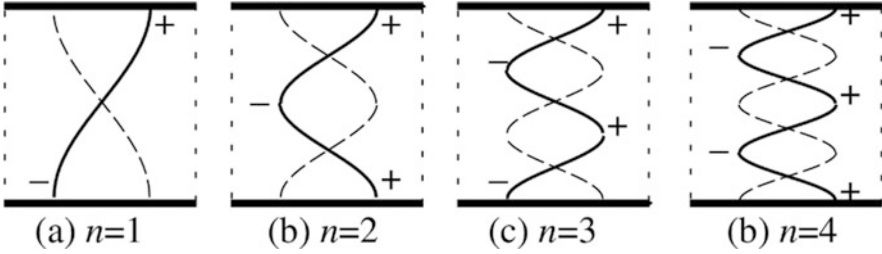

Fig. 8.8 Vertical standing wave pattern

where n is the resonance order appeared in Eq. (8.1). When $f_r \sim f_a$, we can derive the following relation from Eqs. (8.8) and (8.21);

$$2\left(f_a - f_r\right)/f_a \sim \gamma^{-1} \sim \begin{cases} 8k_t^2/n^2\pi^2 & n: \text{ odd} \\ 0 & n: \text{ even} \end{cases}. \tag{8.22}$$

Equation (8.22) indicates that three important facts: (a) achievable γ^{-1} is limited by $k_t{}^2$ of the employed piezoelectric material, (b) even-order overtones cannot be excited electrically, and (c) γ^{-1} decreases rapidly with an increase in n.

Figure 8.8 shows the standing wave pattern of resonances with different n. Because of stress free on the top and bottom surfaces, the displacement takes a maximum there. When n is even, the displacement polarity at the top surface is in-phase with that on the bottom surface. Then the resonance cannot be excited and detected electrically, and γ^{-1} is zero for the case. Even when n is odd, periodicity of the distribution causes cancellation of excited electric fields, and thus γ^{-1} becomes very small when n is large.

It should be noted that Eqs. (8.21)–(8.22) hold only when $h_e = 0$. Since influence of electrodes is not negligible in general, we often characterize piezoelectric strength of the resonator by the "effective" electromechanical coupling factor $k_e{}^2$ defined by

$$k_e^2 = \frac{(\pi f_r/2f_a)}{\tan\left(\pi f_r/2f_a\right)}. \tag{8.23}$$

or its approximated forms of

$$k_e^2 = \frac{\pi^2}{4}\frac{f_a - f_r}{f_a}. \tag{8.24}$$

Figure 8.7 also shows $k_e{}^2$ calculated by Eq. (8.23) as a function of R at $f = f_a$. It is seen that $k_e{}^2$ increases with an increase in R at $f = f_a$, and is going to converge to $\pi^2/8 = 1.234$. This value is the coefficient appearing in Eq. (8.22), and originates from unmatching of the excitation electric field with the acoustic wave field. When R is large, the electrodes can be regarded as the mass and the piezoelectric plate

behaves like a spring. Then the stress field in the plate becomes uniform, and is matched with the excitation electric field. This positive effect of the electrode mass loading was first reported by Lakin et al. [10].

It should be noted that the figure of merit are often evaluated by $M_r = Q_r k_e^2$ and $M_a = Q_a k_e^2$ instead of $M_r = Q_r/\gamma$ and $M_a = Q_a/\gamma$ defined in Eqs. (8.9) and (8.10).

8.4 Resonator Structures

For many years, piezoelectric thin plates required for BAW resonators have been manufactured by mechanical thinning and polishing of piezoelectric plates of quartz and ceramics. Due to difficulty in mechanical processes, practical limit of h was circa a few tens of micrometers, and thus the fundamental resonance frequency was limited in the high frequency (HF) range (<30 MHz). Although use of harmonic resonances with $n \neq 1$ extends this limit, it results in significant increase in γ or decrease in k_e^2.

Smythe and Angove applied anisotropic chemical etching for thinning quartz plates, and this extended applicability of quartz resonators close to the GHz range [11].

In 1980–1981, three groups independently proposed high frequency BAW resonators fabricated by the thin film and micromachining technologies [12–14]. This technology extended applicability of BAW resonators to the ultra high frequency (UHF) and super high frequency (SHF) ranges.

Figure 8.9a shows the proposed device structure called the film bulk acoustic resonator (FBAR). Bottom electrode, piezoelectric film, and top electrode are sequentially deposited and patterned on a supporting substrate (Si). Then the substrate is partially removed from the back side by chemical etching [12–14] or deep reactive ion etching [15], and the free standing diaphragm is realized.

Satoh et al. proposed to use the sacrificial layer technique for the air gap fabrication (see Fig. 8.9b) [16]. First, two additional layers are deposited and patterned, and then bottom electrode, piezoelectric film, and top electrode are successively deposited and patterned. Finally, first additional (bottom) layer is etched away chemically and the air gap is created under the composite diaphragm.

In this process, sticking of the diaphragm to the base substrate is troublesome. The second additional layer is aimed at keeping the distance large and avoiding this problem.

Taniguchi et al. proposed use of bending of the composite diaphragm caused by the internal stress to keep the air gap height [17]. This can eliminate the second additional layer.

Ruby et al. proposed to use the surface micromachining for the same purpose (see Fig. 8.9c) [2]. First, the top surface of the supporting substrate is partially etched, and the etched portion is filled with another material such as phosphosilicate glass, which is used as a sacrificial layer. Remaining fabrication steps are identical with those described above.

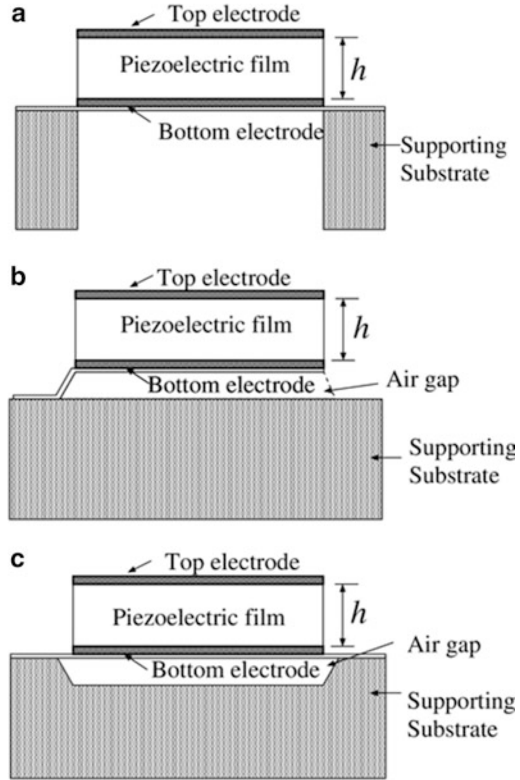

Fig. 8.9 FBAR structures. (**a**) Back-side etched. (**b**) Sacrificial-layer etched. (**c**) Front-side etched

Lakin et al. proposed to use the Bragg reflection instead of the air cavity to isolate the composite membrane acoustically from the base substrate [18]. Figure 8.10 shows this type of proposed device structure called the solidly mounted resonator (SMR). Thin films of low and high acoustic impedance Z_a with quarter wavelength layer are stacked alternately, and they act as the Bragg reflector. SiO_2 is used for low Z_a layers while W or Ta is chosen for high Z_a layers. Due to penetration of acoustic energy into the Bragg reflector, achievable k_e^2 is a little smaller than that in the FBAR structure [19].

It should be noted that the layer thicknesses are slightly modified from quarter wavelengths so that strong reflection occurs not only for the longitudinal vibration but also for shear ones [20]. This modification gives significant enhancement of the Q factors.

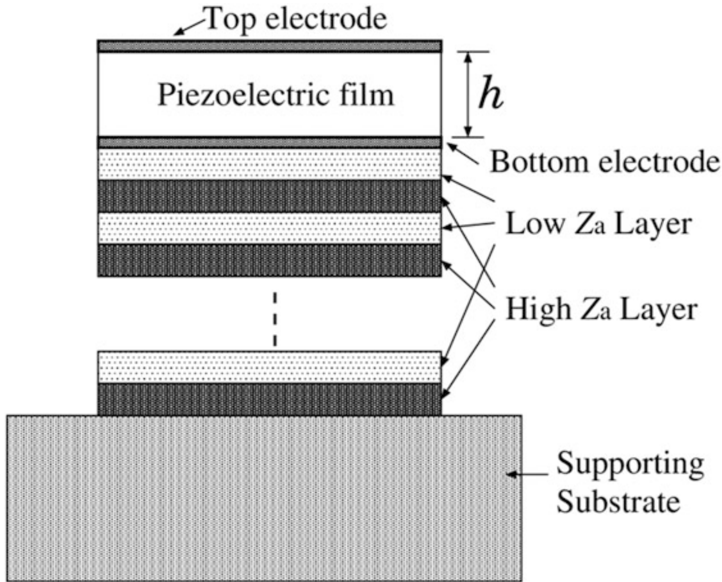

Fig. 8.10 SMR structure

8.5 Material Choice

Choice of the piezoelectric material is determinative for designing high performance RF BAW resonators. That is, k_t^2 limits achievable fractional frequency bandwidth for filter applications.

Aluminum nitride (AlN) is widely used for the purpose because of its several distinct features: low propagation loss, high electrical resistivity, and compatibility with CMOS fabrication processes and equipment [21, 22]. Although various materials such as zinc oxide (ZnO) [12–14, 16] and lead zirconate titanate (PZT) [23, 24] have been investigated extensively for the use, realized performances are much worse than those attained by AlN and far from practical use.

In general, piezoelectric films used in these resonators are polycrystalline, and resonator performances are significantly dependent on various film properties such as crystallinity, orientation, grain size, and binding strength among grains, and they must be uniform through the wafer and/or batches for mass production. Thus appropriate techniques and/or apparatus must be selected for the film deposition [22, 25].

Recently, Sc doping in AlN films is paid much attention owing to its drastic enhancement of the electromechanical coupling [26–28]. When the Sc content is 43 at.%, k_t^2 takes a maximum value about five times larger than non-doped AlN films. Yokoyama et al., proposed co-doping of Mg and Zr for the same purpose [29].

In general, stiff materials have small acoustic attenuation. With an increase in the doping amount, BAW velocities in these films decrease and the acoustic attenuation becomes large.

Molybdenum (Mo) [2], tungsten (W) [19], and ruthenium (Ru) [30] are often used for the electrodes because their large acoustic impedance offers increase in k_e^2 described in Sect. 8.3, and they act as a good seed layer for the AlN growth.

Another important merit of these materials is compensation of the internal stress generated during the AlN deposition. This property is crucial for realization of the free standing membrane in the FBAR structures. In many cases, AlN films with good crystal quality possess large internal stress.

Amorphous silicon dioxide (SiO_2) possesses a quite unique feature in acoustics. Namely, SiO_2 becomes stiff with temperature T. In contrast, most of all materials including AlN, Mo, and Ru become soft with T. Thus the temperature coefficient of the resonance frequency (TCF) can be improved by inclusion of SiO_2 in the resonator structure [31, 32].

It should be noted that SiO_2 is non-piezoelectric and relatively lossy. Thus the TCF compensation by SiO_2 is only possible at an expense of the k_e^2 and Q reduction. In general, SMRs offer better TCF but worse Q than FBARs because SiO_2 is used in the Bragg reflector [19].

There is another aspect to be paid much attention when fabricating a BAW resonator with SiO_2 layers. That is, properties of SiO_2 are very dependent on the deposition technique, apparatus, and conditions, and thus appropriate deposition environments must be endeavored for the current purpose [33].

8.6 Lateral Wave Propagation

Since real BAW resonators possess three-dimensional structures, we must take their influences into account.

Let us consider, as an example, the FBAR structure shown in Fig. 8.11. When the center portion of the resonator vibrates, excited acoustic waves may also propagate

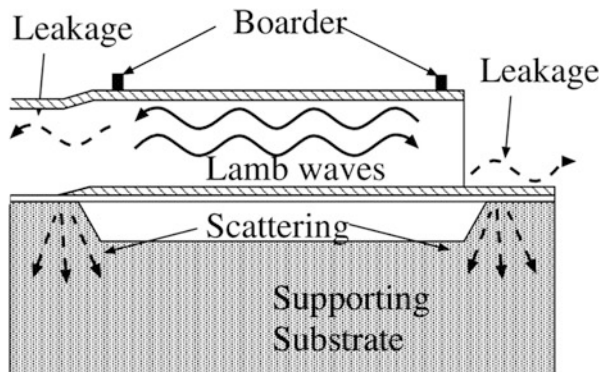

Fig. 8.11 FBAR structure and Lamb wave propagation and leakage

laterally in the diaphragm. Acoustic waves guided in a plate are called Lamb waves. Since leakage of excited Lamb waves causes deterioration of the resonator Q, its suppression is necessary.

The energy leakage can be suppressed by designing side edges to cause the total reflection for all Lamb modes and confine wave energy in the resonator area. However, this strategy causes another problem. That is, due to phase lag with propagation, trapped Lamb modes cause unnecessary spurious resonances close to the main resonance. They are called the transverse mode resonances or inharmonic overtones. The most important but never ending design theme is their suppression without badly affecting the Q factor of the main mode.

The resonance condition of the transverse modes is given by

$$\beta_y W - \angle\Gamma_y = n_y \pi, \tag{8.25}$$

where β_y is the wavenumber of Lamb modes along the surfaces, W is the electrode width, n is the order of the lateral resonance, and Γ_y is the reflection coefficient at the side edges, respectively.

Figure 8.12 shows lateral standing pattern of the Lamb modes when the lateral edges are mechanically free. In this case, the displacement takes a maximum there. It should be noted that, similar to the longitudinal resonances, electrical excitation efficiency will be decreased significantly with an increase in n_y (or β_y) because of mutual cancellation of charges induced by the sinusoidal field.

By a simple analogy from electromagnetic waveguides, readers may think the relation between β_y and ω, namely, the dispersion relation is given by

$$\beta_y = \sqrt{(\omega/V)^2 - (n\pi/h)^2} = V^{-1}\sqrt{\omega^2 - \omega_r^2},$$

where h is the plate thickness and ω_r is the thickness resonance frequency. This equation indicates that waveguide modes exhibit cutoff nature and can propagate laterally only when $\omega > \omega_r$. However, it is more complex for acoustic waveguide cases and cannot be expressed in a closed form even when anisotropy is ignored. This is because the mutual conversion occurs between longitudinal and shear bulk

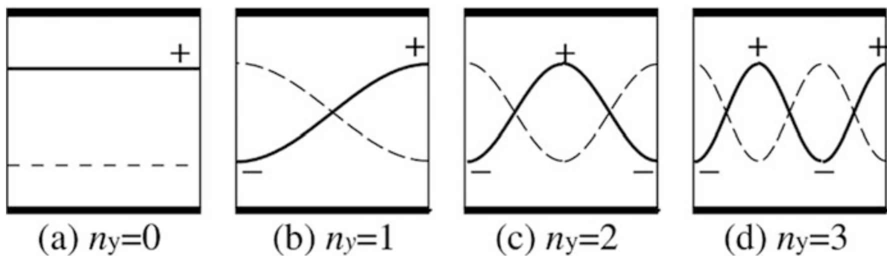

Fig. 8.12 Lateral resonance patterns

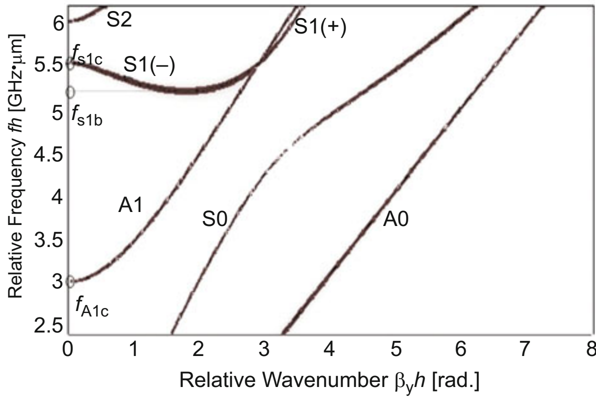

Fig. 8.13 Dispersion relation of Lamb modes in the AlN plate

waves at the top and bottom surfaces and its influence to the Lamb wave propagation is significant. Existence of anisotropy and piezoelectricity makes the analysis more complex. Detailed discussions on acoustic waveguides are seen in Ref. [34].

Figure 8.13 shows the horizontal wavenumber β_y of Lamb modes propagating in an AlN plate with $h_e = 0$ as a function of f. In the figure, Sn and An indicate the nth order symmetric and anti-symmetric Lamb modes, respectively. A branch of the first-order symmetric (S_1) mode intercepts with the vertical axis at $f = f_{S1c}$ (5.55 GHz • μm/h), which corresponds to the resonance frequency f_r of the main TE mode. When $f_{S1b} < f < f_{S1c}$, the S_1 mode can propagate laterally, and it may cause spurious lateral resonances after reflections at side edges. On the other hand, when $f < f_{S1b}$ and $f > f_{S1c}$, the S_1 mode is cut off, and the spurious resonances do not occur.

Two branches of the S1 mode meet at $f = f_{S1b}$, and both of them cannot propagate laterally when $f < f_{S1b}$. This variation of β_y with respect to ω, i.e., $\partial\beta_y/\partial\omega < 0$, is often called the Type-II dispersion.

In other device structures and materials, $\partial\beta_y/\partial\omega$ is quite often positive near the cut off frequency corresponding to the fundamental resonance. This type is called the Type-I dispersion, and the transverse resonances occur at frequencies above the fundamental resonance in the case.

Other Lamb modes exist in the structure. When β is large, these modes are hardly excited electrically because sinusoidal variation causes mutual cancellation of excited vibration. A1 and S2 modes correspond to the first and second-order thickness shear resonances, respectively, at the cut off, which are not excitable electrically when c-axis oriented AlN films are used. Thus only the S1 mode close to the cutoff ($f = f_{S1c}$) is efficiently excitable electrically.

Equation (8.25) indicates that resonance frequencies with $n_y \neq 0$ can be set far from the main resonance frequency with $n_y = 0$ when W is small. But it is not acceptable for filter applications because reduced electrode area results in increased resonator impedance. Furthermore, reduction of the electrode size results in that of the resonator Q factor. Thus it is not practical to connect multiple resonators with small electrode area electrically in parallel.

As a practical solution, electrodes are often shaped into a polygon with nonparallel edges to smear out spurious resonances. This technique is called apodization [35, 36]. It may cause Q deterioration of the main resonance due to relatively large attenuation of Lamb waves with propagation.

One interesting idea is the so called piston mode structure [37], where the resonator side edges are designed to be $\angle\Gamma_y = 0$. As shown in Fig. 8.12, charges induced on the electrodes will be cancelled out due to the sinusoidal field variation of higher-order modes ($n_y > 0$). On the other hand, the fundamental mode ($n_y = 0$) is excitable and detectable electrically because of uniformity of the displacement field.

This idea seems simple and easy to realize. But it is not true. This is because oblique incidence of longitudinal waves to the boundaries causes conversion to shear waves and vice versa, and Lamb modes incident to side edges will cause additional phase shift and/or conversion to the other modes. Namely, electrode edges cause significant scattering of the TE vibration to Lamb modes.

As shown in Fig. 8.11, top and bottom electrodes and/or the piezoelectric film are often extended to peripherals for the electrical connection. They may cause not only the phase shift and mode conversion but also energy leakage.

It is known that these effects can be reduced by defining boarders for efficient reflection of Lamb modes [38]. An example is the overlay (mass-loading) on the top electrodes shown in Fig. 8.11. Under proper design, the mode conversion is well suppressed and large Γ_y is achievable. Furthermore, the piston mode operation is possible by designing the perimeter region so that $\angle\Gamma_y = 0$ at its inner edge [39, 40].

8.7 Summary

This chapter described basic properties and modeling of piezoelectric BAW resonators.

Due to the limited space, all rigorous and/or detailed discussions are intentionally omitted. Also, discussions on several important aspects such as history, filter applications, packaging, fabrication, and integration could not be included in this chapter due to the same reason.

Readers who are willing to know them more in detail, please refer to Refs. [41, 42].

References

1. Vig JR (2000) Quartz crystals and oscillators: a tutorial. http://www.am1.us/Local_Papers/U11625%20VIG-TUTORIAL.pdf
2. Ruby R, Bradley P, Oshmyansky Y, Chien A (2001) Thin film bulk wave acoustic resonators (FBAR) for wireless applications. In: Proc. IEEE ultrason. symp., pp 813–821

3. Lam CS (2008) A review of the recent development of MEMS and crystal oscillators and their impacts on the frequency control products industry. In: Proc. IEEE ultrason. symp., pp 694–704
4. Rosenbaum JF (1988) 10.5 Butterworth-Van Dyke equivalent circuit. In: Bulk acoustic wave theory and devices. Artech House, London, pp 389–191
5. Hashimoto K (2000) 5.4 Impedance element filters. In: Surface acoustic wave devices in telecommunications. Springer, Berlin, pp 149–160
6. Larson JD, Bradley P, Wartenberg S, Ruby RC (2000) Modified Butterworth-Van Dyke circuit for FBAR resonators and automated measurement system. In: Proc. IEEE ultrason. symp., pp 863–868
7. Feld DA, Parker R, Ruby R, Bradley P, Dong S (2008) After 60 years: a new formula for computing quality factor is warranted. In: Proc. IEEE ultrason. symp., pp 431–436
8. Mason WP (1964) Piezoelectric crystals and mechanical resonators. In: Mason WP (ed) Physical acoustics: principles and methods, vol IA. Academic Press, New York, pp 335–416
9. Kino GS (1987) Chapter 1: Sound wave propagation. In: Acoustic waves: devices, imaging, and analog processing. Prentice-Hall, Englewood Cliffs, pp 1–81
10. Lakin KM, Belsick J, McDonald JF, McCarron KT (2001) Improved bulk wave resonator coupling coefficient for wide bandwidth filters. In: Proc. IEEE ultrason. symp., pp 827–831
11. Smythe R, Angove R (1988) Chemically-milled UHF SC-Cut resonators. In: Proc. IEEE freq. contr. symp., pp 73–77
12. Grudkowski T, Black J, Reeder T, Cullen DE, Wagner RA (1980) Fundamental-mode VHF/UHF miniature acoustic resonators and filters on silicon. Applied Physics Letters 37: 993–995
13. Nakamura K, Sasaki H, Shimizu H (1981) A piezoelectric composite resonator consisting of a ZnO film on an anisotropically etched silicon substrate. Japanese Journal of Applied Physics 20:111–114
14. Lakin KM, Wang J (1981) Acoustic bulk wave composite resonators. Applied Physics Letters 39(3):125–128
15. Nishihara T, Yokoyama T, Miyashita T, Satoh Y (2002) High performance and miniature thin film bulk acoustic wave filters for 5 GHz. In: Proc. IEEE ultrason. symp., pp 969–972
16. Satoh H, Ebata Y, Suzuki H, Narahara C (1985) An air gap type piezoelectric composite resonator. In: Proc. IEEE freq. contr. symp., pp 361–366
17. Taniguchi S, Yokoyama T, Iwaki M, Nishihara T, Ueda M, Satoh Y (2007) An air-gap type FBAR filter fabricated using a thin sacrificed layer on a flat substrate. In: Proc. IEEE ultrason. symp., pp 600–603
18. Lakin KM, McCarron KT, Rose RE (1995) Solidly mounted resonators and filters. In: Proc. IEEE ultrason. symp., pp 905–908
19. Ruby R (2007) Review and comparison of bulk acoustic wave FBAR, SMR technology. In: Proc. IEEE ultrason. symp., pp 1029–1040
20. Marksteiner S, Kaitila J, Fattinger GG, Aigner R (2005) Optimization of acoustic mirrors for solidly mounted BAW resonators. In: Proc. IEEE ultrason. symp., pp 329–332
21. Wang JS, Lakin KM (1981) Sputtered AlN films for bulk-acoustic-wave devices. In: Proc. IEEE ultrason. symp., pp 502–505
22. Michin S, Oshmyansky Y (2009) Chapter 7: Thin film deposition for BAW devices. In: Hashimoto K (ed) RF bulk acoustic wave filters for communications. Artech House, Boston, pp 173–196
23. Misu K, Nagatsuka T, Wadaka S, Maeda C, Yamada A (1998) Film bulk acoustic wave filters using lead titanate on silicon substrate. In: Proc. IEEE ultrason. symp., pp 1091–1094
24. Larson JD, Gilbert SR, Xu B (2004) PZT material properties at UHF and microwave frequencies derived from FBAR measurements. In: Proc. IEEE ultrason. symp., pp 173–177
25. Aigner R, Elbrecht L (2009) Chapter 5: Design and fabrication of BAW devices. In: Hashimoto K (ed) RF bulk acoustic wave filters for communications. Artech House, Boston, pp 91–115

26. Akiyama M, Kamohara T, Kano K, Teshigahara A, Takeuchi Y, Kawahara N (2009) Enhancement of piezoelectric response in scandium aluminum nitride alloy thin films prepared by dual reactive cosputtering. Advanced Materials 21(5):593–596
27. Moreira M, Bjurström J, Katardjev I, Yantchev V (2011) Aluminum scandium nitride thin-film bulk acoustic resonators for wide band applications. Vacuum 86:23–26
28. Matloub R, Artieda A, Sandu C, Milyutin E, Muralt P (2011) Electromechanical properties of $Al_{0.9}Sc_{0.1}N$ thin films evaluated at 2.5 GHz film bulk acoustic resonators. Applied Physics Letters 99(9):092903-1–092903-3
29. Yokoyama T, Iwaki Y, Onda Y, Nishihara T, Sasajima Y, Ueda M (2014) Effect of Mg and Zr co-doping on piezoelectric AlN thin films for bulk acoustic wave resonators. IEEE Transactions on Ultrasonics, Ferroelectronics, & Frequency Control 61(8):1322–1328
30. Yokoyama T, Nishihara T, Taniguchi S, Iwaki M, Satoh Y, Ueda M, Miyashita T (2004) New electrode material for low-loss and high-Q FBAR filters. In: Proc. IEEE ultrason. symp., pp 429–432
31. Nakamura K, Ohashi Y, Shimizu H (1986) UHF bulk acoustic wave filters utilizing thin ZnO/SiO_2 diaphragms on silicon. Japanese Journal of Applied Physics 25(3):371–375
32. Zou Q, Bi F, Tsuzuki G, Bradley P, Ruby R (2013) Temperature-compensated FBAR duplexer for band 13. In: Proc. IEEE ultrason. symp., pp 236–238
33. Matsuda S, Hara M, Miura M, Matsuda T, Ueda M, Satoh Y, Hashimoto K (2011) Correlation between temperature coefficient of elasticity and Fourier transform infrared spectra of silicon dioxide films for surface acoustic wave devices. IEEE Transactions on Ultrasonics, Ferroelectronics, & Frequency Control 58(8):1684–1687
34. Auld BA (1989) Chapter 10: Acoustic waveguide. In: Acoustic waves and fields in solids, vol II. Krieger, Malabar, FL, pp 63–220
35. Lason JD, Ruby RC, Bradley P (1999) Bulk acoustic wave resonator with improved lateral mode suppression. US Patent 6,215,375 B1, 1999
36. Ruby R, Larson JD, Feng C, Fazzio S (2005) The effect of perimeter geometry on FBAR resonator electrical performance. In: Technical digest, IEEE MTT-S microwave symp., pp 217–220
37. Kaitila J, Ylilammi M, Ellä J (1999) Resonator structure and a filter comprising such a resonator structure. US Patent 6,812,619 B1, 1999
38. Feng H, Fazzio RS, Ruby R, Bradley P (2004) Thin film bulk acoustic resonator with a mass loaded perimeter. US Patent 7280007 B2, 2004
39. Fattinger GG, Marksteiner S, Kaitila J, Aigner R (2005) Optimization of acoustic dispersion for high performance thin film BAW resonators. In: Proc. IEEE ultrason. symp., pp 1175–1178
40. Kaitila J (2009) Chapter 3: BAW device basics. In: Hashimoto K (ed) RF bulk acoustic wave filters for communications. Artech House, Boston, pp 51–90
41. Rosenbaum JF (1988) Bulk acoustic wave theory and devices. Artech House, Boston
42. Hashimoto K (ed) (2009) RF bulk acoustic wave filters for communications. Artech House, Boston

Chapter 9
Shear Piezoelectric MEMS Resonators

D.T. Chang and D.J. Kirby

High Q, low loss, small size, and the potential for high-frequency operation are the primary benefits of shear piezoelectric MEMS resonators. The mechanical Q of a device strongly determines the overall frequency stability of the resonator/oscillator under test. In particular, piezoelectric crystals such as quartz can be carefully oriented to provide frequency stabilization over temperature. Thickness-shear-mode (TSM) piezoelectric resonators have been fabricated in the MHz–GHz frequency range using wafer-level processing suitable for volume manufacturing of frequency control devices. This chapter discusses the fundamentals of shear-mode operation and provides examples of simulated and fabricated devices and their performance and applications.

9.1 Introduction to MEMS Resonators

Miniaturization of crystal resonators for frequency control applications has driven technology development toward MEMS components. MEMS resonators are attractive for use as oscillators by virtue of their reduced cost, size, weight, and power (CSWaP), combined with the potential for integration with electronics. When designing crystal oscillators for frequency sources, the resonator frequency stability is of paramount importance. In general, thermal frequency variation and quality factor, Q, of the resonator play a dominant role in overall frequency stability.

The aspects of MEMS resonator systems determining efficient, low-noise operation and high-frequency stability are the *transduction technique*, *vibration mode type*, and the *material system*. Examples of MEMS resonator transduction

D.T. Chang (✉) • D.J. Kirby
HRL Laboratories LLC, 3011 Malibu Canyon Road, Malibu, CA 90265, USA
e-mail: dtchang@hrl.com

© Springer International Publishing Switzerland 2017

H. Bhugra, G. Piazza (eds.), *Piezoelectric MEMS Resonators*,
Microsystems and Nanosystems, DOI 10.1007/978-3-319-28688-4_9

techniques include *electrostatic*, *piezoelectric*, *piezoresistive*, *magnetic*, and *thermal*. Examples of vibration modes are *flexural*, *contour*, *extensional*, and *shear*. Material systems for MEMS devices commonly include *silicon*, *polysilicon*, *quartz*, *AlN*, $LiNbO_3$, $LiTaO_3$, *ZnO*, *PZT*, and *GaN*.

Piezoelectric transduction exploits a reciprocal mechanical strain induced with applied electric field. With an AC voltage applied, the fluctuating mechanical strain excites a vibration. By comparison, electrostatic (capacitive) transduction uses electrodes across an air gap to produce alternating electrostatic forces necessary to drive the device into motion. In contrast the piezoresistive mechanism, used mainly for sensing as opposed to excitation, utilizes an induced change in flexure of an element to provide a change in measured resistance. For magnetic transduction, a uniform magnetic field applied to a magnetic material causes the material to deflect, thereby mechanically actuating the structure. And for thermal devices, an oscillating voltage passing through a resistive medium results in an alternating ohmic loss component. An element subjected to varying losses experiences heating and cooling which, via thermomechanical coupling, can resonantly actuate the structure. In each of the excitation categories, amplitude of mechanical vibration builds according to the Q of the resonant mode. Modal vibration amplitude is Q times larger on resonance compared with off resonance. The mechanical Q of the resonant mode is important as it strongly determines the overall frequency stability of the component under test.

MEMS resonators support *flexural*, *contour*, *extensional*, and *shear* modes with the vibration mode type generally classifying the resonator type. Resonant frequencies are determined by the material properties and the mechanical dimensions of the resonator. The general operating frequency range of each of these resonator classes is summarized in Table 9.1.

Lower-frequency devices (10 kHz–10 MHz) are typically flexure-mode resonators such as a polysilicon beam [1]. Next higher in frequency are the *AlN* or $LiNbO_3$ contour-mode resonators (CMR) which vibrate in a body dilation mode in the range 10 MHz–10 GHz [2, 3]. Shear-mode devices, for example, quartz and silicon thickness-shear-mode resonators, operate up to 1–2 GHz [4–6]. Finally, the higher-frequency devices operating up to 20 GHz include thickness extensional resonators which vibrate across the thickness of the piezoelectric device. Examples include the thin-film bulk acoustic resonator (FBAR) devices, commercially available in aluminum nitride (*AlN*) [7, 8].

Table 9.1 Operating frequency range versus vibration mode of resonators

Vibration mode	Operation frequency range
Flexure	10 kHz–10 MHz
Contour	10 MHz–10 GHz
Shear	10 MHz–2 GHz
Thickness extensional	500 MHz–20 GHz

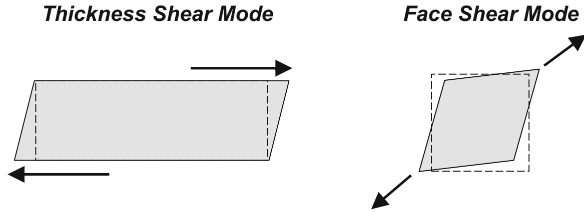

Fig. 9.1 Thickness-shear- and face-shear-mode schematics

9.2 Piezoelectric Shear Modes

Narrowing our focus to piezoelectric shear resonators, devices can support either "*thickness*"-shear or "*face*"-shear modes. Examples of the distortion occurring for a thickness-shear mode and a face-shear mode are shown in Fig. 9.1.

Piezoelectric thickness-shear modes exhibit shearing displacement along one axis which is perpendicular to the device thickness. These modes are electrically excited by an electric field along the Y-axis (direction of thickness) and shear along the crystal X- or Z-axes. Resonance frequencies of the thickness-shear modes occur when the thickness contains an odd integral number of half wavelengths. (Even modes are eliminated due to charge conservation.) Thickness-shear modes have high Q and low impedance. Quartz face-shear devices typically use CT- and DT-cut crystals and distort along more than one axis. Face-shear resonators are not yet as well developed because of their susceptibility to interference from flexural modes [9].

9.3 Piezoelectric Thickness-Shear Principles

For a crystal to be piezoelectric, it must have no center of symmetry (non-centrosymmetric). The piezoelectric effect is a reciprocal effect converting mechanical pressure into an electric field or an electrical field into mechanical strain energy.

At rest and in the absence of any applied potential E, the net charge on the surface of a piezoelectric crystal is zero since all charges within the material sum to zero. However, with a potential bias applied across opposite crystal faces, the surface charge is locally non-zero and a strain or dimensional change takes place. With an applied AC potential, a vibration mode is created in the structure. As the charges change sign with the applied field, the resulting strain follows the field, creating a vibration mode. The material and dimensions of the structure determine the absolute frequency of the resonant modes, and on resonance the vibration amplitude is amplified by the Q-factor of the mode.

Evaluating the total strain in the crystal, one needs to sum the strain developed under the piezoelectric effect plus the strain derived from Hooke's law for a non-piezoelectric material. Hooke's law for a non-piezoelectric material states that

$$T_{ij} = c_{ijkl} S_{kl} \tag{9.1}$$

or

$$S_{ij} = s_{ijkl}T_{kl} \tag{9.2}$$

where T = applied stress, S = strain, c = the components of Young's modulus (elastic stiffness coefficients), and s = the elastic compliance coefficients (inverse of c). Note that for isotropic uniaxial cases, the stiffness is a single value of the Young's modulus, E, whereas for anisotropic materials, stiffness has a tensor representation as in Eqs. 9.1 and 9.2. For a piezoelectric material, an applied stress (T) or strain (S) produces a contribution to electric polarization (P) through the piezoelectric strain coefficients (d) or the piezoelectric stress coefficients (e) as in Eqs. 9.3 and 9.4 [10]:

$$P_i = d_{ijk}T_{jk} \tag{9.3}$$

or

$$P_i = e_{ijk}S_{jk} \tag{9.4}$$

Conversely, when placed in an electric field E, a piezoelectric crystal develops strain which deforms the structure as represented in Eqs. 9.5 and 9.6:

$$S_{jk} = d_{ijk}E_i \tag{9.5}$$

or

$$T_{jk} = e_{ijk}E_i \tag{9.6}$$

The first subscript denotes the direction of the electric polarization or of the electric field, and the last two subscripts denote the direction of stress or strain. Hence summing Eqs. 9.2 and 9.5, the total strain S can be expressed as a function of the piezoelectric strain by

$$S_{ij} = s_{ijkl}T_{kl} + d_{kij}E_k \tag{9.7}$$

Similarly, summing polarization contributions from the applied stress (Eq. 9.3) and from the applied electric field (Eq. 9.8),

$$P_i = \varepsilon_0 \chi_{ij} E_j \tag{9.8}$$

And, using the well known electric displacement equation,

$$D = \varepsilon_0 E + P \tag{9.9}$$

Where ε_0 = permittivity of free space, 8.854×10^{-12} F/m.

We can sum Eqs. 9.3 and 9.8 and subsequently convert to electric displacement D. Therefore, we complete the pair of piezoelectric constitutive equations with Eq. 9.10:

$$D_i = d_{ikl}T_{kl} + \varepsilon_{ik}E_k \tag{9.10}$$

An alternate form of the pair of Eqs. 9.7 and 9.10 can be written for the total stress T in terms of the piezoelectric stress as in Eqs. 9.11 and 9.12:

$$T_{ij} = c_{ijkl}S_{kl} - e_{kij}E_k \tag{9.11}$$

$$D_i = e_{ikl}S_{kl} + \varepsilon_{ik}E_k \tag{9.12}$$

where $\varepsilon =$ dielectric permittivity coefficients. Note that the stress and strain tensors are symmetric and therefore $d_{ijk} = d_{ikj}$ and similarly $e_{ijk} = e_{ikj}$. The piezoelectric stress e and strain d coefficients are related through the elastic stiffness constants, c.

Considering the strain arising from the applied electric field as in Eq. 9.7, represented in matrix notation, we can write that the strain (S) and electric field (E) are related by the piezoelectric strain coefficient matrix d. To convert from tensor notation to matrix condensed notation, the first tensor subscript is retained, and the following two subscripts are replaced with a single value according to Table 9.2:

$$\begin{bmatrix} S_{xx} \\ S_{yy} \\ S_{zz} \\ S_{yz} \\ S_{zx} \\ S_{xy} \end{bmatrix} = \begin{bmatrix} d_{11} & d_{21} & d_{31} \\ d_{12} & d_{22} & d_{32} \\ d_{13} & d_{23} & d_{33} \\ d_{14} & d_{24} & d_{34} \\ d_{15} & d_{25} & d_{35} \\ d_{16} & d_{26} & d_{36} \end{bmatrix} \begin{bmatrix} E_x \\ E_y \\ E_z \end{bmatrix} \tag{9.13}$$

In Eq. 9.13, the shearing terms are the cross terms of the strain coefficients, S_{yz}, S_{zx}, and S_{xy}. For thickness-shear-mode resonators, the resonator thickness lies in the crystal Y-direction. Therefore, the thickness-shear terms are generated in the YZ- and XY-planes via the components S_{yz} and S_{xy}, whereas the term S_{zx} corresponds to "in-plane" shearing.

Considering piezoelectric materials, it is useful then to compare the strength of the piezoelectric stress/strain coefficients. Many thin-film piezoelectrics such as *AlN*, *ZnO*, and *PZT* have three significant piezoelectric coefficients, d_{31} (or e_{31}), d_{33} (or e_{33}), and d_{15} (or e_{15}), which can be exploited to induce strains/stress in

Table 9.2 Conversion between tensor notation and matrix notation

Tensor notation, jk	11	22	33	23,32	31,13	12,21
Matrix notation, p	1	2	3	4	5	6

Table 9.3 Piezoelectric strain coefficients d ($\times 10^{-12}$ C/N) [10]

Material	d_{11}	d_{14}	d_{22}	d_{31}	d_{33}	d_{15}
α-Quartz	2.31	−0.67	0	0	0	0
$LiNbO_3$	0	0	20.8	−0.85	6.0	69.2
$LiTaO_3$	0	0	7.5	−3.0	5.7	26.4

Table 9.4 Piezoelectric stress coefficients e (C/m^2) [10–12]

Material	e_{11}	e_{14}
α-Quartz	0.171	0.0403
$La_3Ga_5SiO_{14}$	−0.431	0.108
$La_3Ga_{5.5}Ta_{0.5}O_{14}$	−0.54	0.07

different directions. Lithium niobate ($LiNbO_3$) and lithium tantalate ($LiTaO_3$) have four non-zero components, $d_{21} = -d_{22}$ (or $e_{21} = -e_{22}$), d_{31}(or e_{31}), d_{33} (or e_{33}), and d_{15} (or e_{15}) [10]. However, quartz (SiO_2), langasite ($La_3Ga_5SiO_{14}$, LGS), and langatate ($La_3Ga_{5.5}Ta_{0.5}O_{14}$, LGT) are of the same crystal class and have only two non-zero components, d_{11} (or e_{11}) and d_{14} (or e_{14}) [10–12]. Values of some available piezoelectric strain coefficients d are given in Table 9.3, and the piezoelectric stress coefficients e are given in Table 9.4.

Although alpha (α)-quartz has moderate to small values for the piezoelectric strain coefficients, d, it is attractive for frequency control applications because of its potential for high Q and low impedance. Alpha-quartz belongs to the trigonal crystal system with point group 32. A crystal has X-, Y-, and Z-axes along which the material properties are defined. The Z-axis of the crystal is defined as parallel to the trigonal c-axis of crystal symmetry. A phase transition occurs at $T = 573$ °C, at which temperature α-quartz transforms to β-quartz and is no longer piezoelectric. Any further discussion of quartz in this chapter assumes it is in the α-phase.

Examining more closely, quartz crystals have many piezoelectric strain terms equal to zero, and the trigonal symmetry reduces the generalized matrix of Eq. 9.13 to that of Eq. 9.14:

$$\begin{bmatrix} S_{xx} \\ S_{yy} \\ S_{zz} \\ S_{yz} \\ S_{zx} \\ S_{xy} \end{bmatrix} = \begin{bmatrix} d_{11} & 0 & 0 \\ -d_{11} & 0 & 0 \\ 0 & 0 & 0 \\ d_{14} & 0 & 0 \\ 0 & -d_{14} & 0 \\ 0 & -2d_{11} & 0 \end{bmatrix} \begin{bmatrix} E_x \\ E_y \\ E_z \end{bmatrix} \tag{9.14}$$

In this case, as can be seen from Eq. 9.14, shearing can develop in quartz, langasite, or langatate with either E_x or E_y applied. All other d terms corresponding to E_z are zero. From Table 9.3, for α-quartz, we have the piezoelectric strain coefficients $d_{11} = 2.3 \times 10^{-12}$ C/N and $d_{14} = -0.67 \times 10^{-12}$ C/N. The corresponding piezoelectric stress coefficients are $e_{11} = 0.171$ C/m^2 and $e_{14} = 0.0403$ C/m^2 as seen in Table 9.4. The absolute value of $2d_{11}$ compared with d_{14} is such that the S_{xy} dominates over S_{zx} for applied electric field E_y. Note that in order to use d_{11} for thickness-shear modes in quartz, we must apply E_y. For the case of finite E_y and

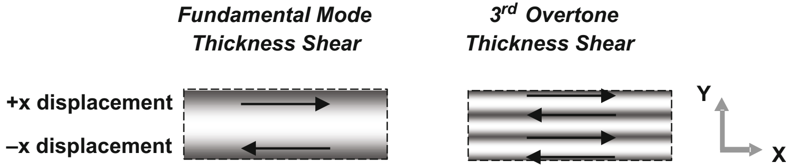

Fig. 9.2 Schematic of *AT*-cut quartz crystal *X*-displacement for the fundamental and third overtone thickness-shear modes. An integral number of half wavelengths exist through the crystal thickness

E_x and $E_z = 0$, the piezoelectric strain coefficient d_{11} produces an S_{xy} component of strain resulting in a thickness shearing displacement of the crystal in the *XY*-plane.

Pictorially, an *AT*-cut quartz crystal shears in the *X*-direction, through the thickness, *Y*, and about the *Z*-axis as presented in Fig. 9.2. In both the fundamental-mode and a third overtone thickness-shear mode, the top and bottom surfaces of the crystal undergo maximum *X*-displacement in opposite directions. For the fundamental mode, a single minimum displacement (null) occurs between these two maxima, forming a half shear-mode wavelength through the thickness. For the third overtone mode, three half wavelengths are formed between the two surfaces of the crystal.

9.4 Quartz Crystal Cut Angles

Thickness-shear modes can be generated in quartz using *AT*-, *SC*-, *BT*-, *FC*-, and *IT*-cut crystals. These cuts are desirable because they lie on the locus of the zero temperature coefficient curves and therefore have the potential to provide a high degree of frequency stability over temperature [13, 14].

Crystals are cut with reference to the *X*-, *Y*-, and *Z*-axes. In the case of a *Y*-cut crystal, the *Y*-axis lies perpendicular to the crystal plate, and the thickness of the crystal plate lies along the *Y*-axis. Similarly, *X*- and *Z*-cut plates lie perpendicular to the *X*- and *Z*-axes, respectively. The quartz blank material is orientated differently before wafer and device fabrication to form the varying quartz cuts. Thus, for each cut, the transduction/excitation field interacts with a modified version of the material.

AT- and *SC*-cuts (modified *Y*-cuts) are the most effective quartz cuts to achieve temperature compensation for high-frequency devices. A classic *AT*-cut quartz crystal is a singly rotated *Y*-cut such that the quartz plate rotates about the *X*-axis and from the *Z*-axis toward the *XY*-plane by 35.25° (35° 15′) as illustrated in Fig. 9.3. In this case, shearing occurs in the *X*-direction. In contrast, an *SC*-cut crystal is a doubly rotated *Y*-cut. As an example, the quartz is first rotated by $\phi = 22.4°$ about the *Z*-axis from *X* toward *Y* and subsequently by $\theta = 33.88°$ again about the *X*-axis and from the *Z*-axis toward the *XY*-plane [15]. An *SC*-cut crystal

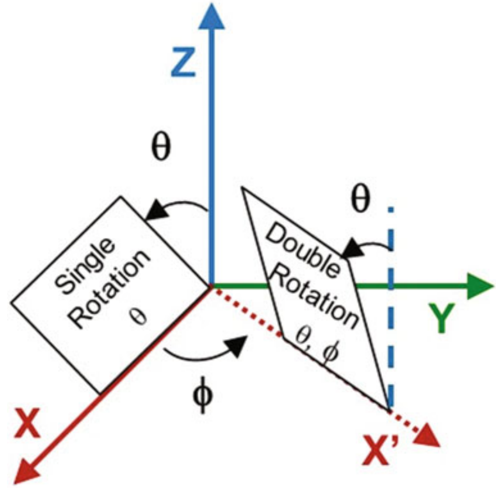

Fig. 9.3 Crystal orientation angles defining singly rotated (e.g., *AT*-cut) and doubly rotated (e.g., *SC*-cut) quartz crystals

has a small out-of-plane shearing component in the *Y*-axis. These two crystal cuts offer quite different frequency-temperature (*f*-*T*) performance. The highest stability crystal oscillators typically use *SC*-cuts. Although they are more difficult and costly to manufacture, they offer in-plane stress compensation and therefore higher thermal frequency stability over *AT*-cut crystals.

Additionally, it is useful to examine the piezoelectric coupling constant, *K*, for each crystal cut. This is a dimensionless number derived from the material properties and provides an indication of the strength of the piezoelectric effect for a given material. Quartz has low coupling factor *K* compared with other piezoelectric materials, but is still desirable for its high Q and low electrical impedance. Values of the electromechanical coupling factor $K = 8.8\,\%$ for *AT*-cut quartz and $K = 4.99\,\%$ for *SC*-cut quartz. The electromechanical coupling coefficient ${k_t}^2$ represents the efficiency of coupling from an electric field to a mechanical mode and is readily derived from *K* using Eq. 9.15 [16]:

$$k_t^2 = \frac{K^2}{1 + K^2} \tag{9.15}$$

For *AT*-cut quartz the electromechanical coupling coefficient is approximately 0.77 % and approximately 0.25 % for *SC*-cut quartz.

9.5 Frequency Dependence on Plate Dimensions

The resonant frequency of a piezoelectric plate is primarily dependent on the plate thickness and material properties as described in Eq. 9.16 with thinner plates providing higher fundamental frequencies:

$$f_n = \frac{n}{2t}\sqrt{\frac{c_{ij}}{\rho}} \tag{9.16}$$

$n = n$th harmonic
$c_{ij} =$ elastic stiffness coefficient
$\rho =$ density
$t =$ plate thickness

The lateral dimensions of the plate are scaled appropriately as the plate thickness varies for a desired fundamental operating frequency. Electrodes included on the top and bottom surfaces of the plate confine the thickness-shear mode. Dimensions of the plate and the electrodes are scaled in such a way as to maintain effective modal trapping within the electrode region; otherwise, the resonator Q is spoiled and frequency stability compromised.

For quartz, the elastic stiffness coefficient $c_{66} \sim 3 \times 10^{10}$ (1/Pa) and density $\rho = 2649$ kg/m^3, and therefore as a convenient estimate for the fundamental thickness-shear mode of quartz, the resonant frequency can be approximated by the ratio of 1.6 GHz to the plate thickness in microns as in Eq. 9.17:

$$f_0 = \frac{1.6\ \text{GHz}}{t\ (\mu\text{m})} \tag{9.17}$$

Note that due to mass loading effects, the actual resonant frequency of the device is reduced by the electrode metal.

9.6 Thickness-Shear-Mode Simulation

As an example of an *AT*-cut quartz thickness-shear-mode (TSM) resonator, Fig. 9.4 shows a finite element analysis (FEA) fundamental-mode eigenfrequency result, in which the top and bottom surfaces of the quartz under the electrodes experience a displacement in the *X*-direction. The crystallographic axes appear in each figure. For the purposes of simulation, the quartz plate is fixed on one edge by an absorbing strip, similar to a perfectly matched layer (PML) boundary condition. The quartz plate is 1.5 μm thick for 1 GHz operation. Aluminum electrodes are of 120×120 μm^2 area and 0.04 μm thick. Notice that the region surrounding the electrodes does not encounter significant displacement and that the shear mode is "energy trapped" under the electrodes. The arrows in the center of the electrode indicate the magnitude of displacement in the *X*-direction. Dark regions represent larger *X*-displacement, whereas light regions represent minimal *X*-displacement. Referring to the *XY*-plane side view, the maximum displacement of the top surface occurs in the $-X$-direction, while for the lower surface, maximum displacement is in the $+X$-direction. The simulation shows a confinement of energy under the electrode region with little or no energy leaking to the edges of the quartz plate.

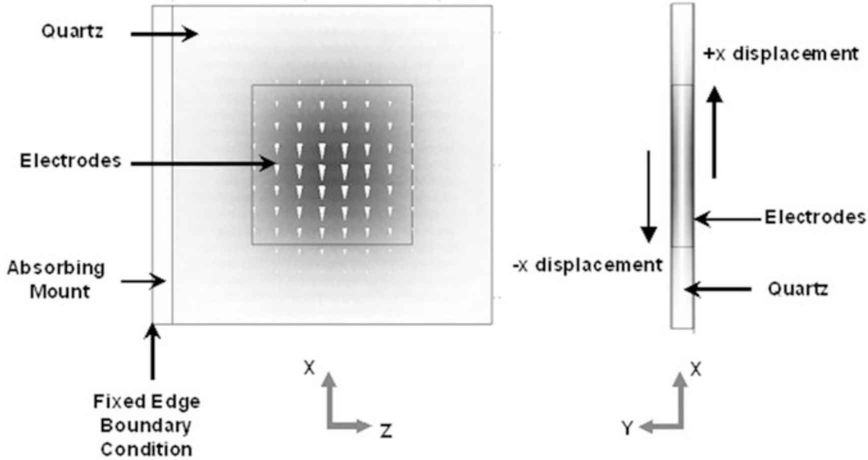

Fig. 9.4 Simulation of displacement associated with thickness-shear mode. Displacement is limited to the electrode region and occurs in the $+X$-direction (*bottom* of quartz) and in the $-X$-direction (*top* of quartz)

9.7 Frequency Dependence on Temperature

Referring back to the thickness-frequency relation of Eq. 9.16, taking the log of both sides and then differentiating, we obtain the fractional frequency of a resonator for varying temperature, also known as the linear temperature coefficient of frequency (TCF):

$$\log(f_n) = \log\left(\frac{n}{2}\right) - \log(t) + \log\left(\frac{1}{\sqrt{\rho}}\right) + \log\left(\sqrt{c_{ij}}\right) \tag{9.18}$$

$$\mathrm{TCF} = \frac{d\,(\log f_n)}{dT} = \frac{1}{f_n}\frac{df_n}{dT} = \frac{-1}{t}\frac{dt}{dT} - \frac{1}{2\rho}\frac{d\rho}{dT} + \frac{1}{2c_{ij}}\frac{dc_{ij}}{dT} \tag{9.19}$$

We see that the TCF is dependent on the thickness, the density, and the elastic stiffness change over temperature. The magnitude of the components of Eq. 9.19 affecting the frequency stability is primarily determined by the crystal cut. The TCF can approach zero for certain cuts when the contribution from the elastic coefficients balances those of the thermal expansion and density change with temperature. The orientation of the crystal cut is therefore a key component of resonator design.

The crystal cut additionally defines the vibrational modes that can exist in the resonator. *AT*- and *SC*-cut quartz typically have low TCF and support thickness-shear vibrational modes. An *AT*-cut quartz crystal can exhibit a frequency variation of less than 15 ppm over a wide temperature range of −35 to +85 °C leading

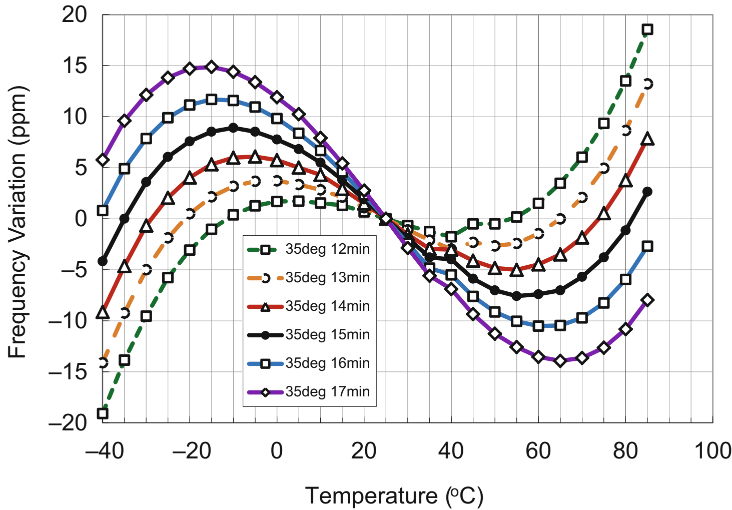

Fig. 9.5 Thickness-shear-mode frequency dependence on temperature for varying *AT*-cut quartz angles

to high thermal frequency stability without the need for further temperature compensation. An *SC*-cut offers in-plane stress compensation and therefore higher thermal frequency stability over *AT*-cut crystals.

An example of simulated frequency variation versus temperature for varying quartz angle of cut is shown in Fig. 9.5 for a 500 MHz *AT*-cut thickness-shear-mode resonator. Note the upper and lower turnover temperatures at approximately $T = -15$ °C and $T = +65$ °C representing zero frequency-temperature slope. The frequency variation is <15 ppm for the standard *AT*-cut quartz angle of 35°15′ (solid circle symbol). As the quartz cut angle is rotated in the positive direction, the steepness of the curve (temperature coefficient of frequency) increases and the overall ppm excursion also increases. As the cut angle is decreased, the S-shape of the curve flattens out and the overall frequency variation is reduced. In the center of the temperature variation, the frequency excursion can become quite flat until the turnover points merge together. At this point, typically over a slightly large temperature range, the temperature coefficient of frequency is zero. However, the frequency change at the temperature extremes can become quite large under this condition, as seen in the curve for the cut angle 35°12′ of Fig. 9.5 (open square symbols). Note that the final f-T behavior is modified slightly for specific resonator designs.

For comparison with *AT*-cut, an f-T curve for an *SC*-cut quartz resonator thickness-shear mode is shown in Fig. 9.6. The doubly rotated *SC*-cut offers a difference in shape of the curve, exhibiting a much flatter region near $T = 100$ °C, bounded by lower and upper turnover points. The inflection point lies between these two turnovers where the second derivative of the slope changes sign. As θ increases,

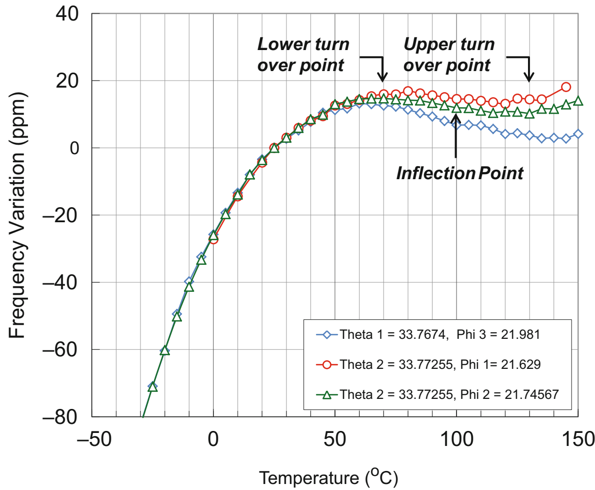

Fig. 9.6 Thickness-shear-mode frequency dependence on temperature for varying SC-cut quartz angles

the lower turnover temperature decreases. And as ϕ increases, the inflection point temperature increases. More specifically, as θ increases, the two turnover points separate in temperature, and the frequency change (ppm) between the turnovers increases. Thus, the crystal cut is important for determining f-T performance and placing the turnover temperatures at desired locations for appropriate frequency stability. For comparison silicon has a linear thermal coefficient of frequency of approximately 30 ppm/°C, demanding a higher level of temperature compensation for high precision applications.

Another important consideration of resonator frequency stability is activity dips. An activity dip is either a frequency jump or a dip in the Q of the desired resonant mode. Activity dips occur when flexural modes close in frequency to the thickness-shear mode interfere with and extract energy from the desired mode. Figure 9.7 shows a simulated f-T and Q versus temperature of an ideal *AT*-cut resonator without any frequency jumps or dips in Q. In general, *SC*-cut crystals exhibit fewer activity dips than *AT*-cut counterparts. Activity dips are avoided through resonator design by minimizing the presence of spurious flexural modes within the vicinity of the thickness-shear mode. Stable shear MEMS resonators approaching GHz have shown $f \times Q$ products close to 1×10^{13} Hz.

9.8 The Equivalent Circuit

The inherent electrical parameters used to describe a resonator can be related to their mechanical counterparts as summarized in Table 9.5. The force applied to a system corresponds to an applied voltage, the displacement of a mass corresponds

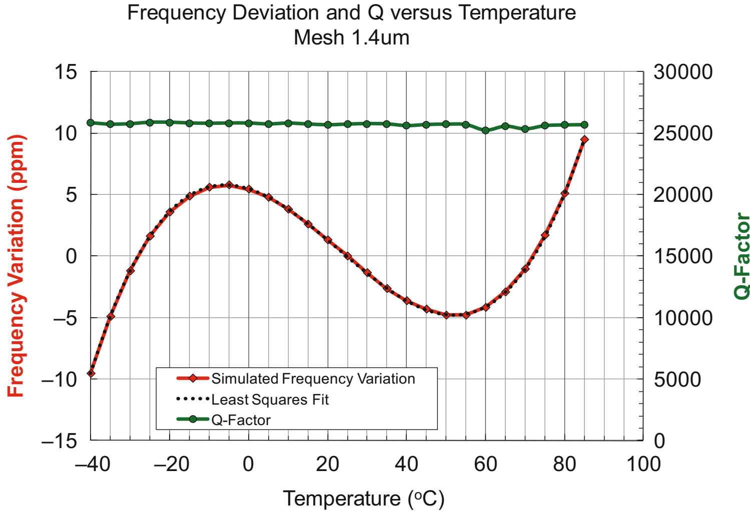

Fig. 9.7 Simulated frequency and Q versus temperature of an ideal *AT*-cut resonator without any activity dips

Table 9.5 Correspondence of mechanical to electrical resonator parameters

Mechanical parameter	Electrical parameter
Force (F)	Voltage (V)
Displacement (x)	Charge (q)
Velocity (v)	Current (I)
Compliance ($1/k$)	Capacitance (C)
Damping (C_m)	Resistance (R)
Mass (m)	Inductance (L)

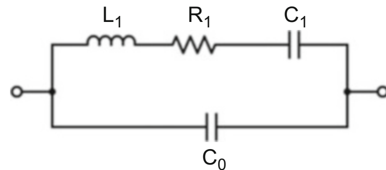

Fig. 9.8 Butterworth-Van Dyke equivalent circuit of a piezoelectric resonator

to a charge on the capacitor, and the velocity of a component relates to the current. Continuing, for the elements of a mechanically vibrating system, the compliance of the structure relates to a motional capacitance, damping is described via a motional resistance, and the effective mass of the structure is associated with a motional inductance.

A schematic of the Butterworth-Van Dyke equivalent circuit model used to describe a piezoelectric resonator is presented in Fig. 9.8 in which C_0 is the static capacitance of the electrodes sandwiching the dielectric material. L_1, C_1, and R_1 represent the motional arm of the resonator, i.e., the mechanically vibrating body.

The relationships between equivalent circuit parameters are summarized in Eqs. 9.20–9.24 [17]:

$$C_0 = \varepsilon_0 \varepsilon \frac{A}{t} \tag{9.20}$$

where ε_0 = permittivity of free space, ε = dielectric permittivity of piezoelectric material, A = electrode area, and t = resonator thickness.

For the motional arm of Butterworth-Van Dyke model, the series resonant frequency is given by ω_0,

$$\omega_0 = \frac{1}{\sqrt{L_1 C_1}} \tag{9.21}$$

$$f_0 = \frac{1}{2\pi} \sqrt{\frac{1}{L_1 C_1}} \tag{9.22}$$

and quality factor

$$Q = \frac{\omega_0 L_1}{R_1} \tag{9.23}$$

Substituting for either L_1 or ω_0 from Eq. 9.21, we have

$$Q = \frac{1}{2\pi f_0 R_1 C_1} = \frac{1}{R_1} \sqrt{\frac{L_1}{C_1}} \tag{9.24}$$

With the equivalent circuit parameters in hand, one can predict the impedance, Z (V/I), or the related admittance, $Y = 1/Z$ (I/V), response of a resonator. A simulated example admittance (Y) response for a 1 GHz AT-cut resonator is shown in Fig. 9.9. For the Butterworth-Van Dyke RLC circuit, the impedance of the motional arm Z_1 is given by Eq. 9.25

$$Z_1 = R_1 + j\omega L_1 + \frac{1}{j\omega C_1} \tag{9.25}$$

and the impedance of the static arm Z_2 is

$$Z_2 = \frac{1}{j\omega C_0} \tag{9.26}$$

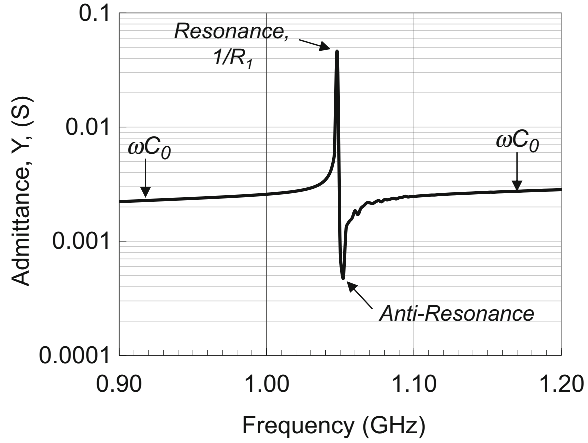

Fig. 9.9 Admittance of a 1 GHz quartz resonator showing the resonance peak ($1/R_1$) and the off-resonance static capacitance C_0

The total impedance Z_t of the resonator is the sum of the static and motional impedances in parallel:

$$\frac{1}{Z_t} = \frac{1}{Z_1} + \frac{1}{Z_2} = \frac{1}{R_1 + j\omega L_1 + \frac{1}{j\omega C_1}} + j\omega C_0 \tag{9.27}$$

On resonance, the real part of the impedance $|Z_R| \sim R_1$. The complex impedance (reactance) of the resonator $|Z_C| \sim 1/\omega C_0$. Therefore, the peak of the resonance in the admittance plot is approximately the inverse of the motional resistance, ($1/R_1$), of the resonator, and the static capacitance C_0 is derived from the value of the admittance off resonance (ωC_0).

9.9 Fabrication of Thickness-Shear Devices

To achieve fundamental-mode resonance in the UHF range, one has to employ wafer-scale micromachining techniques used in MEMS device fabrication. Miniaturization of quartz resonators using key processing enablers such as high aspect-ratio plasma quartz etching and wafer bonding allows the creation of novel piezoelectric structures that are impossible to achieve with the traditional quartz resonator manufacturing process. An example of the thickness-shear-mode quartz MEMS resonator fabrication process is illustrated in Fig. 9.10.

The starting materials for this process are (1) a double-side polished *AT*-cut single crystal quartz wafer, (2) a silicon handle wafer, and (3) a host substrate such as a *GaAs* or a high-resistivity silicon wafer. The process begins with a plasma cavity etch into the silicon handle wafer to later accommodate the top metal electrodes of the quartz wafer. The quartz wafer is metallized with electrodes (*Al* or *Au*) and

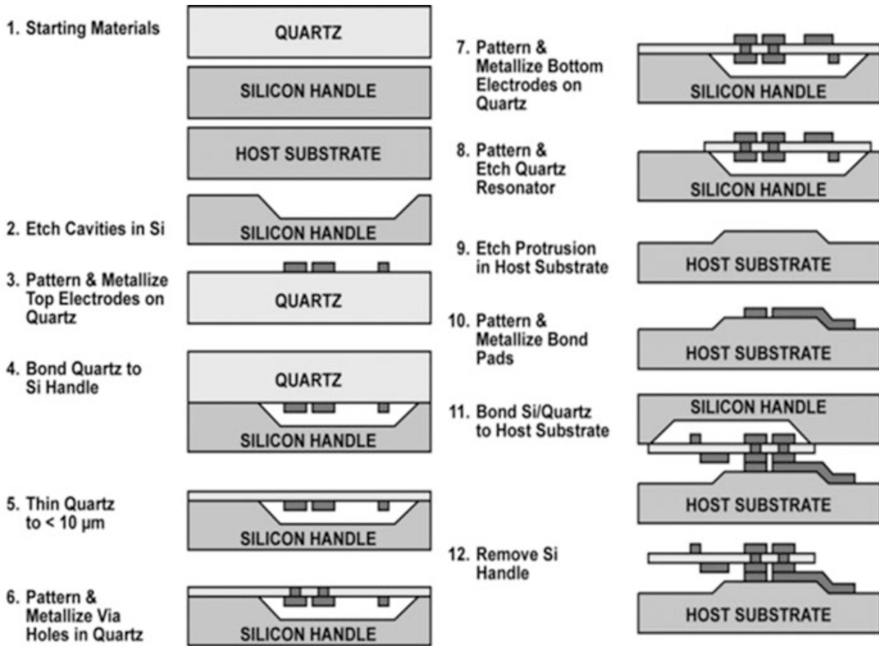

Fig. 9.10 Fabrication process of quartz shear-mode resonator

then aligned and directly bonded to the silicon handle wafer using plasma-assisted room-temperature bonding in a wafer aligner and bonder. The bonded quartz is subsequently thinned to a thickness of approximately 10 μm using wafer grinding and chemical mechanical polishing techniques. The final target thickness is achieved to less than 5 μm with a combination of argon ion milling and hydrofluoric acid-based wet etching. A deep reactive ion etching (DRIE) with CF_4 chemistry creates the through-wafer vias. Bottom-side metallization deposits electrodes matching the previous topside electrode metal (*Al* or *Au*), and also the metal interconnects to bridge the topside metallization to bottom-side bonding pads. The thin sheet of quartz on the silicon handle is then patterned and etched using a second DRIE step to delineate the resonators [18]. The host substrate is first patterned and etched to form protrusions on its surface, creating a spacing underneath the quartz resonator for when it is bonded to the host. *Au* and *In* metals are then deposited on the protrusions to form the bond pads for the subsequent thermal compression bond. In the bonding step, the silicon/quartz pair is aligned to the host substrate using a wafer aligner and then bonded at 100 °C in a wafer bonder using a compression pressure of approximately 10 MPa. Finally, the silicon handle wafer is removed using either an SF_6 plasma etch or a wet TMAH process to release the individual quartz resonators on the host substrate. Completed resonators are shown in both the microscope photographs (Fig. 9.11) and SEM images (Fig. 9.12).

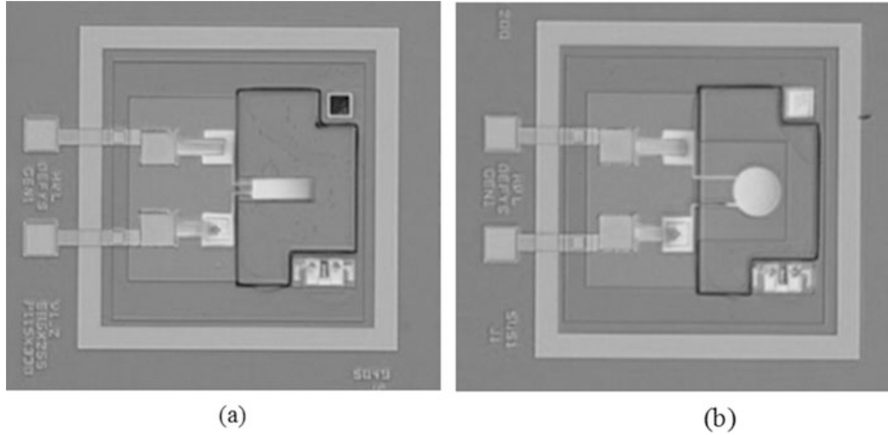

Fig. 9.11 Photographs of fabricated (**a**) rectangular shear-mode resonator and (**b**) disc shear-mode resonator

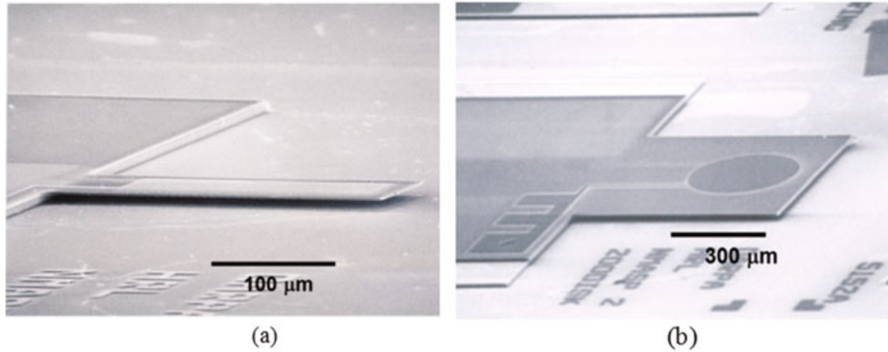

Fig. 9.12 SEM photos of fabricated (**a**) rectangular shear-mode resonator and (**b**) disc shear-mode resonator

9.10 Examples of Prototype Devices

The piezoelectric shear-mode resonator can be electrically represented by a Butterworth-Van Dyke model with equivalent circuit parameters, capacitors C_0 and C_1, inductor L_1, and resistor R_1 as shown previously in Fig. 9.8. The resonant frequency f_0, quality factor Q, and the equivalent circuit parameters can be measured by an RF impedance analyzer. Table 9.6 shows the equivalent circuit parameters of a typical 635 MHz AT-cut resonator fabricated using the quartz MEMS process previously described in Fig. 9.10.

Piezoelectric resonators are key elements in electronic systems since they provide important frequency control functions. One of the most important applications of shear-mode quartz crystal resonators is the stabilization of frequency sources.

Table 9.6 Measured Butterworth-Van Dyke model equivalent circuit parameters for a rectangular *AT*-cut quartz resonator

Parameter	Value
R_1, motional resistance	56.1 Ω
C_1, motional capacitance	0.309 fF
L_1, motional inductance	203 μH
C_0, static capacitance	0.415 pF
f_0, series resonant frequency	635.09955 MHz
Q, quality factor	14,463
$f_0 \times Q$ product	9.19×10^{12} Hz

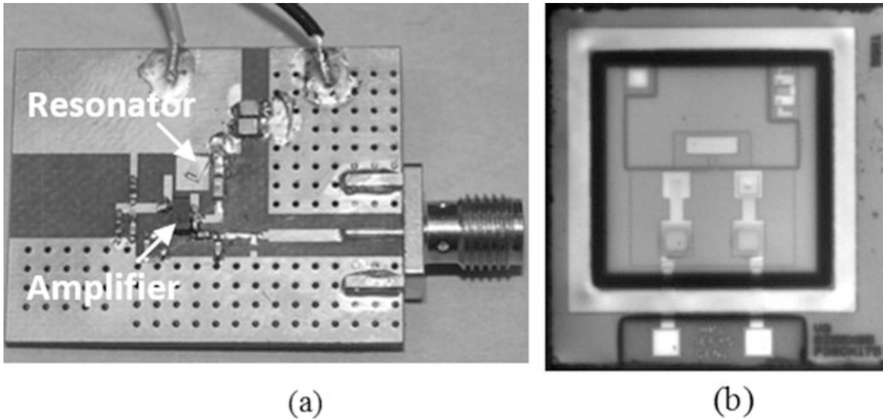

Fig. 9.13 (**a**) Photograph of a 645 MHz oscillator with a quartz MEMS shear-mode resonator and (**b**) an infrared image of an encapsulated resonator viewed through its silicon cap

The frequency sources, or oscillators, provide (1) the carrier signals for electronic communications and navigation systems and (2) the clock signals for data processing and digital communication systems. A shear-mode resonator, when combined with a gain element such as an amplifier in a feedback network, will oscillate when the Barkhausen stability criteria are met, i.e., sufficient loop gain $\geq$1 and proper phase shift in the loop ($2n\pi$ radians).

Figure 9.13 shows an oscillator constructed with a 645 MHz quartz MEMS resonator mounted on a printed circuit board. An infrared image of the vacuum encapsulated resonator is shown on the right. To understand the stability of the oscillator, one performs phase noise measurements typically with a signal source analyzer to determine the spectral purity of the oscillator signal as a function of the offset frequency from the carrier. Figure 9.14 shows a phase noise measurement of the 645 MHz oscillator with the shear-mode resonator.

Vibration can cause a significant increase in the noise level of a piezoelectric frequency source such as a quartz MEMS shear-mode oscillator. In oscillators operating on high-vibration mobile platforms, the vibration-induced phase noise is usually the greatest compared with all other noise sources. UHF quartz MEMS oscillators have been tested on a shaker table to determine acceleration sensitivity,

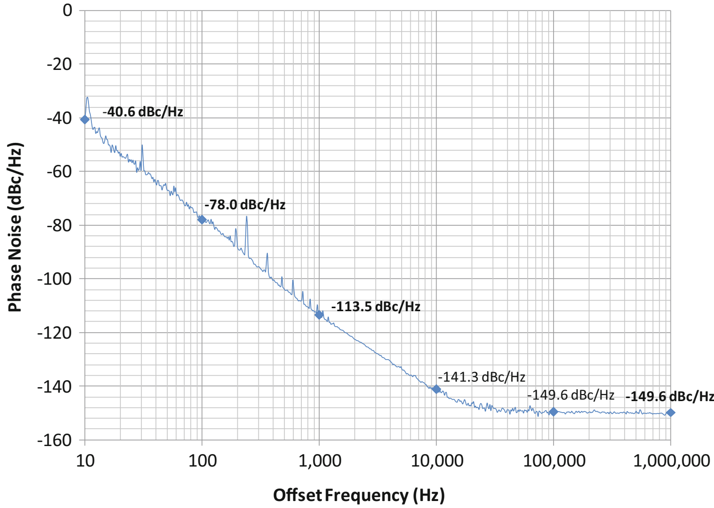

Fig. 9.14 Phase noise response of a 645 MHz oscillator with a shear-mode resonator

Γ, and fractional frequency change per g. Figure 9.15 shows the measured out-of-plane acceleration sensitivity Γ for a 645 MHz oscillator with a 0.5 g peak amplitude sinusoidal input from 10 Hz to 1 kHz. The measured Γ is approximately 5.0×10^{-10}/g. For comparison, predicted vibration sensitivities from quartz FEA models for 500 MHz shear-mode designs and 0.5 g peak sinusoidal vibration inputs have yielded $\Gamma = 1.8 \times 10^{-10}$/g, 9×10^{-13}/g, and 3.0×10^{-15}/g for the out-of-plane and two in-plane axes, respectively. MEMS resonators have exhibited reduced acceleration sensitivity compared with macroscale counterparts by virtue of their significantly lower mass.

Another important application of piezoelectric shear-mode resonators is their use as monolithic crystal filters [19] in RF front ends. High-performance communication systems require narrow-band, low insertion loss filters for high sensitivity, channel selectivity, and noise rejection. Filter bandwidth and insertion loss are dependent on electromechanical coupling coefficient, k_t^2. As k_t^2 increases, bandwidth increases and insertion loss decreases and approaches zero. Insertion loss is also dependent on the product of $k_t^2 \times Q$, and therefore the high-quality factor of quartz offsets its lower k_t^2 value to enable low insertion loss.

Two or more resonators separated by a quartz acoustic gap form a monolithic crystal filter [20]. The filters can have identical resonator electrodes to form a symmetric design or different electrodes resulting in an asymmetric configuration. The asymmetric design minimizes anharmonic modes in the stop band of the filter. Using the quartz MEMS fabrication process outlined in Fig. 9.10, filters with both symmetric and asymmetric electrodes have been designed and fabricated. A photograph of a completed device is shown in Fig. 9.16 with asymmetric electrodes of $80 \times 64\ \mu m^2$ and $67.5 \times 80\ \mu m^2$.

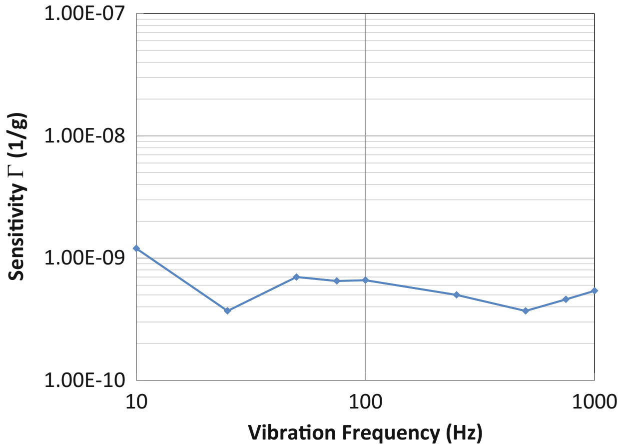

Fig. 9.15 Acceleration sensitivity, Γ, of the 645 MHz oscillator

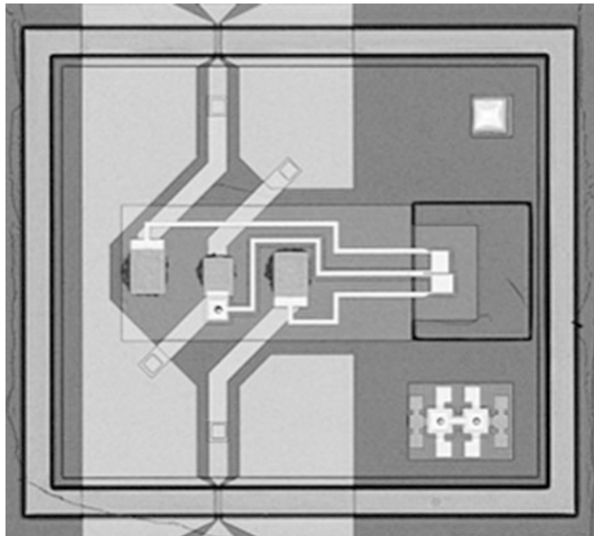

Fig. 9.16 A UHF monolithic crystal filter formed with two asymmetric resonators

The *AT*-cut quartz crystal filter of Fig. 9.16 has a demonstrated insertion loss of −2 dB and bandwidth of approximately 800 kHz (0.2 %) with a center frequency of 366 MHz. In addition, the center frequency is highly stable over temperature as expected for *AT*-cut resonators. Figure 9.17 shows a typical S_{12} scattering parameter of the asymmetric monolithic crystal filter comprised of two shear-mode quartz MEMS resonators.

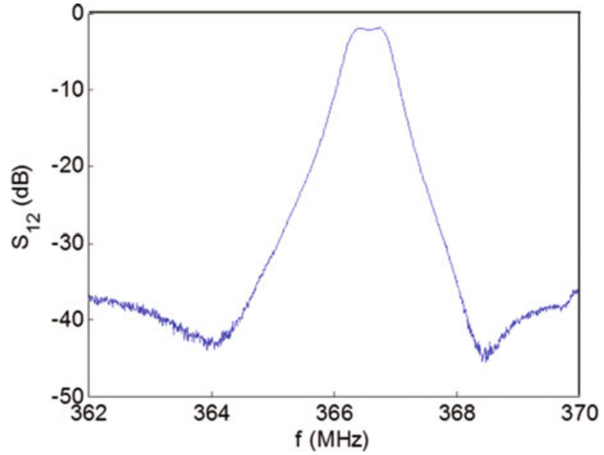

Fig. 9.17 S_{12} scattering parameter of an asymmetric monolithic crystal filter with a center frequency of 366 MHz based on two quartz MEMS shear-mode resonators

9.11 Future Development

Alpha (α)-quartz undergoes a phase transition to the beta (β)-phase (trigonal to hexagonal phase transformation) at a Curie temperature of 573 °C. Because of this phase transition, quartz is not suitable for very high-temperature bulk acoustic wave resonator applications. For high-temperature and harsh operating environments, langasite (*LGS*, $La_3Ga_5SiO_{14}$) and some of its isomorphs such as langatate (*LGT*, $La_3Ga_{5.5}Ta_{0.5}O_{14}$) have been shown to operate as capable high-temperature replacements of shear-mode quartz resonators. *LGT* has a parabolic frequency-temperature characteristic that can be compensated, and its frequency quality factor product, $f \times Q$, of 1.6×10^{13} Hz is comparable to that of *AT*-cut quartz resonators [12]. In addition, *LGT* and *LGS* have piezoelectric coefficients that are 3× larger than that of quartz, thus rendering them good candidates as the next-generation piezoelectric materials for shear-mode resonator applications once their crystal growth and fabrication process mature.

9.12 Summary

Piezoelectric shear-mode MEMS resonators offer high Q, low loss, and a high degree of frequency stability over temperature and vibration. This technology permits flexibility in design that allows customization of device characteristics for a wide range of applications. Wafer-level fabrication techniques enable the production of devices suitable for high-performance frequency control applications such as compact oscillators and RF front-end filters.

References

1. Demirci MU, Nguyen CT-C (2003) Higher-mode free-free beam micromechanical resonators. In: IEEE international frequency control symposium proceedings, pp 810–818
2. Rinaldi M, Zuniga C, Piazza G (2009) Ultra-thin-film AlN contour-mode resonators for sensing applications. In: IEEE international ultrasonics symposium proceedings, pp 714–717
3. Wang R, Bhave SA (2012) Thin-film lithium niobate contour-mode resonator. In: IEEE international ultrasonics symposium proceedings, pp 303–306
4. Kirby DJ et al (2013) Optimizing UHF quartz MEMS resonators for high thermal stability. In: Joint UFFC, EFTF and PFM symposium proceedings, pp 699–702
5. Kubena RL et al (2013) UHF quartz MEMS oscillators for dynamics-based system enhancements. In: Joint UFFC, EFTF and PFM symposium proceedings, pp 1–8
6. Chandrahalim H, Weinstein D, Bhave, SA (2005) Thickness shear mode vibrations in silicon bar resonators. In: IEEE ultrasonics symposium proceedings, pp 898–901
7. Ruby RC et al (2001) Thin film bulk wave acoustic resonators (FBAR) for wireless applications. In: IEEE ultrasonics symposium proceedings, pp 813–821
8. Nishihara T et al (2002) High performance and miniature thin film bulk acoustic wave filters for 5 GHz. In: IEEE ultrasonics symposium proceedings, pp 969–972
9. Zhang S et al (2011) Face shear piezoelectric properties of relaxor-$PbTiO_3$ single crystals. Appl Phys Lett 98:182903
10. Halliburton LE, Martin JJ, Koehler DR (1985) Properties of piezoelectric materials. In: Gerber EA, Ballato A (eds) Precision frequency control, vol 1. Academic Press, Inc., New York, pp 1–40
11. Rosenbaum JF (1988) Bulk acoustic wave theory and devices. Artech House, Inc., Norwood, pp 455–457
12. Smythe RC (1998) Material and resonator properties of langasite and langatate: A progress report. In: IEEE international frequency control symposium proceedings, pp 761–765
13. Vig J (2014) Quartz crystal resonators and oscillators for frequency control and timing applications. Retrieved from http://www.ieee-uffc.org/frequency-control/learning-vig-tut.asp.Ch3
14. Valdois M, Sinha BK (1989) Experimental verification of stress compensation in the SBTC-cut. IEEE Trans Ultrason Ferroelectr Freq Control 36(6):643–651
15. IEEE Standards (1987) IEEE standard on piezoelectricity. ANSI/IEEE Std 176. IEEE, New York, pp 25–28
16. Rosenbaum JF (1988) Bulk acoustic wave theory and devices. Artech House, Inc., Norwood, p 146
17. Bottom VE (1982) Introduction to quartz crystal unit design. Van Nostrand Reinhold Company, New York, pp 67–87
18. Chang DT et al (2003) Optimized DRIE etching of ultra-small quartz resonators. In: IEEE International frequency control symposium proceedings, pp 829–832
19. Kubena RL et al (2016) MEMS-Based UHF Monolithic Crystal Filters for Integrated RF Circuits. J Microelectromech Syst 25(1):118–124
20. Halliburton LE, Martin JJ, Koehler DR (1985) Properties of piezoelectric materials. In: Gerber EA, Ballato A (eds) Precision frequency control, vol 1. Academic Press, Inc., New York, pp 199–216

Chapter 10
Temperature Compensation of Piezo-MEMS Resonators

Wanling Pan

10.1 Introduction

Piezo-MEMS resonators have been used in functional blocks such as oscillators that provide reference signals in timing applications. In such applications, the total frequency variation of generated signals over a temperature range is often required to be as low as possible, often no more than a few parts per million (ppm), and sometimes in the order of a few parts per billion (ppb). A resonator's resonance frequency often drifts as a result of temperature variation, due to the dependency of its material properties and physical dimensions on temperature. Without special design, the total frequency variation of a piezo-MEMS resonator usually well exceeds what is required by the application, and is higher than its quartz counterparts. To reduce the frequency variation, compensation techniques need to be implemented. Such techniques are applied to either the resonator itself, or the oscillator circuitry, or the package. External to the resonator, compensating electric circuits are designed to build voltage-controlled crystal oscillators (VCXOs), temperature compensated crystal oscillators (TCXOs), and temperature controlled chambers are used in oven controlled crystal oscillators (OCXOs). These techniques do not change the intrinsic properties of the resonators, but control the external circuits or the environment to achieve frequency accuracy and stability. The alternative approach, which targets the temperature sensitivity of the resonator itself, and is often used in conjunction with the external compensating techniques, would be the focus of this chapter.

W. Pan (✉)
Maxim Integrated, Inc., San Jose, CA, USA
e-mail: wanling@ieee.org

© Springer International Publishing Switzerland 2017

H. Bhugra, G. Piazza (eds.), *Piezoelectric MEMS Resonators*,
Microsystems and Nanosystems, DOI 10.1007/978-3-319-28688-4_10

10.2 Temperature Sensitivity of Resonance Frequency

The resonance frequency of a resonator is a function of the elastic constants of its materials and its physical dimensions. The temperature sensitivity of frequency therefore mainly comes from two sources—the temperature coefficients of each material's elastic constants, and the thermal expansion coefficient (CTE) of each material. Between these two factors, the temperature coefficients of the elastic constants are usually at least an order of magnitude larger than the CTEs of the materials, and play the dominant role. The aforementioned frequency function, and therefore a resonator's *frequency–temperature* (f–T) relationship, depends on the resonance mode and, if anisotropic materials exist, on the directions of vibration as well. For example, for a single crystalline Si resonator, the temperature sensitivity of the length extensional (LE) mode is different from that of the Lamé mode. For the same LE mode, the orientation of the resonator body also dictates its frequency and therefore the f–T relationship. In a resonator consisting of multiple materials, the contribution to the overall temperature sensitivity by each material can be different for different modes, such as in the case discussed in [1]. Other factors, including the mechanical or electrical stress applied to the resonator, or the electrical architecture, may also affect a resonator's f–T characteristics.

A resonator's frequency sensitivity to temperature is often measured by either the total range of frequency variation within a specific temperature range, or the temperature coefficient of frequency (TCF) at a certain temperature point, given by

$$\mathrm{TCF} = \frac{1}{f}\frac{\mathrm{d}f}{\mathrm{d}T}, \tag{10.1}$$

where f is the frequency and T is the temperature. Relative values such as parts per million (ppm) or parts per billion (ppb) are commonly used to measure the total range of variation, while the rate of frequency change with respect to temperature, ppm/K (°C) or ppb/K (°C), is used to measure the TCF. For many common applications, the specified temperature ranges of operation are typically from tens of degrees below 0 °C up to more than 100 °C. The TCF value is also often given by the slope of the linear approximation of the *frequency–temperature* relationship to represent the overall trend in a specified temperature range, and is commonly referred to as the "linear TCF." The *frequency–temperature* plot of a typical piezo-MEMS resonator is shown in Fig. 10.1. In this example, the total frequency variation over 200–400 K is about 6000 ppm, and the linear TCF is about $-30\,\mathrm{ppm/K}$ in this temperature range.

Two approaches of temperature compensation are commonly implemented, namely passive compensation and active compensation. In the passive compensation approach, the intrinsic property of the resonator body is designed such that the frequency drift due to temperature change is reduced. In the active compensation approach, an external actuation technique is usually implemented to cancel out the frequency drift from temperature change. Although piezo-MEMS resonators are the

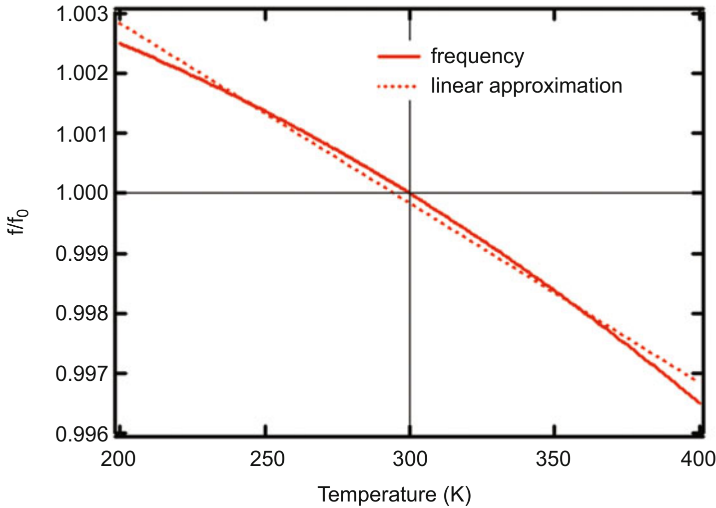

Fig. 10.1 The frequency vs. temperature plot of a typical piezo-MEMS resonator, where f_0 is the resonance frequency at 300K

focus of this chapter, the operation principles of many temperature compensation techniques of non-piezoelectric resonators, such as silicon-only resonators, can often be applied to them as well.

10.3 Passive Compensation Techniques

The passive compensation techniques target the intrinsic properties of the resonator to change its temperature sensitivity. Common techniques are based on the resonator body's composition, the material properties, and the resonator's physical shape and dimensions.

10.3.1 Compensation by Resonator Composition Design

The frequency of each resonance mode is dependent on its characteristic elastic modulus *E*, which is a function of one or more elastic constants. The majority of piezoelectric and substrate materials used in MEMS resonators, such as AlN, ZnO, $LiNbO_3$, $LiTaO_3$, Si, and SiGe, often have negative temperature coefficients of elastic modulus (TCEs) for the common resonance modes in the temperature range of interest. As a result, typical uncompensated piezo-MEMS resonators made of such materials have negative TCFs, and often have frequency variations of

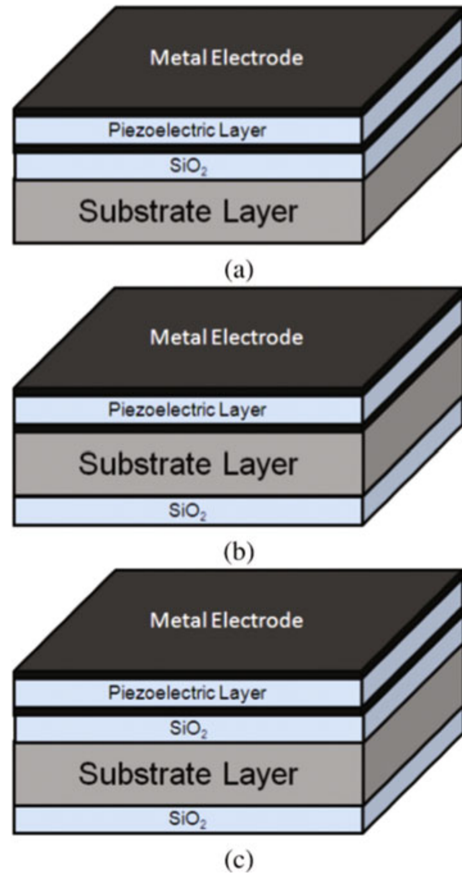

Fig. 10.2 Typical composite piezo-MEMS resonator stack configurations with SiO_2 compensation layer(s), a piezoelectric layer, and a substrate layer (a) the SiO_2 layer is between the substrate and the piezoelectric layer, (b) the SiO_2 layer is separated from the piezoelectric layer by the substrate layer, and (c) the substrate layer is sandwiched between two SiO_2 layers

a few thousand ppm in their targeted operation temperature range (e.g., -40 to $+125\,°C$). To compensate for this, materials with positive TCEs, such as SiO_2, can be introduced to the resonator body. Typically, one or more layers of the compensating material are deposited or grown in the resonator body, forming a composite structure. Figure 10.2 shows some examples, in which SiO_2 layers are introduced to a resonator with a piezoelectric layer and a substrate layer. When the thickness of SiO_2 is comparable to that of the other layers, this technique can be very effective. The use of SiO_2 also benefits from its well-established deposition and growth techniques in the semiconductor industry. The effectiveness and ease of implementation have made this technique one of the most widely adopted methods in passive temperature compensation.

Based on this principle, a temperature compensated thickness mode bulk wave resonator with a total frequency variation of $\sim$300 ppm in the temperature range of ~-70 to $150\,°C$ was designed and reported in [2]. The resonator incorporated SiO_2 layers in its volume to compensate for the negative TCE of its AlN piezoelectric

layer. In another work, Artieda and Muralt [3] implemented an SiO_2/AlN/SiO_2 structure to reduce the linear TCF of a third-harmonic thickness mode resonator to 4 ppm/°C.

Similar compensation effectiveness is also achieved in lateral-extensional mode resonators. Abdolvand et al. [4] reported a MEMS oscillator based on a metal-ZnO-metal-Si-SiO_2 resonator that was fabricated from a silicon-on-insulator (SOI) wafer and had a structure similar to that of Fig. 10.2b. The buried oxide layer of the SOI wafer was used for temperature compensation. A linear TCF of −2 ppm/°C was measured on an oscillator based on it.

The original and compensating materials in a resonator usually have positive and negative TCEs of the same order of magnitude. Therefore, a multi-layered composite structure requires that these layers have similar thicknesses to have a low overall TCF. In order to take advantage of the low damping in single crystalline silicon, many piezo-MEMS resonators are designed to include an Si layer of more than 10 μm thickness, especially in those of the piezoelectric-on-Si type [5]. To achieve effective compensation in such cases, SiO_2 layers of more than a few microns need to be grown or deposited, which can be challenging in fabrication. To address this concern, multiple designs have been proposed to compensate for the TCF of resonators of such thicknesses. In one approach, proposed by Tabrizian et al. [6, 7], arrays of SiO_2 pillars were embedded in the silicon body. These oxide pillars were fabricated by the deposition of LPCVD SiO_2 into etched trenches inside the Si layer of an AlN-on-Si resonator. In this approach, the volume ratio between SiO_2 and Si is increased by the multiple embedded SiO_2 pillars (Fig. 10.3). With this method, the overall frequency variation of as low as 90 ppm was achieved in the temperature range of −20°C to 100°C with a composite 24 MHz AlN-on-Si resonator with Si of 20 μm thickness.

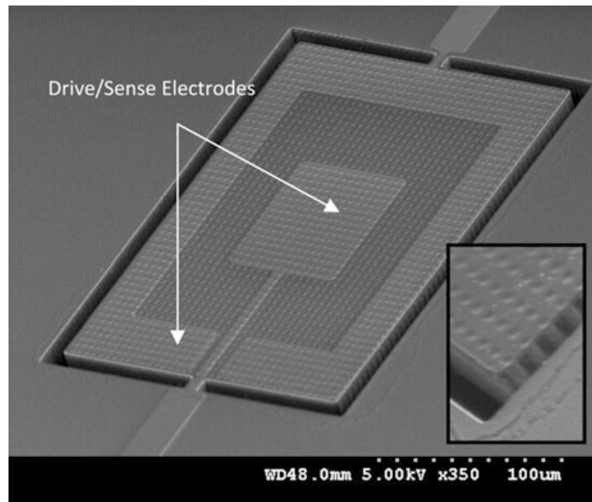

Fig. 10.3 An AlN-on-silicon resonator with embedded SiO_2 pillars [6] (courtesy of the Transducer Research Foundation and Farrokh Ayazi)

Although effective in temperature compensation, this approach faces a few technical challenges in design and fabrication. The requirement of a high quality factor mandates void-free filling of SiO_2 inside the etched Si trenches. Very well controlled Si etching and SiO_2 deposition of high aspect ratio are therefore needed. Extra steps are needed to form a smooth surface for AlN deposition. A second disadvantage of this structure is the lower quality factor of the resulting resonator, which mainly come from the larger damping in SiO_2 compared to that in single crystalline Si, and from the mechanical mismatching between the two materials. The highest quality factor of resonators of such structures at room temperature is reported to be $\sim$10,000, which is noticeably lower than the typical value of 15,000 for AlN-on-Si resonators of similar dimensions. In fact, nearly all the resonators using SiO_2 as the compensating material show degraded quality factor compared to the uncompensated ones with single crystalline silicon only.

10.3.2 Compensation by Material Properties Engineering

Other than introducing a positive-TCE material to the resonator body, the intrinsic elastic properties of the original structural material, such as Si, can be engineered for temperature compensation. It has been demonstrated that the elastic constants of semiconductors, such as Si or Ge, are affected by their doping levels [8, 9]. Such an effect was further investigated in [10–12] and has been applied to MEMS resonators for temperature compensation in various studies.

Following the methods discussed in [8] and [10], it is calculated that the elastic constants c_{11} and c_{12} of Si, as well as their temperature dependencies, are dependent on the doping level (Fig. 10.4), while c_{44} is insensitive to it. Therefore, if a resonator's frequency is dependent on c_{11} and c_{12}, temperature compensation is possible by changing the doping level of the Si layer. For example, for a rectangular-shaped resonator that works in the length extensional mode, with its vibration mainly along the $\langle 110 \rangle$ direction of silicon, if the volume of the resonator body is dominated by Si, its resonance frequency is roughly determined by

$$E_{110} = \frac{4(c_{11}^2 + c_{11}c_{12} - 2c_{12}^2)c_{44}}{2c_{11}c_{44} + c_{11}^2 + c_{11}c_{12} - 2c_{12}^2}. \tag{10.2}$$

The E_{110}–*temperature* relationship for different doping levels is plotted in Fig. 10.5a. It is seen that in the 200–400 K temperature range, the overall temperature coefficient of E_{110} becomes less negative with increased doping, and the TCF is expected to be reduced for such a resonator with higher doping level.

An AlN-on-Si resonator with such an orientation was reported in [5]. Degenerately doped Si (resistivity $< 0.001\,\Omega$ cm) was the dominant material (thickness being $60\,\mu$m as compared to AlN of $< 1\,\mu$m). The resonator had a linear TCF of -12.0 ppm/°C, a reduction of more than 50 % as compared to a resonator with a similar structure but lower Si doping level (resistivity of 0.01–0.02 Ω cm) (Fig. 10.6).

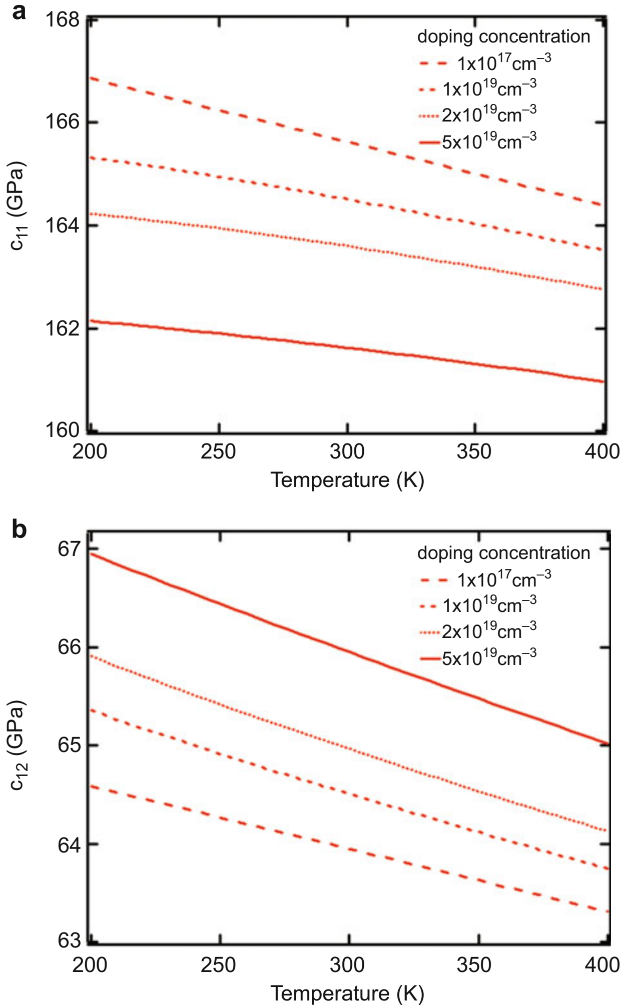

Fig. 10.4 The elastic constants c_{11} and c_{12} vs. temperature for N-doped silicon at different doping levels. (**a**) c_{11} vs. temperature. (**b**) c_{12} vs. temperature

Furthermore, the changes of the elastic constants by doping can be combined with the adjustment of resonator orientation to further reduce the frequency variation. For an Si-dominated resonator working at the same length extensional mode as the previous example, when the major mode of vibration is along the $\langle 100 \rangle$ direction, the resonance frequency will roughly be determined by the elastic modulus

$$E_{100} = c_{11} - \frac{2c_{12}^2}{c_{11} + c_{12}} \qquad (10.3)$$

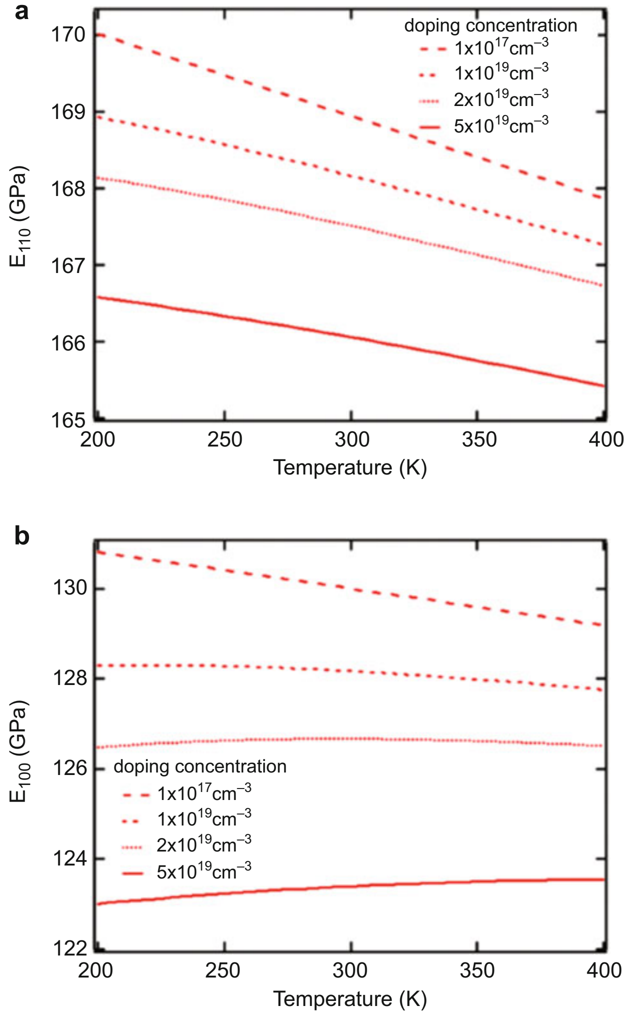

Fig. 10.5 The elastic modulus E vs. temperature for N-doped silicon in different crystalline directions. (**a**) E_{110} vs. temperature. (**b**) E_{100} vs. temperature

It is seen from Fig. 10.5b that with the increase of the doping level, the linear approximation of the temperature coefficient of E_{100} and therefore the linear TCF of the resonator will change from negative to positive in the 200–400 K range. The turnover temperature, defined as the temperature where TCF $= 0$, can be adjusted either by doping or by the orientation of the resonator body, to reduce the total frequency variation in the target temperature range. As the *frequency–temperature* plot is usually approximately parabolic, the turnover temperature is preferred to be at the center of the temperature range of interest to minimize the overall frequency variation.

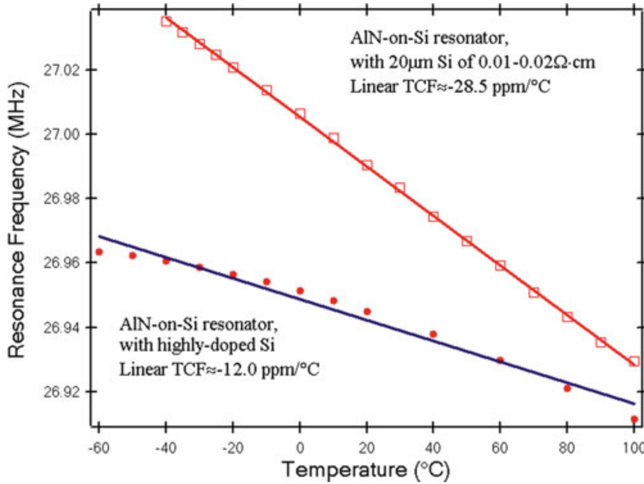

Fig. 10.6 Measured reduction in TCF of piezo-MEMS resonator with degenerately doped Si

Besides N-type dopants, P-type dopants can have similar effects in temperature compensation. Samarao and Ayazi [13] reported reduced TCF of $-1.5\,\text{ppm}/°\text{C}$ on $5\,\mu\text{m}$ thick silicon MEMS resonators using degenerate boron doping, and $-2.72\,\text{ppm}/°\text{C}$ on $20\,\mu\text{m}$ thick resonators using boron-assisted aluminum doping.

Opposite to doping, it has also been discovered that temperature compensation can be achieved by charge carrier depletion in the semiconductor material [14]. In essence, in a depleted semiconductor material, the change in free charge flow from temperature variation is minimized, which results in minimized changes in the electronic and mechanical energies. Such depletion can be obtained by the creation of PN-junctions in the resonator body, either by doping [14] or by bonding layers of opposite polarities [15].

10.3.3 Other Passive Compensation Techniques

Resonator composition design and material engineering are two of the most widely studied methods in temperature compensation. Other less conventional techniques have also been investigated. Notably, Samarao et al. [16] proposed a concave-shaped silicon bulk acoustic resonator (CBAR) for TCF reduction. In this design, the flanks of a conventional rectangular silicon bulk acoustic resonator (SiBAR) are curved, with the actuation electrostatic force applied to the center of the resonator, as illustrated in Fig. 10.7. Linear TCF of $-6.31\,\text{ppm}/°\text{C}$ was measured on a CBAR on a $\sim$0.001 Ω cm Si wafer, as compared to $-21.46\,\text{ppm}/°\text{C}$ for a rectangular-shaped resonator on the same wafer. On the other hand, the insertion loss of CBAR is significantly worse than that of a conventional rectangular resonator, with typical values of more than 50 dB reported [14, 16], and more spurious modes are expected from resonators of such irregular shapes [17].

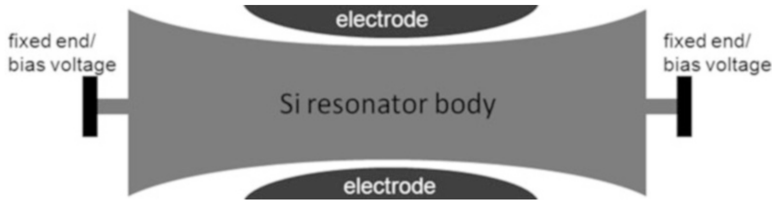

Fig. 10.7 Schematic view of a concave silicon bulk acoustic resonator (CBAR) with reduced TCF, as proposed in [16]

10.4 Active Compensation Techniques

In the previous section passive compensation techniques are discussed. In those cases, the *frequency–temperature* characteristics is usually fixed once the resonator is fabricated. In some applications, it is desired that the frequency of a fabricated resonator can be adjusted real-time to compensate for temperature change. In such situations, active compensation techniques provide more flexibility than the passive techniques.

Active compensation can be achieved by changing the electrical or mechanical properties of the resonator. In one of the designs, a piezoelectric resonator is constructed such that its overall electrical impedance is controlled by a variable air gap, as shown in Fig. 10.8a [18–20]. The air gap, which also provides acoustic isolation for the piezoelectric layer, is controlled by a DC voltage between the top and bottom electrodes, and in effect functions as a tunable capacitor that can be used to adjust the series frequency of the resonator. The equivalent electrical circuit near the resonance frequency is shown in Fig. 10.8b. A maximum continuous tuning range of 3900 ppm was achieved on an AlN-based MEMS resonator with electrostatic actuation. This tuning range is equivalent to the frequency drift from more than 100 °C of temperature change. Compared to tuning with a discrete variable capacitor, this integrated approach reduces the fabrication complexity and overall dimensions, and has a higher quality factor by eliminating the resonator–capacitor interconnections. On the other hand, the air gap increases the insertion loss of the resonator, and the range of electrostatic tuning is restricted by the pull-in effect. These factors may have limited the application of this method.

Alternatively, frequency tuning can be achieved by inducing mechanical stress in the resonator. In [21], the mechanical spring constant of a flexural mode piezoelectric resonator was adjusted by an electrostatic force applied by a DC tuning voltage. A tuning range of 3100 ppm was reported with less than 4 V of DC voltage on a 33 kHz resonator.

Similar to the OCXOs, heaters can be utilized in the resonator or package design, to achieve frequency tuning by heating, or to achieve frequency stability by maintaining the working temperature of the resonator. In one such ovenized structure [22], an AlN-based resonator with integrated aluminum heaters was built with tuning efficiency of more than 1200 ppm/mW. A recent implementation [23]

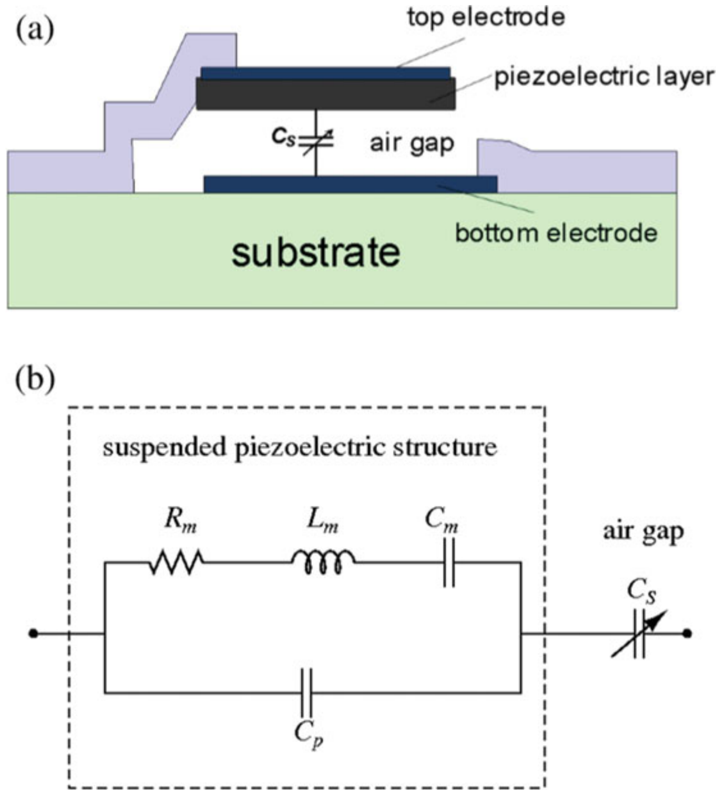

Fig. 10.8 A piezoelectric resonator with a variable air gap for frequency tuning. (**a**) Schematic view of the tunable resonator. (**b**) Equivalent circuit of the tunable resonator

provided a more complete solution by integrating a resistance temperature detector (RTD), a heater, and thermal isolation on the same substrate (Fig. 10.9). Such a design achieved 5 ppm frequency stability across an ambient temperature range of 105 °C.

Mechanical and thermal stresses can be obtained by the same element to achieve frequency tuning, as proposed in [24]. In one of the embodiments, the main resonator body is attached to two U-shaped tuning beams, as shown in Fig. 10.10. A DC current is injected into the tuning beams, causing an increase in their temperatures. As a result, the tuning beams will have different thermal expansions than the resonator body, and mechanical stress is induced in the resonator. This stress, combined with the heating of the resonator by the beams, can be used to adjust the resonance frequency considerably.

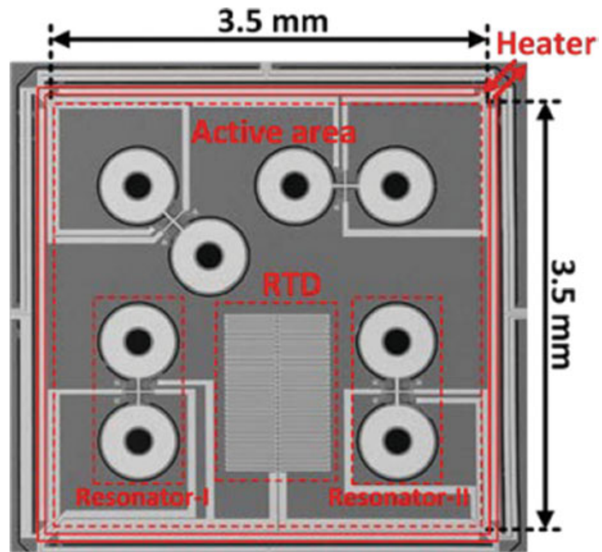

Fig. 10.9 An ovenized MEMS resonator with an integrated RTD, a heater, and thermal isolation [23] (courtesy of the Transducer Research Foundation and Mina Rais-Zadeh)

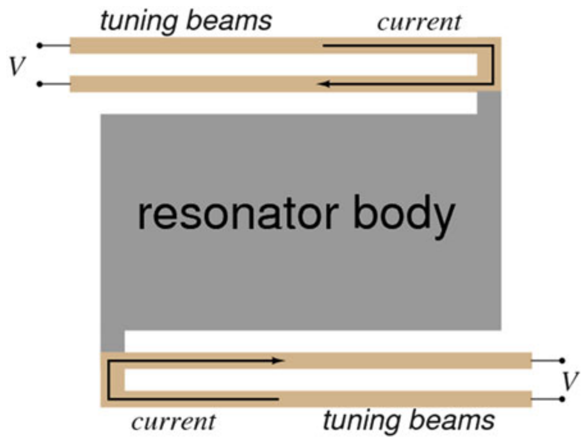

Fig. 10.10 Schematic view of a tunable resonator with thermally actuated tuning beams [24]

Compared to the passive compensation techniques, active compensation has limited adoption at the resonator device level, and is still mostly achieved by components external to the resonator itself, as in the VCXOs, TCXOs, and OCXOs. This may be largely due to the technical complexities in integrating the tuning elements in the device structure.

References

1. Pan W (2014) Periodical signal generators having microelectromechanical resonators therein that support surface wave and bulk acoustic wave modes of operation with different temperature coefficients of frequency. U.S. Patent No. 8,680,931
2. Lakin KM, McCarron KT, McDonald JF (2000) Temperature compensated bulk acoustic thin film resonators. In: IEEE ultrasonics symposium, 2000
3. Artieda A, Muralt P (2008) High-Q AlN/SiO_2 symmetric composite thin film bulk acoustic wave resonators. IEEE Trans Ultrason Ferroelectr Freq Control 55(11):2463–2468. doi: 10.1109/TUFFC.953
4. Abdolvand R, Mirilavasani H, Ayazi F (2007) A low-voltage temperature-stable micromechanical piezoelectric oscillator. In: Solid-state sensors, actuators and microsystems conference, 2007
5. Pan W, Ayazi F (2010) Thin-film piezoelectric-on-substrate resonators with Q enhancement and TCF reduction. In: IEEE 23rd international conference on micro electro mechanical systems (MEMS), 2010
6. Tabrizian R et al (2010) Temperature-stable high-Q AlN-on-silicon resonators with embedded array of oxide pillars. In: Solid-state sensors, actuators, and microsystems workshop, 2010
7. Tabrizian R et al (2012) A 27 MHz temperature compensated MEMS oscillator with sub-ppm instability. In: IEEE 25th international conference on micro electro mechanical systems (MEMS), 2012
8. Keyes, RW (1967) Electronic effects in the elastic properties of semiconductors. Solid State Phys 20:37–90
9. Hall JJ (1967) Electronic effects in the elastic constants of n-type silicon. Phys Rev 161:756–761
10. Pensala T, Jaakkola A, Prunnila M, Dekker J (2011) Temperature compensation of silicon MEMS resonators by heavy doping. In: IEEE international ultrasonics symposium (IUS), 2011
11. Pensala T, Prunnila M, Jaakkola A (2012) Bulk acoustic wave propagation characteristics in degenerately n-doped Si. In: IEEE international frequency control symposium (FCS), 2012
12. Jaakoka A, Prunnila M, Pensala, T (2012) Temperature compensated resonance modes of degenerately n-doped silicon MEMS resonators. In: IEEE international frequency control symposium (FCS), 2012
13. Samarao AK, Ayazi F (2009) Temperature compensation of silicon micromechanical resonators via degenerate doping. In: IEEE international electron devices meeting (IEDM), 2009
14. Samarao AK, Ayazi F (2010) Intrinsic temperature compensation of highly resistive high-Q silicon microresonators via charge carrier depletion. In: IEEE international frequency control symposium (FCS), 2010
15. Pan W (2014) Methods of forming micro-electromechanical resonators having passive temperature compensation regions therein. U.S. Patent 8,785,229
16. Samarao AK, Casinovi G, Ayazi F (2010) Passive TCF compensation in high Q silicon micromechanical resonators. In: IEEE 23rd international conference on micro electro mechanical systems (MEMS), 2010
17. Samarao AK, Ayazi F (2011) Combined capacitive and piezoelectric transduction for high performance silicon microresonators. In: IEEE 24th international conference on micro electro mechanical systems (MEMS), 2011
18. Pan W et al (2005) Design and fabrication of a surface micromachined frequency tunable film bulk acoustic resonator with an extended electrostatic tuning range. In: IEEE international ultrasonics symposium (IUS), 2005
19. Pan W et al (2006) A surface micromachined electrostatically tunable film bulk acoustic resonator. Sens Actuators A 126:436–446

20. Pan W et al (2006) A comparison between tunable FBARs with an integrated and with a discrete variable MEMS capacitor. In: IEEE 19th international conference on micro electro mechanical systems (MEMS), 2006
21. Serrano DE et al (2012) Electrostatically tunable piezoelectric-on-silicon micromechanical resonator for real-time clock. IEEE Trans Ultrason Ferroelectr Freq Control 59:358–365. doi: 10.1109/TUFFC.2012.2204
22. Kim B et al (2010) Ovenized and thermally tunable aluminum nitride microresonators. In: IEEE Ultrasonics Symposium (IUS), 2010
23. Wu Z et al (2014) Device-layer ovenization of fused silica micromechanical resonators for temperature-stable operation. In: Solid-state sensors, actuators, and microsystems workshop, 2014
24. Pan W (2014) Microelectromechanical resonators with thermally-actuated frequency tuning beams. U.S. Patent No. 8,633,635

Chapter 11
Computational Modeling Challenges

Mattan Kamon

11.1 Introduction

Accurate modeling of piezoelectric MEMS Resonators is key to reducing fabrication cycles or diagnosing issues with fabricated devices. Analytic models provide a first pass at assessing device performance but are idealized and do not represent actual device performance to sufficient accuracy, especially for the high-order bulk modes utilized in MEMS oscillators and filters. Computational modeling by the finite-element method has taken great strides in capturing greater detail in both geometry and physical behavior of these resonators. While continuing improvements in computational power have aided in this progress, it is the advances in both algorithms and methodology in coupling physical domains that have enabled greater accuracy compared to fabricated devices. In this chapter we review the key challenge areas in resonator design for which advances in computational modeling provide predictive value.

The first challenge we discuss is efficiently computing the electrical frequency response over a broad frequency range. This is not a difficult problem for flexural mode devices or devices whose size is on the order of an acoustic wavelength such as piezoelectric micromachined ultrasonic transducers (pMUTs). However, bulk mode resonator designs for oscillator or filter applications can be many wavelengths in multiple dimensions. Broad frequency sweeps on fully three-dimensional (3D) computational models using conventional techniques can take days of computation time for an accurate result. To circumvent this bottleneck, a first-pass model is often simplified by reducing the simulation geometry to a 2D cross section (even though most devices exhibit 3D effects) and/or by reducing the number of frequency points to be simulated. Both of these simplifications risk missing important features of

M. Kamon, Ph.D. (✉)
Coventor, Inc, Waltham, MA, USA
e-mail: matt@coventor.com

© Springer International Publishing Switzerland 2017

H. Bhugra, G. Piazza (eds.), *Piezoelectric MEMS Resonators*,
Microsystems and Nanosystems, DOI 10.1007/978-3-319-28688-4_11

the response, such as spurious modes within frequency band of interest. In the next section, we review these computational modeling challenges and discuss fast frequency sweep algorithms which make solution of the full 3D problem feasible.

Reducing energy loss in resonators is vital to meet the phase noise requirements for MEMS oscillators and to reduce insertion loss for MEMS filters. Many different physical phenomena contribute to this loss. Understanding which phenomena are relevant is necessary to design to reduce this loss. While some of the physical phenomena are still topics of fundamental research, computational modeling is successful at predicting anchor loss, thermoelastic dissipation, and gas damping. We review these mechanisms and discuss considerations in the accurate modeling of these phenomena.

For the applications in this book, it is generally desirable for the resonator response to vary linearly with the applied voltage amplitude. However at some input power level, nonlinear terms in the governing equations become significant and degrade the performance of the device. For instance, in filters, nonlinearity creates intermodulation distortion. Residual stress in the fabrication process is another form of nonlinearity that shifts the operating point of the device. Both of these forms of nonlinearity are significant and have not been thoroughly studied with computational methods for piezoelectric MEMS resonators. We end the chapter with a discussion of progress on these topics to date.

11.2 Challenges in Computing the Frequency Response

The frequency response is central to designing a resonator to meet specification. In this section we provide conceptual motivation by first discussing the complexity of the frequency response for piezoelectric MEMS multiwavelength bulk mode resonators and show that three-dimensional analysis is key to capturing an accurate response. We then review the governing equations and finite element formulation to show why standard eigenmode analysis is not enough, and a frequency response computation is necessary, but often infeasible in three dimensions. We finish the section by describing the challenge in computing this frequency response over a broad range and methods that make that feasible.

11.2.1 Motivation

Ideally, a resonator should resonate at the desired frequency for the given application. An initial design can be created based on analytic formula however the measured frequency is typically different due to non-idealities in the fabrication process such as non-infinite extent, nonvertical sidewalls, and anchoring structures. Also, oscillation at only one frequency is desired, but every solid is capable of supporting multiple resonant modes and it is the job of the designer to insure those

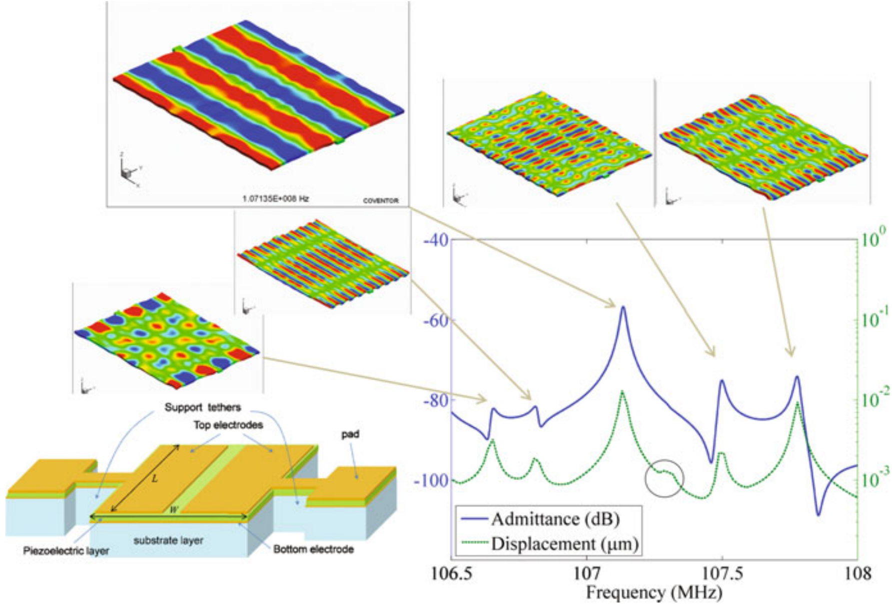

Fig. 11.1 Excited modes for a piezoelectric resonator operating in its fifth extensional mode. Four spurious modes appear in the admittance response with their 3D modes shapes shown. One spurious mode only appears in the displacement response (*black circle*)

other *spurious* modes do not interfere with the desired operation of the device. These non-idealities are difficult to approximate analytically and have made finite-element simulation critical to creating real-world designs. Computing a fast and accurate frequency response is thus central to the design process.

As an example, consider the frequency response of a suspended aluminum nitride (AlN) resonator on a thin single crystal silicon substrate shown in Fig. 11.1. This design is similar to [1, 2] but is given a simple electrode pattern for demonstration. Figure 11.1 shows that when the electrodes are driven with a harmonic voltage, the desired 5th order extensional mode resonates at 1.071 MHz. However, five other spurious modes also appear in the response within only a 1.5 % window of this peak. Notice that only four of those modes appear in the electrical admittance response. The fifth one, shown in the black circle, is excited mechanically by the electrical stimulus, but does not appear in the electrical response because its particular strain pattern creates no net current at the electrodes. The solid also supports at least four additional resonant modes within this frequency range which are not excited at all by this particular electrode pattern.

To further emphasize the complexity of this behavior, note that the modes would not be well represented by one particular two-dimensional cross-section. The modes at 1.068 MHz, 1.071 MHz, and 1.078 MHz are uniform enough in the x-direction that a YZ-plane two-dimensional analysis would approximate these, but the modes at

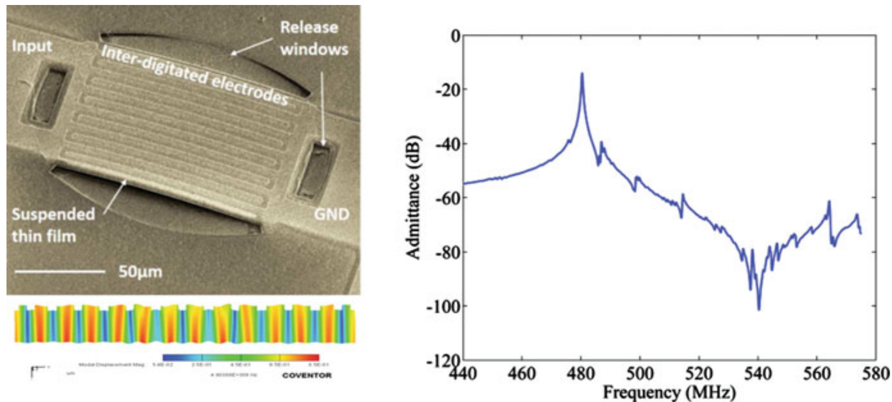

Fig. 11.2 Lithium niobate laterally vibrating resonator, mode shape cross-section, and frequency response. Numerous spurious modes exist apart from expected resonance and anti-resonance. SEM image courtesy of S. Gong, U. of Illinois

1.066 and 1.075 MHz would be completely missed in the corresponding frequency response. Three-dimensional (3D) computational analysis is thus required to capture these features in the response.

Even if the electrode patterns can be appropriately designed to excite the desired mode more directly as is done in [2] using inter-digitated fingers, spurious modes can still remain. Consider the Lithium Niobate resonator from [3] shown in Fig. 11.2. This is the S0 mode of the class of resonators described in Chap. 4. It is formed from an X-cut of Lithium Niobate and oriented 30° to $Y+$. As described in Chap. 4, if this resonator is used as part of an RF filter, ideally the frequency response between resonance and anti-resonance should be free of spurious modes but is shown in Fig. 11.2 to have a handful of spurious modes. Some of these spurs are only captured with 3D analysis. Through the use of 3D finite-element analysis, electrode patterns can be optimized to reduce spurs [4] or optimize electromechanical coupling and reduce insertion loss [5].

11.2.2 Computing the Frequency Response

Computational methods for predicting the behavior of designs whose dimensions are on the order of an acoustic wavelength or less are straightforward to apply. For multiwavelength resonators however, the computational resources needed to accurately resolve the features in the frequency response can be large enough to be impractical. This is especially true in a production environment which requires multiple, automated simulation studies to explore a design space or explore the impact of temperature variation. In the rest of this section, we review the methods

and challenges involved in applying the finite-element method to the designs of Figs. 11.1 and 11.2.

The piezoelectric effect couples the elastic behavior of the solid to the electrostatic behavior. The equations of elastodynamics (Newton's second law) and electrostatics (Gauss's law), in time harmonic form, are

$$\begin{aligned} \sigma_{ij,j} + F_i &= -\omega^2 \rho u_i \\ D_{i,i} - q &= 0 \end{aligned} \tag{11.1}$$

where σ_{ij} is the Cauchy stress tensor, F_i are the components of the applied mechanical body force per unit volume, ρ is the mass density, ω is the angular frequency, u_i are the components of the displacement, D_i are the components of the electric displacement and q the applied electric volume charge. Einstein notation is used in which repeated indices imply summation, and a comma followed by a subscript implies differentiation by that Cartesian component, that is $A_{,j}$ is $\partial A/\partial x_j$. Displacements for bulk resonators are typically small to allow the assumption of linearity. The equations are then coupled through the piezoelectric coefficients in the linear constitutive relations

$$\begin{aligned} \sigma_{ij} &= C_{ijkl}\varepsilon_{kl} - e_{kij}E_k \\ D_i &= e_{ikl}\varepsilon_{kl} + \epsilon_{ik}E_k \end{aligned} \tag{11.2}$$

where C_{ijkl}, ϵ_{ik}, and e_{kij}, are the elastic, dielectric, and piezoelectric material properties, respectively. E_k is the electric field which is related to the electric potential through $E_i = -\phi_{,i}$. Assuming infinitesimal strain, the strain tensor, ε_{kl}, is related to the displacements by

$$\varepsilon_{ij} = \frac{1}{2}\left(u_{i,j} + u_{j,i}\right). \tag{11.3}$$

The relations in (11.2) and (11.3) represent a linearization around a static operating point. Residual stress from the fabrication process and thermal effects can impact that operating point and alter the resonator behavior as will be described later in this chapter. Also, including only the linear terms in (11.2) and (11.3) assumes small strain and electric field. This assumption breaks down when the resonator is driven at higher power levels as will be discussed briefly at the end of the chapter.

The finite element method has been used to model piezoelectric structures since the early 70s [6, 7]. To solve a piezoelectric resonator model with the finite element method, the resonator geometry is divided into a mesh of discrete elements as shown in Fig. 11.3 for the resonator of Fig. 11.2. The solution for the displacement and potential fields is approximated by a linear combination of mechanical, ψ_n^S, and electrical, ψ_n^E, shape functions scaled by the values of displacement and potential fields at the (shared) nodal points between the elements [8]

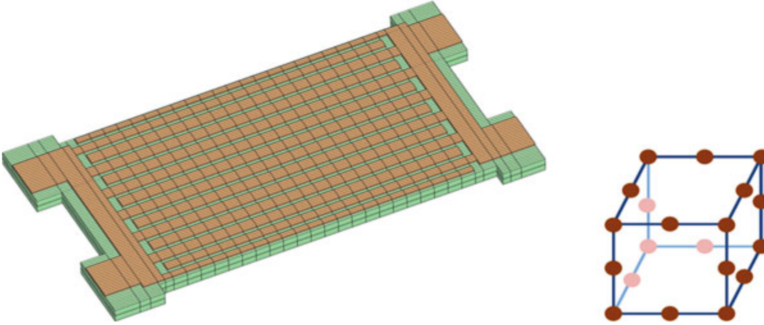

Fig. 11.3 Mesh for lithium niobate resonator (*left*) and sample illustration of an element with nodes (*right*)

$$u_i(x) \approx \sum_{n=1}^{N} \widehat{u}_{in} \psi_n^M(x), \qquad \phi(x) \approx \sum_{n=1}^{N} \widehat{\phi}_n \psi_n^E(x) \tag{11.4}$$

where N is the number of nodes, $\hat{u}_{in}$ and $\widehat{\phi}_n$ are the displacement and potential at the nodal points, and ψ_n^S and ψ_n^E are typically linear or quadratic functions nonzero only over the elements connected to node n. By substituting (11.4) into (11.1)–(11.3) and enforcing that (11.1) be satisfied under an appropriate testing inner-product, we arrive at a finite-dimensional matrix approximation for (11.1)

$$-\omega^2 \begin{bmatrix} M_{11} & 0 \\ 0 & 0 \end{bmatrix} \begin{bmatrix} \widehat{u} \\ \widehat{\phi} \end{bmatrix} + \begin{bmatrix} K_{11} & K_{12} \\ K_{21} & K_{22} \end{bmatrix} \begin{bmatrix} \widehat{u} \\ \widehat{\phi} \end{bmatrix} = \begin{bmatrix} \widehat{f}_1 \\ \widehat{q} \end{bmatrix} \tag{11.5}$$

The system above has *4N* rows and columns (or slightly less due to materials that lack a potential because they are not piezoelectric). M_{11}, K_{ij} are sparse since the shape functions are spatially nonzero only locally near each node.

For resonator applications, body forces, $\widehat{f}_1$, and charges, $\widehat{q}$, are typically zero. To apply electrical excitation, boundary conditions are applied so that the metal regions are constrained to known equipotentials, $\widehat{\phi}_e$, and the surface charge density, $\widehat{q}_e$, that develops at the piezoelectric-metal interface becomes the unknown. Rewriting (11.5) compactly,

$$-\omega^2 Mx + Kx = f \tag{11.6}$$

where $x = \left[\widehat{u}; \widehat{\phi}; \widehat{q}_e\right]$, $f = \left[0; 0; \ \widehat{\phi}_e\right]$ and M and K are the 2×2 block matrices of (11.5) modified for the application of $\widehat{\phi}_e$. Additional governing equations related to energy loss mechanisms, such as gas damping, thermo-elastic damping, or acoustic radiation through the anchors, will be covered later in the chapter. If those physical domains are included in (11.1) and (11.2), then (11.6) becomes, after factoring out x,

$$\left(-\omega^2 M + j\omega D + K\right) x = f \tag{11.7}$$

where $j = \sqrt{-1}$. The first step in evaluating a design is typically to compute the natural frequencies of the design. To do so, the generalized eigenvalue problem of the homogeneous version of (11.6) (or 11.7) is solved

$$Kv = \lambda M v \tag{11.8}$$

to find the eigenvalues λ_i, and corresponding eigenvectors, v_i, that satisfy (11.8). The angular natural frequencies, ω_i, are found from $\lambda_i = \omega_i^2$ and the mode shapes such as shown in Fig. 11.1 are defined by the displacement subvector of v_i. The frequency of the desired resonant mode can be determined by visually searching through the mode shapes to find the known expected shape. This must be done in a manual fashion because the electrical excitation, f, in (11.7) plays no role in (11.8). Thus an electrode pattern designed to excite the desired mode plays little role in an eigenmode analysis and every natural frequency is on the same footing. For piezoelectric micromachined ultrasonic transducers (pMUTs), this is not a problem because the location of the mode that will be excited is known (near zero frequency). However for bulk mode designs such as shown in Fig. 11.2, there are 476 modes within the frequency range shown. Any manual searching, even if guided by an analytic estimate, is unacceptable because parameter sweeps involving many simulations cannot be automated. This is because the modes can change order: a mode with index i for one simulation is not guaranteed to have the same index if the design or the temperature changes. Secondly, an eigenmode analysis only reports the frequency of resonance, but says nothing about how well the design is able to excite that mode compared to the other nearby modes. For both of these reasons, computing the frequency response is required over eigenmode analysis.

Computing the resonator frequency response in the most naïve approach involves forming f based on the desired equipotentials, ϕ_e, and then for each frequency ω_i, solve the linear system in parentheses in (11.7) for the unknown x. A final post-processing step is then applied by integrating appropriate terms of $\widehat{q}_e$ from x to compute the net charge (current) at that frequency.

The difficulty is that many frequency points are necessary to resolve features in the frequency response particularly for the typical quality factors of $Q > 1000$. In addition, each frequency point is expensive because a fine mesh (large number of nodes) is necessary to resolve features accurately. This is shown in Fig. 11.4a where 60 frequency points miss the main resonance, the small spur to the left, and barely capture the spurs to the right. In comparison 1680 points resolve the features but would require 7 h to compute for a moderate mesh of size $N = 17{,}715$ nodes.

Even small spurs matter and resolving them can require a fine mesh. For instance, the frequency shift with temperature varies for different modes [9] and a mode that moves too close to the main resonance can degrade phase noise performance for an oscillator. In Fig. 11.4b, a coarse mesh with $N = 32{,}983$ captures well the fifth-order extensional mode from Fig. 11.1 but the spurious modes are more accurately captured for a finer mesh with $N = 219{,}194$. Computing the response for the fine

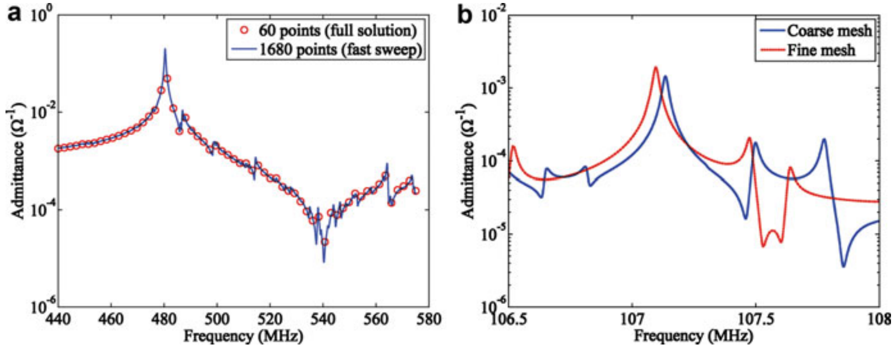

Fig. 11.4 The need for many frequency points and a large number of nodes. (**a**) Sixty frequency points are inadequate to resolve features in the response of the Lithium Niobate resonator. (**b**) Even if the coarse mesh captures the main resonance, a fine mesh is necessary to capture the spurs

mesh in Fig. 11.4b by multiple solves of the full system of (11.7) would then take days of computation time.

Fast frequency sweep methods can attain speed similar to that of eigenmode analysis and also account for the impact of the excitation, f. To do so, fast frequency sweep methods typically project the original system matrices, M, D, K, onto a subspace that is much smaller than the original system, but still captures the relevant dynamics. For example, in solid and structural mechanics, it is common to apply *mode superposition* by choosing an appropriate subset of the eigenmodes to define the subspace [10]. Given n eigenvectors as columns of the matrix $V = [v_1\ v_2 \ldots v_n]$, where $n \ll 4N$, the reduced $n \times n$ system matrices would be

$$\tilde{M} = V^T MV, \quad \tilde{D} = V^T DV, \quad \tilde{K} = V^T KV, \quad \tilde{f} = V^T f \tag{11.9}$$

The frequency response is then computed on the reduced system

$$\left(-\omega^2 \tilde{M} + j\omega \tilde{D} + \tilde{K}\right) \tilde{x} = \tilde{f} \tag{11.10}$$

which takes an insignificant amount of time compared to the original eigenmode computation since n is on the order of 100's. If V includes all the eigenmodes that significantly influence the response within the frequency range of interest, then the frequency sweep of (11.10) will be sufficiently accurate compared to (11.7).

As noted previously, many of the eigenmodes of (11.8) are not excited by the electrode pattern and thus do not appear in the frequency response. Thus the computation time to extract all the eigenmodes in the frequency range of interest is unnecessary. In the electronic design automation community, Krylov subspace methods have been used to form the matrix V, rather than the eigenvectors [11]. Applying a Krylov subspace method would choose a set of column vectors that span the same vector subspace as repeated multiplication of $K^{-1}f$ by $K^{-1}M$,

Table 11.1 Comparison of wall-clock time to perform fast sweep versus direct solution of (11.7) on a quad-core computer

Number of nodes (N)	Degrees of freedom ($\sim 4N$)	Number of frequency points	Solution time	
			Fast sweep	Direct solution
17,715	67,176	1680	15 min	7 h
89,336	347,676	1900	2.5 h	74 h

Direction solution times are projected from time for 60 points

$$\text{colspan}\{V\} = \text{span}\left\{K^{-1}f, K^{-1}MK^{-1}f, \ldots, \left(K^{-1}M\right)^{n-1}K^{-1}f\right\} \tag{11.11}$$

The repeated multiplication by $K^{-1}M$ is similar to a standard eigenmode algorithm for (11.8), however because the excitation vector f is used, V only contains the subspace that the electrode pattern can excite. The number of vectors in V is thus less than the number of eigenmodes, and is thus cheaper, and faster, to compute.

To apply either of these methods to the coupled piezoelectric system of (11.1) requires modification for the multidomain nature of the system at hand and the difference in structure of the system in (11.5) compared to the pure mechanical or purely electrical systems. Various implementations exist of differing speed and accuracy. For instance, using the implementation in [12], computing the 60 points with the direct sweep on (11.7) for Fig. 11.4a takes the same wall-clock time as computing the entire 1680 points with a fast sweep on a 4-core laptop computer. If the mesh is refined for further accuracy, the speed improvement becomes even more critical, since a direct sweep can take days. Table 11.1 compares the computation time for the Lithium Niobate resonator of Fig. 11.2 for two different mesh sizes. Fast sweep is about 30 times faster than direct sweep reducing the computation time from days to hours. The speed of fast sweep makes multiple 3D simulations that explore design tradeoffs feasible.

11.3 Modeling Energy Loss Mechanisms

Energy loss in resonators is measured by the quality factor, Q, which is a measure of the energy lost per harmonic cycle compared to the energy stored,

$$Q = 2\pi \frac{E_{stored}}{E_{lost}}$$

Maximizing the quality factor is important for piezoelectric MEMS resonators to reduce phase noise in oscillator applications and reduce insertion loss in filters [13]. For pMUTs, Q is related to the peak displacement sensitivity [14] and is important to improve resolution for mass sensing [15].

Various energy loss mechanisms contribute to the final Q of a given design according to

$$\frac{1}{Q} = \frac{1}{Q_{gas}} + \frac{1}{Q_{anchor}} + \frac{1}{Q_{thermoelastic}} + \frac{1}{Q_{interfacial}} + \frac{1}{Q_{other}} + \ldots \tag{11.12}$$

The challenge of modeling Q is in determining which mechanisms are relevant for a given class of resonators or even a certain design. For capacitive, low frequency (kHz), small-gap, flexural MEMS resonators in air, gas damping, Q_{gas}, is typically dominant and has been studied extensively. However, for MEMS bulk resonators, gas damping is less important due to the small displacements, larger gaps to the substrate, and larger stored strain energy in the bulk for a similar displacement of a flexural design. In addition, the air squeezed in the gaps behaves more as a spring than damper at higher frequencies as will be discussed later in this section.

For high frequency bulk resonators as well as pMUTs, loss from acoustic energy scattered into the substrate through the anchoring mechanism, Q_{anchor}, plays a significant role [13, 16, 17]. Anchor loss has been shown to play less of a role for AlN contour mode resonators above 370 MHz at which point thermoelastic dissipation and interfacial losses are suspected to be dominant [13]. Other loss mechanisms related to phonon-phonon and electron–phonon interaction are suspected to be relevant at higher frequency or when other mechanisms are mitigated [18, 19] but have not been shown to be relevant to recent piezoelectric MEMS resonators.

In this section we explore the computational modeling of anchor loss, thermoelastic dissipation, and gas damping. These mechanisms are sufficiently understood that their computational modeling can be applied to the design process. The understanding of interfacial loss [20], which is suspected to be related to the crystal lattice mismatch between the electrodes and piezoelectric material, is still a topic of research and thus will not be covered.

11.3.1 Anchor Loss

The means by which a MEMS resonator is attached to the substrate provides a parasitic route for acoustic energy to leave the resonator and propagate into the substrate. This lost energy is often called *anchor loss, substrate loss, clamping loss, or support loss* and is one of the most important loss mechanisms for piezoelectric MEMS resonators.

For released MEMS resonators, the large acoustic mismatch with the air causes acoustic wave reflection, thus acoustic loss is limited to acoustic waves transmitted through the suspension structures to the substrate. For certain types of these resonators, analytic methods have been applied to estimate loss [21, 22]. The most straightforward idea to reduce anchor loss for MEMS resonators whose size is on the order of an acoustic wavelength, whether bulk or flexural, is to choose thin suspensions that are one-quarter of an acoustic wavelength and placed at nodal

points on the resonator [23, 24]. However, these techniques do not eliminate all anchor loss and are not generally applicable when the width of the anchor is not small compared to a wavelength. In addition, geometric detail such as sidewall angles and filleting is not typically included in analytic modeling but has been shown to have significant impact on the computed loss [13].

Finite-element analysis can be applied when analytic techniques do not offer enough predictive value. To model the acoustic energy propagating into the substrate, it would be impractical to add the entire substrate to the finite-element model since the system in (11.7) would be too large to even form. Instead, both computational and analytic techniques assume that once energy leaves the resonator it never returns. For analytic techniques this corresponds to modeling the substrate as a semi-infinite half-space. In a finite-element context, this corresponds to modeling only a small section of substrate and then terminating the outer boundary with special absorbing elements that ideally do not reflect incident acoustic energy. This assumption implies that the region outside the modeling domain does not impart energy back into the resonator. As we shall see later in this section, that assumption must be treated carefully.

Two common techniques for absorbing finite elements are high-order Absorbing Boundary Conditions (ABC) and Perfectly-Matched-Layer (PML) (see [25] for a comparison). The model of the substrate is truncated on the order of a wavelength from the anchor location and the absorbing elements are used to prevent reflection of incident waves back into the resonator. Ideally, these elements absorb all energy that is imparted upon them, and the measure of the stored strain energy at resonance divided by this absorbed (lost) energy gives Q_{anchor}.

The first application of absorbing elements to MEMS was in [26] and a thorough comparison to analytic results in the context of MEMS was done in [27].

As an example, consider the fifth-order extensional mode resonator from Fig. 11.1 attached to a substrate shown in Fig. 11.5. Absorbing elements (not shown) were used on the bottom and four sides of the substrate which causes the displacement amplitude to decay as it propagates away from the anchor. Q_{anchor} is around 7000 which is similar to that reported in [1].

Modeling anchor loss is not just about capturing geometric detail and applying appropriate absorbing elements, but also properly modeling the acoustic paths in the substrate to avoid the artificial isolation of interacting structures. For instance, instead of modeling one large section of substrate in Fig. 11.5, one could use a small block around each anchor separately. This would similarly absorb all the energy that leaves the anchor, but would not capture any interaction between the anchors.

An example of interaction between anchors is the electromechanical dual beam resonator filter analyzed in [28]. Two clamped-clamped beams are coupled with a cross beam that stiffens the out-of-phase mode, shown in Fig. 11.6a. The in-phase mode is at a slightly lower frequency than the out-of-phase mode thus creating a band-pass filter. If each anchor included its own piece of substrate with absorbing elements, then the amplitude of oscillation at both frequencies would be identical. However, by anchoring both anchors of both beams to a single substrate structure

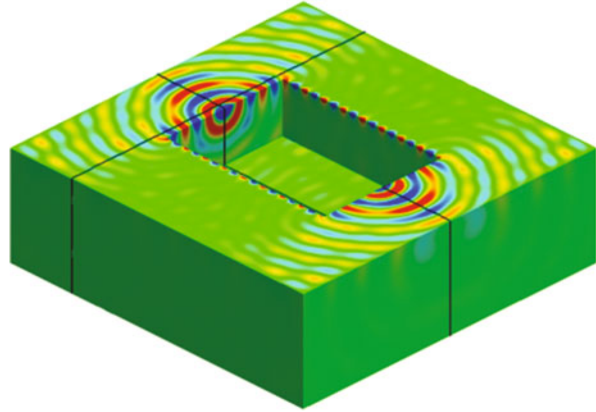

Fig. 11.5 Acoustic energy propagating into substrate from resonator (hidden) from Fig. 11.1. Absorbing elements are on the bottom and four sides of the substrate (not shown)

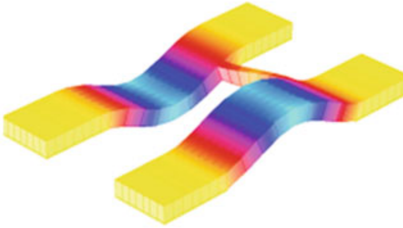

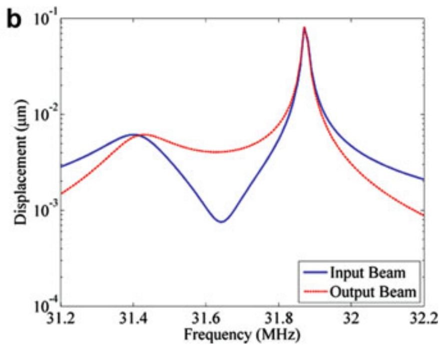

Fig. 11.6 (**a**) Dual beam resonator filter in out-of-phase-mode at 31.87 MHz (**b**) Frequency response of filter showing significantly more damping for in-phase mode

(not shown), the anchor loss of the in-phase mode is significantly greater than the out-of-phase mode as shown in Fig. 11.6b. This is seen in experiment as 7 dB of insertion loss for the in-phase mode, and only 1 dB for the out-of-phase mode [28].

The out-of-phase mode has much less anchor loss because the deformations at the anchors destructively interfere generating a low amplitude acoustic wave compared to the in-phase mode. In this case, the separation of the resonators is small compared to a wavelength. The behavior for half-wavelength separation would be the opposite.

A more subtle case of artificial isolation from absorbing elements was shown to occur when modeling the undercut in a 60 MHz AlN resonator [29]. If one assumes the energy that leaves the anchors never returns, then applying absorbing elements around the edge of the undercut region would suffice. Doing so always suppresses reflections from the edge, however those reflections were shown to be significant for certain anchor sizes. The impact on the acoustic pattern in the undercut region for one of those cases is shown in Fig. 11.7. The impact on Q was similarly severe, over predicting Q by factors of 2–10 in these cases.

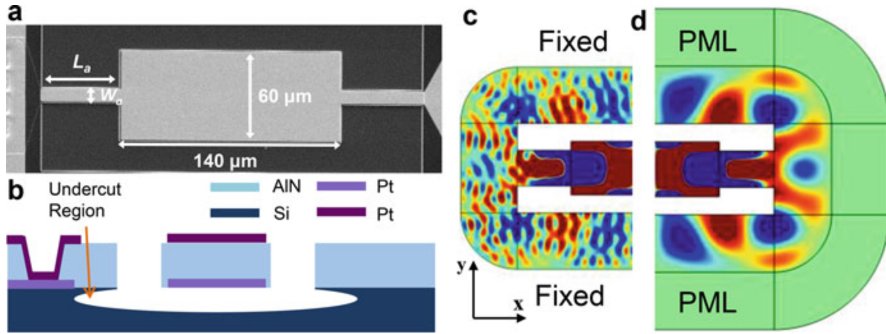

Fig. 11.7 Absorbing elements can absorb too much. Using fixed conditions instead and an alternate method of measuring lost energy results in a better match to experiment for this particular W_a and L_a. (**a**) Top view SEM of 60 MHz laterally-vibrating AlN resonator, (**b**) Cross-sectional illustration of resonator showing that release process undercuts aluminum nitride, (**c**) x-component displacement from finite-element analysis for $W_a = 40$ μm and $L_a = 60$ μm when a fixed boundary condition is applied to the outer edge of the undercut region (**d**) x-component displacement when fixed boundary condition is replaced with a PML boundary. Images courtesy J. Segovia-Fernandez and G. Piazza, CMU

11.3.2 Thermoelastic Dissipation

The equations governing thermoelastic dissipation (TED) are well understood [30]. The elastic portions of (11.1)–(11.3), which contain no loss mechanisms, imply that for an elastic vibrating solid, the elastic stored energy will be reversibly recovered as kinetic energy after a quarter cycle of oscillation. The volume change from this strain field also creates a local temperature variation in the solid which oscillates with the elastic energy. For the small dimensions in MEMS, the time constants for modes of heat transfer can be of similar order as the period of oscillation. In this case, irreversible heat transfer from the temperature gradient can occur during each cycle which appears as lost elastic energy.

To understand why volume change creates the temperature variation mentioned above, note that the converse is well known: for a positive thermal expansion coefficient, an increase in temperature is easily observed to cause expansion and a decrease in temperature to cause compression. Conversely, but not as easily observed, expansion of a solid leads to a decrease in temperature, and similarly, compression leads to a rise in temperature. In [31] this is explained by the second law of thermodynamics. Entropy is constant for a small, adiabatically sealed volume (no heat transfer across boundaries) when undergoing a reversible applied force. If that force is compressive, the volume will decrease. The decrease in entropy from the decrease in volume must be compensated by a rise in temperature to keep entropy constant. Conversely, if the force is tensile, the increase in volume must lead to a decrease in temperature. See [31] for a detailed derivation. Now consider a small volume within a resonating solid. When the period of oscillation is very small compared to thermal time constants, the temperature oscillates fast enough that a

small volume within the resonator is effectively adiabatic. Thus entropy remains constant and the elastic energy is recovered at every cycle. In contrast, when the mechanical and thermal rates are about equal, the system is not adiabatic, and the thermal gradients result in heat transfer out of the small volume. In this case, entropy is not constant which is observed as elastic energy being irreversibly converted to heat.

To add thermoelastic dissipation to the governing piezoelectric equations, we add a third equation to (11.1) for local entropy balance [30] assuming small temperature deviations from the reference temperature

$$q_{i,i} + T_0\dot{S} = 0 \tag{11.13}$$

where q_i are components of heat flux, T_0 is the reference temperature, S is the entropy and the superposed dot implies time differentiation. The thermoelastic coupling is seen through the additions to the constitutive relations

$$\begin{aligned}\sigma_{ij} &= C_{ijkl}\varepsilon_{kl} - \lambda_{ij}T \\ S &= \lambda_{ij}\varepsilon_{ij} + \beta T \\ q_i &= -k_{ij}T_{,j}\end{aligned} \tag{11.14}$$

where T is the change in temperature from T_0, k_{ij} are the thermal conductivities, $\lambda_{ij} = C_{ijkl}\ \alpha_{kl}$ where α_{kl} are the linear coefficients of thermal expansion, and $\beta = C_v/T_0$ where C_v is the heat capacity at constant volume. The last relation is Fourier's law of heat conduction. Piezoelectric terms have been dropped for simplicity (see [32] for the full thermopiezoelectric formulation).

The added term in the stress–strain relationship of (11.14) adds the stress due to thermal expansion. By substituting the second and third relations in (11.14) into (11.13) we arrive at the traditional heat equation plus an added source term proportional to the strain rate.

Zener first explored thermoelastic dissipation analytically for a beam [33]. He used the mechanical eigenmodes and thermal eigenmodes of the *uncoupled* elastic and heat equations. Based on their overlap (similarity in shape), Zener estimated the thermoelastic loss from multiple thermal modes. Other authors extended this idea [34]. However, all these approaches were limited to simple mechanical structures. Solving for geometrically complex structures and mode shapes via the finite element method was first done in [35] and is now common for modeling thermoelastic loss.

As an example Fig. 11.8 shows the thermoelastic loss corresponding to the extensional mode resonator shown in Fig. 11.1. The TED energy density shown indicates the regions of greatest loss that gives a $Q_{TED} \sim 120{,}000$. Since $Q_{anchor} \sim 7000$, little effort should be made to reduce TED for this particular design until the anchor loss can be minimized. But for designs for which TED dominates, finite element simulation predicts the loss well for design modifications such as slots in beams to disrupt heat transfer [36, 37].

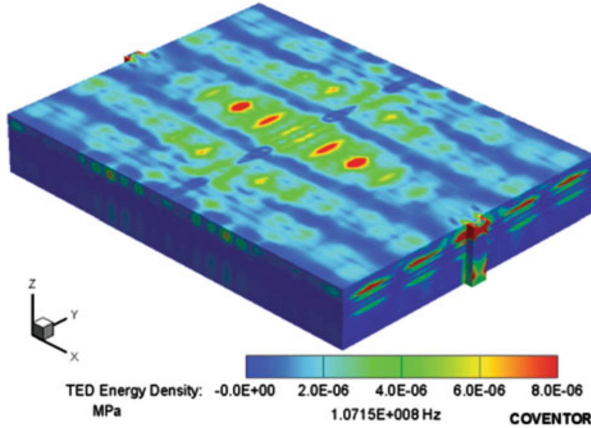

Fig. 11.8 Density of thermoelastic energy loss for 5th order extensional mode displacement field of Fig. 11.1

An advantage of the Zener analytic approach is that it gives weighting factors to the different thermal eigenmodes proportional to their contribution to TED. In [36], the design guidance from Zener's approach was combined with finite-element modeling by using the uncoupled *numerical* mode shapes from finite element analysis so that the thermal heat flow contributing to TED could be visualized and the design modified to minimize its impact.

11.3.3 Fluid Damping

Whether liquid or gas, the fluid surrounding a resonating solid impacts the effective mass, spring, and damping of the resonant mode. This effect is most pronounced in ultrasonic transducers immersed in water since the density of the water is commensurate with that of the vibrating membrane. For instance, in [17], a 25 MHz pMUT's resonance frequency dropped by 25 % when immersed in water due to the added mass of moving the water at every cycle [38]. Quality factor has also been observed to fall from low 100's in air to single digits in water [17, 39] due to acoustic radiation [38].

For MEMS bulk acoustic wave resonators in air, the impact of the fluid is far less prominent but has been shown to degrade the quality factor. For instance, in [40], the quality factor of an AlN-on-Silicon width-extensional resonator's fundamental mode at 35.4 MHz dropped by 30 % in air at atmospheric pressure from its value of 10,100 in vacuum. This corresponds to a $Q_{air} = 25{,}000$ according to (11.12). For the same resonator in its third mode at 107 MHz, Q dropped by 11 % from 4500, which

corresponds to $Q_{air} = 36{,}000$. This increase in Q_{air} with frequency is consistent with loss from viscous fluid flow which we discuss briefly in this section. Note that even if Q_{air} were constant with frequency, the quality factor in vacuum generally diminishes with frequency, lessening the impact of Q_{air} at RF frequencies. In addition, for timing applications, vacuum packaging is required to avoid incremental mass loading from air molecules depositing on the resonator over time. For these reasons, the loss from air damping in MEMS bulk mode resonators has not been thoroughly studied. In this section, we only briefly review the relevant domains governing the fluid dissipation for a resonator in air at atmospheric pressure.

When the motion of the solid resonator creates a shearing motion in the surrounding fluid, the fluid particles, which cannot support a shear stress, flow against each other in response to that shear. This is the case for in-plane motion of a resonator. The friction between the particles in that motion results in energy loss which can be quantified in terms of the viscous penetration depth δ [41]

$$\delta = \sqrt{\frac{2\mu}{\rho\omega}} \tag{11.15}$$

where μ is the viscosity of air, ρ the density of air, and ω the angular oscillation frequency. This penetration depth characterizes the length scale of the velocity waves dissipating into the fluid from the resonator surface. It is within this penetration depth that most of the viscous dissipation in the fluid occurs, and its magnitude relative to the resonator length dimension L can be used to determine the relative contribution of the fluid to the dissipation of the resonator. What's more, since δ is proportional to $1/\sqrt{\omega}$, also is able to characterize the frequency-dependent effects of fluid damping for a given resonator geometry. Consider the notional test case of a silicon sphere of radius $R = 10$ μm (the L of this case) undergoing translational oscillations in air. Following an approach similar to [42],

$$Q_{air} = \frac{m}{6\pi\mu R\,(1 + R/\delta)} \tag{11.16}$$

where m is the mass of the sphere. Figure 11.9a plots (11.15) and (11.16) for air at atmospheric pressure. At low frequencies, with a correspondingly large δ, $1/Q_{air}$ varies with a ω^{-1} relationship in a Stokes flow regime. In this regime, δ is also typically on the scale of or larger than any gaps typical of MEMS structures. The viscous flow resulting from squeezing fluid from a gap is significantly larger than that described by (11.16). For general resonator geometries, squeeze-film damping has been extensively studied due to the small gaps of capacitive MEMS and is quantified later in this section.

As frequency increases and δ decreases, viscous effects create dissipation in a thin boundary layer of decay constant δ encompassing the resonating body. $1/Q_{air}$ for the sphere decreases with a $1/\sqrt{\omega}$ relationship proportional to δ. Above 100 MHz for the sphere in Fig. 11.9a, the loss from air becomes much less significant compared to other loss mechanisms.

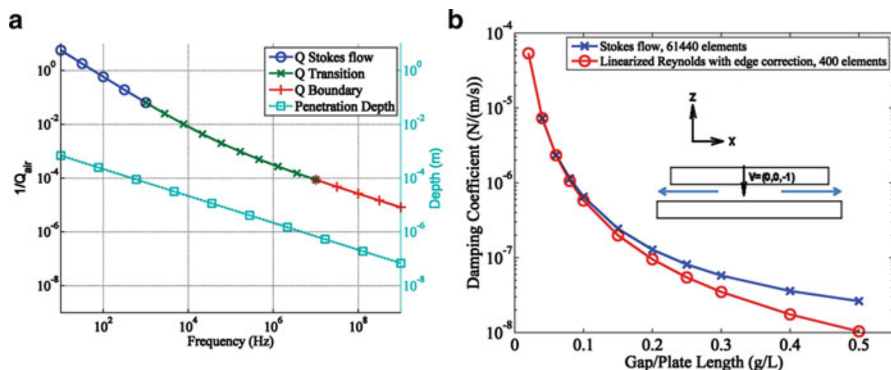

Fig. 11.9 (**a**) Quality factor of air at atmospheric pressure for oscillating sphere of radius $R = 10$ μm. (**b**) Damping in air as a function of gap under different flow assumptions for $L = 50$ μm plate with motion normal to the gap

Although the oscillating sphere case gives an order of magnitude of the fluid damping expected from a resonator of a given oscillation frequency and length dimension, the particular oscillation mode and geometry of the resonator can serve to increase or decrease the fluid damping. Computational methods can be applied to solve for the case of general resonator geometry. A simple example is the damping as a function of gap size shown in Fig. 11.9b. The damping at low frequency drops by more than two orders of magnitude as the gap grows from $g/L = 0.02$–0.2. Most of these results can be computed in seconds to minutes on realistic resonator geometries by solving the linearized Reynold's equation on the 2D surface with correction for flow through perforations [43]. However for $g/L > 1/10$, a more computationally intensive Stokes flow solution gives higher accuracy [44]. For high frequency and very small gaps such that $\delta > g$, the thin fluid film behaves more like a spring than a damper. For instance, neglecting rarefaction effects, for $g/L \sim 0.2$ and $f > 40$ MHz, fluid spring forces dominate and the damping declines as the frequency is raised higher. Gaps for piezoelectric MEMS resonators are typically not so small. Computational methods could also be applied for this high frequency case with $\delta \ll g$ should such analysis prove relevant in the future.

11.4 Static and Dynamic Nonlinearity

The governing equations of (11.1)–(11.3) assume small enough displacements that it is sufficiently accurate to only include the linear terms in the constitutive relationships (11.2) and the strain–displacement relationship (11.3). There are two exceptions to this related to piezoelectric MEMS resonators that are beginning to be studied. The first is the presence of a static residual stress from the fabrication process that can be viewed as shifting the operating point for the linearization. The second exception is the dynamic nonlinearity from applying high power. Dynamic nonlinearity is, for example, the origin of intermodulation distortion in filters. We end this chapter by discussing progress to date on the computational modeling of these effects.

11.4.1 Residual Stress

Stress remaining in thin-film MEMS after the deposition process is referred to as *residual stress*. This stress is due partly to thermal expansion mismatch between adjacent layers, but also due to a host of other deposition related phenomena [45] whose effect is called *intrinsic stress*.

In pMUTs, degradation of the electromechanical coupling coefficient has been attributed to residual stress [46] and poor computational prediction when not modeled [47]. The resonance frequency and electromechanical coupling are very sensitive to residual stress in the plane of the membrane. To model this computationally, the quadratic terms for in-plane strain must be added to (11.3) because the linear terms are small since most of the motion is out-of-plane [48]. The added strain energy from the quadratic terms has the effect of shifting the mechanical stiffness proportional to the residual stress. Specifically, K_{11} in (11.5) is replaced by $K_{11} + K_g$ where K_g is proportional to the residual stress, σ_0. The strong sensitivity of resonance frequency and dynamic displacement predicted by finite-element modeling is shown in Fig. 11.10a for the 50 μm radius pMUT of [47].

For suspended single-material films with only thin electrodes, such as the Lithium Niobate resonator of Fig. 11.2, residual stress from the film transfer process can potentially cause significant mechanical failures on release. The structures are anchored at four locations to compensate but still typically exhibit significant curvature upon release. Since the structures are a single material, this implies the form of the stress is not just a uniform plane stress, but also a *stress gradient* through the thickness of the film. For instance, a linearly varying stress that changes by 100 MPa between the top and bottom resonator surfaces causes the static deformation as shown in Fig. 11.10b. Lithium Niobate resonators exhibit this shape upon release but in greater amplitude indicating the form of the stress requires further investigation.

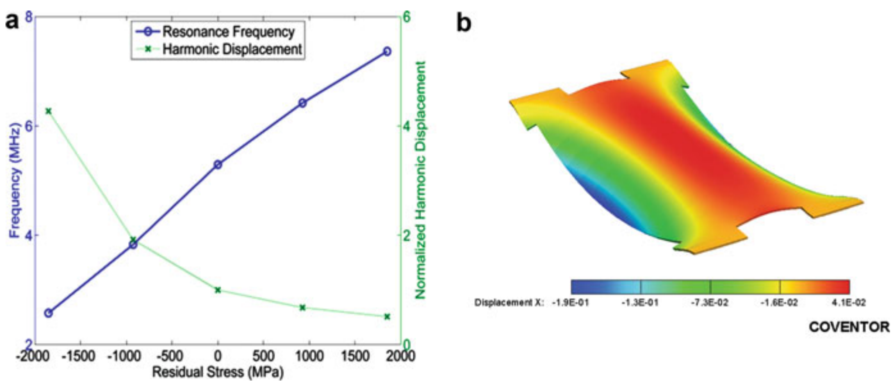

Fig. 11.10 Residual stress on PZE resonators (**a**) Effect of uniform residual stress on 50 μm pMUT. (**b**) Exaggerated static displacement normal to the film due to stress gradient through thickness for Lithium Niobate resonator of Fig. 11.2

11.4.2 Nonlinearity from High Power

For oscillator and filter applications, nonlinearity limits the power handling of the device. Modeling of this nonlinearity in piezoelectric MEMS resonators has largely been analytic to date. In [49] second-order terms for the piezoelectric coefficients in (11.2) for a gallium-nitride resonator are connected to a change in motional resistance at high power levels. However, most recent work on nonlinearity has focused on self-heating [49–51]. The energy loss in the resonator that is converted to heat raises the temperature, which typically lowers the resonance frequency. This change in resonance changes the impedance of the resonator at a given frequency which either increases or decreases the amplitude of oscillation and thus couples back to a change in the temperature. This coupling between heat generation and impedance is a nonlinear relationship that must be solved to determine the steady-state amplitude of oscillation and temperature for each frequency. In [51], this coupling is modeled with a single degree-of-freedom heat flow model in which the entire resonator is assumed at a single temperature, T, and the heat is assumed to be generated uniformly over the resonator. This simple one-temperature model is shown to exhibit a Duffing-like behavior which matches measurement for a Lithium Niobate resonator similar to Fig. 11.2. However such an approach cannot work well in the general case because the heat generation and temperature are distributed over the resonator body rather than lumped as a single temperature.

Computational modeling can further refine the analysis of thermal nonlinearity by using a distributed model of heat generation and temperature [52]. In [51] the frequency was expressed as a function of a single temperature through the temperature coefficient of frequency (TCF). In contrast, the solution of the distributed heat flow equation permits one to determine a *power coefficient of frequency* (PCF). To find the nonlinear frequency response, the unknown absorbed power, P is solved for at each frequency using the equation for power absorbed by an impedance $Z(P)$ terminating a transmission line of characteristic impedance Z_0

$$P = \frac{4Z_0 \mathrm{Re}\{Z(P)\}}{|Z(P) + Z_0|^2} P_{in} \tag{11.17}$$

where P_{in} is the power from the vector network analyzer. $Z(P)$ is the impedance as a function of power calculated from the extracted motional RLC components for the nominal case as is done in [51] as a function of temperature. For instance, for the resonator of Fig. 11.2, the mode shape exhibits the greatest displacement near the center as shown in Fig. 11.11a. For some total power absorbed, P, the finite-element model distributes this power as a heat profile proportional to the square of this displacement. After solving the steady-state heat equation, a nonuniform temperature profile results as shown in Fig. 11.11b. That profile is used to create a spatial distribution of elastic constants which can be used in (11.2) to compute a shifted frequency which determines the PCF. The PCF is then used in a BVD model to express the change in motional RLC components to be used in (11.16). The result of that nonlinear solution for various power levels is shown in Fig. 11.11c.

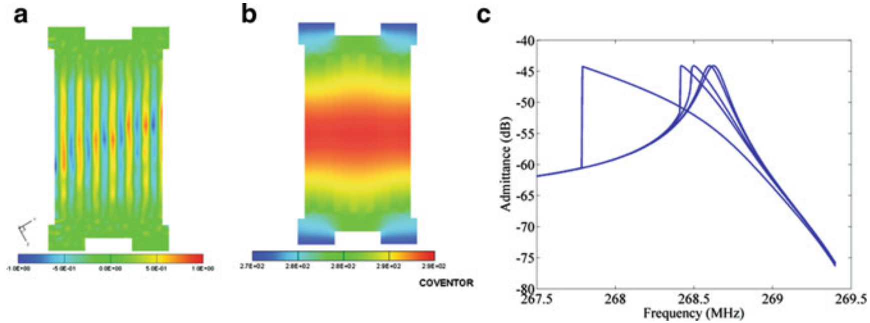

Fig. 11.11 Thermal nonlinearity captured by a distributed heat generation and flow model. (**a**) 3D S0 mode shape shifted in frequency due to temperature profile shown in (**b**). (**c**) Nonlinear frequency response for $P_{in} = -10, -4, 2, 4, 10$ dBm

11.5 Conclusion

In this chapter we explored the various methods of computational modeling that aid in addressing challenges in piezoelectric resonator design and verification. We first showed the importance of three-dimensional modeling in computing an accurate resonator frequency response and showed that fast sweep algorithms make this computation feasible. Second, we discussed the importance of loss mechanisms and showed that computational methods for anchor loss, thermoelastic dissipation, and fluid damping can predict the loss from these mechanisms. Residual stress is particularly important to microfabricated resonators and we showed that its effect and particularly the effect of the stress gradient can be modeled computationally to predict device performance. Lastly, and still to be explored, computational modeling can aid in predicting nonlinearity. We showed that thermal nonlinearity can be modeled by combining a distributed heat flow model with an analytic modeling technique.

Acknowledgements The author would like to thank Stuart Traux for the description of fluid damping at high frequency and the helpful review of this text, Rahul Jhaveri for many of the simulations contained here, and Professor Songbin Gong for the many discussions on the topics contained here.

References

1. Bhugra H, Wang Y, Pan W, Lei D (2011) High performance pMEMS™ oscillators – the next generation frequency references. In: IEEE international electron devices meeting (IEDM), Washington, DC, 2011, pp 20.1.1–20.1.4
2. Ho GK, Abdolvand R, Ayazi F (2007) High-order composite bulk acoustic resonators. In: IEEE 20th international conference on micro electro mechanical systems, 2007. MEMS, pp 791–794

3. Gong S, Piazza G (2013) Design and analysis of lithium-niobate-based high electromechanical coupling RF-MEMS resonators for wideband filtering. IEEE Trans Microw Theory Tech 61(1):403–414
4. Song Y-H, Gong S (2015) Spurious mode suppression in SH0 lithium niobate laterally vibrating MEMS resonators. In: 2015 IEEE international electron devices meeting (IEDM), 2015
5. Pulskamp J, Bedair S, Polcawich R, Smith G, Martin J, Power B, Bhave S (2012) Electrode-shaping for the excitation and detection of permitted arbitrary modes in arbitrary geometries in piezoelectric resonators. IEEE Trans Ultrason Ferroelectr Freq Control 59(5):1043–1060
6. Allik H, Hughes T (1970) Finite element method for piezoelectric vibration. Int J Numer Methods Eng 2:151–157
7. Benjeddou A (2000) Advances in piezoelectric finite element modeling of adaptive structural elements: a survey. Comput Struct 76(1–3):347–363
8. Hughes TJR (2000) The finite element method: linear static and dynamic finite element analysis. Dover Publications, Mineola, NY
9. Wang S, Bahr B, Li S-S (2015) Temperature coefficient of frequency modeling for CMOS-MEMS bulk mode composite resonators. IEEE Trans Ultrason Ferroelectr Freq Control 62(6):1166–1178
10. Bathe K-J (1996) Finite element procedures. Prentice Hall, Upper Saddle River, NJ
11. Odabasioglu A, Celik M, Pileggi LT (1997) PRIMA: passive reduced-order interconnect macromodeling algorithm. In: Proceedings of the 1997 IEEE/ACM international conference on computer-aided design, Washington, DC, USA, 1997, pp 58–65
12. Coventor, Inc (2015) CoventorWare – MEMS simulation suite. Coventor, Inc, Waltham, MA, http://www.coventor.com
13. Segovia-Fernandez J, Cremonesi M, Cassella C, Frangi A, Piazza G (2015) Anchor losses in AlN contour mode resonators. J Microelectromech Syst 24(2):265–275
14. Lu Y, Horsley DA (2015) Modeling, fabrication, and characterization of piezoelectric micromachined ultrasonic transducer arrays based on cavity SOI wafers. J Microelectromech Syst 24(4):1142–1149
15. Park KK, Lee HJ, Crisman P, Kupnik M, Oralkan O, Khuri-Yakub BT (2008) Optimum design of circular CMUT membranes for high quality factor in air. *In: IEEE International Ultrasonics Symposium (IUS)*, pp 504–507
16. Ho GK, Abdolvand R, Sivapurapu A, Humad S, Ayazi F (2008) Piezoelectric-on-silicon lateral bulk acoustic wave micromechanical resonators. J Microelectromech Syst 17(2):512–520
17. Lu Y, Heidari A, Horsley DA (2015) A high fill-factor annular array of high frequency piezoelectric micromachined ultrasonic transducers. J Microelectromech Syst 24(4):904–913
18. Chandorkar SA, Agarwal M, Melamud R, Candler RN, Goodson KE, Kenny TW (2008) Limits of quality factor in bulk-mode micromechanical resonators. In: IEEE 21st international conference on Micro electro mechanical systems, MEMS 2008, pp 74–77
19. Tabrizian R, Rais-Zadeh M, Ayazi F (2009) Effect of phonon interactions on limiting the fQ product of micromechanical resonators. In: Solid-state sensors, actuators and microsystems conference, 2009. International TRANSDUCERS 2009, pp 2131–2134
20. Hao Z, Liao B (2010) An analytical study on interfacial dissipation in piezoelectric rectangular block resonators with in-plane longitudinal-mode vibrations. Sensor Actuat Phys 163(1): 401–409
21. Judge JA, Photiadis DM, Vignola JF, Houston BH, Jarzynski J (2007) Attachment loss of micromechanical and nanomechanical resonators in the limits of thick and thin support structures. J Appl Phys 101(1):013521
22. Hao Z, Ayazi F (2007) Support loss in the radial bulk-mode vibrations of center-supported micromechanical disk resonators. Sensor Actuat Phys 134(2):582–593
23. Hao Z, Pourkamali S, Ayazi F (2004) VHF single-crystal silicon elliptic bulk-mode capacitive disk resonators – part I: design and modeling. J Microelectromech Syst 13(6):1043–1053

24. Li S-S, Lin Y-W, Xie Y, Ren Z, Nguyen CT (2004) Micromechanical 'hollow-disk' ring resonators. In: 17th IEEE international conference on micro electro mechanical systems, 2004 (MEMS), pp 821–824
25. Rabinovich D, Givoli D, Bécache E (2010) Comparison of high-order absorbing boundary conditions and perfectly matched layers in the frequency domain. Int J Numer Methods Biomed Eng 26(10):1351–1369
26. Bindel DS, Govindjee S (2005) Elastic PMLs for resonator anchor loss simulation. Int J Numer Methods Eng 64(6):789–818
27. Frangi A, Bugada A, Martello M, Savadkoohi PT (2013) Validation of PML-based models for the evaluation of anchor dissipation in MEMS resonators. Eur J Mech A Solids 37:256–265
28. Park Y-H, Park KC (2004) High-fidelity modeling of MEMS resonators – part II: coupled beam-substrate dynamics and validation. J Microelectromech Syst 13(2):248–257
29. Segovia-Fernandez J, Xu C, Cassella C, Piazza G (2015) An alternative technique to perfectly matched layers to model anchor losses in MEMS resonators with undercut suspensions. In: 18th international conference on solid-state sensors, actuators and microsystems (TRANSDUCERS), 2015, pp 985–988
30. Nowacki W (1986) Thermoelasticity, 2nd edn. Pergamon Press, Oxford
31. Chandorkar SA, Candler RN, Duwel A, Melamud R, Agarwal M, Goodson KE, Kenny TW (2009) Multimode thermoelastic dissipation. J Appl Phys 105(4):043505
32. Aşkar Altay G, Cengiz Dökmeci M (1996) Fundamental variational equations of discontinuous thermopiezoelectric fields. Int J Eng Sci 34(7):769–782
33. Zener C (1937) Internal friction in solids. I. Theory of internal friction in reeds. Phys Rev 52(3):230
34. Lifshitz R, Roukes ML (2000) Thermoelastic damping in micro-and nanomechanical systems. Phys Rev B 61(8):5600
35. Antkowiak B, Gorman JP, Varghese M, Carter DJD, Duwel AE (2003) Design of a high-Q, low-impedance, GHz-range piezoelectric MEMS resonator. In: 12th international conference on TRANSDUCERS, solid-state sensors, actuators and microsystems, 2003, vol 1, pp 841–846
36. Duwel A, Candler RN, Kenny TW, Varghese M (2006) Engineering MEMS resonators with low thermoelastic damping. J Microelectromech Syst 15(6):1437–1445
37. Abdolvand R, Johari H, Ho GK, Erbil A, Ayazi F (2006) Quality factor in trench-refilled polysilicon beam resonators. J Microelectromech Syst 15(3):471–478
38. Peake W, Thurston E (1954) The lowest resonant frequency of a water-loaded circular plate. J Acoust Soc Am 26(2):166
39. Bernstein JJ, Finberg SL, Houston K, Niles LC, Chen HD, Cross LE, Li KK, Udayakumar E (1997) Micromachined high frequency ferroelectric sonar transducers. IEEE Trans Ultrason Ferroelectr Freq Control 44(5):960–969
40. Lavasani HM, Abdolvand R, Ayazi F (2015) Single-resonator dual-frequency AlN-on-Si MEMS oscillators. IEEE Trans Ultrason Ferroelectr Freq Control 62(5):802–813
41. Landau LD, Lifshitz EM (1987) Fluid mechanics, 2nd edn. Pergamon Press, Oxford
42. Blom FR, Bouwstra S, Elwenspoek M, Fluitman JHJ (1992) Dependence of the quality factor of micromachined silicon beam resonators on pressure and geometry. J Vac Sci Technol B 10(1):19–26
43. Yang Y-J, Kamon M, Rabinovich VL, Ghaddar C, Deshpande M, Greiner K, Gilbert JR (2001) Modeling gas damping and spring phenomena in MEMS with frequency dependent macro-models. In: The 14th IEEE international conference on micro electro mechanical systems, 2001. MEMS 2001, pp 365–368
44. Frangi A, Spinola G, Vigna B (2006) On the evaluation of damping in MEMS in the slip–flow regime. Int J Numer Methods Eng 68(10):1031–1051
45. Senturia SD (2007) Microsystem design. Springer, New York, NY
46. Cho J, Anderson M, Richards R, Bahr D, Richards C (2005) Optimization of electromechanical coupling for a thin-film PZT membrane: I. Modeling. J Micromech Microeng 15(10): 1797–1803

47. Sammoura F, Smyth K, Bathurst S, Kim SG (2012) An analytical analysis of the sensitivity of circular piezoelectric micromachined ultrasonic transducers to residual stress. *In: IEEE International Ultrasonics Symposium (IUS)*, pp 580–583
48. Geradin M, Rixen DJ (2014) Mechanical vibrations: theory and application to structural dynamics. John Wiley, New York, NY
49. Wang S, Popa LC, Weinstein D (2015) Piezoelectric nonlinearity in GaN Lamb mode resonators. In: 18th International conference on solid-state sensors, actuators and microsystems (TRANSDUCERS), 2015, pp 989–992
50. Segovia-Fernandez J, Piazza G (2013) Thermal nonlinearities in contour mode AlN resonators. J Microelectromech Syst 22(4):976–985
51. Lu R, Gong S (2015) Study of thermal nonlinearity in lithium niobate-based mems resonators. In: 18th international conference on solid-state sensors, actuators and microsystems (TRANSDUCERS), 2015
52. Jhaveri R, Lu R, Gong S, Kamon M (2016) Distributed and thermo-acoustically coupled modeling for accurate prediction of thermal nonlinearity in piezoelectric MEMS resonators. In: Solid-state sensors, actuators, and microsystems workshop, Hilton Head, SC

Part III
Manufacturing and Reliability of Piezoelectric MEMS Resonators

Chapter 12
Fabrication Process Flows for Implementation of Piezoelectric MEMS Resonators

Roozbeh Tabrizian

Since the first demonstration of thin-film piezoelectric resonators [1], high performance MEMS devices including low insertion loss resonators and filters [2, 3], small form factor energy harvesters [4], large-force actuators [5], and highly sensitive resonant sensors [6–8] have been successfully demonstrated using piezoelectric materials such as AlN, ZnO, and PZT. Thin film AlN has been of great interest mainly due to the high quality of its film growth and CMOS compatibility, as well as well-developed process recipes. The processing advantages in addition to the superior piezoelectric and acoustic properties of AlN, including large wave propagation velocity [9] and low thermoacoustic dissipation [10], have made it a popular choice for piezoelectric transduction of MEMS resonant devices.

Both the transverse and longitudinal piezoelectric effects of AlN thin films have been used to actuate and sense different micromechanical resonant devices. A thin AlN film sandwiched between two metal layers is typically deposited on a substrate, and various devices have been fabricated by patterning the stack (including substrate, and AlN and metal electrode layers).

In order to take advantage of the more efficient longitudinal piezoelectric effect of AlN, resonant devices are typically designed to operate in their thickness modes where the propagation of the bulk acoustic wave is predominantly orthogonal to the plane of the AlN film [2, 11]. For these modes, the resonance frequency is mainly determined by the thickness of layers in the stack and is approximately independent of the device lateral dimensions. Alternatively, transverse piezoelectric effect of the AlN deposited on the substrate surface can be used to actuate and sense resonant structures into a lateral mode where the propagation of acoustic wave is parallel with the plane of AlN film [3, 12]. The resonance frequency of these modes is mainly

R. Tabrizian (✉)
University of Florida, Gainesville, FL, USA
e-mail: rtabrizian@ece.ufl.edu

© Springer International Publishing Switzerland 2017

H. Bhugra, G. Piazza (eds.), *Piezoelectric MEMS Resonators*,
Microsystems and Nanosystems, DOI 10.1007/978-3-319-28688-4_12

a function of device lateral dimensions enabling the implementation of resonators with different resonance frequencies on the same substrate.

Depending on the application and required specifications of the MEMS resonator, piezoelectric transducer stack may serve simultaneously as the structural body, or be integrated on an arbitrary face of a micro-/nano-structure that is patterned in a semiconductor or insulator substrate. This chapter reviews the details of the fabrication process flow of piezoelectrically transduced resonators, with a focus on AlN as the piezoelectric material. Both piezo-only and piezo-on-substrate configurations will be considered, and few examples of process variations that result in more flexible and/or sophisticated transduction configurations or on-chip electronic integration will be discussed.

12.1 Introduction

A typical process flow for implementation of a piezoelectrically transduced resonator (called piezo-resonator hereafter) includes acoustic cavity formation and transduction stack preparation/integration. While the piezoelectric properties (i.e., electromechanical coupling coefficients) of the deposited films are highly correlated with processing condition and substrate preparation, the acoustic performance of the resonant device can be tailored by opting for proper structural substrates and device geometries. Figure 12.1 (left) schematically shows a piezo-on-substrate device where the resonator is composed of the transduction layer (i.e., piezoelectric film sandwiched between metallic electrodes) stacked on the top surface of a structural body of silicon and silicon dioxide layers. The deposition of the transduction stack can be done before or after formation of the acoustic cavity. Figure 12.1 (right) shows a piezo-only resonator where the transduction stack simultaneously serves as the sole structural body.

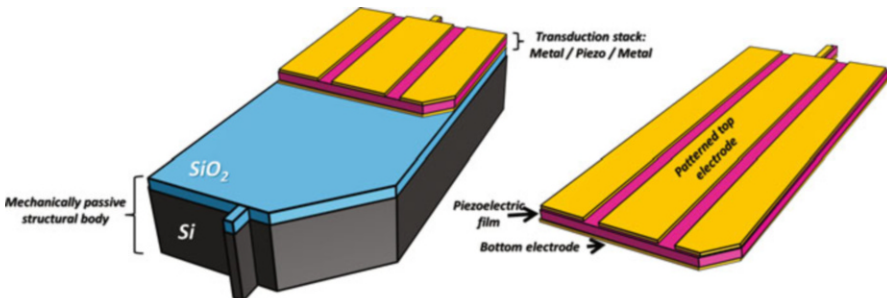

Fig. 12.1 (*Left*) Piezo-on-substrate and (*right*) piezo-only resonator

12.2 Deposition of Piezoelectric AlN

While the piezoelectric properties (i.e., electromechanical coupling coefficients) of the film are defined by its texture and crystallinity, transduction stack deposition is the most important step in implementation of a piezo-resonator, and directly affects its electromechanical transduction efficiency and transmission loss. The most frequent techniques for deposition of piezoelectric AlN films are RF magnetron sputtering [13], metal-organic chemical vapor deposition (MOCVD) [14], and molecular beam epitaxy [15]. Among these techniques RF magnetron sputtering is the most popular for implementation of MEMS resonators for industrial and consumer electronic applications, as it offers low processing temperature, high deposition rate, and good texture and piezoelectric property.

Typically the AlN thin film is sandwiched between metallic electrodes that serve for the application of electric field across AlN or collecting electromechanically induced charges during vibration. Different metals have been used as electrode material for AlN piezoelectric transducers, including platinum, molybdenum (Mo), gold, aluminum, iridium, and ruthenium [16]. Since the AlN is deposited on top of the bottom metal layer (Fig. 12.1), the crystalline quality of AlN layer is highly correlated with the choice of bottom electrode material. While deposited films have a polycrystalline structure in RF magnetron sputtering deposition, in order to have good piezoelectric properties (i.e., a large piezoelectric electromechanical coupling), deposition should be well-characterized to imitate the (0002) crystallographic orientation of Wurtzite AlN, where the polar direction is along the *c*-axis. Therefore, in order to get a large piezoelectric electromechanical coupling the *c*-axis of the AlN film should be aligned with the preferred direction of applied electric field between bottom and top electrodes. The quality of *c*-axis orientation of sputtered AlN film can be characterized by full width half maximum (FWHM) of the X-ray rocking curve around the desired diffraction peak of (0002) AlN. Figure 12.2 (left) shows the X-ray diffraction pattern of a 700 nm AlN film with a FWHM of 1.65°. Figure 12.2 (right) compares the FWHM of AlN films deposited using RF magnetron sputtering with MOCVD films, showing higher crystallinity of MOCVD films with a cost of lower deposition rates.

It is shown that the coupling factor (k_t^2) of the AlN film decreases dramatically for FWHMs higher than 4° [18]. Besides low FWHMs, other important characteristics of the film that directly or indirectly affect the performance of the piezoelectrically transduced resonators include film stress, repeatability of film thickness and thickness variation across the deposition area.

Figure 12.3 shows an AlN cluster sputter tool equipped with the dual-target S-gun magnetrons [19] customized to improve the *c*-axis alignment of the deposited film to be perpendicular to the substrate.

The most important requirements for the sputter deposition of piezoelectric AlN with Mo metal electrodes are [20]: (1) effective pre-clean, further smoothening and activation of the surface in vacuum environment right before film sputtering;

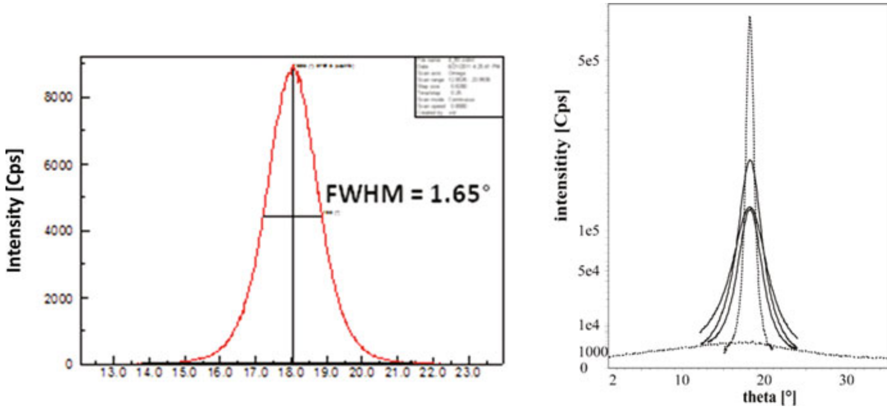

Fig. 12.2 (*Left*) X-ray rocking curves of 700 nm AlN film deposited on Mo layer and (*right*) comparison between X-ray diffraction curves of MOCVD (*dashed line*) and RF magnetron sputtered (*solid lines*) AlN films [17]

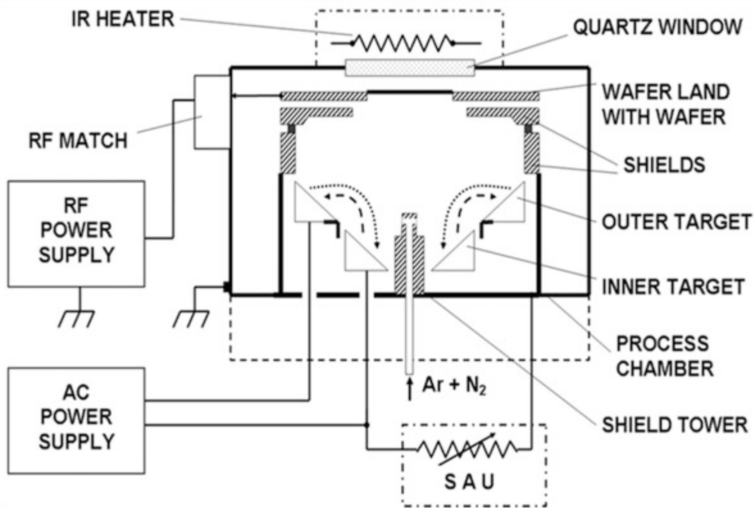

Fig. 12.3 Schematic diagram of the Endeavor-AT process module equipped with the S-gun magnetron for ac reactive sputtering [21]

(2) formation of highly textured bottom Mo electrode with satisfactory thickness enabling growth of more thorough columnar grains; (3) heteroepitaxial growth of highly *c*-axis oriented AlN film on Mo electrode.

Since the texture of bottom metal film is of primary importance to obtain well-oriented AlN [18–21], the FWHM of the AlN (0002) X-ray rocking curve directly correlates with FWHM of the Mo (110) diffraction peak [21]. Figure 12.4 (left) shows the X-ray diffraction pattern of a 200 nm AlN sputtered on Mo film [16].

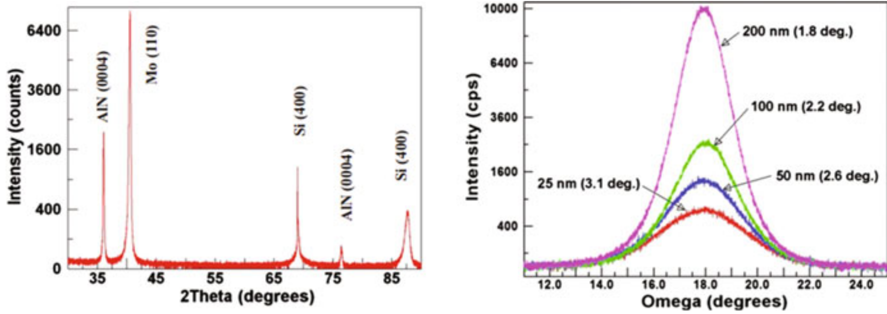

Fig. 12.4 (*Left*) X-ray diffraction patterns of 200 nm AlN films deposited on Mo; (*right*) X-ray rocking curves of different thickness AlN films deposited on Mo [16]

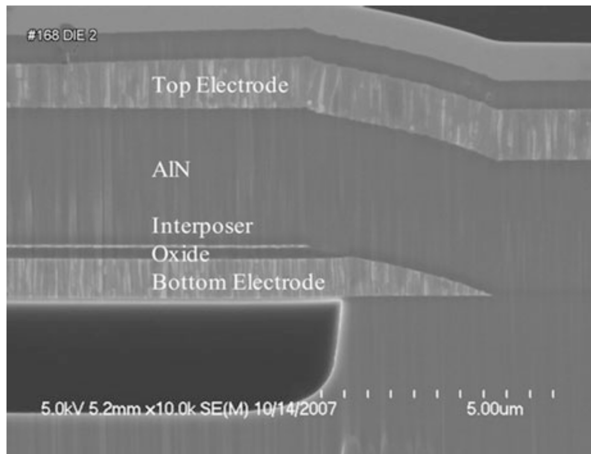

Fig. 12.5 Cross sectional SEM image of an FBAR showing AlN film with columnar texture sandwiched between bottom and top electrodes [24]

Furthermore, it is shown that the thickness of the AlN plays an important in defining the piezoelectric property of the film. Specifically, it can be very challenging to get highly piezoelectric films for nm-level thicknesses [16]. Figure 12.4 (right) compares the FWHM of AlN films with different thicknesses sputtered under similar condition and on Mo electrodes.

An effective technological approach to improve crystallinity of the Mo bottom electrode is to deposit thin AlN seed layer underneath the metal [21]. This effect can be explained by the coherent heteroepitaxial nucleation [22]. It is shown that even very thin AlN-seed layer with thickness as low as 10 nm can drastically improve the crystallinity of the bottom metal electrode, while optimal thickness of the seed layer is in the range of 20–40 nm [23].

Figure 12.5 shows the columnar texture of AlN film sandwiched between electrodes, in an FBAR cross-section [24].

12.3 Fabrication Process Flow of Piezo-Only Resonators

While in piezo-only resonators, the transduction stack simultaneously serves as the sole structural body, depending on the vibration mode of the resonator, in-plane geometry definition of the stack is used to define the mode shape and frequency, and/or acoustic energy trapping. Furthermore, except for solidly mounted resonators [25] where the energy trapping in *c*-axis direction is done through formation of brag reflectors out of several layers of materials with large acoustic impedance mismatch, other piezo-only resonators (i.e., FBARs and in-plane bulk acoustic/contour mode resonators) should be released from the substrate to facilitate vertical levitation required for their free vibration.

A typical process flow for realization of either of these configurations is summarized in Fig. 12.6.

A silicon substrate is first covered by a dielectric such as silicon dioxide/nitride (step 1 in Fig. 12.6) that serves for passivation and protection of the bottom metal electrodes during dry release in the final step. The bottom metal layer is then deposited followed by the sputtering of an AlN with desired thickness, which is later patterned to provide access to bottom electrodes (step 3). In this step an isotropic wet etch of AlN (e.g., in 50 °C tetramethylammonium hydroxide) can be used to provide high etch selectivity over bottom electrode and also provide a slopped sidewall of etched AlN to facilitate conformal coverage during top metal deposition; this is required to enable electric contact between top and bottom metal layers wherever desired. Then the second metal layer is sputtered to serve as top electrode for electromechanical transduction and also provide planar access to the bottom electrode through conformal step coverage (step 4). Finally trenches are dry-etched around the device using a chlorine/fluorine-based recipe in an inductively coupled plasma (ICP) reactive ion etching (RIE) system. Smooth sidewalls of the

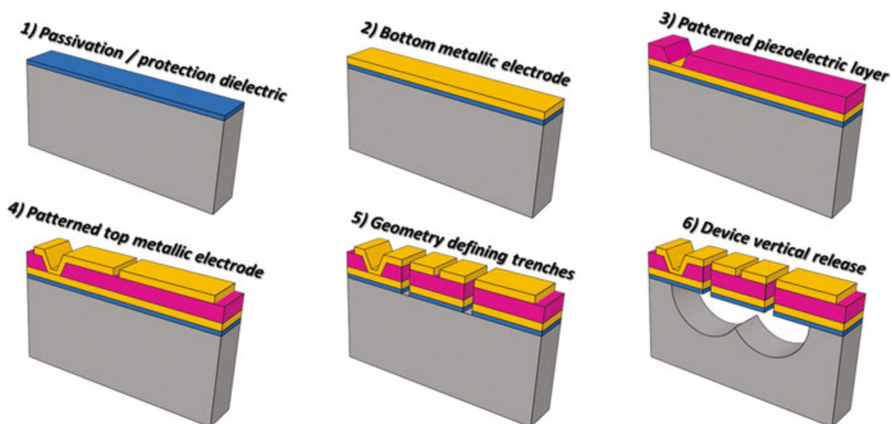

Fig. 12.6 A typical fabrication process flow for implementation of a piezo-only resonator

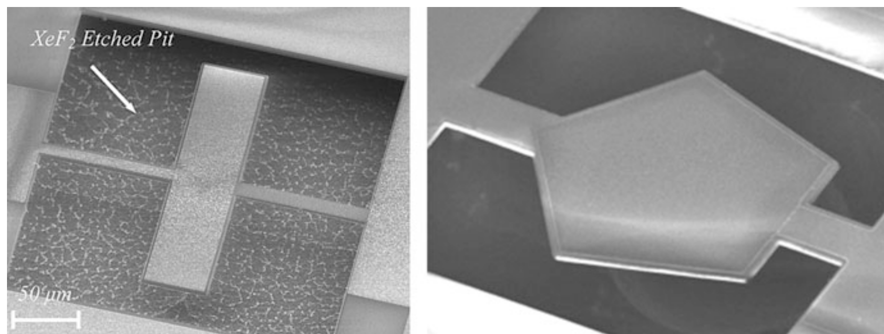

Fig. 12.7 SEM image of (*left*) a contour mode [12] and (*right*) an FBAR [24] piezo-only AlN resonator

trench are desirable to prevent destructive dispersion of acoustic waves as reflected from stress-free sidewalls that define the in-plane geometry of the device (step 5). Finally the device is released by isotropic dry etching of the silicon substrate (step 6) in xenon difluoride. Figure 12.7 shows an FBAR (right) and a rectangular contour mode resonator (left) formed using a similar process.

12.4 Fabrication Process Flow of Piezo-on-Substrate Resonators

Although in-plane piezo-only resonators are providing a much larger electromechanical coupling compared to their capacitive silicon counterparts [26], their quality factor (Q) is usually 10–100 times smaller. This can be attributed to several dissipation mechanisms exclusive to piezoelectric transduction stack [27] including charge redistribution loss, rough electrode surfaces, large acoustic attenuation of metals, and the stress discontinuity at the piezo–metal interface.

An alternative approach that takes advantage of the large electromechanical coupling of piezoelectric transduction while improving the device Q is to integrate the transduction stack on the top surface of a semiconductor or insulator structural body with low intrinsic acoustic dissipation. Depending on the ratio between piezoelectric film thickness and that of substrate, significantly higher Qs can be achieved by the cost of decreased electromechanical coupling, as piezoelectric transduction is loaded by a thick mechanically passive structure [3]. Furthermore, the thermoacoustic properties [28] of the resonator can be engineered in such a piezo-on-substrate structure through heavy doping of the substrate [29] or formation of composite structures by integration of a material with an opposite temperature sensitivity of elastic moduli [30]. Figure 12.8 schematically shows two piezo-on-substrate structures. In Fig. 12.8 (left) the transduction stack is integrated on a silicon dioxide-on-silicon resonator. In Fig. 12.8 (right) the transduction stack

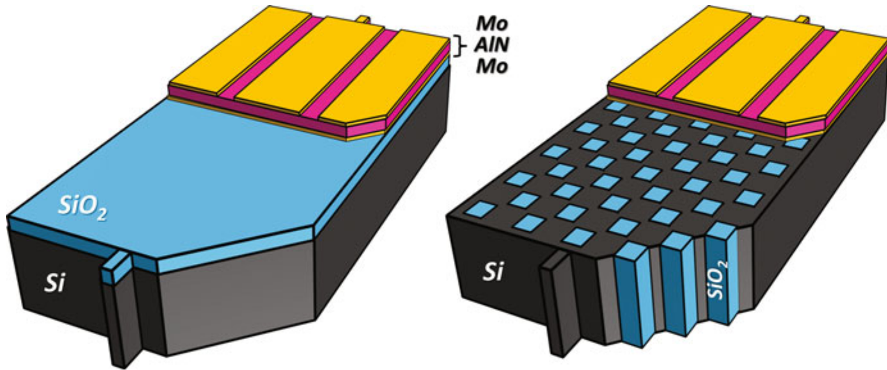

Fig. 12.8 (*Left*) Piezo-on-silicon dioxide-on-silicon and (*right*) piezo-on-SilOx resonator

is placed on top of a composite structure formed by embedding silicon dioxide (SiO_2) pillars in a silicon rectangular parallelepiped (forming SilOx [30]). Such a composite structure can compensate the large linear temperature sensitivity of piezo-only or piezo-on-silicon resonators using the opposite temperature sensitivity of SiO_2.

Figure 12.9 schematically summarizes the process flow for AlN-on-SilOx resonator. The SiO_2 pillar matrix is formed by etching square-shaped trenches inside the device layer of a silicon-on-insulator (SOI) wafer (step 2). These trenches are then filled by multiple deposition and etching steps of low-pressure chemical vapor deposition SiO_2. An additional thin layer of SiO_2 is left on the surface of the structure to provide a smooth surface that is required for the deposition of a high-quality AlN film (step 3). The transduction stack is then sputtered on the top surface of the composite structure and patterned to define top metal electrodes and provide access to bottom metal layer (steps 4–6). Then trenches with straight sidewalls are etched over the entire stack to form device stress-free boundaries (step 7). Having different materials in the stack, trench etching step may be performed in different etching tools using various dry etch recipes. While chlorine/fluorine-based anisotropic RIE in an ICP system is required to pattern the transduction stack and top SiO_2 layer, etching straight trenches in silicon substrate should be performed in a DRIE system using Bosch process [31]. Finally the device is released by etching through silicon holes from wafer backside followed by etching buried oxide layer in an ICP system. The last step may be replaced by using a silicon handle layer that is patterned with cavities underneath resonators prior to bounding handle and device layers.

Figure 12.10 shows the SEM image of a temperature stable piezo-on-SilOx bulk acoustic resonator.

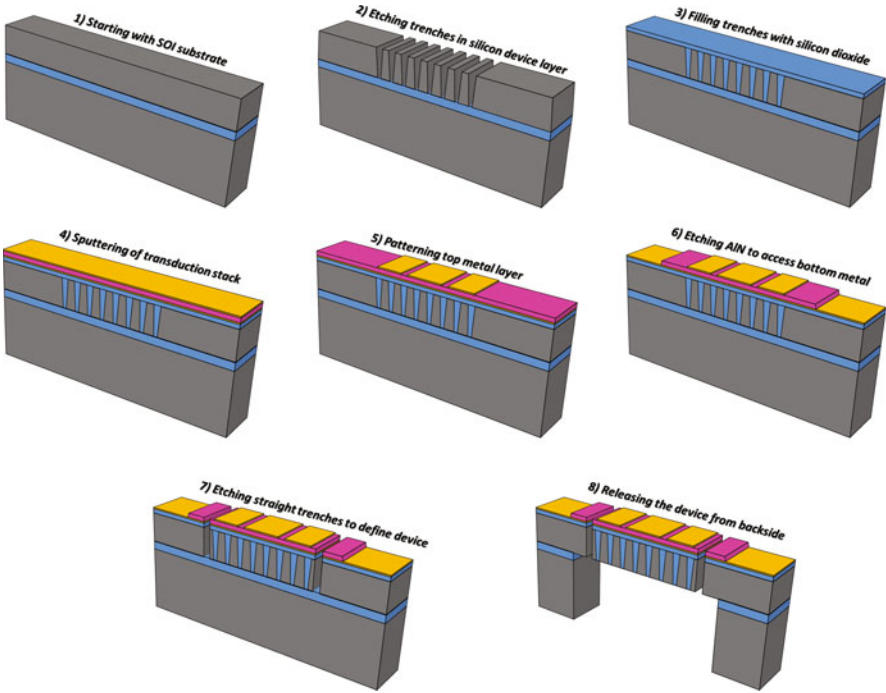

Fig. 12.9 The fabrication process flow for implementation of a piezo-on-SilOx resonator

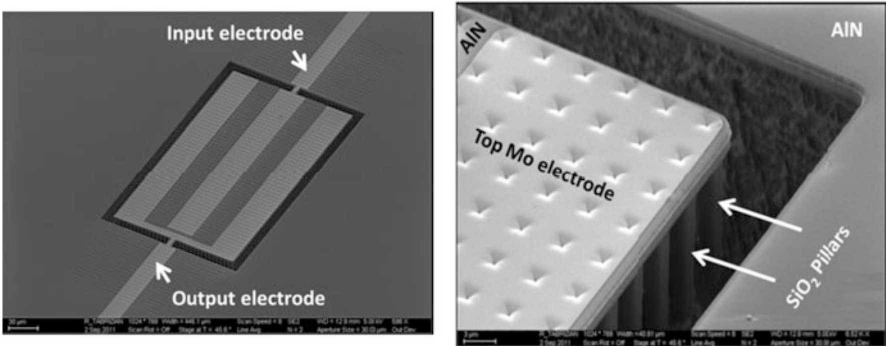

Fig. 12.10 (*Left*) Temperature-stable AlN-on-SilOx resonator. (*Right*) SiO_2 pillars extruding from the resonator sidewall

12.5 Sidewall AlN Process for 3D Transduction of MEMS Resonators

While FBARs are benefiting from large longitudinal piezoelectric electromechanical coupling by having a vibration polarization parallel to the *c*-axis, in in-plane bulk acoustic/contour mode resonators smaller transverse coupling results in higher motional resistance of the device. However, in in-plane devices, the resonance frequency can be defined by the lateral dimensions of the structure in the same batch, and over a wide frequency range. In order to take advantage of the more efficient longitudinal piezoelectric effect of AlN as well as lithographical frequency definition of in-plane bulk acoustic resonators, an alternative approach can be used where piezoelectric transduction of laterally vibrating micromechanical resonators is provided using AlN films deposited on the sidewalls of silicon microstructures [32]. This transduction configuration brings the more efficient longitudinal piezoelectric effect of AlN to high Q laterally vibrating micro-resonators to create a spurious free frequency response with low motional impedance and lithographically defined resonance frequency. Furthermore, extension of AlN transducer into the third dimension (i.e., on the sidewalls) provides a large transduction area without excessive consumption of chip surface area. These advantages make sidewall AlN transduction attractive for implementation of low motional resistance resonators and filters spreading across a wide frequency spectrum on the same substrate as well as small form factor micromechanical energy harvesters and switches.

Realization of high quality AlN transducers on the sidewalls of a silicon microstructure requires preparation of a smooth surface on the sidewalls of the patterned microstructure. Smooth surfaces are required for the uniform growth of *c*-axis oriented AlN films that exhibit strong piezoelectric properties. To reduce the sidewall roughness that is resulted from the DRIE of silicon (e.g., scalloping and striation), 100 mm diameter Si (100) wafers with patterned microstructures are taken through three consecutive steps. First, wafers are annealed in a nitrogen ambient at 1050 °C for 2 h. Enhanced surface mobility of silicon atoms resulted from high flow rate (20 sccm) of heated nitrogen reduced sidewall scalloping resulted from Bosch DRIE process. This step is followed by dry oxidation of wafers at 1100 °C to from $\sim$50 nm of sacrificial oxide. This oxide layer is then removed in hydrofluoric (HF) acid, leaving nearly smooth sidewall surfaces. Finally, wafers surface is etched by low-energy (100–200 eV) argon ions using a capacitively coupled RF (13.56 MHz) plasma source in vacuum environment. This step is performed right before film sputtering steps. Figure 12.11 compares the surface smoothness of the sidewall before and after this process.

Having a smooth sidewall, AlN layer with highly uniform thickness can be achieved on the sidewalls. Figure 12.12 summarizes the process flow for implementation of silicon bulk acoustic resonators with top and sidewall AlN transducers.

The fabrication process of one-port silicon bulk acoustic resonators (SiBAR) with top and sidewall AlN requires only two masks and three steps (Fig. 12.12). First, the resonator body is patterned in the silicon device layer of a thick SOI wafer

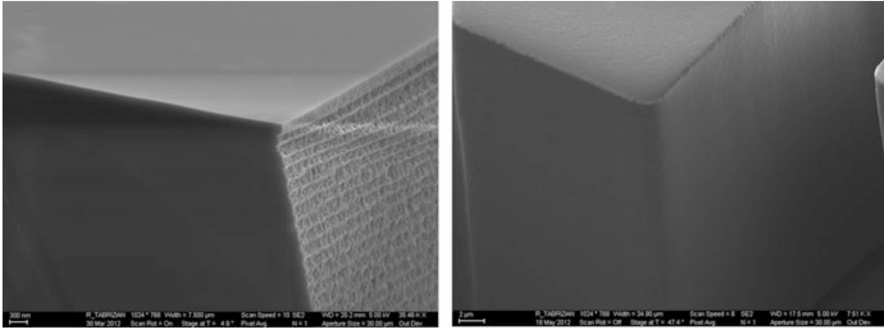

Fig. 12.11 (*Left*) Sidewall surface after Bosch DRIE etching and (*right*) after DRIE etching and surface smoothening processes

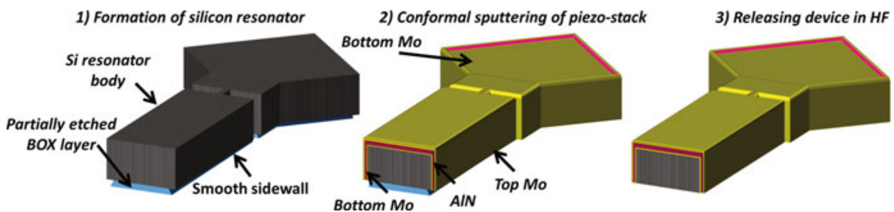

Fig. 12.12 The fabrication process flow for implementation of a silicon bulk acoustic resonator with top and sidewall AlN transducers

and the sidewalls are smoothened (step 1). This is followed by sputter deposition of a thin AlN layer sandwiched between bottom and top Mo electrodes on the resonator top surface and sidewalls. Then, the top Mo and AlN layers are etched from one pad of the resonator to access the bottom Mo which serves as an electrical signal ground (step 2). Finally, the device is released by etching the buried oxide layer in HF acid (step 3). Figure 12.13 shows an SEM image of a fabricated one-port SiBAR with AlN on sidewalls and top surface and schematic of the electrical interface for its characterization/measurement.

Figure 12.14 (left) shows the cross-sectional SEM image of the resonator before release in HF. Figure 12.14 (right) shows the continuity of AlN and Mo films from the top surface to sidewalls at the edges of the resonator, with sidewall AlN thicknesses approximately half of the top surface AlN. The bottom Mo serves as ground for sidewall and top AlN layers. An input signal is applied to the continuous top Mo.

Uniform thickness of AlN sidewall film results in efficient actuation of the desired width-extensional resonance mode over the entire thickness of the resonator and eliminates charge cancellation in the sensing mechanism.

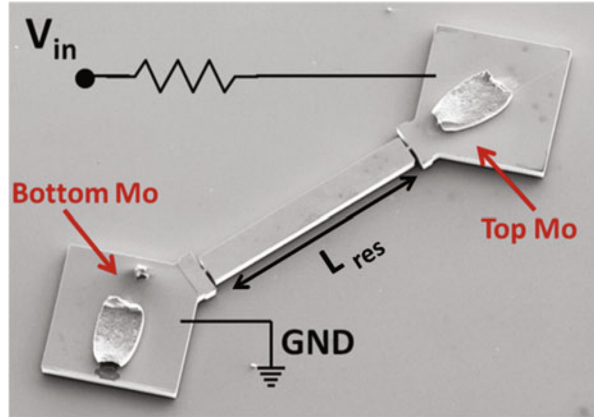

Fig. 12.13 SEM image of the resonator and the electrical interface scheme for measurement

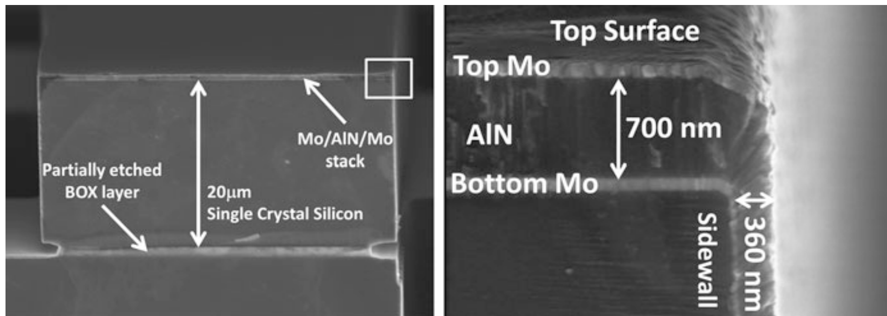

Fig. 12.14 (*Left*) SEM picture of the device cross section; BOX layer partially etched to enable full release in HF. (*Right*) Continuity of AlN and Mo films from the top surface to sidewalls at the edges of the resonator

12.6 Fabrication Process Flow for AlGaN/GaN Resonators with Integrated HEMT Read-Out

Gallium nitride (GaN) is a wide bandgap semiconductor material showing strong piezoelectric properties [33]. When equipped with a thin AlGaN layer on top forming AlGaN/GaN heterostructure, this platform facilitates co-integration of high electron mobility transistors (HEMT) and acoustic resonators. Such an integration is considered as a potential for realization of monolithic AlGaN/GaN frequency references without a need for external circuitry [34, 35]. Such an integrated system is inherently immune to parasitics resulted from interconnects and also packaging issues. Furthermore, integration of the HEMT on the acoustic cavity can further improve the performance of the frequency reference as it provides inherent signal filtering and amplification prior to introduction of additional feed-through.

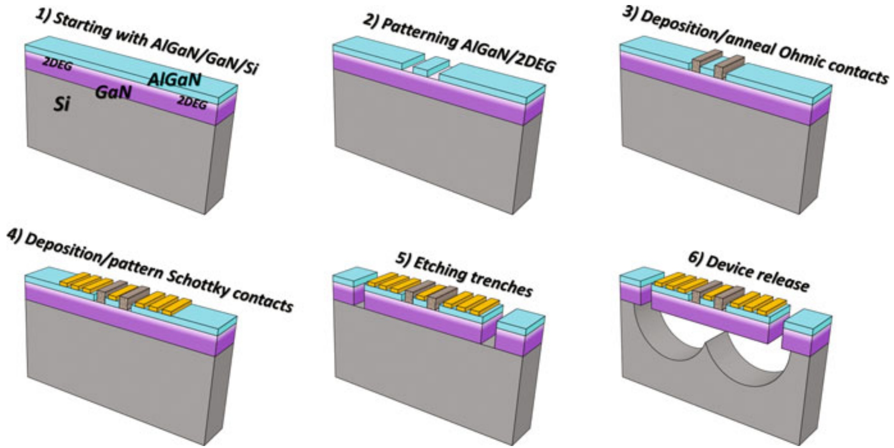

Fig. 12.15 Fabrication process flow for GaN piezo-resonators with integrated HEMT electronics

The AlGaN/GaN piezo-resonators are fabricated using MOCVD grown GaN-on-high resistivity Si (111) as the starting substrate. Depending on the application, the total thickness of the GaN-based stack can be 1–2 μm with the top AlGaN layer in the range of 100–200 Å [36].

Figure 12.15 summarizes the fabrication process flow for implementation of GaN piezo-resonators integrated with HEMTs.

The fabrication starts with defining the active area of the HEMTs (step 2 in Fig. 12.15). The top AlGaN layer is plasma etched to remove 2D electron gas (2DEG) outside of the active/device area. Next the ohmic contacts are formed using a stack of titanium/aluminum/titanium/gold (e.g., Ti/Al/Ti/Au = 200/1000/450/550 Å) followed by 30–60 s of annealing in nitrogen environment at 800 °C to drive the dopants into the 2DEG channel (step 3). Next, nickel/gold stack (e.g., Ni/Au = 100 nm/30 nm) is deposited to form the Schottky contacts used as the interdigitated fingers for piezoelectric transduction as well as the gate contacts of the HEMTs (step 4). Then, a 1–2 μm SiO_2 is deposited on the devices to both serve as the mask for the following trench etch step as well as passivation of the 2DEG surface. This is followed by etching trenches through the GaN layer to access the silicon substrate (step 5). Finally the device is released through isotropic dry etch in xenon difluoride. The SiO_2 mask/passivation layer should also be thinned using plasma etch, to leave only ~100–200 nm-thick SiO_2 on the devices for passivation and/or temperature compensation purposes. Figure 12.16 shows the SEM image of the fabricated device [37]. The HEMT is placed in the middle of the resonator for vibration sensing and signal amplification.

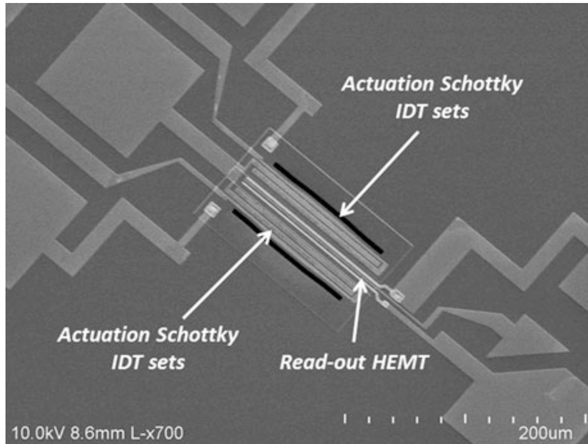

Fig. 12.16 SEM image of a resonant HEMT device, where actuation is done by two separate sets of IDTs at the two sides of the acoustic cavity. The read-out HEMT is located at the middle of the cavity at a location of maximum stress [37]

References

1. Lakin KM, Wang JS (1981) Acoustic bulk wave composite resonators. Appl Phys Lett 38(3):125–127
2. Pan W, Abdolvand R, Ayazi F (2008) A low-loss 1.8 GHz monolithic thin-film piezoelectric-on-substrate filter. In: Proc. 21st IEEE international conference on micro electro mechanical systems (MEMS 2008), Tucson, AZ, Jan 2008, pp 176–179
3. Pan W, Ayazi F (2010) Thin-film piezoelectric-on substrate resonators with Q enhancement and TCF reduction. In: 23rd IEEE international conference on micro electro mechanical systems (MEMS 2010), pp 727–730
4. Jeon Y, Sood R, Jeong J-H, Kim S-G (2005) MEMS power generator with transverse mode thin film PZT. Sensors Actuators A 122(1):16–22
5. DeVoe DL, Pisano AP (2007) Modeling and optimal design of piezoelectric cantilever microactuators. J Microelectromech Syst 6(3):266–270
6. Fu JL, Ayazi F (2010) Dual-mode piezo-on-silicon resonant temperature and humidity sensor for portable air quality monitoring systems. In: IEEE sensors conference, Waikoloa, Big Island, Hawaii, 2010, pp 2131–2135
7. Tabrizian R, Ayazi F (2014) Dual-mode vertical membrane resonant pressure sensor. In: Proc. of IEEE international micro electro mechanical systems conference (MEMS 2014), San Francisco, CA, January 2014, pp 120–123
8. Tabrizian R, Ayazi F (2013) Acoustically-engineered multi-port AlN-on-silicon resonators for accurate temperature sensing. In: Proc. of IEEE international electron devices meeting (IEDM 2013), Washington, DC, December 2013, pp 1811–1814
9. Dubois MA, Muralt P (1999) Properties of aluminum nitride thin films for piezoelectric transducers and microwave filter applications. Appl Phys Lett 74(20):3032–3034
10. Pandey DK, Singh D, Yadav RR (2007) Ultrasonic wave propagation in IIIrd group nitrides. Appl Acoust 68(7):766–777
11. Krishnaswamy SV, Rosenbaum J, Horwitz S, Vale C, Moore RA (1990, December) Film bulk acoustic wave resonator technology. In Ultrasonics symposium, 1990. IEEE proceedings. IEEE, pp 529–536

12. Piazza G, Stephanou PJ, Pisano AP (2006) Piezoelectric aluminum nitride vibrating contour-mode MEMS resonators. J Microelectromech Syst 15(6):1406–1418
13. Shiosaki T, Yamamoto T, Oda T, Kawabata A (1980) Low-temperature growth of piezoelectric AlN film by rf reactive planar magnetron sputtering. Appl Phys Lett 36(8):643–645
14. Yang CM, Uehara K, Kim SK, Kameda S, Nakase H, Tsubouchi K (2003, October) Highly c-axis-oriented AlN film using MOCVD for 5GHz-band FBAR filter. In: 2003 IEEE symposium on ultrasonics, vol 1. IEEE, pp 170–173
15. Sitar Z, Paisley MJ, Yan B, Ruan J, Choyke WJ, Davis RF (1990) Growth of AlN/GaN layered structures by gas source molecular-beam epitaxy. J Vac Sci Technol B 8(2):316–322
16. Felmetsger VV, Laptev PN, Graham RJ (2011) Deposition of ultrathin AlN films for high frequency electroacoustic devices. J Vac Sci Technol A 29(2):021014
17. Tonisch K, Cimalla V, Foerster C, Romanus H, Ambacher O, Dontsov D (2006) Piezoelectric properties of polycrystalline AlN thin films for MEMS application. Sensors Actuators A Phys 132(2):658–663
18. Naik RS, Lutsky JJ, Reif R, Sodini CG, Becker A, Fetter L, Huggins H, Miller R, Pastalan J, Rittenhouse G, Wong YH (2000) Measurements of the bulk, c-axis electromechanical coupling constant as a function of AlN film quality. IEEE Trans Ultrason Ferroelectr Freq Control 47(1):292–296
19. Felmetsger V, Laptev P, Tanner S (2008) Crystal orientation and stress in ac reactively sputtered AlN films on Mo electrodes for electro-acoustic devices. In: Proceedings of the IEEE international ultrasonic symposium, Beijing, 2008, vol 1, pp 2146–2149
20. Felmetsger VV, Laptev PN (2010) New generation of S-Gun magnetron for AlN reactive sputtering. In: The forth international symposium on acoustic wave devices for future mobile communication systems, Chiba, University, Japan, 3–5 Mar 2010, vol 1, pp 145–152
21. Tabrizian R, Felmetsger V, Ayazi F (2011) A sidewall AlN process for efficient 3D piezoelectric transduction of MEMS. In: Proc. technologies for future micro-nano manufacturing workshop, Napa, California, Aug 2011, pp 23–27
22. Kamohara T, Akiyama M, Ueno N, Nonaka K, Kuwano N (2006) Influence of molybdenum bottom electrodes on crystal growth of aluminum nitride thin films". Appl Phys Lett 89:071919
23. Felmetsger V, Laptev P, Tanner S (2008) In: Proceedings of the IEEE international ultrasonics symposium, Beijing, 2–5 Nov 2008, pp 2146–2149
24. Ruby R, Small M, Bi F, Lee D, Callaghan L, Parker R, Ortiz S (2012) Positioning FBAR technology in the frequency and timing domain. IEEE Trans Ultrason Ferroelectr Freq Control 59(3):334–345
25. Lakin KM, McCarron KT, Rose RE (1995, November) Solidly mounted resonators and filters. In: Ultrasonics symposium, 1995. IEEE proceedings. IEEE, vol 2, pp 905–908
26. Pourkamali S, Ho GK, Ayazi F (2007) Low-impedance VHF and UHF capacitive silicon bulk acoustic wave resonators—Part I: Concept and fabrication. IEEE Trans Electron Dev 54(8):2017–2023
27. Tabrizian R, Rais-Zadeh M (2015, June). The effect of charge redistribution on limiting the kt 2. Q product of piezoelectrically transduced resonators. In: 2015 18th international conference on solid-state sensors, actuators and microsystems (TRANSDUCERS), 2015 transducers. IEEE, pp 981–984
28. Tabrizian R, Ayazi F (2014) Thermo-acoustic engineering of silicon microresonators via evanescent waves. Appl Phys Lett 106(26):263504
29. Samarao AK, Ayazi F (2012) Temperature compensation of silicon resonators via degenerate doping. IEEE Trans Electron Dev 59(1):87–93
30. Tabrizian R, Casinovi G, Ayazi F (2013) Temperature-stable silicon oxide (SilOx) micromechanical resonators. IEEE Trans Electron Dev 60(8):2656–2663
31. Bean KE (1978) Anisotropic etching of silicon. IEEE Trans Electron Dev 25(10):1185–1193
32. Tabrizian R, Ayazi F (2011) Laterally excited silicon bulk acoustic resonators with sidewall AlN. In: 16th international conference on solid-state sensors, actuators and microsystems (Transducers 2011), Beijing, China, June 2011, pp 1520–1523

33. Rais-Zadeh M, Gokhale V, Ansari A, Faucher M, Theron D, Cordier Y, Buchaillot L (2014) Gallium nitride as an electromechanical material. IEEE J Microelectromech Syst 23(6):1252–1271
34. Bahr B, Popa LC, Weinstein D (2015) 1 GHz GaN-MMIC monolithically integrated MEMS-based oscillators. In: IEEE int. solid state circuits conf. (ISSCC 2015), San Francisco, CA, 22–26 Feb 2015
35. Ansari A, Gokhale V, Roberts J, Rais-Zadeh M (2012) Monolithic integration of GaN-based micromechanical resonators and HEMTs for timing application. In: IEEE international electron device meeting (IEDM'12), San Francisco, CA, Dec 2012, pp 15.5.1–15.5.4
36. Ansari A, Rais-Zadeh M (2014) A thickness-mode AlGaN/GaN resonant body high electron mobility transistor. IEEE Trans Electron Dev 61(4):1006–1013
37. Ansari A, Tabrizian R, Rais-Zadeh M (2015) A high-Q AlGaN/GaN phonon trap with integrated HEMT read-out. In: 18th international conference on solid-state sensors, actuators and microsystems (Transducers 2015), Alaska, USA, June 2015, pp 2256–2259

Chapter 13
Reliability and Quality Assessment (Stability and Packages)

Robert Gubser

13.1 A Long and Demanding History Sets the Demands for the Resonators

The every growing human demand or need to communicate has been the driving force that began to define the need for frequency control devices. The need to control a radiated signal with information imbedded and then to be recovered by a receiving device (all forms of transmitted and received communications). The technical community found that devices that used mechanical stability to set a resonant frequency were capable of offering the needed performance if the mechanical element could be excited and operate in an electrical circuit. The piezoelectric devices offered this solution where mechanical and electrical operation is coupled together.

The quartz crystal, piezoelectric silicon dioxide, provided the initial solutions that have been used. These devices have a long history compared to most other electronic devices being used in the twenty-first century.

R. Gubser (✉)
PRA Inc., Norfolk, VA, USA
e-mail: bobg@prainctest.com

© Springer International Publishing Switzerland 2017

H. Bhugra, G. Piazza (eds.), *Piezoelectric MEMS Resonators*,
Microsystems and Nanosystems, DOI 10.1007/978-3-319-28688-4_13

1880	Piezoelectric effect discovered (the Curies)
1905	First hydrothermal growth of quartz in the laboratory—by G. Spezia
1917	Application of piezoelectric effect in sonar
1918	Piezoelectric oscillator
1926	First quartz crystal-controlled broadcast station
1927	Temperature-compensated quartz cut discovered
1927	First quartz crystal clock built
1934	First practical temperature-compensated cut developed (AT cut)
1949	AT-cut design greatly improved (contoured and high Q)
1956	Commercially grown synthetic or cultured quartz available
1956	First temperature-compensated crystal oscillator (TCXO) described
1964	Color burst crystal (3.579545 MHz) for recovering the color information on a color TV finally sold at <US$1 each
1967	Crystal filters with delay compensation and 1.01 to 1 shape factor from −3 dB to −60 dB realized, 24 crystals at 250 KHz
1972	The XY-cut tuning fork developed for quartz watches
1974	The SC cut was predicted and verified in built in 1976
1976	Hughes Aircraft was the largest producer of watches using quartz. They were unique and used the SL cut
1982	The first use of dual-mode vibration, oscillator function, and a temperature sensor

This long history with devices for:

- Military communication
- Radar timing needs
- Telephone–telecom industry
- Many timing control needs brought on by the ever expanding semiconductor industry’s capabilities
- Medical needs
- Vehicle critical operations (engine control, breaking, etc.)
- Entertainment industry

The piezoelectric resonators are coupled to semiconductor IC to form oscillators which provide the timing signal(s) for the end use systems. These combined assemblies of technologies demands well chosen assembly processes that are precisely controlled.

This results in a lengthy set of specifications to assure achievement of the needed quality and reliability.

13.2 The Challenges of FCP Devices: Longevity and Critical Applications Are Common

The piezoelectric resonators are often in critical applications, and these devices must perform for many years. Often these are life critical applications:

- Pacemakers
- Medical monitoring equipment
- Machine monitoring and motor control applications
- Telecommunication of all types (cable, fiber, RF, etc.)
- Automobiles and emergency vehicles
- GPS or its equivalent versions
- Military applications (both offensive and defensive)

These applications often include severe environmental conditions.

13.3 Where Did the Rules of Evaluation Come from?

The frequency control resonators have many diverse applications, and to assure performance in these applications, tests have been derived to verify the performance. When any failure has been found and there is a realization that a test is needed to make sure that failure mode is not pervasive in the product.

The resonator portion of these devices is in a hermetically sealed region or cavity, and the integrity of this cavity is critical to the device performance; hence, many tests or rules are applied to assure this.

Essentially the rules have grown with time to assure the product meets the expectations of how the product is being used. Most telecom applications have limited mechanical stresses; these applications focused on signal integrity and longevity of performance. Automotive applications tend to have less signal integrity needs, and the operating environment can be very difficult. Wide temperature range with severe transitions, high shock, and vibration are encountered. Hence, the mechanical and temperature portion of the evaluation and specification is emphasized.

For many in the FCP business, when they see a +200 °C evaluation, they know this is for the "downhole" drilling industry.

If very high shock evaluation is dictated, then the product could be in a munitions application.

The rules for evaluating these FCP products shall continue to evolve as technology creates new conditions and the applications continue to expand. There will be customer unique specifications and evaluation procedures, and as this broadens, there will be formal specifications and procedures. The current JEDEC and similar specifications followed this path.

13.4 The Challenges of an IC and Electromechanical Device

These piezoelectric resonators convert mechanical energy to electrical signals and vice versa. This results in a product sensitive to virtually all possible stresses applied to the package.

- Mechanical forces applied to the package (both static and dynamic) can alter the electrical signal. For example, package rotation or position can have different aging rates due to forces of gravity. Vibration can result in increased electrical noise output (increased jitter and phase noise).
- Temperature, both transient and static, changes the mechanics of the resonator and hence the performance. The rate of change is critical; during rapid changes the mechanical portion is not in an isothermal condition resulting in different stresses compared to the static or slow changing temperature.
- Exceptional rapid temperature changes can result in damage to the hermetic seals on the resonator region or cavity. Also, rapid changes may permanently alter the mechanical properties of the resonator, for example, alter the electromechanical coupling.
- The mechanical portion has elastic limits. Any mechanical stress or electrical stress that induces an excessive mechanical stress can alter the devices performance in the short and long time periods.
- Plastic packaging of these products increases the susceptibility to problems; the plastic package provides very limited protection to the resonator. Add to this that the plastic offers no protection from humidity and can amplify this by absorbing moisture and therefore adding stresses to the resonator portion further emphasizes the challenges of plastic packaging.

These piezoelectric MEMS and quartz assemblies are often configured as sensors to measure changes in the environment; one should expect those configured as precision signal generators are going to be desensitized to the environment but not totally eliminating these changes.

13.5 With FCP Long History, So Much Is a Level of Expectation

Many of the piezoelectric devices made and shipped today have one- or two-page specifications. When new products are developed, they are targeted to meet these short lists of expectations. Unfortunately this is exceptionally short sighted.

The resonators are all similar or identical whether the application is for ultra precisions and longevity or for a simple consumer application. The end users understand this, and they expect that a consumer application part will have most of the performance characteristics of the precision part. This is the “implied specification” when one states the resonator part is a quartz crystal or an equivalent to a quartz crystal part.

The bill of materials and the process steps are identical whether the device has a one-page or a long lengthy specification. Why wouldn’t the end user expect similar performance?

All piezoelectric resonators are expected to perform to a long list of performance characteristics.

There are various groups worldwide that have written the documents on how to test and qualification tests for these electromechanical devices. Those documents published by and for the US Military are common in the whole world industry and are often referred to.

There are automotive specifications (AEC, IEC, JEDEC, JIS (Japan)) which all are similar and are often used interchangeably.

13.6 US Military Standards

Often used US Military quality and reliability specifications with their associated test procedure definitions are listed here.

Some of these documents were written many years ago when the quartz crystal was the only precision frequency control item in use. These are often being applied to the more recent MEMS-based resonators.

Mil-PRF-55310D	Section 4.8.35. Reporting operating conditions
MIL-STD-202	Test methods for electronic and electrical component parts
Mil-STD-202 M210	Condition B resistance to soldering heat
MIL-STD-790	Established reliability and high-reliability qualified product list (QPL) systems for electrical, electronic, and fiber-optic part specifications
MIL-STD-810	Environmental engineering considerations and laboratory tests
Mil-STD-883 1014 A1	Fine leak test
Mil-STD-883 1014 C1	Gross leak test
Mil-STD-883 M1007	Low storage temperature test
Mil-STD-883 M1010	Condition B temperature cycling
Mil-STD-883 M2009	External visual inspection
Mil-STD-883 M2011	Bond strength
Mil-STD-883 M2016	Physical dimensioning
Mil-STD-883 M2019	Die shear
MIL-STD-1285	Marking of electrical and electronic parts
MIL-0-55310B	Document aging and its measurement. A version since 1976 and B version in 1988

Copies of these documents are often available online at https://assist.daps.dla.mil/quicksearch/ or https://assist.daps.dla.mil.

13.7 JEDEC Standards

Commonly applied JEDEC standards to piezoelectric resonators:

JESD22-B102e2	Recommended to use this as an interim
JESD22-A101-B	Temperature/humidity/bias testing
JESD22-A102C	Pressure cooker testing (PCT)
JESD22-A103B	High-temperature storage (HTS)
JESD22-B103B	Mechanical vibration
JESD22-A104D	Temperature cycling
JESD22-B104C	Mechanical shock
JESD22-B105C	Condition A lead integrity
JESD22-B105C	Condition B lead integrity
JESD22-B107A	Solvent resistant/marking permanency
JESD22-A108C	High-temperature operating life (HTOL)
JESD22-A110-B	High accelerated stress testing (HAST)
JESD22-A113-B	Moisture resistance test
JESD22-A114D	ESD human body model (HBM)
JESD22-A115C	ESD machine model (MM)
JESD22-C101E	ESD charge device model (CDM)
JESD78	Latch up

There have been some suggestions to drop some of the ESD testing, not do all three types. This is not recommended, for example, the signal leads to the resonator often have limited protection (the protection circuits tend to reduce the device performance in both frequency stability and jitter). ESD protection and performance become a trade-off issue. Some may say the resonators is internal the package and therefore these circuit nodes are protected. Unfortunatley this may not be true, these are in many cases multi die packages where the critical signal leads may be more vulnerable than expected.

13.8 Other Standards

IPC/EIA J-STD-002A	Solderability

Infant mortality testing:

The mechanical resonator may have degraded performance after being idle for many days. For example: a case where contamination may settle on the resonator is being a unique condition for these electromechanical devices resulting in the finished device failing to proivide the output signal when the device is powered up.

A suggested test uses a large number of units (3000–5000 devices) and performs the initial part of the HTOL test. Set up and perform the first 2 days of an HTOL test, and any failure results in the failure of the entire group.

Any nonquartz crystal piezoelectric resonator development should be cognizant of the following quartz-based resonator documents. This is another case of end user expectation:

MIL-C-3098x crystal specification

MIL-C-3098H version in 1997
MIL-C-3098G in 1979
MIL-C-3098K with amendment 1 in 2011

IEC 60122-1, Quartz Crystal Units of Assessed Quality, Part 1: Generic Specification, Third Edition

ECA-512 Standard Methods for Measurement of the Equivalent Electrical Parameters of Quartz Crystal Units, 1 kHz to 1 GHz

13.9 In-Process and Production Monitoring

The in-process monitoring to assure the quality and longevity of the device must be chosen carefully:

- Timely enough to permit prompt feedback to the processing
- Low cost
- Effective to assure the quality is being maintained

There are three key items that meet these requirements, and these items are indicative of the process being under control:

- Resonator resistance or Q
  The resonator was formed correctly and the piezo portion is operating correctly. The resonator is sealed correctly (under a vacuum in most cases).
- Frequency
  The resonator structure is being repeatedly made to the qualified process.
- Seal integrity (leak test)
  This test can be the most difficult. The resonator cavity size limits the ability to do most leak tests. A 1- or 2-day aging measurement may be the only way to get indications of a good seal. The high-temperature coefficient of the resonator makes this method difficult to implement.

Sample quantities for all lots of resonators should be taken and tested. Any changes in the average and the distribution should require an evaluation of what has changed in the process.

13.10 Other Specifications for Frequency Control Products

There are additional requirements that are essential for many applications of the piezoelectric resonator supplied as a complete oscillator. These parameters would need to be supported the same as the above requirements.

These requirements have been applied to quartz crystal oscillators but are not stated on the datasheets. The needed results were achieved by the natural of the piezoelectric quartz resonator, a case of expected and implied performance but not stated.

13.10.1 Response to Temperature Change

The piezoelectric MEMS resonators are typically used in a PLL circuit to permit the exact user requested frequency is the output of the oscillator. The PLL circuit is also sensing temperature and changes the PLL feedback to correct for the MEMS resonator temperature coefficient.

If the temperature sensor on the PLL IC and the MEMS resonator are not perfectly coupled, there is a strong possibility of a large out-of-tolerance frequency shift until the stable thermal condition is achieved.

13.10.2 Perturbations

This is where the frequency makes a significant step change for a small change in temperature. These would be step changes in the order of a few ppm.

The quartz crystal resonators have these perturbations and by design they can be eliminated, but any change in the fabrication process or flaw in the resonator shape these perturbation flaws reappears.

Several have touted that the piezoelectric MEMS are free of this type of erroneous response. Unfortunately they have been found in the products being delivered. The problems stemming from the resonator flaw can be measured. For almost all oscillators, there is a small amount of the resonator signal on the output, and this can be recovered with a spectrum analyzer, therefore knowing the frequency jump was in the resonator.

13.10.3 Power Supply Noise Sensitivity

The device datasheets are normally derived from data taken in a laboratory environment. Actual use will be in systems where there is noise on the power supply

terminals. A "rule of thumb" would be to hope for 50 mV PP at any frequency from DC to 200 MHz and in practice accept 100 mV PP on the supply terminals. In many cases it is worse, but with some good PCB layout and RF bypassing, a level 100 mV PP should be attainable.

This externally injected noise must not significantly alter the device performance. The resonator and the accompanying circuit must be tolerant of this noise.

13.10.4 System-Injected Noise

The MEMS-based resonators and associated IC are most often packaged in a plastic package that is susceptible to radiated and inductively coupled noise. For example, what happens if the assembly is operated near a switching regulator? This is a case of both capacitively coupled and inductively coupled noise. Care has to be exhibited when designing the package and the circuit to protect sensitive nodes.

13.10.5 Low-Frequency Wander

This is a parameter that does not appear on most piezoelectric resonator datasheets. The quartz resonators did not have this low-frequency condition of output noise; with the much higher temperature coefficient of frequency change of the MEMS resonator, in some cases as high as −30 ppm/°C, this is now a significant parameter to contend with.

This is truly a low-frequency jitter condition that is ignored until one finds their new design and the circuit does not meet specifications.

This large temperature coefficient is corrected by a temperature compensation function built into the PLL circuit. The PLL is continually adjusting the compensation circuit which is a step change in the output frequency.

This is easily measured with a period averaging frequency counter such as the Keysight (Agilent) 531xx or 53200 series. Vary the measurement time or gate time from 0.001 mS to 1 S. Frequency jumps or changes will be noted that are unique to the MEMS resonator-controlled devices. The longer gate time will average these jumps; hence, changing the gate time will assist in indicating the internal circuit timing that is creating these jumps (Figs. 13.1 and 13.2).

13.10.6 Long-Term Aging

The performance of the resonator versus time is important, essentially how long will the resonator be providing a signal that is within specification.

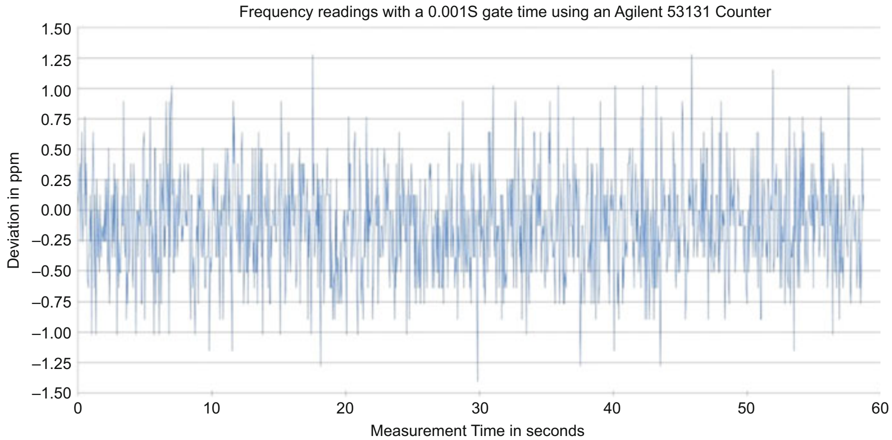

Fig. 13.1 Typical MEMS-based XO with a CMOS output and the temperature constant at about 25 °C and 3.300 V V_{DD}. The counter resolution is about ±0.1 ppm

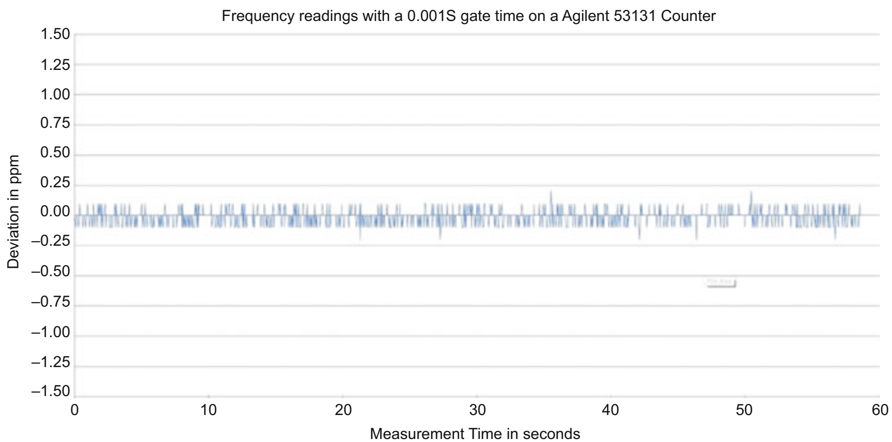

Fig. 13.2 Typical quartz crystal-based XO with a CMOS output and the temperature constant at about 25 °C and 3.300 V V_{DD}. The counter resolution is about ±0.1 ppm (Note: the noise or wander is limited by the counters resolution)

The level of expectation has been set by the quartz crystal resonator; in today's ceramic hermetically sealed packages, the resonators routinely can achieve ±10 ppm over a 10–20-year period.

Often it is stated that the need is much less, "oh it's a consumer part and will be discarded in 2 or 3 years"; so aging is not important. Think of the number of items such as copiers/printers, kitchen appliances, our cars, radios, etc. where the product life will be much greater than 2 or 3 years.

Often a quartz resonator specification is stated as ±3 ppm for the first year and then ±2 ppm after the first year. The end users of this type of product also understand that the aging rate is declining logarithmically every year. Therefore, at year 10 it is far less than ±2 ppm per year. The piezoelectric MEMS resonators have not demonstrated a similar logarithmic slowing or the rate if declining is far lower than quartz.

The MEMS industry and the various MEMS design technologies have resulted in a widespread aging performance.

13.10.7 EMI Radiation

The signal radiated from the resonator and associated internal electronics is important to meet various RF noise emission specifications.

The piezoelectric resonators operating with PLL circuits have many more challenges compared to the simple quartz crystal oscillator. The crystal oscillator has the base resonator frequency and then the harmonic multiples of the frequency. The piezoelectric MEMS devices with the PLL have many other frequency components besides the basic resonator to control; also the resonator is often a noninteger multiple of the output frequency.

13.11 What Are the Expectations of the Future?

13.11.1 The Device Sizes

Sizes will continue to decline for all FCP technologies. No sector has reached a limit or physics “hard stop” at this time.

13.11.2 The Device Supply Voltages and Power

The resonators are all passive, so the supply voltages are only limited by the circuitry placed around the resonator. Also, the power consumed in the resonator is already in the uW range in almost all cases; therefore, the associated electronics determines the power consumption and that it is ever decreasing.

13.11.3 The Device Cost

The cost will continue to decline. The various technologies used to achieve these FCP devices will continue to compete for the available timing control needs of a system.

13.11.4 Self-Test

The resonators (the electromechanical device) that set the performance of the device are typically fully isolated from the end user. There is no way to know with what margins the resonator is operating under. In fact, in practice most resonators are only operated in the final configuration, and the margins are never measured.

It is practical today with the IC capabilities to measure the resonator performance and report this to the rest of the system. For example, what is the operating resistance of the resonator? Built-in self-test (BIST) will be implemented in the coming years.

Chapter 14
Large Volume Testing and Calibration

Minfan Pai

Large volume testing is expected in manufacturing for production. It is one of the operations that could be the determining factor for the success of an MEMS product. The function of the testing is to ensure that every part manufactured is a good part. Today, MEMS products, such as motion sensors and microphones for smart phones, are often just a portion of the many components used in the final product form—if any one of them is defected, the entire system may fail at any time. Hence, the impact of a defected die could be much bigger than just a component failure and would possibly cause situations such as production line down, schedule delay, unhappy customers, and moreover, a tarnished company reputation which affects future sales and even the sales of other product lines. The product quality is, therefore, one of the most important measures of the usability of an MEMS product. Additionally, the control of the test cost is quite often an on-going task for MEMS manufactures. Testing for MEMS could be many times more complex than that of typical semiconductor products. If not managed well, it could significantly affect the cost margin and render the product uncompetitive. In this chapter, we will use the piezoelectric MEMS resonators developed by Integrated Device Technology, Inc. (IDT) as examples to discuss the techniques used in MEMS manufacturing testing in details. Methodologies used in both test rejections and test time reduction (for test cost management) are discussed.

The construction of IDT's piezoelectric MEMS resonator products takes more of a traditional approach which consists of a separate MEMS and ASIC dies. The MEMS die is attached on top of the ASIC die, which sits on the lead frame, before they are wire bonded and plastic molded and diced into the final component product form [1]. A teardown view of the product is shown in Fig. 14.1. This approach permits the opportunity to test the MEMS and ASIC dies (if needed) individually

M. Pai, Ph.D. (✉)
Integrated Device Technology, Inc., San Jose, CA, USA
e-mail: minfanpai@yahoo.com

© Springer International Publishing Switzerland 2017

H. Bhugra, G. Piazza (eds.), *Piezoelectric MEMS Resonators*,
Microsystems and Nanosystems, DOI 10.1007/978-3-319-28688-4_14

Fig. 14.1 Teardown of an IDT piezoelectric MEMS oscillator in a plastic package (Reproduced from Bhugra et al. 2011)

before the final test performed on the final assembled products. It enables screening of defected MEMS or ASIC die components before committing them to the final assembly, so the impact from the cost incurred by yield loss is not accumulative. In other words, the manufacturer does not need to pay for the cost of an ASIC die, the assembly, the package, and the final test, for each corresponding defected MEMS die.

Of course, some other MEMS resonator products are now taking the integrated approach [2, 3]. MEMS and ASIC wafers are bonded together after being fabricated separately, or they are processed together on the same wafer as an integral part, producing complete functioning dies once diced. With this approach, MEMS and ASIC are typically tested together through ASIC, since they are electrically connected. The overall testing process may be simplified; however, the freedom in designing adequate testing strategies for the product could be reduced. Care must to be taken to make sure the effectiveness of the test is sufficient. Despite the differences, many of techniques we discuss next should still apply, depending on the specific construction of the MEMS products in question.

Our emphasis is on the MEMS die testing as it relates directly to the core of the MEMS products. The procedures involved in the final test step on assembled parts (with MEMS and ASIC dies in packages) are more tightly associated with the specific designs of the control ASIC for each case. We first discuss how the MEMS resonator dies are tested at wafer level before the assembly. And in the last section, we touch upon the calibration aspect conducted in the final test on the final assembled parts.

Since many MEMS resonator products utilize similar working principles and sharing basic structural and/or processing elements, readers should find the discussions and examples applicable to various resonator technologies or even other MEMS product types.

14.1 Purpose of Testing in Manufacturing

As mentioned previously, the primary purpose of testing in manufacturing is to screen out bad parts for final products. Similar to practices used in semiconductor products, it can be accomplished by passing them through automatic testers which evaluate against a set of predetermined test limits that complies with the specification sheet defined for the products.

But that is not all. Another equally important purpose of manufacturing testing is to reduce infantile mortality rate and improve overall product reliability. Because MEMS is in general a more complex technology than ICs, which functions not only in the electrical domain but mechanical, the testing procedures dealing with reliability aspect is inevitably a lot more complicated and extensive.

Piezoelectric MEMS resonators are no exception. Like many other MEMS manufacturers who had experienced in the development stage, resonator makers found themselves needing to explore various new and special techniques for effective testing in manufacturing.

Occasionally, temporary measures may need to be implemented in test to address certain fab or assembly issues that arose and could not be resolved in a timely manner so that the production is not interrupted.

The data collected from large volume manufacturing testing are very useful as well. They can be analyzed to track the stability of the wafer fabrication process and provide feedbacks to the fab for continuous improvements. In addition, due to the extended coverage of the data which could not have been obtained otherwise, they are proven invaluable for designers in devising the next-generation products.

14.2 Considerations in Testing in Manufacturing

It is important to understand that the goal in testing in manufacturing is different from the device characterization testing conducted in the product development stage. The setup and methods used in characterization measurements might not be suitable for directly porting to large volume testing in manufacturing.

First, let us consider a device characterization scenario. One may need to understand the temperature dependence of the resonance frequency of a particular resonator design. Measurement accuracy is usually a top priority as it pertains to the thorough understanding of the device for assisting either in device designs or improvements. However, there are also situations where you only need to understand the general trending of the devices across various designs. Do you need the frequency drift measurement accuracy within ±0.1 PPM or ±1 PPM? Do you need the temperature control accuracy within ±0.1 °C or maybe just ±1 °C? The decision comes down to your need for the data. Next, the questions will be on the capability of the measurement equipment and the oven for temperature tests. You may need to conduct a gauge R&R study (gauge repeatability and

reproducibility) for the measurement setup. You may also need to investigate whether the temperature measured from the oven chamber accurately reflects the temperature of the device and if a wait time between measurements for thermal stabilization and equilibrium is required.

The thinking process is similar when first setting up the tests for manufacturing, yet the requirements need to be modified as the objectives are now different. Ability to differentiate between bad parts from the good in the most efficient manner should now be the dominant factor in designing the setup and methodology for manufacturing testing.

For example, at manufacturing, you may care more about the distribution of the resonance frequency of all dies on wafer rather than the absolute frequency reading of each die at highest level of accuracy. Or, perhaps you do not really need the exact phase shift information at resonance of all dies on wafer. You can then consider eliminating this particular test.

In many cases, the test cost for MEMS products is a significant portion of the total cost of the product manufacturing. Thus, it is essential for the success of the product to keep the test cost at minimum—which directly translates to actions to minimize test time and number of test insertions. It could be a long and on-going effort to meet the test cost target, as many of the knowledge required is obtained through manufacturing practices.

14.3 Forming a Testing Strategy

Forming a testing strategy in manufacturing is the most important part of the preparation process. It usually starts at the development stage when you have an MEMS device that can be stably fabricated with reasonable yields and you are ready to ramp it up for high volume production. Large amount of data will need to be collected and analyzed to understand all of the device’s characteristics and possible failure modes. The process would involve exploring devices through various extreme electrical and environmental conditions plus reliability testings, aiming to find out their limits and understand the failure mechanisms. An appropriate test setup and effective rejection methods can, therefore, be derived.

The studies also need to take backend assembly processes into account, such as wafer grinding and dicing, etc. The impacts from these processes to the electrical or physical assessments during test need to be evaluated. For example, some devices may be extremely sensitive to ESD (electrostatic discharge) that they could be destroyed or behave erroneously after the event happening during wafer saw. One should then consider conducting the tests, or inserting additional tests for checking, after the wafers are sawn in this case.

A lot of times with the information available at hand, it is still not easy to determine the proper test limits or criteria to use for certain tests. It is suggested that

the most conservative and stringent ones should be considered first and gradually relaxed when deemed suitable based on the more data collected into the production phase.

Lastly, the test hardware, including wafer probers, electrical test equipment, handlers, vision systems, and computers, is, of course, another great subject in preparing for large volume testing. Tool capability, accuracy, cost, size, throughput, flexibility, and scalability are the default consideration factors. Most importantly, the selection of the hardware should be supporting the test strategies formed.

14.4 Methods of Rejection

In this section, we will begin with using IDT's piezoelectric resonator products as example to illustrate how various rejection methods can be used in large volume manufacturing testing. Note that not all of the methods we will be discussing are meant for adoption in manufacturing test together as a whole. They are simply provided to readers as case study scenarios and their implementations should depend on the need of the actual product at hand.

We will divide the methods in two main categories: electrical and visual rejections. Electrical rejections evaluate directly the electrical functionality of the products, which are closer to practices in typical IC tests. Visual rejections deal with mechanical construction of the device. Because MEMS devices bear mechanical elements and usually have a protective cap structure fabricated at wafer level (wafer level packaging), any compromise in mechanical aspects affecting both may degrade device's performance. The visual rejections are, therefore, more related to the reliability aspect in the tests.

14.4.1 Electrical Rejections

IDT's piezoelectric resonator is a two-port device. For electrical performance assessment of a resonator die at manufacturing, S21 parameters are measured using a network analyzer with a wafer prober at wafer sort. From the data obtained, quantities describing the properties of the resonance peak, referred as resonance parameters, are extracted. They include peak frequency (F), Q factor (Q), insertion loss (IL), and phase (Ph). The following sections discuss various electrical rejection methods primarily based on these extracted parameters.

Resonance Check

The very first step in electrical rejection is simply to check whether a resonator is resonating or not. More specifically, devices without a distinguishable resonance

peak at electrical excitations that swept across the expected frequency range are rejected. These include resonators with exceptional weak peaks as well as ones without a peak at all.

There are a few ways to reject these types of bad dies. The easiest and quickest is to check the detected insertion loss level after searching for the peak by finding the maximum point across the measured spectrum. If the value is very close to the representative feedthrough level (no peak) or substantially lower than what a normal peak should be (a weak peak), then the die should be rejected. Usually this can be done with just one very fast sweep across the expected frequency range of the device. A second approach is to check if a die has a measureable Q factor. Even a device exhibits a resonance peak but with a very weak one that its Q factor is essentially zero (or not measureable), then it has to be rejected. These screening criteria can be both used, if necessary, to ensure non-functioning bad dies are rejected effectively.

Spec Limits Rejection

Screening based on spec limits is easy to understand. These are the minimum and maximum allowable values set on the resonance parameters, F, Q, IL, and Ph, respectively. If measured parameters fall out of the predetermined limits, they are considered not possessing the full expected normal functionality of the device and should be rejected.

Setting the spec limit values is not a trivial matter. At the minimum, the knowledge should come from device designers as well as the data collected from pilot wafer lots. Designers understand the expected working range reflected in the parameters through simulations and modeling conducted in the design phase. The wafer data demonstrate the achievable and reproducible device performances and reveal the extent of variations dictated by the foundry's process capabilities. Furthermore, by way of reliability testing, there are weaknesses of the device that can be learned, which may allow establishment of correlations of failures to device resonance parameters. For instance, devices with Q factors below a certain value may be linked to nonideal cap sealing conditions and thus have a high possibility of latent failure in certain environmental conditions.

Another factor to consider in determining the spec limits may come from the IC side. When designing the ASIC that pair with MEMS resonators, electrical models describing the MEMS device's performance are used. Although IC designers would typically institute a broader operation range with margins than the models predicted, the spec limits should safely guarantee that the dies passing through tests will work with the ASIC properly in high volume production setting over process corners. In some special cases, there may be a need to tighten certain parameters to meet a specific performance requirement for a product variant, the specs are modified accordingly.

Dynamic Spec Limits Rejection

Along with the fixed-value spec limits discussed, dynamic spec limits can be implemented. It is aimed at removing outliers that stem from wafer processing variations and localized defects.

MEMS devices usually comprise of a number of material/structural layers. Variations from each of the layers due to processing could push the device's performance in the same or opposite directions. The resonance parameters measured at completion of processing then reflect the compounded effects. Normally speaking, the distribution of each of the parameters would follow a bell curve, or, be *normally distributed*. If devices existed with one or more parameters distinctively located outside of the main distribution, it implies that the processing condition at the location on wafer might be somewhat abnormal. It may be a point defect caused by residues or contaminants, or it could be any other processing issues affecting a localized area. Although their resonance parameters do not necessarily fall out of the fixed spec limits and the dies may still appear to function normally in the test conditions, as a precaution and for quality control, the devices may elected to be rejected to minimize reliability concerns.

The dynamic spec limits are determined statistically based on the measurements of the whole wafer. The limits could change from wafer to wafer as they are meant to address the particular processing variations of the wafer under test. In Fig. 14.2 the relation of the fixed and dynamic spec limits is illustrated.

To establish the dynamic spec limits values for a wafer, one evaluates the overall parameter distribution and measures each of the die on wafer against it. A simple way is to calculate the mean and standard deviation of the parameter of interest (which describe a normal distribution) and reject the outlier dies that situated outside of the distribution, defined by a predetermined distance away from the mean.

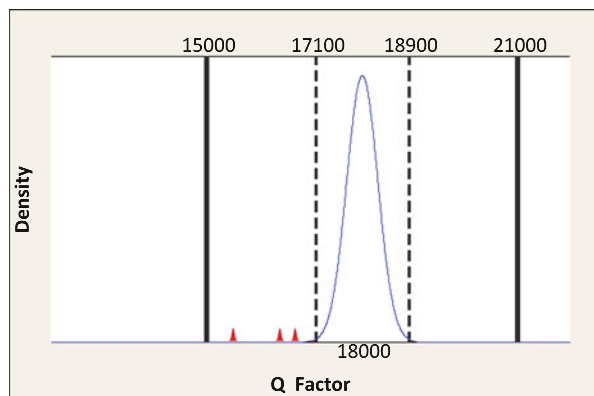

Fig. 14.2 Illustration of the dynamic test limits and the fixed test limits

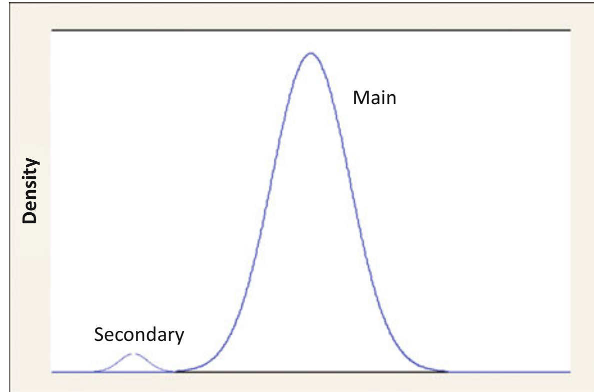

Fig. 14.3 Illustration of a parameter distribution having a significant secondary distribution

For example, if the outlier criterion is set to 3σ, then a passing die should satisfy the condition:

$$P < m + 3\sigma \quad \text{and} \quad P > m - 3\sigma,$$

where P is the measured parameter value of the die, m is the calculated mean, and σ is the calculated standard deviation. The outlier criterion is determined based on knowledge learned from the observations and analysis of historical wafer data, by which the process outliers can be reasonably identified. Similar discussions in outlier control can be found in [4].

A simple adoption of the above rejection may not be sufficient, however, if the characteristic of the parameter distribution is not perfectly normally distributed. For example, consider a parameter distribution having a main distribution and a secondary distribution as illustrated in Fig. 14.3. The secondary distribution may have come from a defect area on wafer covering an appreciable number of dies. A simple calculation of the mean and the standard deviation do not properly represent the actual distribution and will not effectively reject the outliers. One way to improve this situation is to implement "recurring" rejections, that is, a new mean and a new standard deviation value is recalculated every time an outlier is removed until there are no more outliers. The technique is applied to all of the resonance parameters independently so that the final selected group of dies is efficiently exclude of dies within the unwanted secondary distribution.

Yield Limit Rejection

Over of few multiple wafer fabrication runs in production phase, a typical wafer yield number can be established which reflects processing capability and stability of the fab process. A wafer yield limit can be set accordingly as an indicator and be used to automatically trigger a warning or rejection of an abnormal yielding wafer

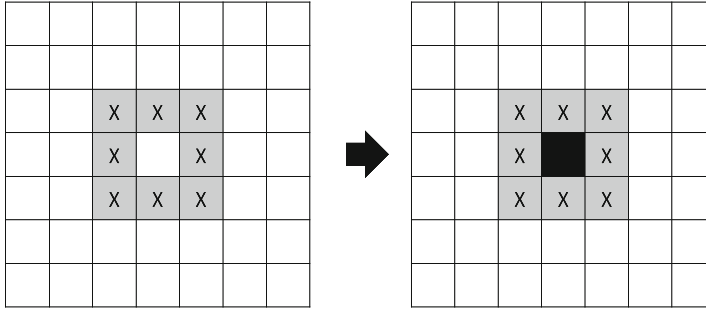

Fig. 14.4 An example of geographical-based rejection. The center good die is rejected due to existence of surrounding bad dies

or wafer lot. Engineers should investigate in the case of a sudden yield drop (a yield outlier) and determine if it is a fab or test issue and make recommendations for disposition. The yield limit should be reviewed periodically and renewed to reflect any improvement made to the fab process.

Geographical Rejection Including Expansion

Geographical-based rejection method is commonly practiced in semiconductor world for outlier control [5]. The rejection is based on the geographical relation to the surrounding electrical bad dies on wafer. Examples are shown in Fig. 14.4. An electrically tested good die is rejected if it is surrounded by a certain number of bad dies in its immediate adjacent proximity.

An extension of this method is called "expansion." During IDT's resonator development, it was found that the yield loss attributed to cap wafer bonding voids usually appears in circular pattern. A unique electrical signature allows for accurate detection of these defected dies, however, the minimally affected dies occasionally found at the periphery of the voids with only a tiny structural defect present a bigger challenge. An algorithm which considers bond void areas and geographically expands the region by a die or two at the periphery was proven to be effective in rejection of the defects. An illustration of the expansion rejection is shown in Fig. 14.5.

Rejection by Electrical Signature

Unique electrical signatures in resonance parameter data may be found to correlate to certain failure modes or defect modes. One example associated with cap wafer bonding void is mentioned above. The signatures are highly dependent of the

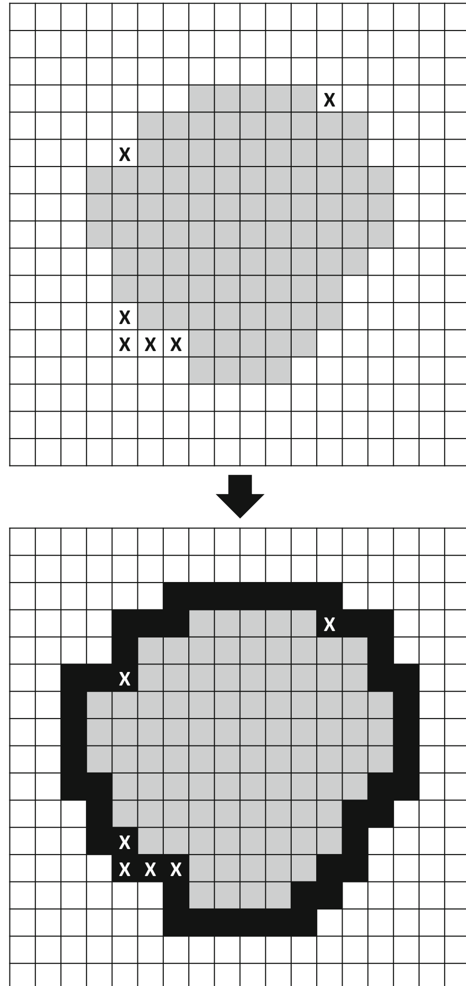

Fig. 14.5 An example of expansion rejection. "x" denotes the dies with minute cap defects that were not detected electrically but rejected by expansion

MEMS process and its processing sequence; therefore, they do vary case by case and need to be identified through analyses at development phase. Other types of defects with electrical signatures may include bond pad shorting, ESD, etc.

Rejection by electrical signature may not necessarily improve the overall rejection efficiency—as these defect types having significant deviation from regular parameter values very likely would have been rejected readily by spec limits alone. But the method does provide the next level of insights into the defect types. It is beneficial not only for future process improvement but for more advanced rejection algorithm development such as the expansion algorithm discussed previously.

Rejection Beyond Resonance Parameters

Resonator measurements showing minor irregularities on the profiles of the resonance spectrum around the peak may be observed at high volume production. Some of them may be found to correlate to certain processing defects, while others may actually be caused by random nonideal contact conditions during wafer probe. In any case, for outlier control, decisions may be made to reject dies with these irregularities due to uncertainty. Because the variations on the profile are usually quite subtle that they could not be detected based on the spec limit screening alone, a more complex spectrum analysis are required for this type of rejection.

14.4.2 Visual Rejections

Visual rejections rely on analyses of wafer inspection data taken upon completion of the wafer fabrication or at selected critical processing steps as needed. The inspections are done with automated imaging tools which scan through the entire wafer surfaces with magnification and resolution suitable for the need of the targeted analysis. Individual images corresponding to every die on wafer can be registered and retrieved by the imaging analysis programs.

As can be anticipated, the imaging control during inspection plays an important role in the efficiency and accuracy in the imaging analysis. Any nonideal imaging situations, such as out-of-focus, tilt, shift, and exposure and contrast variations, can drastically increase the complexity for analysis. Moreover, processing irregularities such as debris and surface etching topography can complicate the situation even more. Therefore, besides improving on the imaging front, it is equally important that a well-designed analysis algorithm takes all of these factors into account.

As will be seen, the use of visual rejections is more so depending on the specific MEMS product in question, since the die's physical construction is very much determined by the particular MEMS designs and processes. In the following, we will use IDT's resonator products as examples to discuss various types of implementation in visual rejections.

Seal Defect Rejection

Figure 14.6 shows the schematic of IDT MEMS die's cross section. The completed device wafer is first bonded to a cap wafer using a polymer adhesion layer. The polymer holds the two wafers together so that subsequent processing steps on the cap wafer can be carried out. As polymer is intrinsically permeable, a metal layer covering the bond interface exposed around the peripheral of the dies is necessary to ensure a hermetic seal. This processing step is called metal seal. More detailed descriptions of the construction of the device can be found in [6–8].

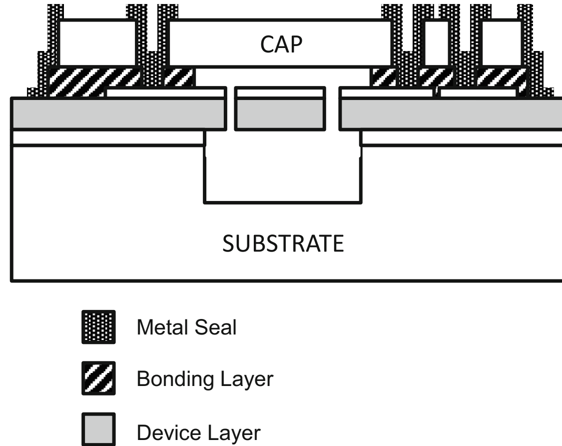

Fig. 14.6 Cross-sectional schematic view of the IDT piezoelectric MEMS resonator with a cap fabricated at wafer level (Reproduced from Bhugra et al. 2014)

The effectiveness of the seal is of upmost importance. Stability and reliability of the device could be severely compromised if the seal is not perfect. If any leak path exists, moisture could reach into the cavity where active device resides and condensate on the device's surface. It could also be absorbed by the aluminum nitride piezoelectric layer. In either case, frequency shift and Q degradation will result due to loading. Under extreme conditions, corrosions of the electrode metals may even occur and render the device nonfunctional.

Unlike electrostatic-based resonators, most of which require a high vacuum to retain their Q to function, piezoelectric resonators are not as sensitive and may still function within the normal range even if the vacuum is breached. This is advantageous as, if somehow the seal is compromised, a device in the field may still continue to work without failing. Nonetheless, it does make defect detection at manufacturing more difficult. A nonelectrical rejection method is, therefore, needed to be developed.

It was observed that the edge profile of the metal seal around the die periphery is a very good indicator for the quality of the seal. This correlation was established through studies involving measurements and de-processing analyses under various test conditions. If edge profile is incomplete—featuring either a notch or any broken sections—there is a high chance of existence of openings in the metal leading to the exposure of the polymer layer at the bonding interface. Algorithms aiming to detect any imperfections around the seal's edge profiles can thus assure that all passing dies are with the metal seal layer properly fabricated.

Delaminated Cap Rejection

Like most MEMS products today, IDT's resonator dies constitute of a cap that provides protection for the active device from the outside environment. The cap is typically fabricated at wafer level using wafer bonding techniques. At the end of

the process, the completed wafers are diced into individual dies—each completed with a cap on top. Depending on the process flow's design, separation of the cap from its wafer form into individual caps can be done by an etching step on the cap wafer, or simply by the wafer saw process during the backend processing.

During the cap separation, localized wafer bonding defects, if exist, could cause the individual caps in the affected region to delaminate and fly off due to insufficient adhesion. In most cases, as discussed in the previous section, the delaminated dies can be easily detected electrically because either the metal bond pads are completely gone along with the caps or the resonator structures are severely damaged from follow-on processing without a protective cap in place. The real concern here would be the ones that still have most of its cap structure in place but partially delaminated. As mentioned previously that piezoelectric resonators are insensitive to vacuum leaks, they could still be tested normal while posing high reliability risks.

Similar to metal seal detection, algorithms can be established to visually detect dies with partially delaminated caps. This can be done by detecting the outer profile of the cap structure. If a corner is missing then the profile would deviate from its standard shape. It can also be done by detecting certain features on the cap—it could be labels or markings, etc. Again, this is highly dependent on the process and the design.

Bond Void Rejection

Besides cap wafer bonding, there is a second processing step involving wafer bonding in IDT's design. The single-crystal silicon resonator body layer, as illustrated in Fig. 14.6, is constructed using direct wafer bonding technique. A silicon-on-insulator (SOI) wafer is bonded to a silicon substrate wafer with pre-etched cavities. After backgrinding on the SOI, a well-defined silicon layer suspended above the cavities is formed. This kind of direct wafer bonding process is very commonly used in MEMS manufacturing. Covalent bond is formed by pressing two highly polished silicon surfaces together and annealing at elevated temperature without any intermediate adhesion materials. The process is extremely sensitive to surface roughness, residues, and contaminants. Any tiny particles could generate bond voids much larger in size after bonding.

Comparing to cap defects discussed previously, this type of bond voids is even harder to detect both electrically and visually—as it is hidden underneath the wafer surface. What is worse, the voids could have kept perfectly under vacuum during wafer probe until dicing. Some would mitigate this issue by performing a partial dicing which reveals the bond interface early in the process for wafer probe. Or, the wafer probe is conducted while on tape after it is diced.

Most likely the upper portion of the dies reside within bond voids would completely fall off during the pick-and-place process at assembly, rendering them nonfunctional and failing at final test. However, if a die is situated at the edge of

a bond void, it is more likely that it may still be partially bonded and passes the electrical and visual rejections all the way up to the final test. Again, these are the dies with potential reliability risk and should be addressed.

To detect these bond voids, acoustic micro imaging (AMI) data taken right after the bonding process can be utilized [9]. IR imaging may be used as well; however, depending on the die size the resolution may be too low to discern die-level defects. These imaging techniques are commonly used during the development phase for detecting major bond failures or for qualifying a bond process. Algorithms that identify bond voids and match the imaging data to the wafer die map can determine exactly which dies are located around the bond voids for rejection. The expansion concept discussed in geographical rejection methods can also be applied for extra precaution.

Edge Die Rejection

Same as IC fabrication practices, exclusion zone is applied to MEMS wafer to avoid either picking dies or placing dies during mask design in regions around the wafer periphery with large processing deviations. The zone is defined by a predetermined distance extending inward from the wafer edge. Due to rectangular reticle shape constraint, there will be some dies that are fully or partially placed within the zone. Regardless, they are rejected automatically from the assembly wafer maps to minimize risk.

In IDT's case, it was found that the standard practice of the exclusion zone described above is not sufficient. Owning to the topography generated from prior processing steps, the very first front row of dies facing wafer periphery appear to have a higher chance of bearing distorted cap structures as fabricated, even if they are not inside the exclusion zone. The abnormity on the cap structures prevents complete metal sealing and increases reliability risk (again, the dies can still be tested normal electrically). Consequently, these front rows of dies facing wafer periphery are treated as dummy dies and are also excluded from the final assembly maps automatically. Note that the dies cannot be directly removed from the designs in the photo mask, as the problem would simply propagate to the next first rows of dies facing the wafer edge.

Delaminated Metal Pad Rejection

Detection of delaminated metal pads can be implemented as preventive measure to address occasional random occurrence of substandard adhesion of bond pads to the die surface. Although the occurrence should be extremely low for a well-controlled production process, assembly line could be interrupted even if there is just one problematic die on wafer. A die with delaminated bond pads may cause problems during wire bond, impacting assembly throughput as a result.

Electrical rejection cannot effectively screen out dies with delaminating bond pads. As long as they are still partially attached to the die surface, probe tips would simply push the metal layer down and still make good electrical contact during probing. For this reason, the detection has to be visual based. Since partially delaminated pads tent to curve upwards slightly due to intrinsic stress, they would appear with shades on the die images. Algorithms can be developed to detect the minor shading gradients on the pad surfaces for rejection.

14.5 Test and Rejection Analyses Flow

As illustrated in Sect. 14.4, it is a fairly lengthy and complex procedure to reach to the conclusion of die selection on wafer for assembly. The procedure involves inspection imaging, wafer probing, plus the electrical and visual data analyses. The final assembly wafer map generation cannot be arrived until all data are collected and analyzed.

For visual data collection, especially of final completed wafer inspection, it is preferred to be taken prior to wafer probe and before releasing from the fab so that the data accurately reflect the state from processing and are not influenced by artifacts from handling. In addition, visual analyses can be performed as soon as any set of data becomes available, and need not wait until the receipt of electrical data. An example of the test and analysis flow is shown in Fig. 14.7.

14.6 Consideration in Test Implementation

In this section, we will discuss a few topics for consideration when implementing large volume testing. It is aimed for improving efficiency, throughput, and minimizing possible mistakes.

14.6.1 Defect Coding System

The information resulting from all of the test data, after electrical and visual rejection analyses, can be quite complex. Every single die on wafer could have multiple datasets describing its electrical and visual attributes. It is, therefore, convenient and essential to implement a defect coding system so that the properties of any fabricated dies can be quickly retrieved and understood. Each die after analyses will be tagged with the defect code. The design of the coding system should be kept brief and simple and yet covers necessary information.

The benefit of implementing such a system is multifold. Firstly, it helps product engineers to quickly quantify the condition of a fabricated wafer or wafer lot. Various types of wafer maps and Pareto charts can be generated for further analysis

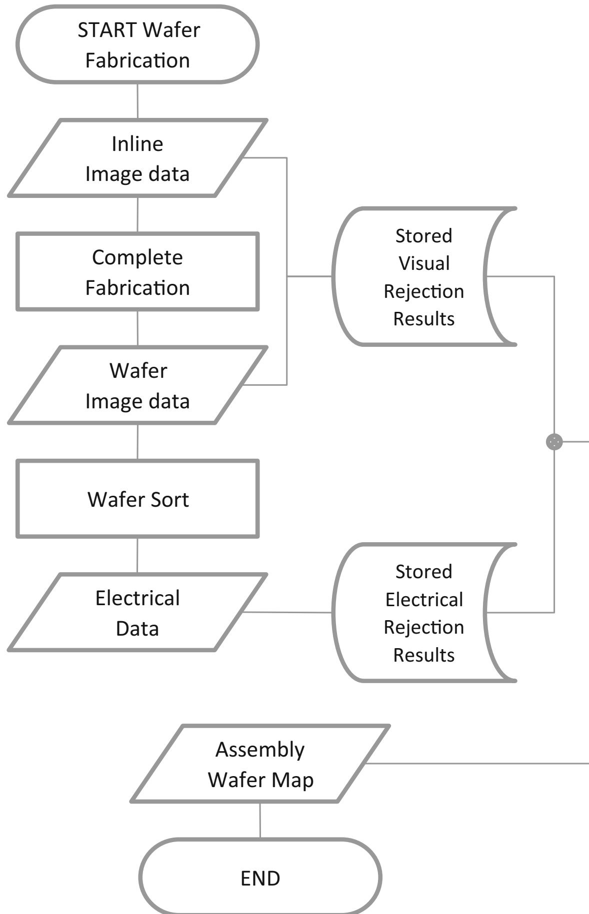

Fig. 14.7 An example of test and rejection analyses process flow

and monitoring. Secondly, the information can be helpful for process engineers to understand issues related to wafer processing and provide feedbacks to fabs for improvements. Thirdly, it is an efficient tool for failure analysis where establishing correlations between multiple factors to failures are commonly practiced.

14.6.2 Interface Design for Test Programs

User interface design for manufacturing test programs is not a trivial matter. At wafer sort, for example, it is important to have a simple and robust user interface which leaves no room for operator errors. Any mistakes resulting wrong data recorded may eventually allow for bad dies shipping to the end customers.

Unless necessary, there should be no options for changing or configuring any test conditions. The production version of the test program should be separated from the one used for development, or at least it is password-protected for enabling the switching between the two modes of operation. Additionally, file locations and filenames of test data should be automatically set by a rule following predetermined file structures, preventing possibility of mixing of wrong data files.

Another common problem in manufacturing testing is mixing up of wafers. Implementation of laser wafer ID marking for automatic wafer registration at the cassette loading on prober is preferred. Otherwise, an effective wafer checking and verification procedure should be installed and followed.

It is also a very useful feature if all testing conditions can be logged, which provide traceability whenever needed.

14.6.3 Calibration of Prober Setup

Calibration of test setup with network analyzers is performed with a CAL kit specifically designed for the probes or probe cards format used. The CAL kit is in the form of a small rectangular ceramic substrate with gold metal patterns on the surface, which allows for a full SOLT (Short, Open, Load, and Through) calibration.

Ideally, calibration of the prober setup should be done regularly to ensure accuracy and consistency of the measurements for every wafer. At the very least, it is desirable to perform a calibration every time before commencing to the probing of a test lot so that any possible condition changes that could have been affecting the original calibration state is accounted for.

However, the calibration procedure is quite cumbersome in the manufacturing setting where automatic probers with cassette wafer loading mechanisms are typically employed. Loading of the CAL kit onto the wafer chuck would require mounting it to a dummy wafer and manually adjusted or aligned by an operator. This process is impractical and severely affecting throughput.

If wafer fabrication process allows, equivalent calibration structures can be designed and directly fabricated on the wafer surface on production wafers. This resolves the need for the frequent special loading of the CAL kit. And calibration can simply be done, if preferred, at the start of each wafer probe and fully automated.

14.6.4 Data Processing and Automation

MEMS resonator wafers typically have fairly high number of total die per wafer (DPW) due to their small device size. With the implementation of both the electrical and visual rejection schemes, the amount of data generated per wafer for processing in manufacturing could be daunting. To ensure immediate availability

of the assembly wafer maps upon completion of wafer probes, the speed of data processing is crucial especially because the electrical data, as discussed, cannot be analyzed until the whole wafer's probe data are acquired.

The bottleneck in overall data processing, however, lies in the imaging analyses part, since the size of data itself is much larger than that of electrical and the computing required for the analyses is far more complex. Besides computing power, intelligent designs in the analysis algorithms are often the key to substantially minimizing the data processing time.

The management in the timing of data processing also helps. For example, the wafer bonding imaging data is available prior to the completion of the wafer fabrication and certainly before the wafer sort. This analysis step can then be performed once the data are available. And during wafer sort, those analyses results can be automatically retrieved and applied to the latest set of the test data for final conclusion.

Finally, since in production the wafer sort is mostly done in cassettes loaded with full wafer lots, batching-processing concept can be utilized in the data processing for rejection. With the capability designed in, the computer program can automatically retrieve all required data from the various data depositories and process them one wafer by one wafer sequentially from the lot. At the end of data processing, assembly maps for each wafer in the lot can be automatically generated within a short period of time upon the completion of wafer probe.

14.7 Test Time Reduction

As discussed briefly in Sect. 14.2 that test cost could be one of the determining factors for the success of an MEMS product. At manufacturing, test cost is basically directly calculated from the test time. Investment in activities to achieve test time reduction goals can be well justified in the end when the final product cost is lowered as a result. Care must be taken so that accuracy is not sacrificed during the reduction process. Finding solutions call for detailed analysis in both the test hardware and software for every action and command and look for ways to make the execution faster. Below we discuss a few examples for consideration in working toward test time reduction.

14.7.1 Multi-site Testing

The most straightforward way for immediate test time improvement is to deploy parallel, multi-site testing. In this case, multiple sets of network analyzers with a probe card capable of probing the corresponding number of dies in parallel are

adopted. Before deployment, one needs to take into consideration the probe card designs and stepping schemes during the mask's reticle design so that minimal number of stepping is required to cover all of the dies across the entire wafer.

14.7.2 Test Program Optimization

In software, there are also a few things that can be done to optimize the test program for efficiency.

Procedures for testing resonators typically include first searching for the resonance peak over the expected frequency range, followed by one or two narrower sweeps over the resonance peak. The final close-up sweep is necessary for meeting the resolution and accuracy requirements for the resonance parameter extraction. Understanding the different goals for the measurement sweeps, the sweeping condition settings (such as number of points and IF bandwidth) can be adjusted accordingly to optimize the speed while satisfying the requirements.

Some intelligence in the program can be implemented as well to reduce test time. For example, the second narrow sweep can be omitted if the first wide sweep did not find any resonance peak. Additionally, if the characteristic of frequency distribution on wafer is known, some frequency tracing capabilities may be possible when stepping over dies, allowing skipping of the first wide sweeps in some cases to save time.

14.7.3 Hardware or Software

Certain tasks in tests can be done either with the hardware or with software. Examination of the execution speed in both cases can help determine the better way for test time control.

One example is for the resonance parameter extraction step done after the S21-parameter measurement on network analyzers. The extraction may seem taking no time, however, due to high DPW, the total time can add up considerably when going through all the dies on an entire wafer. As an alternative way, the extraction computation can be moved to PC after wafer probe. For one, the time spent offline in the background from the prober for computation does not count directly to the incurred test cost. For two, the computation with optimized algorithm over the acquired full dataset (instead of one at a time) can be so much faster that it takes only a fraction of the time to complete.

Another example is for offline calibration correction. When the feature is turned on on network analyzers, the correction based on the factors saved during calibration is applied to the S21 measurement for every die probed. Just as resonance parameter extraction, once this computation is moved to after the wafer probe as a post-processing step, considerable test time can be saved.

14.7.4 Data File Formats

Determining a right data file format is essential when implementing manufacturing testing for MEMS products. As discussed, the amount of data gathered from each resonator die testing is quite large. They include S21 parameters and multiple imaging data, as well as the reduced dataset after the rejection analyses. A well designed data file format will maximize the efficiency for data saving and retrieving as well as computation. It can expedite both the testing processes and the analyses processes, contributing significantly to overall test time reduction efforts.

14.8 Calibration

One of the major differences between MEMS oscillators and quartz oscillators to date is that MEMS oscillators typically utilize fractional-N synthesizer phase-locked loop (PLL) in the architecture [10, 11], allowing it to be programmed at different frequencies as needed prior to product shipment. This adoption is in part due to a fundamental difference in the MEMS resonator manufacturing, where individual dies are produced in batch on the wafer level. The native frequency of each die as fabricated is thus heavily influenced by the variations of wafer processing across the wafer, exhibiting a spread much larger than the specifications typically required for the targeted applications. A calibration step during manufacturing becomes necessary to register the actual frequency output reading from the resonator-based reference oscillator so that the feedback divider can be programmed accordingly for the targeted final frequency output.

Another reason of using the fractional-N PLL is to address the inherently larger temperature coefficient of frequency (TCf) from silicon structural material, on which most MEMS resonators are based. If uncompensated in any way (actively and passively), the frequency drift over temperature easily exceeds all of the targeted applications. Constant-adjusting feedback divider values properly set with respect to ambient temperatures can provide the compensation function needed for the device. Again, due to wafer processing variations, the profiles of the TCf curves may vary slightly from die to die. Another calibration procedure is, therefore, necessary to evaluate the exact temperature profile of the resonator die and provide the information necessary for the feedback divider for active temperature compensation.

The calibrations mentioned above are typically conducted at the final test step where the completed assemble units are fed to automatic test equipment (ATE) via handlers. The first calibration step, which involves the reading of the reference oscillator frequency, is quite straightforward. The values required for PLL programming are calculated and stored to the EEPROM on the ASIC chip. The second calibration step is more complicated. Usually more than one test insertions at various ATE temperature set points are necessary to capture the TCf profile of the die for the required compensation. The number of insertions and exact temperature

set points are strongly depending on the characteristics of the devices dictated by their designs and processes. The calibration strategy versus targeted product specification on the temperatures also plays an important role in the test plan.

14.9 Conclusion

Large volume testing and calibration are important processes in manufacturing piezoelectric MEMS resonators-based products. Procedures and strategies for transitioning from the tests done at development phase to high-volume manufacturing are discussed, including detailed analyses in electrical and visual rejections, as well as considerations for test implementation and optimization.

References

1. Bhugra H, Lee S, Pan W, Wang Y, Lei D (2011) Reliability of next generation high performance pMEMS resonator oscillators. Paper presented at the frequency control and the European frequency and time forum, 2011 joint conference of IEEE international, San Francisco, 1–5 May 2011
2. Emmanuel PQ (2009) IC-compatible MEMS structure. US Patent 7,514,760, 7 Apr 2009
3. Small M, Ruby R, Ortiz S, Parker R, Zhang F, Shi J, Otis B (2011) Wafer-scale packaging for FBAR-based oscillators. Paper presented at the frequency control and the European frequency and time forum, 2011 joint conference of IEEE international, San Francisco, 1–5 May 2011
4. JEDEC Standard (2012) Special requirements for Maverick product elimination and outlier management. JEDEC Solid State Technology Association, Arlington
5. Singh AD, Nigh P, Krishna CM (1997) Screening for known good die (KGD) based on defect clustering: an experimental study. Paper presented at international test conference, Washington, 1–6 Nov 1997
6. Bhugra H, Lee S, Pan W, Pai M, Lei D (2014) Commercialization of world's first piezoMEMS resonators for high performance timing applications. Paper presented at the 27th IEEE international conference on micro electro mechanical systems, San Francisco, 26–30 Jan 2014
7. Bhugra H, Kei K, Wang Y (2011) Methods of forming packaged micro-electromechanical devices. US Patent 7,955,885, 7 Jun 2011
8. Lei K, Pai M, Pan W (2011) Methods of packaging microelectromechanical resonators. US Patent 8,426,233, 23 Apr 2011
9. Adams T (2010) Bonded wafer yield increased by acoustic imaging. Wafer & Device Packaging and Interconnect, pp 36–38
10. Cioffi K, Lacroix D (2008) Frequency and temperature compensation synthesis for a MEMS resonator. US Patent 7,449,968, 11 Nov 2008
11. Patridge A, Lutz M (2009) Frequency and/or phase compensated microelectromechanical oscillator. US Patent 7,532,081, 12 May 2009

Part IV
Real World Implementations

Chapter 15
High Frequency Oscillators for Mobile Devices

Jan H. Kuypers

Wireless communication has become ubiquitous today, with almost two billion smartphone users worldwide. The data to be transmitted to the user is modulated onto a carrier frequency, typically in the range of 700 MHz to 3.5 GHz and broadcasted from a base station. For the user to retrieve the actual data, the receiver must demodulate the data from the high-frequency carrier. This is done by reproducing the carrier frequency locally in the cell phone, often referred to as local oscillator (LO) and using the LO to demodulate the received cellular signal. For correct reception the frequency for the demodulation of cellular data typically requires a tolerance of less than ± 2 ppm error and hence a precise frequency reference is needed. In the past only quartz crystal based oscillators and resonators have been able to provide the required performance for mobile devices. Today's quartz crystal frequency references are based on resonators operating at 19.2, 26, 38.4, and 52 MHz. These frequencies are multiplied to generate the much higher LO frequency with the use of a fractional-N synthesizer, also referred to as frac-N phase locked loop (PLL). The final accuracy of the LO is given by the accuracy of the reference device and the step size of the frac-N PLL, which today allows for ppb resolution.

This chapter introduces the challenge of developing a quartz crystal replacement based on piezoelectric thin film resonators fabricated using microelectromechanical system (MEMS) technology (Fig. 15.1). Very often quartz crystal resonator technology is dismissed as 90-year-old technology, suggesting it is outdated, which could not be more wrong. At present, all wireless communication functionality found in a handset, including cellular, WiFi, FM, Bluetooth, and GPS relies on quartz based frequency references. There has been an immense development to reduce size, package height, cost, and frequency errors over the years. At the same

J.H. Kuypers (✉)
Sand 9, Inc., Boston, MA, USA
e-mail: Jan.Kuypers@Qorvo.com

© Springer International Publishing Switzerland 2017

H. Bhugra, G. Piazza (eds.), *Piezoelectric MEMS Resonators*,
Microsystems and Nanosystems, DOI 10.1007/978-3-319-28688-4_15

Fig. 15.1 Photograph of a miniature chip-scale packaged (CSP) MEMS resonator including an integrated temperature sensor and heater for calibration with dimensions of 1.5 mm × 1.1 mm × 0.5 mm

time, there has been a strong trend to consolidate the different frequency sources that were traditionally allocated to individual functions, i.e., the VC-TCXO for the cellular transceiver with ±2 ppm stability, the high-stability TCXO for GPS with ±0.5 ppm stability, the XO with ±50 ppm stability for WiFi, the XO with ±50 ppm stability for FM and Bluetooth, and yet another MHz crystal with ±50 ppm stability for the application processor, as well as two 32 kHz crystal resonators to provide real time clock capabilities to the cellular transceiver and the application processor. The development of consolidation began around 2002 for 2G transceivers with the goal to eliminate the expensive cellular VC-TCXO [1]. This initiated the rise of the digitally compensated crystal oscillator (DCXO) and the decline of the crystal timing content in mobile phones. The 2G (GSM/GPRS/EDGE) implementation was particularly elegant as it relied on a single quartz crystal with ±50 ppm stability without the use of a temperature sensing device to correct for temperature related drift. The frequency error was adjusted based on the frequency control burst transmitted by GSM base stations. Today, all mobile platforms are moving towards one single quartz crystal component combined with a temperature sensor to supply a reference frequency as well as time base to all phone functions. It is needless to say that the technical challenges to have one frequency reference to support the two most stringent systems, i.e., GPS/GNSS in regard to overall stability and close-in phase noise, as well as WiFi 802.11 ac for ultimate far-out phase noise floor, are immense. The resulting cost savings of using only one crystal component were significant, yet had severe financial repercussions on the quartz timing industry, as suppliers had steadily increased their capacities to meet the rising demand of mobile devices. The resulting price deterioration has also affected the success and business case for adopting MEMS timing solutions in the mobile space, as explained later.

The zero-IF cellular RF front-end shown in Fig. 15.2 features the simplest implementation of the possible timing architectures. It contains one VC-TCXO as frequency reference and a fractional N-phase locked loop (PLL) to synthesize the local oscillator required for down-conversion for receiving and up-conversion for transmission. Fractional N-PLLs were introduced in 2005 to support multi-mode operation, at first dual mode to both support GSM/GPRS/Edge and CDMA, as otherwise two frequency references would have been necessary [2].

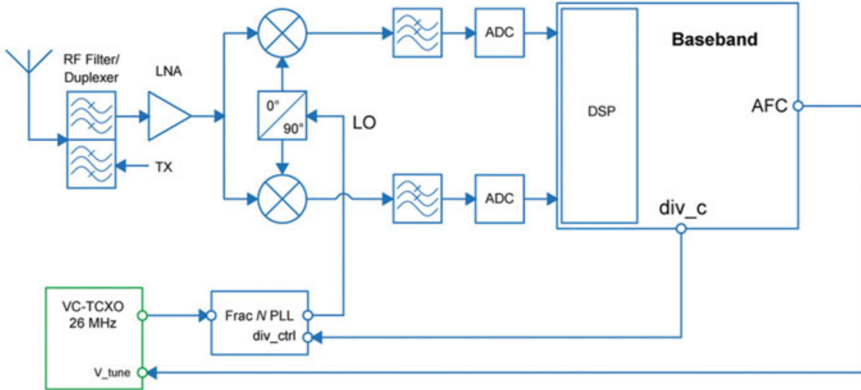

	VC-TCXO	Xtal only	DCXO	MEMS DCXO
Year of wide use*	1980	2010	2012	-
Oscillator circuit on-chip	No	Yes	Yes	Yes
Compensation	Analog	Analog	Digital	Digital
Clock sharing	No	No	Yes	Yes
Factors	++ Was main solution ++ Simple system architecture ++ Excellent performance + Still in use as of 2015 - Large external component -- High cost -- Multiple dedicated references	++ Cost (Xtal + sensor) + External component size - Chip area increase -- Temp.-comp. now on chip -- Complex system architecture -- Calibration on phone board - Analog tuning dependence - Frequency stability + Current consumption	++ Cost (Xtal + sensor) + Analog chip area reduction -- Temp.-comp. now on chip -- Complex system architecture -- Calibration on phone board - Frequency stability + Current consumption + Frequency step-size control ++ Low power mode ++ Clock re-use -- Re-use challenges for GNSS	Similar to DCXO, except: ++ Size ++ Cost (integrated temp sensor) ++ Co-packaged reference ++ Transceiver ships with pre-calibrated reference inside ++ No Calibration on phone board + No Xtal sourcing required + Frequency step-size control + Frequency stability -- Requires timing architecture changes to accommodate ±8,000 ppm initial frequency offset and -160 ppm to +15 ppm variation over temp.
Frequency synthesis architecture				

Fig. 15.2 Illustration of a traditional implementation of a VC-TCXO based cellular transceiver. The table below compares the architectures commonly found in cellular transceivers over the years. *The year of being widely used is challenging to define, as many transceiver companies either skipped architectures, did not offer all products in one architecture, or did not integrated or clock-share to the same degree

15.1 Understanding the Diversity of Timing Requirements in Mobile Devices

In order to understand the importance of frequency stability and required performance for mobile applications it is best to review the requirements for GPS. The block diagram in Fig. 15.3 shows the simplified architecture of a GPS receiver. It contains a reference oscillator to demodulate the navigation messages of the satellites. The messages are all broadcasted on the L1 carrier (1.57 GHz) and are down-converted to an intermediate frequency (IF) by multiplying it with a frequency close to the L1 carrier, referred to as the local oscillator (LO). The LO frequency is generated from a stable reference source, for example a temperature compensated crystal oscillator (TCXO) operating at 26 MHz by means of a phase-locked loop. The main requirements for a good GPS reference are (a) excellent phase noise close to the carrier and (b) excellent short-term stability.

In order to establish the position accurately the navigation message of the satellites is used. It is encoded at only 50 bit/s and hence is modulated very close to the carrier. Any noise in the reference oscillator close to its carrier is also up-converted in the PLL, so that in the mixing step of LO and L1 carrier this noise is introduced. Any noise in the reference oscillator will limit estimating the phase of the navigation message. In order to achieve this phase noise requirement, a resonator with high quality factor (>5000 at 26 MHz) should be used, but the resonator may not have excessive acoustic flicker noise. In addition, a current of 200–900 μA for the oscillator core is required based on a Pierce or Colpitts type oscillator circuit to meet the phase noise requirements.

In order to improve the position estimate phase coherent integration is used over a typically 10–20 ms long window. Any drift of the reference clock within this time frame will reduce the degree of phase coherence and hence will limit the desired improvement in SNR, which in turn will limit the position accuracy.

For the purpose of tracking the time and date a second frequency reference is used that consumes a minimum amount of power. This function is often referred to as real-time clock (RTC). The requirements for this clock are: very low power consumption (<1 μA), as it is always on and good long-term frequency accuracy, typically <10 ppm/year. Most commonly a 32,768 kHz tuning fork quartz crystal is used for this purpose.

Although both components are referred to as frequency reference they both fulfill very different requirements and will typically require different technical solutions. As a rule of thumb, good phase noise requires >200 μA of current in the oscillator core. However, as mentioned in the introduction the trend is to consolidate all time and frequency references into a single solution. This means that a MHz resonator also needs to be used as the basis for the RTC. The inherent advantage is the cost and board space savings, as well as the improved temperature stability from now having an AT-cut frequency error, of well under ±50 ppm versus 0 to –150 ppm for a z-cut tuning fork crystal. The biggest challenge though is to control the current consumption for this solution. The key is that the high performance phase noise is

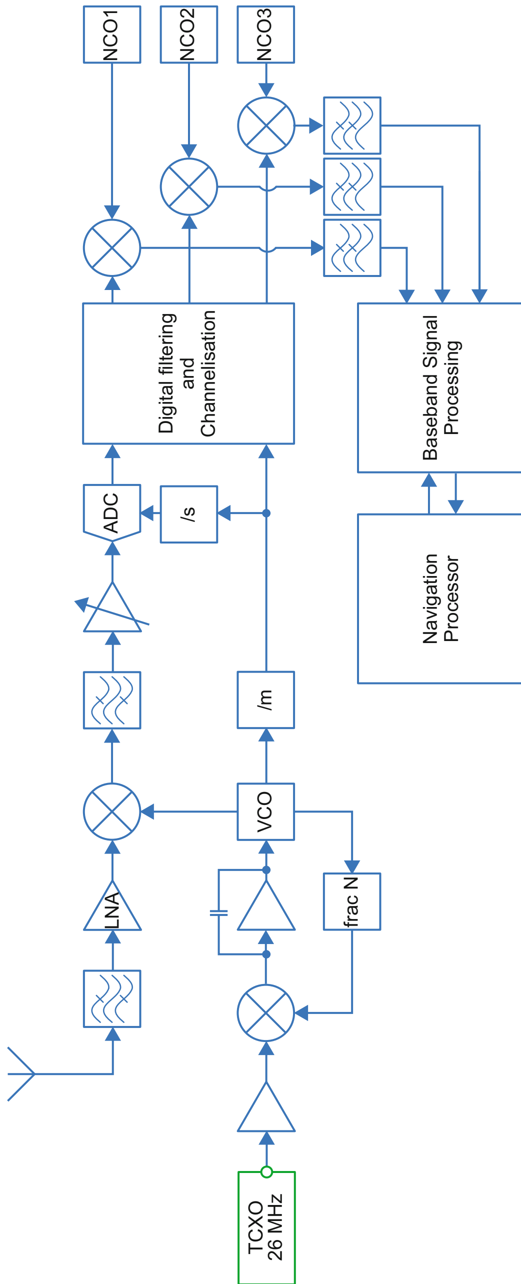

Fig. 15.3 Illustration of a generic TCXO-based GPS receiver implementation

only required during receiving or transmitting, so that the oscillator can be current starved to just support oscillation. As a result, the oscillator core current of for example 600 μA can be dropped to 50 μA. Typically dropping the current will affect the phase in the oscillator and hence there will be a systematic phase shift between operating in the low-power mode and high-performance mode that has to be addressed at the system level.

15.2 Significance of Acoustic Devices

From an integrated circuit stand-point requiring external timing components for a system to function has always been a nuisance. Since the 1920s with the rise of quartz crystal resonators being used as reference frequency component there has always been the quest for a circuit solution. Nevertheless, the initial accuracy, temperature stability and quality factor of piezoelectric resonators based on quartz where the only solution to solve the carrier synchronization problem encountered in wireless communication. In order for the receiving party to correctly demodulate a broadcasted signal it had to be able to regenerate the same carrier frequency. Almost 100 years later quartz resonators are still the preferred choice for most frequency references. In the meantime, quartz resonator technology has advanced tremendously in regard to initial frequency accuracy, frequency stability, size, availability, and cost.

15.2.1 The Significance of Resonator Q

The most common oscillator configurations encountered today are the Pierce and Colpitts configuration due to their simplicity, excellent short-term stability, and ability to support low power consumption. Stable oscillation occurs if the gain of the active circuit component is large enough to compensate for all losses, and the phase integrated around the loop is either a multiple of 360° or 180°, depending on whether the amplifier is non-inverting or inverting. These criteria are referred to as Barkhausen criteria. A resonator is best understood as a phase–frequency discriminator with a bandpass function. For the oscillator that means that it will have enough gain around resonance, but the phase condition determines at what frequency the oscillation occurs.

Assuming as an example that in steady-state oscillation the oscillator circuit without the resonator provides 350° of phase shift, then the resonator will provide the missing 10° of phase. If an additional phase perturbation $+\Delta\varphi$ is introduced into the oscillator loop then the resonator will compensate for this additional phase shift by operating at $10° - \Delta\varphi$. Figure 15.4 shows the admittance and phase of the impedance for two 26 MHz crystal resonators. Both resonators are identical in geometry, but for the difference in loss. As one can see from Fig. 15.4b the phase

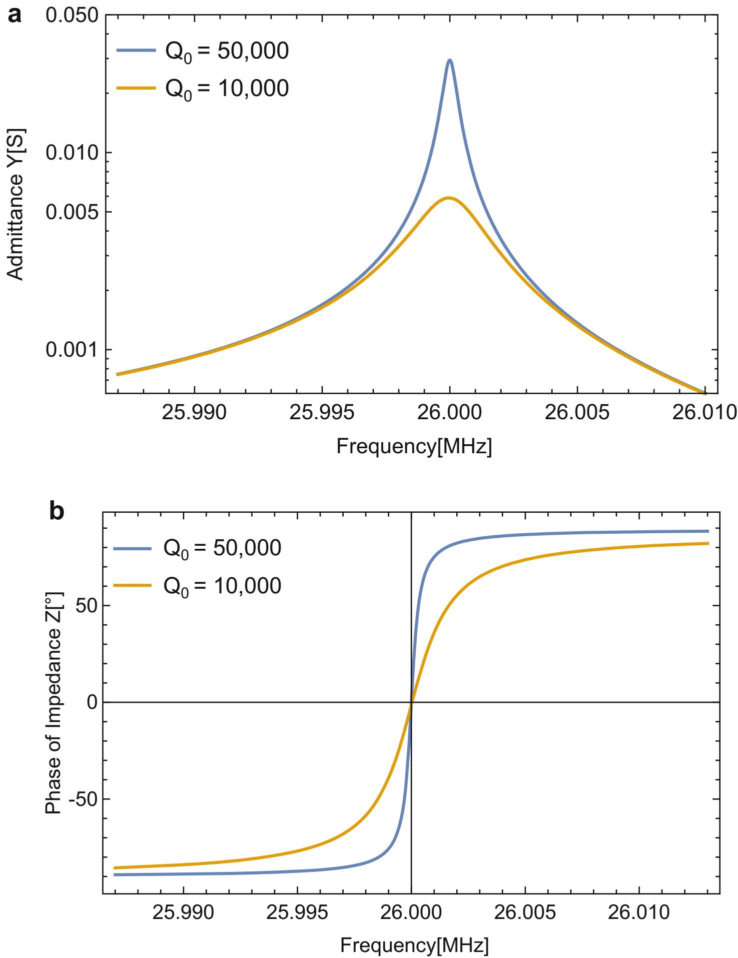

Fig. 15.4 Admittance and phase of the impedance of two 26 MHz crystal resonators with identical geometries, but different loss

slope is much steeper for the high Q resonator. The significance of the higher Q is apparent in regard to any phase perturbation introduced into the oscillator loop. As seen from Fig. 15.4b, the same $\Delta\varphi$ causes less frequency variation for the higher Q resonator. That means any noise or drift of circuit components affecting the phase of the oscillator, effectively a movement on the *y*-axis of Fig. 15.4b, will cause a smaller shift in frequency. That means, the higher the Q in the oscillator circuit, the more stable in frequency and phase the output will be. This is the key to later understand the importance of Q in regard to oscillator phase noise and why crystal oscillators can tolerate significant temperature variation of the circuit components.

It should be noted that when referring to the Q factor of a resonator it corresponds to the unloaded Q_0 factor. Once a resonator is "loaded" with surrounding oscillator circuitry the Q drops from Q_0 to Q_L. As a rule of thumb, the effective or loaded Q_L in the oscillator circuit is designed to be around half of the unloaded Q_0 [3].

15.2.2 What Is Preventing Us Today From Using an Integrated Circuit Solution to Provide Time and Frequency

The main reason why attempts to replace crystal oscillators with integrated solutions has failed is that the phase noise performance within 10 kHz of the carrier, as well as the frequency stability do not meet the requirements for wireless data transmission. The vast majority of wireless communication requires frequency stabilities of the carrier of at least ±50 ppm, and often as low as ±0.5 ppm. That means that the reference frequency component must be able to maintain this stability over a typical temperature operating range from −30 °C to +85 °C. The best LC-oscillators reported to date using on-chip temperature compensation claim to achieve ±100 ppm [4], which is not good enough. AT-cut quartz resonators (without oscillator circuit) can achieve ±15 ppm. Although, the circuit components that are part of any crystal oscillator circuit will possess large temperature dependencies the high quality factor of the quartz resonator component makes it insensitive to these changes, as discussed earlier.

15.3 Phase Noise in Oscillators

The phase noise $\mathscr{L}(f)$ of an oscillator is an important measure of its spectral purity and stability. Historically it was often referred to as the ratio of signal power contained within a 1 Hz bandwidth at a frequency offset from the carrier compared to the power of the main oscillation. This definition does not discriminate between the amplitude modulated (AM) noise from the phase modulated (PM) noise that we are after. This was addressed with a new definition in the IEEE Std 1139-1999 defining the phase noise $\mathscr{L}(f)$ as half of the double-sideband spectral density of phase fluctuations [5]. Predicting oscillator phase noise is quite challenging and depends mostly on good models describing the noise terms. An excellent reference is given by Rhode [6].

In literature the phase noise in oscillators is often estimated with Leeson's equation, e.g., [7], as

$$\mathcal{L}_1(f) = \frac{FkT}{2Q_L^2 P_{avg}} \left(\frac{f_0}{f}\right)^2$$

where Q_L corresponds to the loaded Q factor of the resonator, P_{avg} to the average power delivered to the resonator, F is the noise figure of the active circuitry, k the Boltzmann constant, T the absolute temperature, f_0 the oscillation frequency, and f the frequency offset from the carrier. The astute reader will have noticed the use of a factor of two in the denominator and not four. This is due to the use of P_{avg}, rather than the original incident power expression P_{inc} given by Leeson.

The Leeson equation is very powerful, but it neglects the power transfer through the resonator. This has led to misconception in parts of the MEMS community that ultimate resonator Q_0 makes for exceptional oscillator phase noise. Including the power transfer, we can rewrite Leeson's equation as:

$$\mathcal{L}_2(f) = \frac{FkT}{32Q_0^2(Q_L/Q_0)^2(1-Q_L/Q_0)^2 P_{avg}} \frac{(R_{out}+R_{in})^2}{R_{out}R_{in}} \left(\frac{f_0}{f}\right)^2$$

where R_{in} and R_{out} correspond to the input and output impedance of the oscillator circuit surrounding the resonator, and Q_L and Q_0 correspond to the loaded and unloaded Q factor of the resonator. Only for the special case of $Q_L = Q_0/2$ both expressions are identical. Replacing Q_L with

$$Q_L = Q_0 \frac{R_m}{R_m + R_{out} + R_{in}} \tag{15.1}$$

makes this even more apparent. Normalized phase noise of both expressions is shown in Fig. 15.5. W.l.o.g. we can set $R_{out} = R_{in} = Q_o = FkT = P_{avg} = f_0 = 1$, leading to the result shown below. It is evident that if there is a significant load mismatch of R_m to the circuit this will cause the phase noise to deteriorate. This is not captured in Leeson's original expression.

As we will see later any crystal oscillator also contains flicker noise introduced by the active circuitry. One other contributor less well known is the acoustic flicker noise in oscillators. Although the underlying mechanisms and theory are not fully understood a good empirical expression has been obtained for quartz bulk acoustic wave (BAW) resonators [8]. The understanding of flicker noise in regard to surface acoustic wave (SAW) resonators where a lot of work was done in the early 90s [9–11] and in MEMS resonators based on piezoelectric thin films is still very basic. What is known is that smaller devices exhibit higher flicker noise than larger devices, that acoustic flicker noise can originate from a quartz substrate or piezoelectric thin film itself, and that devices with less electrode coverage suffer less flicker noise, with the indication that the electrode material, its morphology and interface play a key role [9–11].

Applying the approach given by Parker [12, 13] we can include both the active and acoustic flicker noise term. For simplification we will replace the FkT/P_{avg} term with the variable NF, referring to the noise floor observed far from carrier. For the oscillator noise we can then write:

$$\mathcal{L}_3(f) = L_r L_{fr} + L_a (1 + L_{fr})$$

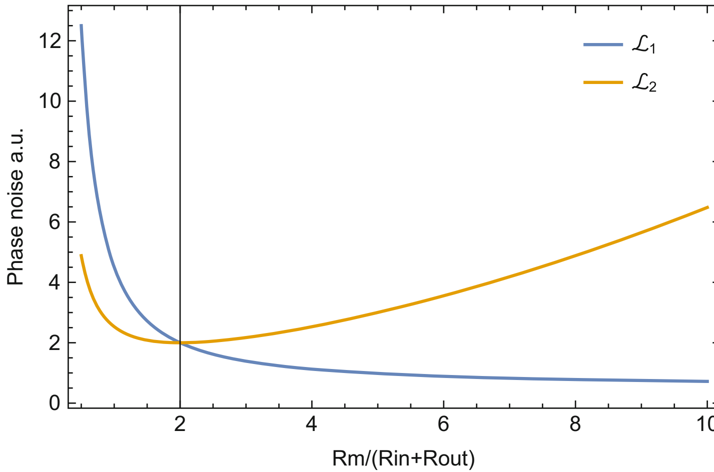

Fig. 15.5 Comparison of the normalized phase noise predicted by the adjusted Leeson's equation and the more rigorous expression including the impedance mismatch of the resonator element to the circuit

where

$$L_{\mathrm{fr}} = \frac{1}{32Q_0^2(Q_{\mathrm{L}}/Q_0)^2(1-Q_{\mathrm{L}}/Q_0)^2}\frac{(R_{\mathrm{out}}+R_{\mathrm{in}})^2}{R_{\mathrm{out}}R_{\mathrm{in}}}\left(\frac{f_0}{f}\right)^2$$

and

$$L_{\mathrm{a}} = NF\cdot\frac{f_{\mathrm{c}}}{f} + NF$$

where f_{c} corresponds to the flicker noise of the active circuitry. Similarly the acoustic flicker noise contribution according to [12] is given as

$$L_{\mathrm{r}} = NF\cdot\frac{f_{\mathrm{cr}}}{f}$$

where f_{cr} corresponds to the flicker noise of the resonator. The phase noise for an oscillator including the flicker noise from the active circuitry and acoustic component, using the Q_{L} expression Eq. 15.1 above is then given as:

$$\mathcal{L}_3(f) = NF\frac{(R_{\mathrm{in}}+R_{\mathrm{m}}+R_{\mathrm{out}})^4}{32Q_0^2R_{\mathrm{in}}R_{\mathrm{m}}^2R_{\mathrm{out}}}\left(\frac{f_{\mathrm{cr}}f_0^2}{f^3}+\frac{f_{\mathrm{c}}f_0^2}{f^3}+\frac{f_0^2}{f^2}\right)+NF\frac{f_{\mathrm{c}}}{f}+NF$$

This expression can be very useful in the reverse way to fit the terms to experimental data and understand the underlying limitations. This approach, quite fittingly has been referred to as "oscillator hacking" [14]. The sequence of fitting is to first match *NF* from the flat region or noise floor on a single sideband phase noise

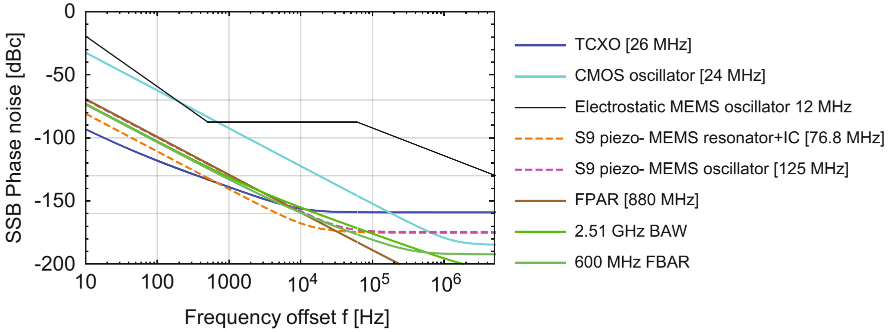

Fig. 15.6 Comparison of different oscillator technologies reported in literature fitted and scaled to a common 26 MHz frequency output, including a quartz crystal based TCXO [15], CMOS oscillator [16], electrostatic MEMS oscillator [16], piezoelectric AlN based MEMS oscillator [17–19], as well as BAW oscillators based on AlN piezoelectric thin films [20, 21]

measurement, for example taken with a Keysight E5052 signal source analyzer. It should be noted, that in rare cases the noise floor might be elevated due to a poor design of a subsequent buffer amplifier. The next step is to then fit iteratively the other terms under the best possible assumption that $Q_\mathrm{L} = Q_0/2$. This fitting procedure was applied to different resonator technologies. The phase noise was then scaled to a nominal output frequency of 26 MHz using the 20Log(N) conversion, resulting in Fig. 15.6.

First of all, it should be noted that the noise floor for all oscillators operating higher than 26 MHz has to be treated with caution, as the noise floor is typical limited by the IC technology and available power, so that during the down conversion according to the 20Log(N) rule the results are not physical. Comparing these results show that a CMOS oscillator solution can achieve excellent noise floor compared to the TCXO, but loses on the close-in phase noise due to the lack of the resonator Q, e.g., 20 for an LC oscillator and 50,000 for a TCXO. For a digital clock with low jitter a CMOS oscillator can be a good choice, as long as the high power requirements to achieve this noise floor can be supported by the application. Electrostatic oscillators are somewhat of a peculiarity in that they require digital compensation techniques to account for initial frequency offsets and temperature drift. Typically a lower frequency resonator of 5–52 MHz is used and a fractional-N (frac-N) phase-locked loop (PLL) is used to synthesize the output frequency with a very high precision. The strength of this solution is the versatility to provide any frequency in the 1–100 MHz range. The down-side is the elevated phase noise "hump" for electrostatic oscillators using frac-N PLLs in the 1–100 kHz range due to dithering of the dividers.

The more interesting observation of the phase noise data between 100 Hz and 1 kHz offset is that all technologies scale with $1/f^3$, except for the superior quartz resonators scaling with $1/f^2$ and the electrostatic MEMS scaling with $1/f^4$. It is hard to ignore that the close-in phase noise for all resonator technologies based

on aluminum nitride piezoelectric thin films, whether it be a bulk wave [20, 21] or plate wave device [17–19], is dominated by acoustic flicker noise. The source of acoustic flicker noise in AlN piezoelectric thin film resonators as well as in SAW resonators is still not understood. The reason why the close-in phase noise for the Sand 9 MEMS resonator is about 10 dB superior to other AlN based resonators is unclear. A possible explanation could be that the majority of the Lamb wave resonator stack consists of single crystalline silicon and thermally grown silicon dioxide, and that the acoustic energy stored in these layers is not affected as much as the energy stored in the electrodes and piezoelectric thin film. More trivial reasons for elevated phase noise levels are the electrical flicker noise of the amplifier, power supply noise, or poor noise figure. Nonlinear oscillators in principal can suppress the flicker noise from the active circuitry, due to the appearance of infinite acoustic Q at resonance. However, acoustic flicker noise is added by the resonator itself and as such does not benefit from nonlinearity.

In order to confirm the piezoelectric MEMS resonators as the source of the observed flicker noise a modern test bench based on the technique used to measure the passive phase noise in SAW oscillators reported for example in [22] was used. Figure 15.7 illustrates the equipment and setup used.

One of the repercussions of the significant acoustic flicker noise observed in the MEMS and FBAR based technologies is that the close-in phase noise scales at 30 dB per decade and not 20 dB per decade as found for high-Q quartz resonator based oscillators. This loss of 10 dB phase noise per decade is often a big challenge and one needs to ensure that the requirements of the targeted application can be met. As mentioned earlier, the close-in phase noise is of particular importance for GPS/GNSS applications. The in-depth evaluation of Sand 9's standalone MEMS resonators for GNSS applications performed by Integrated Navigations Systems Ltd. [23, 24] and cellular performance evaluated by Intel [25] has shown on-par performance with current crystal oscillators.

15.4 Historical Developments of the Sand 9 Piezoelectric MEMS Resonator

In the following section the historical developments, product and design decisions are introduced that lead to miniature timing solutions including a chip-scale packaged MEMS based VC-TCXO as well as a MEMS resonator with an integrated temperature sensor and heater for calibration.

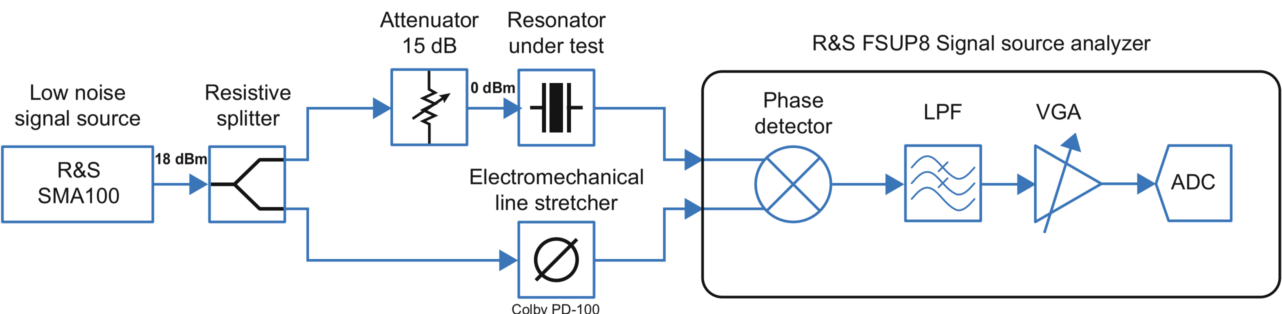

Fig. 15.7 Setup to measure the acoustic flicker noise in resonators. During the initial calibration the phase shifter is adjusted to obtain quadrature at the phase detector to mix out the carrier and obtain zero volt at the ADC. The phase fluctuations of a resonator inserted into the measurement branch cause deviations from quadrature and due to the linear relationship around the quadrature crossing produce a linear signal close to DC related to the acoustic flicker noise. All MEMS resonators tested exhibit a clear $1/f$ trend in the range of 1 Hz to 1 kHz before hitting the noise floor

15.4.1 Early Prototypes

Often new product ideas in MEMS arise out of research groups that have developed a pool of unit processes. These process modules can be leveraged to develop early prototype devices for a proof of concept and can be showcased with investors. This was the case at Sand 9, where first devices were fabricated at the clean room facilities at Boston University and later Harvard's Center for Nanoscale Systems. Thereafter, devices were fabricated at a smaller local foundry with the help of AlN deposition services provided by Tegal, and later OEM group. The first goal was to develop early resonator prototypes and to convince ourselves that cellular performance phase noise observed in simulation was indeed possible with resonators having unloaded quality factors below 3500. Early-on it became clear that any analog pulling capability of the resonator would degrade the phase noise performance, either by capacitively pulling the resonator away from its series resonance and hence higher motional resistance and degraded Q, or by introducing a phase shift in the oscillator, with a larger tuning range requiring a lower Q resonator, as explained below in more detail. Hence, the first goal was to reduce the linear temperature coefficient of frequency (TCF) of the resonator, as to reduce the total required tuning range of the frequency error over temperature from approximately 3000 ppm to less than 200 ppm. This passive temperature compensation was achieved with silicon dioxide that has the rare property of becoming stiffer with increasing temperature, and it had been used successfully for the thermal compensation in ZnO FBAR devices as early as 1981 [26]. In order to guarantee the long-term stability of the MEMS resonator frequency only materials that were considered stable and had high self-migration temperature were adopted in the resonator stack. To avoid instabilities from plasma enhanced chemical vapor deposited (PECVD) silicon dioxide, single crystal silicon was oxidized. In order to account for the large compressive stress in thermal oxide of about 300 MPa/μm, a symmetrically balanced structure was proposed. The layer stack of the resonator is illustrated in Fig. 15.8. A simple rectangular plate can support a vast number of acoustic modes. A mode referred to as symmetrical S0 Lamb Wave mode was chosen for the main operation. For the right plate width, this mode shows very low velocity dispersion with thickness changes in the stack, so that the reference frequency is not very sensitive to fabrication tolerances. This mode also provides significant electromechanical coupling of 0.5–3.5 % depending on the exact layer thicknesses. The single crystal silicon acts as mechanical support for the oxide early on in the process, but also enables very high acoustic Q in excess of 13,000 at 80 MHz. So far comparable Q factors in AlN based devices without silicon have only been observed for electrode-less resonators [27, 28], possibly due to the frequent use of Pt and Al, known for their viscous losses. One can argue that the theoretical electromechanical coupling factor of $k_t^2 \approx 3.5$ % for an S_0 Lamb wave propagating in a thin AlN plate is traded for a higher Q, as the $k_t^2 \approx 0.8$ % reduces for this more complex stack.

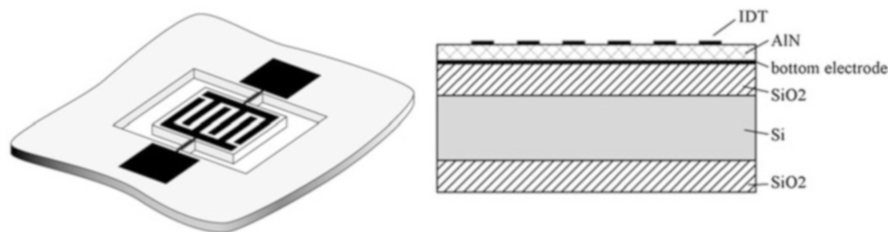

Fig. 15.8 Illustration of a simple 2-port Lamb wave resonator and cross section of the layer stack

As explained below in more detail, the AlN Lamb wave resonators were targeted to have a resonance frequency of 124.5 MHz. Figure 15.9a shows scanning electron microscope (SEM) images of very early 2-port resonators. The large extracted shunt capacitance $C_{0,1}$ and $C_{0,2}$ on the ports provided in Fig. 15.9c is due to the ground bottom electrode being unpatterned for these early devices and the use of rather large bondpads.

These early prototypes were assembled in standard ceramic leadless chip carriers (LCC) with wirebonding. These early devices had significant process imperfections, the deposition of the various layers was not optimized for stress and device performance, and the geometry was not ideal in regard to stress sensitivity, Q and spurious mode suppression. Nevertheless, based on pairing these early devices with discrete circuitry we were able to demonstrate best-in-class performance for MEMS oscillators, including phase noise performance, temperature stability, and power consumption [29] (Fig. 15.10).

The measured phase noise across the tuning range is shown in Fig. 15.11a. Across the tuning range of ±200 ppm a slight degradation of the phase noise of about 4 dBc/Hz at 1 kHz offset is observed. The worst case phase noise values at 123.9 MHz are −88 dBc/Hz at 100 Hz offset, −116 dBc/Hz at 1 kHz offset, −140 dBc/Hz at 10 kHz offset, and −151 dBc/Hz for the noise floor. Relating this to a 19.2 MHz reference, as commonly used in cellular transceivers today, results in −104 dBc/Hz at 100 Hz offset, −132 dBc/Hz at 1 kHz offset, and −156 dBc/Hz at 10 kHz offset, which is more than adequate for a cellular transceiver. To demonstrate the temperature compensating capability the frequency error over temperature was measured and the polynomial coefficients for compensation computed. Finally, with the compensation of the microcontroller turned on a temperature stability of less than 2.5 ppm was demonstrated over a range from −40 °C up +85 °C, Fig. 15.11c.

15.4.2 A Chip-Scale Package VC-TCXO Replacement Using Piezoelectric MEMS Resonators

With the initial proof of concept using discrete IC components and wirebonded MEMS resonators, we set out to develop a fully integrated solution. The biggest

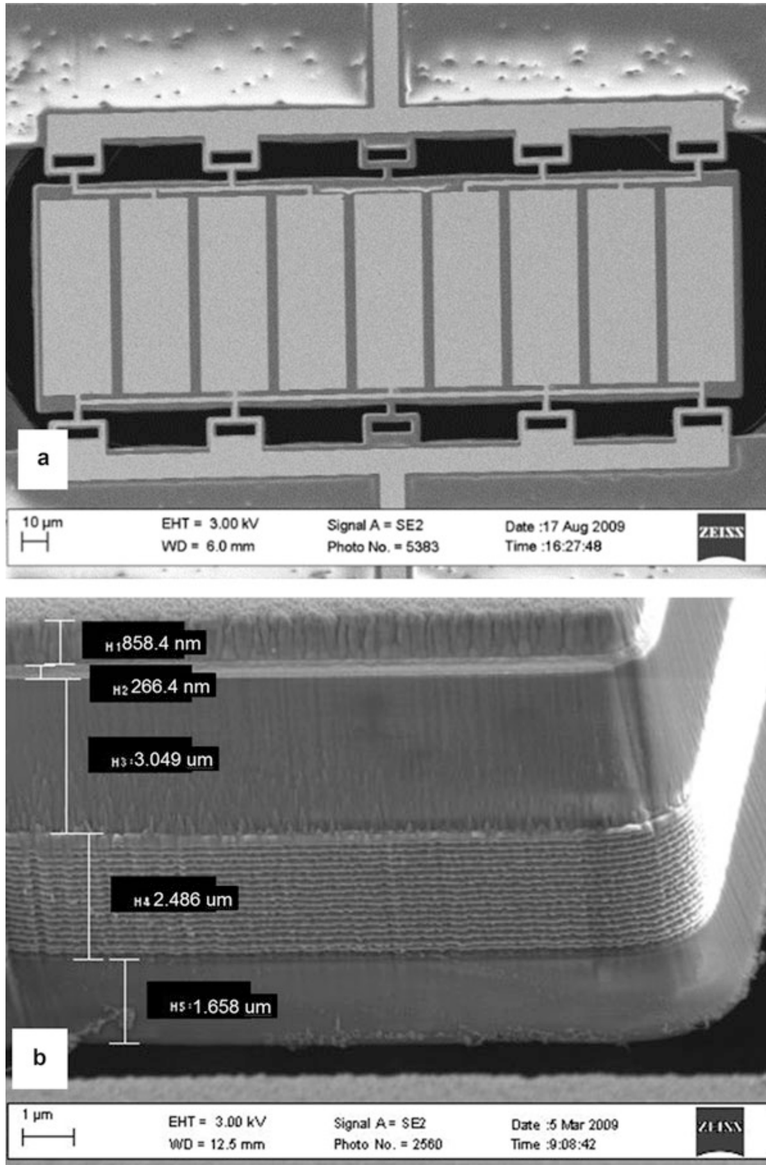

Fig. 15.9 Illustration of a very early 2-port Lamb wave resonator (**a**), and cross section of an early layer stack clearly showing the silicon device layer etched with DRIE, sandwiched between the temperature compensating silicon dioxide layers (**b**). The frequency response is shown across different frequency ranges showing good agreement with a basic BVD equivalent circuit model expanded to include shunt branches on the two ports (**c**), (**d**), and (**e**)

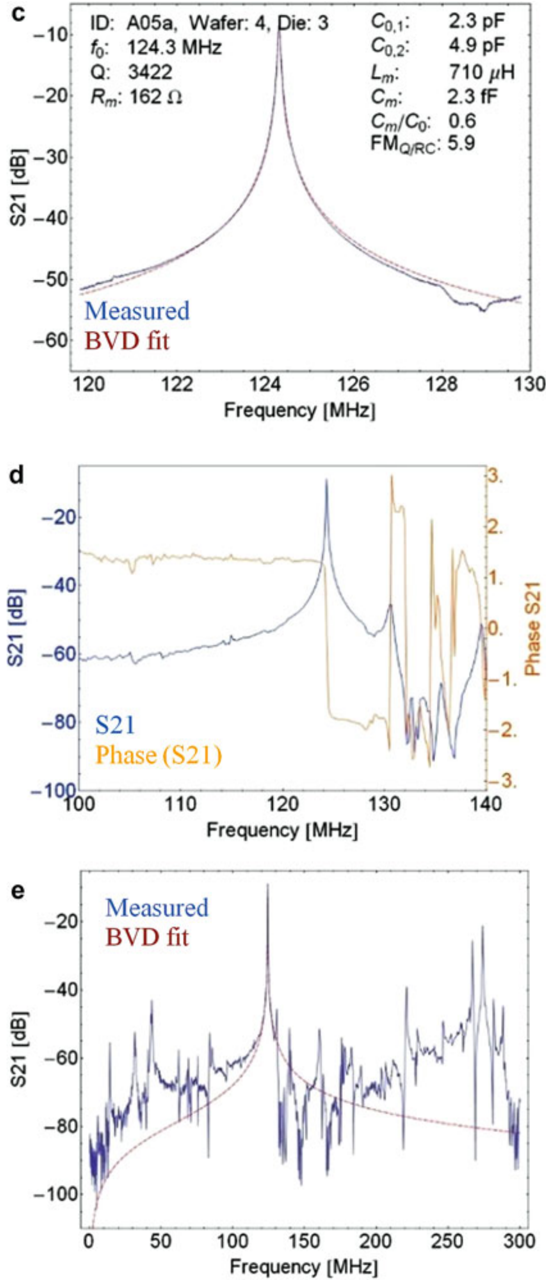

Fig. 15.9 (continued)

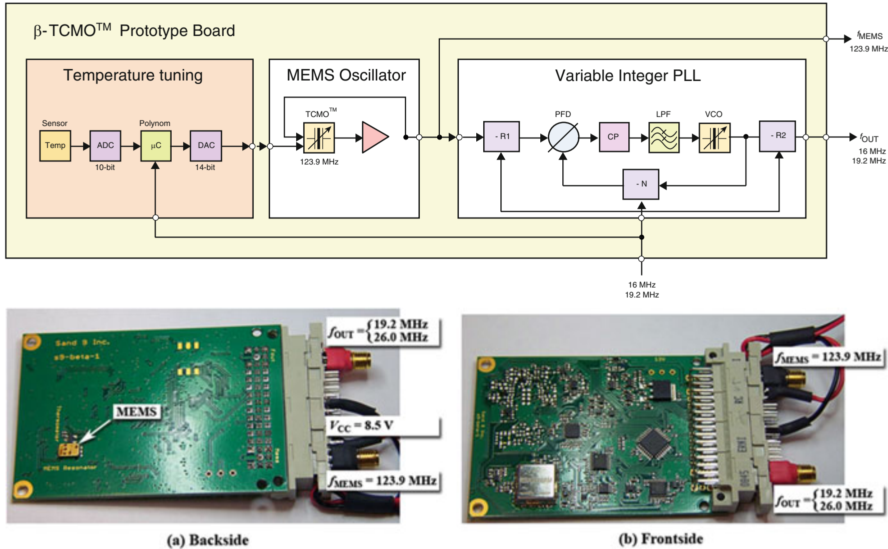

Fig. 15.10 Evaluation board (EVB) developed for the first 2-port temperature compensated MEMS resonators using a phase tuning technique as part of the oscillator. In addition the EVB contained a temperature sensor placed next to the LCC MEMS package, as well as a microcontroller to apply an analog polynomial compensation to the phase shifter in the oscillator. The board also contained a frequency synthesizer to produce an output frequency referenced to the MEMS oscillator with arbitrary frequency for the ease of customer evaluation

unknown was whether we could obtain similar performance in our ASIC compared to the high-end discretes used for the early prototypes. One of the biggest concerns was the introduction of noise within the IC into the oscillator loop. For the IC technology in order to balance low flicker noise and low power a 0.18 µm SiGe Bi-CMOS process was selected.

The fabrication process to build the chip-scale package MEMS oscillator is shown in Fig. 15.12. Originally this was a 6″ process that was later transferred to an 8″ tool set with some modifications. First, an engineered SOI wafer with built-in cavity is formed. One way is to oxidize an SOI wafer and bond this to a plain silicon wafer with a preformed cavity, resulting in (1). SOI device layer thickness uniformity, annealing, SOI handle wafer removal, as well as wafer edge quality are aspects to be considered. As for the TSV solution three different approaches were developed at three different foundries. Low resistance, planarity, as well as low RF parasitics are the prime challenges. In the early implementation on 6″ the backside routing and interconnects to the TSVs were formed early on, as shown in (3). This was still possible as 400 µm thick 6″ MEMS wafers can be readily processed without major yield impact. However, to support the trend of cellular transceivers going from 1.1 to 0.6 mm in height, the sequence needed to be changed to thin the MEMS wafer after bonding. The MEMS resonator (4) is formed by the deposition of the electrode and piezoelectric thin-film layers shown in Fig. 15.8. It is important

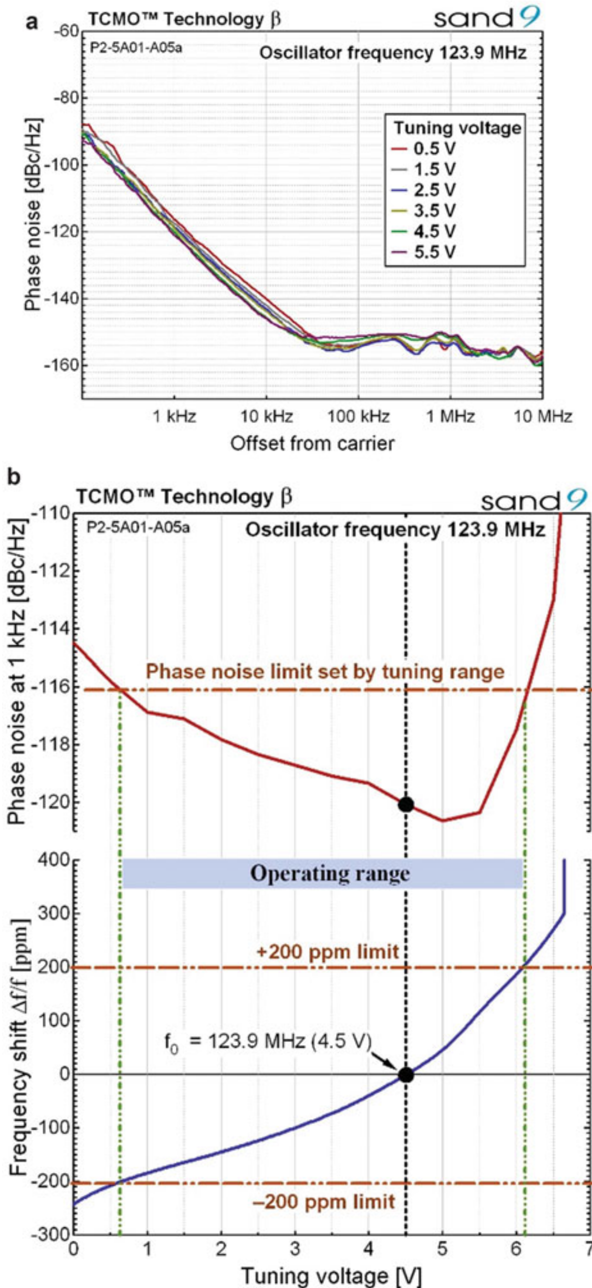

Fig. 15.11 (**a**) Measured phase noise versus tuning voltage of the first MEMS prototypes packaged in an LCC package, using an evaluation board with a discrete oscillator and microcontroller, shown in Fig. 15.10. (**b**) Phase noise variation across the ±200 ppm tuning range, showing a slight degradation. (**c**) Frequency error over temperature after calibration and active analog temperature compensation using a phase shifter controlled by the microcontroller

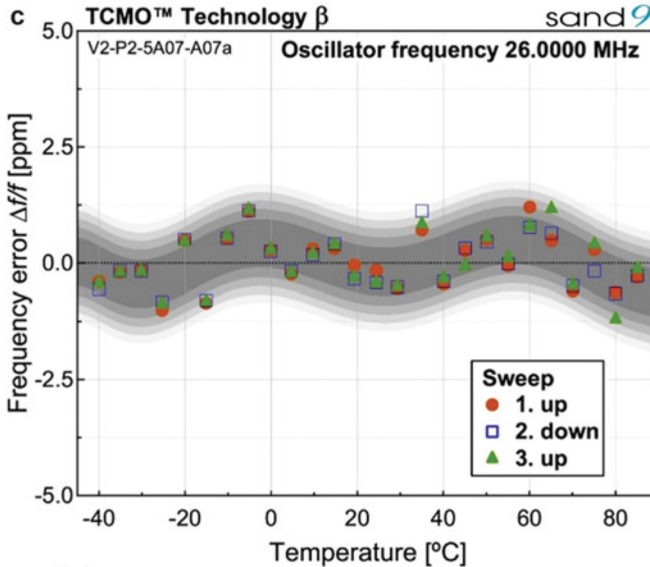

Fig. 15.11 (continued)

to control the stress of the different layers to avoid excessive bow of the membrane and cracking of anchor features during release. The stress control is readily achieved with deposition pressure and bias, keeping the thickness dependence in mind. The resonator is formed in a sophisticated dry etch chemistry releasing the suspended acoustic plate above the cavity. The hermetic seal and electrical interconnects are formed (5) by eutectic bonding. After bonding the IC wafer is thinned. Depending on the assembly technology CSP balls are formed on the backside after opening the routing layer and depositing suitable UBM metallization.

Later on, with the shift of the industry to using only a quartz resonator and having the oscillator circuit integrated into the cellular transceiver or connectivity solution, the same process was leveraged to fabricate "resonator-only" CSP die. Instead of bonding to an IC wafer a silicon dummy wafer is used as a cap for the resonator wafer.

The first product that the engineering team at Sand 9 worked on was a cellular grade VC-TCXO. Early 2008 quartz based cellular VC-TCXOs would feature about ±2.5 ppm frequency stability over temperature, consume around 3.5 mA of current and would sell in very high volume in a 2.5 mm × 2.0 mm package for more than $0.50 (Fig. 15.13).

The decision early on was to accept the manufacturing spread of the initial frequency of ±10,000 ppm and to assume that the customers would be able to compensate for the initial offset with a one-time calibration. 124.5 MHz was chosen for the initial frequency of the MEMS oscillator, because detailed analysis by Juergen Schoepf and Reimund Rebel revealed that the spurious frequency content in the local oscillator (LO) generated by using a frac-N PLL in the cellular transceiver would be uncritical for all common cellular bands. This analysis was

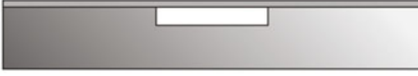

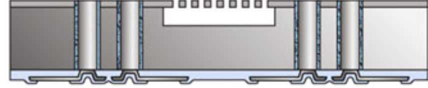

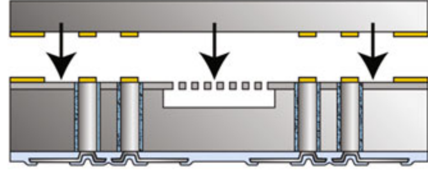

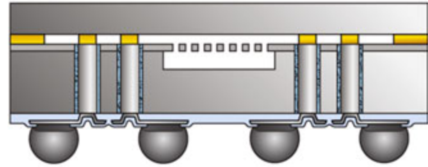

Fig. 15.12 Simplified fabrication process used for the chip-scale packaged MEMS VC-TCXO

rather sophisticated as it took all higher harmonics into account, as well as the ±10,000 ppm spread of the oscillator. At the same time, the higher reference frequency would provide a better phase noise performance in the system due to a higher comparison frequency at the phase–frequency discriminator (PFD) in the PLL. It was estimated that the use of a 124.5 MHz oscillator over a 19.2 MHz oscillator would provide a 8.1 dB improvement due to the reduced up-conversion of the white noise at the PFD. Going to even higher frequencies, i.e., beyond 130 MHz leads to an overall penalty due to the performance degradation inherent to typical CMOS PFD implementations.

The voltage tuning capability of the TCXO is important for the transceiver to be aligned to the carrier frequency. Typically VC-TCXOs would have a tuning range between ±8 ppm and ±13 ppm. This tuning as well as any temperature compensation that occurs within the VC-TCXO must be analog, to avoid any phase or frequency discontinuities that would prevent successful cellular data transmission (Fig. 15.14).

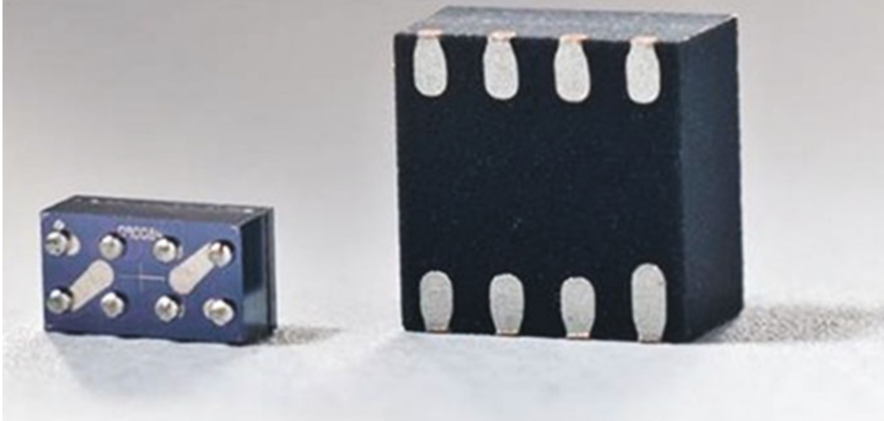

Fig. 15.13 Miniature chip-scale packaged MEMS VC-TCXO in 1.5 mm × 1.1 mm × 0.5 mm form factor (**a**). The form factor for a 2.0 mm × 2.0 mm × 0.9 mm dual-flat no-leads (DFN) package containing the CSP die is shown in (**b**)

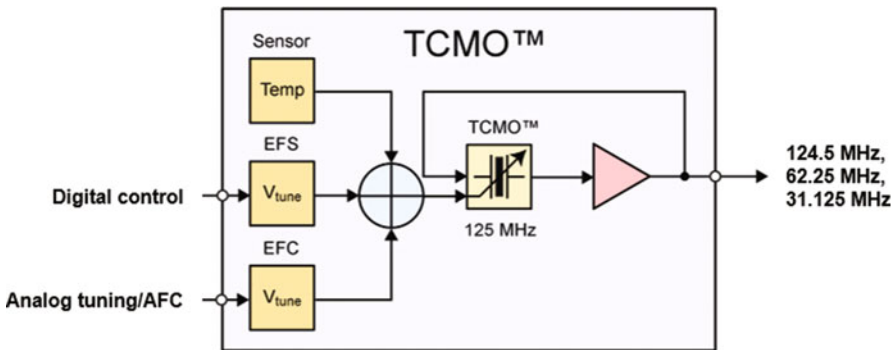

Fig. 15.14 Block diagram of the MEMS solution to replace VC-TCXOs. The temperature compensated MEMS oscillator (TCMO) contains a temperature sensor followed by an analog temperature compensating circuit to compensate for the temperature dependence of the MEMS resonator. In addition, a voltage control for carrier synchronization is provided. The TCMO further supports a digital 2-wire bus that can be used to program a frequency offset into the part, as well as set a binary divider to divide-by-2, and divide-by-4

15.4.3 Piezoelectric MEMS Concept for a 125 MHz VC-TCXO

The oscillator tuning concept was based on using the resonator as a phase–frequency discriminator, so that additional phase shift introduced by the IC in the oscillator loop would be compensated for by the resonator and hence cause a resulting frequency shift. This is illustrated in Fig. 15.15a.

As seen from Fig. 15.15 the tuning range is inversely proportional to the loaded Q_L of the resonator, i.e., the wider the resonance peak or its 3 dB bandwidth,

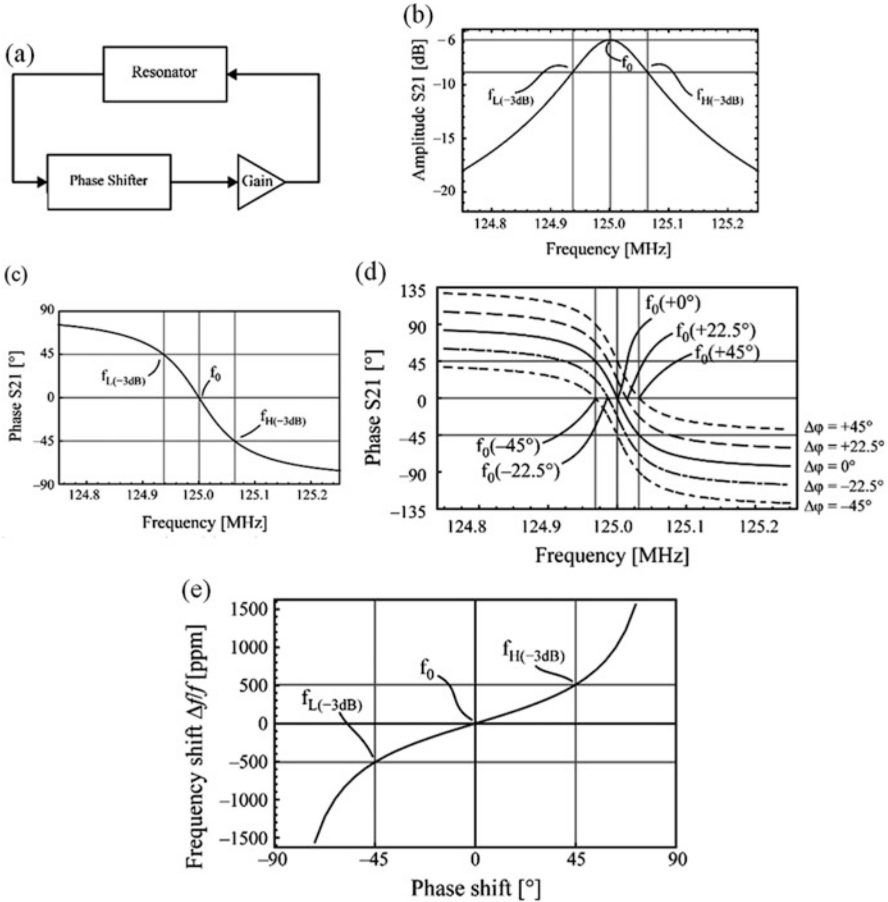

Fig. 15.15 The block diagram of a phase-tunable oscillator is shown in (**a**). The amplitude characteristics of the MEMS resonators are shown in (**b**). The phase relationship for the MEMS resonator is shown in (**c**). Assuming a phase shift of 0° of the resonator at resonance and 0° phase shift of the amplifier in (**a**), according to the Barkhausen criteria the circuit will cause oscillations at the resonance frequency of the MEMS resonator, if the amplifier has enough gain to compensate for all losses in the loop. The phase condition for the initial oscillation is shown in (**d**), together with the cases where the phase shifter introduces an additional phase shift in the loop. The introduction for example of +22.5° of phase shift by the phase shifter, due to the Barkhausen criteria will force the MEMS resonator to operate at −22.5°, resulting in a frequency shift according to the phase–frequency relationship of the resonator, shown in (**c**). The effective tuning relationship is shown in (**d**)

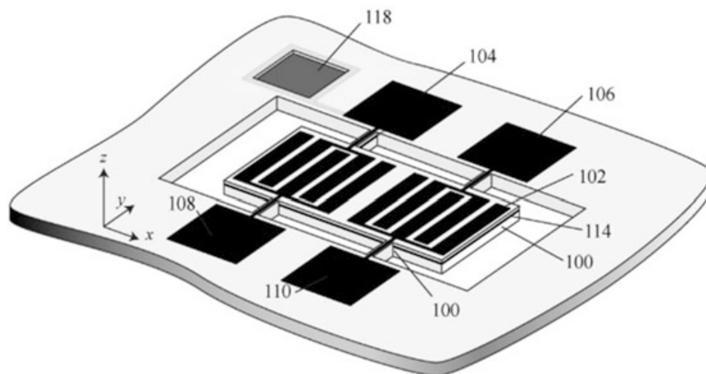

Fig. 15.16 Illustration of a 4-port piezoelectric thin film resonator with a common ground electrode, designed for excitation of the S_0 mode

the further it can be pulled for a ±45° phase shift. That meant to cater for the temperature variation in the MEMS resonator and the external VC pulling range a minimum tuning target of ±200 ppm was set. Assuming a phase tuning range of the IC of ±45°, this equates to the 3 dB bandwidth of S21 and results in Q_L to not exceed 2500. Following the rule of thumb from above that for best phase noise performance the unloaded resonator Q_0 should equal twice the loaded Q_L, the resonator Q_0 was not to exceed 5000. To account for manufacturing variations of Q the target Q_0 was set to 3500. Back in 2008 the general perception was that it would be impossible to meet cellular performance with such low Q_0. The MEMS community thought that in order to achieve the GSM cellular phase noise target of −130 dBc/Hz at 1 kHz offset for a 13 MHz carrier one would need Qs in the 100,000–1,000,000 range. However, in-depth harmonic balance simulations suggested that we should be able to meet cellular performance even with such moderate Q. In order to suppress common mode noise in the oscillator, a differential oscillator concept was chosen, which meant that a 4-port MEMS resonator was needed (Fig. 15.16).

A simple sagittal plane simulation based on a Green's function based model for the 4-port plate wave resonator to compute the transfer function in shown in Fig. 15.17.

As can be seen the symmetric structure shows excellent suppression of the common mode at resonance. The antisymmetric modes occurring around 0.875 and 1.125 of the normalized frequency in Fig. 15.17 have a phase of 180° and hence despite their low insertion loss do not support oscillation.

The impedance of the resonator is matched to the circuit requirements with the number of electrodes and aperture. It should be noted though that for the design of the resonators the Lamb wave dispersion in the transverse direction has to be taken into account, and hence a 3D FEM simulation is required to avoid spurious modes. One of the main challenges is that the A_0 mode is also excited in this structure

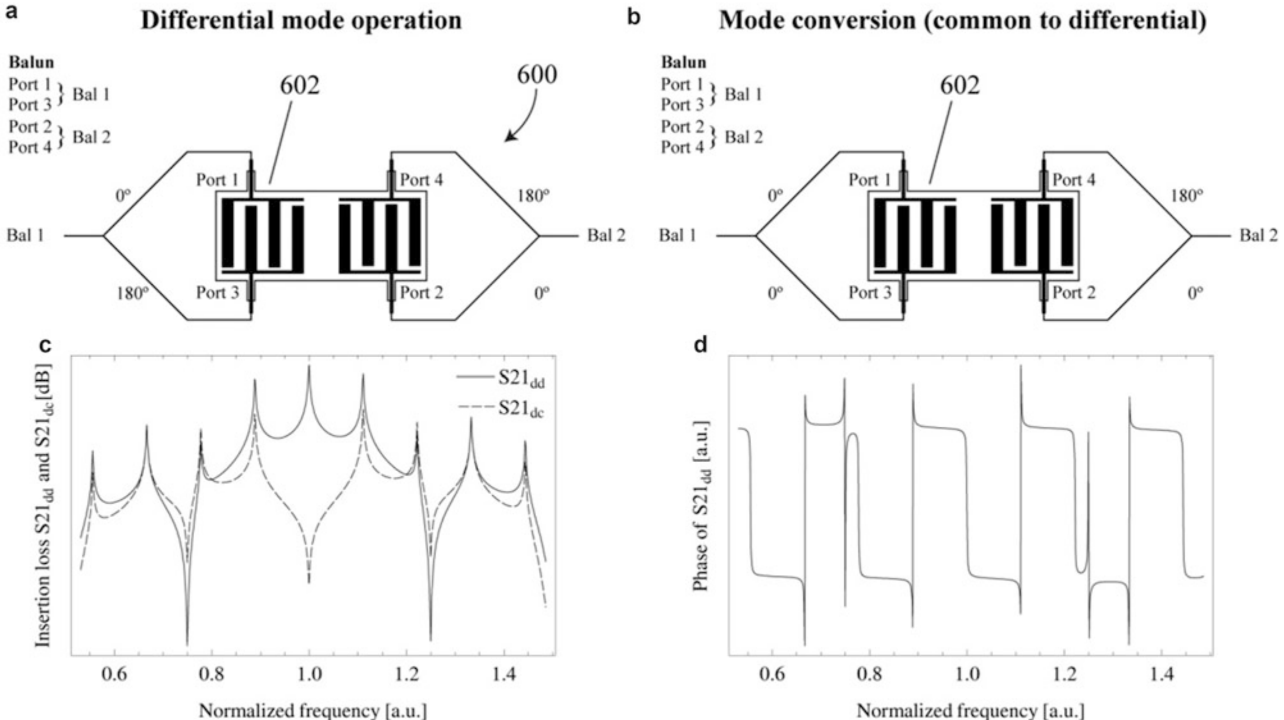

Fig. 15.17 Illustration of a 4-port piezoelectric thin film resonator with a common ground electrode, designed for excitation of the S_0 mode. The two configurations show the operation of the differential mode excitation and its resonance, as well as the excellent suppression when feeding the resonator with a common mode signal. The key is the symmetric layout of the IDT on the input port

having the same wavelength. Due to the phase velocity of the A_0 mode being about four times lower than the S_0 mode for this stack, unwanted oscillation at ≈30 MHz can occur. In order to provide the required tuning range, the resonator Q_0 has to be artificially clamped to 3500 by designing the anchors to be lossy. The answer to use a multitude of anchors to limit the Q_0 of the S_0 mode and at the same time suppress the A_0 mode due to the torsional displacement on the anchors for the A_0 mode seems straight forward. However, the anchors are also the key mechanism to transduce package stress into the acoustic resonator. Initial axial loading estimations used to justify the first design turned out to be insufficient and more complex 3D FEM simulations on the final package geometry were necessary. It turns out that external axial stresses paired with package warpage, due to soldering or die attach give rise to much higher internal loads. Early resonator designs with ten anchors displayed ±10 ppm frequency shifts using a 3-point bending setup with 90 mm spaced anvils and a center displacement of ±1 mm. Careful redesign reduced the stress sensitivity by a factor of 100, enabling a true package-insensitivity, required for any type of co-packaged oscillator product.

Figure 15.18a shows an early resonator design after removing the capping CMOS circuit. The frequency error over temperature for the differential resonator is shown in Fig. 15.18c. Due to process variation of the layer thicknesses a frequency tuning range of −160 ppm to +15 ppm needs to be catered for. As the oscillator circuit was designed to supply ±200 ppm of tuning range there was no need to reduce the spread of the variation over temperature of the oscillation frequency with the assistance of ion beam trimming. This simplified the process, its cost and throughput with a reduced need for metrology and trim equipment.

In order to provide a circuit description for improved oscillator IC design a Verilog-A model was developed on the basis of a closely matching 4-port BVD model, shown in Fig. 15.19. The model consists of six acoustic branches that are all identical in case of a symmetric plate design. The shunt branches, containing a series resistance and capacitance, are related to the capacitance between the port traces and the underlying device silicon layer being grounded, as well as the static capacitance of the electrodes to the ground plane underneath the AlN layer. The small resistance term is due to the silicon device ground plane.

An effective fitting routine was developed to extract circuit models from wafer level RF probe data. The resulting fit provides a close match around resonance, as shown in Fig. 15.18. This enabled the effective simulation and optimization of the oscillator circuit.

The concept of the analog oscillator tuning is described in Fig. 15.20. At its core it involves taking the differential output signal of the resonator and creating two vectors that are 90° out of phase. These vectors are then weighted and added, resulting in an effective phase ranging from 0° to −90°. With appropriate design of the phase around the oscillator loop contributing +45° of phase, the desired phase control in the range of ±45° is enabled. An early circuit implementation is shown in Fig. 15.20b, the center tapped RC input impedance creates the two phase vectors that are weighted with the current source of the two differential stages, resulting in an effective phase shift through the circuit.

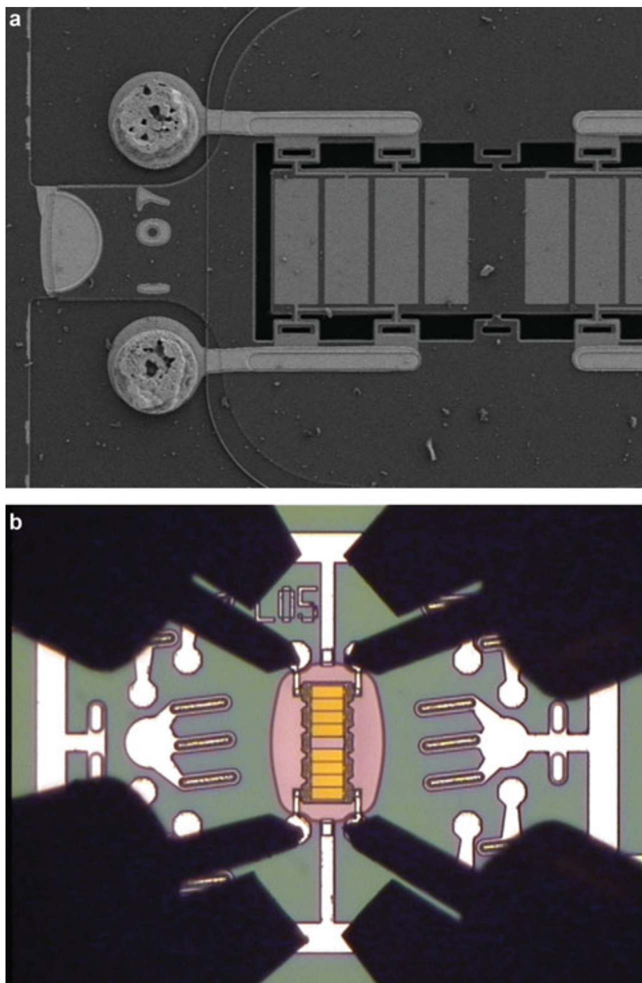

Fig. 15.18 (**a**) Early 125 MHz resonator designs after removing the CMOS capping die. (**b**) Microscope image of differential on-wafer level 4-port GSSG-GSSG probing. (**c**) Frequency error over temperature for the differential S0 MEMS resonator. (**d**) Narrowband differential RF measurement $S21_{dd}$ of the MEMS resonator (using ports 1 and 3 as input, and ports 2 and 4 as output). (**e**) Wideband $S21_{dd}$ measurement including the adjacent antisymmetric modes that have their phase crossing at 180° and do not cause oscillation. The *dashed line* corresponds to a best fit of a 4-port BVD model, introduced below

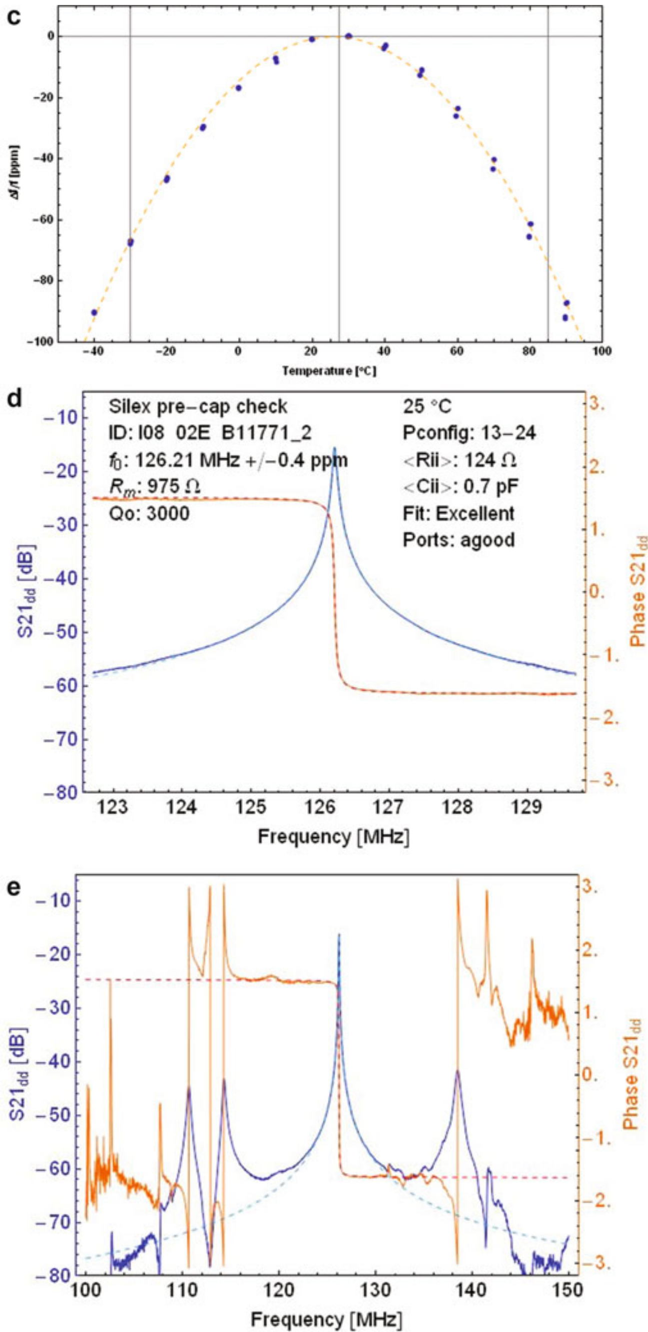

Fig. 15.18 (continued)

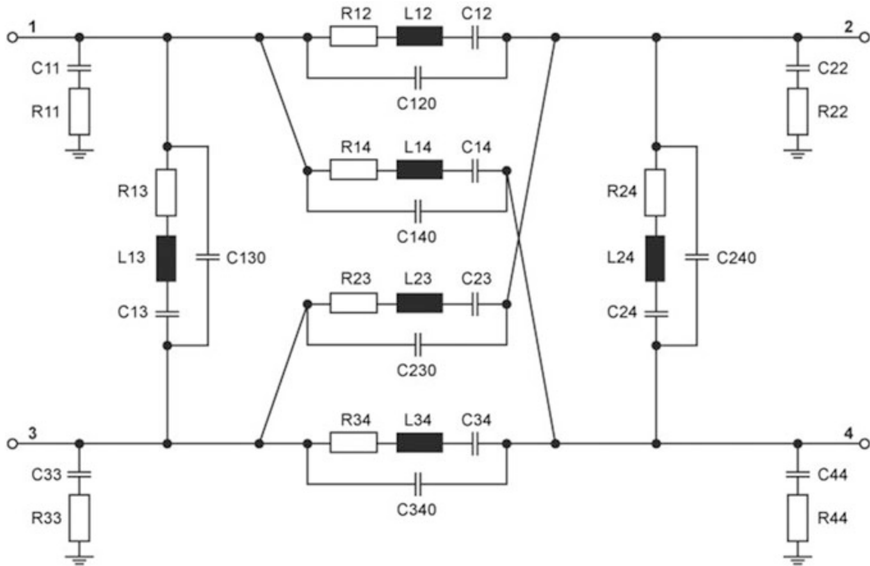

Fig. 15.19 Four port equivalent circuit model closely describing the differential MEMS resonator around resonance

The temperature compensation is achieved by generating a control voltage for the differential stages based on an analog computing function. Rather than resorting to an analog implementation of a polynomial function a more advanced circuit was developed [30] (Fig. 15.21).

As already mentioned thermal oxide with its unique positive temperature coefficient of stiffness is used to compensate for the large negative temperature drift in the Lamb wave resonator inherent to the other materials used in the stack. As seen from Fig. 15.18 despite having a zero first order temperature coefficient of frequency, a strong second order residual remains. In addition to a negative first order characteristic of the stiffness over temperature for most materials, a strong second order characteristic is also observed. For silicon this behavior is well known [31], whereas resonators purely based on AlN and SiO_2 also display a strong second order term [32].

The typical frequency error over temperature normalized to 25 °C for the developed stack at 124.5 MHz determined from measurements is given by

$$\frac{\Delta f}{f} = TCF1 \cdot \Delta T - 0.022 \cdot \Delta T^2 + 5.28 \quad 10^{-6} \cdot \Delta T^3 \text{ [ppm]}$$

where ΔT is the temperature difference to 25 °C, and TCF1 corresponds to the linear first order coefficient determined by the process stability. A typical range for TCF1 without trimming or other extraordinary measures is less than ±1 ppm/K. The third order frequency error over temperature amounts to ±1.5 ppm from −40 °C to +85 °C. It is very stable and appeared to be independent of the thickness

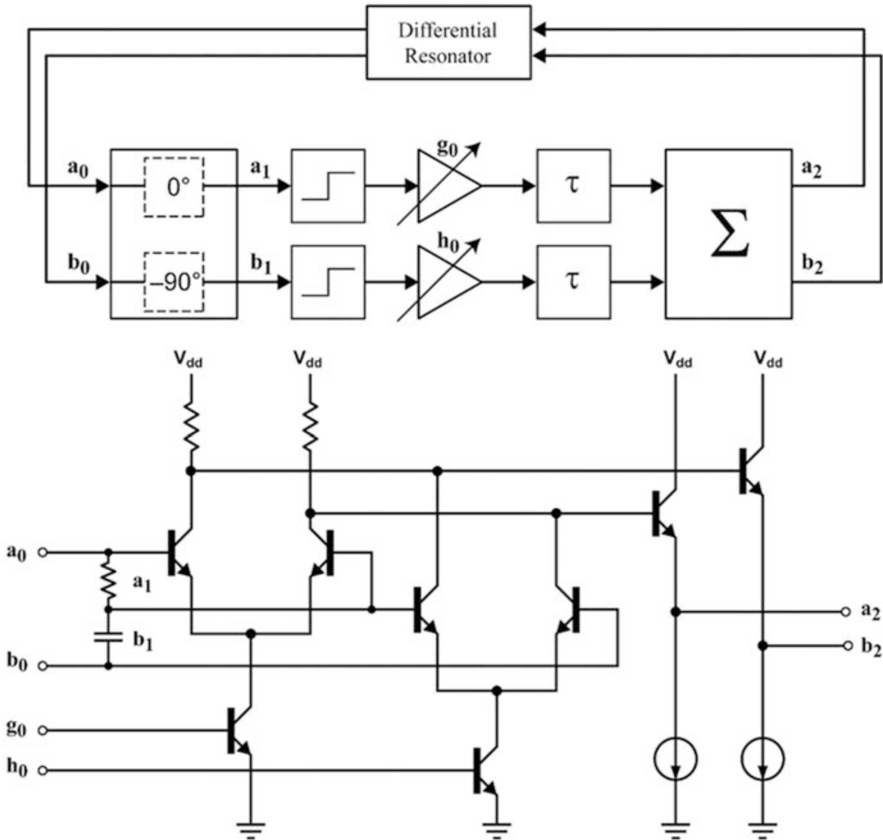

Fig. 15.20 Differential oscillator tuning circuit developed for the AlN MEMS based VC-TCXO. The RC-phase splitter creates two signals that are 90° out of phase and can be weighted according to signals g_0 and h_0. As a result, the phase of the differential output signal a_2, b_2 can be tuned ±45°

variations. For the V_{tune} temperature compensating circuit the third order error is not specifically accounted for with a third order term. However, it is mitigated with an additional linear term that is applied at negative temperatures.

For a typical TCXO calibration the oscillator is ramped over temperature and a suitable compensation function is programmed to the oscillator. It is then once again tested over temperature to assure that the frequency error over temperature for the TCXO meets the specifications, i.e., less than ±2.0 ppm.

In order to reduce the test time and cost associated, as well as to enable the MEMS VC-TCXO to be tested and calibrated at an Outsourced Semiconductor Assembly and Test facility (OSAT), this novel tuning circuit was developed. It has the unique property that it is calibrated during the actual measurement and no second test is required to confirm the accuracy. As such the entire MEMS VC-TCXO is

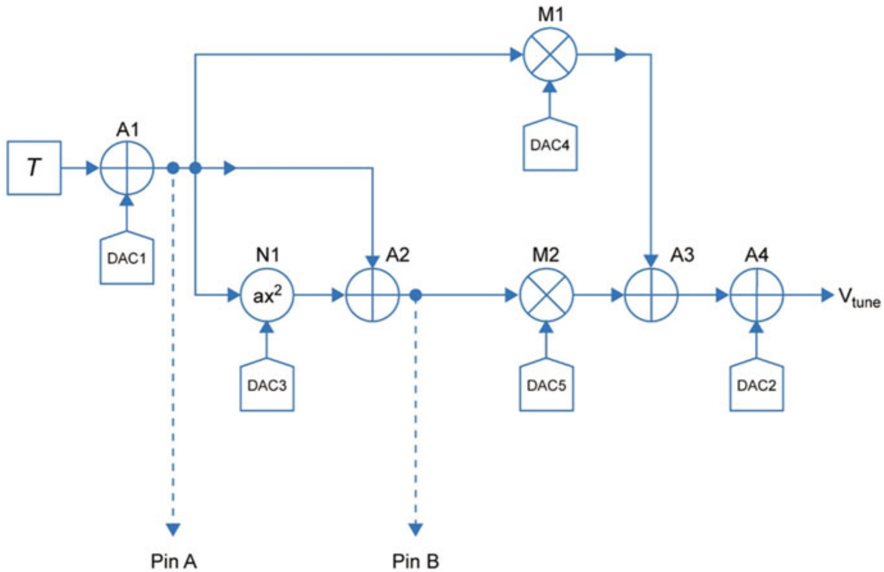

Fig. 15.21 Analog circuit generating the phase tuning voltage for frequency compensation over temperature. This second order polynomial compensation function is fundamental to the MEMS VC-TCXO

compensated with tests at three different temperatures, without the need for lengthy in-oven testing. The details of the calibration sequence are found in [30].

The first order challenges for this implementation are to ensure a stress insensitive MEMS resonator design in combination with a low clamped Q_0. The linearity of the tuning and of the temperature sensor in the circuit must be ensured. Last, because the implementation relies on phase tuning the oscillator, any noise introduced into the tuning signal V_{tune} will directly modulate the oscillator, causing phase noise deterioration. This is avoided with a low pass filter on the phase tuning port that is designed to still be fast enough to provide compensation during large thermal ramp rates. The frequency error over temperature is shown in Fig. 15.22.

The start-up time of the oscillator is shown in Fig. 15.23. Achieving this extraordinary fast start-up time despite the low pass filter on the tuning port is not straightforward and requires a unique circuit solution [33].

The measured phase noise of the CSP MEMS oscillator is shown in Fig. 15.24. It displays a $1/f$ characteristic between 1 and 10 kHz, as well as a characteristic $1/f^3$ behavior between 100 Hz and 1 kHz. As explained earlier this is due to the acoustic flicker noise in the MEMS resonator. For offsets smaller than 100 Hz the noise introduced in the phase tuning circuit dominates and causes almost a 50 dB/decade increase in phase noise to the 10 Hz offset.

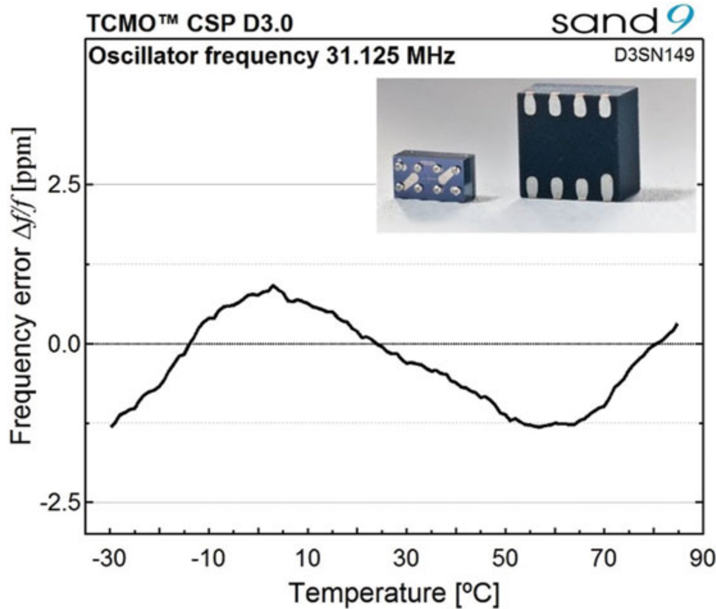

Fig. 15.22 Frequency error over temperature for the miniature 124.5 MHz CSP MEMS VC-TCXO, with the internal frequency divider set to four

15.5 Integrated MEMS Resonator

In 2008 in an effort to reduce cost, the wide use of VC-TCXOs for cellular applications was rethought. The idea was to purchase low cost packaged quartz crystals and provide the oscillator circuitry and temperature compensation as part of the cellular transceiver IC. As a result, the interest in an MEMS VC-TCXO dropped and instead there was a strong pull for a miniature MEMS resonator that would be compatible with this new approach and would lend itself to co-packaging. In 2011 the first efforts began working with the Intel cellular team to develop the world's first System in Package (SiP) cellular transceiver with an integrated frequency reference [34]. This transceiver did not require additional quartz crystal (Xtal) based frequency references and led to the realization of the first modem to rely solely on a MEMS resonator as the frequency source. The transceiver IC designed in a 65 nm CMOS process was initially designed to support a 26 MHz Xtal resonator and was modified to support the use of a 76.8 MHz chip-scale packaged (CSP) MEMS resonator (Fig. 15.25).

The trend in mobile and connectivity solutions over the past years has been to reduce the number of reference frequencies, as well as the overall number of discrete reference frequency components by sharing the frequency between different functional blocks. Furthermore, the goal has been to move away from expensive high-stability temperature compensated crystal oscillators (TCXO) and

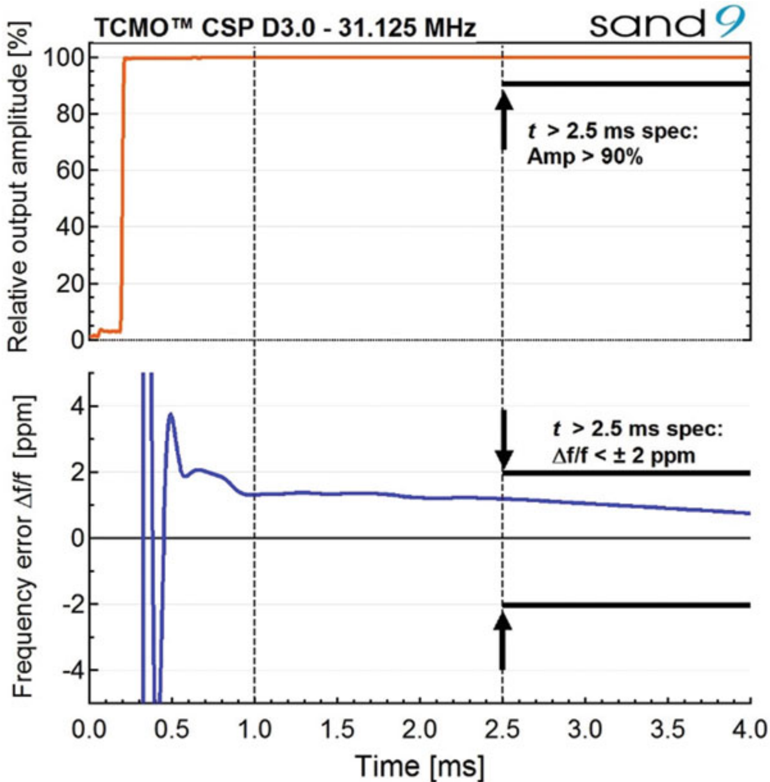

Fig. 15.23 Start-up time of the miniature MEMS VC-TCXO, showing exceptional frequency accuracy already after 1 ms

to use simple Xtals instead. This has had several repercussions. With consolidating frequency references the expectations in regard to their performance has increased. It is driven by the most stringent system requirements, typically GPS/GNSS on the close-in phase noise and overall frequency stability, as well as cellular/WiFi on the far-out phase noise. To meet the stringent frequency stability requirements over temperature the Xtal resonator frequency is compensated with the information from a temperature sensor, either integrated into the Xtal package or from a discrete external temperature sensor. The clear cost advantage is offset by the need to perform the temperature calibration, offset calibration, learning algorithms and active temperature compensation on the component manufacturer's side. However, as it provides full control over the frequency compensation over temperature, there is a potential to exceed the stability of a ±0.5 ppm TCXO. Despite the ability for better performance, related product differentiation and cost reduction, only few commercial solutions exist in the market today that have surpassed the technical challenges of a Xtal based implementation. The biggest obstacle has been the temperature estimation uncertainty during thermal transients, as they frequently

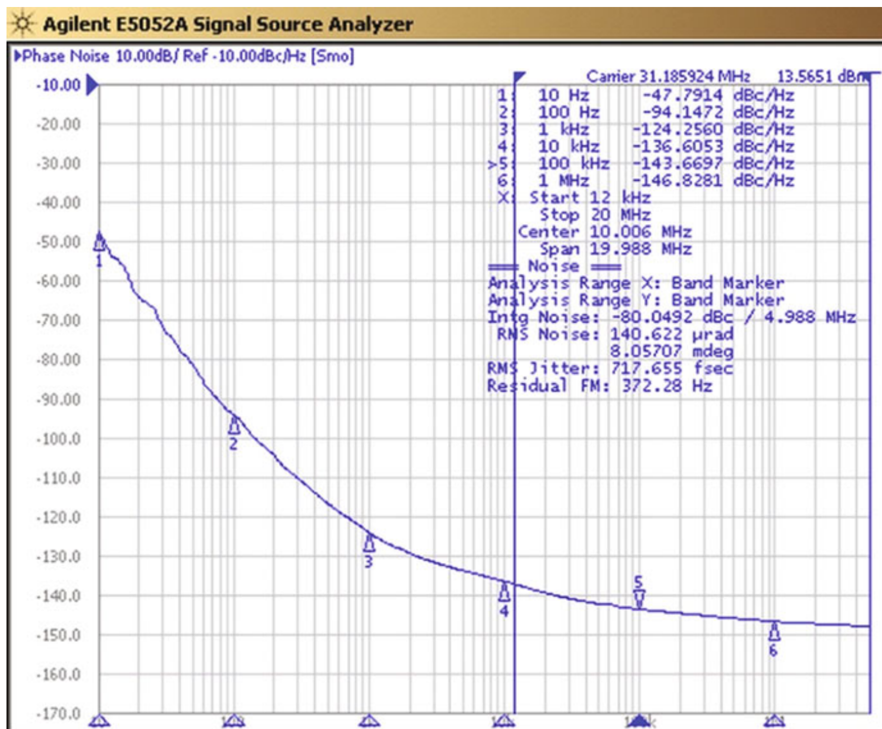

Fig. 15.24 Measured phase noise of the CSP MEMS VC-TCXO. Displaying less than −130 dBc/Hz at 1 kHz offset when referenced to 13 MHz

occur in phones or tablets. The estimation challenges arise due to the time lag between sensor and resonator, as well as their geometric separation.

The 76.8 MHz MEMS resonator used in this work was designed to overcome this challenge. The CSP MEMS resonator replaces the Xtal resonator and the temperature sensor by offering an integrated temperature sensor with a thermal response that is 2–3 orders of magnitude faster than integrated TSX or discrete Xtal and temperature sensor solutions. The integrated MEMS approach enables close prediction of frequency correction in the most challenging thermal environments.

15.5.1 Integrated Cellular Transceiver

The Intel transceiver IC was based on a commercially available 65 nm CMOS multi-band HSPA+/EDGE/GPRS solution. Circuit modifications were performed to support a MEMS resonator operating at 76.8 MHz instead of a 26 MHz Xtal resonator. The 76.8 MHz piezoelectric MEMS resonators were fabricated in Sand 9’s aluminum nitride MEMS process provided by GlobalFoundries. The MEMS

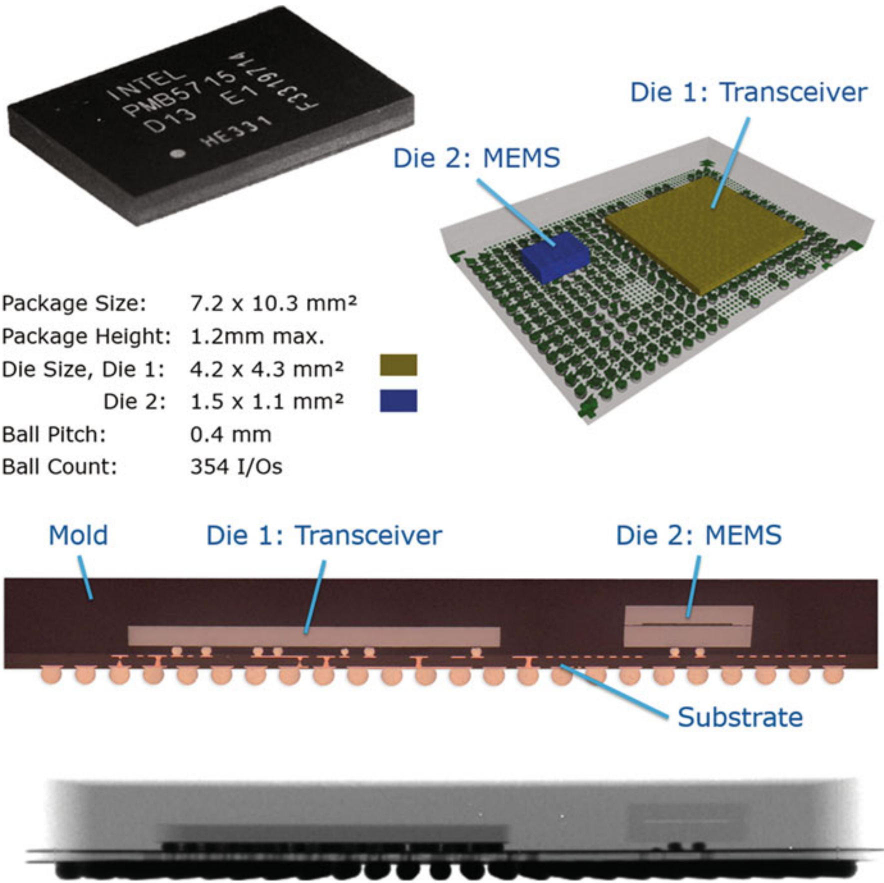

Fig. 15.25 Photograph of the Intel cellular transceiver SiP module and a 3D X-ray image revealing the MEMS die and cellular transceiver die (*top*). The cross section and X-ray image below reveal the Intel transceiver IC and co-packaged MEMS resonator CSP in a side-by-side flip chip configuration. This work still used the larger MEMS die with $1.5 \times 1.1 \times 0.5$ mm^3 as used for the VC-TCXO

resonators were based on the stack introduced earlier for the 124.5 MHz MEMS oscillator providing a typical frequency error (FT error) over temperature of less than 150 ppm over an extended temperature range from −30 °C to +110 °C. In the DCXO approach, the Xtal FT error of ±20 ppm is improved based on a temperature reading and digital compensation. The MEMS CSP features an integrated temperature sensor for this purpose. The resonator design is optimized to be stress insensitive and prevent activity dips related to spurious modes. The frequency characteristics and equivalent circuit model of a CSP MEMS are shown in Fig. 15.26. The extracted lumped element values are provided in Table 15.1.

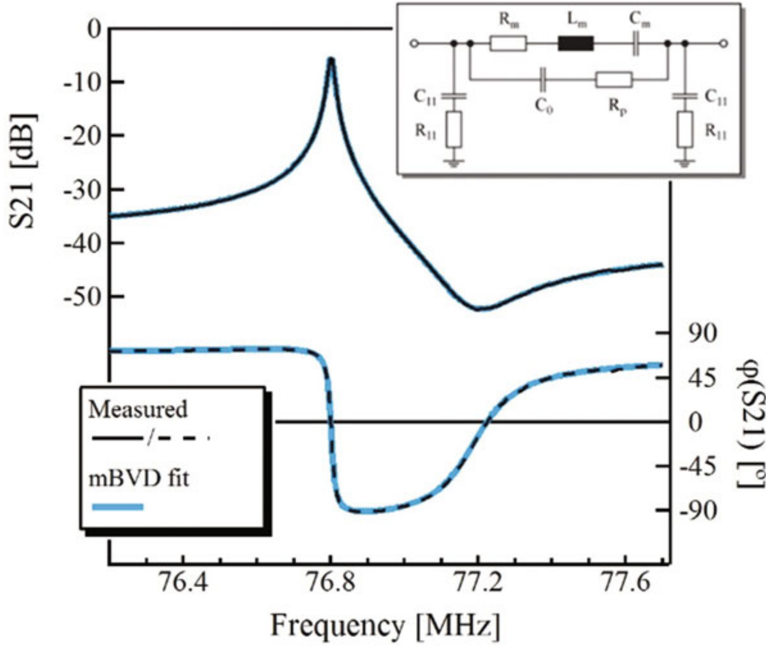

Fig. 15.26 Insertion loss and phase of the 76.8 MHz chip-scale packaged MEMS resonator measured with an Agilent E5071C ENA using Cascade SGS RF probes for probe on bump. The insert shows the equivalent circuit model used for the parameter extraction around resonance

Table 15.1 Typical equivalent circuit parameters of the 76.8 MHz MEMS resonator extracted from the mBVD model shown in the insert in Fig. 15.26

Parameter	Value	Parameter	Value
f_0	76.8 MHz	f_0 init. offset	±8000 ppm
Q_0	11,000	C_0	0.24 pF
R_m	80 Ω	R_p	1.8 kΩ
L_m	1.84 mH	C_{11}	3.5 pF
C_m	2.334 fF	R_{11}	50 Ω

15.6 Results

To compare the performance an individually packaged transceiver operating with an external 26 MHz crystal (DCXO) was compared to an external 76.8 MHz MEMS in CSP package (DCMO-ext), as well as the fully integrated transceiver with the integrated MEMS resonator (DCMO-SiP). For the DCXO the oscillator was running at 26 MHz, whereas for the DCMO implementations the oscillator operated at 76.8 MHz. The current consumption from a 1.8 V supply was 2.4 mA higher for the DCMO. The battery drain in a mobile device would only be 1.2–1.5 mA higher, depending on battery voltage and DC-DC converter efficiency (Fig. 15.27).

A Rohde and Schwarz FSQ8 was used in the FM demodulation mode to measure start-up time. The results represent the average of ten measurements where the normalized frequency error was computed to the final settled frequency. The transceiver clock enable trigger ***ref_clk_en*** was used as the time reference. The typical start-up time for the DCXO to reach ±1 ppm stability was measured as 1.8 ms, compared to 0.5 ms for the DCMO-ext and DCMO-SiP, as shown in Fig. 15.28.

The transmitter modulation accuracy was determined by measuring the error vector magnitude (EVM) on the transmitted WCDMA Tx signal using the FSQ8 equipped with the vector signal analysis option. The EVM was measured from 897 MHz (band 8) to 1.95 GHz (band 1), with the corner cases reported in Table 15.2. No significant impact of the reference clock is observed.

Next, the phase noise of the reference clock was measured with an Agilent E5052 signal source analyzer with the results shown in Fig. 15.29. The DCXO measurement is at 26 MHz, and the DCMO measurement is at 25.6 MHz, using an internal divider (i.e., 76.8/3). As seen from the results in Fig. 15.29, the phase noise for the DCMO is about 2 dB higher than for the DCXO, meeting the requirements. It should be noted, that in practice the LO can be generated directly off the 76.8 MHz output, so that another 4–5 dB are gained, thus exceeding the DCXO result. This margin in phase noise can be traded off for a reduction in current consumption (Fig. 15.29).

This project demonstrated the first implementation of a SiP cellular transceiver with integrated frequency reference. The taken data validates the feasibility of using a MEMS resonator with reasonable current drain for cellular transceiver applications and demonstrates the potential for a reduced footprint and bill of materials in a highly integrated cellular solution by co-packaging the devices.

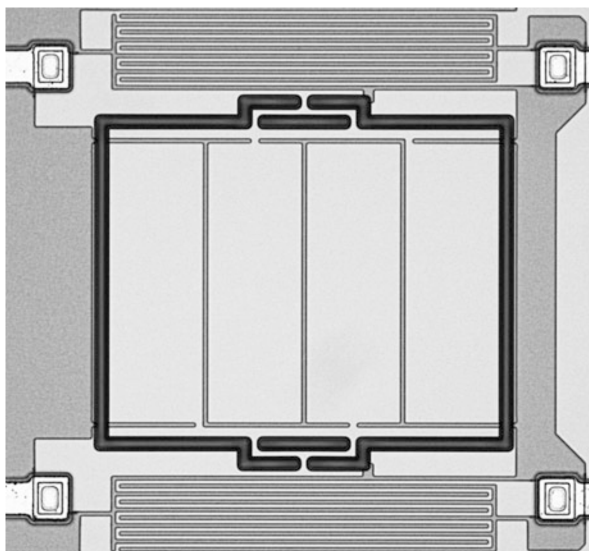

Fig. 15.27 Microscope image of the 76.8 MHz low-stress design with a mean Q_0 of 11,000. The integrated temperature sensor in form of a meander-type resistive temperature detector (RTD) is visible adjacent to the resonator plate

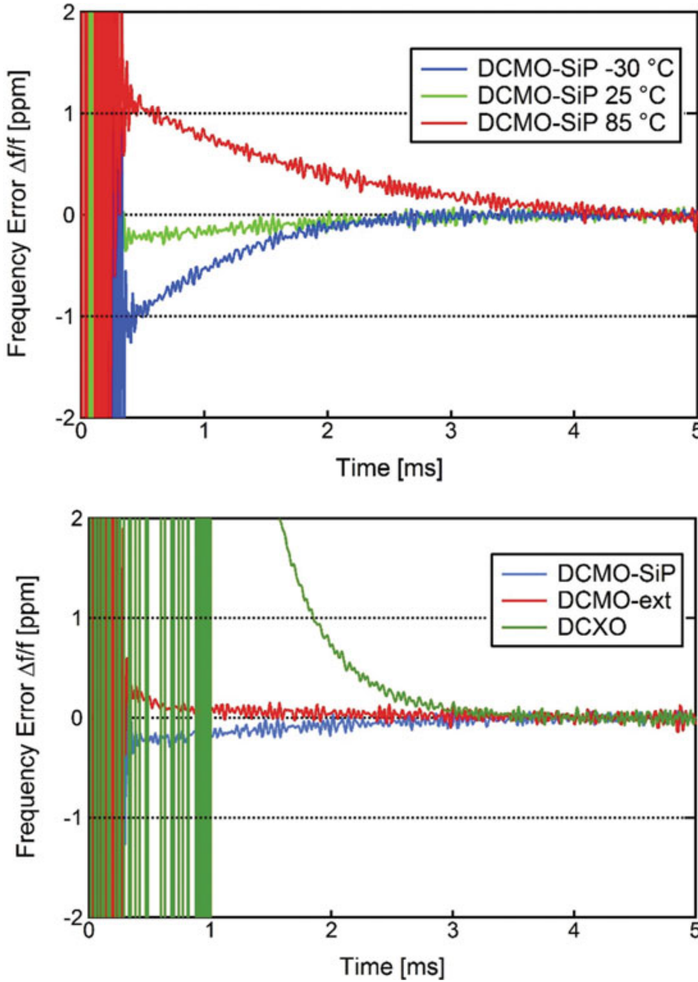

Fig. 15.28 Start-up time of the quartz resonator and MEMS resonator based cellular transceiver. The MEMS resonator showing a superior start-up time

15.7 Understanding the MEMS Timing Business

Before light-headily venturing into founding a company or creating an R&D effort within an existing company to seek to capture part of the $4B timing market there are a few high-level considerations to make. First of all, it is important to note that the timing market is very diverse, catering to the different demands of the end application. As an example, for a high-end frequency reference for a stationary application we might be able to accept a larger form factor and higher power consumption to obtain ultimate phase noise and frequency stability, whereas for

Table 15.2 EVM data for QPSK at low and high frequency measured at 25 °C

Reference	Power [dBm]	Condition	EVM RMS [%]
DCXO	0	$f = 897.4$ MHz	3.0
		$f = 1952.4$ MHz	3.1
DCMO-ext	0	$f = 883.8$ MHz	2.9
		$f = 1922.9$ MHz	2.9
DCMO-SiP	0	$f = 883.8$ MHz	3.0
		$f = 1922.9$ MHz	3.1

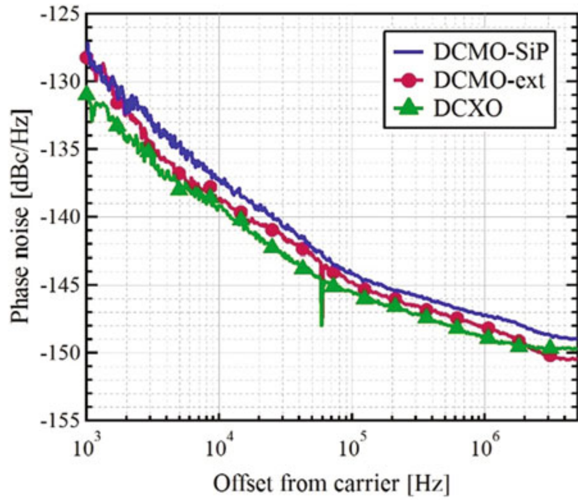

Fig. 15.29 Phase noise measured with an Agilent E5052 signal source analyzer. The measurements are taken at 25 °C, without impedance matching or buffer to the 50 Ω impedance with a carrier power of around 1 dBm

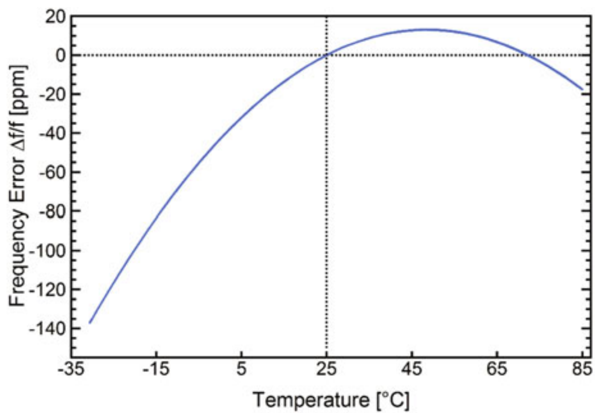

Fig. 15.30 Frequency error over temperature shown for the 76.8 MHz CSP MEMS resonator used in the cellular transceiver

a mobile phone application, low power consumption and size are traded off just to the point where the phase noise and frequency stability requirements can still be met. As such a "one fits all" MEMS timing solution does not exist and the choices early on in the technology determine what market segment can be captured. For a comparison the total addressable market for the different crystal timing categories are shown in Fig. 15.31.

Within these categories, in particular for the OCXOs, there are a few very high ASP parts (>$10) with very specific and extremely challenging requirements with volumes in the 1000 per year. Oscillators within the ASP bracket of $1–10 with volumes in the 10,000–100,000 per year still require high performance and very challenging metrics. Then there are mid-performance tier parts, e.g., as used in cell phones ($0.03–0.4), as well as the ubiquitous low-end timing devices in the <$0.05 range, both in principle having volumes for specific products in the 100M+ range. In order to justify the business case and significant investment required to develop a MEMS timing solution the available market metric is a key consideration.

An estimate of the cost to develop a MEMS timing product from scratch and to bring it to market probably lies in the range of $50M to $150M, depending on the level of synergies of existing infrastructure and technology. Taking the aforementioned discussion on annual volumes and TAM into account, and assuming a focus on a single product, only the high-volume segment for mid-performance

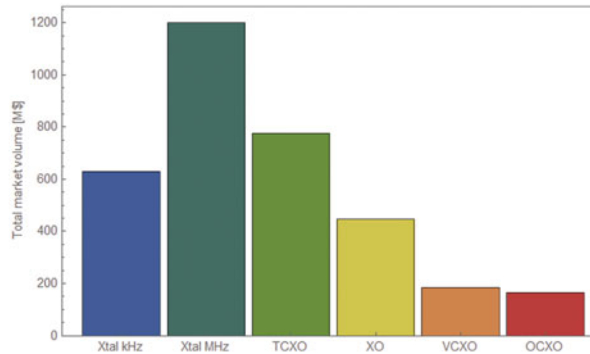

Fig. 15.31 Total market volume for the different timing devices as of 2012 [35]

Xtal and TCXOs can be justified from a return of investment (ROI) point of view today. Although referred to as mid-performance tier, the technical requirements as discussed in the preceding sections are still very challenging.

To understand the business case in more detail, let us assume as an example, that a fully processed 200 mm MEMS wafer will cost between $500 and $2000, depending on the volume, required processes, number of steps, and actual yield. For a 1 mm × 1 mm die size one can expect to yield approximately 30,000 components, resulting in a cost of $0.017–0.06 per component. This does not include packaging, test, shipping, and operating expenses beyond the fab cost. This example helps to immediately understand the importance of the die size, as well as the importance of a wafer-level package to reduce additional down-stream packaging costs. Even more important is the challenge to make money.

Assuming the cost of a fully tested and packaged die to be $0.03 and the sales price for a high volume application to be $0.06 with annual sales of 100M pieces, the mere $6M revenue is insufficient to sustain the operating expenses and illustrates the current challenges of this industry.

15.8 The Business Case for MEMS Cellular Timing Devices

Back in 2008, as shown in Fig. 15.31 the business case to go after quartz crystal VC-TCXOs with a lower cost and smaller MEMS based VC-TCXO solution made sense. VC-TCXOs were selling in very high volume into mobile phones for prices well in excess of $0.50 per part. In the following years it became evident that smartphone technology was taking over the position of PCs as the technology driver. The addition of connectivity (FM, Bluetooth, WiFi, GPS) into Smartphones had the attractive effect that the number of timing components grew, see Table 15.3, which had a significant impact on the overall timing content for cell phones, also shown in Fig. 15.32.

One needs to interpret Fig. 15.32 keeping in mind the low percentage of smartphone users early on relative to the world's mobile phone users. The rise of GPS TCXOs in Fig. 15.32 is representative of this development. The predictions for 2018 see smartphone users making up the majority of all cell phone users world-wide [40]. The strong decline in total timing content in 2008 with the adoption of Xtal-only architectures was somewhat compensated with the rise of smartphones and not having consolidated the timing devices, with a prime example shown in Table 15.2 for the 2010 iPhone. However, as the MHz Xtal adoption continues, GPS/GNSS is enabled with a mere MHz Xtal, as well as timing references being consolidated, the total timing content continuously declines, to arrive at one MHz Xtal and one temperature sensor to do the job. Another fact is the decline of 32 kHz crystal tuning fork devices, that are used for real time clock (RTC) applications, in conjunction with power management ICs as to periodically wake, e.g., the processor and then send it back to sleep to conserve power. The RTC functionality is now often

Table 15.3 Comparison of timing content for the iPhone 4 [36] and the iPhone 6 [37, 38] representative of the evolution of timing content in high-end smartphones

	iPhone 4 GSM (2010) [36]	iPhone 6 GSM (2014) [37, 38]
Number of timing devices	6	3
Application processor, cellular, connectivity, GPS	• 26 MHz TCXO (2.0 × 1.6 mm^2) • 33.6 MHz TCXO (2.5 × 2.0 mm^2) • 37.4 MHz Xtal (2.0 × 1.6 mm^2) • 24 MHz Xtal (2.0 × 1.6 mm^2) • (2) 32.768 kHz Xtal (2.0 × 1.2 mm^2)	• 19.2 MHz Xtal (2.0 × 1.6 mm^2) General time and frequency distribution by Qualcomm Power management IC
Motion processor	NA (Introduced with iPhone 5S [39])	M8 motion co-processor requires: • 24.0 MHz Xtal (1.6 × 1.2 mm^2) • 32.768 kHz Xtal (2.0 × 1.2 mm^2)

In 2014, due to the Qualcomm power management IC (PMIC) distributing one 19.2 MHz reference across the phone removed the need for at least four of the timing devices

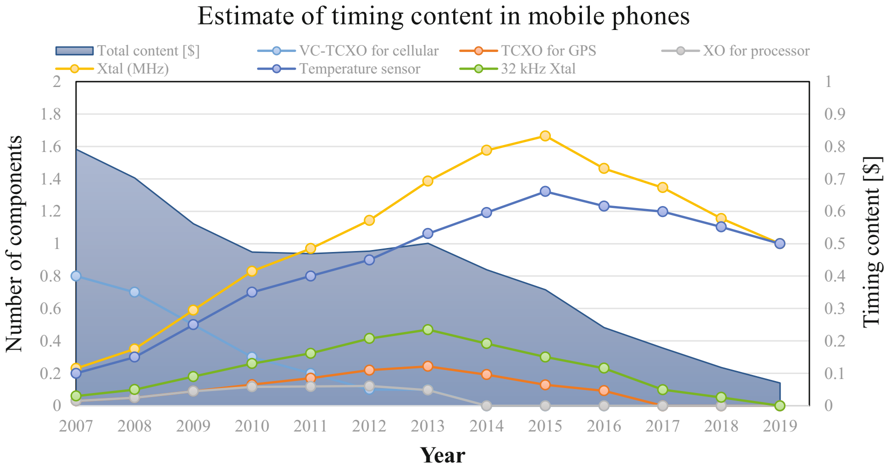

Fig. 15.32 Estimates of the author showing the shift in timing content away from VC-TCXOs towards the adoption of a MHz Xtal solution for cellular transceivers around the years 2007–2011. The rise of smartphones initially stalls the falling trend for the total timing content; however, it then continues with the consolidating approach of distributing timing across the platform. Achieving the final goal of a single frequency reference is closely tied to overcoming the challenges with a DCXO approach for GPS/GNSS. The decline of the 32 kHz Xtals in handsets is due to the trend to synthesize a time reference from a MHz crystal at a small power penalty

being achieved by dividing down the MHz Xtal's frequency at the penalty of higher power. This can be significantly improved with an oscillator implementation that can operate in a low-power mode.

It is interesting to note in regard to Table 15.2 that in 2014 two additional Xtals were introduced after the Qualcomm PMIC had been very effective in replacing all other timing components. These components are related to the introduction of a motion co-processor beginning with the iPhone 5S, with the goal to acquire and process the increasing amount of sensor data in a dedicated processor allowing the main application processor to conserve power.

The trend that timing devices might be added to achieve new functionality is only temporary until time and engineering resources develop a solution to use a single reference. One possible scenario that could break this trend is, if a timing device with novel performance becomes a requirement. An example of such advanced performance would be the use of a highly accurate clock for indoor navigation that requires better short-term stability than available with the DCXO approach. A very low-power MEMS OCXO implementation could provide this benefit.

15.9 Where Are We Today?

In the last 10 years quartz timing industries have faced technology developments unparalleled in history and in many cases had to restructure and reinvent their revenue model due to the changes in the timing architecture in mobile phones. As a result, competing with quartz technology during this phase has been a tremendous challenge. This technology has been evolving so quickly that with targeting the status quo and competing on cost one cannot succeed, as it requires constantly updating direction and redefining the business case. To succeed against quartz timing is to understand where the performance requirements will be 5–10 years out and to try to get there first, accepting a high risk of getting it wrong.

If Sand 9 had targeted a resonator-only product back in 2008 with a focus on miniature size the products would have had a lead of more than 7 years on quartz crystal timing technology and would have gained 10 % year-on-year in regard to a form factor reduction, as illustrated in Fig. 15.33.

The true potential for MEMS to be disruptive is apparent from comparing the die size trends for offering a MEMS VC-TCXO in an overmolded package and offering a CSP MEMS resonator as bare die. For the case of trying to imitate a pin-to-pin compatible crystal VC-TCXO in an overmolded package with a die size of 1.5 mm × 1.1 mm × 0.5 mm, initially requiring a $2.0 \times 2.0 \times 1.1\ \text{mm}^3$ package makes it impossible to get on par with quartz as seen from the chart above. An additional 2 year slip getting this technology to market puts it 4 years behind the

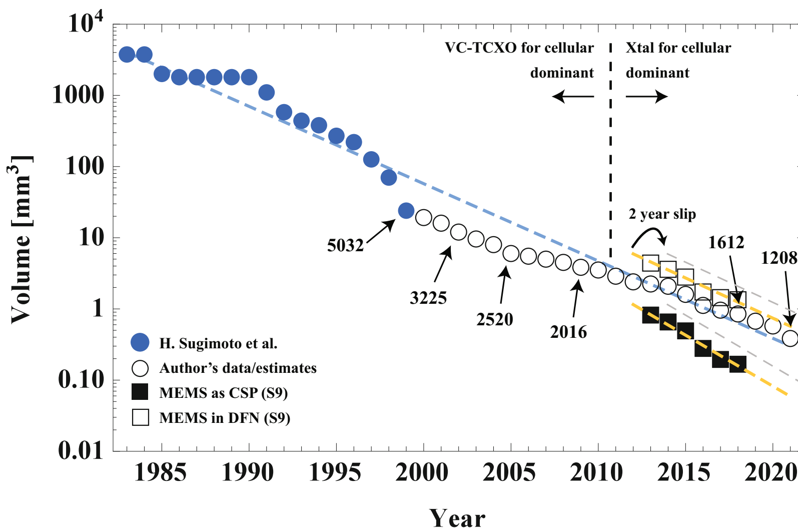

Fig. 15.33 Historic evolvement and prediction of the size of the cellular timing solution. It shows the aggressive year-on-year size reduction. MHz Xtals with 1612 footprint are already found in for example the iPhone 6, but are not used for the cellular functionality, which is still in a $2.0 \times 1.6 \times 0.65\ \text{mm}^3$ package [37, 38]

status quo, not to mention that the leading suppliers will already be selling at higher ASPs to the aggressive adopters. In comparison, the package size trajectory for a CSP MEMS resonator is already more than 5 years ahead of the crystal market. Even a 2 year slip due to the ability to leverage different device scaling laws than an AT-cut strip resonator enables to reduce die size faster with a 10 % gain on quartz every year.

15.9.1 When Is the MEMS Timing Revolution Going to Happen?

The reality is, that if we are asking ourselves this question the revolution has not happened yet, and that is because the semiconductor industry has not seen a clear return on investment (ROI) with enabling MEMS as a timing solution. Prior to replacing VC-TCXOs and consolidated timing the total timing content in a high-end phone was well in excess of $1. Eventually, with one temperature sensor and one MHz Xtal the incremental cost savings of possibly $0.02 for adopting a cheaper MEMS solution is not attractive enough to justify the engineering resources needed to enable it. That does not mean that MEMS timing is not being closely followed by these industries. To understand when it is going to happen requires to understand why it has not happened earlier. First, electrostatic MEMS oscillator solutions have not met the requirements for 4G cellular or GPS/GNSS applications. Second, the oscillator solution for mobile applications is on the way out. Too many intricate performance trade-offs in power and control of the oscillator (e.g., switching between low-power mode and high-power mode and dealing with the transitions) are made today so that one oscillator solution will not find wide application and is simply undesirable. That means MHz CSP resonators are the only way to succeed. In order to be easily adopted into the current consolidated timing architecture found in handsets requires the MEMS to have identical ESR and static capacitance, as well as on-par or better frequency stability over temperature, and initial frequency accuracy as a 2016 foot print MHz Xtal. A MEMS resonator device that fulfills all these criteria does not exist today, but is technically feasible. This device will be further referred to as "Looks Like Quartz" (LLQ) device.

15.9.2 How to Imitate a Xtal with an LLQ?

First of all, electrostatic MEMS resonators are physically unable to imitate the equivalent circuit of an AT-cut strip resonator due to the lack of electromechanical coupling [41]. The equivalent circuit model for a generic 26 MHz Xtal is shown in Fig. 15.34, with typical lumped element values of $R_m = 20\ \Omega$, $L_m = 10.7$ mH, $C_m = 3.5$ fF, and $C_0 = 1$ pF. Depending on the placement, packaging and resulting

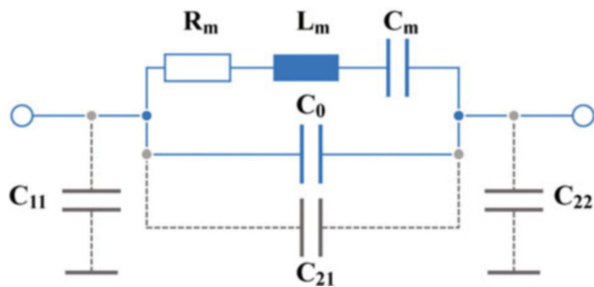

Fig. 15.34 Equivalent circuit representation based on a Butterworth–Van Dyke (BVD) model of a Xtal resonator, including parasitic capacitances

routing, parasitic capacitances in the range of 0.2–0.5 pF are common for the shunt capacitances C_{11} and C_{22}, as well as 0.1–0.4 pF for C_{21}, that have to be taken into account.

Computing the electromechanical coupling coefficient according to the IEEE definition:

$$k_t^2 = \frac{\pi}{2}\frac{f_s}{f_p}\frac{1}{\tan\left(\frac{\pi}{2}\frac{f_s}{f_p}\right)} \approx \frac{\sqrt{C_0}\pi \cot\left(\frac{\sqrt{C_0}\pi}{2\sqrt{C_0+C_m}}\right)}{2\sqrt{C_0+C_m}} \approx \frac{\pi^2}{8}\frac{C_m}{C_0}$$

yields k_t^2 values depending on the parasitics in the range of 0.43–0.23 % for this case. Piezoelectric thin film MEMS devices on silicon can easily provide k_t^2 in excess of 0.7 %. This means that a MEMS LLQ solution based on a piezoelectric thin film can be made smaller than current Xtals, yet mimic their electrical performance. Last, one of the biggest misconceptions in the past 10 years has been the need for very high-Q and very low ESR, also referred to as R_m. In general a piezoelectric MEMS resonator in the 40–80 MHz range with a minimum unloaded Q_0 of 7000 and maximum R_m value of 110 Ω should be capable to achieve cellular and GPS/GNSS performance, unless it suffers from elevated acoustic flicker noise. Although this ESR seems considerably higher than a typical 2.0×1.6 mm^2 footprint MHz Xtal with a maximum ESR of 60–80 Ω [42] the trend towards Xtals with smaller form factor will inevitably require oscillator designs to support higher ESR values. Going to a 1612 footprint will cause the ESR to increase by as much as 25–35 % [43], not to mention the increase going to a future 1208 footprint.

Initial frequency accuracy is required for ease of a widespread adoption and will require frequency trimming, widely used today in SAW and BAW filter manufacturing. However, for a multilayer stack this will significantly affect the linear TCF. Solutions to individually correct both for frequency offsets and temperature characteristics have been proposed [44]. The low dispersion sensitivity, i.e., moderate frequency shift with thickness, allows for a controlled trim process [44].

The biggest challenge for an LLQ today is the requirement to meet a ±50 ppm frequency stability over temperature of the intrinsic MEMS resonator. This arises from the stability specifications of the connectivity module that historically has utilized an uncompensated XO, or today just a simple MHz crystal without further compensation. As seen earlier, despite perfect compensation of the first order

temperature coefficient of frequency (Fig. 15.30), the frequency error due to a strong second order component still amounts to about 200 ppm. The only solution to address this second order terms is to engineer at least one of the materials in the resonator stack to have a significant positive second order temperature coefficient of stiffness. The most reasonable approach is to leverage the strong thermoelectromechanical interaction in silicon with doping [45]. It has been shown for silicon that with very high doping levels not only the first order TCF can be reduced [46], but also the second order TCF can be zero [47–53]. The latter work addresses the concern that high doping does not affect the aging characteristics. Several manufacturing related challenges have yet to be solved, so that a commercial product featuring piezoelectric thin film actuation with less than ±50 ppm frequency error over temperature for a direct quartz crystal replacement is still several years away.

15.10 The Value of MEMS Timing

The key factor that will determine the future of MEMS timing and its commercial success is the ability to place a value on integration. Rather than seeing MEMS timing as a silicon component replacing a quartz component, it is the value of having an integrated timing source. Traditionally an IC relying on a reference clock is only testable after the phone board's assembly. An IC with integrated timing is fully functional out of the box. Frequency offsets and temperature learning data can be programmed during final test and hence the performance of the IC can be guaranteed. If the host IC has a high ASP (>$5) and the aspect of having a co-packaged miniature timing source included provides significant product differentiation and competitive advantages to achieve higher sales, then the value is no longer measured in regard to a fractional cost saving of using a MEMS versus quartz component, but in terms of the host IC. In short, the question will be whether the ROI, after having to include the cost of the MEMS timing device, deal with the added complexity with packaging and testing, as well possibly reengineer the timing architecture is still significant.

15.11 Conclusions

Back in late 2008 when the author joined Sand 9 as acoustic device design engineer to work on a MEMS timing solution targeting cellular VC-TCXOs the only risks seemed to be technical in nature: can a MEMS solution meet the stringent aging criteria of less than 1 ppm/year, can the cellular phase noise requirements be met, and can the current consumption be below 3.5 mA. These were big enough problems to worry about, and with a strongly growing demand for mobile phones, and only a moderate price erosion for cellular VC-TCXOs the business case seemed solid.

Although we were eventually able to achieve the technical goals, the status of the technology as well as the market had already moved on. By 2010, cellular VC-TCXOs featured current consumptions of below 1.2 mA, and were already on the path of being designed out, so that prospective customers were asking for MEMS resonator solutions to replace the MHz Xtal components. Besides the need to realign on a much simpler packaged resonator, the business case had eroded. Not enough, the general strive to a single frequency reference with frequency sharing also meant that our solution with a temperature stability of -160 ppm to $+15$ ppm based on a zero first order TCF was not sufficient to meet the ± 50 ppm stability requirement that historically has been demanded for connectivity solutions (FM/Bluetooth/WiFi). As a result, this required either the transceiver manufacturer to re-architect their entire transceiver, baseband, connectivity and GPS solution for a <$0.20 component, or for us to modify our technology. The latter, as mentioned above would have required the reduction of the second order TCF for example using a heavily doped silicon layer, as well as the use of trimming to get rid of the initial frequency offset of ± 8000 ppm. This would have delayed the time to market for at least another 18 months. Instead, the hope was to identify an early adopter for a cellular only solution to validate our technology in a high-volume application, and extend the compatibility to a more general timing solution.

In summary, based on the efforts between 2008 and 2014 at Sand 9 we were able to validate that AlN based piezoelectric MEMS resonators can be co-packaged with cellular transceivers and can meet the stringent requirements for cellular 2G/3G/4G, connectivity, as well as GPS/GNSS. As such, the deployment of MEMS timing in cellular phones is determined by the business case rather than the technical feasibility. The technologies to extend the status quo to a drop-in MHz quartz crystal replacement to avoid re-architecting today's cellular single-source timing solution, in form of ion beam trimming and highly doped silicon seem within reach. Nevertheless, it will be several years to bring this to the maturity level for a 200 mm high-volume process.

In the near-term, it is more likely that MEMS resonators will find application in lower volumes as co-packaged timing source for high ASP products, where a clear value can be placed on product differentiation that is unrelated to differential cost savings using a MEMS over a quartz device.

Acknowledgements The author would like to acknowledge the technical contributions to the related products and technology by Juergen Schoepf, Reimund Rebel, Guiti Zolfagharkhani, Alexei Gaidarzhy, Florian Thalmayr, Andrew Sparks, Gabriele Vigevani, Darren Weninger, Kim Chung, Tung Shen Chew, Oscar Mendoza, as well as the Intel team: Greg Chance, Thorsten Meyer, Stephan Stoeckl, Burkhard Neurauter, Giuseppe Patane, Bernhard Neubauer, Gerald Minichshofer, Emad Hegazi, Walaa Mohamed, Mostafa Sayed Abdulaleem Ismail, and David H. Gaied. Special thanks go to Tony Haddrell and Peter Anderson at Integrated Navigation Systems Ltd. for their work on evaluating MEMS resonators for GNSS receivers.

References

1. Lam CS (2008) A review of the recent development of MEMS and crystal oscillators and their impacts on the frequency control products industry. In: Ultrasonics symposium, 2008. IUS 2008. IEEE, pp 694–704, 2–5 Nov 2008. doi:10.1109/ULTSYM.2008.0167
2. Qualcomm (2004) Qualcomm announces high-speed HSDPA solution to drive advanced data services for WCDMA (UMTS). https://www.qualcomm.com/news/releases/2004/05/13/qualcomm-announces-high-speed-hsdpa-solution-drive-advanced-data-services. Accessed 24 May 2015
3. Everard J (2000) The fundamental theory of low noise oscillators with special reference to some detailed designs. In: IEEE frequency control symposium Tutorial. http://www.ieee-uffc.org/frequency-control/learning/pdf/everard.pdf. Accessed 24 May 2015
4. McCorquodale MS (2008) Self-referenced, trimmed and compensated RF CMOS harmonic oscillators as monolithic frequency generators. In: Proc. 2008 Int'l frequency control symposium, pp 408–413
5. IEEE standard definitions of physical quantities for fundamental frequency and time metrology—random instabilities. In: IEEE Std 1139–1999, 1999, p 2. doi: 10.1109/IEEESTD.1999.90575
6. Rhode UL, Newkirk DP (2000) RF/wireless oscillators, RF/microwave circuit design for wireless applications. Wiley, New York, pp 716–847
7. Leeson DB (1966) A simple model of feedback oscillator noise spectrum. Proc IEEE 54(2):329–330. doi:10.1109/PROC.1966.4682
8. Walls FL, Handel PH, Besson R, Gagnepain JJ (1992) A new model of 1/f noise in BAW quartz resonators. In: Frequency control symposium, 1992. 46th, proceedings of the 1992 IEEE, pp. 327, 333, 27–29 May 1992. doi:10.1109/FREQ.1992.269996
9. Parker TE, Andres D (1993) Dependence of SAW resonator 1/f noise on device size. In: Frequency control symposium, 1993. 47th, proceedings of the 1993 IEEE international, pp 178, 185, 2–4 Jun 1993. doi:10.1109/FREQ.1993.367394
10. Parker TE, Andres D (1994) 1/f noise in surface acoustic wave (SAW) resonators. In: Frequency control symposium, 1994. 48th, proceedings of the 1994 IEEE international, pp 530, 538, 1–3 Jun 1994. doi:10.1109/FREQ.1994.398287
11. Parker TE, Andres D, Greer JA, Montress GK (1994) 1/f noise in etched groove surface acoustic wave (SAW) resonators. In: Ultrasonics, ferroelectrics, and frequency control, IEEE transactions on, vol. 41, no. 6, pp 853, 862, Nov 1994. doi:10.1109/58.330266
12. Parker TE (1987) Characteristics and sources of phase noise in stable oscillators. In: 41st annual symposium on frequency control. 1987, pp 99, 110, 27–29 May 1987. doi: 10.1109/FREQ.1987.201009
13. Parker TE, Montress GK (1992) Spectral purity of acoustic resonator oscillators. In: Frequency control symposium, 1992. 46th, proceedings of the 1992 IEEE, pp 340, 348, 27–29 May 1992. doi:10.1109/FREQ.1992.269994
14. Rubiola E (2006) The Leeson effect—phase noise and frequency stability in feedback oscillators. In: FEMTO-ST, Besancon, France. http://rubiola.org. Rev. 1.2, 27 Apr 2006, Chap. 2, p 29. Accessed 24 May 2015
15. NT2016SA phase noise (26 MHz). http://www.ndk.com/images/pn_NT2016SA.pdf. Accessed 24 May 2015
16. McCorquodale MS Self-referenced CMOS oscillators. In: Workshop, 2009 international microwave symposium. http://web.eecs.umich.edu/~mmccorq/seminars/mccorquodaleRFIC09.pdf. Accessed 24 May 2015
17. "Sand 9 Internal measurements—76.8 MHz zero-TCF 'Lugano' evaluation", Temperature sensing Xtal replacement, chip-scale packaged MEMS resonator with integrated temperature sensor and heater with silicon dummy cap, Feb 2014
18. "Sand 9 Internal measurements—125 MHz zero-TCF 'Innsbruck' evaluation", chip-scale packaged MEMS oscillator with BiCMOS oscillator circuit in wafer cap, Jan. 2013

19. Avramov I, Arapan L, Katardjiev I, Strashilov V, Yantchev V (2009) IC-compatible power oscillators using thin film plate acoustic resonators (FPAR). In: Ultrasonics symposium (IUS), 2009 IEEE international, pp 855, 858, 20–23 Sept 2009. doi:10.1109/ULTSYM.2009.5441502
20. Petit D, Cesar E, Bar P, Joblot S, Parat G, Berchaud O, Barbier D, Carpentier JF (2008) Thermally stable oscillator at 2.5 GHz using temperature compensated BAW resonator and its integrated temperature sensor. In: Ultrasonics symposium, 2008. IUS 2008. IEEE, pp 895, 898, 2–5 Nov 2008. doi:10.1109/ULTSYM.2008.0216
21. Pang W, Ruby RC, Parker R, Fisher PW, Larson JD III, Grannen KJ, Lee D, Feng C, Callaghan L (2007) 11E-3 a thermally stable CMOS oscillator using temperature compensated FBAR. In: Ultrasonics symposium, 2007. IEEE, pp 1041, 1044, 28–31 Oct 2007. doi:10.1109/ULTSYM.2007.263
22. Montress GK, Parker TE, Loboda MJ (1989) Residual phase noise measurements of VHF, UHF, and microwave components. In: Frequency control, 1989, proceedings of the 43rd annual symposium on, pp 349, 359, 31 May–2 Jun 1989. doi:10.1109/FREQ.1989.68889
23. Haddrell T, Anderson P (2014) Use of MEMS resonators in GNSS receivers. In: White paper prepared by Integrated Navigation Systems Ltd., p 25, V0.9, 10 Jan 2014
24. Anderson P, Haddrell T, Kuypers JH, Sundstrom R, Weninger D (2014) Integrating high performance MEMS resonators with a smartphone GNSS receiver. Abstract submitted to ION GNSS 2014 conference, proceedings unpublished
25. Chance G, Meyer T, Stoeckl S, Neurauter B, Patane G, Neubauer B, Minichshofer G, Kuypers JH, Schoepf J, Rebel R, Weninger D, Chung K, Chew TS, Mendoza O (2014) Integrated MEMS oscillator for cellular transceivers. In: Frequency control symposium (FCS), 2014 IEEE international, pp 1–3, 19–22 May 2014. doi:10.1109/FCS.2014.6859910
26. Nakamura K, Sasaki H, Shimizu H (1981) ZnO/SiO2-diaphragm composite resonator on a silicon wafer. Electron Lett 17(14):507–509
27. Hung L-W, Nguyen CT-C (2010) Capacitive-piezo transducers for higher Q contour-mode AlN resonators at 1.2 GHz. In: Tech. Digest, 2008 solid-state sensor, actuator, and microsystems workshop, Hilton head, South Carolina, 6–10 Jun 2010, pp 463–466
28. Hung L-W, Nguyen CT-C (2015) Capacitive-piezoelectric transducers for high- Q micromechanical AlN resonators. J Microelectromech Syst 24(2):458–473. doi: 10.1109/JMEMS.2014.2332991
29. Kuypers JH, Zolfagharkhani G, Gaidarzhy A, Rebel R, Chen DM, Stanley S, LoCascio D, Schoepf KJ, Crowley M, Mohanty P (2010) High performance MEMS oscillators for communications applications. In: Proceedings fourth international symposium on acoustic wave devices for future mobile communication systems, pp 137–144
30. Rebel R, Kuypers JH, LoCascio D (2010) Methods and apparatus for calibration and temperature compensation of oscillators having mechanical resonators. US 8729976, Priority date 13 July 2010
31. Bourgeois C, Steinsland E, Blanc N, deRooij NF (1997) Design of resonators for the determination of the temperature coefficients of elastic constants of monocrystalline silicon. In: IEEE international frequency control symposium 1997, pp 791–799
32. Lin C-M, Yen T-T, Lai Y-J, Felmetsger VV, Hopcroft MA, Kuypers JH, Pisano AP (2009) Experimental study of temperature-compensated aluminum nitride Lamb wave resonators. In: Frequency control symposium, 2009 joint with the 22nd European frequency and time forum. IEEE international, pp 5–9, 20–24 Apr 2009, doi:10.1109/FREQ.2009.5168132
33. Newman BM, Badillo DA, Rebel R, Schoepf KJ, Asmani M (2011) Power on reset circuit and method of use. US8736319, Priority date 26 Oct 2011
34. Chance G, Meyer T, Stoeckl S, Neurauter B, Patane G, Neubauer B, Minichshofer G, Kuypers JH, Schoepf J, Rebel R, Weninger D, Chung K. Chew TS, Mendoza O (2014) Integrated MEMS oscillator for cellular transceivers. In: Frequency control symposium (FCS), 2014 IEEE international, pp. 1–3, 19–22 May 2014, doi:10.1109/FCS.2014.6859910
35. Evans-Pughe C Oscillators - the new wave. http://eandt.theiet.org/magazine/2012/10/oscillators-new-wave.cfm. Accessed 22 Oct 2015
36. http://eetimes.jp/ee/articles/1011/17/news130.html. Accessed 22 Oct 2015

37. iFixit010: https://www.ifixit.com/Teardown/iPhone+6+Teardown/29213. Accessed 22 Oct 2015
38. iFixit011: http://www.electronicproducts.com/iPhone_6_Plus-whatsinside_text-171.aspx. Accessed 22 Oct 2015
39. http://en.wikipedia.org/wiki/Apple_M7. Accessed 22 Oct 2015
40. http://www.emarketer.com/Article/2-Billion-Consumers-Worldwide-Smartphones-by-2016/1011694
41. Kaajakari V. http://www.ieee-uffc.org/frequency-control/learning/pdf/Kaajakari-MEMS_Resonators_v2b.pdf. Accessed 22 Oct 2015
42. Datasheet - NDK crystal used in iPhone 6 according to [iFixit010, iFixit011]. http://www.ndk.com/images/products/catalog/c_NX2016SF-STD-CTZ-1_e.pdf]. Accessed 22 Oct 2015
43. Datasheet TXC Xtal. http://www.txccorp.com/download/products/xtal/8Q.pdf. Accessed 22 Oct 2015
44. Thalmayr F, Kuypers J, Schoepf J. US Patent 8,689,426
45. Keyes RW (1967) Electronic effects in the elastic properties of semiconductors. Solid State Phys 20:37–90. doi:10.1016/S0081-1947(08)60217-9
46. Shahmohammadi M, Harrington BP, Abdolvand R (2012) Zero temperature coefficient of frequency in extensional-mode highly doped silicon microresonators. In: Frequency control symposium (FCS), 2012 IEEE international, pp 1–4, 21–24 May 2012. doi:10.1109/FCS.2012.6243640
47. Thalmayr F, Sparks A, Kuypers J, Vigevani G. US Patent disclosure, 11/18/2011, 11/16/2012
48. Vigevani G, Thalmayr F, Kuypers J NSF reports submitted 7/2013, 12/2013
49. Ng EJ, Hong VA, Yang Y, Ahn CH, Everhart CLM, Kenny TW (2015) Temperature dependence of the elastic constants of doped silicon. J Microelectromech Syst 24(3):730–741. doi:10.1109/JMEMS.2014.2347205
50. Pensala T. Temperature stable silicon and piezo-MEMS for timing and frequency reference applications. Presentation at http://ifcs-eftf2015.org/sites/ifcs-eftf2015.org/files/pensala.pdf. Accessed 4 Dec 2015
51. Jaakkola A, Pekko P, Dekker J, Prunnila M, Pensala T (2015) Second order temperature compensated piezoelectrically driven 23 MHz heavily doped silicon resonators with ±10 ppm temperature stability. In: Frequency control symposium & the european frequency and time forum (FCS), 2015 joint conference of the IEEE international, pp 420–422, 12–16 Apr 2015. doi:10.1109/FCS.2015.7138871
52. Jaakkola A, Prunnila M, Pensala T, Dekker J, Pekko P (2015) Design rules for temperature compensated degenerately n-type-doped silicon MEMS resonators. J Microelectromech Syst 24(6):1832–1839. doi:10.1109/JMEMS.2015.2443379
53. Jaakkola A, Gorelick S, Prunnila M, Dekker J, Pensala T, Pekko P (2014) Long term stability and quality factors of degenerately n-type doped silicon resonators. In: Frequency control symposium (FCS), 2014 IEEE international, pp 1–5, 19–22 May 2014. doi:10.1109/FCS.2014.6859866

Chapter 16
BAW Filters and Duplexers for Mobile Communication

Robert Aigner

16.1 Introduction

While there is no broad consensus RF bulk acoustic wave (BAW) technology should actually be listed as an RF-MEMS technology, most experts would agree BAW is a true success story. In fact—at this point in time—no other "true" RF-MEMS technology comes even close to BAW in terms of market penetration and revenue generated. It is a prime example for an innovation having a profound impact on size and performance of devices most persons consider a necessity in daily life: the smartphone. Without the selectivity of high-performance acoustic filters, none of the advanced cellular voice and data services would exist. There is an insatiable demand for higher wireless data rates across all boundaries of society and geography. Why has BAW flourished way beyond the predictions in recent years?

The allocated frequency spectrum is very limited, and the most favorable frequencies are already occupied by cell phone bands, by governmental agencies, or by unlicensed bands with restricted transmission range. All new wireless systems released are forced to deploy relying on less favorable frequency bands that have noisy or "oversensitive" neighbors—sometimes both. The commercial viability of these new bands depends at least in part on equipment makers' ability to solve neighborhood problems. BAW filters play a key role in minimizing interference between systems operating in different bands. The reason for the spectacular growth of BAW is the high number of smartphones shipped, multiplied by the large number of bands a typical smartphone is equipped to operate in.

This chapter aims to provide background information on applications, their requirements, and how those link into technology features late-generation BAW technology offers.

R. Aigner (✉)
Qorvo, Inc., Orlando, FL, USA
e-mail: Robert.Aigner@Qorvo.com

© Springer International Publishing Switzerland 2017

H. Bhugra, G. Piazza (eds.), *Piezoelectric MEMS Resonators*,
Microsystems and Nanosystems, DOI 10.1007/978-3-319-28688-4_16

16.2 Short History of BAW

Filters based on acoustic waves have their origins in the 1950s when quartz crystals became broadly available and enabled filters to become far more selective than LC-based filter circuits. In the 1970s surface acoustic waves (SAWs) on various piezoelectric crystal materials entered the scene for filters with a frequency range up to about 100 MHz [1]. Those filters were predominantly used as intermediate frequency (IF) filters in heterodyne receivers. Starting in the mid-1980s, enhancements to SAW filter processes made them a viable solution for frequencies up to 1 GHz. The production volumes for acoustic filters remained very low until cell phones became affordable for a wide public in the mid-1990s. During that time, RF-SAW filters were used mostly in the receive path between antenna and low-noise amplifier, while the transmit path used LC filters or ceramic filters. LC filters show very poor selectivity as the Q-values of inductors are constrained by restive losses. Ceramic filters on the other side can be very selective, but they have a very large footprint and height. "Direct conversion" receiver architecture took hold in the industry around year 2001 which led to the demise of SAW IF filters in cell phone architectures. As a side effect, this made RF filtering at the antenna much more demanding. SAW IF filters had been good business for many suppliers which were now looking to replace the revenue lost with new filter products. About at the same time, cell phones started adding support for multiple bands as needed for international roaming. Size of phones had shrunk steadily for more than a decade, but with multiple bands supported in one phone, pressure was building to radically reduce the size and thickness of the RF filters. BAW technology arrived just at the right time to respond to this challenge.

Attempts to make a BAW filter using thin film materials go back to the 1970s. Those were ultimately unsuccessful due to the poor quality of piezoelectric thin films available at that time. Most early work was related to a device concept we would today classify as a film bulk acoustic resonator (FBAR) in which a free-standing membrane is used to prevent the acoustic wave from escaping into the substrate. In the late 1980s the early pioneers set out again to conquer the challenge of thin film quality. The first to succeed making a real product in the RF frequency range was Ken Lakin. He circumvented the challenges of making a free-standing membrane by introducing an acoustic Bragg reflector using multilayers of dissimilar materials [2]. The concept and name BAW solidly mounted resonator (SMR) was born. Ken Lakin was first in depositing high-quality AlN thin films with strong preferential c-axis orientation. He succeeded getting piezo coefficients close enough to a monocrystal—as needed to achieve sufficient coupling coefficient and quality factor for a practical BAW filter. He founded the company TFR Technologies in 1989 which focused on specialty BAW filters for space and military applications. The first products were delivered to customers in 1997. The facility exists to this day as part of Qorvo (whose predecessor TriQuint acquired TFR in 2004) and continues to supply small volumes of highly specialized filters. Independent of the activities

at TFR a small group at HP labs around Rich Ruby started to investigate the FBAR concept in 1993 [3]. In 1999 they had mastered the challenges of making membranes and growing excellent AlN on a bottom electrode. The level of performance they reached was suitable for commercialization, and they smartly chose duplexers for the PCS CDMA band at 1.9 GHz as their lead product to go in production with. Their selling point was a dramatic reduction in size and thickness compared to existing duplexers. Early products emerged in 2001 around the time HP spun out all non-computer divisions into Agilent. By year 2004 Agilent had a solid grip on the market for PCS duplexer and had sent conventional ceramic duplexers into obsolescence. The wireless division of Agilent was spun out to form Avago in 2005 which to this day is a leading player in BAW/FBAR (note: Avago announced to change its name to Broadcom in May 2015). The third contender in commercializing BAW filter was a group at Infineon which started out as a secret project between Siemens (later Infineon) and cell phone maker Nokia in 1997. The author of this chapter had the honor to lead this effort between 1997 and 2005. The group's innovations eliminated several of the shortcomings acoustic reflectors had suffered from and succeeded to launch a first BAW-SMR filter to the cell phone market in 2001 [4]. That group also introduced localized ion beam etching as method to correct for manufacturing variations in frequency across a wafer. A moderate amount of BAW filters for GSM phones were shipped in the years to follow. The activity later faltered when Nokia lost interest in BAW and Infineon's management misjudged how important filters would soon become in RF systems.

Following HP/Agilent/Avago's (/Broadcom's) highly publicized product launch in the early 2000s a large number of semiconductor companies started efforts to develop BAW. At the peak around 2005, there were at least 11 companies actively developing BAW, many of which had unrealistic goals and schedules and/or poor strategic alignment. The challenges of BAW technology are easily underestimated, in particular how to achieve very high coupling coefficient, Q-values, and spurious mode suppression—all at once—and finally manufacture BAW filters at very high yields. Five contenders reportedly terminated BAW development between 2007 and 2009. Infineon sold the BAW business to competitor Avago in 2008. Following the acquisition of TFR Technologies in 2004, TriQuint entered the race for the cell phone BAW market. The author joined TriQuint in 2006 to lead this effort. Production readiness was achieved in early 2009 followed by an immediate ramp into high volume. In the years between 2009 and 2012, TriQuint (now Qorvo) and Avago (now Broadcom) fought a fierce battle in court which resulted in a settlement and patent cross license agreement. As a side effect, some of the minor players were scared away from pursuing the most attractive applications for BAW filters, effectively leaving Avago (now Broadcom) and TriQuint (now Qorvo) as the only two vendors for BAW filters. The years following 2012 brought extreme growth for both companies. By the end of year 2015, the total accumulated number of BAW and FBAR filter chips out in the field will have surpassed 20 billion units.

16.3 Types of Filters Used in Smartphones

Frequency bands allocated to various cellular systems differ significantly from one another. The relative bandwidth is very different from band to band as is the width of the guardbands designated for each. Modern smartphones have multiple antennas embedded which allows them to operate properly in various usage situations and to support concurrent use of Wi-Fi and GPS during voice and data transfer. The architects of an RF system (often also referred to as the RF front end) for a phone define how receive and transmit signals for all bands are connected to multiple antennas using RF switches and networks containing acoustic filters. The RF signals are then routed to a transceiver integrated circuit (IC). There are several types of filter networks which can be distinguished:

Transmit (Tx) filter:
Transmit filters are placed between the output of power amplifiers and antenna. As such they are subjected to maximum transmit power of 1 W (30 dBm) in certain operating conditions of a phone. The main purpose they serve is to eliminate out-of-band emissions which will interfere with other RF applications. The insertion loss of Tx filters is a critical parameter; any loss added to the Tx path will increase the current consumption of the power amplifier significantly. Self-heating effects can occur and have to be managed in order to guarantee proper function and lifetime. Nonlinear effects in a Tx filter can create significant problems. Several LTE bands released in the recent years use time division duplex (TDD). Those systems would typically rely on Tx filters to control emissions into other bands.

Receive (Rx) filter:
Receive filters are found between antenna and the first low-noise amplifier (LNA) in the signal chain. Power levels of the receive signal are generally very low. The Rx filter protects the LNA from interference sources which often are very close in frequency and very strong in amplitude. Without the Rx filters, intermodulation with interferers would be unmanageable. The insertion loss of an Rx filter directly impacts the receiver sensitivity. Nonlinear intermodulation effects in the filter itself have to be prevented.

Duplexer:
Many of the classical and new bands have separate frequency allocations for receive (Rx) and transmit (Tx) working in frequency division duplex (FDD). Those bands all require duplexers to enable simultaneous Rx and Tx operation. A duplexer is a circuit combining a Tx filter and Rx filter (e.g., described above) such that both filters are matched to one common antenna port for their respective passbands. The interference in this case includes the system's own Tx signal as well as the broadband noise from the power amplifier and mixers. For the respective other bands, each filter is therefore designed to provide extreme rejection levels. What is referred to as isolation between Rx and Tx port is a crucial parameter for duplexers. Typical requirements for isolation are 55 dB.

Diplexer:
In many aspects a diplexer looks similar to a duplexer. Two filters are matched to one port in such a way that the presence of the other filters has as little as possible impact on insertion loss in the passbands. The main difference is that often there is no provision made to support simultaneous receive and transmit of paired bands; hence, rejection requirements are far less demanding than in a duplexer. Diplexers are often used to share an antenna between various applications such as cellular voice with Wi-Fi or GPS. Not all diplexers contain acoustic filters; depending on specs, some are just LC networks. In special cases acoustic filters are used in band-reject configuration rather than in the classical band-pass configuration.

Quadplexer:
A combination of usually two Tx and two Rx filters matched to one common antenna port (the name is sometimes used for other cases too). Quadplexers can in the simplest case be a combination of two duplexers with additional low-pass and high-pass LC networks. This would be possible if the bands are spaced far from each other in frequency. While previous generations of quadplexers did not require cross isolation from each RX port to each other TX port, this will change with the introduction of carrier aggregation (CA) when receive bandwidth in multiple bands is bundled to achieve a higher data rate.

Hexplexer:
The extension of a quadplexer with usually three Tx and three Rx filters matched to an antenna port. Hexplexers are truly challenging to design and manufacture. The out-of-band losses of all filters accumulate unfavorably and present themselves as loss for the passband of each of the filters. Matching at the common port is also becoming very challenging.

Interstage filter:
Typically used to eliminate noise emissions before they enter a mixer or amplifier. Traditionally it is placed at the output of an LNA in the receive path or at the input side of a power amplifier in the transmit path. Most of the interstage filters have been eliminated in order to save cost and space. As a consequence other filters and duplexers closer to the antenna need to meet even more stringent rejection requirements than in earlier generation phones.

All the “hard” filtering in cell phones is accomplished with acoustic filters. Lumped element (LC) filters are unable to meet the selectivity and loss requirements. The limitation stems mostly from the quality factors (Q) of inductors which are limited to about 50 and from comparably large manufacturing tolerance of inductor and capacitors. Surface acoustic wave (SAW) filters have been deployed in wireless devices since nearly the beginning of the modern wireless industry. They continue to be used in very large numbers for Rx filters at frequencies below 2 GHz and for duplexers mostly below 1 GHz. Many of the LTE bands released in recent years are at frequencies above 2 GHz and/or have very challenging rejection requirements in close proximity to the passband. At higher frequency SAW starts to show progressively higher losses making it difficult to achieve steep filter skirts and

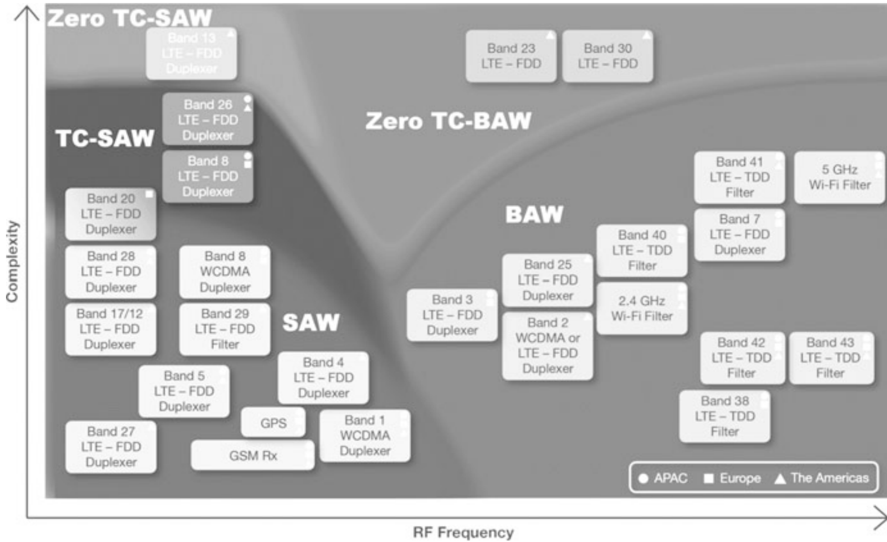

Fig. 16.1 Application space for acoustic filters (revision Feb. 2015)

low insertion loss. BAW is ideally suited for the frequency range above 1.5 GHz because Q-values don't degrade with frequency as much; Q-values of 2500–4000 are state of the art. Device size for BAW is scaling favorably with increasing frequency. While it is possible to use BAW also at lower frequencies, it is in most cases not economical to do so because SAW can deliver nearly same performance at lower cost. Figure 16.1 maps the application space for RF filters with most of the important bands marked. The "complexity" on the y-axis is a measure for how challenging the filter solution is for each of the bands; it will also correlate with cost. SAW, BAW, and their derivate technologies each have staked out a domain in which they are the preferred solution. It should be mentioned that several of the bands were recently repurposed from GSM to LTE or from WCDMA to LTE, making it harder for filters to comply. Examples for this include Band 8, which is a transitioning to LTE but still used for WCDMA in many regions; it is therefore showing up twice in Fig. 16.1. The phone manufacturer may elect to use a cheaper filter for a phone being mostly used in a region with WCDMA-only or a high-end filter if the service provider wants to offer LTE.

16.4 Evolution of Size and Performance

The RF section of a smartphone occupies less than 1/3 of the total available board space—a number that has not changed significantly over the past years—while the number of filters present has increased nearly ten times. Without aggressive steps to

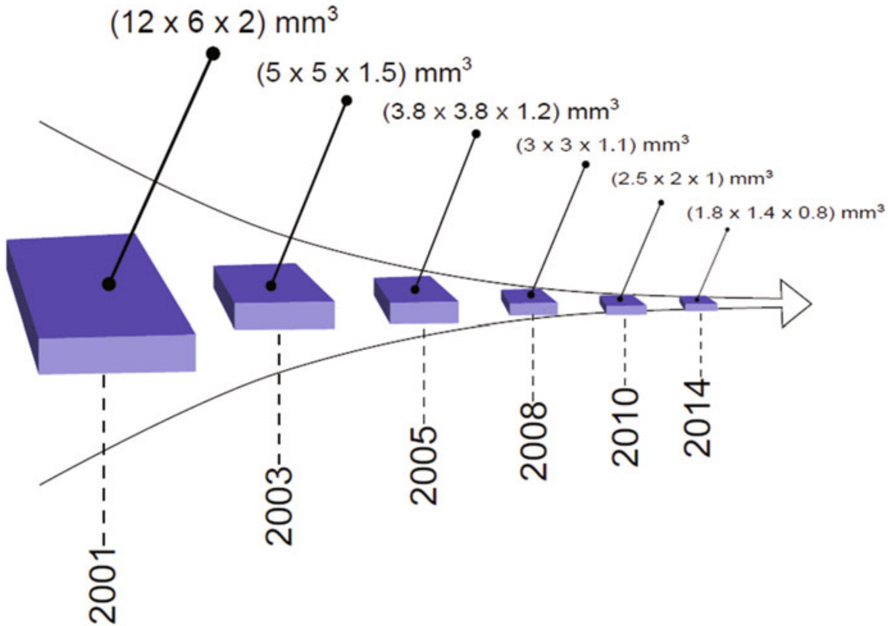

Fig. 16.2 Evolution of the size of duplexers

shrink size and integrate filters into RF modules, the total board space needed for filters would be impossible to fit into a late-model smartphone. The first-ever BAW duplexer on the market by Agilent/Avago/Broadcom had a footprint of 12×6 mm^2 and about 2 mm height. While this is huge by today's standards, it was back then a dramatic improvement over ceramic duplexers which were at least 5 mm thick. The evolution of size for single duplexers is shown in Fig. 16.2. The area consumed by a single filter function is expected to continue shrinking at a rate of 20 % per year. To sustain this rate of shrinkage, both the filter chip and the package need to be upgraded constantly. In the package inductors and interconnects need to be compacted aggressively, and additional metal layers are needed. At the same time the maximum acceptable thickness of filters and duplexers keeps decreasing and is currently <0.8 mm for duplexers and <0.5 mm for single filters. A wafer-level-packaged BAW chip has a thickness down to 0.2 mm.

Evolution of filter size is easy to observe; the improvement in performance over the years is harder to quantify but no less impressive. Performance is a summary expression for multiple aspects of filter characteristics each of which will be discussed in later sections. In filters there are always compromises to be made between insertion loss and rejection, bandwidth and return loss, and insertion loss and linearity—just to mention a few. Hence, it can be misleading to judge filters based on just one parameter. Fact is that a filter or duplexer from 5 years ago will fall short of today's requirements in all parameters. Product cycles are typically

less than a year, and customers expect significant improvements compared to the previous generation. There are several reasons the pressure on filter performance is so high:

- More bands in a phone require more switching and routing of RF signals which introduces additional losses. Also, adding more bands to an antenna requires to make compromises for all bands. Antenna designers are facing the challenge to squeeze antennas for a modern smartphone into the few spaces which are suitable.
- Battery capacity does not keep up with the increase in current consumption due to added features and heavier usage. A main complaint of smartphone users is how fast the battery drains. Lower insertion loss RF filters bring a significant benefit for current consumption of the power amplifiers.
- Regulations regarding emissions and signal quality are getting more stringent with every new band added. In the United States the Federal Communication Commission (FCC) regulates spectrum usage. Bands have been expanded in bandwidth often by reducing guardbands and packing bands more densely into suitable spectrum. Some bands have been re-designated from satellite-only to bands with terrestrial transmitters, thus changing the signal strength and emissions which can interfere with other systems drastically.

16.5 Insertion Loss

In most cases the insertion loss (IL) of a filter is at the very top of a specification or data sheet. The impact of insertion loss on total efficiency of the transmit chain is dramatic. For example, a 3 dB insertion loss equates to 50 % of the transmit power wasted in the filter. In combination with power amplifiers—which themselves have efficiency in a 40–50 % range converting DC to RF power—this means the battery will have to supply 2 W for a 0.5 W RF signal at the antenna. In the receive chain the insertion loss of the filter directly adds to the noise figure (NF) of the receiver. When receive signals are weak—for a far-away base station, inside of buildings, a hand covering the antenna, or other reasons—a lower insertion loss makes the difference between a dropped call and an uninterrupted connection.

Insertion loss of acoustic filters is caused by resistive losses, material (viscous) losses, and acoustic wave leakage in and between the elements constituting the filter. Most BAW filters are constructed as ladder-type filters of individual BAW resonators. The Q-value of a BAW resonator describes the composite of all losses. Resistance effects play a bigger role at the frequency where impedance is minimum, referred to as resonance frequency f_s. The *Q-value at resonance* is often referred to as Q_s, while the corresponding *Q-value at anti (or parallel) resonance* is referred to as Q_p. The insertion loss of a filter correlates very well with Q_s and Q_p. Additional losses occur in interconnects and inductors. Ladder filters usually have the lowest insertion loss in the inner 60 % of the passband. The maximum insertion loss occurs

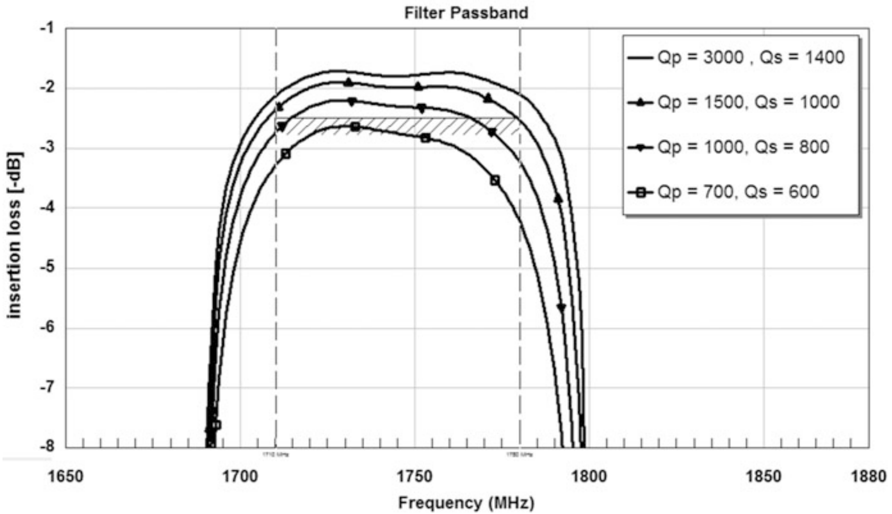

Fig. 16.3 Effect of Qp and Qs on filter performance

almost always at the band edges. Typical requirement for maximum insertion loss ranges from 1.8 to 3 dB. Filter specs also state limits on how much the insertion loss may vary within the passband or within one channel of the passband. This spec-parameter would be referred to as maximum passband ripple. As this will impact the integrity of the signal—depending on the modulation used—an alternative is to specify the error vector magnitude (EVM) the filter causes. EVM is a measure for how much a modulated signal is distorted in amplitude and phase. The lower the Q_s and Q_p of a BAW filter, the more the "shoulders" start to hang. Figure 16.3 shows an example simulated with Q_s and Q_p as a parameter. The insertion loss can be strongly impacted by poor matching to the input and output port impedance. A poorly designed filter can have terrible insertion loss despite using very high Q-value BAW resonators. The best method to separate mismatch-related losses from true filter losses is to apply the mathematical method of simultaneous conjugate matching. How BAW filters are designed to minimize mismatch is described in the next section. As most filters show a temperature drift, the insertion loss specification states a temperature range. More about temperature effects will be discussed in the respective section.

16.6 Port Impedance and Matching

With regard to port impedance, the magic number in RF is 50 (Ω). Most RF measurements are done in a 50 Ω environment, and the majority of RF components are designed to match to 50 Ω ports. 50 Ω just happens to be a very good

compromise for antennas, coax cables, striplines, and also acoustic filters built on piezo materials with relative dielectric constant of 5–50. At 2 GHz a higher port impedance will cause a circuit to be prone to parasitic capacitance, while for a very low port impedance, losses will be adversely affected by series resistance and parasitic inductance.

The reason why excellent matching is a key requirement for transmit filters is the inability of output transistors of power amplifiers to perform well if load impedances is off target. The current consumption, linearity, and gain of an amplifier are optimized to work in a very narrow window of complex load impedance. PA matching networks are typically significantly wider in bandwidth than the passband of a filter, and they will translate the complex impedance the filter presents at its input to a different complex impedance the output transistor favors. However, if the filter presents an impedance which varies wildly within the passband, the matching network can do nothing to correct this problem. The impedance variation of a filter or duplexer is best observed in a Smith chart for S11 or S22. The desired situation is to have a very tight locus for the entire passband, as opposed to a big swirl with many lobes and ends sticking out. However it is often acceptable to have a tight locus which lies off-center on the Smith chart because this can be corrected by the matching network. An S-parameter set can easily be transformed to a different nominal port impedance—even a complex-valued port impedance. A value for best achievable return loss can be calculated accordingly. The filter port to which a power amplifier will connect usually requires to have better than 15 dB return loss. For receive path filters, the matching is important too as it can affect the behavior or the subsequent low-noise amplifier. Requirements are typically less stringent than for transmit, often in a 12 dB return loss range.

BAW resonators behave like regular capacitors for wide ranges of frequency, in particular at very low frequencies; only near the acoustic resonance, the impedance deviates drastically from a capacitor. Wideband rejection of BAW ladder filters is accomplished by a capacitive voltage division from stage to stage of the ladder filter; acoustic resonances don't play any role in this. One should keep in mind that BAW filters create stopband rejection by reflecting the RF signal rather than by absorbing it. As a "rule of thumb," a BAW ladder filter for a 50 Ω port impedance will have an average capacitance in each branch resulting in an impedance close to $j\ 50\,\Omega$ at passband *center frequency* f_c.

A branch could contain just one resonator or two or more resonators and/or additional capacitors as shown in Fig. 16.4. Branches in a ladder filter are either series or shunt branches.

From the desired *port impedance* Z_p and the passband *center frequency* f_c, one can readily back out the *low-frequency capacitance* C_{lf} the branches of the filter will have on average:

$$C_{lf} = \frac{1}{2\pi f_c Z_p} \tag{16.1}$$

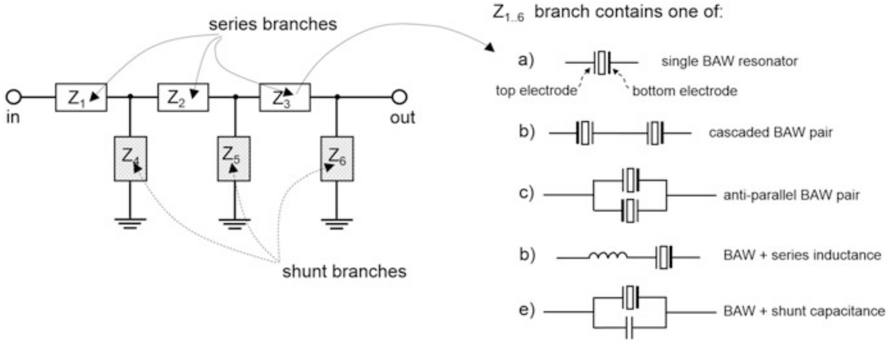

Fig. 16.4 Simplified ladder filter and some examples of elements in each branch

Note that the low-frequency capacitance of a resonator is inversely proportional to passband center frequency. The acoustic resonances are generally placed within a few % of the center frequency of a filter. In a BAW device, the layer stack determines the resonance frequency. *Resonance frequency* f_s can be determined using a Mason model [5] which requires knowledge of thickness, velocity, and mass density of all layers, plus coupling coefficient and *dielectric constant* $\varepsilon_0\ \varepsilon_r$ *of the piezolayer*. With everything else kept constant and all layer thicknesses multiplied by *factor a,* the resonance frequency will change by a factor of *1/a*. Higher resonance frequency requires thinner layers, including the piezolayer. Once *thickness of the piezolayer t* is known, one can calculate the *area of a resonator* A_{res} needed to obtain the low-frequency capacitance. Using the parallel plate capacitor formula,

$$A_{res} = \frac{C_{lf}\ t}{\varepsilon_0\ \varepsilon_r} \tag{16.2}$$

From thickness scaling with $1/f_s$ in combination with equations (16.1) and (16.2), it becomes obvious that resonator area will be inversely proportional to the square of center frequency:

$$A_{res} \propto \frac{1}{f_c^2} \tag{16.3}$$

In essence this is the reason why thin film BAW is commercially not attractive at very low frequencies. The capacitance and area from equations (16.1) and (16.2) will only give a rough estimate where to start when designing a filter. For BAW filters with a small relative bandwidth (<3.3 %), achieving a very good port matching is not difficult. A designer will optimize the resonance frequencies and area of individual resonators until the passband shows low insertion loss and high return loss. The number of series and shunt branches utilized in a ladder filter depends to a large degree on the levels of stopband rejection the filter must meet. In order to increase rejection, one can try to reduce the area of series resonators and increase the

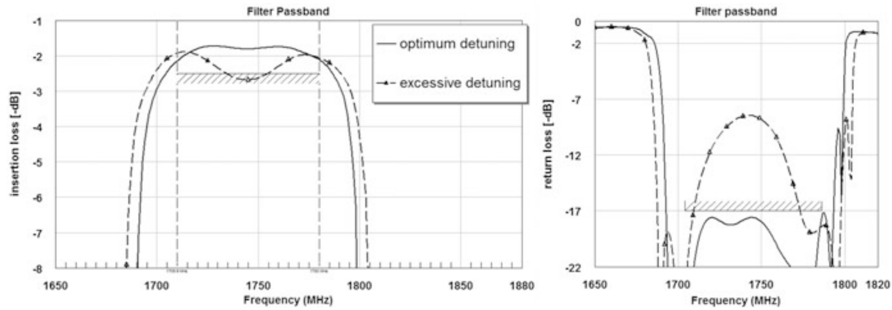

Fig. 16.5 Comparison of a filter with properly set frequencies (*solid lines*) with a filter having excessive detuning between series and shunt resonators (*dashed lines*)

area of shunt resonators. This will gradually degrade the ability to meet matching requirement over the entire passband. The alternative is to add more series and/or shunt branches which will usually show better matched passbands. However, the price to pay is larger total area and a risk of increased insertion loss.

AlN-based BAW filters with larger relative bandwidth (>3.3 %) are more challenging regarding return loss. Novice filter designers are tempted to stretch the bandwidth of a filter by moving the resonance frequencies of series and shunt branches further apart; this indeed creates a wider passband. Unfortunately it will also result in poor return loss in the center of the passband and gradually the center insertion loss will also start to degrade. Figure 16.5 shows an example of a filter which was stretched in bandwidth beyond reasonable limits.

Some relieve can come from adding series inductance to shunt branches, but on the flipside this may negatively impact wideband rejection performance. Other tricks are known to create ladder filters with relative bandwidth up to 8 % using LC branches between filter stages, but this will necessarily lead to a degraded rejection at some frequency region in the stopbands. Piezo materials with higher coupling coefficient such as Sc-doped AlN are especially beneficial for those applications.

In a duplexer the matching of two filters at the (shared) antenna port complicates the situation. Each of the two filters needs to be well matched in its respective passband, while it needs to be highly reflective (low return loss) in the other filter's passband. Moreover, the impedance of the reflective filter must be as high as possible—ideally and "open"—or else that filter will cause mismatch for the passband of the other filter. In many cases this will be implemented using a matching network between the filters and the antenna port. The main objective of the matching network is to rotate the phase of each filter to meet the "open" condition as described above. Figure 16.6 shows a simplified example of a duplexer and how phase rotation is applied. A number of different options exist to implement the matching network.

Early duplexer used microstrip or stripline delay lines as phase shifters, but those are comparatively long and hard to fit into current-generation duplexers. Most duplexers today use LC-based matching networks. Depending on the relative position of receive and transmit frequencies—and the filter topologies chosen—the

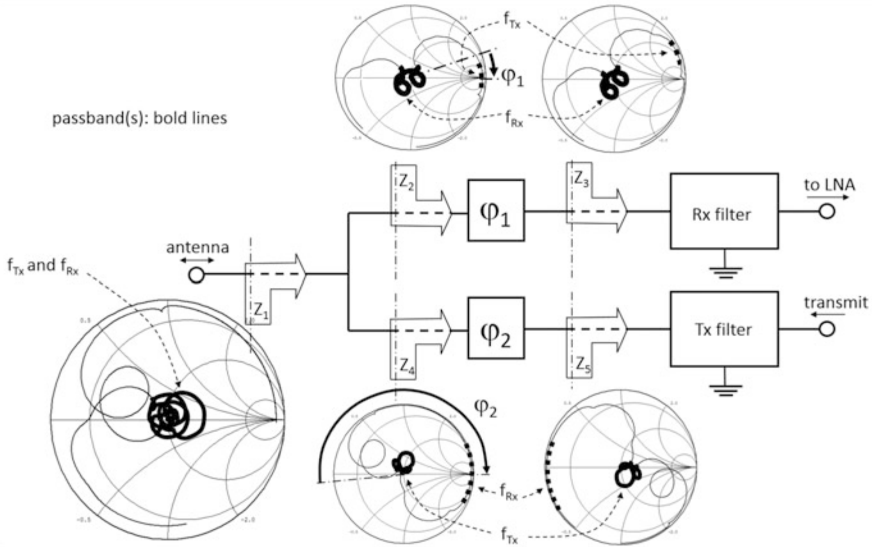

Fig. 16.6 Example of impedance Smith charts for different reference planes in a duplexer

preferred solution is either a low-pass or a high-pass-type matching network. While the low-pass network will create a clockwise rotation of impedance in a Smith chart (as in Fig. 16.6), a high-pass network will create a counterclockwise rotation. Few lucky cases exist when only one of the paths requires a phase shift. The size and *Q*-factor of the inductance needed often make one solution favorable over the other. Due to the nature of a high pass or low pass, there will be an impact observed in the wideband characteristics of the duplexer. Since size of duplexers is severely constrained, the capacitors of the LC network are often eliminated by designing the input impedance of the filters to have capacitive characteristics and/or by using capacitors integrated on the BAW chip (Fig. 16.7).

In Fig. 16.8 the shunt inductance is high-pass type and will create a counterclockwise phase rotation in for both Rx and Tx paths. This is a good choice if both Rx and Tx can be designed to show a capacitive input impedance at the respective frequencies. Shunt-L match does not create a pure phase rotation around the center of the Smith chart; both passbands will see an impedance change which needs to be factored in when designing the BAW filters.

16.7 Rejection and Isolation

Early generations of BAW duplexers used in narrowband (N) CDMA phones served one main purpose: isolate receive and transmit signals from each other to the best possible degree. Isolation is measured between the Tx and Rx port of a duplexer

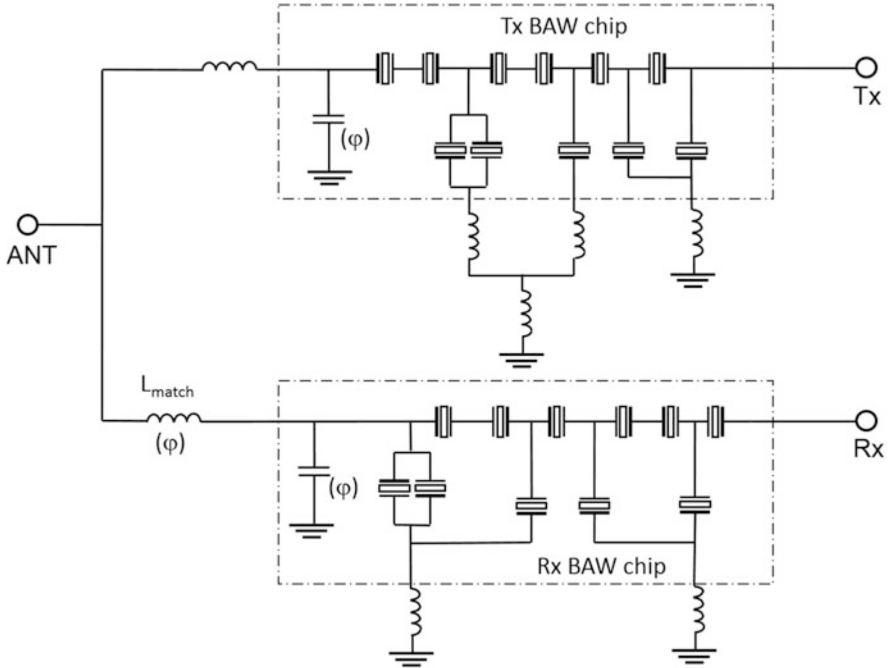

Fig. 16.7 Matching network used for a Band 25 duplexer. There is a shunt capacitance on the antenna port which is integrated into the Tx BAW chip, a series inductor connecting to the Rx chip. The matching network is low-pass type and would also be referred to as series-L match

Fig. 16.8 Shows an example of a Band 7 duplexer with a shunt-L match at the antenna port

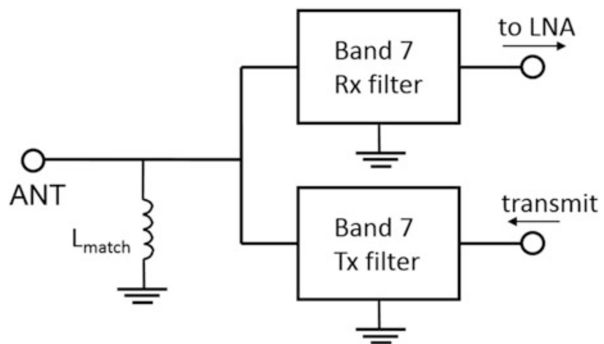

with a nominal termination at the antenna (usually 50 Ω). At Tx frequencies early duplexers had to achieve better than 50 dB isolation, while at Rx frequencies 40 dB isolation was sufficient. Rejection at other out-of-band frequencies was not required because very few other bands were utilized which could interfere. The few sources of interference known in those days were dealt with in other passive filters. With every consecutive generation of BAW duplexers, the specifications for isolation were tightened and new requirement for out-of-band rejection added. With the

advent of WCDMA (3G) around year 2003, the regulatory bodies tightened the limits for phones to operate properly in the presence of interference signals. For duplexers, it was no longer sufficient to have low insertion loss and high isolation. When Wi-Fi found its way into smartphones, it also became important to prevent Tx noise to be emitted into the Wi-Fi band at 2.45 GHz. GPS also became a common feature. Around year 2010, most of the interstage filters were eliminated. In order to prevent receiver de-sense problems (as a result of wideband noise from the power amplifier), the duplexers had to provide additional isolation in the Rx passband. Isolation requirements for duplexers in LTE (4G) are now typically 55 dB for both the Rx and the Tx frequency ranges.

In order to achieve isolation levels of greater than 55 dB in combination with a large number of out-of-band rejection requirements, modern duplexers make use of inductances added into the shunt branches of a ladder filter. Each inductance in combination with the low-frequency capacitance of a BAW resonator forms an LC tank circuit which will increase stopband rejection in a certain frequency range. Essentially this LC tank creates a transmission zero which has a rejection maxima limited just by the out-of-band losses of the acoustic resonator and the Q-factor of the inductor. This is however not without drawbacks as it will degrade rejection at higher frequencies, often referred to as "flyback" (Fig. 16.9).

With inductors added to multiple shunt branches, several rejection regions can be taken care of. A typical case where this method is applied is to increase the rejection of the second and third harmonic tone (H2 and H3) either from the power amplifier or from the filter itself. One of the most severe challenges in small-sized duplexers is to prevent inadvertent coupling between inductances, traces, bond wires, and ground planes. Any shortcut the RF signal finds to go directly from the Tx to the Rx port will cause severe problems with isolation. No matter what degree of rejection each of the filters achieve, the isolation will be limited by this cross talk. Shared ground

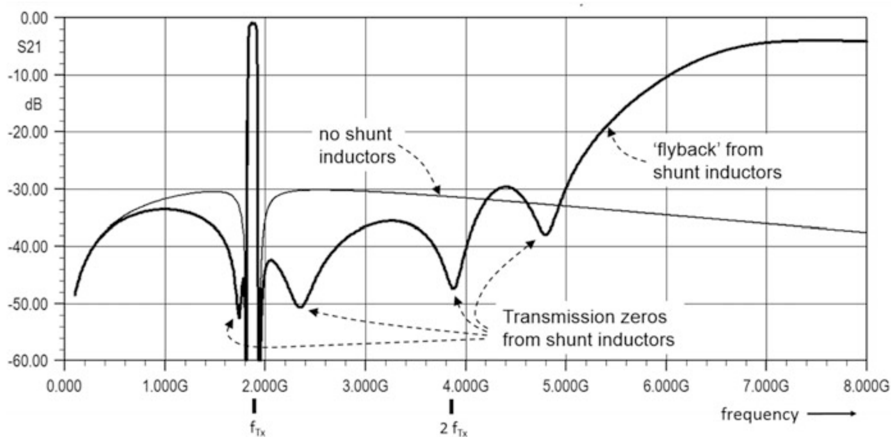

Fig. 16.9 Example of a BAW filter before and after adding inductance to the shunt branches

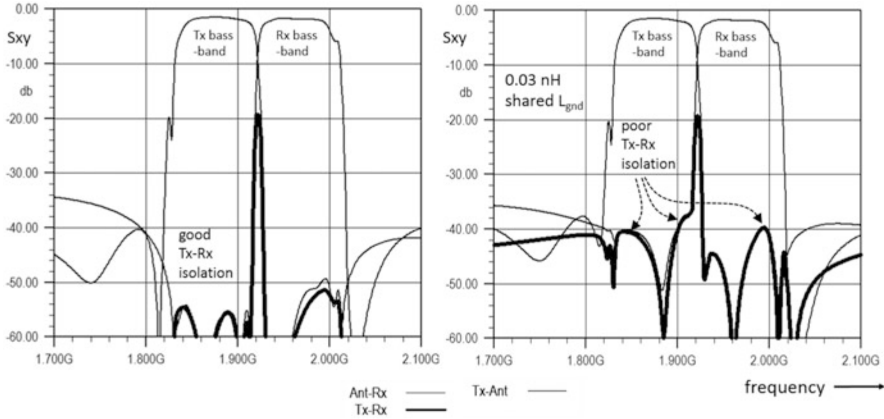

Fig. 16.10 Degradation of Tx-Rx isolation by shared ground inductance. *Left diagram* is a duplexer designed to meet 55 dB isolation in Tx band and 50 dB in Rx band. *Right diagram* shows same duplexer with shared $L_{gnd} = 0.03$ nH and less than 40 dB isolation in either band

inductance between Rx and Tx filters is in particular unforgiving. As the currents flowing in the ground of a Tx filter can be high, it takes only a minute amount of shared inductance to destroy isolation (Fig. 16.10).

As a consequence of the challenging requirements for rejection and isolation, the design of BAW duplexers involves heavy numerical electromagnetic (EM) simulations. For best possible prediction of isolation, the tiniest details of geometry on the BAW chip, all inductors, and traces in the functional substrate and in many cases even the geometry of the customer's phone board must be included. Many legacy duplexers were built on organics laminates with four metal layers. State-of-the-art duplexers utilize organic laminates with up to seven metal layers. Only true 3D EM simulation tools will represent reality to a satisfactory degree, but even then expertise is needed setting up the mesh and ports.

16.8 Power Handling and Reliability

All communication standards beyond 2G require narrowband filtering in the transmit path to meet regulatory requirements. The typical maximum power in transmit operation for a WCDMA and LTE system can be up to 27 dBm at the antenna. This equates to 29–30 dBm at the input of the filters. Typically the required lifetime is >5000 h at maximum power and average operating temperatures of +55 °C. The elevated temperature takes into account that the inner part of phones gets quite warm in normal operation. It is not sufficient for a filter to just survive the 30 dBm transmit power for long enough. Before a phone leaves the factory, it undergoes a calibration of the transmit channels which can lead to peak power exceeding

normal power ratings by a few dB for a short period of time. It is also common to test high transmit power into a severely mismatched antenna port. This is often referred to as “ruggedness” test. The filter (and power amplifier) must tolerate this overload situation without permanent damage. Another aspect of power handling is to check if the filter still meets specifications in presence of self-heating effects. Transmit filters with an inherently poor heat path will face tremendous challenges in both operating lifetime and spec compliance at high-power levels. It is essential to understand all factors contributing to the thermal resistances of the entire device from the individual resonators all the way to the customer’s phone board.

Reliability of BAW filters is qualified with a number of standardized testing procedures which aim to predict how likely a part is to fail “in the field” (in the user’s hands). BAW has an excellent track record of reliability. Whenever modifications are made to the wafer process or packaging process, a new run of qualification tests is needed. In this fast-paced industry, no customer can wait 3 full years to confirm a new part is reliable; hence accelerated testing methods are deployed. The theory behind accelerated testing is the same as used in other areas of microelectronics [6]; lifetime is determined by an Arrhenius equation (exponential function) with a characteristic activation energy. Tests for power handling are performed at significantly higher ambient temperatures to create failures in a shorter time, often referred to as high-temperature operation life (HTOL). As a “rule of thumb” for acoustic filters, every 10 °C increase in ambient temperature will shorten the lifetime of a filter by a factor of 2. When, for example, running a power durability test at +135 °C (80 °C above the temperature relevant for true lifetime), it is sufficient to test if parts survive 10,000 h/256 = 39 h. The effort for such tests is still rather big because part-to-part variations can be significant. A statistically relevant sample quantity much be tested, often more than 50 samples will be needed to ensure there are no early failures in the distribution.

Similar accelerated methods exist for moisture resistance of filters. Section 16.12 provides insights on packaging choices for BAW and ways to achieve moisture resistance. A typical test will run parts in a test chamber at 85 °C and 85 % relative humidity for 500–1000 h and inspect pre- and post-RF data for any signs of frequency shifts or insertion loss degradation. A more extreme test case is known as “pressure cooker” or “autoclave” test. In this case the parts are placed inside a pressure vessel with 100 % relative humidity at a temperature above 100 °C and at a pressure of several atmospheres. Under these severe conditions, moisture diffusion is dramatically enhanced, and weaknesses of parts will be exposed.

Parts will also be exposed to electrostatic discharge (ESD) testing. Several approaches exist which aim to mimic conditions realistically occurring during manufacturing of the phone or during usage. Due to the excellent breakthrough electric field in AlN, a typical BAW should do very well in all categories of ESD test cases. One kilovolt ESD-HBM ratings are commonly achieved. BAW is significantly more robust than, for example, SAW or MIM capacitors often used in integrated active circuits.

Additional tests include high- and low-temperature storage, temperature cycling tests, mechanical tests (“drop tests”), soldering reflow cycles, and other tests often specific to a certain customer.

16.9 Temperature Effects

The temperature coefficient of frequency (TCF) of acoustic filters has become a very important performance parameter in the past 10 years. At room temperature the filter topology chosen and the Q-values of the resonators determine how steep a filter will roll off from passband to stopband. A phone is supposed to work properly in ambient temperatures from −30 °C up to +55 °C. Even though the extremes are rare, they warrant consideration. The components inside the phone can briefly be at −30 °C while powering up a phone from standby but will typically run significantly warmer once steady state is reached. Most filter specifications therefore call out a temperature range of −30 °C up to +85 °C. Over the full temperature range, the temperature drift of a filter may be equally detrimental to performance than a poor Q-value. Excessive temperature drift has plagued conventional SAW filters ever since guardbands have shrunk dramatically for many of the popular LTE bands at or below 1 GHz. Temperature compensated (TC) SAW is a very attractive solution for those bands. BAW has always done relatively well with regard to TCF.

For BAW-SMR and FBAR, the materials and thicknesses of layers used for the acoustic stack determine the TCF. Both types use AlN as a piezolayer and a hard and heavy material (such as tungsten or molybdenum) above and below the piezolayer. Those materials establish a moderately negative TCF. Most of the acoustic energy is confined in those layers; therefore they dominate the overall TCF. FBAR typically shows a TCF of −27 ppm/°C. The similarities between BAW-SMR and FBAR end here. BAW-SMR uses amorphous SiO_2 in the acoustic reflector stack. There is no SiO_2 in a conventional FBAR stack. SiO_2—despite its boring history as a dielectric layer in ICs—is a material with unique temperature characteristics for elastic stiffness. SiO_2 increases in stiffness when temperature increases—which is opposite to nearly all other commonly available materials. As a consequence the SiO_2 in the layer stack will counteract the temperature drift from other layers and bring the TCF closer to zero. Typical values for BAW-SMR are −18 ppm/°C. At 2.5 GHz center frequency, the frequency drift of BAW-SMR over full temperature range will be −2.7 MHz (at +85 °C) and +2.5 MHz (at −30 °C). FBAR will temperature drift about 50 % more; in order to maintain spec compliance at the temperature extremes, more margin in insertion loss and/or rejection needs to exist at room temperature.

Some of the most recently released LTE bands like Band 30 can’t tolerate a TCF exceeding ±5 ppm/°C. Complete temperature compensation can be implemented in BAW-SMR as well as in FBAR by increasing or introducing SiO_2 into the layer stack at a location where acoustic energy density is high. In either case this will

be detrimental for performance, in particular for effective coupling coefficient. The price to pay for full temperature compensation in BAW is a lower limit for relative bandwidth a filter can still achieve.

As indicated earlier in the section about power handling, there will be self-heating effects in transmit filters. For filters with negative TCF, the most critical case is usually a transmit tone at the upper edge of the passband. The temperature increase due to self-heating will move the filter to a lower frequency. Typically the insertion loss for the transmit signal will increase as the tone starts riding down the slope of the filter. This creates a positive feedback condition as higher insertion loss means more power is dissipated and temperature increases further. In extreme cases a thermal runaway condition can occur in which a filter is destroyed very fast. Several factors determine how severe a self-heating issue will affect a filter:

- Transmit power level and spectral distribution of the modulation used
- Dissipated power in the filter
- Thermal resistance from resonators to package and heat sink
- Value of TCF

In terms of thermal resistance and TCF, the construction principle of BAW-SMR is clearly advantageous. Heat dissipated in the piezolayer and electrodes can vertically flow out through the acoustic reflector layers. Keeping the resonators as close as possible to ambient temperature is a key to remain spec compliant at maximum power levels. In an FBAR the heat dissipated in the resonator will have to flow out laterally through the membrane, resulting in much higher thermal resistance and higher temperature at resonator level. For other types of RF-MEMS resonators which are suspended by skinny anchors, the self-heating issue will be dramatically worse, and operation of these devices at high transmit power will be extremely challenging.

16.10 Group Delay

It is inherent for high-order filters to create significant phase angles between sinusoidal input and output signals. It is also fundamental for phase angle to increase significantly throughout the passband, depending on the order of the filter. Group delay is calculated from the negative derivative of phase (in radiant) over frequency. Group delay has the dimension of time and is usually stated in nanoseconds. A large group delay means a signal takes longer to pass a filter; however this is almost irrelevant compared to the travel time of radio waves between base station and a phone. A constant group delay over the passband is desirable but not always easy to achieve. It can cause issues if group delay shows strong variations within the passband of a filter. Group delay variation is getting increasingly important for systems using a high modulation bandwidth as it will cause signal distortion. Limits for group delay variation are either directly stated, or the customer specifies a maximum error vector magnitude (EVM) which is a parameter compounding

magnitude and phase distortions. EVM beyond a few % will affect bit-error rate. Problems with group delay are often related to unwanted acoustic "spurious" modes which can create peaks in the group delay. The spurious modes are usually very narrow in frequency (weakly coupled modes) but can have moderate to high Q-values. The best remedy for spurious mode problems is to design the acoustic layer stack and the edges of the resonators for best possible mode suppression.

16.11 Linearity of Filters and Duplexers

WCMDA and LTE systems have stringent requirements with regard to harmonic emissions and intermodulation effects. In older systems much less attention was paid to such effects, and therefore acoustic filters were considered linear circuits until problems with linearity surfaced in early WCDMA systems [7]. The dominant source of nonlinearity in BAW is directly linked to the nature of the AlN lattice structure and its piezoelectric properties. A good understanding of how various nonlinear effects relate to the constituent piezoelectric equations of AlN has been established [8, 9] in the past years. Nonlinear BAW resonator models exist which predict the behavior well. Nonlinear characterization of BAW filters is tedious work and needs to be done carefully to prevent erroneous results.

Filters for LTE have to meet a large number of spec parameters relating to linearity. In current-generation acoustic filters, there is considerable effort required to achieve compliance. The most common situations for which nonlinear specifications exist are summarized in Table 16.1. Actual numbers will vary significantly depending on antenna configuration and system architecture. Both regulatory requirements and system performance need to be considered.

Several design concepts are known to mitigate the effect of inherent nonlinear effects in acoustic resonators. Nonlinear cancellation techniques [10] are widely

Table 16.1 Example of linearity requirements for many FDD bands

Mixing product	Frequency it occurs	Frequency of "blocker" fB	Situation/problem	Typical spec
H2	2* fTX	–	Emission of 2nd harmonic during TX	−45 dBm
H3	3* fTX	–	Emission of 3rd harmonic during TX	−55 dBm
IMD2L	fB + fTX	90–300 MHz	Falls into own RX band(s) and kills receive sensitivity	−110 dBm
IMD2H	fB − fTX	2*fTX +90 to 300 MHz		
IMD3L	2*fTX − fB	fTX − 90 to 300 MHz		
IMD3H	2*fB − fTX	fTX + 45 to 150 MHz		

Worst case occurs for maximum transmit power and when mixing product lines up with receive channel

used today, but they are not absolute because full cancellation would require perfect symmetry/anti-symmetry of resonator pairs (see Fig. 16.4b, c). In practical filter layouts, it is hard to achieve better than a 30 dB improvement for any mixing product from cancellation techniques alone. It should be noted that cancellation schemes work well for even-order nonlinearities (like H2 and IMD2), but they don't work for odd order (H3 and IMD3). Luckily the third-order nonlinearity is very small in conventional AlN-based BAW resonators. Another consideration in duplexers is how mixing products propagate through a circuit. In every stage of a filter, there will be a balance between attenuation for out-of-band tones (like H2 or H3) with newly created tones. The designer of a filter has the option to create LC traps for certain tones in some of the stages, but for this to be effective, one needs to understand where a tone is generated and how it propagates. In duplexers, the resonators close to the antenna port are the most critical ones and deserve the most attention. This is the location where Tx signals and strong interference signals exist simultaneously. Mixing between them can create intermodulation falling right into the Rx passband. Once created, those cannot be filtered out and will hit the receiver input at full strength.

16.12 Packaging and RF Module Integration

Between 25 and 65 % of the surface area of an acoustic filter will be resonator surfaces which need to vibrate freely. In contrast to semiconductor ICs, a BAW resonator cannot be directly encapsulated with the approaches commonly used in ICs. In BAW-SMR the upper surface of the resonators needs to remain free of additional mass loading and contamination. Fortunately the handling of BAW-SMR wafers during sawing and assembly is not difficult as the wafers are mechanically very robust (but residues and debris must be removed properly afterwards). In comparison FBAR wafers with released membranes are very delicate to handle. Residues can creep under the membranes through the release holes, and cleaning processes can fracture membranes. Sawing with blades and a water-jet is not a good idea either. Historically most SAW and BAW filters have relied on hermetic ceramic packages. By definition, a hermetic package prevents moisture from diffusing into the cavity which houses the acoustic resonators. A classical hermetic package uses a ceramic carrier and welded metals seals. There is a significant size and cost penalty using hermetic packages, and therefore they are losing market share rapidly. The metals and oxides used in BAW will not tolerate direct exposure to humid environment. In the best case the frequency will start drifting; in the worst case the resonator structure will be damaged by corrosion. Glues or polymers have high diffusion rates and absorption for moisture and will not suffice on the long run to prevent degradation. A true moisture barrier is needed; there are several choices how to implement it. A hermetic wafer-level package as used for FBAR requires a wafer bonding with a metal seal ring and through Si vias for electrical interconnects [11], all of which increase the cost of a completed wafer significantly. In BAW-SMR

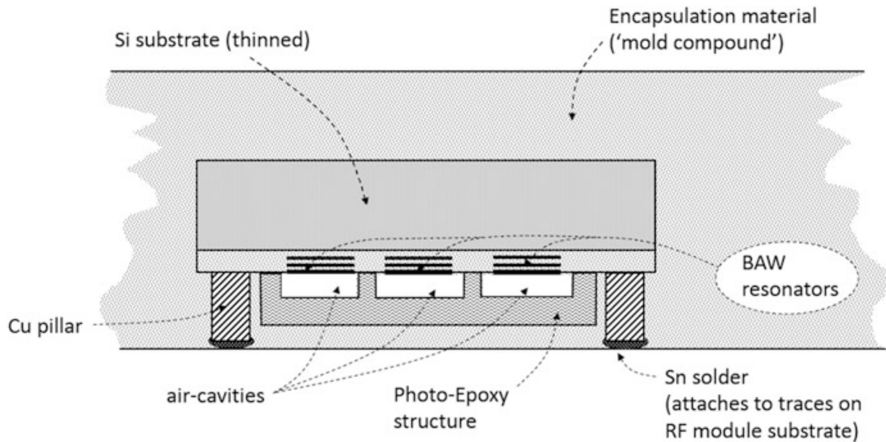

Fig. 16.11 Shows a simplified cross section of a wafer-level package (WLP) for BAW-SMR

technology, it is possible to use thin passivation layers to protect the entire device structure from moisture; the bottom electrode is deeply buried in the layer stack and not subjected to the ambient anyways. This is in stark contrast to FBAR in which both top and bottom electrodes are vulnerable to moisture attack. The ability to make a BAW-SMR filter moisture resistant with a deposited passivation layer has proven to be a key enabler for low-cost packaging. Photo-defined polymers are therefore an excellent choice for BAW-SMR, but not used on FBAR as of today. The only function of the polymer wafer-level package on a BAW-SMR is to prevent encapsulation material from getting into direct mechanical contact with the top electrode (Fig. 16.11).

As pointed out earlier, a major driver in the smartphone business is size. In order to achieve the smallest possible implementation of an RF front end, the successful players in this market go to great length in integrating filters, passive components, power amplifier, SOI switches, and CMOS controller circuits into tiny spaces. Those RF modules contain a mix of different technologies which can be a challenge for packaging/assembly. The most densely packed RF modules contain only flip-chip devices and occasionally a few capacitors and inductors as surface-mount devices (SMD). The majority of inductors are today embedded into a multilayer laminate. Wire-bonded ICs and filters are starting to disappear from late-generation RF modules as wire bonds require more space between components than flip chip.

One big challenge of large RF modules is to guarantee all bands, modes, and functions work properly before shipping a product to a customer. Complex test procedures are required to test RF modules. Each component added into a module will imply higher risk for yield loss at final test. For example, in a module with 20 components of which each has a 3 % fail rate, the total yield would only be $0.97^{20} = 0.54 = 54\,\%$. Obviously this can have disastrous consequences for the financial success of a product and company. The best method to prevent one filter or

IC from sending a whole RF module to the trash bin at the end of the manufacturing line is to test each component thoroughly before using it. This is often referred to as "known good die" approach. In RF filters this is not trivial to accomplish as a filter behaves different with and without the inductances to the signal pins and shunt branches present. Extensive correlation studies are needed to establish parameter limits for a filter to be declared fit to be used in a module.

16.13 Filter Design Methodology

Designing a BAW product involves making a number of decisions on filter topology, process options, frequency positioning of resonators, and packaging options. At the very beginning of the design flow comes a thorough analysis of the requirements and specifications. Good judgment needs to be applied to requests from customers as they occasionally have unrealistic expectations and don't understand the trade-offs to be made; equally often customers omit to specify certain parameters (and later come back to complain about them). The review of requirements includes the following aspects:

- Identify critical requirements from system point of view.
- Maximum RF power the filter will be exposed to.
- Situation regarding linearity and intermodulation.
- Constraints on matching circuits and port impedances.
- Size and height constraints.

The filter design flow starts with determining how many series and shunt branches will work best for a certain requirement. A higher number of branches generally increase the rejection levels one can achieve, but at a certain number the insertion loss will also start to increase. In almost all cases the size of the filter will increase for a higher number of branches. In many duplexer designs, the input impedance is more favorable if the antenna-side element is either a series or a shunt branch. There is no general rule if a filter should contain equal number of series or shunt branches or if there is one fewer of either—it all depends on the specific requirements. Shunt branches can be individually grounded through off-chip inductances, or they can be tied together on the chip and share a ground connection. The option to modify the inductance and create some additional transmission zeros in the wideband characteristics is often helpful. Often an earlier generation of a similar BAW filter will be used as an initial starting point to figure out how many branches are appropriate. For an initial exploration of filter topology and grounding configuration (common ground, split ground, combination of both), the designer will usually model the ground inductances as lumped elements and the resonators with a Butterworth-van Dyke (BVD) model [12]. The BVD model is formulated such that size dependency of resonator parameters is predicted for the specific BAW process used. Initially the frequencies and areas of all resonators

will be undetermined; however some limits and constraints will be applied. Ground inductances and matching elements may also be available for optimization. The advantage of this approach is the speed at which circuit simulators can crunch through millions of optimization cycles; the BVD model is numerically extremely efficient. Suitable optimization algorithms will quickly converge to a reasonably looking passband and stopbands or—if the topology is chosen poorly—fail to find a promising solution at all. An experienced designer will know how to change the filter topology based on the results obtained. In addition to changing the number of branches in a ladder filter, often there will be a need to address a situation where one resonator wants to have smaller area than constraints allow. In many cases this can be resolved by replacing a single resonator (see Fig. 16.4a) with a cascaded pair of resonators (Fig. 16.4b). Effectively this allows increasing the impedance in a branch by up to a factor of 2 if needed. Different reasons to insert cascaded resonators will be described later. BAW-SMR has the option to provide MIM capacitors which can be used in various parts of the circuit for matching and phase shifters or to reduce effective coupling coefficient in certain branches (Fig. 16.4e). Those MIM caps are a side product of metal layers in the reflector and don't add any cost at all. The basic implementation of "reflector MIM caps" is described in [13]. Once a satisfying passband response (insertion loss and return loss) along with required stopband rejection is achieved, the filter topology becomes one of the candidates to enter the next round of evaluations (Fig. 16.12).

Any step beyond basic filter topology studies requires full 3D electromagnetic (EM) simulations of the interconnections, inductors, traces, and all other elements having relevant geometrical size. For this purpose, detailed layout work for the filter and package/module will have to be done—even though this is by no means a final version of a layout for a product. The EM result will reveal parasitic effects that were not considered in the initial lumped element simulations. In Rx or Tx filters, the discrepancy will mostly be in the rejection regions and wideband performance. In duplexers additional issues with isolation could be revealed. Discrepancies are usually important enough to require significant redesign of the

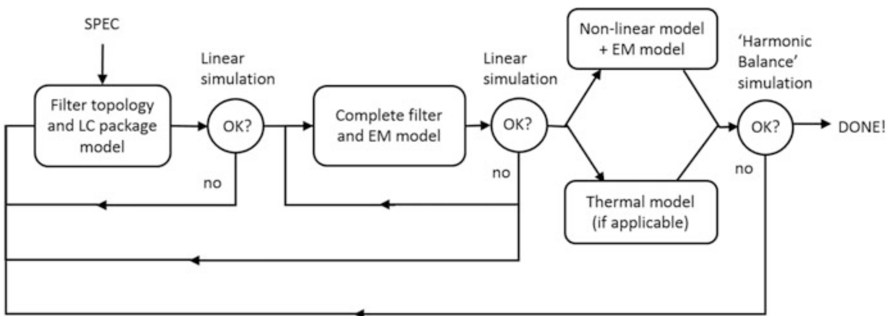

Fig. 16.12 Design flow diagram for BAW product

filter and package/module layout. This again is an area for which human intuition and experience is key. In complex products, several iterations may be required until satisfying small-signal response across the entire frequency range is achieved.

Next—if the filter is specified to endure transmit power—a calculation of dissipated power density [W/mm^2] will be performed to identify resonators with a potential for overheating. In critical cases a full 3D thermal model will be calculated. Should a certain resonator show concerning temperature increase at max transmit power, the designer has two options:

(a) Reduce thermal resistance to ambient. In flip-chip devices, this can be accomplished adding bumps to facilitate better heat flow. Package/module design must also take thermal requirements into account.
(b) Replace one resonator with a series-cascaded resonator pair, of which each is two times the area of the original resonator. This method reduces the power density by a factor of 4. The downside is that chip area will likely have to grow in size.

In either case it will be necessary to redo the EM simulation with the modified layout and confirm small-signal behavior is still meeting expectations and then repeat the thermal simulation. In very rare cases the BVD model will have to be supplemented with a Mason model to check and re-optimize for higher-order acoustic modes at very high or very low frequencies.

Finally, a BAW will have to be modeled for nonlinear effects such as IMD2, IMD3, H2, and H3. Nonlinear BAW models must be run on harmonic balance solvers which slow down simulations dramatically compared to small-signal linear solvers. It is not efficient to use a nonlinear model from the very start because optimization cycles for the basic filter design would take a lot more time to converge. Experienced designers will predict upfront which resonators in a filter are the biggest risk and consider countermeasures. Often times the nonlinear simulations are performed just to verify the countermeasures are effective. One thing to point out is that nonlinear simulations can only be accurate if the 3D EM simulations predict the wideband behavior accurately. If, for example, an error exists for high-frequency rejection, the nonlinear simulation cannot predict H2 and IMD2 accurately at all. Depending on size constraints in a product, nonlinear cancellation techniques [10] may not be possible in all branches of the filter. Simulations will help the designer to determine in which branches the dominant nonlinear effects are created and find the best compromise between size and nonlinear performance. In a typical duplexer, all resonator branches near the antenna port will rely on nonlinear cancellation techniques. Series cascaded resonator pairs are very common in series branches of Tx filters as they also help improve power handling. In many cases shunt branches will use antiparallel resonator pairs which is a good solution as long as the resulting resonator areas are still above reasonable limits. Using inductance in the shunt branches will also allow to place transmission zeros at the frequency of H2, but designers need to choose wisely in which of the shunt branches this is most beneficial. What is surprising to novices is that a good small-signal rejection for H2 in a filter is not a guarantee for good nonlinear H2 performance. Small-signal

rejection at H2 frequency sums up from stage to stage, but if a branch close to the output generates most of the H2 problem, the earlier stages are of no help. Generally with all methods applied properly, it is feasible to meet linearity requirements in LTE systems, but often the resulting filter is larger and shows higher insertion loss than a filter designed without linearity requirements in mind. It is therefore very important to understand the environment the filter is supposed to work in and not over-engineer the nonlinear performance. Depending on antenna design, the H2 and H3 tones remaining after a filter will be more or less critical.

16.14 Solutions for Carrier Aggregation in Long-Term Evolution (LTE)

In order to support inter-band carrier aggregation (CA), the RF front end must allow multiple signals to be routed between antenna and transceiver simultaneously. At the current time, the development is mostly focused on downlink (=receive)-CA which will allow higher download data rates, but there are discussions going on to also use uplink-CA in the future. There are a number of additional challenges to be addressed:

- Multiple filters need to be connected and impedance matched to one common port. For the passband frequency of each of the filters, the sum of the input admittances of all other filters should be very close to zero to prevent degradation of insertion loss.
- Each RX filter must show very high rejection and isolation for all possible transmit frequency scenarios. Adding frequency ranges for which additional rejection is required will increase insertion loss for the passband.
- The TX filter must have rejection and isolation for all receive frequencies to be covered. Similar to above, this increases insertion loss.
- The scenarios for which IMD2 and IMD3 mixing products can fall into one of the RX bands will multiply with the number of RX bands.

Band combinations are still evolving as is the architecture to best address the challenges above. In any case an RF subsystem to serve multiple bands for carrier aggregation will be extremely complex to design. The roll-out of CA on a significant scale is expected in 2016, and in most of the cases it will be limited to two Rx bands receiving with one of the corresponding Tx bands transmitting. This can be accomplished with a CA-compatible quadplexer. Looking further out into the future, there will be three or more Rx bands aggregated which will require hexplexers or worse. With every additional filter added, the risk of one critical parameter falling short of expectations is increasing dramatically. Without the performance improvements achieved in past years, it would be inconceivable to address the challenges of current RF modules. It is fully expected the key parameters for BAW will continue to improve, in most cases through hard and tedious work on process

details but occasionally through a lucky break. The complexity of those products is tremendous and will challenge the creativity of BAW designers and the ingenuity of device physicists for years to come. On a positive final note, the profits created from those products will provide well-paying jobs to design and technology experts for the foreseeable future. As a colleague and industry veteran nicely puts it: LTE can as well be interpreted to stand for “long-term employment.”

References

1. Morgan DP (2000) A history of surface acoustic wave devices. Int J High Speed Electron Syst 10:553
2. Lakin KM et al (1995) Solidly mounted resonators and filters. Proceedings of 1995 IEEE ultrasonics symposium, Seattle, 7–10 Nov 1995
3. Hashimoto K (2009) RF bulk acoustic wave filter for communications, Chapter 5. Artech House, Norwood, MA
4. Aigner R et al (2002) Advancement of MEMS into RF-filter applications. Proceedings of IEDM2002, San Francisco, 8–11 Dec 2002, pp 897–900
5. Mason WP (1950) Piezoelectric crystals and their application in ultrasonics. Van Nostrand, Princeton, NJ
6. Gan Z, Wang W (2012) Semiconductor process reliability in practice. McGraw-Hill, New York
7. Aigner R et al (2005) Behavior of BAW devices at high power levels. Proceedings of IEEE IMS-MTT-S, Long Beach
8. Feld D et al (2010) Determination of the nonlinear physical constants in a piezoelectric AlN film. Proceedings of 2010 IEEE ultrasonics symposium, San Diego, 11–14 Oct 2010
9. Rocas E et al (2013) Electro-thermo-mechanical model for bulk acoustic wave resonators. IEEE Trans Ultrason Ferroelectr Freq Control 60(11):2398
10. Aigner R (2005) US patent 7,365,619, 22 Jun 2005
11. Feld D et al (2003) A wafer level encapsulated FBAR chip molded into a 2.0 mm × 1.6 mm plastic package for use as a PCS full band Tx filter. Proceedings of 2003 IEEE ultrasonics symposium, Honolulu, 5–8 Oct 2003
12. Larson JD et al (2000) Modified Butterworth-Van Dyke circuit for FBAR resonators and automated measurement system. Proceedings of 2000 IEEE ultrasonics symposium, San Juan, 22–25 Oct 2000
13. Aigner R et al (2012) Recent advances in BAW technology. Proceedings of International Chiba Symposium on acoustic wave devices, Chiba/Japan, Dec 2012

Index

A

Absorbing Boundary Conditions (ABC), 267
Acoustic attenuation coefficient, 143
Acoustic charge transport (ACT), 73
Acoustic devices
  resonator Q, 340–342
  time and frequency, 342
Acoustic micro imaging (AMI), 324
Active compensation techniques, 252–254
Activity dip, 232–233
Akheiser loss mechanism, 138
Alder's approach, 106–107
AlGaN/GaN heterostructure, 2DEG
  bulk wave RBT, 85–87
  conduction band bending, 74–75
  fabrication process flow, 294–296
  flexural RBT, 85
  high-*Q* MEMS resonators, 75
  piezoelectric transduction, 80
  piezoresistive transduction, 80–83
  resonator f.*Q* values, limits of, 79, 91–94
  sensing mechanism, 88–89
Aluminum nitride (AlN) thin films
  AlN-ScN alloy thin films, 30–33
  BAW resonators, piezoelectric coefficient, 3, 214
  CMOS compatible, 4
  DC-pulsed sputter process, 8
  electric field, 7–8
  hardness and stiffness constants, 3
  high sound velocity, 4
  high thermal conductivity, 3
  magnetron sputtering, 4
  melting point, 4
  MOPVE process, 8
  properties and characterization, 21–30
  reactive magnetron sputter deposition
    c-axis-textured, piezoelectric thin films, 9–17
    oxygen impurities and regrowth issue, 20–22
    substrate roughness, impact of, 18–20
  relative dielectric constant, 3
  RF MEMS applications, 4
  wurtzite structure
    "Berry's phase" method, 6
    lattice constants, 4
    N-and Al-polar films, 4–6
    nucleation, 6–7
    poisson ratio, 6
    thermal CVD technique, 7
Amorphous silicon dioxide (SiO_2), 214, 215
Anchor loss
  absorbing elements, 268–269
  analytic methods, 266–267
  finite-element analysis, 267
  in-phase mode, 267–268
  out-of-phase mode, 267–268
Arrhenius equation, 403
AT-cut quartz thickness-shear-mode (TSM) resonator
  admittance resonance peak and off-resonance static capacitance, 234–235
  electromechanical coupling coefficient, 228
  frequency variation *vs.* temperature, 230–231
  orientation angles, 227–228
  simulated *f-T* and Q *vs.* temperature, 232–233

© Springer International Publishing Switzerland 2017

H. Bhugra, G. Piazza (eds.), *Piezoelectric MEMS Resonators*,
Microsystems and Nanosystems, DOI 10.1007/978-3-319-28688-4

AT-cut quartz thickness-shear-mode (TSM) resonator (*cont.*)
X-displacement
fundamental and third overtone shear-mode, 227
simulation, 229–230

B

BAW. *See* Bulk acoustic wave (BAW)
"Berry's phase" method, 6
Bond void rejection, 323–324
Bosch DRIE process, 290, 292
Bragg reflector, 141, 388
Bulk acoustic wave (BAW)
AIN, 214
BVD model
anti-resonance quality factors, 206
capacitance ratio, 206
electromechanical equivalent circuit, 204, 205
harmonic resonances, 204
input admittance, 205
modification, 206, 207
multiple resonances, 206, 207
physical model, 204
Q factor, 208
resonance frequency, 206
TCF, 208
thickness resonance, 204
vector network analyzer, 208
carrier aggregation, LTE, 412–413
FBAR structures, 212, 213, 215, 218
filter design methodology, 409–412
filters and duplexers, linearity of, 406–407
filter types, smartphones
acoustic filters, 390–392
diplexer, 391
duplexer, 390
hexplexer, 391
LTE, 392
quadplexer, 391
receive (Rx) filter, 390
transmit (Tx) filter, 390
WCDMA, 392
group delay, 405–406
high frequency oscillators, 343
history of, 388–389
insertion loss, 394–395
Lamb wave propagation, 215–217
lateral resonance patterns, 216
leakage, 215, 216
$LiNbO_3$ thin film
asymmetrical mode (A0), 106, 110–111
high electromechanical coupling, 106
intrinsic electromechanical coupling, Alder's approach, 106–107
SH0 acoustic waves, 107, 109–110
shear horizontal mode, 106
symmetrical lateral (S0) mode, 106–109
Mason's equivalent circuit
electromechanical coupling factor, 211–212
input admittance, 209
resonance and anti-resonance frequencies, 210
resonator structure, 209
standing wave pattern, 211
packaging and RF module integration, 407–409
piston mode structure, 218
port impedance and matching
ladder filters, 396
low-pass/high-pass-type matching network, 399
Mason model, 397
microstrip/stripline delay lines, 398
parallel plate capacitor formula, 397
phase rotation, 398, 399
RF components, 395
Sc-doped AlN, 398
series and shunt branches, 396–398
Smith chart, 396, 399
power handling and reliability, 402–404
rejection and isolation, 399–402
SiO_2, 215
size and performance, evolution of, 392–394
SMR structures, 213, 214
temperature effects, 404–405
Butterworth–Van Dyke (BVD) model, 84, 409
anti-resonance quality factors, 206
capacitance ratio, 206
electromechanical equivalent circuit, 204, 205
flexural piezoelectric resonators, 156–157
harmonic resonances, 204
input admittance, 205
modification, 206, 207
multiple resonances, 206, 207
physical model, 204
Q factor, 208
resonance frequency, 206
shear-mode resonators, 233–235, 237–238
TCF, 208
thickness resonance, 204
vector network analyzer, 208

C
Calibration, 330–331
Carrier aggregation (CA), 391, 412–413
Chemical solution deposition (CSD), 40, 42–43
Chip-scale package (CSP)
  high frequency oscillators, 335, 336
  VC-TCXO replacement
  cellular grade, 354, 356
  discrete IC components and wirebonded, 349, 352
  eutectic bonding, 354
  fabrication process, 352, 355
  initial frequency, 354
  PFD, 355
  SOI wafer, 352
  stress control, 354
  voltage tuning capability, 355, 356
Complementary metal-oxide semiconductor (CMOS), 74
Computational modeling
  energy loss
    Anchor loss, 266–269
    fluid damping, 271–273
    modeling *Q*, 266
    quality factor, 265
    TED, 269–271
  frequency response
    eigenmode analysis, 263
    fast frequency sweep methods, 264, 265
    finite element method, 261, 262
    frequency points, 263, 264
    Gauss's law, 261
    Krylov subspace method, 264, 265
    motivation, 258–260
    Newton's second law, 261
  pMUTs, 257
  static and dynamic nonlinearity
    high power, 275–276
    residual stress, 274
Concave-shaped silicon bulk acoustic resonator (CBAR), 251, 252
Coupling factor. *See* Electromechanical coupling factor
Cross-sectional Lamé-mode resonator (CLMR) technology, 189–190
Cross-sectional Lamé-mode transformer (CLMT), 189

D
Data file formats, 330
Data processing, 327–328
Deep reactive ion etching (DRIE), 75, 236
Defect coding system, 325–326
Delaminated cap rejection, 322–323
Delaminated metal pad rejection, 324–325
Disc shear-mode resonator, 236–237
Dissipation mechanisms, piezoelectric transduction stack, 289
DRIE. *See* Deep reactive ion etching (DRIE)

E
Edge die rejection, 324
Electrical rejections
  dynamic spec limits, 317–318
  electrical signatures, 319–320
  geographical-based rejection, 319, 320
  resonance check, 315–316
  resonance parameters, 321
  spec limits, 316
  yield limitation, 318–319
Electromechanical coupling factor
  AlN-based thin-film piezoelectric resonators, 147–148
  BVD model, 146
  definition, 146
  figure of merit, 148
  one-port piezoelectric resonator, impedance for, 146
  piezoelectric coupling factor, 144–145
  ZnO-based micro-resonators, 147
Electron cyclotron resonance-based reactive ion etching (ECR-RIE), 46–48
Electrostatic discharge (ESD) testing, 403
Electrostatic (capacitive) transduction, 222
Error vector magnitude (EVM), 371, 373, 395, 405, 406
EVM. *See* Error vector magnitude (EVM)

F
Fabrication process flow
  AlGaN/GaN resonators, integrated HEMT read-out, 294–296
  piezoelectric AlN films, deposition of, 285–287
  piezo-only resonators, 284, 288–289
  piezo-on-substrate resonators, 284, 289–291
  sidewall AlN process, 3D transduction of MEMS resonators, 292–294
  transduction stack, 284
  VC-TCXO replacement, 352, 355
Face-shear mode resonators, 223
Fast frequency sweep methods, 264, 265

FBAR. *See* Film bulk acoustic resonator (FBAR)
Federal Communication Commission (FCC), 394
FEM-supported double beam laser interferometry (FEM-DBLI), 30
Ferroelectric random access memory (FRAM), 40, 42, 47–49
Figure of merit (FoM), 148
Film bulk acoustic resonator (FBAR), 212, 213, 215, 218, 388
Finite element method (FEM) model, 156–157, 167, 169
Flexural piezoelectric resonators
  energy methods, vibration analysis
    BVD equivalent circuit model, 156–157
    piezoelectric force and elastic strain energy, 157–158
  mechanics of laminates
    cross section and coordinate definitions, 153, 154
    flexural rigidity, 155
    natural frequency, 155
    neutral axis, 154, 155
    thin-film piezoelectric coefficients, 155–157
  one-dimensional resonators
    clamped–clamped beam analysis, 158–161
    natural frequencies, 162
    two-port resonator, 162–164
  two-dimensional resonators
    elastic strain energy, 164
    in-plane strain and stress components, 164
    piezoelectric strain energy, 165
    PMUT, 170–172
    round plates, 168–170
    square plates, 165–167
Frac-N phase locked loop (PLL), 335, 345
FRAM. *See* Ferroelectric random access memory (FRAM)
Frequency division duplex (FDD), 390
Frequency stability, 221
frequency–temperature plot (f——T) correlation, 244
Full width half maximum (FWHM), 285, 286

G

Gallium nitride (GaN), M/NEMS, 294, 295
  electromechanical resonators, 90
  high-*Q* MEMS resonators, 75
  IV–IV, III–V, and II–VI semiconductors, bandgaps of, 75–76
  oscillators, MMIC technology, 89–91
  passive piezoelectric transduction
    AlGaN/GaN HEMTs, 2DEG, 74–75, 80
    bottom and top electrodes, 77–78
    Lamb-mode resonators, 78–80
  physical resonant sensors
    AlGaN/GaN HEMTs, 2DEG, 88–89
    micromechanical resonators, 86, 90–92
    pH sensors, 89
    resonant temperature sensors, 88
    uncooled infrared (IR) sensing, 88
  piezoelectric coupling coefficient, 76–77
  piezoresistive transduction, 80–83
  resonant body transistors
    finite transduction efficiency, 83–84
    flexural, 85
    Lamb wave and thickness mode RBT, 85–87
    transistor sensing, 84–85
  resonator f.*Q* values, limits of, 79, 91–94
  silicon substrates, 74–75
Gauss's law, 261
Geographical-based rejection, 319, 320

H

HEMT. *See* High electron mobility transistors (HEMT)
Hermetic ceramic packages, 407
Heteroepitaxial nucleation, 287
Heterojunction acoustic charge transport (HACT), 73–74
High bulk acoustic wave resonators (HBARs), 105
High electron mobility transistors (HEMT), 294–296
High frequency oscillators
  acoustic devices
    resonator Q, 340–342
    time and frequency, 342
  battery voltage and DC-DC converter, 370, 371
  business timing, 372, 374, 375
  cellular timing devices, 375–377
  chip-scale packaged, 335, 336
  DCMO-ext and DCMO-SiP, 371, 372
  early prototypes
    AlN Lamb wave resonators, 349
    evaluation board, 349, 352
    leadless chip carriers, 349
    2-port Lamb wave resonator, 348–351
    tuning range, 349, 353–354
  EVM, 371, 373
  factor reduction, 378

FM and bluetooth, 336
GPS, 336
integrated MEMS resonator
functional blocks, 366
Intel transceiver IC, 368–370
SiP, 366, 369, 371
Xtal package, 367–368
LLQ, 379–381
local oscillator, 335
mobile devices, 338–340
overmolded package, 378–379
phase noise
acoustic flicker noise, 343, 344
Agilent E5052 signal source analyzer, 371, 373
bulk acoustic wave, 343
close-in phase noise, 345–346
equipment and setup, 346, 347
frac-N PLLs, 345
IEEE Std 1139-1999, 342
Leeson's equation, 342, 343
loaded and unloaded Q factor, 343
normalized phase noise, 343, 344
oscillator hacking, 344
26 MHz frequency output, 345
timing revolution, 379
timing, value of, 381
VC-TCXO (*see* Voltage controlled, temperature compensated oscillators (VC-TCXO))
WiFi, 336
High-resolution transmission electron microscopy (HR-TEM), 12
High-speed high electron mobility transistors (HEMTs)
bulk wave RBT, 85–87
conduction band bending, 74–75
fabrication process flow, 294–296
flexural RBT, 85
high-*Q* MEMS resonators, 75
piezoelectric transduction, 80
piezoresistive transduction, 80–83
resonator f.*Q* values, limits of, 79, 91–94
sensing mechanism, 88–89
High-temperature operation life (HTOL), 403
Hooke's law, 223–224

I
Inductively coupled plasma (ICP) RIE reactors
GaN resonator, 75
$LiNbO_3$ thin films, 112–117
PZT thin film, 46, 48
Inductively coupled plasma (ICP) system, 288
Infrared (IR) sensing, 88
Insertion loss (IL), 394–395
Integrated Device Technology (IDT). *See* Rejection methods
Interdigital transducers (IDTs), 85–87
Intermediate frequency (IF) filters, 388
Internet of Things (IoT), 175
Inverted mixing order (IMO) process, 42
Ion-sensitive field-effect transistor (ISFETs), 89

J
JEDEC standards, 304

K
"Known good die" approach, 409
Krylov subspace method, 264, 265

L
Large volume testing
ASIC dies, 312
manufacturing testing
analyses process flow, 325, 326
data file formats, 330
data processing and automation, 327–328
defect coding system, 325–326
device characterization, 313–314
hardware/software, 329
infantile mortality rate, 313
multi-site testing, 328–329
product reliability, 313
testing strategy, 314–315
test program optimization, 329
test setup, calibration, 327
thinking process, 314
user interface design, 326–327
plastic package, 311, 312
rejection methods
analyses process flow, 325, 326
electrical (*see* Electrical rejections)
visual, 321–325
Lateral-field-excitation (LFE), 189
Laterally vibrating piezoelectric MEMS resonators
AlN laterally vibrating resonator
advantages, 184, 186
AlN NPR technology, 194–197
graphene electrode, 190–191
k_t2 and *Q* values, AlN CLMRs, 188–190

Laterally vibrating piezoelectric MEMS resonators (*cont.*)
micro-acoustic resonators, RF PCM switches, 191–193
9.9 GHz AlN resonators, SEM of, 186–188
post-CMOS compatible 4-mask fabrication process, 186–187
electromechanical coupling coefficient and quality factor, 182–183
equivalent electrical circuit, 179–181
flexural beam resonators, FBARs and QCMs, 194
frequency scaling, criteria for, 185
GaN resonators, 184
$LiNbO_3$ thin film
asymmetrical mode (A0), 106, 110–111
electromechanical coupling and quality factor, 118–119
MBVD model of, 118, 120
S1 and A1 mode devices, 122
SAWs, AlN FBARs and CMRs, 123–125
SEM image of, 118
SH0 mode devices, 107, 109–110, 118, 119, 121–122
S0 mode devices, 106–109, 118–121
temperature compensation techniques, 125
LN thin film, 184, 186, 188
mechanical lumped elements, electrical equivalents for, 177–179
MEMS/NEMS resonant sensors, 193–194
micromachining techniques, 186–188
mock-up view of, 176
PZT thin-films, 184
semiconducting/insulating material, 183
thin-film piezoelectric film, 176, 183
wave equation, 176–177
Lateral overtone bulk acoustic wave resonators (LOBARs), 105
Leadless chip carriers (LCC), 349
Lead zirconate titanate (PZT) thin films, 3
actuator applications, 39
deposition
CSD, 40, 42–43
IMO process, 42
material properties, 44, 46
metal/conducting oxides, 41–42
MOCVD, 40, 42
parameters, 40
RF/ion-beam deposition, 40
silicon, 40–41
TiO2/Pt, 41
transverse piezoelectric stress constant, 44
2-MOE-based solution process, 42–43
XRD pattern, 44–45
Zr/Ti gradient, 44–45
device design concerns, 50–53
laterally vibrating piezoelectric resonators, 184
patterning techniques
actuators, single-etch and multiple-step etch process, 48–49
ECR/RF reactor, 46–48
ICP-RIE, 46, 48
ion milling, 49–50
singlemask layer etching process, 48–49
wet etching techniques, 46–47
resonator applications
acoustic filters, 61, 65
contour-mode resonators, center frequency tuning, 59, 61
DC-bias tunability, 58–60
electromechanical coupling, 55–56
FBAR PZT, series and parallel resonance frequencies of, 59, 62
figure of merit, 62–64, 66
flexure-mode resonators, 53
k_{33} dielectric constant and dielectric loss tangent, unipolar responses, 59, 60
length-extensional 2-pole and SAW filters, 56
limitations of, 62
mechanical quality factor *vs.* resonator center frequency, 57, 58
mechanical quality factor *vs.* year results obtained, 57, 58
out-of-plane flexural disc array resonator, 60, 62, 63
piezoelectric stress constant, unipolar response, 59, 61
PZT-on-single-crystal silicon resonator, 56–57, 59
representative published results for, 53, 54
resonator center frequency *vs.* year results obtained, 53, 55
10.8 MHz PZT-on-Si 2-pole IF filter, 60, 63, 64
two-port resonator, 58, 60
Leeson's equation, 342, 343
Length extensional (LE) mode, 244
Lithium niobate ($LiNbO_3$) thin films
benefits of, 100

bulk acoustic wave modes
asymmetrical mode (A0), 106, 110–111
high electromechanical coupling, 106
intrinsic electromechanical coupling, Alder's approach, 106–107
SH0 acoustic waves, 107, 109–110
symmetrical lateral (S0) mode, 106–109
high electromechanical coupling and quality factor, 99–100
historical development
crystal-ion-slicing technique, implantation process, 101–102
Czochralski technique, grown with, 100–101
electro-optic properties, 100
RF-MEM platform, 103
SAW devices, 100
$LiNbO_3$ LVRs
electromechanical coupling and quality factor, 118–119
MBVD model of, 118, 120
S1 and A1 mode devices, 122
SAWs, AlN FBARs and CMRs, 123–125
SEM image of, 118
SH0 mode devices, 118, 119, 121–122
S0 mode devices, 118–121
temperature compensation techniques, 125
material properties, 103–105
micromachining process
epitaxially grown thin films, 118
ion milling, 112, 114, 115
RIE, 113–116
RIE-ICP, 112–117
UV laser ablation, 112
wet etching techniques, 112
Local oscillator (LO), 338
Long-term evolution (LTE), 390–392, 404, 406, 412–413
Looks Like Quartz (LLQ) device, 379–381
Low-noise amplifier (LNA), 390

M
Magnetic transduction, 222
Mason model, 397, 411
Mason's equivalent circuit model
electromechanical coupling factor, 211–212
input admittance, 209
resonance and anti-resonance frequencies, 210
resonator structure, 209
standing wave pattern, 211
MBE. *See* Molecular beam epitaxy (MBE)
Metal-organic-chemical vapor deposition (MOCVD), 40, 42, 74, 78, 285, 286, 295
Metal organic phase vapor epitaxy (MOPVE), 8
Modified Butterworth-Van Dyke (MBVD) model, 118, 120
Molecular beam epitaxy (MBE), 74, 78, 285
Monolithic microwave integrated circuits (MMICs), GaN, 76–77
Lamb-mode resonators, 78–79
oscillators, 89–91
silicon substrate, 75

N
Newton's second law, 261
Nonlinear cancellation techniques, 406, 411

P
Passive compensation techniques
CBAR, 251, 252
material properties engineering
elastic constants, 248, 249
elastic modulus *E vs.* temperature, 248–250
frequency–temperature plot, 250
N-type dopants, P-type dopants, 251
Si doping level, 248, 251
resonator composition design
AlN-on-Si resonator, 247, 248
piezoelectric and substrate materials, 245
SiO_2 layers, 246–247
Perfectly-Matched-Layer (PML), 267
Phase-frequency discriminator (PFD), 355
Phononic crystals, 141
Piezoelectric micromachined ultrasonic transducer (PMUT), 170–172, 257
Piezoelectric transduction, 222
Piezoresistive transduction, 80–83, 222
Potassium hydroxide (KOH), 75
Power supply noise sensitivity, 306–307
Pressure cooker/autoclave test, 403
PZT thin films. *See* Lead zirconate titanate (PZT) thin films

Q
Quality assessment. *See* Reliability assessment
Quality factor (*Q*)
BVA quartz crystal resonators, 144
damped mass-spring system, 134

Quality factor (*Q*) (*cont.*)
definition, 133–134
electrical losses, 135
extrinsic losses, 135, 136
air/fluid damping, 141–142
ohmic loss, 142
support loss, 140–141
surface loss, 142
figure of merit, 148
fluctuation-dissipation theorem, 135
frequency response, 134–135
intrinsic loss, 135
acoustic attenuation coefficient, 143
dielectric loss, 136–137
phonon-electron interaction loss, 139–140
phonon-phonon interaction loss, 137–139
piezoelectric loss, 137
mechanical/elastic losses, 135
micro-fabricated thin-film piezoelectric resonators, 144
piezoelectric loss, 135
Quartz crystal microbalances (QCMs), 194
Quartz MEMS shear-mode resonators
asymmetric monolithic crystal filter, 239–241
BVD equivalent circuit model, 237–238
645 MHz oscillator
acceleration sensitivity, 238–240
encapsulated resonator, infrared image of, 238
phase noise response of, 238–239
thickness-shear mode
AT-cut crystals (*see AT*-cut quartz thickness-shear-mode (TSM) resonator)
fabrication process, 235–237
frequency dependence, plate dimensions, 229
piezoelectric stress/strain coefficients, 226–227
SC-cut crystals, 227–228, 231–232

R

RBT. *See* Resonant body transistors (RBT)
Reactive ion etching (RIE) system, 46–48, 288
Reactive magnetron sputter deposition, AlN thin films
c-axis-textured, piezoelectric thin films
film stress and piezoelectric coefficient $d_{33,f}$, 12–14
hardware and process, 9–10
polarity, 16–17
Pt substrate, TEM cross section of, 14, 16
sapphire substrate, TEM plan view image of, 14, 16
substrate self-bias voltage, orientation selection, 15–17
Thornton's growth zone model, 14–15
X-ray diffraction pattern, 12
ZrN deposition, 10–11
oxygen impurities and regrowth issue, 20–22
substrate roughness, impact of, 18–20
Real-time clock (RTC), 338
Rectangular shear-mode resonator, 236–237
Rejection methods
analyses process flow, 325, 326
electrical rejections
dynamic spec limits, 317–318
electrical signatures, 319–320
geographical-based rejection, 319, 320
resonance check, 315–316
resonance parameters, 321
spec limits, 316
yield limitation, 318–319
visual rejections
bond voids, 323–324
delaminated cap rejection, 322–323
delaminated metal pads, 324–325
edge die rejection, 324
efficiency and accuracy, 321
seal defect, 321–322
Reliability assessment
device cost, 310
device supply voltages and power, 309
FCP devices
evaluation, rules of, 301
implied specification, 302–303
longevity and critical applications, 300–301
frequency control products
EMI radiation, 309
long-term aging, 307–309
low-frequency wander, 307, 308
perturbations, 306
power supply noise sensitivity, 306–307
system-injected noise, 307
temperature change, 306
history, 299–300
IC and electromechanical device, 301–302
infant mortality testing, 304–305
in-process monitoring, 305
JEDEC standards, 304
MIL-C-3098x crystal specification, 305

production monitoring, 305
self-test, 310
US Military Standards, 303
Residual stress, 274
Resonance frequency, 244–245
Resonant body transistors (RBT)
finite transduction efficiency, 83–84
flexural, 85
Lamb wave and thickness mode RBT, 85–87
transistor sensing
equivalent circuit, 84–85
RGTs, 84
Resonant gate transistor (RGT), 84
RIE system. *See* Reactive ion etching (RIE) system
Ruggedness test, 403

S
SAWs. *See* Surface acoustic waves (SAWs)
Secondary ion mass spectrometer (SIMS), 49–50
Self-heating effects, 403, 405
Shear piezoelectric MEMS resonators
benefits of, 221
face-shear mode, 223
quartz crystal resonators
asymmetric monolithic crystal filter, 239–241
BVD equivalent circuit model, 237–238
frequency sources/oscillator, stability of, 238–240
TSM (*see* Thickness-shear-mode (TSM))
Silicon bulk acoustic resonators (SiBAR), 292, 293
Silicon dioxide (SiO_2) pillar matrix, 290, 291
Silicon-on-insulator (SOI), 290, 323
Smart sensor systems, 175
Solidly mounted resonator (SMR), 213, 214, 388
Spec limit rejection, 316
Surface acoustic waves (SAWs), 73–74, 100, 106, 388, 391
Surface-mount devices (SMD), 408
System-injected noise, 307
System in Package (SiP), 366, 369

T
Temperature coefficient of elasticity (TEC), 88
Temperature coefficient of frequency (TCF), 88, 208, 230–232, 244, 404–405
Temperature compensated crystal oscillator (TCXO), 338
Temperature sensitivity, 244–245
Thermal transduction, 222
Thermoelastic damping (TED), 138–139
Thermoelastic dissipation (TED), 269–271
Thickness-field-excitation (TFE), 189
Thickness-shear-mode (TSM)
BVD model, 233–235
AT-cut quartz crystal (*see AT*-cut quartz thickness-shear-mode (TSM) resonator)
fabrication process, quartz resonators, 235–237
frequency dependence, plate dimensions, 228–229
high Q and low impedance, 223
Hooke's law for non-piezoelectric material, 223–224
mechanical and electrical parameters, 232–233
MHz–GHz frequency range, 221
piezoelectric crystal, 223–224
piezoelectric effect, 223
piezoelectric stress/strain coefficients, 224–227
SC-cut quartz crystal
activity dips, 232
electromechanical coupling coefficient, 228
frequency variation *vs.* temperature, 231–232
higher thermal frequency stability, 228, 231
orientation angles, 227–228
piezoelectric coupling constant, 228
shearing displacement, 223
tensor and matrix notation, 225
Thornton's growth zone model, 14
3D electromagnetic (EM) simulations, 402, 410
Time division duplex (TDD), 390
Transduction technique, 221–222
2D electron gas (2DEG), 74–75, 295
Two-port resonators
cross section of, 162–163
equivalent circuitmodel, 162–164
two-port circular resonator, 162–163

U
User interface (UI) design, 326–327
U-shaped tuning beams, 253, 254
US Military Standards, 303

V
Verilog-A model, 360, 363
Vibration mode type, 222
Visual rejections
  bond voids, 323–324
  delaminated cap rejection, 322–323
  delaminated metal pads, 324–325
  edge die rejection, 324
  efficiency and accuracy, 321
  seal defect, 321–322
Voltage controlled, temperature compensated oscillators (VC-TCXO)
  chip-scale package replacement
    cellular grade, 354, 356
    discrete IC components and wirebonded, 349, 352
    eutectic bonding, 354
    fabrication process, 352, 355
    initial frequency, 354
    PFD, 355
    SOI wafer, 352
    stress control, 354
    voltage tuning capability, 355, 356
  125 MHz VC-TCXO
    analog circuit, 363, 365
    analog oscillator tuning, 363, 364
    CMOS capping, 360–362
    CSP MEMS oscillator, 365, 368
    4-port MEMS resonator, 358
    frequency error, 363–366
    Green's function, 358, 359
    phase-tunable oscillator, 356, 357
    silicon, 363
    start-up time, 365, 367
    stress sensitivity, 360
    test time and cost, 364–365
    Verilog-A model, 360, 363
  zero-IF cellular RF front-end, 336–337

W
Wafer-level package (WLP), 407, 408
Wurtzite structure
  "Berry's phase" method, 6
  lattice constants, 4
  N-and Al-polar films, 4–6
  nucleation, 6–7
  poisson ratio, 6
  thermal CVD technique, 7

X
Xenon difluoride (XeF_2), 75
X-ray diffraction (XRD)
  AlN thin films, 12, 31
  PZT thin film, 44–45

Y
Yield limit rejection, 318–319